CHECK

NIST GCR 01-808

Seismic Behavior of Partially-Grouted Masonry Shear Walls, Phase 2: Effectiveness of Bed-Joint Reinforcement

Arturo E. Schultz
Robert S. Hutchinson

Department of Civil Engineering
University of Minnesota
Minneapolis, Minnesota

February 2001

NIST

United states Department of Commerce
Technology Administration
National Institute of Standards and Technology

1901-2001
NIST CENTENNIAL

NIST GCR 01-808

Seismic Behavior of Partially-Grouted Masonry Shear Walls, Phase 2: Effectiveness of Bed-Joint Reinforcement

Prepared for
U.S. Department of Commerce
Structures Division
Building and Fire Research Laboratory
National Institute of Standards and Technology
Gaithersburg, MD 20899-8611

By
Arturo E. Schultz
Robert S. Hutchinson
Department of Civil Engineering
University of Minnesota
Minneapolis, Minnesota

February 2001

U.S. Department of Commerce
Donald L. Evans, *Secretary*
Technology Administration
Karen H. Brown, *Acting Under Secretary of Commerce for Technology*
National institute of Standards and Technology
Karen H. Brown, *Acting Director*

Structural Engineering Report No. ST-98-6

SEISMIC BEHAVIOR OF PARTIALLY-GROUTED MASONRY SHEAR WALLS: PHASE 2 - EFFECTIVENESS OF BED-JOINT REINFORCEMENT

by

Arturo E. Schultz and Robert S. Hutchinson

A report to the
NATIONAL INSTITUTE OF STANDARDS AND TECHNOLOGY
Building and Fire Research Laboratory
Research Contract No. USDOC/60NANB6D0121

Department of Civil Engineering
University of Minnesota
Minneapolis, Minnesota

December 1998
(revised December 1999)

ABSTRACT

A recently completed project on partially-grouted masonry shear walls is documented. This project forms part of an ongoing research program on masonry structures at the Building and Fire Research Laboratory of the National Institute of Standards and Technology (NIST). This report and project draw from and build upon previous work conducted at NIST, including a comprehensive literature review (Yancey et al., 1991), simulated seismic load tests of unreinforced masonry walls (Woodward and Rankin, 1983; 1984a; 1984b; 1985a; 1985b) and reinforced masonry walls (Yancey and Scribner, 1989), and numerical analyses employing empirical formulations (Fattal and Todd, 1991; Fattal, 1993a; Fattal, 1993c) and finite element models (Yancey). The previous NIST research culminates with a preliminary draft outlining a research program on partially-grouted masonry shear walls (Schultz, 1994; Fattal, 1993b). This program calls for simulated seismic load experiments of partially-grouted masonry walls, and numerical analyses, both empirical and finite element modeling of shear wall behavior.

The current research project on partially-grouted masonry shear walls addresses walls which have vertical reinforcement concentrated at a few locations, such as jambs, and only these cells are grouted. In the present project, all horizontal reinforcement is provided by welded wire grids that are placed in the bed joints of the masonry. The construction and testing of a series of six partially-grouted concrete masonry shear walls is described. The principal variables are height-to-length aspect ratio and horizontal reinforcement ratio.

Specimen configuration, test setup, instrumentation, and testing procedure, are presented, along with a detailed discussion of observed behavior of the partially-grouted shear walls and measured response to the cyclic loading histories. The discussion includes modes of response, global force-displacement characteristics, and local deformation response. An assessment of the shear resistance characteristics of the test specimens is also summarized. The shear resistance characteristics studied include initial stiffness, shear strength at first cracking, and shear strength at ultimate. In addition, a discussion on minimum horizontal reinforcement ratio for adequate seismic performance is also discussed.

Key Words: bed joints, building technology, cracking strength, cyclic load tests, horizontal reinforcement, masonry, partial grouting, seismic loading, shear strength, shear wall, stiffness, wire reinforcement

ACKNOWLEDGEMENTS

The research program described in this report was designed by the first author while he was employed at the NIST, and the shear wall tests were conducted by Gerry Cheok. The assistance and advice of the technical staff of the Structures Division (NIST), including Frank Rankin, Max Peltz and Erik Anderson, was essential to the successful completion of these tests. Analysis of the test data and preparation of the final report was made possible by the generous financial support of the NIST to the University of Minnesota. Special thanks go to NIST staff members Gerry Cheok and John Gross for their review of this report.

Special thanks go to the National Concrete Masonry Association, especially Mark Hogan (President), Robert Thomas (Director of Engineering and Research), and Larry Breeding (Senior Lab Technician). Their support included donation of the concrete block, construction of the masonry wall panels, and ample technical advice on the design and construction of masonry test specimens. This support is gratefully acknowledged. Special thanks also go to Hanns Baumann and the Baumann Research and Development Corporation (Newport Beach, CA) for donating the welded wire grids used as bed-joint reinforcement for the partially-grouted masonry shear walls.

TABLE OF CONTENTS

ABSTRACT ii
ACKNOWLEDGEMENTS iii
TABLE OF CONTENTS iv
LIST OF TABLES vii
LIST OF FIGURES xi
1. INTRODUCTION 1
1.1 Background 1
1.2 Literature Review 2
1.3 Scope and Objectives 6
1.4 Requirements for Horizontal Reinforcement 7
2. EXPERIMENTAL PROGRAM 10
2.1 General 10
2.2 Description of the Program 10
2.3 Specimen Designations 14
3. SPECIMEN DETAILS 15
3.1 Masonry Wall Panel Configuration 15
3.2 Vertical Reinforcement 16
3.3 Horizontal Reinforcement 16
3.4 Precast Concrete Header/Footer Beams 17
3.5 Fabrication Procedure 18
3.6 Material Tests 19
4. TESTING PROCEDURE 22
4.1 Test Setup 22
4.2 Loading History 22
4.3 Instrumentation 24
5. GENERAL BEHAVIOR OF SHEAR WALL SPECIMENS 25
5.1 Timelines 25
5.2 Crack Patterns 26
(a) Wall Specimen 2 27
(b) Wall Specimen 4 27
(c) Wall Specimen 6 28
(d) Wall Specimen 8 29
(e) Wall Specimen 10 29

(f) Wall Specimen 12 30
5.3 Mode of Response 31
(a) Long Walls (H/L=0.5) 31
(b) Intermediate Walls (H/L=0.7) 31
(c) Short Walls (H/L=1) 32
(d) Idealized Wall Behavior 32
6. FORCE-DISPLACEMENT RESPONSE TO CYCLIC LOADING 34
6.1 Lateral Displacements 34
6.2 Force-Displacement Response 37
6.3 Force-Displacement Envelopes 39
6.4 First Major Event (FME) 40
6.5 Initial Stiffnesses 42
6.6 Energy Dissipation Capacity 45
7. LOCAL RESPONSE TO CYCLIC LOADING 47
7.1 Vertical Reinforcement Strains 47
7.2 Horizontal Reinforcement Strains 50
7.3 Masonry Surface (LST) Strains 55
7.4 Gross (LVDT) Strains 58
7.5 Wall Displacements 60
8. ASSESSMENT OF SHEAR RESISTANCE CHARACTERISTICS 63
8.1 Initial Stiffness Estimates 64
8.2 Cracking Shear Strength 68
8.3 Average Shear Stress at Ultimate Conditions 72
8.4 Shear Strength Prediction 76
(a) Fattal 76
(b) Shing et al. 76
(c) UBC 78
(d) NEHRP Provisions 79
(e) Discussion 80
8.5 Minimum Horizontal Reinforcement Ratio 80
9. SUMMARY, CONCLUSIONS AND RECOMMENDATIONS 84
9.1 Summary 84
9.2 Observations and Conclusions 85
9.3 Recommendations for Future Research 87
10. REFERENCES 89

11. TABLES 93
12. FIGURES 246
APPENDIX. SHEAR WALL SPECIMEN 14 368
A.1 Introduction 368
A.2 Welded Wire Confining Reinforcement Grids 369
A.3 Fabrication and Testing of Wall Specimen 14 369
A.4 Force-Displacement Response 370
A.5 Global Behavior 372
A.6 Local Response 373
A.7 Shear Strength Calculations 374
A.8 Concluding Remarks 375

LIST OF TABLES

Table 2.1 Experimental Priorities in Masonry Research Plan 93
Table 2.2 Schedule of Nominal Properties for Specimens in Priority I 94
Table 2.3 Estimated Minimum Horizontal Reinforcement Ratios for Phase 2 Specimens . . 95
Table 3.1 Dimensions of Concrete Masonry Units 96
Table 3.2 Mix Designs by Weight for Masonry Materials
(a) Masonry Mortar 98
(b) Masonry Grout 99
Table 3.3 Summary of Compression Strengths of Masonry Materials
(a) At Various Ages 100
(b) Companion Specimen Tests. 101
Table 3.4 Material Test Specimen Schedule 102
Table 3.5 Masonry Prism Tests
(a) 28-Day Moist-Cured Specimens 103
(b) Companion Air-Cured Specimens 104
Table 3.6 Masonry Mortar Cube Tests
(a) 28-Day Tests of Moist-Cured Masonry Mortar 105
(b) Tests of Air-Cured Masonry Mortar at Various Ages 106
(c) 7-Day Tests of Moist-Cured Header Beam Mortar 107
(d) 7-Day Tests of Moist-Cured Footer Beam Mortar 108
(e) 28-Day Tests of Moist-Cured Header Beam Mortar 109
(f) 28-Day Tests of Moist-Cured Footer Beam Mortar. 110
Table 3.7 Masonry Grout Specimen Tests
(a) 28-Day Tests of Moist-Cured Specimens 111
(b) Tests of Air-Cured Specimens at Various Ages 112
Table 3.8 Cube Tests of Anchorage Plug Grout
(a) 7-Day Tests of Moist-Cured Header Beam Grout. 113
(b) 7-Day Tests of Moist-Cured Footer Beam Grout 114
(c) 28-Day Tests of Moist-Cured Header Beam Grout 115
(d) 28-Day Tests of Moist-Cured Footer Beam Grout 116
Table 3.9 Concrete Masonry Unit Tests 117
Table 3.10 Tension Test Results for Vertical Reinforcing Bars 118
Table 3.11 Tension Test Results for Longitudinal Wires in Horizontal Reinforcing Grids . 119
Table 4.1 Vertical (Axial) Load Variation During Tests 120
Table 4.2 Location of LST Transducers 121
Table 5.1 Timeline for Test of Wall Specimen 2 122
Table 5.2 Timeline for Test of Wall Specimen 4 132
Table 5.3 Timeline for Test of Wall Specimen 6 142
Table 5.4 Timeline for Test of Wall Specimen 8 151
Table 5.5 Timeline for Test of Wall Specimen 10 161
Table 5.6 Timeline for Test of Wall Specimen 12 170
Table 6.1.1 Positive Peak Lateral Displacement During the Simulated Seismic Drift Tests . 180
Table 6.1.2 Negative Peak Lateral Displacement During the Simulated Seismic Drift Tests. 181
Table 6.1.3 Average Peak Lateral Displacement During the Simulated Seismic Drift Tests . 182
Table 6.2.1 Positive Peak Shear Force During the Simulated Seismic Drift Tests 183
Table 6.2.2 Negative Peak Shear Force During the Simulated Seismic Drift Tests 184

Table 6.2.3 Average Peak Shear Force During the Simulated Seismic Drift Tests 185
Table 6.3.1 Deformation Capacities 186
Table 6.4.1 Shear Force and In-Plane Lateral Displacement at First Visible Cracking 187
Table 6.4.2 Shear Force and In-Plane Lateral Displacement at Proportional Limit 188
Table 6.4.3 Shear Force and In-Plane Lateral Displacement at Stiffness Change 189
Table 6.5.1 Initial Stiffnesses Inferred from Experimental Data 190
Table 6.6.1 Energy Dissipation Indices 191
Table 7.1.1 Summary of Vertical Reinforcement Strains for Wall Specimen 2 192
Table 7.1.2 Summary of Vertical Reinforcement Strains for Wall Specimen 4 193
Table 7.1.3 Summary of Vertical Reinforcement Strains for Wall Specimen 6 194
Table 7.1.4 Summary of Vertical Reinforcement Strains for Wall Specimen 8 195
Table 7.1.5 Summary of Vertical Reinforcement Strains for Wall Specimen 10 196
Table 7.1.6 Summary of Vertical Reinforcement Strains for Wall Specimen 12 197
Table 7.2.1 Summary of Horizontal Reinforcement Strains for Wall Specimen 2 198
Table 7.2.2 Summary of Horizontal Reinforcement Strains for Wall Specimen 4 199
Table 7.2.3 Summary of Horizontal Reinforcement Strains for Wall Specimen 6 200
Table 7.2.4 Summary of Horizontal Reinforcement Strains for Wall Specimen 8 201
Table 7.2.5 Summary of Horizontal Reinforcement Strains for Wall Specimen 10 202
Table 7.2.6 Summary of Horizontal Reinforcement Strains for Wall Specimen 12 203
Table 7.2.7 Composite Drift Indices For Horizontal Reinforcement Strains 204
Table 7.3.1 Summary of Masonry Surface (LST) Strains in Wall Specimen 2 205
Table 7.3.2 Summary of Masonry Surface (LST) Strains in Wall Specimen 4 206
Table 7.3.3 Summary of Masonry Surface (LST) Strains in Wall Specimen 6 207
Table 7.3.4 Summary of Masonry Surface (LST) Strains in Wall Specimen 8 208
Table 7.3.5 Summary of Masonry Surface (LST) Strains in Wall Specimen 10 209
Table 7.3.6 Summary of Masonry Surface (LST) Strains in Wall Specimen 12 210
Table 7.3.7 Composite Drift Indices for Masonry Surface Strains at Tension Threshold .. 211
Table 7.4.1 Summary of Gross (LVDT) Strains in Wall Specimen 2 212
Table 7.4.2 Summary of Gross (LVDT) Strains in Wall Specimen 4 213
Table 7.4.3 Summary of Gross (LVDT) Strains in Wall Specimen 6 214
Table 7.4.4 Summary of Gross (LVDT) Strains in Wall Specimen 8 215
Table 7.4.5 Summary of Gross (LVDT) Strains in Wall Specimen 10 216
Table 7.4.6 Summary of Gross (LVDT) Strains in Wall Specimen 12 217
Table 7.5.1 Wall Displacement Profiles (LVDT) for Wall Specimen 2 218
Table 7.5.2 Wall Displacement Profiles (LVDT) for Wall Specimen 4 219
Table 7.5.3 Wall Displacement Profiles (LVDT) for Wall Specimen 6 220
Table 7.5.4 Wall Displacement Profiles (LVDT) for Wall Specimen 8 221
Table 7.5.5 Wall Displacement Profiles (LVDT) for Wall Specimen 10 222
Table 7.5.6 Wall Displacement Profiles (LVDT) for Wall Specimen 12 223
Table 7.5.7 Linear Correlation of Displacements for Wall Specimens 224
Table 8.1 Initial Stiffness Estimates 225
Table 8.2.1 Cracking Shear Strength from Shing's Formula 226
Table 8.2.2 Cracking Shear Strength from Proposed Formula 227
Table 8.3.1 Average Net and Gross Area Shear Stresses
(a) Series 1 228
(b) Series 2 229
Table 8.3.2 Material Properties for Shear Strength Estimates 230

Table 8.3.3 Calculated Average Ultimate (Gross Area) Shear Stresses Nominal Properties and Original Matsumura-Fattal Formula
(a) Series 1 . . . 231
(b) Series 2 . . . 232
Table 8.3.4 Calculated Average Ultimate (Gross Area) Shear Stresses for Actual Properties and Original Matsumura-Fattal Formula
(a) Series 1 . . . 233
(b) Series 2 . . . 234
Table 8.3.5 Calculated Average Ultimate (Gross Area) Shear Stresses Using Actual Properties and Modified Matsumura-Fattal Formula
(a) Series 1 . . . 235
(b) Series 2 . . . 236
Table 8.4.1 Calculated Shear Strength at Ultimate Using Actual Properties and Modified Matsumura-Fattal Formula
(a) Series 1 . . . 237
(b) Series 2 . . . 238
Table 8.4.2 Calculated Shear Strength at Ultimate Using Actual Properties and NEHRP Formula
(a) Series 1 . . . 239
(b) Series 2 . . . 240
Table 8.4.3 Calculated Shear Strength at Ultimate Using Actual Properties and UBC Formula
(a) Series 1 . . . 241
(b) Series 2 . . . 242
Table 8.4.4 Calculated Shear Strength at Ultimate Using Actual Properties and Shing's Formula
(a) Series 1 . . . 243
(b) Series 2 . . . 244
Table 8.5 Updated Minimum Horizontal Reinforcement Ratios for Phase 2 Specimens . 245

Table A.1 Masonry Material Compression Tests
(a) Masonry and Mortar . . . 378
(b) Grout . . . 379
Table A.2 Tension Test Results for Horizontal Reinforcing Grids in Wall Specimen 14 . 380
Table A.3 Location of LST Transducers for Wall Specimen 14 . . . 381
Table A.4 Timeline for Test of Wall Specimen 14 . . . 382
Table A.5 Peak Lateral Displacements for Wall Specimen 14 . . . 392
Table A.6 Peak Shear Forces for Wall Specimen 14 . . . 393
Table A.7 Deformation Capacity for Wall Specimen 14 . . . 394
Table A.8 Shear Force and Lateral Displacement at First Major Event for Wall Specimen 14 . . . 395
Table A.9 Initial Stiffnesses Inferred from Experimental Data for Wall Specimen 14 . . . 396
Table A.10 Energy Dissipation Indices for Wall Specimen 14 . . . 397
Table A.11 Summary of Vertical Reinforcement Strains for Wall Specimen 14 . . . 398
Table A.12 Summary of Horizontal Reinforcement Strains[1] for Wall Specimen 14 . . . 399
Table A.13 Composite Drift Indices for Horizontal Reinforcement Strains in Wall Specimen 14 . . . 400

Table A.14 Summary of Masonry Surface (LST) Strains in Wall Specimen 14 401
Table A.15 Composite Drift Indices for Masonry Surface (LST) Strains in Wall Specimen 14 402
Table A.16 Summary of Gross (LVDT) Strains in Wall Specimen 14 403
Table A.17 Wall Displacement Profiles (LVDT) for Wall Specimen 14 404
Table A.18 Average Ultimate (Gross Area) Shear Stresses for Wall Specimen 14 405
Table A.19 Calculated and Measured Shear Strengths at Ultimate for Shear Wall 14 406

LIST OF FIGURES

Fig. 3.1 Masonry Wall Panel Configurations 246
Fig. 3.2 Test Specimen Configuration 247
Fig. 3.3 Welded Wire Grid Configuration 248
Fig. 3.4 Precast Concrete Header/Footer Beams 249
Fig. 3.5 Precast Concrete Header/Footer Beam Sections 250
Fig. 4.1 Test Setup 251
Fig. 4.2 In-Plane Displacement History 252
Fig. 4.3 Vertical Load Variation for Shear Wall No. 8 253
Fig. 4.4 Location and Designation of LVDT Transducers 254
Fig. 4.5 Location and Designation of LST Transducers 255
Fig. 4.6 Location and Designation of Strain Gages on Vertical Reinforcement 256
Fig. 4.7 Location and Designation of Strain Gages on Horizontal Reinforcement 257
Fig. 5.1 Photograph of Wall Specimen 2 at End of Test 258
Fig. 5.2 Photograph of Wall Specimen 4 at End of Test 258
Fig. 5.3 Photograph of Wall Specimen 6 at End of Test 259
Fig. 5.4 Photograph of Wall Specimen 8 at End of Test 259
Fig. 5.5 Photograph of Wall Specimen 10 at End of Test 260
Fig. 5.6 Photograph of Wall Specimen 12 at End of Test 260
Fig. 5.7 Final Crack Pattern for South Face of Wall Specimen 2 261
Fig. 5.8 Final Crack Pattern for South Face of Wall Specimen 4 261
Fig. 5.9 Final Crack Pattern for South Face of Wall Specimen 6 262
Fig. 5.10 Final Crack Pattern for South Face of Wall Specimen 8 262
Fig. 5.11 Final Crack Pattern for South Face of Wall Specimen 10 263
Fig. 5.12 Final Crack Pattern for South Face of Wall Specimen 12 263
Fig. 6.1.1 In-Plane Lateral Displacement History for Wall Specimen 2 264
Fig. 6.1.2 In-Plane Lateral Displacement History for Wall Specimen 4 264
Fig. 6.1.3 In-Plane Lateral Displacement History for Wall Specimen 6 265
Fig. 6.1.4 In-Plane Lateral Displacement History for Wall Specimen 8 265
Fig. 6.1.5 In-Plane Lateral Displacement History for Wall Specimen 10 266
Fig. 6.1.6 In-Plane Lateral Displacement History for Wall Specimen 12 266
Fig. 6.2.1 Shear Force History for Wall Specimen 2 267
Fig. 6.2.2 Shear Force History for Wall Specimen 4 267
Fig. 6.2.3 Shear Force History for Wall Specimen 6 268
Fig. 6.2.4 Shear Force History for Wall Specimen 8 268
Fig. 6.2.5 Shear Force History for Wall Specimen 10 269
Fig. 6.2.6 Shear Force History for Wall Specimen 12 269
Fig. 6.2.7 Force-Displacement Relations for Wall Specimen 2 270
Fig. 6.2.8 Force-Displacement Relations for Wall Specimen 4 271
Fig. 6.2.9 Force-Displacement Relations for Wall Specimen 6 272
Fig. 6.2.10 Force-Displacement Relations for Wall Specimen 8 273
Fig. 6.2.11 Force-Displacement Relations for Wall Specimen 10 274
Fig. 6.2.12 Force-Displacement Relations for Wall Specimen 12 275
Fig. 6.2.13 Shear Force Capacity vs. Aspect Ratio 276
Fig. 6.2.14 Shear Force Capacity vs. Horizontal Reinforcement Ratio 276
Fig. 6.3.1 Force-Displacement Envelopes for Walls with $\rho_h = 0.056\%$ 277

Fig. 6.3.2 Force-Displacement Envelopes for Walls with $\rho_h = 0.11\%$ 277
Fig. 6.3.3 Force-Displacement Envelopes for Walls with $H/L = 0.5$ 278
Fig. 6.3.4 Force-Displacement Envelopes for Walls with $H/L = 0.7$ 278
Fig. 6.3.5 Force-Displacement Envelopes for Walls with $H/L = 1.0$ 279
Fig. 6.3.6 Deformation Capacity vs. Aspect Ratio 280
Fig. 6.3.7 Deformation Capacity vs. Horizontal Reinforcement Ratio 280
Fig. 6.4.1 Lateral Stiffness Envelope for Wall Specimen No. 2 281
Fig. 6.4.2 Lateral Stiffness Envelope for Wall Specimen No. 4 281
Fig. 6.4.3 Lateral Stiffness Envelope for Wall Specimen No. 6 282
Fig. 6.4.4 Lateral Stiffness Envelope for Wall Specimen No. 8 282
Fig. 6.4.5 Lateral Stiffness Envelope for Wall Specimen No. 10 283
Fig. 6.4.6 Lateral Stiffness Envelope for Wall Specimen No. 12 283
Fig. 6.4.7 Average Shear Force at First Cracking vs. Aspect Ratio 284
Fig. 6.4.8 Average Shear Force at First Cracking vs. Reinforcement Ratio 284
Fig. 6.5.1 Initial Stiffnesses vs. Aspect Ratio 285
Fig. 6.5.2 Initial Stiffnesses vs. Horizontal Reinforcement Ratio 285
Fig. 6.6.1 Energy Dissipation for Walls with $\rho_h = 0.056\%$. 286
Fig. 6.6.2 Energy Dissipation for Walls with $\rho_h = 0.11\%$. 286
Fig. 6.6.3 Energy Dissipation for Walls with $H/L = 0.5$ 287
Fig. 6.6.4 Energy Dissipation for Walls with $H/L = 0.7$ 287
Fig. 6.6.5 Energy Dissipation for Walls with $H/L = 1.0$ 288
Fig. 7.1.1 Strains in Vertical Rebars vs. Lateral Drift in Wall Specimen 2 289
Fig. 7.1.2 Strains in Vertical Rebars vs. Lateral Drift in Wall Specimen 4 290
Fig. 7.1.3 Strains in Vertical Rebars vs. Lateral Drift in Wall Specimen 6 291
Fig. 7.1.4 Strains in Vertical Rebars vs. Lateral Drift in Wall Specimen 8 292
Fig. 7.1.5 Strains in Vertical Rebars vs. Lateral Drift in Wall Specimen 10 293
Fig. 7.1.6 Strains in Vertical Rebars vs. Lateral Drift in Wall Specimen 12 294
Fig. 7.2.1 Strains in Horizontal Grids vs. Lateral Drift in Wall Specimen 2 295
Fig. 7.2.2 Strains in Horizontal Grids vs. Lateral Drift in Wall Specimen 4 297
Fig. 7.2.3 Strains in Horizontal Grids vs. Lateral Drift in Wall Specimen 6 299
Fig. 7.2.4 Strains in Horizontal Grids vs. Lateral Drift in Wall Specimen 8 301
Fig. 7.2.5 Strains in Horizontal Grids vs. Lateral Drift in Wall Specimen 10 303
Fig. 7.2.6 Strains in Horizontal Grids vs. Lateral Drift in Wall Specimen 12 305
Fig. 7.2.7 Drift Ratios at Target Horizontal Reinforcement Strains for Wall Specimen 2 307
Fig. 7.2.8 Drift Ratios at Target Horizontal Reinforcement Strains for Wall Specimen 4 308
Fig. 7.2.9 Drift Ratios at Target Horizontal Reinforcement Strains for Wall Specimen 6 309
Fig. 7.2.10 Drift Ratios at Target Horizontal Reinforcement Strains for Wall Specimen 8 310
Fig. 7.2.11 Drift Ratios at Target Horizontal Reinforcement Strains for Wall Specimen 10 311
Fig. 7.2.12 Drift Ratios at Target Horizontal Reinforcement Strains for Wall Specimen 12 312
Fig. 7.2.13 Influence of Aspect Ratio on Net Composite Drift Indices for Horizontal Reinforcement Strains 313

Fig. 7.2.14 Influence of Reinforcement Ratio on Net Composite Drift Indices for Horizontal Reinforcement Strains 314
Fig. 7.3.1 Masonry Surface Strains vs. Lateral Drift in Wall Specimen 2. 315
Fig. 7.3.2 Masonry Surface Strains vs. Lateral Drift in Wall Specimen 4. 317
Fig. 7.3.3 Masonry Surface Strains vs. Lateral Drift in Wall Specimen 6. 319
Fig. 7.3.4 Masonry Surface Strains vs. Lateral Drift in Wall Specimen 8. 321
Fig. 7.3.5 Masonry Surface Strains vs. Lateral Drift in Wall Specimen 10 323
Fig. 7.3.6 Masonry Surface Strains vs. Lateral Drift in Wall Specimen 12 325
Fig. 7.3.7 Masonry Surface Tension Strain Response (LST) for Wall Specimen 2 327
Fig. 7.3.8 Masonry Surface Tension Strain Response (LST) for Wall Specimen 4 328
Fig. 7.3.9 Masonry Surface Tension Strain Response (LST) for Wall Specimen 6 329
Fig. 7.3.10 Masonry Surface Tension Strain Response (LST) for Wall Specimen 8 330
Fig. 7.3.11 Masonry Surface Tension Strain Response (LST) for Wall Specimen 10 331
Fig. 7.3.12 Masonry Surface Tension Strain Response (LST) for Wall Specimen 12 332
Fig. 7.3.13 Influence of Aspect Ratio on Net Composite Drift Indices for Masonry Surface Strains 333
Fig. 7.3.14 Influence of Reinforcement Ratio on Net Composite Drift Indices for Masonry Surface Strains 334
Fig. 7.4.1 Gross (LVDT) Strains vs. Lateral Drift in Wall Specimen 2 335
Fig. 7.4.2 Gross (LVDT) Strains vs. Lateral Drift in Wall Specimen 4 337
Fig. 7.4.3 Gross (LVDT) Strains vs. Lateral Drift in Wall Specimen 6 339
Fig. 7.4.4 Gross (LVDT) Strains vs. Lateral Drift in Wall Specimen 8 341
Fig. 7.4.5 Gross (LVDT) Strains vs. Lateral Drift in Wall Specimen 10 343
Fig. 7.4.6 Gross (LVDT) Strains vs. Lateral Drift in Wall Specimen 12 345
Fig. 7.5.1 Displaced Profiles for Wall Specimen 2. 347
Fig. 7.5.2 Displaced Profiles for Wall Specimen 4. 347
Fig. 7.5.3 Displaced Profiles for Wall Specimen 6. 348
Fig. 7.5.4 Displaced Profiles for Wall Specimen 8. 348
Fig. 7.5.5 Displaced Profiles for Wall Specimen 10. 349
Fig. 7.5.6 Displaced Profiles for Wall Specimen 12. 349
Fig. 7.5.7 Masonry Sliding Response in Wall Specimen 10 350
Fig. 7.5.8 Masonry Sliding Response in Wall Specimen 12 351
Fig. 7.5.9 Correlation Between TTF and External Displacements for Wall Specimen 2 . . 352
Fig. 7.5.10 Correlation Between TTF and External Displacements for Wall Specimen 4 . . 352
Fig. 7.5.11 Correlation Between TTF and External Displacements for Wall Specimen 6 . . 353
Fig. 7.5.12 Correlation Between TTF and External Displacements for Wall Specimen 8 . . 353
Fig. 7.5.13 Correlation Between TTF and External Displacements for Wall Specimen 10 . 354
Fig. 7.5.14 Correlation Between TTF and External Displacements for Wall Specimen 12 . 354
Fig. 8.1 Shear and Flexural Deformations in Elastic Shear Walls 355
Fig. 8.2 Shear Resistance Mechanisms at First Cracking 356
Fig. 8.3.1 Dependance of Net Area Shear Stresses at Ultimate on Aspect Ratio 357
Fig. 8.3.2 Dependance of Net Area Shear Stresses at Ultimate on Reinforcement Ratio. . . 358
Fig. 8.3.3 Dependance of Gross Area Shear Stresses at Ultimate on Aspect Ratio 359
Fig. 8.3.4 Dependance of Gross Area Shear Stresses at Ultimate on Reinforcement Ratio . 360
Fig. 8.3.5 Calculated Gross Area Shear Stresses at Ultimate 361
Fig. 8.4.1 Calculated Shear Strengths at Ultimate. 362

Fig. 8.4.2 Calculated Shear Strengths vs. Aspect Ratio for Lightly-Reinforced Specimens 363
Fig. 8.4.3 Calculated Shear Strengths vs. Aspect Ratio for Heavily-Reinforced Specimens 364
Fig. 8.4.4 Calculated Shear Strengths vs. Reinforcement Ratio for Stocky Specimens . . . 365
Fig. 8.4.5 Calculated Shear Strengths vs. Reinforcement Ratio for Intermediate Specimens 366
Fig. 8.4.6 Calculated Shear Strengths vs. Reinforcement Ratio for Slender Specimens. . . 367

Fig. A.1 Welded Wire Grid Configuration for Wall Specimen 14 407
Fig. A.2 Final Crack Pattern for South Face of Wall Specimen 14 408
Fig. A.3 In-Plane Lateral Displacement History for Wall Specimen 14 409
Fig. A.4 Shear Force History for Wall Specimen 14 409
Fig. A.5 Force-Displacement Relations for Wall Specimen 14 410
Fig. A.6 Force-Displacement Envelopes for Wall Specimen 14 411
Fig. A.7 Lateral Stiffness Envelope for Wall Specimen 14 411
Fig. A.8 Energy Dissipation for Wall Specimen 14 412
Fig. A.9 Strains in Vertical Bars vs. Drift in Wall Specimen 14 413
Fig. A.10 Strains in Horizontal Grids vs. Drift in Wall Specimen 14 414
Fig. A.11 Drift Ratios at Target Horizontal Reinforcement Strains for Wall Specimen 14. . 416
Fig. A.12 Masonry Surface Strains vs. Drift in Wall Specimen 14 417
Fig. A.13 Masonry Surface Tension Strain Response (LST) for Wall Specimen 14 419
Fig. A.14 Gross (LVDT) Strains vs. Drift in Wall Specimen 14 420
Fig. A.15 Displaced Profiles for Wall Specimen 14 422
Fig. A.16 Masonry Sliding Response in Wall Specimen 14 423
Fig. A.17 Correlation Between TTF and External Displacements for Wall Specimen 14 . . 424

1. INTRODUCTION

1.1 Background

Since 1993, the Building and Fire Research Laboratory (BFRL) at the National Institute of Standards and Technology (NIST) has been studying the seismic performance of partially-grouted masonry (PGM) shear walls as part of the NIST research program on the seismic design of masonry walls. This effort is part of the U.S. National Earthquake Hazard Reduction Program (NEHRP), and it culminates a 15 year long program with previous thrusts that have focused on the resistance characteristics of unreinforced concrete block walls, including the influence of cyclic loading (Woodward and Rankin, 1983), vertical compression stress (Woodward and Rankin, 1984a), wall aspect ratio (Woodward and Rankin, 1985b), strengths of block and mortar (Woodward and Rankin, 1985a), and horizontal reinforcement without vertical steel (Yancey and Scribner, 1989). In addition, other studies have addressed finite element methods for modeling shear wall response to cyclic lateral loads (Yancey; Chang and Love, 1998; Shing and Cao, 1997) and development of empirical shear strength equations (Fattal, 1993a; 1993c; Fattal and Todd, 1991).

Following its longstanding commitment to assist the construction industry through the development of design codes and standards, the BFRL hosted the Council for Masonry Research (CMR) in a workshop to seek guidance on how NIST can best serve the masonry industry (Fattal, 1993b). The concerns that were voiced most prominently in the workshop were related to construction costs, and total costs in masonry construction are more seriously impacted by labor than any other factor. Fully-grouted and reinforced masonry construction, as used presently in regions of high seismic risk of the U.S., is much more labor-intensive than other types of masonry construction, yet, the degree of seismic resistance it affords may not be necessary for regions of moderate seismicity if a less labor-intensive alternative can be identified. Among the potential alternatives discussed during the workshop, the CMR strongly recommended that NIST investigate the seismic behavior of partially-grouted masonry walls.

Partially-grouted masonry is defined as construction using hollow units in which only those vertical and horizontal cells that contain reinforcement are grouted. To further limit the amount

of grouting, vertical reinforcement can be concentrated in fewer cells, particularly along the jambs of wall panels. A second issue of high priority that was identified by the Council for Masonry Research in the NIST workshop (Fattal, 1993b) is the replacement of horizontal reinforcement in bond beams with bed joint reinforcement in the form of welded wire grids. This practice promises to reduce the labor costs associated with forming and grouting bond beams, as well as accelerate the erection of masonry walls. Yet, the seismic performance of partially-grouted masonry has not been studied in a systematic manner, so seismic design procedures for this construction form simply do not exist.

1.2 Literature Review

An extensive literature review conducted by NIST researchers on masonry shear wall tests (Yancey et al., 1991) serves as the backdrop for current research activities at NIST on the seismic resistance of partially-grouted masonry construction. However, there are several noteworthy papers, some which summarize the observed seismic performance of a similar type of construction, while others describe simulated seismic load tests of masonry shear walls which are reinforced horizontally with ladder-type wire grids in the bed joints. The observations and conclusions in these studies have an influence on the overall direction and selection of the amount and type of horizontal reinforcement for the shear walls to be tested in the NIST Masonry Research Program.

The concept of partially-grouted masonry for lateral load resistance is not without precedent, as it shares similarities with a popular type of masonry construction in Latin America and elsewhere which is known as confined masonry (Casabbone, 1994). Confined masonry comprises unreinforced masonry walls, usually made using clay masonry units, which are erected between vertical gaps that serve to cast tie columns after all masonry has been placed. Tie beams are placed at regular vertical spacings with at least one tie beam at each floor. Thus, a "confinement" frame of lightly-reinforced tie columns and tie beams is cast after the masonry mortar has hardened. Shrinkage of the concrete frame serves to confine the unreinforced masonry panel, as well as to provide structural redundancy and more uniform distribution of lateral forces to the masonry. This system has been reasonably successful throughout Latin America in mitigating seismic damage to low-rise masonry structures (Schultz, 1994).

Hidalgo and Luders (1987) tested 29 reinforced masonry shear wall specimens, made using either concrete block or hollow clay units, under cyclic lateral load histories and constant vertical load. Some of the specimens were partially-grouted, and some of these were reinforced horizontally with welded wire grids, while others utilized hot-rolled, deformed reinforcing bars in grouted bond beams. Horizontal reinforcement ratios varied from 0 to 0.12% of gross vertical area. Hidalgo and Luders noted that not all of the bed-joint horizontal reinforcement was able to participate in the resistance to lateral loads. Brittle fracture of the longitudinal wires at the welded intersections was observed in those bars that attracted load first, even though other longitudinal bars had not reached nominal capacity.

In an earlier paper on the same experimental study, Luders and Hidalgo (1986) report the results of the first 17 shear wall tests. Based on experimental observations, they observed that the effectiveness of bed-joint reinforcement, when used as shear reinforcement for masonry shear walls, is lower than that of deformed bars in grouted bond beams. They concluded that the contribution of bed-joint reinforcement to peak shear strength is less than the force calculated at nominal yield. Luders and Hidalgo recommended the use of welded bed joint reinforcement for masonry shear walls, but at a lower efficiency ratio than hot-rolled reinforcing bar. They observed masonry shear wall strength to be linearly proportional to the total cross-sectional area of wire reinforcing grids, but, for equal amounts of horizontal reinforcement, this reinforcement enhanced shear wall strength by only 55% of the increase provided by hot-rolled reinforcing bars.

Sanchez et al. (1992) report the results of three cyclic load tests of confined masonry shear walls. This research was meant to address mid-rise structures (4 to 10 stories), for which inclined cracking of the confined masonry panels have been observed during strong ground shaking. Horizontal reinforcement was placed in the bed joints of the masonry panels to mitigate this observed mode of damage. Of the three specimens, one had no horizontal reinforcement, while the other two had either bed joint reinforcement, in the form of wire grids, or cold-drawn corrugated wire reinforcement embedded in the bed joints. Sufficient horizontal steel was used to provide horizontal reinforcement ratios of approximately 0.11% in the last two specimens. Both specimens with horizontal reinforcement exhibited approximately twice the deformation capacity as did the specimen with no horizontal reinforcement.

However, the specimen with cold-drawn wire demonstrated 50% more lateral load capacity than did the wire grid specimen, even though both specimens had the same amount of horizontal steel. It was also observed that the wire reinforcing grids failed in a brittle manner at the welded intersections, whereas the cold-drawn wire displayed a "necked down" region at the fracture points. Sanchez surmises that brittle rupture of the wire reinforcing grids prevented widespread development of horizontal steel strength, resulting in the reduced shear strength of the masonry panels, thus confirming the conclusions set forth by Hidalgo and Luders (1987). Yet, tension tests of the horizontal reinforcement indicated approximately the same elongation in both the cold-drawn wire and the welded wire grids.

Shing and Noland (1992) reported on reinforced masonry shear wall tests designed to illustrate the behavior of welded wire grids as bed-joint reinforcement, as well as to investigate the influence of heat treatment of the girds. Two specimens were built with a horizontal reinforcement ratio equal to 0.07%, but one was reinforced with heat-treated wire grids, and the other utilized untreated grids. Both reinforcements were supplied by the same manufacturer, and the shear wall specimens were nearly identical to another specimen tested by Shing et al. (1989; 1990a; 1990b) as part of the TCCMAR program. Horizontal reinforcement in the TCCMAR specimen, comprising hot-rolled deformed bars in fully-grouted bond beams, provided a reinforcement ratio equal to 0.14%. The yield strength of the rebar was lower than that of the both types of grids, so, the difference in horizontal steel forces at nominal yield is not as large as the horizontal reinforcement ratios suggest. Observed global behavior, including cracking and ultimate shear strengths, deformation capacity, and hysteretic characteristics, was nearly identical for all three specimens. Shing and Noland concluded that, in addition to ductile reinforcement, ductile behavior in shear-critical walls requires some minimum amount of horizontal reinforcement. They do not elaborate on the minimum horizontal reinforcement concept, but, they suggested that it may be difficult for commonly-available wire grids to provide the necessary amount of horizontal reinforcement for ductile behavior. However, Shing and Noland supported the notion that welded bed-joint reinforcement could be used to supplement horizontal steel in grouted bond beams.

Schultz (1994; 1997) studied the concept of minimum horizontal reinforcement for ductile behavior of masonry shear walls subjected to in-plane seismic loading analytically. He

postulated two models for minimum amounts of horizontal reinforcement. One was based on the horizontal reinforcement having sufficient strength after inclined cracks form in the masonry to resist the force carried by the masonry upon diagonal crack formation. The second model was based on the horizontal reinforcement having sufficient toughness to absorb the energy released by the masonry upon diagonal crack formation. Diagonal cracking strength was adapted from experimental data reported by Shing (1989), and an expression developed by Shing (1990a; 1990b) was used to describe peak shear strength. The lengths of horizontal reinforcement participating in energy absorption were obtained assuming a uniform distribution of constant bond stress along the bars. On the basis of this study, Schultz concluded that strength rather than energy controls the minimum amount of horizontal reinforcement for hot-rolled reinforcing bars. In addition, strength can also be the controlling criterion for wire grids if elongation is at least 10% elongation and the ratio of tensile strength to yield strength is at least equal to 1.25. Minimum horizontal reinforcement ratio expressions were also proposed.

Aguilar et al. (1996), studied confined wall specimens similar to those reported by Sanchez (1992). These specimens were constructed using solid clay bricks and cold-drawn wire, and had as much vertical compression on the net area as did Sanchez's specimens. The experimentally observed performance was better than that of their earlier grid specimen (Sanchez, 1992), but wall shear strength was very low, with reported values of average ultimate shear stresses on the order of 0.6 MPa (87 psi). However, this study also shows that improvements were noted in the behavior for walls with wire reinforcement over that for walls with welded wire grids, because the latter were very brittle in comparison with the cold-drawn wire. Aguilar also investigated a minimum horizontal reinforcement expression which requires more steel than the one proposed by Schultz (1997).

Yoshimura et al. (1996) conducted tests on the seismic behavior of confined masonry walls made using hollow concrete block and used hot-rolled bar instead of wire reinforcement. As part of their study, Yoshimura et al. considered the amount of horizontal reinforcement as well as special detailing of reinforcement to provide confinement along the jambs of the wall and improved anchorage of the horizontal reinforcement in the tie-columns including spirals and hooks. These wall specimens had a modest amount of vertical compression stress (0.84 MPa on the net area of masonry). Yoshimura et al. report reasonably good seismic performance

including adequate levels of deformation capacity, and higher shear stresses than previously reported for confined masonry walls (Sanchez, 1992).

1.3 Scope and Objectives

Study of partially-grouted masonry that utilizes bed-joint reinforcement, and how these practices affect the seismic performance of masonry shear walls, are the principal focus of the current phase of the NIST Masonry Research Program. A preliminary plan of the research program for partially-grouted masonry shear walls which focuses on these two issues was drafted by Fattal (1993b). A more detailed document further develops and refines the partially-grouted masonry phase of the NIST Masonry Research Program was prepared by Schultz (1994). The revised plan (Schultz, 1994) discusses the expected influences of key variables on shear wall strength, describes the test specimens and testing procedure, and summarizes complementary numerical analyses. It also addresses the issue of minimum horizontal reinforcement in masonry shear walls.

The revised plan was implemented in a combined experimental and analytical effort, and it includes the participation of researchers at NIST as well as in several U.S. universities. Specific objectives of the current phase of the NIST masonry research program include experimental verification of the influence of horizontal reinforcement ratio, type of horizontal reinforcement and height-to-length aspect ratio on the seismic performance of partially-grouted masonry walls. Other objectives of the program include the verification of finite element modelling techniques using physical data generated by the partially-grouted masonry shear wall experiments, and validation and calibration of empirical design equations for partially-grouted masonry shear walls.

Since the preparation of the revised research plan, two series of six partially-grouted masonry shear wall specimens have been designed, fabricated and tested at the BFRL. Because the placement of reinforcing bars and grout necessitates the use of hollow masonry units with large openings, the research effort has focused on concrete block masonry. In addition, only some of the parametric combinations identified in the NIST research program were selected for experimentation. A companion report (McGee et al., 1998) discusses the first of two series of

six partially-grouted masonry shear wall tests conducted at the BFRL. The specimens in the first series of shear wall tests utilized bond beams for the placement of horizontal reinforcement, and horizontal reinforcement ratio (ρ_h) and height-to-length aspect ratio (H/L) were the principal experimental variables. The present report documents the second series of partially-grouted masonry shear wall tests, in which horizontal reinforcement is provided by welded wire grids that are placed in the bed joints of the masonry. The same values for horizontal reinforcement ratio and height-to-length aspect ratio that were used in the first series of tests are also used for the second series as well.

This report is organized in eight chapters plus this introduction. The next three chapters describe the experimental program (Chapter 2), the construction details (Chapter 3), and the testing procedure (Chapter 4), respectively. The subsequent four chapters address the observations made during the experiments, including a general description of shear wall behavior (Chapter 5), details of the overall force-deformation response (Chapter 6), and a description of the localized deformation response (Chapter 7), as well as an assessment of shear resistance characteristics (Chapter 8). Summary, conclusions and recommendations complete the report in Chapter 9.

1.4 Requirements for Horizontal Reinforcement

The preceding studies clearly demonstrate that welded bed-joint reinforcement, as it is commonly produced, may not be conducive to ductile shear wall response. Rapid cooling of the molten metal at the welded intersections embrittles the steel, and premature fracture is common at these locations due to limited strain capacity. This property tends to make welded bed-joint reinforcement unsuitable for horizontal reinforcement in masonry shear walls subjected to earthquake forces, because premature fracture prevents widespread bridging of cracks, and this feature is necessary for the redistribution of shear stresses and uniform distribution of cracks that are sought in ductile wall behavior. It is also apparent that increasing the ductility of bed joint reinforcement alone is not sufficient, as the amount of horizontal reinforcement also affects the behavior of masonry shear walls. To modify the brittle nature of masonry walls reinforced with welded bed-joint reinforcement, it is imperative that both the quality of reinforcing steel and the amount of horizontal reinforcement be addressed.

Several alternatives can be exercised to improve steel quality in reference to welded bed-joint reinforcement. First, bed-joint reinforcement can be heat-treated after fabrication to eliminate the embrittlement produced by rapid cooling during the welding process. Or, the welding process can be improved by controlling weld heat and rate of cooling. Alternatively, a tougher steel can be used to fabricate this reinforcement. For example, stainless steels typically have maximum elongations that are two to three times as large as those for low-carbon structural steels. Furthermore, through the addition of alloying agents (such as in 321 and 347 stainless steels), or by limiting the carbon content (such as in 304L stainless steel), commercially-produced stainless steels can be modified to allow welding (Flinn and Trojan, 1986). It is also noted that the use of bed-joint reinforcement manufactured from stainless steel is now common in the U.K. and Canada, as improved corrosion resistance is sought. It may not be necessary, however, to resort to the use of expensive steels, as cold-drawn carbon wire can be manufactured under strict quality control to ensure a minimum elongation of as much as 10%.

A shear wall must have a minimum amount of horizontal steel, in addition to ductile horizontal steel, if this reinforcement is to participate in the resistance to cyclic, in-plane lateral loads. The minimum criterion proposed by Schultz is used in this study. However, the feasibility and practicality of using large amounts of bed joint reinforcement still remains a contentious issue. Shing and Noland (1992) used heat treated, bed-joint reinforcement welded using No. 9 gage wire (3.8-mm or 0.15-in. diameter) at every bed joint and still could not provide enough horizontal reinforcement for ductile shear wall response. The largest nominal wire size that is most commonly used for bed joint reinforcement is No. 9 gage, yet, it is possible to fabricate grids using larger diameter wires, such as No. 6 gage wire (4.8-mm or 0.19-in diameter), and such reinforcement should fit within a typical 9.5-mm (3/8-in.) bed joint. This wire gage provides a modest increase of 27% in wire diameter, but, it gives rise to a 60% increase in wire cross-sectional area. Even larger wires can be used if the cross wires are butt-welded to the longitudinal wires so as to minimize overall thickness of the grids. Other alternatives include grids in which longitudinal wires have a low-profile rectangular section and grids with two longitudinal wires on either side of the cross wires. The former have been used in western Europe to minimize joint thickness (M. Catani, personal communication, 1994), and the latter are available commercially in the U.S.

On the basis of the minimum horizontal reinforcement criterion proposed by Schultz, grids with wire diameters as large as #5 gage wire with a 6% minimum elongation are specified in this study. These welded wire grids were fabricated by Baumann Research and Development Corporation of Newport Beach, California, and were donated to NIST for the partially-grouted masonry shear wall tests. This product was selected for use in the present work because it represents a general class of welded steel wire products. Its use in the research summarized herein should not be construed as an endorsement by the authors, the University of Minnesota or the National Institute of Standards and Technology.

2. EXPERIMENTAL PROGRAM

2.1 General

This report documents experimental activities conducted as part of the second phase of the first priority of the NIST Masonry Research Plan. The first priority of this plan addresses the effectiveness of bed-joint reinforcement in partially-grouted masonry shear walls relative to the seismic performance of shear walls in which hot-rolled deformed bars in grouted bond beams serve as the horizontal reinforcement. Of critical interest are the in-plane shear resistance characteristics of partially-grouted masonry walls subjected to cyclic load histories. Due to the magnitude and scope of the NIST Masonry Research Program on the Seismic Resistance of Partially-Grouted Masonry Shear Walls, a note is in order to justify the breadth and depth of this program.

The amount of experimental research dedicated to the in-plane shear strength of masonry walls has grown considerably during the last two decades, yet, a complete understanding of masonry shear wall behavior still proves to be elusive. There are marked differences in the observed influence of certain parameters when comparing shear strength test results from different sources (Yancey et al., 1991; Fattal and Todd, 1991). These discrepancies can be attributed to differences in testing programs (loading conditions, specimen configuration, test setup, etc.), as well as the large number of parameters which influence the behavior of masonry shear walls. Given this assessment of the current state-of-the-art, strict control of parametric variations in experimental investigations of masonry shear wall behavior becomes a necessity.

2.2 Description of the Program

The NIST Masonry Research Plan comprises an ambitious program to test 42 shear-critical partially-grouted masonry walls under in-plane, cyclic lateral loads. The focus on shear-critical walls is not to be taken as an endorsement of such members, but simply as a necessity in order to observe and measure shear resistance characteristics of partially-grouted masonry walls at ultimate conditions. Twenty-six of these wall specimens were to be made using hollow concrete block and remaining 22 were to be made using hollow, structural clay brick. The

seven research priorities in the NIST Masonry Research Plan are listed in Table 2.1, along with a brief description of the basic objective in each priority. The first priority is further subdivided into two phases with the second phase focusing on shear walls with bed-joint reinforcement which is documented in this present document. The first phase of Priority I includes tests of partially-grouted wall specimens which are nominally identical to those in Phase 2, except that the horizontal reinforcement was provided by hot-rolled deformed bars in grouted bond beams. These tests are documented separately in a parallel report (McGee, et al., 1998).

Phase 2 comprises twelve parametric combinations numbered sequentially and organized in two phases of six wall tests each (Table 2.2). All twelve walls in Phase 2 for the wall specimens were made using hollow concrete block masonry units. The tests of the odd-numbered walls constitute Phase 1, while the even-numbered parametric combinations refer to the concrete masonry wall specimens are included in Phase 2.

Three height-to-length aspect ratios ($r = H/L$) are included in both phases, one for stocky wall panels ($r_1 = 0.5$) which have length L = 2845 mm (112 in.), another for intermediate wall panels ($r_2 = 0.7$) with L = 2032 (80 in.), and a third ratio for square wall panels ($r_3 = 1.0$) with L = 1422 mm (56 in.). As an explanatory note, it is recognized that walls between floors in low-rise construction tend to be longer than they are high, making it commonplace for aspect ratios to be smaller than unity. Fattal (1993b) recognized that little experimental information is available for aspect ratios less than unity, and the scarce information available suggests that aspect ratio has a marked influence on masonry wall shear strength in this region. In addition, there is reason to believe that the increase in shear strength with decreasing aspect ratio reaches a saturation point, and that this limit exists in the range of $0 < r < 1$.

For modularity in testing, the height of all wall specimens was kept constant while the length was varied to generate the three aspect ratios described above. Variations in specimen height are not easily accommodated in the NIST Tri-directional Testing Facility (TTF), as it is designed for a few, discrete heights. A single height of masonry H = 1626 mm (64 in.) was preferred initially to maintain uniformity with the bulk of previous masonry shear wall tests at NIST, yet, a height H = 1422 mm (56 in.) was selected for all specimens for the following reasons. First, specimens that are 1626 mm (64 in.) tall require a length of 3252 mm (128 in.)

to produce an aspect ratio equal to 0.5, but the maximum practical width that can be accommodated in the TTF is 2845 mm (112 in.). Second, in erecting the panels, an odd number of courses were sought so that the single bond beam may be placed at mid-height rather than at an offset from mid-height. It was also deemed undesirable to use more than one bond beam per specimen as "concentration of reinforcement" is one of the goals of the partially-grouted masonry research program. The three aspect ratios selected earlier, namely 0.5, 0.7 and 1.0, are compatible with wall lengths equal to 2845 mm (112 in.), 2032 mm (80 in.), and 1422 mm (56 in.), respectively, given a single wall height of 1422 mm (56 in.).

Nominal properties for the six shear wall specimens in each of the two phases of Priority I are given in Table 2.2. Two types of horizontal reinforcement are called for, either hot-rolled reinforcing bar in grouted bond beams, or welded steel wire grids placed in the mortar bed joints. However, the bed joint reinforcement had to be fabricated from steel that was moderately ductile, and this was assured by specifying a minimum elongation equal to 0.10, and a minimum ratio of tensile strength to yield stress (f_u/f_y) equal to 1.25. Two horizontal reinforcement ratios, defined on the basis of the gross area of masonry, are included in the first priority, namely $\rho_{h1} = 0.05\%$ and $\rho_{h2} = 0.12\%$. The smaller of these two values (ρ_{h1}) is less than the minimum value included in most masonry design specifications, while ρ_{h2} is larger than the design minimum value (Schultz, 1997). Larger amounts of horizontal reinforcement were impractical due to congestion of reinforcement, particularly for the bond beam specimens.

From the viewpoint of parametric control, selection of a single vertical reinforcement ratio for all specimens was desirable, but it was found to be impractical for walls with different aspect ratios. It was difficult, if not impossible, to fit enough vertical bars in the exterior cells of the stocky specimens ($r_1 = 0.5$) to produce the target reinforcement ratio. In order to limit the use of grouting, the research plan recommends that all vertical reinforcement be contained in the exterior cells of the test specimens (Fattal, 1993b; Schultz, 1994). Yet, the amount of vertical reinforcement that can be provided in this manner was constrained by dimensional limitations regarding the placement of several bars in a single cell.

A note is made regarding the failure mode of the masonry shear wall specimens in this study. In seismic design practice, flexural failures of masonry shear walls are preferred over shear

failure. Yet, in the present study, flexural failure is precluded by using sufficient vertical reinforcement to allow the observation of shear distress and failure in the laboratory. Design practices which target shear failure of masonry walls are not endorsed in this report, and they are used in the present study only to enable the measurement of shear strength of partially-grouted masonry shear walls.

In order for a single vertical reinforcement ratio to ensure an adequate margin of safety against flexural failure, a magnitude equal to at least 0.3% based on gross area was needed for the concrete block specimens (Schultz, 1994). However, larger vertical reinforcement ratios only worsen the congestion problem. Thus, a different approach was adopted, and a single vertical reinforcement scheme with a constant cross-sectional area of vertical steel was adopted for all specimens in the Phases 1 and 2 of the first priority of the NIST Masonry Research Program (Table 2.2). By using a constant cross-sectional area, instead of a constant reinforcement ratio, the congestion problem was avoided in the stocky specimens ($r_1 = 0.5$). Also, by selecting the required vertical steel area on the basis of the slender panels ($r_3 = 1.0$), all specimens were guaranteed to fail in shear, as the flexural strength condition is most severe for the slender panels. However, this measure did not ensure a constant vertical reinforcement ratio for all specimens. Two #6 hot-rolled, deformed bars, providing 568 mm^2 (0.88 in.^{2}) of cross-sectional area, were used to reinforce each exterior cell of the partially-grouted masonry walls.

A masonry compression strength equal to 13.8 Mpa (2000 psi) was assumed for all specimens in both phases of Priority I. In addition, a nominal compression stress equal to 10% of the compression strength, or $\sigma_c = 1.38$ Mpa (200 psi), was assumed on the net area of the walls. Current code provisions for structural design of masonry in the U.S. (MSJC, 1995; ICBO, 1997) do not allow compression service stresses in excess of $0.225f'_m$ on the net area, and this requirement translates to a maximum compression stress equal to 3.10 Mpa (450 psi) for the concrete block masonry in the NIST research plan (f'_m = 13.8 Mpa, or 2000 psi). Furthermore, bending compression and slenderness effects may further reduce this allowable stress. Thus, a net area compression stress which is on the order of 1.38 Mpa (200 psi) is considered to be representative of long-term loads in typical masonry walls, and a larger vertical stress on the net area is difficult to justify on the basis of loadbearing masonry construction in the U.S.

Schultz, (1994; 1997) derived expressions for minimum horizontal reinforcement ratio in masonry shear walls, one which is based on a strength criterion, and another based on an energy criterion. The strength criterion calls for enough horizontal steel so that the resultant shear force released by the masonry upon diagonal cracking can be resisted by the reinforcement. The energy criterion requires sufficient horizontal reinforcement so that the elastic strain energy release associated with diagonal cracking of the masonry can be absorbed by the horizontal steel without fracture. Table 2.3 summarizes the ratios required by each criterion for all specimens in the second phase of Priority I. In calculating these ratios, which are based on the gross area of masonry, the height, effective thickness and gross thickness of masonry in all specimens was taken as 1422 mm (56 in.), 64 mm (2 1/2 in.), and 194 mm (7 5/8 in.), respectively. Also, it is assumed that the welded wire grids have a minimum elongation of 0.10 and a minimum ratio of tensile strength to yield stress equal to 1.25. For all shear wall specimens in Phase 2, the strength criterion controls, and the corresponding minimum ratio is 0.043% based on the gross area of masonry. The horizontal reinforcement ratios in the experimental program should serve to provide additional validation for the expressions proposed by Schultz (1994; 1997).

2.3 Specimen Designations

The specimen designations used in Tables 2.2 and 2.3 comprise four descriptive groups of characters, the first which is CO for concrete block masonry. The second group, which begins with the letter R, indicates aspect ratio. The numerical pairs 05, 07 or 10 represent aspect ratios equal to 0.5, 0.7 and 1.0, respectively. The third group identifies with the letter B those specimens with horizontal reinforcement in bond beams, and those with bed-joint reinforcement with the letter J. The next pair of numbers are the first two decimal digits of the horizontal reinforcement ratios expressed in percentages, with 05 and 12 representing horizontal reinforcement ratios equal to 0.05% and 0.12%, respectively. The last group of characters, beginning with the letter Q, indicate axial stress, and the numeral 10 represents a vertical compression stress equal to 10% of masonry compression strength.

3. SPECIMEN DETAILS

The construction of the partially-grouted shear wall specimens in Phase 2 are documented in the following chapter. Masonry panel configuration and geometry are described, along with test setup, reinforcement details, fabrication procedure, material tests, and the header/footer precast beams that were used to attach the specimens to the testing platform.

3.1 Masonry Wall Panel Configuration

To achieve the objectives of the experimental phase of the NIST research program on partially-grouted masonry shear walls, the wall elevations shown in Fig. 3.1 were selected for the three aspect ratios in this study. All concrete masonry specimens were to be made using blocks with 194 mm (7 5/8 in.) x 397 mm (15 5/8 in.) nominal dimensions. The concrete masonry units satisfied the ASTM C90 specification for load-bearing concrete block (ASTM, 1985a), and they were 55% solid. Actual dimensions measured for three concrete blocks selected at random are given in Table 3.1. Head and bed joints with an approximate thickness of 9.5 mm (3/8 in.) were used to provide effective dimensions of 203 mm (8 in.) x 406 mm (16 in.) for the masonry units.

All masonry was face-shell bedded using Type S mortar which satisfied ASTM C270 (ASTM, 1989b). As noted in Fig. 3.1, only those cells containing reinforcement were filled with grout, and coarse grout was specified which met the requirements of ASTM C476 (ASTM, 1983). The mix designs for the mortar and grout used to build the masonry panels are given in Tables 3.2(a) and 3.2(b). Standard tests for material properties of the masonry materials and steel reinforcement are summarized in Section 3.6.

A total of seven courses in each panel were used to provide a nominal height of masonry equal to 1422 mm (56 in.). The 2845 mm (112 in.), 2032 mm (80 in.) and 1422 mm (56 in.) lengths, respectively, for the stocky ($r_1 = 0.5$), intermediate ($r_2 = 0.7$) and slender ($r_3 = 1.0$) panels is achieved by varying the number of masonry units in each course (Fig. 3.2). All panels had a nominal thickness of 203 mm (8 in.). The grouting pattern is shown in Fig. 3.2 for a slender panel specimen ($r_3 = 1.0$). For all of the specimens, only the exterior cells

contained vertical reinforcement, and only these cells were grouted. Horizontal reinforcement was provided in the form of welded steel wire grids which were placed in each bed joint between courses of masonry.

3.2 Vertical Reinforcement

Two #6 hot-rolled, deformed reinforcing bars, providing 568 mm^2 (0.88 $in.^2$) of steel area, were used to reinforce each exterior cell of the concrete block masonry walls. This vertical reinforcement provided a total cross-sectional area equal to 1136 mm^2 (1.76 $in.^2$). Because the lengths of the specimens varied with aspect ratio, these steel areas produced different vertical reinforcement ratios, depending on the aspect ratio of the wall. The vertical reinforcement ratios, based on gross area of horizontal sections, is given in Table 2.2. All vertical steel was specified as Grade 60 hot-rolled, deformed reinforcing bar.

Two straight pieces of #6 reinforcing bar, approximately 2210 mm (87 in.) long, were placed in each exterior cell of the specimens. The bars extended above and below the 1422-mm (56 in.) height of masonry, and the ends of the bars extend into pockets in the precast concrete header/footer beams. High-strength, non-shrink grout served to anchor the bars in these pockets, as described in section 3.4. The ends of the vertical bars were threaded over a 51-mm (2 in.) length at either end. A pair of steel nuts and a steel plate serve to anchor the bar securely in the grout pocket.

3.3 Horizontal Reinforcement

The specimens with bed joint reinforcement had welded (ladder-type) wire reinforcing grids that meet ASTM A82 specifications (ASTM, 1985b) placed in the bed joints. The wire grids were made using cold-drawn carbon steel wire with a minimum specified elongation of 8%. In addition, the cross wires were butt-welded to the longitudinal wires, as noted in Fig. 3.3, so that the overall thickness was one wire diameter, and the welding process was specified to be controlled so as to minimize embrittlement from rapid cooling of the welded intersections. The specifications for the welded wire grids also required that fracture of longitudinal wires should occur away from the welded intersections.

Two different wire grids were used. For the specimens with $\rho_{h1} = 0.05\%$, a grid with No. 9 Gage (3.76 mm or 0.148 in. diameter) longitudinal wires and cross wires was used, while a grid with No. 5 Gage (5.26 mm or 0.207 in. diameter) longitudinal wires and cross wires is used for the specimens with $\rho_{h2} = 0.12\%$. The latter utilizes slightly larger longitudinal wires than are typically allowed in 9.5 mm (3/8 in.) bed joints. However, the mason was able to accommodate the grid in the bed joints without having to increase the average thickness of the joints. At one end of each grid, the bed joint reinforcement was placed such that cross-wires engage at least one of the vertical bars in the grouted cells. At the other end of the grid, excess lengths of longitudinal wires were bent in a 90° angle around one of the vertical bars in the grouted exterior cell.

3.4 Precast Concrete Header/Footer Beams

In-plane shear and vertical compression stresses were applied to the walls by means of stiff precast concrete header/footer beams (Fig. 3.4). It is customary for masonry shear walls specimens for use in-plane cyclic load tests to feature large concrete footers to anchor vertical reinforcement. Often, the header beams are either eliminated if the specimen is a cantilever wall. In the present study, the specimens were fixed against rotation top and bottom, so a header beam was required as well as the footer. These beams also served the auxiliary purposes of anchoring the vertical reinforcement and providing easy connection to the upper and lower crossheads of the TTF platform.

Previous experimental studies at NIST on masonry shear walls did not utilize such header/footer beams. However, all but one of these studies involved unreinforced walls, and the only study on reinforced masonry utilized walls that had only horizontal reinforcement (Scribner and Yancey, 1989). It is essential that vertical reinforcement in masonry shear wall specimens be anchored such that the ultimate strength of the vertical bars can be developed. Otherwise, uncharacteristically large amounts of slip of reinforcing bars in tension can take place, resulting in uplift of the heel of the wall and reduction in flexural strength. This situation is more acute for slender walls ($r_3 = 1.0$).

The header/footer beams that were fabricated for the present study are shown in Fig. 3.4. By precasting these members, large savings in labor and materials were gained, as a pair of these beams would otherwise have to be built for each wall specimen. Only one pair of header/footer beams for each of the three aspect ratios were built, and these members were reused for the entire testing program.

The precast concrete header/footer beams (Fig. 3.5) are prismatic members with rectangular cross-section. These members feature multiple vertical openings of small diameter that (1) enable lifting of the specimen using high-strength threaded rods, and (2) allow placement of the high-strength post-tensioning rods to attach the specimen to the TTF. In addition, the header/footer beams feature a pair of pockets in the shape of a truncated right pyramid, in which the vertical reinforcing bars of the wall panel were anchored. A pair of vertical bars were anchored in each pocket for each wall test, and a steel plate, held in place by two steel nuts, served as mechanical anchorage.

The truncated right pyramid configuration was employed to facilitate the removal of the grout plug following a test. By placing a barrier (i.e. wax) to break bond between the grout and the concrete beam, the grout plugs could be removed without damaging the header and footer beams. Vertical stirrup pairs are placed at 76-mm (3 in.) spacing resisted flexural shear in this region. In addition, horizontal ties are used to confine the pyramid, and, shearheads fabricated from structural steel tubes were used to resist punching shear in the concrete above the pockets.

The header/footer beams were cast using a lightweight concrete, with a nominal 28-day compression strength equal to 34.5 MPa (5000 psi) and a weight density of 1920 kg/m^3 (120 lb/ft^3). This was done to reduce the overall weight of the header/footer beams while still retaining sufficient strength to withstand the rigors of transportation and testing in the laboratory.

3.5 Fabrication Procedure

The masonry walls were built by a licensed mason. All six masonry panels were built at one time, and companion prisms (grouted and ungrouted), mortar cubes and grout cubes were

made simultaneously. The masonry was laid on platforms to provide a smooth, level surface of fabricated wood which allowed placement of the vertical reinforcing bars. Wire grids for bed joint reinforcement were placed in the bed joint specimens with each course of masonry. Exterior cells were grouted 24 hours after all seven courses have been placed. External support at the top of the vertical rebars was necessary when the panels were constructed.

After a period of at least one week, the panels were positioned using leveling shims on a bed of mortar on top of the precast concrete footer. The portions of vertical reinforcing bars which protruded below the masonry panel were inserted through the access tubes and into the pockets of the footer beam (Fig. 3.5). Anchor plates and steel nuts were attached at the appropriate location at the bottom of the vertical bars. Shims and another bed of mortar were placed on top of the masonry panel, and the header beam was lowered into position. The top of the vertical bars were placed through the access tubes and into the pockets of the header beam, and steel nuts and plates were attached to the bars. Anchorage of the vertical bars was provided by filling the pockets in the header and footer beams with superplasticized high-strength, non-shrink grout. The grout was pumped through an inlet, and an outlet was used to determine by visual inspection when the pockets were filled.

Once the grout in the header/footer pockets had matured at least 7 days, the specimens, which by now comprised the masonry panel and the header and footer beams, were placed in the TTF. The specimens were lifted using the overhead crane by means of high-strength threaded rods that are bolted to the footer beam. A bed of gypsum cement was placed below the footer and above the header to provide sufficient surface contact for uniform transfer of stresses between the TTF crossheads and the header and footer beams on the specimens.

3.6 Material Tests

A variety of compression tests of masonry materials were conducted, and a summary of compression strengths is given in Table 3.3(a) for the 28-day tests of specimens that were moist-cured, and Table 3.3(b) for companion specimens that were cured in air next to the masonry wall panels. A schedule of all compression tests of masonry materials is given in Table 3.4.

Prism compression tests, according to ASTM specifications, were conducted for the concrete masonry (ASTM, 1980) using a height-to-thickness (*h/t*) ratio equal to 2. Sufficient tests were conducted to characterize grouted and ungrouted prisms (Table 3.5). The prisms were moist-cured by sealing them in polyethylene bags from the day they were built until the day they were capped and tested. The air-cured companion specimens were stored next to the masonry wall panels and allowed to cure under the same conditions exposed to laboratory air. It is worth noting that the 28-day strength of moist-cured ungrouted prisms had an average value of 13.7 Mpa (1990 psi), which is very close to the target nominal strength of 13.8 Mpa (2000 psi). Grouted prisms that were moist-cured had a 28-day strength in excess of 17.2 Mpa (2500 psi).

Masonry mortar cube tests and masonry grout specimen tests, as specified in ASTM C109 (ASTM, 1988a) and ASTM C1019 (ASTM, 1984), respectively, supplemented the tests described above. Compression strength tests results are summarized in Tables 3.6 and 3.7, respectively. It is noted that the mortar used for the bed joints between the masonry panels and the header/footer beams was prepared at a later time than the mortar used for the seven courses of masonry. In addition to the masonry grout, high-strength non-shrink grout of the type used for grouting prestressing tendons was used to anchor the vertical bars in the grout pockets of the header and footer beams. This material was also sampled and tested using standard procedures, and the corresponding cube strengths are listed in Table 3.8. Finally, unit compression tests for the concrete block, as described in ASTM C140 (ASTM, 1980), were conducted, and the net area block strength is given in Table 3.9.

Tension coupon tests for vertical and horizontal reinforcing steel were also included in the program. The No. 6, hot-rolled, deformed bar used to reinforce the exterior vertical cells had average values for yield stress, tensile strength and elongation that are typical for Grade 60 steel reinforcing bar (Table 3.10). The welded wire grids, on the other hand, fell short of expectations. This reinforcement was specified to be manufactured using wire with an elongation in excess of 8%, and that fractures should occur away from the welded intersections. In addition, the minimum elongation of the welded material was specified to meet or exceed 6%. However, as noted in Table 3.11, the average elongation was 0.0434 and 0.0604 for the No. 9 gage and No. 5 gage longitudinal wires, respectively. Furthermore, the yield stress was almost equal to the tensile strength, with the latter being only 4.7% and 7.1%

larger than the former for the No. 9 gage and No. 5 gage wire, respectively. It was also noted that the longitudinal wires had to be tested with the cross-wires in place, as the removal of these wires was found to damage the longitudinal wires and lead to premature failure during the coupon tensile tests.

4. TESTING PROCEDURE

4.1 Test Setup

The assembled specimens were transferred for testing in the tri-directional test facility (TTF) using the setup shown in Fig. 4.1. The TTF is a multiaxial testing machine which is capable of applying force or displacement histories along 6 directions (translations and rotations along three orthogonal axes). The TTF comprises a pair of crossheads (one fixed and one moving), six hydraulic actuators, a hydraulic power supply, electronic controls for the power supply and actuators, and a high-speed, multi-channel data acquisition system. A dedicated computer controls the TTF, which is a closed-loop system, and the data acquisition system. A detailed description of the TTF is found elsewhere (Woodward and Rankin, 1984b).

The specimens were placed in the TTF such that the plane of the wall was directed along the east-west axis of the TTF. A 457-mm (18 in.) deep concrete spacer beam was placed between the specimen and lower crosshead to span the clear height of the TTF. A bed of hydrocal (gypsum cement) mortar was placed between the header/footer beams and the TTF crossheads to allow for uniform transfer of stresses. High-strength post-tensioning rods were used to connect the header/footer of the specimen to the TTF. These rods were post-tensioned using a torque wrench once a hydrocal mortar bed had attained sufficient strength (2 to 3 hours).

4.2 Loading History

A displacement history was imposed on the specimen along the east-west axis of the TTF (i.e. along the in-plane horizontal direction of the masonry wall panel), while a constant vertical force resultant was maintained. The lower crosshead of the TTF is fixed, thus all motion of the base of the wall specimens was restricted. The top crosshead, which is the one capable of motion, was operated by appropriate instructions from the TTF control system to constrain rotation along three orthogonal axes and translation along the north-south axis of the TTF (i.e. perpendicular to the plane of the masonry wall panel). Thus, east-west displacements and vertical displacements were specified at each increment of each cycle of the loading history for all wall specimens.

The east-west displacement history conformed to the Sequential Phased Displacement procedure developed as part of the TCCMAR program (Porter and Tremel, 1987). An idealized plot of this procedure is shown in Fig. 4.2, where it can be seen that cycles of reversing displacements of increasing amplitude are applied to the specimen until failure. Initial displacements were applied to the walls in the elastic range, and these cycles were specified in groups of three cycles with equal peak displacements. These cycles gave way to the inelastic displacement cycles once a benchmark displacement was reached. The benchmark displacement is known as the first major event (FME), which was defined in this program as the formation of the first inclined or vertical crack that traversed through at distance equal to at least one(-half) of the depth of a masonry course.

Two distinct types of inelastic displacement cycles were featured in the program, including degradation cycles, during which peak displacement amplitude decreased between successive cycles, and stabilization cycles in which peak displacement amplitude was maintained constant from one cycle to the next. These displacements were applied in small increments, and at a slow loading rate. The specimens were inspected visually for cracks or other surface damage at peak displacement for each loading direction of each cycle. Failure of the specimens was defined at the instant when a loss of shear strength was observed which was equal to 25% or more of the peak strength observed previously in that loading direction.

The TTF is a displacement-controlled testing machine, so that vertical load had to be specified as a displacement. This procedure required calibration of vertical load and displacement, so that a specified displacement produced the desired load. However, these calibrations differed from one wall to the next, and they were proportional to the axial stiffnesses of the wall specimens. Axial stiffness was affected by the state of wall damage which increased progressively with increasing east-west displacement. Lateral movement also generated second-order changes in wall geometry which also affected axial load. Thus, vertical displacements were specified on the basis of calibrations which changed continuously during the tests. For this reason, displacement increments were small, and axial load was only approximately constant during the tests. A sample axial load history is shown in Fig. 4.3, and Table 4.1 lists mean values and standard deviations in measured axial load for all six walls, as well as the target load for a nominal vertical stress equal to 1.38 MPa (200 psi).

4.3 Instrumentation

The shear wall specimens were instrumented with linear variable differential transducers (LVDT), linear strain transducers (LST), and electrical resistance strain gages, respectively, to monitor wall displacements, masonry strains, and reinforcement strains on both the vertical bars (VRB) and the welded wire grids (HRG). The LVDT, LST, VRB and HRG instrumentation schemes, respectively, are given in Figs. 4.4, 4.5, 4.6 and 4.7.

Total lateral displacement of the wall was measured using LVDTs attached to a steel frame that was erected adjacent to the TTF (Fig. 4.4). Two other LVDTs were used to determine the change in length of the principal diagonals, and 6 LVDTs were used to measure the vertical shortening/elongation of the exterior cells. A pair of LVDTs were also used to monitor liftoff/crushing of the wall toe/heel. The linear strain indicators (LST), which are strain amplifying devices utilizing strain gages mounted on leaf springs, were placed at various locations to monitor local strains in the masonry (Fig. 4.5 and Table 4.2). Electrical resistance strain gages attached to the vertical reinforcing bars (Fig. 4.6) and to the horizontal grids (Fig. 4.7), and were used to monitor strain changes in the reinforcement.

The instruments described above are in addition to the internal load cells and displacement transducers in the hydraulic actuators of the TTF. Note that the control software for the TTF generates global force and displacement signals that define the translation and rotation of the upper crosshead along three orthogonal axes. These global forces and displacements are in equilibrium with and kinematically consistent to the forces and displacements in the individual actuators. These signals were sampled, digitized, recorded, and stored along with the strains and displacements measured on the masonry panels.

5. GENERAL BEHAVIOR OF SHEAR WALL SPECIMENS

Certain basic aspects of masonry shear wall behavior were noted on the basis of visual observations during the simulated seismic drift tests. These observations facilitate the formulation of a qualitative overall assessment of wall response to the cyclic drift histories. The observations were mostly visual such as crack formation, growth and propagation, spalling and crushing damage, but they also included sounds emitted by the specimens during the tests. These observations serve as outward manifestations of shear wall specimen behavior and distress, and, taken together with force-displacement traces from x-y pen plotters they provided an immediate assessment of the overall behavior of the specimens. This chapter is meant to convey some of this information to the reader, and it is complemented with select values of force and displacement measurements that are described in Chapter 6. The assessment of overall behavior draws upon crack patterns (sketches and photographs) and tabular timelines (taken from laboratory logbooks) to document overall behavior of the partially-grouted shear wall specimens.

5.1 Timelines

A summary list of the important events in each shear wall test is given in Tables 5.1-5.6. For each event, these tables include the number corresponding to the point in the loading history, the cycle group, the cycle number, the current displacement and force, and specific comments describing or pertaining to the event. The point in the loading history refers to the processed records, and is intended as a marker identifying the particular location of the event listed in the timeline. The cycle group and number refer to the pattern in which the drift cycles were imposed, as described in Chapter 4. Drift cycles occurring before the first major event (FME) are labeled elastic (i.e. cycle group E*n*), and those occurring after the FME are inelastic (i.e. cycle group xD_c). Elastic cycle groups typically have three repetitions for each new peak drift (i.e. cycle numbers 1-3), while inelastic cycle groups have a total of five cycles (D1-D3, S1 and S2). The displacement and force values noted in Tables 5.1-5.6 correspond to the global east-west quantities recorded by the TTF.

The comments included in the timeline describe briefly the nature of each event listed in the table. Each wall history comprises from 3000 to as many as 4000 points, and, of these, only a few hundred have been selected for the timeline tables (typically 200 to 300). The comments in the timeline tables include highlights of the drift history, such as negative and positive peaks, the ends of cycles and beginning of subsequent cycles, and the beginning and end of a given day of testing. The timelines also include events that indicate significant changes in wall behavior, such as the cracking associated with the first major event, other cracking, spalling and crushing damage, as well as an assortment of various sounds.

It was noted on various occasions during the shear wall tests that the specimens emitted audible sounds (i.e. loud "bangs", "pops" or "cracks"), and these were accompanied by changes in the force-displacement relations that were being monitored on the x-y pen plotters. These sounds were interpreted as instances of fracture of the welded wire grids that were being used as horizontal reinforcement. It is quite probable that even though many of the wire grid fractures were identified with these audible sounds, others went unnoticed. Nevertheless, these sounds serve as an important record of wall behavior.

In addition to the instances of grid fractures, another type of sonic event (described as loud "thuds" during the tests) was identified with sliding behavior of the masonry with respect to the header and footer beams. Sliding displacements were inferred as the difference between absolute displacement measurements in the test specimens as these responded to the cyclic drift histories, and these displacements are described in greater detail in Chapter 7. As noted in Chapter 7, sliding displacements were present to some degree throughout most of the tests, yet, only a few instances of audible sounds associated with sliding are present in the permanent record of the tests. These instances of sliding appear to be those few instances in which large displacements took place in a sudden manner, while most sliding displacements evolved in a gradual manner which followed the application of the cyclic drift histories.

5.2 Crack Patterns

The formation, propagation and growth of cracks on the masonry panels provides a valuable medium whereby the basic mechanisms of response to the cyclic drift histories can be

visualized. Photographs of the specimens after testing are provided in Fig. 5.1-5.6, and more detailed crack patterns are given in Fig. 5.7-5.12. These figures comprise hand-drawn sketches prepared on the basis of visual assessment of cracking immediately after the tests. Space limitations preclude the reporting of crack patterns at intermediate stages of testing. In the crack patterns no differentiation is made between cracks of different widths, even though a great variation in crack width can be appreciated in the photographs (Fig. 5.1-5.6). Also, spalling is indicated in the crack patterns by cross-hatching. The following narrative was prepared, on the basis of the observed crack patterns, to summarize the most important features of the process of crack formation and progression for each of the specimens.

(a) Wall Specimen 2

Cracks initiated during cycle group $1.0D_c$ in the head joints of both end units of the top course. These vertical cracks propagated halfway through the 6th course and then turned outward 45° towards the jambs. During the $1.5D_c$ and $2D_c$ cycles, these cracks extended downward through the 2nd, 3rd and 4th courses in a vertical orientation but tapering slightly outward towards the jambs.

Parallel vertical cracks along the jambs were noted during the $3D_c$ cycle group at a distance of one-half of a masonry unit from the two edges. In addition, short inclined cracks formed in both top corners, and some horizontal cracking was noted in the bed joints of the first three courses during these cycles.

During the $4D_c$ and $5D_c$ cycles, inclined cracks were observed to form at third points along the top of the masonry, and these cracks propagated towards the nearest bottom corners. In addition, extensive crushing and spalling damage was observed in the top four courses of the masonry during the cycles of groups $4D_c$, $5D_c$ and $6D_c$.

(b) Wall Specimen 4

Cracking initiated during cycle group $1.0D_c$ when vertical cracks formed in the top mortar joint and propagated through the end units of the top (7th) course. These vertical cracks turned

outward 45° (i.e. towards the jambs) once they had traversed half-way through the 6th course. During the second cycle of group $1.5D_c$ these cracks continued to propagate downward (sloping slightly outward towards the jambs) through the 5th, 4th and 3rd courses.

During the $2D_c$ cycles, a diagonal crack was formed at the top east corner of the panel and it propagated towards the bottom west corner through courses 4, 5, 6 and 7 alternating through head and bed joints in stairstep fashion. New inclined cracks formed in the $3D_c$ cycles beginning at third points along the top mortar joint and propagating downward through the height of the panel towards the farthest bottom corner. Near the center of the panels, these cracks progressed in a stairstep pattern by cracking through mortar head and bed joints. But, away from the center of the panel the cracks propagated through the masonry units.

Cycle group $4D_c$ saw extension and widening of existing cracks, as well as the formation of multiple cracks similar to those already present in the panel. Some crushing and spalling damage was noted in courses 6 and 7. During the cycles of group $5D_c$, widespread crushing and spalling was noted in courses 3 through 7, and horizontal cracking was observed in the central portion of the bed joint for the 3rd course (i.e. the horizontal joint between courses 2 and 3). The cycles in group $6D_c$ featured further crushing and spalling damage of the panel.

(c) Wall Specimen 6

Cracking began during the $1.0D_c$ cycles with a vertical crack in the head joint of the exterior half-unit at the west end of the top course. This unsymmetric pattern remained throughout the $1.5D_c$ cycles, and it was not until the $2D_c$ cycles that vertical cracking began in the west end of the top course. However, these vertical cracks did not develop much further, as diagonal cracks (45°) formed during the $3D_c$ cycles at both top corners and radiated towards the opposite bottom corners.

During the $4D_c$ cycles, the crack pattern changed once again, as inclined cracks were initiated in the mid-length of the top joint and radiated downward towards either bottom corner. This pattern of cracking was better developed in the east side of the panel than the west side. Some crushing and spalling damage was noted in the top two courses. The cycles of group $5D_c$

experienced further development of these inclined cracks, and the crushing and spalling damage extended down to the 4th and 5th courses. Damage during cycle group $6D_c$ was limited to extensive spalling and crushing of the top half of the masonry panel.

(d) Wall Specimen 8

Cracks initiated in cycle group $1.0D_c$ in the head joints of both end units of the top course. These vertical cracks propagated halfway through the 6th course and then turned outward 45° towards the jambs. During the $1.5D_c$ cycles, these cracks extended downward through the 4th course in a vertical orientation but tapering slightly outward towards the jambs. The $2D_c$ cycles saw extension of these cracks through the 3rd and 2nd course, in addition to the formation of short inclined cracks in both top corners. In addition, the entire bottom joint cracked during these cycles.

During the $3D_c$ cycles, additional development of the vertical cracks along the jambs was noted, but most damage was limited to crushing and spalling of the top course. During the cycles of groups $4D_c$, $5D_c$ and $6D_c$, damage was confined to crushing and spalling throughout the top one-half of the masonry panel.

(e) Wall Specimen 10

Initial cracking occurred during cycle group $1.0D_c$ when vertical cracks formed in the top mortar joint and propagated into the end units of the top (7th) course. In addition, the bottom (bed) joint cracked partially along both ends. During the cycles of group $1.5D_c$, the vertical cracks at the ends of the top course propagated through the 6th course. And, these jamb vertical cracks continued to propagate during cycle group $2D_c$, during which time they traversed through courses 3, 4, and 5 while maintaining their vertical attitude.

Diagonal cracks initiated during the $3D_c$ cycles which propagated through the entire height of the masonry. Near the center of the panels, these cracks progressed in a stairstep pattern, but away from the center of the panel they fractured the masonry units. New inclined cracks formed at third points along the top of the masonry panel during the group $4D_c$ cycles,

beginning at third points along the top mortar joint and propagating downward through the height of the panel towards the farthest bottom corner. Crushing and spalling was observed at various locations in courses 2 through 7.

During the cycles of group $5D_c$, the inclined crack pattern described above became more fully developed with additional crack formation in the bottom east corner of the panel. This pattern was repeated for the bottom west corner during the cycles of group $6D_c$. In addition, the severity and distribution of spalling and crushing damage increased progressively during cycle groups $5D_c$, $6D_c$ and $8D_c$, and, at the end of the test crushing and spalling was the only visible form of new damage to the masonry panel.

(f) Wall Specimen 12

Cracking began during the $1.0D_c$ cycles with a vertical crack in the head joint of the exterior half-unit at the west end of the top course, as well as a vertical crack in the unit at the east end of the top course, and stairstep cracks in courses 2 and 3 near the mid-length of the panel. A diagonal crack (45°) formed during the $1.5D_c$ cycles spanning from the upper east to the lower west corners of the panel. Short stairstep cracks formed at various locations in the panel during these cycles as well. During the $2D_c$ cycles, another diagonal crack which radiated from upper west to lower east corners was fully developed, and additional cracking along the other diagonal was also observed.

The crack pattern remained unremarkable during the next four cycle groups. The formation of short horizontal and inclined cracks was observed in the top four courses during the group $3D_c$ cycles. And, additional cracking along the upper east to lower west diagonal were noted during cycle group $4D_c$, as well as minor crushing in courses 1, 2 and 3. The latter pattern of progressive crushing and spalling damage continued during the group $5D_c$ and $6D_c$ cycles.

It was not until the cycles of group $8D_c$ that a change in the cracking mode was observed. As further diagonal cracking took place in the cycle group, the orientation of these cracks shifted until the new cracks were initiating along the third point of the top panel near the west jamb and radiating towards the lower east corner of the panel. However, this change in cracking mode

did not continue as the group $10D_c$ cycles witnessed mostly extensive crushing and spalling damage throughout the masonry panel. This damage had continued unabated and in a progressive manner through the cycles of group $8D_c$.

5.3 Mode of Response

The crack patterns described in the preceding section include important similarities and differences between specimens of a given aspect ratio. These observations are summarized in the following paragraphs, and are used to develop a qualitative assessment of the mode of response of the shear wall specimens to cyclic drift histories. Similarities in the behavior of walls with the same aspect ratio suggest that the mode of response is linked to the ability of the walls to transfer horizontal forces to the base are subject to the limitations imposed by the geometric configuration. The differences suggest that the response was also affected by the amount of horizontal reinforcement.

(a) Long Walls (H/L=0.5)

Long walls (Specimens 2 and 8) responded initially with vertical cracks at the interfaces of the grouted and ungrouted masonry along the jambs during the $1.0D_c$ cycle groups. These cracks quickly propagated downward, and by the end of the $2D_c$ cycle groups, they had extended through most of the height of the panels. Aside from further development of these cracks, and crushing and spalling of the masonry, the mode of response of the long walls did not change throughout the remainder of the tests. Most of the masonry in the central and lower one-half of the long wall specimens did not crack at all, particularly for Wall Specimen 2.

(b) Intermediate Walls (H/L=0.7)

Intermediate walls (Specimens 4 and 10) responded initially with vertical cracks at the interfaces of the grouted and ungrouted masonry along the jambs during the $1.0D_c$ cycle groups. However, these walls developed diagonal cracks early in the drift history (during cycle groups $2D_c$ and $3D_c$, respectively), and these diagonal cracks gave way to inclined cracks spanning from third points at the top of the masonry to the opposite corner at the base of the

panels (during cycle groups $3D_c$ and $4D_c$, respectively). Aside from localized spalling and crushing, no further change in the crack patterns and modes of response was observed for the remainder of the cyclic drift tests.

(c) Short Walls (H/L=1)

Short walls (Specimens 6 and 12) responded initially with vertical cracks at the interfaces of the grouted and ungrouted masonry along the jambs during the $1.0D_c$ cycle groups. However, almost immediately (cycle group $1.5D_c$) diagonal cracks were formed in both loading directions of both specimens. This mode of response remained effective for a significant portion of the tests, as the specimens did not give any outward indication of change for several cycle groups. Towards the end of the tests (cycle groups $4D_c$ and $8D_c$, respectively), the mode of response changed as new inclined cracks formed at third-points (Specimen 6) or mid-point (Specimen 12) along the top of the masonry and radiating to the opposite bottom corner of the panels. Aside from localized spalling and crushing, no further change in the crack patterns and modes of response was observed for the remainder of the cyclic drift tests.

(d) Idealized Wall Behavior

In all cases damage to the walls was initiated by vertical cracks at the top of the walls near the jambs. This cracking was undoubtedly in response to large stress concentrations at the interfaces between grouted and ungrouted masonry, and it is an obvious weakness of partially-grouted masonry. However, this mode of cracking had the greatest impact on the behavior of the long walls (H/L=0.5) and had the least impact on the short walls (H/L=1).

If vertical cracking damage of the jambs did not affect more than the top few courses of masonry, the walls were able to change their mode of response to more efficient diagonal struts, as evidenced by diagonal cracks. Such was the case with the intermediate (H/L=0.7) and short (H/L=1) walls. In order to switch to a diagonal strut mechanism, the horizontal reinforcement had to be intact through the vertical cracks in order to bridge this interruption in the horizontal flow of stresses.

Eventually, damage to jambs from vertical cracking, grid fracture, vertical bar yielding, and compression/tension from overturning rendered the jambs ineffective. That is, the effective stiffness of the jambs decreased sufficiently to complete the diagonal strut mechanisms. Thus, horizontal shear stresses applied to the top of the header beam accumulated along the top of the beam in response to friction between header beam and masonry before being transferred into the compression struts. Thus, the mode of response changed from diagonal struts (spanning along opposite top and bottom corners of the panels) to inclined struts which initiated at third-points and mid-points along the top of the masonry panels.

Long walls (H/L=0.5) were not observed to crack diagonally or along inclined struts because stress transfer was concentrated along the jambs, and the central portion of these walls remained relatively stress-free. Also, the presence of additional horizontal reinforcement delayed the damage that rendered the jambs ineffective, so that the change from diagonal to inclined struts occurred later in the tests of heavily-reinforced specimens (10 and 12) than in those of the lightly-reinforced specimens (6 and 8). It is also presumed that additional reinforcement in Specimen 8 prevented as much cracking as was observed for lightly-reinforced Specimen 2.

6. FORCE-DISPLACEMENT RESPONSE TO CYCLIC LOADING

From the vantage point of seismic design, some of the most important measurements made during the simulated seismic drift tests of partially-grouted masonry walls are associated with the lateral displacements and the corresponding shear forces, because considerations relating to displacement and force capacity permeate modern seismic design procedures. Consequently, data of the type presented in this Chapter are needed to justify design code provisions for partially-grouted masonry shear walls. This Chapter discusses lateral displacement histories, as well as corrections made to this data. Shear force histories are also presented, and the hysteretic relation between shear force and displacement is investigated. Envelopes of force-displacement response are constructed, and deformation capacities are extracted from these envelopes. This Chapter also includes discussion of the first major event (FME), initial stiffnesses of the walls, and energy dissipation capacities.

6.1 Lateral Displacements

The simulated seismic loading tests were conducted by imposing an in-plane drift on the top of the wall specimens. Thus, the TTF developed the necessary forces, depending upon the stiffnesses of the specimens, to produce the desired in-plane drift, as well as those forces needed to constrain the other degrees-of-freedom at the top of the walls (i.e. vertical translation and out-of-plane drift, as well as in-plane, out-of-plane and torsional rotations). As noted in Chapter 4, the in-plane drift histories at the top of the walls followed a specified pattern of cycles before and after the first major event (FME).

Displacement histories are shown in Fig. 6.1.1-6.1.6 for the tests of shear wall specimens 2, 4, 6, 8, 10 and 12, respectively. The measured global displacements in the in-plane lateral direction are plotted against the integer count (i.e. Point) for each load step of the tests. In general, the displacement histories are unremarkable, and they illustrate the pattern of cycles with increasing displacement amplitude that is described in Chapter 4. The displacements histories also demonstrate clearly that the shear wall specimens with the larger amount of horizontal reinforcement (8, 10, and 12) were tested to larger displacements over more cycles than those with less horizontal reinforcement (2, 4, and 6).

Peak displacements Δ_{max} (i.e., maximum displacements measured during the tests) are listed in Tables 6.1.1-6.1.3 for all wall specimens in Series 2, as well as the associated drifts which are expressed as a percentage of the height of masonry (1422 mm or 56 in.). Peak displacements and drifts are reported in each loading direction (Tables 6.1.1 and 6.1.2), as well as the average of the two loading directions (Table 6.1.3). In addition, the data points corresponding to the peak displacements are given, as well as the in-plane shear force recorded at the instant of peak displacement ($V_{\Delta,max}$). Because these forces occurred well after peak load V_{max} had been recorded (i.e., maximum loads measured during the tests), the ratios of load at peak displacement ($V_{\Delta,max}$) to peak load (V_{max}) are also given in Tables 6.1.1-6.1.3 to provide some indication of load deterioration.

The tests were stopped only after the resisting in-plane shear force had deteriorated significantly below the peak value recorded during the tests. In all cases, the reduction in in-plane shear resistance was such at the time the tests were stopped, that the specimens exhibited load capacities which varied between 1/4 and 1/2 of peak resistance. Due to the difficulty in predicting maximum load response for a cycle at a given displacement target, it was difficult to impose a narrower range of in-plane shear strength reductions as a criterion for ending the tests. The consequence of this variability in the criterion to end the tests is that the peak displacements (Δ_{max}) recorded during the tests do not represent any consistent definition of deformation capacity. A more appropriate measure of the ability of the walls to deform inelastically is discussed later in this chapter.

All tests were carried out to drifts that exceeded 1% of masonry height, and in some cases (Specimens 8 and 12), peak drift ratio approached 2%. Even though these peak drifts cannot be taken as a consistent set of deformation capacities, it is nonetheless interesting to notice the trends that the data suggest. Both peak drift and the ratio of lateral load at peak drift to peak lateral load ($V_{\Delta,max}/V_{max}$) for the specimens with the larger amount of horizontal reinforcement (Wall Specimens 8, 10, and 12) exceeded those for the specimens with the smaller amount of horizontal reinforcement (Specimens 2, 4, and 6) at all aspect ratios (0.5, 0.7, and 1.0). This trend suggests that the larger amount of horizontal reinforcement allowed the walls to retain more of their lateral load capacity over a broader range of deformations. This property, usually defined as ductility or toughness, is investigated in greater detail in this chapter.

The in-plane global displacement data for all wall tests was corrected for an extraneous displacement component introduced by the testing system. Due to excess tolerance in the force actuator used to impose the in-plane drift histories, there was a region in the displacement range of the tests during which the force actuator exhibited flexibility that was of the same order of magnitude as that of the wall specimens. This phenomenon occurred when the force actuator passed through its neutral position (i.e. zero force and displacement position) as it unloaded from one direction and began loading in the opposite direction. This compliance of the testing system (in the region of low lateral forces) introduced an extraneous displacement component in the measured in-plane global displacement history, but this displacement component was very small and did not exceed much over 1 mm (0.04 in.) in any of the tests. This displacement is of little consequence to all aspects of these tests except initial in-plane stiffness of the walls. Because initial stiffness (i.e. lateral stiffness of the walls prior to any visible damage) was one of the objectives of this program, it was necessary to correct the data. These corrections made it necessary to characterize the stiffness of the test setup in the in-plane lateral direction, and to extract the unwanted "testing system" displacement from the in-plane global displacement histories.

After the data for all wall tests was processed, it was determined that there was a measurable amount of sliding between the top and bottom surfaces of the masonry panels and the adjacent header and footer beams. During initial stages of the shear wall tests, these displacements were present because of the manner in which the vertical reinforcement detail in the header and footer beams was constructed. As noted in Chapter 3, the research plan called for the bars to be inserted into sleeves in the header/footer beams and anchored by means of steel plates and nuts embedded in high-strength grout plugs within the header and footer beams. The portion of the vertical bars in the sleeves that led to the grout plugs was supposed to be filled with high-strength grout (or a cementitious material of equivalent strength), in order to provide stiff and strong anchorage for the vertical bars in the header and footer beams.

The above procedure was verified in the shear wall tests of Series 1, but, as noted in Chapter 3, it was not followed in connecting the headers and footers of Wall Specimens 2, 4 and 6, and the footers of Wall Specimens 8, 10, and 12. Thus, the vertical bars for the shear wall specimens in Series 2 could not develop dowel resistance until the masonry panels had

translated relative to the footer beams, and in some cases the header beams, enough to overcome the tolerance between the sleeves and the rebar. In most cases, the effective tolerances were small (less than 2.5 mm or 0.1 in.) and the associated displacements did not affect the shear wall tests except for the initial stages (i.e., prior to the FME).

Sliding displacements after the initial stages of the shear wall tests were larger. These displacements were afforded by inelastic deformations of the rebar acting as dowels, and there is evidence of yielding in the vertical rebar strain histories (see Chapter 7). However, regardless of their magnitude, the measured global in-plane lateral displacement histories were not corrected to remove the sliding displacement components. The general topic of sliding displacements is addressed in more detail in Chapter 7. In the present study, it was decided not to correct the measured global in-plane displacement histories to remove the sliding component. This decision was due, in part, with the fact that the tests were controlled using the displacement signals with the sliding components. Furthermore, as noted in Chapter 7, there is insufficient displacement data to correct (or replace) the in-plane lateral displacement histories for all wall tests. Finally, it is believed that some sliding between masonry walls and foundations or floor slabs may be present anyway in the seismic response of masonry buildings.

6.2 Force-Displacement Response

The histories of the in-plane shear forces applied to the masonry shear walls are plotted in Fig. 6.2.1-6.2.6. The force histories give a clear indication of the deterioration in shear force capacity, and, once again, the heavily reinforced walls (8, 10 and 12) demonstrate somewhat less deterioration of shear force capacity with drift than do the lightly-reinforced walls (2, 4, and 6). However, height-to-length aspect ratio had an even larger impact on shear force deterioration, with the walls with the lowest aspect ratios ($H/L = 0.5$) demonstrating the most stable response and the walls with the highest aspect ratios ($H/L = 1$) being the least stable.

Peak shear forces are summarized in Tables 6.2.1 and 6.2.2 for positive and negative loading directions, and the average forces for the two loading directions are given in Table 6.2.3. Average peak shear forces are plotted against aspect ratio in Fig. 6.2.13, and against horizontal

reinforcement ratio in Fig. 6.2.14. These tables and figures indicate that, except for Wall Specimen No. 8, shear force capacities decrease with increasing aspect ratio and increase with increasing horizontal reinforcement ratio. Tables 6.2.1-6.2.3 also indicate some randomness in the displacement at peak shear strength, with some specimens like Wall No. 8 attaining peak strength very early in the test (i.e. at a drift equal to 0.2%), while others like Wall No. 12 attained peak strength towards the end of the test (i.e. at a drift equal to 1.1%).

Force-displacement relations are given in Fig. 6.2.7-6.2.12 for all six tests of specimens with bed joint reinforcement. For each wall, two plots are given, one for the initial elastic cycles (i.e. before the FME), and a second one for the subsequent inelastic (post-cracking) cycles. From these force-displacement relations, it is noted that most of the shear walls, particularly the long walls (H/L=0.5) responded to the cyclic drift histories in a stable manner. For all specimens, the initial response was approximately linear and characterized by large stiffnesses. The force-displacement hysteresis curves widened as peak displacement increased, thus, the shear walls were able to dissipate energy by hysteresis. For the long walls (Fig. 6.2.7 and 6.2.10), the hysteresis loops strongly resemble ideal elastoplastic behavior, and these walls also had little deterioration of shear strength over a wide range of imposed drifts.

The intermediate and short walls demonstrated "pinching" behavior, i.e. reduction in unloading stiffness at low lateral load levels. It can be observed in Fig. 6.2.7-6.2.12 that deterioration of post-peak strength and pinching of the hysteresis loops became more pronounced with increasing height-to-length aspect ratio. The walls with the lowest aspect ratio (Wall Specimens 2 and 8) experienced a reduction in peak resistance of about 25%, followed by subsequent stabilization and a slight increase in resistance. The responses of the other walls were marked by a more rapid post-peak decrease in load resistance. However, none of the walls failed suddenly, and all specimens were tested at least until the peak resistance for a given group of cycles dropped below 75% of maximum peak resistance.

The increase in horizontal reinforcement from a ratio of 0.056 to 0.10% is seen to improve both peak strength, and decrease post-peak deterioration. The improved strength characteristics are most clearly evident for the intermediate (H/L=0.7) and slender (H/L=1) walls. However, even the long walls seem to have benefitted from the increase in horizontal

reinforcement (Fig. 6.2.7 and 6.2.10). Some of these enhancements can be noted by comparing Fig. 6.2.8 and 6.2.11 for the intermediate walls, and Fig. 6.2.9 and 6.2.12 for the slender walls. The improvement is not only evident as peak displacement amplitude increases from one set of cycles to another, but also during the stabilization cycles when three cycles with identical drift demands.

6.3 Force-Displacement Envelopes

Force-displacement envelopes were produced for all wall tests by collecting the force-displacement coordinate pairs for which displacements exceeded the previous maximum displacement. The resulting envelopes had an irregular appearance arising from the sudden changes imposed by the drift history. In order to "smooth" the force-displacement envelopes, an 11-point moving average was applied to the force history, and the resulting envelopes are plotted in Fig. 6.3.1-6.3.6. The envelopes are grouped by horizontal reinforcement ratio in Fig. 6.3.1-6.3.2, and by aspect ratio in Fig. 6.3.3-6.3.5.

The force-displacement envelopes indicate that the responses of the wall specimens were essentially linear during the early cycles of the tests, i.e. up to the FME. Once the specimens were deflected beyond the displacements that produced the vertical cracks, wall response to the imposed drifts became highly nonlinear. The envelopes (Fig. 6.3.1-6.3.2) also indicate that, in general, peak lateral resistance decreased markedly with increasing aspect ratio. However, this trend was not as apparent in the post-peak range. Horizontal reinforcement ratio did not have as pronounced an effect on peak lateral load resistance as did aspect ratio, even though the walls with larger horizontal reinforcement ratios (8, 10, and 12) developed slightly larger strengths (Table 6.2.3) than did the ones with lesser amounts of horizontal reinforcement (2, 4, and 6). In contrast, horizontal reinforcement ratio did appear to have a marked influence on the ability of the masonry walls to maintain peak load resistance over a large range of drifts.

The ability of a structural element to maintain peak load resistance over a large range of deformations is a measure of the "toughness" of the element. One way of quantifying the toughness of a structural element is through a parameter known as deformation capacity (Δ_u) which represents the ability of a yielding system to deform inelastically while maintaining most

of its load capacity. Another manner for quantifying toughness is through measures of energy dissipation capacity, and this parameter is discussed in section 6.6 in relation to the response of the shear wall specimens to the simulated seismic drift tests.

The deformation capacities of the shear wall specimens (Δ_u) were obtained from the force-displacement envelopes as that displacement at which in-plane shear force capacity had decreased permanently to less than 75% of the maximum shear force registered for a given wall in a given loading direction. The capacities Δ_u and the corresponding drift ratios Δ_u/H are given in Table 6.3.1, and they are plotted against aspect ratio and reinforcement ratio, respectively, in Fig. 6.3.6 and 6.3.7. In Fig. 6.3.3, the long walls (Nos. 2 and 8) are seen to undergo reductions in lateral load capacity below 75% of the maximum load capacity early in the tests, only to exceed the 75% margin at larger displacements. Consequently, deformation capacity Δ_u was not deemed to have been attained until the load resistance of the walls dropped permanently below 75% of the current maximum load.

The deformation capacities, averaged in both loading directions, shown in Table 6.3.1 exceed a drift ratio of 0.75% in all cases. In Fig. 6.3.7, horizontal reinforcement ratio is seen to have a modest and consistent beneficial effect on deformation capacity: Increases in deformation capacity of 17, 13 and 66% were obtained, respectively, for walls with aspect ratios of 0.5, 0.7, and 1 as ρ_h was increased from 0.056 to 0.11%. No consistent trend in deformation capacity is seen for aspect ratio (Fig. 6.3.6).

6.4 First Major Event (FME)

The first major event (FME) in all tests of Series 1 and 2 comprised vertical cracking of the top course of masonry at the interface between ungrouted and grouted masonry. In some cases these cracks propagated through head joints, while in others they propagated through the concrete masonry units. This cracking marked the first instance of outward damage to the masonry walls, beyond which displacement the walls continued to develop additional cracks. The FME also served to delineate elastic and inelastic behavior for the specimens. Consequently, the definition of the FME, and the corresponding shear forces and in-plane lateral displacements are of great importance.

Three methods were investigated for determining the first major event (FME) in the response histories of the six masonry shear wall specimens. The first method for defining the FME was the same technique used during the shear wall tests. The FME was deemed to have occurred when the first vertical cracks were observed visually in a given loading direction. The shear force and displacement, as well as the Point (integer count for the response histories), at which the first visible cracking was noted served as the coordinates for the FME and were recorded. These values are given in Table 6.4.1 for each loading directions, as well as the averages for both loading directions. It was initially assumed that FME forces and displacements defined on the basis of first visible cracking would not be as accurate as those defined using analytical techniques, since cracks may have formed prior to becoming visible. Also, during the simulated seismic drift tests, the wall specimens were checked for cracks only at the peak displacements for each cycle.

The second method for defining the FME utilizes the limit of proportionality of the smoothed force-displacement envelopes. The limit of proportionality is taken to represent the onset of damage to the masonry walls due to the cracks that represent the FME. The proportional limit is defined as the lateral load and displacement which mark the first significant departure from a nearly linear force-displacement relationship in each loading direction. These values are summarized in Table 6.4.2 for all six shear wall specimens, as well as the average forces and displacements in both loading directions.

The third method identifies changes to the stiffnesses of the shear walls as by-products of the FME. Thus, forces and displacements at the first significant decrease in wall lateral stiffness serve to represent the FME. The stiffnesses of the wall specimens were defined as the ratios of lateral load to lateral displacement for each point in the force-displacement envelopes, and these stiffnesses were plotted against the displacements from the force-displacement envelopes to define stiffness envelopes (Fig. 6.4.1-6.4.6). The stiffness envelopes were scanned visually to identify the first significant drop in stiffness (i.e., beyond which stiffness drops markedly and consistently for the remainder of the load history), and thus identifies the FME. The corresponding forces and lateral displacements representing these stiffness changes in each loading direction are given in Table 6.4.3.

Upon comparing the shear forces obtained using the three techniques for defining the FME, it can be seen that there are no significant differences. Upon comparing the FME displacements, it can be noted that the "first visible cracking" and the "proportional limit" techniques give similar values. The only significant difference is the FME displacement for Wall Specimen 4, for which "first visible cracking" value is 33% larger than the "proportional limit" value. The displacements obtained using the "stiffness change" technique, however, are consistently smaller than those obtained using the other two techniques.

On the basis of the observations above, the "first visible cracking" technique was deemed the most appropriate for defining the FME. First, the "first visible cracking" technique was found to be consistent with the "proportional limit" technique, and the "stiffness change" technique was found to be susceptible to numerical instability (i.e. division by zero or small numbers). Second, FME displacements defined using "first visible cracking" were used during the tests to define all of the seismic drift targets. Third, the FME defined from "first visible cracking" comprises a specific Point in the response histories, whereas the other two techniques identify coordinates in the force-displacement and stiffness envelopes only.

Shear forces at first cracking (i.e., "first visible cracking") are plotted against aspect ratio in Fig. 6.4.7 and against reinforcement ratio in Fig. 6.4.8. These plots clearly indicate that there is a strong and consistent trend in cracking shear strength with aspect ratio. Cracking shear strength is seen to decrease in a linear manner with increasing aspect ratio. It is equally apparent that cracking shear strength is independent of horizontal reinforcement ratio. Conceptually, it is difficult to justify any correlation between horizontal reinforcement ratio and shear strength at first cracking, and the experimental data bear this out. The only exception is the cracking shear strength for Specimen 12 (ρ_h = 0.056%), which is significantly higher than that for Specimen 6 (ρ_h = 0.11%) and could be attributed to horizontal reinforcement ratio. However, even in relation to aspect ratio, the cracking strength of Specimen 6 seems to be low.

6.5 Initial Stiffnesses

Initial stiffness is a property that is difficult to measure accurately. It cannot be obtained with precision from the stiffness histories defined in section 6.4, because it has been determined that

there was sliding present in the displacement data used to define these stiffness envelopes, as well as the force-displacement envelopes. It was noted earlier that the shear wall tests in Series 2 (section 6.1) included sliding in the response of the specimens to the imposed in-plane drift histories. This sliding response, which was not observed for the shear wall specimens in Series I, was due to improper connection between vertical reinforcing bars and the header and footer beams. These sliding displacements are included in the measured global in-plane lateral displacement history even during early cycles before the masonry walls showed any sign of cracking. Consequently, stiffnesses inferred from such measurements cannot be compared with estimates that do not include sliding displacement, nor can they serve as true estimates of the inherent resistance of the masonry panels to lateral movement.

For the previous series of shear wall tests in this program, the force-displacement envelopes were used to obtain estimates of the initial stiffnesses of the shear walls (Schultz, 1994). All force-displacement data up to 40% of proportional limit for each shear wall was used for linear regression analysis. The slope of the lines defined by linear regression were taken as the initial stiffnesses, and these inferred stiffnesses were found to compare well with analytical estimates.

In the present study, an alternative technique was used to infer the initial stiffnesses of the masonry shear walls. The measured displacements obtained from the LVDT's attached to the masonry panel near the top and bottom of the panels (i.e. instruments TOPHOR and BOTHOR, respectively, as noted in Chapter 4) capture most of the lateral deformation of the masonry panels. For a given value of shear force V on the masonry wall, the lateral deformation is equal to the relative lateral displacement Δ_o between these devices (i.e. the difference between the displacement measured by TOPHOR and BOTHOR). Initial stiffness thus, is calculated as the ratio of shear force to relative lateral displacement, or $K_o = V/\Delta_o$.

The only problem with the procedure described above is that the relative lateral displacement Δ_o does not span the entire height of masonry, so the stiffness K_o only represents behavior between the targets for the LVDT's (TOPHOR and BOTHOR). However, it is shown analytically in Chapter 8 that the calculated relative lateral displacement for an elastic panel between the LVDT target points Δ_o is equal to 86% of the relative displacement between Δ the top and bottom of the masonry (i.e. $\Delta_o = 0.86\Delta$). This relationship holds as long as the targets

are located $H/14$ from the top and bottom edges of the masonry. Consequently, the calculated stiffness for each panel K is equal to 86% of the stiffness K_o between the LVDT targets ($K = V/\Delta = 0.86V/\Delta_o = 0.86K_o$).

One of the features noted in section 6.2 regarding the measured force-displacement data at early stages of the tests is the pinching of the force-displacement relations (Fig. 6.2.7a-6.2.12a). This reduction in stiffness, which is believed to be due in part to the sliding response of the masonry along the interfaces with the header and footer beams, precludes the use of linear regression on force-displacement data from early stages of the tests to infer the initial stiffnesses of the shear wall specimens. As an alternative, the effective stiffness for the largest cycles in the initial uncracked and undamaged state of the walls was used. These cycles were taken as those for which peak load did not exceed 50% of the load at the FME, and the cycle effective stiffness was computed as the slope of the line segment connecting the force-displacement coordinate pairs at instances of peak positive and peak negative response. The relative lateral displacements were defined using the measured displacement of the LVDT's attached near the top and bottom of the masonry, but with a finite offset (~$H/14$). Following the discussion in the preceding paragraph, the stiffness between top and bottom of the masonry was taken as 86% of the previously described slope.

Details of the calculation of the inferred initial stiffnesses are summarized in Table 6.5.1. Initial stiffnesses are also plotted in Fig. 6.5.1 against aspect ratio and in Fig. 6.5.2 against horizontal reinforcement ratio. This data shows a clear correlation between initial stiffness and aspect ratio, with the longer walls (H/L=0.5) having the largest stiffnesses and the shortest ones (H/L=1) having the smallest initial stiffnesses. The decay in initial stiffness as H/L increases from a value of 0.5 to 0.7 is much greater than the reduction in stiffness between aspect ratios of 0.7 and 1.0. This behavior can be represented analytically, and details regarding this issue are included in Chapter 8. Finally, it is worth noting that horizontal reinforcement ratio does not appear to have any consistent influence on initial stiffness (Fig. 6.5.2). This observation supports the notion that there was no significant damage to the walls during those early cycles from which data was used to calculate initial stiffnesses.

6.6 Energy Dissipation Capacity

Energy dissipation capacity is the second of two measures of toughness, the other being deformation capacity (section 6.3). Cumulative energy dissipation was evaluated by integrating each cycle of the force-displacement history and accumulating these areas. These values were then normalized by one-half of the product of the force and displacement at the FME to define the energy dissipation index, and thus account for the varying strengths and stiffnesses of the walls. Cumulative energy dissipation indices at the end of each cycle were paired with the current maximum displacement to define an energy dissipation-peak displacement relation (Fig. 6.6.1-6.6.5). The "stepped" appearance of these plots is due to the energy that is accumulated in cycles D2, D3, S1, and S2 in each cycle group. Since cumulative energy dissipation is plotted against previous maximum displacement, the horizontal ordinate does not change as the vertical one increases.

The energy dissipation indices (Fig. 6.6.1-6.6.5) exhibit a nearly linear relation between dissipated energy and peak displacement demand in all walls. Cumulative energy dissipation indices are also given in Table 6.6.1 at lateral displacements equal to 0.25, 0.5, 0.75, 1.0 and 1.25% of wall height, as well as at peak displacement (Δ_{max}) for each shear wall specimen.

In relation to the energy dissipation indices given in Table 6.6.1, it is noted that at early stages of the simulated seismic drift tests (i.e. drift ratios equal to 0.25% and 0.5%), all shear wall specimens exhibited small energy dissipation indices, and these were about same for all walls. By the time drift ratio had increased to 0.75%, the long walls were beginning to indicate a greater capacity to dissipate energy by hysteresis. It also appears quite evident that increasing the aspect ratio decreases the ability for the wall to dissipate energy.

What is most striking about the energy dissipation data (Table 6.6.1), as well as the energy dissipation envelopes (Fig. 6.6.1-6.6.5), is that horizontal reinforcement ratio had no significant effect on energy dissipation capacity. Because the walls with more horizontal reinforcement had larger deformation capacities (section 6.3) and less strength deterioration (section 6.2), they were able to endure more cycles of simulated seismic drift. Consequently, the energy dissipation indices at peak displacement (@ Δ_{max}) for the walls with ρ_h = 0.11%

(Wall No. 8, 10, and 12) greatly exceed those for the walls with ρ_h = 0.056% (Wall No. 2, 4 and 6) due to the larger number of drift cycles during which to accumulate hysteretic energy.

7. LOCAL RESPONSE TO CYCLIC LOADING

A wide array of instruments and transducers were used to measure the local response of the partially-grouted shear wall specimens during the cyclic load tests. These instruments and their locations are described in Chapter 4, and they include strain gages bonded the vertical (VRB) and horizontal reinforcement (HRG), linear strain transducers (LST) adhered to the south face of the shear wall specimens, and linear voltage displacement transducers (LVDT) attached to various target locations on the shear wall surfaces. There instruments were used to measure reinforcement strains, masonry strains (local and gross) and wall displacements. These measurements are used in the following sections to describe the local response of the partially-grouted shear wall specimens to the cyclic loading.

7.1 Vertical Reinforcement Strains

Strains in vertical reinforcement were monitored using electrical resistance strain gages. The strain gages (VRB) and installation procedure are described in Chapter 4, and gage designations and locations are summarized in Fig. 4.6. All gages on vertical reinforcement were placed on the bars near the top or bottom of the masonry. The selection of this location was predicated on the assumption that the largest strains in the bars would occur near the bed joints at the top or bottom edges of the masonry panels, and that these bed joints would be the first horizontal locations to crack and develop sizable crack widths. Both vertical bars in the wall jambs at each location were instrumented with one strain gage.

A summary of the strain gage histories is provided in Tables 7.1.1 to 7.1.6, respectively, for Wall Specimens 2, 4, 6, 8, 10 and 12. The summary tables include the data points and drift ratios at which the gages reached three different strain targets. These targets include the measured yield strain of 0.00237 and peak strain response, as well as the limit of reliable strain measurement. Strain data is deemed to be unreliable if the bar ruptures, or if the gage, bond (between gage and bar) or lead wire fail. The latter two are believed to be the most common occurrences, and these are characterized in the strain histories as highly erratic trends accompanied by large, sudden changes in strain. Even though several gages (usually 1 to 3 gages per shear wall specimen) are deemed to have failed during the tests, post-test

disassembly of the specimens indicated that none of the bars ruptured or suffered extensive post-yield straining.

Drift is reported for each strain target at the instant that the strain in question was attained. A second drift value representing the previous peak drift experienced by the wall is also reported if it exceeds current drift (i.e., the first value reported). That the wall underwent a larger value of drift before the current strain limit was attained can be explained by differences in response along the two loading directions (e.g., current strain limit in tension when the previous peak drift occurred while the gage was in compression), or other peculiarities of local strain behavior in inelastic, inhomogeneous, hysteretic systems.

Typical strain gage histories are plotted in Fig. 7.1.1 to 7.1.6 for Wall Specimens 2, 4, 6, 8, 10 and 12. Due to space limitations, data is shown for only two gages per specimen. Data for one gage at the top of each specimen, and for another at the bottom, are reported. The strain histories are plotted as the horizontal ordinate against the corrected TTF lateral displacement. The strain-displacement histories (Fig. 7.1.1-7.1.6) exhibit features typically found in reinforcing bars that are loaded in fully-reversed cycles of load. These features include small strain amplitudes at early stages of the tests (Fig. 7.1.1a) as cracks initiate and grow with the load history, thus mobilizing straining of the rebar. The strain-displacement cycles are also slightly asymmetric about the horizontal axis (Fig. 7.1.2), as loading in one direction produces tension strain increments and loading in the other direction produces smaller increments of compression strain. In the tension loading direction, the rebar alone is responsible for resisting external load, whereas in the compression direction, the masonry contributes most to load resistance. Lastly, the strain-displacement cycles for some gages (Fig. 7.1.2a and 7.1.4a) display a continuous increase in permanent deformation as the test progresses, thus serving to indicate the degree of inelastic behavior.

One feature of vertical rebar response to cyclic loading that was common to all wall specimens is yielding and inelastic straining of the reinforcement. On the average, five of the eight strain gages in each test measured strains that exceed the strain at first yield for the reinforcement (0.00237). Furthermore, post-yield strain demand was moderately large for those gaged locations, with strain ductility factors as large as 7 (Tables 7.1.1-7.1.6). It is also worth

noting that strains at the top of the bars were consistently larger than those at the bottom, and exterior bars attracted larger strains than interior bars.

The last observation in the preceding paragraph is not surprising, as exterior bars have a larger moment arm to the center of rotation of the wall than interior bars. However, an explanation for the difference in strain demand between top and bottom bars is somewhat more elusive. It is possible that the weight of the masonry may have assisted the bottom bars by offsetting some of the tension strain demand from overturning. However, the weight of the masonry is quite small relative to the magnitude of external loading. Another possible explanation may be related to the greater amount of damage to the top course of masonry than the bottom course. Thus, it is postulated that there is a more efficient transfer of stress from rebar to a more competent masonry from the base of the wall to the bottom gage than there is along the damaged masonry at the top of the panel to the top gages. The net result is a greater reduction of strain demand at the base of the wall over the demand at the top.

The observation regarding the yielding of vertical bars is interesting in its own right. The vertical reinforcement in the masonry shear wall specimens was not expected to yield at all during the tests. In the document summarizing the NIST masonry research plan, Schultz (1994) describes the design of the shear wall specimens, which had as one of its objectives the design of shear-critical walls. So, the specimens were proportioned and reinforced to fail in shear, and the lateral force at nominal flexural strength was estimated to be at least twice the lateral force at nominal shear strength. Furthermore, the partially-grouted shear wall specimens tested in the first phase of this program, Series 1 (McGee et al., 1998; Schultz, 1994), indicated no yielding of the vertical reinforcing bars, even though the yield strain was approached by some bars in some of the previous tests. It is equally surprising that the peak loads for the walls in Series 1 were very similar to those of the walls in the present series, Series 2. So, the difference in strain demands for the two series of tests cannot be explained on the basis of load alone.

The specimens in Series 2 cracked and were damaged in a different pattern than the specimens in Series 1, and this difference may serve to explain the differences in vertical rebar strain behavior. Because all horizontal reinforcement in the Series 1 specimens was concentrated in a

single bond beam at mid-height, vertical cracking between grouted and ungrouted masonry along the two jambs controlled wall behavior. These cracks extended from the top of the wall to the bond beams and they effectively separated the jambs from the rest of the masonry. Because this cracking rendered the grouted, reinforced jamb elements quite flexible, less of the external loading was resisted by these elements, and sliding friction between the header beam and the top of the remaining masonry made up for any associated decrease in wall resistance to in-plane lateral loads. For the specimens in Series 2, horizontal reinforcement held the wall together for a longer displacement range, thus the reinforcement attracted more stress and strain than those observed in the specimens of Series 1.

7.2 Horizontal Reinforcement Strains

Strains in horizontal reinforcement were monitored using electrical resistance strain gages mounted on the longitudinal wires of the welded grids as described in Chapter 4. Strain gage locations and designations (HRG) are summarized in Fig. 4.7. All wire grids were instrumented with at least four strain gages, one near each end of the two longitudinal wires of grid. The intent of this scheme was to capture those grid strains that are mobilized by vertical cracks which form along the interior boundary of the grouted cell on either jamb of the specimens. Additional gages were installed on longitudinal wires in the middle half-length of the grids for those grids in top and bottom bed joints of the middle course of masonry. These gages were included to capture strains associated with inclined cracks through the center of the wall. It is noted that the first digit of the strain gage designations include the number of the masonry course on which the bed joint rests (e.g. 1 for the first course and 6 for the sixth course), and the second digit serves as an indication of the nearest masonry face (N for the north face and S for the south face). The other digits refer to the location along the plane of the wall (i.e. E for east, W for west and C for center). Thus, the gages were distributed in pairs which should read similar strains (e.g. 6NE and 6SE).

A summary of the strain gage histories is provided in Tables 7.2.1 to 7.2.6, respectively, for Wall Specimens 2, 4, 6, 8, 10 and 12. The summary tables include the data points and drift ratios at which the gages reached two limiting conditions which are labeled, respectively, as the tension threshold and the first yield condition. Drift is reported for each strain target at the

instant that the strain in question was attained, and following the procedure described in the previous section, a second drift value representing the previous peak drift is also reported if it exceeds current drift. The tension threshold is defined as the condition when the strains measured by the gages reaches a tension strain equal to 0.0002 (200 με). At this value of strain, the longitudinal wires would have developed a stress of slightly less than 41.4 MPa (6 ksi), below which the magnitude of loading can be considered unimportant. Another consideration in selecting the strain for the tension threshold has to do with the character of the strain histories: For most gages, the initial portion of the record (at strains less than 0.0002) corresponds to a quiescent period when compared with the subsequent portion of the record (at strains larger than 0.0002) in which the strains rapidly increase in magnitude.

The first yield condition is defined as the first instance in which measured strain exceeds the nominal yield strain which is taken as 0.00280 (2800 με) for the 9-Gage wire (Wall Specimens 2, 4, and 6) and 0.00270 (2700 με) for the 5-Gage wire (Wall Specimens 8, 10 and 12). These nominal yield strains are defined, respectively for the 9-Gage and 5-Gage wire, as 80 and 90% of the yield strain determined from the 0.02% offset method in the wire tension tests (Chapter 3). The full yield strains were not used because the wires used to fabricate the welded grids were not very ductile, and the corresponding stress-strain curves did not exhibit well-defined yield points. On the basis of the stress-strain curves presented in Chapter 3, it was determined that for the 9-Gage and 5-Gage wires, respectively, 80 and 90% of the 0.02% offset yield stress more closely represents the limit of proportionality.

In addition to the two previously described conditions, the data point and drift ratio at the limit of reliable measurement is also included in the summary tables (Table 7.2.1-7.2.6). The limiting condition is defined using the same criterion described in the preceding section for vertical reinforcement. That is, strain data is deemed to be unreliable if either the wire ruptures, or the gage fails, or bond between the gage and wire is lost, or lead wire is severed. As noted in Chapter 5, there is aural evidence of frequent wire grid failures. However, these failures cannot be identified in the strain history. The signal conditioning units for the gages on the wire grids were set to record strains as large as +/-0.05 (50,000 με), except for Wall Specimen 2 for which a strain range of +/-0.005 (5,000 με) was used. Furthermore, high-elongation gages were used along with the appropriate adhesive and curing procedure. Yet, most strain

gage installations that were strained beyond the 0.005 to 0.01 (5,000 to 10,000 με) strain range failed well before the wire reached its tensile breaking strain.

It is worth noting that even though the first instance of yielding listed in Tables 7.2.1-7.2.6 may be in either tension or compression, most gages responded primarily in tension. This was so because the straining mechanism for horizontal reinforcement was driven by the opening of cracks in the masonry. As cracks initiated and the corresponding widths grew with increasing loads, the horizontal reinforcement was strained from an initially unloaded state in cycles of increasing tension strain. Consequently, the reinforcement accumulated permanent tensile deformations during the cyclic load tests.

Typical strain gage histories are plotted in Fig. 7.2.1 to 7.2.6 for Wall Specimens 2, 4, 6, 8, 10 and 12. Due to space limitations, data is shown for only four gages per specimen. Data for one gage each at a top corner and bottom corner of each specimen are shown, as well as gages in the center of the wall and in the mid-height region of one of the jambs. The strain histories are plotted as the horizontal ordinate against the corrected TTF lateral displacement. The strain-displacement histories (Fig. 7.2.1-7.2.6) share many similarities with those for the vertical reinforcing bars, including small strain amplitudes at early stages of the tests, asymmetry about the horizontal axis, and strain cycles that display a continuous unidirectional increase in permanent tensile deformation. In addition, the gages on horizontal bars exhibit sudden increases in strains (e.g. Fig. 7.2.1) which are most likely the result of a masonry crack forming in the vicinity of the strain gage. As a result of these strain "jumps", some gages on horizontal reinforcement generate very large strains, and the failure of the gage installations, as well as the rupture of some of the grids occurred during these sudden strain increases.

In addition to the summary tables and the strain-displacement histories, drift ratios corresponding to the strains at the tension threshold and at first yield are summarized graphically on an outline of the masonry walls in Fig. 7.2.7-7.2.12. These sketches show views of the north face of each wall on which are superimposed the drift ratios corresponding to the strains at the two limiting conditions for each gage location. At each gage location two drift ratios are given, one each for the north (N) and south (S) gages. The drift ratios correspond to the largest drift undergone by the wall specimens in the given loading direction

when the limiting strain condition was attained. Gages for which the limiting condition was never attained are denoted as "*NA*", and dashed lines indicate gages which were not functional. In addition, part of the strain histories in some of the gages became unreliable when the limiting condition was reached, but it is evident that the grids underwent large strains subsequently. For these cases, the drift at the strain limit is taken as an estimate and is shown in italics.

Review of Fig. 7.2.7-7.2.12 indicates that most of the gaged locations saw significant drifts (i.e. the tension threshold was reached), and yielding began at early stages of the tests and was well-distributed throughout the wall specimens. More careful evaluation of Fig. 7.2.7-7.2.12 indicates that top and bottom corners of the wall specimens underwent yielding in all cases. Also, for the short wall specimens (6 and 12), as well as the intermediate wall specimens (4 and 10), the central portion of the masonry panels incurred significant straining of the horizontal reinforcement in the cyclic load tests. The long wall specimens (2 and 8) did not see much straining of the wire grids in the center of the panels. The last two observations are supported indirectly by the pattern of crack growth and formation in the tests (Chapter 5).

Other significant trends are present in grid strain data, but these are not as obvious as those in the preceding paragraph. To uncover these trends, composite drift indices were computed from the data in Fig. 7.2.7-7.2.12 for both limiting strain conditions. The composite drift index for each strain condition (tension threshold and first yield) is defined as the average drift associated with one of two populations of gages. For the gross composite index, all of the functional gages were considered, whereas for the net composite index, only the functional gages that achieved the limiting strain condition were used. Furthermore, for the gross composite drift index, gages with nil readings (i.e. dashed lines) were assumed to have a drift ratio equal to zero, whereas for the net composite index these gages were not considered.

The composite drift indices are listed in Table 7.2.7 for Wall Specimens 2, 4, 6, 8, 10 and 12. On the basis of these indices, the following observations are drawn. Considering either the gross or the net composite drift index, the amount of horizontal reinforcement is not seen to have a strong influence on the drift at the tension threshold. For example, the composite drift indices, particularly the net values, for Wall Specimens 2 and 8 are nearly identical, as are those of Wall Specimens 4 and 10. The only exception is Wall Specimen 12 which has rather

small composite drift indices at the tension threshold. However, height-to-length aspect ratio does appear to have a significant effect on the drift at the tension threshold, with the long specimens (2 and 8) displaying the smallest drifts, and the drifts at the tension threshold increasing seemingly as wall length decreases (i.e. increasing aspect ratio). These trends for the net composite indices are illustrated in Figs. 7.2.13 and 7.2.14.

The observations described above regarding the tension threshold follow logically the idealized behavior of the masonry wall specimens. The tension threshold is most closely associated with initial cracking of the wall, and the amount of horizontal reinforcement should not affect this behavior. Wall length affects the amount of lateral force transferred by horizontal shear from the masonry to the header/footer beams. Some of this stress is resisted by dowel action of the vertical bars, and the long walls generate more horizontal resistance and, therefore, larger dowel force demands for these bars. Under such conditions, long walls should develop vertical cracks and transfer stress to the wire grids earlier in the load history, as is noted in Table 7.2.7. Composite drift indices at first yield, particularly the net values (Fig. 7.2.13-7.2.14), increase with increasing aspect ratio and horizontal reinforcement ratio. Thus, the short wall with the greatest amount of reinforcement (Wall Specimen 12) holds out to a considerably larger drift before yielding than does the long wall with the smallest reinforcement (Wall Specimen 2). This trend is very strong according to the data in Table 7.2.7.

The influence of the aspect ratio can be understood in much the same manner it was considered in the preceding paragraphs, with the longest walls yielding first as a result of earlier cracking and more progressive crack growth which drives the wire grid strains. However, the role of horizontal reinforcement seems to be more complex. Certainly, having more horizontal reinforcement crossing a crack restrains crack width which, in turn, limits the magnitude of tension strain in the grids and delays the drifts observed at the tension threshold. Another explanation may have to do with the larger diameters for the longitudinal wire used to fabricate the grids for Wall Specimens 8, 10 and 12. Larger wires do not collect as much axial stress from bond as do smaller wires, assuming that the cross-section and material properties remain fixed. Thus, the smaller wires should collect stress at a faster rate and yield at earlier drifts than the larger wires.

7.3 Masonry Surface (LST) Strains

Masonry surface strains on the south face of the masonry walls were monitored using linear strain transducers (LST) which were mounted directly on the masonry surface as described in Chapter 4. LST locations and designations are summarized in Fig. 4.5, and specific dimensions are listed in Table 4.2. All wall specimens were instrumented with a total of 15 LST's, except for Wall Specimen 2 which had only 14 transducers. Three LST's were used along each jamb to monitor vertical strains in the masonry, and a single LST served to monitor vertical strain at the center of the masonry. The remaining 8 transducers were used to measure strains along the two diagonal directions near the center of the wall, as well as the associated transverse strains (i.e. normal to the diagonal directions).

A summary of the LST strain histories is provided in Tables 7.3.1 to 7.3.6, respectively, for Wall Specimens 2, 4, 6, 8, 10 and 12. The summary tables include the data point and drift ratio at which the gages reached two limiting conditions which are labeled, respectively, as the tension threshold and the compression threshold. The summary tables include the data points and drift ratios at which the transducers reached two limiting conditions which are labeled, respectively, as the tension and compression thresholds. Drift is reported for each strain target at the instant that the strain in question was attained, and following the procedure described in the previous section, a second drift value representing the previous peak drift is also reported if it exceeds current drift. The tension threshold is defined as the condition when the strains measured by the gages reaches a strain equal to 0.0001 (100 $\mu\varepsilon$). This value of strain approaches the tensile capacity of masonry. In addition, the initial portion of most LST strain histories at strains less than 0.0001 is unremarkable in terms of magnitude and variation of strain when compared with the subsequent portion of the record (at strains larger than 0.0001) in which the strains rapidly increase in magnitude. The compression threshold is defined as the first instance in which measured strain in compression first exceeds 0.002 (2000 $\mu\varepsilon$). This value of strain approaches the compression capacity of the masonry.

In addition to the two previously described limiting strain conditions, the data point and drift ratio at the limit of reliable measurement (i.e., if the spring and the post of the LST are no longer in contact) are also included in the summary tables (Table 7.3.1-7.3.6). Also, peak

tension and compression strains in the reliable portion of the LST strain histories are also given in the summary tables. It is noted that while the measured masonry surface strains demonstrate a preferred direction in either tension or compression: Once a test was underway, the cycles of LST strain drift in either the tension or compression,with tension behavior being more common. Consequently, in many of the transducer locations the masonry accumulated permanent tensile or compressive deformations during the cyclic load tests.

Typical LST strain histories are plotted in Fig. 7.3.1 to 7.3.6 for Wall Specimens 2, 4, 6, 8, 10 and 12. Due to space limitations, data is shown for only four LST transducers per specimen. Data for one transducer each at a top corner and bottom corner of the wall specimens are shown, as well as data for one diagonal transducer and one transverse transducer in the central portion of the wall. All strain histories shown are plotted as the horizontal ordinate against the corrected TTF lateral displacement. The strain-displacement histories (Fig. 7.3.1-7.3.6) share many similarities with those for the gages on vertical reinforcing bars and horizontal reinforcing grids, including small strain amplitudes at early stages of the tests, asymmetry about the horizontal axis, and strain cycles that display a continuous unidirectional increase in permanent deformation. As with the strains from gages on horizontal bars, the masonry surface strains measured using LST transducers exhibit sudden increases or "jumps" in strain (e.g. Fig. 7.3.1b and 7.3.2b) which are most likely the result of cracks in the masonry forming within the gage length of the transducers. As a result of these strain "jumps", some of the LST transducers generate strains of very large magnitudes. These strains do not represent actual masonry strain, but rather crack widths averaged over the gage lengths.

Cursory review of the summary tables indicates that few of the LST transducers measured strains that meet the compression threshold criterion defined earlier, but the tension threshold was reached by many of the transducers. For this reason, drift ratios at the threshold tension strain condition and peak tension strain response are summarized graphically on an outline of the masonry walls in Fig. 7.3.7-7.3.12. These sketches show views of the south face of each wall on which are superimposed the drift ratios corresponding to the threshold tension strain condition and the peak tension strain for each transducer location. The drift ratios correspond to the largest drift undergone by the wall specimens in the given loading direction when the

limiting strain condition was attained. Gages for which the limiting condition was never attained are denoted as "*NA*", and dashed lines indicate gages which were not functional.

Review of Fig. 7.3.7-7.3.12 indicates that more than one-half of the instrumented locations experienced the tension threshold condition, and peak tension strain demand varied widely throughout the array of surface strain transducers for each of the wall specimens. The eight LST transducers in the center of the panel indicate widespread tension straining in this portion of the walls. In addition, for those transducers measuring vertical strains along the jambs, if the threshold tension condition was reached early in the tests (i.e., at small drift ratios), then peak strain demand is likely to be very large at that location. This condition seems to correspond to cases where horizontal and/or inclined cracks formed within the gage length of the LST transducers.

Composite drift indices were computed from the data in Fig. 7.3.7-7.3.12 at the threshold tension strain condition for the LST transducers measuring diagonal or transverse masonry surface strains. The composite drift index for this limiting strain condition is defined as the average drift associated with of all of the functional gages (gross) or of all functional gages that achieved the limiting condition (net). For the gross composite drift index, gages with nil readings (i.e. dashed lines) were assumed to have a drift ratio equal to zero, whereas for the net composite index these gages were not considered.

The composite drift indices are listed in Table 7.3.7 for Wall Specimens 2, 4, 6, 8, 10 and 12. On the basis of these indices, the following observations are drawn. Considering either the gross or the net composite drift index, the amount of horizontal reinforcement is seen to have a very modest influence on the drift at the tension threshold condition. For example, the composite drift indices, particularly the net values, for Wall Specimens 2 and 8 are approximately the same. As expected, height-to-length aspect ratio does appear to have a significant effect on the drift at the tension threshold condition, with the long specimens (2 and 8) displaying the largest drifts, and the drifts at the tension threshold decreasing as wall length decreases (i.e. increasing aspect ratio). These trends for the net composite indices are illustrated in Fig. 7.3.14 and 7.3.14.

The observations described above regarding the tension threshold condition appear to be contrary to those observed for the threshold tension condition in the horizontal reinforcement strain histories in the previous section (Fig. 7.2.13 and 7.2.14). However, the composite drift indices for the horizontal reinforcement strains are dominated by horizontal strains along the jambs, with at least 2/3 of the gages on the grids measuring jamb horizontal strain. Yet, the composite drift indices described in the preceding paragraphs focus exclusively on the diagonal and transverse strains in the central portion of the masonry walls. When it is recognized that the composite drift indices for grid strain and masonry strain are monitoring tension activity in different regions of the walls, these two measures can be seen to complement each other and describe the behavior of the walls in an accurate manner. These indices indicate that long walls respond to horizontal tension in the jambs early in the tests, and there is a delay before the tension strains in the central portion of the long walls build up to the threshold tension strain condition.

The combination of the composite indices for grid strains and masonry strains present a clear assessment of the influence of aspect ratio on wall behavior. The behavior of long walls is dominated by vertical cracks at the jambs which arise from accumulating large shear stress resultants over the horizontal distance from one jamb to the next. In contrast, short walls carry lateral loads by means of diagonal compression struts and tension fields, thus, the response of these walls is dominated by intersecting diagonal cracks.

7.4 Gross (LVDT) Strains

An array of LVDT displacement transducers were used to monitor the movement of various points on the masonry surfaces and the testing equipment during the cyclic drift tests. The locations and designations of the LVDT transducers are summarized in Fig. 4.4. Wall specimens 2, 4, 6 and 8 were instrumented with a total of 16 LVDT's, and Wall Specimens 10, 12 and 14 had 17 displacement transducers. The LVDT's were used for measuring deformation of the masonry, i.e., the displacement of one element on the masonry relative to another element, or for monitoring the translation of the wall or testing equipment, i.e., displacement of masonry or testing equipment relative to a fixed reference. The displacements measured by LVDT's that were monitoring deformation were used to compute gross strains

over the gage length of the transducer. Data from a total of ten LVDT transducers were used to compute gross strains along the both jambs of the wall (including the mortar joint along the base of the wall), and the total (average) strains along both diagonal.

A summary of the gross (LVDT) strain histories is provided in Tables 7.4.1 to 7.4.6, respectively, for Wall Specimens 2, 4, 6, 8, 10 and 12. The summary tables include the data point and drift ratio at which the gages reached a threshold tension limiting condition. Drift is reported for this strain target at the instant that the threshold was attained, and following the procedure described in the previous sections, a second drift value representing the previous peak drift is also reported if it exceeds current drift. Threshold tension strain is defined as the condition when the gross strains reached a tension value equal to 0.0001 (100 με). As with the masonry surface strain, this limiting value of tension strain approaches the tensile capacity of the masonry. In addition, peak gross strain, and the data point and drift ratio at the limit of reliable measurement are also included in the summary tables (Table 7.4.1-7.4.6). As with the LST strain histories, it is noted that the measured gross strains demonstrate a preferred direction in either tension or compression, and the cycles of gross (LVDT) strain drift in either direction with tension behavior being more common. By the end of the tests, many transducer locations had accumulated sizable permanent tensile or compressive strains.

Typical gross (LVDT) strain histories are plotted in Fig. 7.4.1 to 7.4.6 for Wall Specimens 2, 4, 6, 8, 10 and 12. Due to space limitations, strain data is shown from only four LVDT transducers per specimen. Data for one transducer each at a top corner and bottom corner of the wall specimens are shown, as well as data for one transducer at the mid-height of a jamb and one diagonal transducer. Gross strain histories are plotted as the horizontal ordinate against the corrected TTF lateral displacement. These strain-displacement histories (Fig. 7.4.1-7.4.6) share many similarities with those measured by the LST transducers and described in the previous section. These features include small strain amplitudes at early stages of the tests, asymmetry about the horizontal axis, and gross strain cycles that display a continuous unidirectional increase in permanent deformation. As with all previous strain measurements, gross strains exhibit sudden increases in strains (e.g. Fig. 7.4.1a and 7.4.2b) which are most likely the result of a masonry cracking within the gage length of the transducers.

The gross (LVDT) strain histories should resemble the masonry surface (LST) strain histories that were recorded at the same location. Quite often, that relation exists, as can be seen in comparing the strain-displacement history for LVDT WVTTOP (Fig. 7.4.3a) with the history for LST ALPHA (Fig. 7.3.3a) for the test of Wall Specimen 6. However, even though the shape of the two strain histories is comparable, there are some differences, the most important which is magnitude of strain. In comparing the two strain histories mentioned above, a difference of about one order of magnitude can be noted, with the masonry surface strain ALPHA being approximately 10 times larger than gross strain WVTTOP measured at the same general location and during the same test. This difference is to be expected as the gross strains are averaged over a longer gage length than are the masonry surface strains, thus minimizing the contribution of the most highly stressed locations. Gage lengths for the LVDT transducers are listed in Tables 7.4.1-7.4.6, and these are many times larger than the 1 in. (25.4 mm) gage length for the LST transducers.

Once it is accepted that the gross strain magnitudes are likely to be very different from masonry surface strains, then the non-correlation that can be observed in the tension threshold data for the gross strains (Tables 7.4.1-7.4.6) and the masonry surface strains (Tables 7.3.1-7.3.6) can be more easily accepted. This observation renders the gross strains useless for determining local strain demands in the masonry. The most appropriate use for this data is to establish a qualitative assessment of the overall deformation demand, and this qualitative assessment can and should be used to verify local strain demands measured by other means.

7.5 Wall Displacements

The remaining LVDT transducers (6 for specimens 2, 4, 6 and 8, and 7 for Specimens 10 and 12) that were not used for monitoring gross strain (Fig. 4.4) served to measure absolute displacement of the masonry wall (TOPCTR, TOPHOR, MIDHOR, and BOTHOR), or absolute movement of the concrete header (SPACER) and footer (BASHOR) beams, or the top crosshead of the TTF machine (XHEAD). The three records monitoring the lateral movement of the masonry (TOPHOR, MIDHOR and BOTHOR) are used to construct displaced profiles of the masonry walls. These displacements (Tables 7.5.1-7.5.8) are used to calculate drift ratios that are shown in Fig. 7.5.1-7.5.6, along with the drift of the header and footer beams

(SPACER and BASHOR) at the first positive peak displacement (D1) of cycle groups D_c, 2 D_c and 3D_c for Wall Specimens 2, 4, 6, 8, 10 and 12.

Displaced profiles at first cracking (D_c) were essentially linear for all specimens, but as displacement demand increases, the profiles become distorted. The distortion assumes two distinct features; it includes reversal or "loss" of displacement at the TOPHOR and MIDHOR locations, and it displays large relative displacements between LVDT transducers TOPHOR and SPACER. The displaced profiles grow progressively more distorted as the displacement demand exceeds 3D_c with LVDT SPACER out-displacing all others, and with LVDT's TOPHOR and MIDHOR eventually displacing into the negative direction.

The behavior of displacements measured using LVDT transducers TOPHOR, MIDHOR and BOTHOR is controlled by the formation of vertical cracks along the jambs. The outer web of the units along the jambs eventually separates from the rest of the wall, and the displacements in the negative loading direction, as jamb and outer web are in bearing, is not fully reversed as the vertical cracks grow very wide. Consequently, these components of displacement cannot be taken as representative of the rest of the masonry, particularly after the vertical cracks are fully developed. It should be noted from Fig. 7.5.1-7.5.6 that this aspect of wall distortion is more severe for the long walls (Wall Specimens 2 and 8) which also displayed the most marked vertical cracking behavior.

The large lateral displacements measured by LVDT transducer SPACER includes sliding between masonry and header beam. When the importance of these displacements was determined (during the test of Wall Specimen 8), an additional LVDT transducer (TOPCTR) was added to the array of instruments to measure the displacement of the top central portion of masonry (Fig. 4.4). The displacements comprising the difference between header beam displacement (SPACER) and masonry top (center) displacement (TOPCTR) are shown with corrected TTF east-west displacement in Fig. 7.5.7a and 7.5.8a, respectively, for Wall Specimens 10 and 12. The sliding displacement along the bottom of the masonry, calculated as the difference between LVDT transducers BOTHOR and BASHOR is also shown in Fig. 7.5.7b and 7.5.8b.

Plots of sliding displacement for Shear Walls 10 and 12 (Fig. 7.5.7-7.5.8) indicate that sliding behavior was characterized by two principal features; sliding displacement cycles that were synchronized with lateral drift history and a unidirectional accumulation of sliding displacement which is seen as a shifting baseline. Concerning the accumulation of sliding displacement in one direction (i.e., shifting baseline), it is curious to note that these displacements occur in opposing directions at the top and bottom surfaces of masonry. This shifting baseline leads to asymmetry of actual drift demand in the masonry, but the total (double-amplitude) drift demand on the masonry remains unchanged. Fluctuations in sliding displacement from one cycle to the next were generally not larger than 0.25 in. (6 mm) for most of the tests of Walls 10 and 12. Consequently, instantaneous drift demand of the masonry is reduced by 0.25 in. (6 mm) from the amount imposed by the TTF. However, the imposed drift on the walls was not affected much by sliding up to the deformation capacity of the walls (1% drift).

The sliding displacement described above is not unrealistic for masonry that is placed on concrete floors or foundations, and it was not considered necessary in the present study to extract it from the displacement demand imposed by the TTF facility. There is another source of sliding displacement, however, that should not be included in the test data if its magnitude is large enough. During the tests, sliding was also noted between the TTF crosshead (XHEAD) and the header beam (SPACER), as well as between the footer beam (BASHOR) and the laboratory floor. These displacements were kept small by providing large clamping forces between the connected surfaces by means of pre-tensioned, high-strength, steel rods.

The relative displacement between header and footer beams (SPACER - BASHOR) is plotted against corrected TTF displacement in the east-west direction in Fig. 7.5.9-7.5.14 for Shear Wall 2, 4, 6, 8, 10 and 12. The relative displacements are seen to be approximately equal to the TTF displacement. A linear least-squares fit of this displacement data was conducted for all specimens, and the resulting linear expressions are summarized in Table 7.5.7. High correlation coefficients and small vertical intercepts provide a high degree of confidence in this data. In addition, an average value of approximately 0.94 indicates that the loss of displacement by sliding of the test setup represents only 6% of TTF displacement, regardless of the magnitude of displacement. This amount is considered to be small enough that the TTF displacement data need not be corrected further to remove these sliding displacements.

8. ASSESSMENT OF SHEAR RESISTANCE CHARACTERISTICS

One of the major objectives of the NIST Masonry Research Program is the development of reliable tools for the seismic design of partially-grouted masonry shear walls. This objective entails the verification and calibration of design procedures and equations for determining the force requirements and the strength supplied by partially-grouted masonry shear walls. The first issue is directly dependant upon accurate estimates of the initial, in-plane, lateral stiffness of partially-grouted masonry walls. Initial stiffness is required in the seismic analysis of structural systems, and inaccuracies in initial stiffness estimates can lead to errors in the calculation of system period (or frequency). In addition, such an incorrect period calculation will give rise to an incorrect estimate of the design base shear force for the structural system. Furthermore, errors in wall stiffnesses will also lead to inaccurate distribution of lateral forces among the various components of the lateral load system.

The other essential aspect from the view point of design is accurate estimation of actual shear strength. For that reason, shear strength prediction has been an important aspect of the NIST Masonry Research Program. In particular, a shear strength predictive formula developed by Matsumura (1985; 1987) was identified by Fattal and Todd (1991) to be the most accurate among many commonly used formulas in the U.S. for the prediction of shear strength for a large database of masonry shear walls (Yancey et al., 1991), including some that were partially-grouted. Fattal later modified this formula to increase its overall accuracy, including changes that are specific to partially-grouted walls (1993a; 1993c). In formulating the NIST Masonry Research Plan, Schultz (1994) recognized that the Matsumura-Fattal formula exhibits features that seem to parallel previous experimental observations, including the treatment of horizontal reinforcement ratio and vertical compression stress.

The first part of this chapter addresses methods for assessing the initial stiffness of partially-grouted masonry shear walls. The chapter also addresses average shear stresses and shear strength at ultimate conditions. A modification is also proposed for the Matsumura-Fattal shear strength equation to increase prediction accuracy for the partially-grouted masonry shear wall tests in the first two series of the NIST Masonry Research Program. The chapter continues with shear strength at first cracking, and an equation is formulated for the cracking

phenomenon observed during the shear wall tests. The chapter closes with a discussion of minimum horizontal reinforcement for adequate seismic behavior of masonry shear walls.

8.1 Initial Stiffness Estimates

The initial, in-plane, lateral stiffness of masonry walls has been traditionally estimated assuming that they are linear, elastic and homogeneous, and that the contributions of flexural and shear deformations can be calculated separately and combined (Dickey and Schneider, 1996; Drysdale et al., 1994). That is, the flexural displacement Δ_f at the top of a fixed-fixed shear wall (Fig. 8.1a) can be added to the shear displacement Δ_s (Fig. 8.1b) to give a total displacement Δ. Since both Δ_f and Δ_s are generated by the same shear force V at the top of the wall, then the flexibility coefficients Δ/V are also additive. Recognizing that stiffness is the inverse of the flexibility coefficient, the following relation for wall stiffness K is established

$$\frac{1}{K}=\frac{\Delta}{V}=\frac{1}{K_f}+\frac{1}{K_s}=\frac{\Delta_f}{V}+\frac{\Delta_s}{V} \tag{8.1}$$

The flexural displacement for the fixed-fixed wall shown in Fig. 8.1a is given by

$$\Delta_f=\frac{VH^3}{12E_mI} \tag{8.2}$$

where H is wall height and E_m is the modulus of elasticity for masonry. The moment of inertia I is calculated assuming that the face-shell bedded wall has a rectangular section with an effective thickness equal to twice the face-shell thickness t_f. This yields a moment of inertia equal to $t_fL^3/12$. Thus, the flexural stiffness becomes

$$K_f=\frac{2E_mt_f}{\left(\frac{H}{L}\right)^3} \tag{8.3}$$

Assuming that the wall is in a state of pure shear, displacement Δ_s can be expressed as $\gamma H/1.2$, where γ is shear strain, and the denominator represents the shape factor for a rectangular

section (Langhaar, 1962). Shear strain is proportional to shear stress τ and inversely proportional to shear modulus of elasticity G_m for a linear system, thus, shear displacement becomes

$$\Delta_s = \frac{\tau H}{1.2 G_m} \tag{8.4}$$

While the wall is in an uncracked, elastic state, shear stresses have a parabolic distribution through the depth of the wall section. The shear stress at the centroid of the cross section is 1.5 times the average shear stress for a rectangular cross section ($\tau = 1.5V/A_n$). Net area in a face-shell bedded wall is taken as $2t_f L$. Introducing the above definitions for stress and net area, and recognizing that G_m is equal to $0.4E_m$ if Poisson's ratio is taken as 0.25 for masonry (Schneider and Dickey, 1996; Drysdale et al, 1994), then shear displacement becomes

$$\Delta_s = \frac{V\left(\frac{H}{L}\right)}{0.64 E_m t_f} \tag{8.5}$$

And, the corresponding shear stiffness is given by

$$K_s = 0.64 \frac{E_m t_f}{\left(\frac{H}{L}\right)} \tag{8.6}$$

Substituting Eq. (8.3) and (8.6) into Eq. (8.1), and solving for lateral stiffness K, gives the following expression for a masonry wall

$$K = \frac{2E_m t_f}{\left(3\left(\frac{H}{L}\right) + \left(\frac{H}{L}\right)^3\right)} \tag{8.7}$$

Schultz (1994) computed initial stiffnesses for the six walls in Series 1 using Eq. (8.7), and these stiffnesses were compared with initial stiffnesses inferred from the test data (Schultz, 1994). The inferred initial stiffnesses were obtained from the initial portion of the smoothed

force-displacement envelopes. For each masonry wall tested, this data set was fitted with a linear least-squares trend, the slope of which was taken as initial stiffness. And, only portions of the envelopes for which the magnitude of shear force did not exceed 40% of the limit of proportionality were used in this calculation. Generally, the force-displacement data in this range demonstrated a strongly linear relation. Even when a lower bound estimate of $600f'_m$ for modulus of elasticity E_m (Atkinson and Yan, 1990) was used, the inferred stiffnesses were found to be only approximately equal to 3/4 of the calculated stiffnesses. At the time, these differences were attributed to the rapid decay of stiffness with crack initiation in masonry walls, and, because some slip was present between the masonry panels and the header and footer beams. However, the latter appeared to be the factor of greatest importance (Schultz, 1994).

When the exercise described above was repeated for the shear wall specimens in Series 2, the comparison yielded initial stiffness estimates that were, on the average, one-half as large as the inferred stiffnesses. This suggested that slip between the masonry panels and the header and footer beams was significant, the sum of which was as large as the deformation of the masonry panel. Differences in the placement detail for the portion of reinforcing bar protruding through the header and footer beams is most likely responsible for the discrepancy between Series 1 and Series 2. Wet "hydrocal" (i.e., gypsum cement mixed with water) was used to fix the rebars in the access tubes for the specimens in Series 1, whereas a copper sleeve was used for the specimens in the second series. Finite dimensional tolerances were present in the specimens of Series 2, resulting in slip displacements even during the elastic cycles.

To solve this problem, the difference between the LVDT's at the top and bottom of the masonry panel (i.e. transducers TOPHOR and BOTHOR in Fig. 4.4) was used as lateral displacement instead of the global east-west displacement of the TTF crosshead. The former displacement was used to define an interstory displacement which contains only masonry deformation and no slip displacements at the interfaces with the header and footer beams. However, the transducers TOPHOR and BOTHOR were not placed at the edge of the masonry panels, but at a distance e from the interfaces (Fig. 8.1). Thus, the flexural and shear displacements, and the corresponding stiffnesses, need to be modified to reflect this change in measurement location.

Using simple methods for calculating flexural deflections in linear elastic members, the change in flexural deflection Δ_{fe} over the distance e can be defined as

$$\Delta_{fe}=\left(\frac{VH^3}{24E_mI}\right)\left(\frac{e}{H}\right)\left[8\left(\frac{e}{H}\right)^2+3\left(1-2\frac{e}{H}\right)^2\right] \tag{8.8}$$

and the flexural displacement between the locations of the LVDT transducers Δ_{fe} becomes

$$\Delta_{fo}=\left(\frac{VH^3}{12E_mI}\right)\left[1-8\left(\frac{e}{H}\right)^3-3\left(\frac{e}{H}\right)\left(1-2\frac{e}{H}\right)^2\right] \tag{8.9}$$

The corresponding flexural stiffness becomes

$$K_{fo}=\frac{\dfrac{2E_mt_f}{(H/L)^3}}{\left[1-8\left(\dfrac{e}{H}\right)^3-3\left(\dfrac{e}{H}\right)\left(1-2\dfrac{e}{H}\right)^2\right]} \tag{8.10}$$

Recognizing that the dimension e was approximately equal to 102 mm (4 in.) in all tests, and that the height H was held constant at 102 mm (56 in.), the ratio of the flexural stiffness given by Eq. (8.3) to that given by Eq. (8.10) is equal to 0.840. Since shear deformation is assumed to be consistent with the edges of the masonry remaining straight but in a rotated configuration, the shear displacement between the LVDT transducers TOPHOR and BOTHOR is

$$\Delta_{so}=\frac{V\left(\dfrac{H}{L}\right)\left(1-2\dfrac{e}{H}\right)}{0.64E_mt_f} \tag{8.11}$$

and the corresponding shear stiffness becomes

$$K_{so}=0.64\frac{E_mt_f}{\left(\dfrac{H}{L}\right)\left(1-2\dfrac{e}{H}\right)} \tag{8.12}$$

Substituting 102 mm (4 in.) and 1422 mm (56 in.), respectively, for e and H in Eq. (8.12), gives a stiffness that is equal to the value given by Eq. (8.6) and divided by 0.857. Thus, the corrected stiffness for interstory masonry displacements measured between LVDT transducers is approximately equal to the value given by Eq. (8.7) divided by 0.85, the latter which is the average of the correction factors for flexural stiffness (0.840) and shear stiffness (0.857).

Initial stiffnesses for each wall in Series 2 were inferred from the early cycles of the force-displacement histories, for which peak lateral force did not exceed 50% of the force at first cracking (i.e. at the FME). The relative lateral displacements of the masonry panels were defined as the difference in the readings given by LVDT transducers TOPHOR and BOTHOR (Fig. 4.4). Lateral stiffness of the walls was defined as the slope of the line connecting the positive and negative peaks of the force-displacement cycles. These inferred stiffnesses are listed in Table 8.1, along with estimates based on 118% (i.e. 1/0.85) of the value given by Eq. (8.7). Modulus of elasticity E_m was taken equal to $600f'_m$, and a compression strength equal to 15.2 MPa (2200 psi) was used for f'_m. This strength is slightly larger than the average 28-day compression strength of the moist-cured prisms given in Table 3.3. The difference is included to account for the stronger grouted masonry in the exterior cells. The face-shell thickness t_f was taken as 34 mm (1.35 in.) according to Table 3.1

As noted in Table 8.1, aspect ratio (H/L) has a large impact on lateral stiffnesses, but stiffness expression (eq. 8.6) simulates this variation quite well. Calculated stiffnesses are in good agreement with the inferred quantities, and ratios of calculated to inferred stiffnesses range from 0.87 to 1.12 with a mean value of 0.99. It is worth noting that the slip displacement which was removed from the calculations above, may be present in the response of a masonry building to seismic loading depending upon the details at the connections between walls and floors. If specific information regarding these connections is not available, initial stiffness estimates be reduced by 50% to account for slip, on the basis of the present study.

8.2 Cracking Shear Strength

In planning the masonry shear wall tests in the present study, Schultz (1994) relied on a formula for the cracking shear strength of masonry walls which was proposed by Shing et al.

(1989). This formula was developed using test data for fully grouted and reinforced masonry shear walls, and it was meant to predict the shear force at which diagonal cracks are formed in masonry shear walls. The formula is given by

$$V_c = (c_1 \sigma_v + c_2) A_n \sqrt{f'_m} \tag{8.13}$$

where the constants c_1 and c_2, respectively, are equal to 0.0759 and 0.208 when σ_v and f'_m are in MPa, A_n is in mm^2, and V_c is in N. For U.S. customary units (i.e., psi, in^2 and lbs), constants c_1 and c_2 are equal to 0.0063 and 2.5, respectively.

Observations made during the partially-grouted masonry shear wall tests at NIST indicated clearly that the cracking behavior of the walls was different from what has been observed in fully-grouted masonry shear wall tests by others (Shing et al., 1990b; Shing et al. 1989). As noted in Chapter 5, the predominant mode of cracking involved vertical cracks which initiated in the top course of masonry at the interface between grouted and ungrouted masonry. While inclined cracks formed at later stages of testing, these were deemed less important than the vertical cracks because the latter dominated shear wall response to lateral loading. Initiation of vertical cracks, in fact, was treated as the first major event (FME) in all of the partially-grouted masonry shear walls tested at NIST, thus this mode of cracking controlled the magnitudes of drifts that were used for the cyclic drift histories.

In order to further understand the mechanism behind vertical crack formation, and in order to compare experimental observations with predicted cracking strengths, a simple expression for shear strength at vertical cracking was developed. Vertical cracks are assumed to form in response to large horizontal tension stresses induced in the top course of masonry by the horizontal shear stresses that are transferred at the mortar joint between the header beam and the masonry panel (Fig. 8.2a). At vertical crack formation, resistance to horizontal shear is provided by the bed joint (V_f), as well as dowel resistance of the vertical rebar (V_d) and tensile strength of the head joint (V_t). Concentration and localization of tensile stresses in the face-shells at the interface of grouted and ungrouted masonry produces vertical cracks when the tensile strength of the nearest head joint nearest is exceeded (Fig. 8.2b). Large concentrations of horizontal dowel forces from the vertical rebars exacerbate the problem.

Equilibrium of horizontal forces for the free body of the header beam plus the fractured "corner" of masonry shown in Fig. 8.2b requires that

$$V_c = V_f + V_t + 2V_d \tag{8.14}$$

where V_c is the cracking shear strength, and V_f is the sum of the shear resistance resultants V_{f1} and V_{f2}. The shear resistance along the mortar bed joint can be treated using the shear-friction concept in ACI 318-98 (1998), except that the normal force provided by normal reinforcement in the traditional shear friction mechanism is replaced by vertical force on the wall section. For this case, shear strength is given by

$$V_f = \eta A_h \sigma_c = \eta P_v \tag{8.15}$$

where η is the coefficient of friction, A_h is the net horizontal area, σ_v is the net vertical stress, and P_v is the total vertical force acting on the wall. A value of 0.6 is used for the coefficient of friction, as recommended by ACI 318-98 (1998) for new concrete cast against existing concrete that has not been intentionally roughened. Utilization of the shear friction concept eliminates the need to distinguish between cracked and uncracked joints between the header beams and masonry panels.

The tensile resistance of the head joint V_t is expressed as

$$V_t = f_{t,j} A_{v,u} = c_3 \sqrt{f_j'} \, (2t_f)(h_u + t_j) \tag{8.16}$$

The tensile strength of the mortar $f_{t,j}$ is approximated as fraction of the strength given by the formula in ACI 318-98 (1998) for the splitting strength of concrete cylinders. The ACI 318-98 cylinder splitting strength expression is $c_3 f'_c$ where c_8 is equal to 0.556 and 6.7 when stresses are in MPa and psi, respectively. This formula is modified by replacing mortar compression strength f_j' for concrete compression strength f_c', and only 60% of splitting strength is assumed to be effective in direct tension, as noted by Mindess and Young (1981). Thus, the constant c_3 is reduced to 0.332 and 4, respectively, for MPa and psi. The net vertical area on which this tension strength acts ($A_{v,u}$) is assumed to be provided by the head joints which comprise two

vertical rails of hardened mortar that are as thick as the minimum face shell thickness of the masonry t_f, and as tall as one masonry unit (h_u) plus one bed joint (t_j).

Finally, the horizontal dowel resistance generated by the vertical reinforcing bars V_d is assumed to be controlled by the strength of the grout in which the bars are embedded, given the large strength difference in strengths for grout and rebar. It is further assumed that the grout reaches its crushing strength (85% of grout specimen compression strength f'_g) immediately adjacent to one side of the rebar, and over a bar length equal to approximately one rebar diameter. This condition is shown in Fig. 8.2c, and post-test disassembly of the wall specimens confirmed damage patterns consistent with this assumption. Thus, the total resistance provided by all four rebars (two along each jamb) is

$$V_d = 3.4 f'_g d_b^2 \tag{8.17}$$

where d_b is rebar diameter.

Cracking strengths computed using Shing's formula (8.13), and the proposed formula (8.14-8.17) are summarized in Tables 8.2.1 and 8.2.2, respectively. In evaluating shear strengths with Shing's formula, the nominal vertical compression stress on the net area, 138 MPa (200 psi), was used. In addition, masonry compression strength f'_m was taken as 17.3 MPa (2510 psi), which is the average value from all of the companion masonry prisms that were cured in laboratory air and tested at 28 days of age. Similarly, the value for grout strength f'_g which was used to evaluate shear strengths with the proposed cracking strength formula, 18.8 MPa or 2730 psi, was also taken as the average of all 28-day compression strengths for air-cured mortar cube. Exposure to laboratory air is assumed to be a more realistic representation of shear wall curing conditions than moist curing of mortar cubes (by immersion in water) and masonry prisms (by storing in sealed polyethylene bags).

Calculated cracking shear strengths are compared to measured cracking shear forces in Tables 8.2.1 and 8.2.2. Both formulas are seen to provide a reasonably accurate assessment of wall cracking strengths, with a mean value approximately equal to unity, and a standard deviation of 15%. The proposed formula, however, does not tend to overestimate cracking shear strength

as much as Shing's formula. Surprisingly, however, Shing's formula predicts cracking strengths nearly as well as the proposed formula, especially in view of the fact that the former was not developed for the cracking mechanism observed in the partially-grouted shear wall tests, while the latter was specifically tailored to address this mechanism. Both formulas are seen to reproduce the observed trends in shear strength with aspect ratio,but not the apparent increase in cracking shear strength with amount of horizontal reinforcement. The observed strengths at first cracking (Tables 8.2.1 and 8.2.2) are larger for Wall Specimens 8 and 12 (ρ_h = 0.056%), than they are for Wall Specimens 2 and 6 (ρ_h = 0.110%). This observation suggests that the cracks had already formed in the masonry at the time they were first observed.

8.3 Average Shear Stress at Ultimate Conditions

It is useful to investigate measured shear stresses at ultimate conditions because the trends in the experimental data are more clearly visible in the stress format rather than the strength format that was presented in Chapter 7. After reviewing the experimental trends in shear stress at ultimate, this section describes the Matsumura-Fattal shear strength equation as well as a modification that is proposed by the authors to better represent partially-grouted walls. Shear stresses at ultimate conditions were considered for the wall tests in both Series 1 and 2.

Ultimate shear stresses were calculated for each wall specimen by dividing peak lateral load by horizontal area. Average peak lateral load was obtained by averaging the peak values of lateral load in both loading directions, and two values of horizontal area were used. Gross area (A_g) was defined as the product of wall length L and gross unit thickness t_g, while net area (A_n) was taken to be the product of twice the minimum face shell thickness t_f and total wall length L. Since the walls were face-shell bedded, the webs of the masonry were excluded from the net area calculation. Even the areas of exterior webs of end units, which were bedded with mortar, as well as the areas of grouted end cells were neglected in the net area calculation on the assumption that shear stress distribution is best described by that for an elastic, uncracked section. Thus, the contribution of transverse elements of area (i.e. flanges) is negligible.

Gross and net area shear stresses at ultimate are given in Tables 8.3.1(a) and 8.3.1(b), respectively for the shear wall tests in Series 1 and 2. In addition to these two definitions of

shear stresses, these tables also include wall length (L), height-to-length aspect ratio (H/L), horizontal reinforcement ratio (ρ_h) based on both gross and net areas, and shear strength V_u. The gross unit thickness t_g and the face-shell thickness t_f were determined by measurement as described in Chapter 3 (Table 3.1).

The net area stresses at ultimate for Series 1 and 2 are plotted against aspect ratio (H/L) in Fig. 8.3.1a and 8.3.1.b, respectively. Also, these net area stresses are plotted against horizontal reinforcement ratio (ρ_h) in Fig. 8.3.2a and 8.3.2b. Similarly, Fig. 8.3.3 and 8.3.4, respectively, illustrate the dependance of gross area shear stresses against H/L and ρ_h for the shear wall tests in both Series 1 and 2. Comparison of Fig. 8.3.1 with 8.3.3, and Fig. 8.3.2 and Fig. 8.3.4, clearly indicates that the net and gross area stress definitions are nearly identical. The plots of net and gross area shear stresses differ only by a constant, which is the ratio of net to gross wall horizontal areas. Thus, it is not necessary to follow trends in the data for both of these stress definitions, as a single shear stress definition will suffice.

The data shown in Fig. 8.3.1, as well as that in Fig. 8.3.3, indicates that increasing height-to-length aspect ratio (H/L) increases shear stresses at ultimate. That is, the more slender walls exhibit higher shear stresses at ultimate than the stockier walls. In addition, several other important observations are apparent in the data shown in Fig. 8.3.1 and 8.3.3. First, the specimens in Series 1, with the exception of Wall No. 3, exhibited an almost linear increase in shear stress at ultimate with height-to-length aspect ratio over the range studied. It is noted that the shear strength (and average ultimate shear stress) of Wall No. 3 is considered to be an outlier, and study of shear wall strength in subsequent sections confirms this observation. Second, the data for Series 2 (Fig. 8.3.1 and 8.3.2) indicates a nonlinear trend with height-to-length aspect ratio, and there appears to be a saturation point at $H/L = 0.7$ beyond which any increase in shear stress at ultimate with increasing aspect ratio is likely to be small.

In Fig. 8.3.1 and 8.3.3, it is noted that Wall No. 8 is weaker than Wall No. 2, the latter which had less horizontal reinforcement. Thus, the shear strength of Wall No. 8 is considered to be uncharacteristically low. Finally, the shear wall specimens in Series 2 gave consistently higher shear stresses at ultimate than did the specimens in Series 1. As noted in Table 8.3.1, the mean value of shear stress at ultimate for the specimens in Series 2 is 25% larger than the mean shear

stress value for the specimens in Series 1. It is worth noting that the yield stress of the wire grids used as horizontal reinforcement for Series 2 is at least 50% larger than that for the rebar used to reinforce the bond beams in Series 1.

In Fig. 8.3.2 and 8.3.4 it is noted that increasing horizontal reinforcement ratio increases stress at ultimate notwithstanding the two outliers (i.e. Wall No. 3 in Series 1, and Wall No. 8 in Series 2). However, the increase in shear stress afforded by an increase in horizontal reinforcement ratio is very small, even over an almost doubling of horizontal reinforcement ratio (i.e. 0.05% vs. 0.12%). In Fig. 8.3.2 and 8.3.4, the suspiciously high and low strengths, respectively, of Wall Nos. 3 (Series 1) and 8 (Series 2), can be seen clearly. These strength data are clearly contrary to the trends established by the other 10 specimens, for which a beneficial influence in shear strength with horizontal reinforcement is seen in all cases.

To better understand the observed trends in average ultimate shear stress with both reinforcement ratio and aspect ratio, the Matsumura-Fattal shear strength formula is introduced. As part of the NIST masonry research program, Fattal (1993a, 1993c) proposed an empirical expression for predicting the shear strength of fully-grouted and partially-grouted masonry shear walls. The expression is a modification of one developed as part of the Japanese TCCMAR effort (Matsumura, 1985; 1987; 1988), and Fattal used data from a variety of experimental programs to calibrate this expression (Yancey et al., 1991). Fattal demonstrated measurable improvements in the accuracy of shear strength predictions for both fully-grouted and partially-grouted masonry shear walls when using these modifications.

According to Fattal (1993a), nominal shear stress at ultimate (v_n) is given by

$$v_n = v_m + v_s + v_a \tag{8.18}$$

where v_m, v_s, and v_a, respectively, are the contributions of masonry, horizontal reinforcement, and axial compression to shear strength. These quantities are given by

$$v_m = k_0 \, k_u \left[\left(\frac{0.5}{r + 0.8} \right) + 0.18 \right] \sqrt{f'_m \, f_{yv}} \; \left(\rho_v \right)^{0.7} \tag{8.19}$$

$$v_s = 0.011 k_0 \gamma \delta f_{yh} \rho_h^{0.31} \tag{8.20}$$

$$v_a = 0.012\, k_0 f_m' + 0.2\sigma_c \tag{8.21}$$

where ρ_v and ρ_h are the ratios of vertical and horizontal reinforcement, respectively, f_{yv} and f_{yh} are the nominal yield stresses of these reinforcements, respectively, and r is the height-to-length aspect ratio (H/L). The dimensionless factors k_0, k_u, and γ, respectively, are equal to 0.8, 0.64 and 0.60 for partially-grouted masonry. The factor δ is equal to 1.0 for walls with points of inflection at mid-height, such as those in the present tests, and 0.6 for cantilever walls. All of the parameters in Eq. (8.18) - (8.21) which are proportional to masonry area, including f_m', ρ_v, ρ_h, and σ_c, must be defined in terms of gross area of masonry (Matsumura 1987, 1988), and all stress quantities must be in megapascals (MPa).

Average ultimate shear stresses for the walls in Series 1 and 2 were computed assuming nominal material properties (Table 8.3.2) and using the Matsumura-Fattal formula, and these values are listed in Tables 8.3.3(a) and 8.3.3(b), respectively. These stresses were recomputed using actual material properties (Table 8.3.2), and the values are summarized in Tables 8.3.4(a) and 8.3.4(b), respectively, for Series 1 and 2. Finally, the partial grouting parameter k_o in the Matsumura-Fattal formulation was modified to more accurately reflect the influence of grouting on shear strength. Matsumura's original proposition was for a constant value of $k_o = 0.8$ for all cases of partial grouting. However, the degree of grouting in partially-grouted walls can vary considerably, and the partial grouting parameter should encapsulate this variation. Fattal (1993a) indicated that the partial grouting parameter k_o should be a function of the proportion of grouted volume to gross volume (VOL_{gross}), however, he recognized that he had insufficient experimental data to establish this relationship. Following Fattal's suggestion, the partial grouting parameter was further redefined in the current study as

$$k_o = \frac{VOL_{net}}{VOL_{gross}} = \frac{VOL_{gross} - VOL_{void}}{VOL_{gross}} \tag{8.22}$$

where VOL_{void} is the ungrouted volume in the wall. With this modification, the formulation is referred to as the modified Matsumura-Fattal method. Values for the partial grouting parameter

k_o were computed as 0.59, 0.62 and 0.66, respectively, for walls with aspect ratios equal to 0.5, 0.7 and 1.0.

Calculated average ultimate shear stresses based on gross area (Table 8.3.5) are shown in Fig. 8.3.5 for Series 1 and 2. Stresses calculated using the Matsumura-Fattal formulation and both nominal and actual material properties are shown, as well as stresses calculated using the modified Matsumura-Fattal formulation and actual material properties. These plots demonstrate several important aspects. First, modification greatly improves the accuracy of the Matsumura-Fattal equation when used for predicting the strength of partially-grouted shear walls. Second, Wall Nos. 3 and 8 are clearly seen to be outliers, with Wall 3 being uncharacteristically strong and Wall 8 being uncharacteristically weak.

8.4 Shear Strength Prediction

(a) Fattal (1993a)

In seismic design, it is customary to calculate net strength of a section, rather than nominal stresses. Thus, the calculation of shear strength plays a critical role in design. The Matsumura-Fattal formula for average ultimate shear stresses can be easily converted into shear strength (V_n) formulas by multiplying the stresses v_n by area (A_g) of a horizontal section of the wall based on gross dimensions. Tables 8.4.1(a) and 8.4.1(b) summarize these calculations, including comparison with the experimentally-determined shear strength V_u. Other popular shear strength formulas used for seismic design in the U.S. are explored in the following.

(b) Shing et al. (1990)

As part of the US-TCCMAR program, Shing et al. (1990a; 1990b) proposed an expression for estimating the in-plane shear strength of fully-grouted, reinforced masonry walls. Tables 8.4.2(a) and 8.4.2(b) summarize the calculations using this expression. This approach recognizes the contribution of masonry, horizontal reinforcement, and axial compression stress, and, the contribution of the latter is combined with the shear strength component of the masonry. The horizontal shear strength of a wall section at ultimate (V_n) is given by

$$V_n = V_m + V_s \tag{8.23}$$

where V_m and V_s, respectively, are the shear strength contributions of the masonry and horizontal reinforcement. These strengths are given by

$$V_m = \left[c_4 \left(\rho_v f_{yv} + \sigma_c \right) + c_5 \right] A_n \sqrt{f'_m} \tag{8.24}$$

and

$$V_s = \left[\left(\frac{L - 2d'}{s} \right) - 1 \right] A_b f_{yh} \tag{8.25}$$

where L is the length of the wall, d' is the centroidal distance of the vertical tension reinforcement to the nearest jamb, and s is the spacing of horizontal reinforcement. The empirical constants c_4 and c_5, respectively, are equal to 0.0217 $^1/$ MPa (0.0018 $^1/$ psi) and 0.166 MPa (2.0 psi).

The cross-sectional area of the wall (A_n) in Eq. (8.24) is based on the net horizontal section. However, the ratio of vertical reinforcement ρ_v and the axial compression stress σ_c must be defined in a consistent manner, because the products of these two parameters and the net area must be equal to the total area of vertical steel (A_{sv}) and the net compression force P_c, respectively. Since this expression was developed by Shing for fully-grouted walls, the distinction between net and gross section was not necessary. However, for partially-grouted masonry walls, care must be exercised when applying this formula.

The steel strength (V_s) is based on a 45° truss idealization of the masonry wall, in which horizontal reinforcing bars with area A_b are placed at a uniform spacing s along the height of the wall. In the present study, for specimens with bed joint reinforcement, application of Eq. (8.25) is straightforward. But, for bond beam specimens, s is taken as one-half the height of the panel (in the assumption that the top and bottom boundaries represent the edges of adjacent bond beams), and A_b is taken as the total area of steel in the bond beam.

(c) UBC (ICBO, 1997)

The 1997 edition of the Uniform Building Code (ICBO, 1997) includes a formula for the shear strength of masonry walls which recognizes the contributions provided by horizontal reinforcement (V_s) and masonry (V_m). Tables 8.4.3(a) and 8.4.3(b) summarize the calculations using this expression. Nominal shear strength at ultimate is given by

$$V_n = V_m + V_s \tag{8.26}$$

where

$$V_m = C_d A_{mv} \sqrt{f'_m} \tag{8.27}$$

$$V_s = A_{mv} \rho_n f_{yh} \tag{8.28}$$

When using SI units, the coefficient C_d is taken as either 0.2 MPa, for shear-span-to-depth ratios (*M/Vd*) less than or equal to 1/4, or 0.1 MPa, for *M/Vd* greater than or equal to 1. The corresponding C_d limits in U.S. Customary units are 2.4 psi and 1.2 psi, respectively, for *M/Vd* equal to 1/4 and 1. Linear interpolation is used to define C_d for values of *M/Vd* between limits of 1/4 and 1. For aspect ratios equal to 0.5, 0.7, and 1.0 in the present study, values of 0.198, 0.184 and 0.161 MPa (2.385, 2.211, and 1.939 psi), respectively, are used for C_d.

The nominal shear strengths given by Eq. (8.26) cannot exceed the following limit

$$c_6 A_e \sqrt{f'_m} \leq c_7 A_e \tag{8.29}$$

where the constants c_6 and c_7 are equal to 322 (6.0) and 1691 (380), respectively, if V_n is in N (lbs) and f'_m is in kPa (psi) for shear-span-to-depth-ratios (*M/Vd*) less than or equal to 1/4. For *M/Vd* greater than or equal to 1.0, these constants take on values of 214 (4.0) and 1113 (250), respectively. Linear interpolation is allowed if the value of *M/Vd* lies between 1/4 and 1.0. The area A_{mv} is defined as the neat area bounded by wall thickness and wall length along a horizontal plane through the shear wall, thus it is a gross area. The ratio of horizontal

reinforcement ρ_n is determined with respect to a vertical section through the wall and using the horizontal area A_{mv}. The term A_e is defined as the effective area of masonry, and in this study it is taken as the net area of masonry in a horizontal section. The ratio of horizontal reinforcement ρ_h is determined with respect to a vertical section through the wall. If gross sections are used to define this area of masonry, then the horizontal area A in Eq. (8.28) must also be calculated using gross sections.

(d) NEHRP Provisions (*NEHRP* 1997)

In the 1997 Edition of the NEHRP Provisions (*NEHRP*, 1997), nominal shear strength for reinforced masonry walls (V_n) is given by

$$V_n = V_m + V_s \tag{8.30}$$

where the nominal shear strength of the masonry (V_m) for sections not in a plastic hinge zone is

$$V_m = c_8 \left(4 - 1.75 \frac{M}{Vd}\right) A_n \sqrt{f'_m} + 0.25 A_n \sigma_c \tag{8.31}$$

and the shear strength of the horizontal reinforcement (V_s) is

$$V_s = 0.5 A_n \rho_h f_{yh} \tag{8.32}$$

The constant c_8 in Eq. (8.31) is equal to 0.083 MPa (1.0 psi), and the axial load P due to unfactored design loads is taken as the product of net axial compression stress σ_c from unfactored loads and using net area if A_n.

The expression for nominal strength of shear reinforcement (Eq. 8.32) is identical to that in the UBC (Eq. 8.26 - 8.28), but only 50% of this strength is assumed to participate effectively in the overall mechanism of shear resistance at ultimate conditions (Eq. 8.30). Calculated shear strengths using the NEHRP expression are summarized in Tables 8.4.4(a) and 8.4.4(b).

(e) Discussion

Shear strengths calculated using each one of the procedures described above are summarized in Tables 8.4.1 through 8.4.4, and the strengths are plotted against Shear Wall No., horizontal reinforcement ratio, and aspect ratio in Fig. 8.4.1-8.4.6. These plots generally indicate that the modified Matsumura-Fattal approach is more accurate than any other shear strength formula considered. This is true relative to variations in shear strength with aspect ratio (Fig. 8.4.2 and 8.4.3), as well as with horizontal reinforcement ratio (Fig. 8.4.4 - 8.4.6). The improvement in calculation accuracy is noted in the bottom of Tables 8.4.1 through 8.4.6 by means of the average value of the ratio of measured-to-calculated shear strengths, as well as the standard deviation for this quantity. The modified Matsumura-Fattal approach invariably predicted values that were closest to the measured strength, and the standard deviations were less than one-half of that noted for all other formulas.

8.5 Minimum Horizontal Reinforcement Ratio

In the planning stages of the current masonry shear wall research program, consideration was given to the amount of horizontal reinforcement in the wall specimens (Schultz, 1994). In particular, the relationship between the reinforcement ratios for the selected horizontal reinforcing schemes and lower limits on horizontal reinforcement ratio was considered important. In fact, the horizontal reinforcement ratios used in the present study were selected to investigate the validity of formulas for minimum horizontal reinforcement ratio which were proposed by Schultz (1997).

Two formulas for minimum horizontal reinforcement ratio were derived, after a number of idealizations and approximations, such that the horizontal shear force and elastic strain energy released by the masonry upon inclined crack formation be resisted by the horizontal reinforcement. The minimum horizontal reinforcement ratio formulas were verified with experimental observations from cyclic load tests of 24 fully-grouted and reinforced masonry shear walls conducted by Shing et al. (1989; 1990a; 1990b; 1992). By comparing required and provided reinforcement ratios, the proposed formulas were able to identify 9 of the 12 walls that failed in a brittle manner (i.e., shear), as well as 10 of the 12 walls that failed in a

ductile manner (i.e., flexure). Four of the five remaining walls had horizontal reinforcement ratios that were very close in magnitude to the required minimum values according to Schultz (1997). Thus, these formulas were deemed valid and accurate for defining minimum horizontal reinforcement requirements for adequate seismic behavior in fully-grouted and reinforced masonry shear walls.

The minimum horizontal reinforcement ratio, defined on the basis of gross area, for the strength criterion postulated by Schultz (1997) is given by

$$\rho_{h,min} = \frac{3}{2}\left(\frac{t_e}{t}\right)\left(\frac{\sqrt{f'_m}}{f_{yh}}\right)\left(c_9\sigma_c + c_{10}\right) \tag{8.33}$$

where t_e is the effective thickness of partially-grouted masonry (i.e., the net horizontal area per unit length of wall). The constants c_9 and c_{10} are equal to 0.0482 and 0.0623, respectively for SI units (MPa), and 0.004 and 0.75, respectively, for US customary units (psi). The gross area minimum horizontal reinforcement ratio for the energy criterion is given by the following

$$\rho_{h,min} = \left[c_{11}\left(\frac{t_e}{t}\right)\sqrt{\frac{(L/t)}{(H/L)}}\left(c_{12}\sigma_c + c_{13}\right)\right]^{\frac{2}{3}} \tag{8.34}$$

where the constants c_{11}, c_{12} and c_{13} are equal to $2.24\text{x}10^{-4}$, 0.0723 and 0.125, respectively, in SI units (MPa), and $1.56\text{x}10^{-6}$, 0.006 and 1.5, respectively, in US customary units (psi).

Minimum horizontal reinforcement ratios were calculated for the shear walls during the planning stages of this research program. These values, which were presented in Chapter 2 (Table 2.3), were calculated using nominal quantities for masonry compression strength (f'_m), horizontal steel yield strength (f_{yh}), vertical stress on the net area of masonry (σ_c), and gross wall thickness (t = 194 mm = 7 5/8 in.). The effective thickness t_e is taken as the sum of the minimum thicknesses of the two masonry face shells (i.e., t_e = 63.5 mm = 2.5 in.), because the contribution of the grouted regions is assumed to be negligible: these elements serve as flanges to the horizontal wall sections and carry little shear stress. The computed minimum horizontal reinforcement ratios (Table 2.3) suggest that all specimens had enough horizontal

steel to satisfy the strength criterion ($\rho_h > 0.043\%$), and reinforcement ratios for Wall Specimens 6, 8, 10 and 12 were also sufficient to satisfy the energy criterion. But, Wall 2 did not have enough horizontal steel to satisfy the energy criterion ($\rho_h = 0.056\% < \rho_{h,min} = 0.074\%$), while Wall 4 appeared to have nearly enough ($\rho_h = 0.056\% \approx \rho_{h,min} = 0.059\%$). Thus, Walls 2 and 4 were expected to exhibit less ductile failure modes than the other walls.

Minimum horizontal reinforcement ratios were recalculated using actual material strengths (f'_c and f_{yh}) and wall stresses (σ_c), and the revised values are listed in Table 8.5. Measured gross wall thickness t and minimum face-shell thicknesses t_f were determined to be equal to 194.6 mm (7.66 in.) and 33.7 mm (1.33 in.), respectively (Table 3.10). Minimum horizontal reinforcement ratios in Table 8.5, with the updated values for strength, stress and geometry, are seen to vary slightly over those in Table 2.3. However, the overall conclusions regarding likely failure modes, on the basis of the calculated minimum horizontal reinforcement ratios, do not change.

The shear wall tests did not reveal brittle failures for Wall Specimens 2 and 4, and the response and failure modes for these walls were identical to those for the other walls (i.e., Specimens 6, 8, 10 and 12). In fact, all walls failed in shear because they were designed and detailed so that shear controlled the failure mode. However, wall failures were gradual, with cracks widening and additional wire grids rupturing with successive load cycles. All walls underwent many cycles of load (Figs. 6.2.1-6.2.6) and large drift ratios (Table 8.3.1). In addition, all walls suffered multiple wire grid fractures, even though Wall Specimens 6, 8, 10 and 12 satisfied the minimum horizontal ratio for the energy criterion.

Given the disparity between predicted failure modes from the energy criterion (Eq. 8.34) and observed wall behavior, it is concluded that the formula for minimum horizontal reinforcement ratio for the energy criterion is not appropriate for partially-grouted masonry walls with bed joint reinforcement. This problem may attributed to the use of wires with mechanical properties that did not meet the assumptions made in the derivation of Eq. (8.34), namely that $f_{uh}/f_{yh} = 9/8$, and $\varepsilon_u = 5\%$. However, the derivation of this formula is somewhat convoluted with multiple assumptions and idealizations, and it is sensitive to many parameters. Thus, there is little confidence in the use of this equation for partially-grouted masonry walls

reinforced with bed-joint reinforcement comprising welded wire grids, even though it appeared to work well for fully-grouted walls (Schultz, 1997).

In contrast, the minimum horizontal reinforcement ratio formula for the shear strength criterion (Eq. 8.33) appears to be adequate for both partially-grouted masonry shear walls, as well as fully-grouted walls. Given this degree of confidence in this formula, as well as the experimental observations in this study, an important conclusion can be reached regarding the amount of horizontal reinforcement in partially-grouted masonry shear walls. A minimum horizontal reinforcement ratio equal to 0.07% of the gross vertical area, as is currently required by design codes in the U.S. (MSJC, 1999; NEHRP, 1997; ICBO, 1997), may be too large depending upon the degree of partial grouting (t_e/t), material properties (f'_m and f_{yh}), and vertical compression stress (σ_c). Partially-grouted masonry shear walls with gross area horizontal reinforcement ratios equal to 0.056% (Nos. 2, 4, and 6) were found to behave as well as walls with twice as much horizontal reinforcement (Nos. 8, 10, and 12).

9. SUMMARY, CONCLUSIONS AND RECOMMENDATIONS

9.1 Summary

An experimental investigation on the shear resistance characteristics of partially-grouted masonry shear walls is documented. The investigation is part of an ongoing research program at the Building and Fire Research Laboratory on the seismic design of masonry. The present report documents the results from the second phase of the first priority of the NIST Masonry Research Program (Schultz, 1994). The principal objective of this phase was to define the behavior of partially-grouted masonry shear walls in which all horizontal reinforcement is provided by welded grids of cold-drawn steel wire. These grids reside in the mortar bed joint of the masonry units, thus they need not interfere with the placement of the vertical steel.

Six partially-grouted masonry walls were built by a professional mason at the Building and Fire Research Laboratory of the National Institute of Standards. These walls comprised seven courses of hollow concrete masonry units sandwiched between precast concrete header and footer beams. The nominal compression strength of the masonry was assumed to be 13.79 MPa (2000 psi), grade 60 reinforcement (f_y = 414 MPa) was assumed for the vertical steel, and horizontal reinforcement was assumed to have a nominal yield strength equal to 552 MPa (80 ksi). Actual material strengths were 17.3 MPa (2510 psi), 445 MPa (64.6 ksi), 715 Mpa, and 593 Mpa, respectively, for the masonry, vertical steel, No. 9 Ga. horizontal reinforcement, and No. 5 Ga horizontal reinforcement.

Only the exterior vertical cells of the masonry walls were grouted, as these were the only cells containing reinforcement. The principal variables in the tests were the wall height-to-length aspect ratio (r = H/L), and the horizontal reinforcement ratio (ρ_h). All walls had the same height, and aspect ratio was controlled by using three different wall lengths. Aspect ratios equal to 0.5, 0.7 and 1.0 were selected to span a typical range of masonry walls. The amount of horizontal reinforcement was selected to meet or exceed design requirements for ductile behavior as postulated in earlier work by Schultz (1997). Gross area ratios of horizontal reinforcement were nominally 0.05% and 0.12%, and actual values were 0.056% and 0.11%, respectively, depending upon the wire size used for the bed-joint reinforcement.

All six walls in Series 2 were tested using a test protocol that includes a lateral drift history in prescribed groups of cycles, and constant vertical load. All other degrees-of-freedom at the top and base of the walls were fully constrained. The header and footer beams were attached to the upper and lower crossheads of the TTF, and the drift and load histories, as well as the restraint forces at the constrained degrees-of-freedom were generated by a suite of six servo-controlled hydraulic force actuators which received commands from a dedicated computer by means of a feedback loop. Cracks and other forms of surface damage (e.g. crushing, abrasion, splitting) were identified visually and recorded at different stages of the tests. Data from the various displacement transducers, strain gages and other devices was sampled, digitized and stored. The shear wall tests were supplemented by a series of material strength tests for the masonry materials (block, mortar, grout, and masonry prisms), as well as for the steel reinforcement (vertical bars, horizontal cages).

9.2 Observations and Conclusions

Throughout the tests, it was observed that all walls exhibited nearly elastic force-displacement behavior for forces up to at least one-half of the yield strength of the specimen. Inelastic behavior invariably initiated with vertical cracking of the top course of masonry near the section where ungrouted masonry meets the grouted vertical cells. These vertical cracks propagated downward and widened considerably during the tests. For the long walls (i.e., with aspect ratio $H/L = 0.5$), these cracks dominated the force-displacement response over a wide range of displacements. Some diagonal or inclined cracks formed during the tests, but this usually occurred later in the load histories, and it was more prevalent among the more slender walls (i.e, $H/L = 0.7$ and 1.0). Towards the end of the tests, the welded wire grids began to fracture in a sequential manner, as evidenced by loud popping sounds. However, failure of the walls was gradual, as progressive damage was being accumulated by these moderately resilient walls which exhibited a respectable amount of toughness.

During the lateral load tests, the walls were observed to generate large lateral drifts before losing significant amounts of strength through deterioration. It was also noted that the behavior of the stocky specimen appeared to be more stable than that of the slender specimens, with the latter being affected more by inclined crack patterns. However, all specimens had

stable force-displacement hysteresis curves. Typically, all walls were able to dissipate energy through inelastic deformations. Increasing the horizontal reinforcement ratio had a small but positive influence on deformation capacity and shear strength.

The data presented in this report suggests that partially-grouted masonry walls are a viable lateral-load resisting system for seismic design, and that bed joint reinforcement can serve as horizontal reinforcement provided that it meets minimum requirements regarding tensile behavior. Resistance of partially-grouted masonry shear walls to the seismic drift histories was found to be stable and featured high initial stiffness and ample energy dissipation. The lateral load resisting mechanism observed in the tests represents a considerable improvement over that observed for the partially-grouted shear walls with bond beams in the previous phase of the experimental program (Schultz, 1994).

After initial formation of vertical cracks arising from stress concentrations between ungrouted and grouted masonry, the bed joint reinforcement was able to bridge the cracks and allow the masonry to continue carrying stress and form well-developed compression regions. Increasing height-to-length aspect ratio was found to have a beneficial effect on ultimate shear stress, but a detrimental one on toughness (deformation and energy dissipation capacities). Horizontal reinforcement ratio was found to have a modest and beneficial effect on ultimate shear stress and deformation capacity, but it did not affect energy dissipation.

Three procedures for defining the force-displacement characteristics of partially-grouted masonry shear walls were investigated with the objective of verifying design tools. The first procedure was initial lateral stiffness for masonry walls which were estimated from masonry properties and first principles, assuming an elastic panel. These estimates compared well with stiffnesses inferred from the experimental data, as long as slip displacements between the masonry and the header/footer beams were removed from the test data. The measured slip displacements suggest that initial stiffness estimates should be reduced by 50% to account for potential slip displacements. A formula for shear strength of masonry walls at first cracking (Eq. 8.13) proposed by Shing et al. (1989) was found to approximate experimental observations nearly as well as a cracking formula developed as part of this study (Eq. 8.14-8.17) specifically for partially-grouted masonry walls. Finally, a simple modification for

degree of grouting (Eq. 8.22) was proposed for use with the Matsumura-Fattal shear strength formula, and this modification greatly improves the predictive capability of the Matsumura-Fattal shear strength formula (Eq. 8.18-8.21) well beyond that of any other commonly used masonry shear strength formula in the U.S. (Fattal, 1993a).

9.3 Recommendations for Future Research

The following recommendations are drawn on the basis of the study summarized in this report. They are intended to widen the scope of the knowledge base concerning partially-grouted masonry shear by addressing specific issues raised in the present study.

1) Additional partially-grouted masonry shear wall tests from the "matrix" of tests contained in the NIST Masonry Research Program (Schultz, 1994) are strongly recommended. None of the walls in the present study had net vertical compression stresses other than σ_c = 1.38 Mpa (200 psi), and all walls had horizontal reinforcement. It is imperative to study the seismic performance of partially-grouted masonry walls which have no vertical stress and/or no horizontal reinforcement. Furthermore, no clay masonry specimens were included in the present study. At least seven, but preferably 12 tests are recommended, including parametric combinations 13 through 19 in the NIST Masonry Research Plan (Schultz, 1994), as well as some clay masonry walls.

2) An exhaustive attempt should be made to identify welded wire grids, or an equivalent, that are better suited for low-cycle, high-amplitude fatigue applications such as seismic design. Clearly, this wire reinforcement should meet minimum specifications, including a minimum value on elongation. The wire grids in the present study did not meet the specified criteria.

3) The detail for anchoring vertical reinforcement to header/footer beams should be improved to prevent the accumulation of large slip displacements at the interface of the masonry and the header/footer beams.

4) Analyses should be conducted suing a nonlinear finite element analysis package such as FEM/I (Ewing et al.,) to establish a better understanding of how to model partially-grouted

masonry shear walls. In particular, the mechanisms that produced the vertical cracks in the tests of Series 2 are not typically included in finite element formulations.

5) A second analytical effort is needed to define realistic seismic demands for partially-grouted masonry shear walls. Nonlinear dynamic (i.e. time history) and static (i.e. pushover) analyses should be used, as well as floor plans and elevations that are typical in actual masonry building systems.

6) Finally, an effort should be expended to continue to study the use of the modified Matsumura-Fattal shear strength equation, with a view towards generating simple but accurate shear strength equations amenable for building code provisions.

9. REFERENCES

Aguilar, G. Meli, R., Díaz, R. and Vázquez, R., "Influence of Horizontal Reinforcement on the Behavior of Confined Masonry Walls," Proceedings of the *Eleventh World Conference on Earthquake Engineering*, Elsevier Science Ltd., Paper No.1380, 1996.

American Concrete Institute, *Building Code Requirements for Reinforced Concrete*, ACI 318-98, ACI, Farmington Hills, MI, 1998.

American Society for Testing and Materials, "Standard Specification for Grout for Masonry," ASTM C476-83, ASTM, Philadelphia, PA, 1983.

American Society for Testing and Materials, "Standard Specification for Hollow Load-Bearing Concrete Masonry Units," ASTM C90-85, ASTM, Philadelphia, PA, 1985a.

American Society for Testing and Materials, "Standard Specification for Mortar for Unit Masonry," ASTM C270-89, ASTM, Philadelphia, PA, 1989b.

American Society for Testing and Materials, "Standard Specification for Steel Wire, Plain, for Concrete Reinforcement," ASTM A82-85, ASTM, Philadelphia, PA, 1985b.

American Society for Testing and Materials, "Standard Method of Sampling and Testing Grout," ASTM C1019, ASTM, Philadelphia, PA, 1984.

American Society for Testing and Materials, "Standard Methods of Sampling and Testing Concrete Masonry Units," ASTM C140-75, ASTM, Philadelphia, PA, 1980.

American Society for Testing and Materials, "Test Method for Compressive Strength of Hydraulic Cement Mortar," ASTM C109, ASTM, Philadelphia, PA, 1988a.

Casabbone, C, "General Description of Systems and Construction Practices," in *Masonry in the Americas*, SP-147, American Concrete Institute, Detroit, MI, 1994, pp. 21-55.

Chang, P., and Love, A.,"Finite Element Modeling of Masonry Shear Walls," Dept. Of Civil Engrg., Univ. of Maryland, College Park, 283 pp.

Drysdale, R. G., Hamid, A. A., and Baker, L. R., *Masonry Structures, Behavior and Design*, Prentice-Hall, Inc., Englewood Cliffs, NJ, 1994, 784 pp.

Ewing, R., El-Mustapha, A., and Kariotis, J., "FEM/I, A Finite Element Computer Program for the Nonlinear Static Analysis of Reinforced Masonry Building Components," US-Japan Coordinated Program for Masonry Research, Report No. 2.2-1, Ewing/Kariotis/Englekirk & Hart, Rancho Palos Verdes, CA, 1989, 118 pp.

Fattal, S. G., "Strength of Partially-Grouted Masonry Shear Walls Under Lateral Loads," NISTIR 5147, National Institute of Standards and Technology, Gaithersburg, MD, June 1993a, 66 pp.

Fattal, S. G., "Research Plan for Masonry Shear Walls," NISTIR 5117, National Institute of Standards and Technology, Gaithersburg, MD, June 1993b, 33 pp.

Fattal, S. G., "The Effect of Critical Parameters on the Behavior of Partially-Grouted Masonry Shear Walls Under Lateral Loads," NISTIR 5116, National Institute of Standards and Technology, Gaithersburg, MD, June 1993c, 45 pp.

Fattal, S. G., and Todd, D. R., "Ultimate Strength of Masonry Shear Walls: Predictions vs Test Results," NISTIR 4633, National Institute of Standards and Technology, Gaithersburg, MD, October 1991, 46 pp.

Flinn, R. A., and Trojan, P. K., *Engineering Materials and their Applications*, 3rd Ed., Houghton Mifflin Co., Boston, MA, 1986, 742 pp.

Hidalgo, P. and Luders, C., "Resistencia al Esfuerzo de Corte de Muros de Albañileria Armada Sometidos a Solicitaciones Sismicas," XXIV Jornadas Sudamericanas de Ingenieria Estructural, Vol. 1, Porto Alegre, Brasil, 1987, pp. 1-15.

International Conference of Building Officials, *Uniform Building Code*, Whittier, CA, 1997.

Langhaar, H. L. *Energy Methods in Applied Mechanics*, J. Wiley and Sons, Inc., New York, NY, 1962, 350 pp.

Luders, C, and Hidalgo, P., "Influencià del Refuerzo Horizontal en el Comportamiento Sismico de Muros de Albanileria Armada," Cuartas Jornadas Chilenas de Sismologia e Ingenieria Antisismica, Vol. 2, Viña del Mar, Chile, pp. H-139 to H-158, 1986.

Masonry Standards Joint Committee, "Building Code Requirements for Masonry Structures," Publication No. ACI 530-95/ASCE 5-95/TMS 420-95, American Concrete Institute, Farmington Hills, MI, American Society of Civil Engineers, New York, NY, and The Masonry Society, Boulder, CO, 1999.

Matsumura, A., "Effectiveness of Shear Reinforcement in Fully Grouted Hollow Clay Masonry Walls," Fourth Meeting of the Joint Technical Coordinating Committee on Masonry Research, U.S.-Japan Coordinated Earthquake Research Program, San Diego, CA, October, 1988.

Matsumura, A., "Shear Strength of Reinforced Hollow Unit Masonry Walls," *Proceedings,* Fourth North American Masonry Conference, Paper No. 50, Los Angeles, CA, 1987.

Matsumura, A., "Effect of Shear Reinforcement in Concrete Masonry Walls," First Meeting of the Joint Technical Coordinating Committee on Masonry Research, U.S.-Japan Coordinated Earthquake Research Program, Tokyo, Japan, August, 1985.

McGee, S., Chang, P., and Schultz, A. E., "Seismic Behavior of Partially-Grouted Masonry Shear Walls with Bond Beams," Dept. of Civil Engrg., Univ. of Maryland, 1998.

Mindess, S. and Young, J. F. *Concrete*. Prentice-Hall, Inc., Englewood Cliffs, NJ, 1981, 671 pp.

NEHRP Recommended Provisions for the Development of Seismic Regulations for New Buildings, Part 1, Provisions, Federal Emergency Management Agency, 1997.

Porter, M. L. and Tremel, P. M., "Sequential Phased Displacement Procedure for TCCMAR Testing," 3rd Meeting, Joint Technical Coordinating Committee on Masonry Research, US-Japan Coordinated Earthquake Res. Prog., Sapporo, Japan, Oct. 1987.

Sanchez, T. A., Flores, L., Alcocer, S. M., and Meli, R., "Respuesta Sismica de Muros de Mamposteria Confinada con Diferentes Tipos de Refuerzo Horizontal," Report No. ES/02/92, CENAPRED, Mexico City, March 1992, 49 pp.

Schneider, R. R., and Dickey, W. L., *Reinforced Masonry Design*, Prentice-Hall, Inc., Englewood Cliffs, NJ, 1996, 682 pp.

Schultz, A. E., "Minimum Horizontal Reinforcement Requirements for Seismic Design of Masonry Walls," *TMS Journal,* The Masonry Society, Vol. 14, No. 1, pp. 49-64, Aug. 1997.

Schultz, A. E., "NIST Research Program on the Seismic Resistance of Partially-Grouted Masonry Shear Walls," NISTIR 5481, National Institute of Standards and Technology, Gaithersburg, MD 20899, June 1994, 101 pp.

Schultz, A. E., "Performance of Masonry Structures under Extreme Lateral Loading Events," in *Masonry in the Americas*, D. P. Abrams ed., SP-147, American Concrete Institute, Detroit, MI, 1994, pp. 85-125.

Shing, P. B. and Cao, L. "Analysis of Partially Grouted Masonry Shear Walls," Dept. of Civil Engrg., Rep. No. CU/SR-97/2, Univ. of Colorado, Boulder, Feb. 1997, 40 pp.

Shing, P. B., and Noland, J. L., "Shear Behavior of Concrete Masonry Walls with Horizontal Joint Reinforcement," Dept. of Civil, Env. and Arch. Engrg., Univ. of Colorado, Boulder, Oct. 1992, 13 pp.

Shing, P. B., Schuller, M., and Hoskere, V. S., "In-Plane Resistance of Reinforced Masonry Shear Walls," *Journal of Structural Engineering*, ASCE, Vol. 116, No. 3, Mar. 1990a, pp. 619-640.

Shing, P. B., Schuller, M., Hoskere, V. S., and Carter, E., "Flexural and Shear Response of Reinforced Masonry Walls," *ACI Structural Journal*, Vol. 87, No. 6, November-December, 1990b, pp. 646-656.

Shing, P. B., Noland, J. L., and Klamerus, E., "Inelastic Behavior of Concrete Masonry Shear Walls," *Journal of Structural Engineering*, ASCE, Vol. 115, No. 9, Sept. 1989, pp. 2204-2225.

Sveinsson, B. I., McNiven, H. D., and Sucuoglu, H., "Cyclic Loading Tests of Masonry Single Piers, Volume 1 - Additional Tests with Height to Width Ratio of 1," Report No. UCB/EERC-85/15, Earthquake Engineering Research Center, University of California, Berkeley, December 1985, 163 pp.

Woodward, K., and Rankin, F., "Influence of Block and Mortar Strength on Shear Resistance of Concrete Block Masonry Walls," NBSIR 85-3143, National Bureau of Standards, Gaithersburg, MD, April 1985a, 73 pp.

Woodward, K., and Rankin, F., "Influence of Aspect Ratio on Shear Resistance of Concrete Block Walls," NBSIR 84-2993, National Bureau of Standards, Gaithersburg, MD, January 1985b, 65 pp.

Woodward, K., and Rankin, F., "Influence of Vertical Compressive Stress on Shear Resistance of Concrete Block Masonry Walls," NBSIR 84-2929, National Bureau of Standards, Gaithersburg, MD, October 1984a, 61 pp.

Woodward, K., and Rankin, F., "The NBS Tri-Directional Test Facility," NBSIR 84-2879, National Bureau of Standards, Gaithersburg, MD, May 1984b, 44 pp.

Woodward, K., and Rankin, F., "Behavior of Concrete Block Masonry Walls Subjected to Repeated Cyclic Displacements," NBSIR 83-2780, National Bureau of Standards, Gaithersburg, MD, October 1983, 178 pp.

Yancey, C. W. C., Experimental Results Versus Finite Element Predictions for Masonry Shear Walls," NISTIR, National Institute of Standards and Technology, Gaithersburg, MD.

Yancey, C. W. C., Fattal, S. G. and Dikkers, R. D., "Review of Research Literature on Masonry Shear Walls," NISTIR 4512, National Institute of Standards and Technology, Gaithersburg, MD, February 1991, 99 pp.

Yancey, C. W. C., and Scribner, C. F., "Influence of Horizontal Reinforcement on Shear Resistance of Concrete Block Masonry Walls," NISTIR 89-4202, National Institute of Standards and Technology, Gaithersburg, MD, October 1989, 61 pp.

Yoshimura, K. Kikuchi, K. Okamoto, T. and Sánchez, T., "Effect of Vertical and Horizontal Wall Reinforcement on Seismic Behavior of Confined Masonry Walls," Proceedings of the *Eleventh World Conference on Earthquake Engineering*, Elsevier Science Ltd., Paper No. 191, 1996.

Table 2.1 Experimental Priorities in Masonry Research Plan

Priority	Objective
I	Effectiveness of bed joint reinf. vs. hot-rolled, deformed bars in bond beams
II	Contribution of vertical reinforcement in the absence of horizontal steel
III	Effect of zero axial compression stress
IV	Influence of horizontal reinforcement
V	Influence of aspect ratio
VI	Characteristics of hollow clay unit masonry
VII	Influence of axial compression stress

Table 2.2 Schedule of Nominal Properties for Specimens in Priority I

Phase	Specimen		Aspect Ratio	Horizontal Reinforcement		Vertical Reinforcement Ratio (%)	Compressive Stress
	No.	Designation	(*H/L*)	Type	Ratio (%)		(MPa)
1	1	CO-R05-B05-Q10	$r_1 = 0.5$	bond beam	$\rho_{h1} = 0.05$	0.205	$\sigma_{c1} = 1.38$
	3	CO-R07-B05-Q10	$r_2 = 0.7$	bond beam	$\rho_{h1} = 0.05$	0.287	$\sigma_{c1} = 1.38$
	5	CO-R10-B05-Q10	$r_3 = 1.0$	bond beam	$\rho_{h1} = 0.05$	0.410	$\sigma_{c1} = 1.38$
	7	CO-R05-B12-Q10	$r_1 = 0.5$	bond beam	$\rho_{h2} = 0.12$	0.205	$\sigma_{c1} = 1.38$
	9	CO-R07-B12-Q10	$r_2 = 0.7$	bond beam	$\rho_{h2} = 0.12$	0.287	$\sigma_{c1} = 1.38$
	11	CO-R10-B12-Q10	$r_3 = 1.0$	bond beam	$\rho_{h2} = 0.12$	0.410	$\sigma_{c1} = 1.38$
2	2	CO-R05-J05-Q10	$r_1 = 0.5$	joint r/f	$\rho_{h1} = 0.05$	0.205	$\sigma_{c1} = 1.38$
	4	CO-R07-J05-Q10	$r_2 = 0.7$	joint r/f	$\rho_{h1} = 0.05$	0.287	$\sigma_{c1} = 1.38$
	6	CO-R10-J05-Q10	$r_3 = 1.0$	joint r/f	$\rho_{h1} = 0.05$	0.410	$\sigma_{c1} = 1.38$
	8	CO-R05-J12-Q10	$r_1 = 0.5$	joint r/f	$\rho_{h2} = 0.12$	0.205	$\sigma_{c1} = 1.38$
	10	CO-R07-J12-Q10	$r_2 = 0.7$	joint r/f	$\rho_{h2} = 0.12$	0.287	$\sigma_{c1} = 1.38$
	12	CO-R10-J12-Q10	$r_3 = 1.0$	joint r/f	$\rho_{h2} = 0.12$	0.410	$\sigma_{c1} = 1.38$

1 MPa = 145 psi

Table 2.3 Estimated Minimum Horizontal Reinforcement Ratios for Phase 2 Specimens

Specimen		f'_m, MPa (psi)	f_{yh}, MPa (ksi)	σ_c, MPa (psi)	L, mm (in.)	minimum ρ_h (%)	
No.	Designation					Strength	Energy
2	CO-R05-J05-Q10	13.79 (2000)	551.7 (80)	1.38 (200)	2845 (112)	0.0426	0.0741
4	CO-R07-J05-Q10	13.79 (2000)	551.7 (80)	1.38 (200)	2032 (80)	0.0426	0.0592
6	CO-R10-J05-Q10	13.79 (2000)	551.7 (80)	1.38 (200)	1422 (56)	0.0426	0.0467
8	CO-R05-J12-Q10	13.79 (2000)	551.7 (80)	1.38 (200)	2845 (112)	0.0426	0.0741
10	CO-R07-J12-Q10	13.79 (2000)	551.7 (80)	1.38 (200)	2032 (80)	0.0426	0.0592
12	CO-R10-J12-Q10	13.79 (2000)	551.7 (80)	1.38 (200)	1422 (56)	0.0426	0.0467

Table 3.1 Dimensions of Concrete Masonry Units

Dimension†	Location	Block 1	Block 2	Block 3	Mean††
Gross Dimensions	Length	39.65	39.70	39.60	39.642 (0.0289)
		39.60	39.75	39.65	
		39.60	39.65	39.65	
		39.65	39.70	39.50	
	Mean††	39.625 (0.0289)	39.700 (0.0408)	39.600 (0.0707)	
	Width	19.45	19.40	19.45	19.458 (0.0417)
		19.45	19.45	19.45	
		19.45	19.50	19.45	
		19.50	19.55	19.40	
	Mean††	19.463 (0.0250)	19.475 (0.0655)	19.438 (0.0250)	
	Height	19.40	19.45	19.35	19.408 (0.0634)
		19.45	19.50	19.40	
		19.35	19.45	19.30	
		19.40	19.50	19.35	
	Mean††	19.400 (0.0408)	19.475 (0.0289)	19.350 (0.0408)	
Interior Web Thickness	Top	2.65	2.55	2.70	2.633 (0.0764)
	Mid-Height	2.90	2.85	2.80	2.850 (0.0500)
	Bottom	4.50	4.45	5.00	4.650 (0.3041)

†Dimensions in cm (1 cm = 0.394 in.)
††Standard deviation in parentheses

Table 3.1 Dimensions of Concrete Masonry Units (continued)

Dimension†	Location	Block 1	Block 2	Block 3	Mean††
Face-Shell Thickness	Top	3.30	3.30	3.25	3.367 (0.0779)
		3.40	3.30	3.35	
		3.30	3.25	3.40	
		3.35	3.30	3.50	
	Mean††	3.338 (0.0479)	3.388 (0.0854)	3.375 (0.1041)	
	Mid-Height	3.35	3.40	3.35	3.429 (0.0916)
		3.50	3.45	3.35	
		3.30	3.40	3.60	
		3.40	3.50	3.55	
	Mean††	3.388 (0.0854)	3.438 (0.0479)	3.463 (0.1315)	
	Bottom	3.50	3.60	3.45	3.550 (0.0479)
		3.50	3.60	3.35	
		3.45	3.50	3.80	
		3.55	3.55	3.75	
	Mean††	3.500 (0.0408)	3.563 (0.0479)	3.588 (0.2213)	
Exterior Web Thickness	Top	3.40	3.30	3.30	3.308 (0.0801)
		3.25	3.40	3.20	
	Mean††	3.325 (0.1061)	3.350 (0.0707)	3.308 (0.0707)	
	Mid-Height	3.50	3.55	3.50	3.475 (0.1037)
		3.35	3.60	3.35	
	Mean††	3.425 (0.1061)	3.575 (0.0354)	3.425 (0.1061)	
	Bottom	3.65	3.60	3.70	3.608 (0.1158)
		3.45	3.75	3.50	
	Mean††	3.550 (0.1414)	3.675 (0.1061)	3.600 (0.1414)	

†Dimensions in cm (1 cm = 0.394 in.)

††Standard deviation in parentheses

Table 3.2 Mix Designs by Weight for Masonry Materials
(a) Masonry Mortar

Mortar Mix Design by Weight (lbs)		
Material	Weight (lbs) for a Mortar Volume = 1 ft^3	Weight (lbs) for a Mortar Volume = 2 ft^3
Type I Portland Cement	24.0	48.0
Hydrated Lime	3.8	7.6
Mortar Sand	92.4	184.8
Water	19.5	39.0

1 lb = 0.453 kg; 1 ft^3 = 0.0283 m^3

Table 3.2 Mix Designs by Weight for Masonry Materials
(b) Masonry Grout

Grout Mix Design by Weight (lbs)		
Material	Weight (lbs) for a Grout Volume = 1 ft^3	Weight (lbs) for a Grout Volume = 4.5 ft^3
Type I Portland Cement	19.2	86.5
Mortar Sand	64.5	290.1
Pea Gravel	41.9	188.4
Water	14.4	64.9

1 lb = 0.453 kg; 1 ft^3 = 0.0283 m^3

Table 3.3 Summary of Compression Strengths of Masonry Materials
(a) At Various Ages

Description	Age (days)	Compression Strength (psi)
Moist-cured, grouted masonry prisms	28	2540
Moist-cured, ungrouted masonry prisms	28	2100
Moist-cured masonry mortar cubes	28	3180
Air-cured masonry mortar cubes	7	2180
Air-cured, masonry mortar cubes	28	2370
Air-cured, masonry mortar cubes	56	2340
Moist-cured, masonry grout specimens	28	4170
Air-cured, masonry grout specimens	7	3120
Air-cured, masonry grout specimens	28	3630
Air-cured, masonry grout specimens	56	3740
Concrete masonry units	----	3380

1 psi = 0.00690 MPa

Table 3.3 Summary of Compression Strengths of Masonry Materials
(b) Companion Specimen Tests

Description	Compression Strength (psi) for Shear Wall					
	2	4	6	8	10	12
Companion, air-cured, grouted masonry prisms	2090	2140	1910	2350	2120	2400
Companion, air-cured, ungrouted masonry prisms	2280	2450	2690	2500	2490	2660
7-day cube tests of moist-cured mortar for header beam	2720	2700	2220	2280	2510	2660
28-day cube tests of moist-cured mortar for header beam	3200	3280	2760	2900	3320	3440
7-day cube tests of moist-cured mortar for footer beam	2860	2560	2520	2510	2470	2540
28-day cube tests of moist-cured mortar for footer beam	3310	3150	3210	3320	3040	3170
7-day cube tests of moist-cured grout for header beam anchorage plugs	8750	9200	9060	7670	7750	9370
28-day cube tests of moist-cured grout for header beam anchorage plugs	9350	10,490	10,890	9390	9550	10,500
7-day cube tests of moist-cured grout for footer beam anchorage plugs	8260	8590	9060	6650	8720	8510
28-day cube tests of moist-cured grout for footer beam anchorage plugs	9120	10,530	10,890	7630	10,140	9670

1 psi = 0.00690 MPa

Table 3.4 Material Test Specimen Schedule

Type of Test	Specimen Designation	Description
masonry prisms	PG28DM-*i* (*i* = 1-6)	28-day, grouted, moist-cured prisms
	PU28DM-*i* (*i* = 1-6)	28-day, ungrouted, moist-cured prisms
	PGSW*j*-*k* (*k* = 1 or 2)	Companion, grouted, air-cured prisms for shear wall *j*
	PUSW*j*-*k* (*k* = 1 or 2)	Companion, ungrouted, air-cured prisms for shear wall *j*
mortar cubes	*m*M28DM-*n* (*n* = 1-3)	28-day, moist-cured cubes for masonry mortar batch *m*
	1M7DA-*n* (*n* = 1-3)	7-day, air-cured cubes for masonry mortar batch 1
	1M28DA-*n* (*n* = 1-3)	28-day, air-cured cubes for masonry mortar batch 1
	1M56DA-*n* (*n* = 1-3)	56-day, air-cured cubes for masonry mortar batch 1
	M7TSW*j*-*n* (*n* = 1-3)	7-day, moist-cured mortar, top joint of shear wall *j*
	M28TSW*j*-*n* (*n* = 1-3)	28-day, moist-cured mortar, top joint of shear wall *j*
	M7BSW*j*-*n* (*n* = 1-3)	7-day, moist-cured mortar, bottom joint of shear wall *j*
	M28BSW*j*-*n* (*n* = 1-3)	28-day, moist-cured mortar, bottom joint of shear wall *j*
masonry grout specimens	*g*G28DM-*n* (*n* = 1-3)	28-day, moist-cured specimens for grout batch *g*
	2G7DA-*n* (*n* = 1 or 2)	7-day, air-cured specimens for grout batch 2
	2G28DA-*n* (*n* = 1 or 2)	28-day, air-cured specimens for grout batch 2
	2G56DA-*n* (*n* = 1 or 2)	56-day, air-cured specimens for grout batch 2
non-shrink grout cubes	G7TSW*j*-*n* (*n* = 1-3)	7-day, moist-cured grout, header plugs in shear wall *j*
	G28TSW*j*-*n* (*n* = 1-3)	28-day, moist-cured grout, header plugs in shear wall *j*
	G7BSW*j*-*n* (*n* = 1-3)	7-day, moist-cured grout, footer plugs in shear wall *j*
	G28BSW*j*-*n* (*n* = 1-3)	28-day, moist-cured grout, footer plugs in shear wall *j*
masonry units	CMU-*n* (*n* = 1-4)	Compression strength of concrete masonry unit

j = shear wall number (*j* = 2, 4, 6, 8, 10, or 12)
n = mortar cube, grout cube, grout specimen, or concrete masonry units number
m = mortar batch number
g = grout batch number

Table 3.5 Masonry Prism Tests
(a) 28-Day Moist-Cured Specimens

Type of Prism	Specimen Designation	Date Cast	Date Tested	Compression Strength (psi)	
				individual	average
grouted	PG28DM-1	6/17/96*	7/24/96	2850	2540
	PG28DM-2	6/17/96*	7/24/96	2230	
	PG28DM-3	6/17/96*	7/24/96	2540	
ungrouted	PU28DM-1	6/17/96	7/15/86	2030	2100
	PU28DM-2	6/17/96	7/15/86	1760†	
	PU28DM-3	6/17/96	7/15/86	2170	

1 psi = 0.00690 MPa
*Grouted 6/26/96
†This value is considered an outlier and was not used to calculate average strength

Table 3.5 Masonry Prism Tests
(b) Companion Air-Cured Specimens

Type of Prism	Shear Wall No.	Specimen Designation	Date Cast	Date Tested	Compression Strength (psi)	
					individual	average
grouted	2	PGSW2-1	6/17/96*	9/6/96	2400	2090
		PGSW2-2	6/17/96*	9/6/96	1780	
	4	PGSW4-1	6/18/96†	9/27/96	2000	2140
		PGSW4-2	6/18/96†	9/27/96	2280	
	6	PGSW6-1	6/17/96†	3/20/95	1910	1910
		PGSW6-2	6/18/96†	3/20/95	1910	
	8	PGSW8-1	6/17/96†	11/27/96	2350	2350
		PGSW8-2	6/17/96†	11/27/96	2350	
	10	PGSW10-1	6/17/96†	1/3/97	2130	2120
		PGSW10-2	6/17/96†	1/3/97	2110	
	12	PGSW12-1	6/17/96†	1/17/97	2360	2400
		PGSW12-2	6/17/96†	1/17/97	2440	
ungrouted	2	PUSW2-1	6/17/96	9/6/96	2310	2280
		PUSW2-2	6/17/96	9/6/96	2260	
	4	PUSW4-1	6/18/96	9/27/96	2520	2450
		PUSW4-2	6/18/96	9/27/96	2380	
	6	PUSW6-1	6/17/96	11/4/96	2730	2690
		PUSW6-2	6/17/96	11/4/96	2640	
	8	PUSW8-1	6/17/96	11/27/96	2450	2500
		PUSW8-2	6/17/96	11/27/96	2560	
	10	PUSW10-1	6/17/96	1/3/97	2480	2490
		PUSW10-2	6/17/96	1/3/97	2500	
	12	PUSW12-1	6/17/96	1/17/97	2690	2660
		PUSW12-2	6/17/96	1/17/97	2640	

1 psi = 0.00690 Mpa *Grouted 6/26/96 †Grouted 6/27/96

Table 3.6 Masonry Mortar Cube Tests
(a) 28-Day Tests of Moist-Cured Masonry Mortar

Batch No. (Shear Wall No.)	Specimen Designation	Date Cast	Date Tested	Compression Strength (psi)	
				individual	average
1 (8)	1M28DM-1	6/17/96	7/15/96	3330	3350
	1M28DM-2	6/17/96	7/15/96	3340	
	1M28DM-3	6/17/96	7/15/96	3370	
2 (8)	2M28DM-1	6/17/96	7/15/96	2730	2900
	2M28DM-2	6/17/96	7/15/96	3040	
	2M28DM-3	6/17/96	7/15/96	2940	
3 (10, 12)	3M28DM-1	6/17/96	7/15/96	3040	2960
	3M28DM-2	6/17/96	7/15/96	2950	
	3M28DM-3	6/17/96	7/15/96	2890	
4 (10, 12)	4M28DM-1	6/17/96	7/15/96	3230	3370
	4M28DM-2	6/17/96	7/15/96	3440	
	4M28DM-3	6/17/96	7/15/96	3430	
5 (2)	5M28DM-1	6/17/96	7/15/96	3320	3250
	5M28DM-2	6/17/96	7/15/96	3210	
	5M28DM-3	6/17/96	7/15/96	3220	
6 (2, 6)	6M28DM-1	6/17/96	7/15/96	3180	3060
	6M28DM-2	6/17/96	7/15/96	3110	
	6M28DM-3	6/17/96	7/15/96	2870	
7 (6, 4)	7M28DM-1	6/17/96	7/15/96	3240	3310
	7M28DM-2	6/17/96	7/15/96	3240	
	7M28DM-3	6/17/96	7/15/96	3450	
8 (4)	8M28DM-1	6/17/96	7/15/96	3250	3210
	8M28DM-2	6/17/96	7/15/96	3210	
	8M28DM-3	6/17/96	7/15/96	3170	

1 psi = 0.00690 MPa

Table 3.6 Masonry Mortar Cube Tests
(b) Tests of Air-Cured Masonry Mortar at Various Ages

Age (days)	Specimen Designation	Date Cast	Date Tested	Compression Strength (psi)	
				individual	average
7	1M7DA-1	6/17/96	6/24/96	2100	2180
	1M7DA-2	6/17/96	6/24/96	2200	
	1M7DA-3	6/17/96	6/24/96	2250	
28	1M28DA-1	6/17/96	7/15/96	2470	2370
	1M28DA-2	6/17/96	7/15/96	2390	
	1M28DA-3	6/17/96	7/15/96	2250	
56	1M56DA-1	6/17/96	8/12/96	2330	2340
	1M56DA-2	6/17/96	8/12/96	2340	
	1M56DA-3	6/17/96	8/12/96	2350	

1 psi = 0.00690 MPa

Table 3.6 Masonry Mortar Cube Tests
(c) 7-Day Tests of Moist-Cured Header Beam Mortar

Shear Wall	Specimen Designation	Date Cast	Date Tested	Compression Strength (psi)	
				individual	average
2	M7TSW2-1	7/25/96	8/1/96	2980	2720
	M7TSW2-2	7/25/96	8/1/96	2690	
	M7TSW2-3	7/25/96	8/1/96	2680	
4	M7TSW4-1	8/23/96	8/30/96	2730	2700
	M7TSW4-2	8/23/96	8/30/96	2680	
	M7TSW4-3	8/23/96	8/30/96	2700	
6	M7TSW6-1	8/27/96	9/3/96	2190	2220
	M7TSW6-2	8/27/96	9/3/96	2250	
	M7TSW6-3	8/27/96	9/3/96	2230	
8	M7TSW8-1	10/8/96	10/15/96	2280	2280
	M7TSW8-2	10/8/96	10/15/96	2240	
	M7TSW8-3	10/8/96	10/15/96	2310	
10	M7TSW10-1	10/18/96	10/25/96	2510	2510
	M7TSW10-2	10/18/96	10/25/96	2590	
	M7TSW10-3	10/18/96	10/25/96	2420	
12	M7TSW12-1	12/17/96	12/24/96	2760	2660
	M7TSW12-2	12/17/96	12/24/96	2620	
	M7TSW12-3	12/17/96	12/24/96	2590	

1 psi = 0.00690 MPa

Table 3.6 Masonry Mortar Cube Tests
(d) 7-Day Tests of Moist-Cured Footer Beam Mortar

Shear Wall	Specimen Designation	Date Cast	Date Tested	Compression Strength (psi)	
				individual	average
2	M7BSW2-1	7/24/96	7/31/96	2880	2860
	M7BSW1-2	7/24/96	7/31/96	2830	
	M7BSW2-3	7/24/96	7/31/96	2870	
4	M7BSW4-1	8/22/96	8/29/96	2570	2560
	M7BSW4-2	8/22/96	8/29/96	2520	
	M7BSW4-3	8/22/96	8/29/96	2590	
6	M7BSW6-1	8/27/96	9/3/96	2640	2520
	M7BSW6-2	8/27/96	9/3/96	2390	
	M7BSW6-3	8/27/96	9/3/96	----	
8	M7BSW8-1	10/4/96	10/11/96	2570	2590
	M7BSW8-2	10/4/96	10/11/96	2660	
	M7BSW8-3	10/4/96	10/11/96	2540	
10	M7BSW10-1	10/17/96	10/24/96	2480	2470
	M7BSW10-2	10/17/96	10/24/96	2430	
	M7BSW10-3	10/17/96	10/24/96	2490	
12	M7BSW12-1	12/16/96	12/23/96	2560	2540
	M7BSW12-2	12/16/96	12/23/96	2610	
	M7TSW12-3	12/16/96	12/23/96	2450	

1 psi = 0.00690 MPa

Table 3.6 Masonry Mortar Cube Tests
(e) 28-Day Tests of Moist-Cured Header Beam Mortar

Shear Wall	Specimen Designation	Date Cast	Date Tested	Compression Strength (psi)	
				individual	average
2	M28TSW2-1	7/25/96	8/22/96	3130	3200
	M28TSW2-2	7/25/96	8/22/96	3260	
	M28TSW2-3	7/25/96	8/22/96	3200	
4	M28TSW4-1	8/23/96	9/20/96	3330	3280
	M28TSW4-2	8/23/96	9/20/96	3250	
	M28TSW4-3	8/23/96	9/20/96	2700	
6	M28TSW6-1	8/27/96	9/24/96	2740	2760
	M28TSW6-2	8/27/96	9/24/96	2720	
	M28TSW6-3	8/27/96	9/24/96	2810	
8	M28TSW8-1	10/8/96	11/5/96	2910	2900
	M28TSW8-2	10/8/96	11/5/96	2860	
	M28TSW8-3	10/8/96	11/5/96	2930	
10	M28TSW10-1	10/18/96	11/15/96	3280	3320
	M28TSW10-2	10/18/96	11/15/96	3300	
	M28TSW10-3	10/18/96	11/15/96	3380	
12	M28TSW12-1	12/17/96	1/14/97	3490	3440
	M28TSW12-2	12/17/96	1/14/97	3460	
	M28TSW12-3	12/17/96	1/14/97	3380	

1 psi = 0.00690 MPa

Table 3.6 Masonry Mortar Cube Tests
(f) 28-Day Tests of Moist-Cured Footer Beam Mortar

Shear Wall	Specimen Designation	Date Cast	Date Tested	Compression Strength (psi)	
				individual	average
2	M28BSW2-1	7/24/96	8/21/96	3430	3310
	M28BSW1-2	7/24/96	8/21/96	3320	
	M28BSW2-3	7/24/96	8/21/96	3180	
4	M28BSW4-1	8/22/96	9/19/96	3180	3150
	M28BSW4-2	8/22/96	9/19/96	3190	
	M28BSW4-3	8/22/96	9/19/96	3080	
6	M28BSW6-1	8/27/96	9/24/96	3180	3210
	M28BSW6-2	8/27/96	9/24/96	3230	
	M28BSW6-3	8/27/96	9/24/96	3220	
8	M28BSW8-1	10/4/96	11/1/96	3380	3320
	M28BSW8-2	10/4/96	11/1/96	3340	
	M28BSW8-3	10/4/96	11/1/96	3230	
10	M28BSW10-1	10/17/96	11/14/96	3060	3040
	M28BSW10-2	10/17/96	11/14/96	3090	
	M28BSW10-3	10/17/96	11/14/96	2980	
12	M28BSW12-1	12/16/96	1/13/97	3190	3170
	M28BSW12-2	12/16/96	1/13/97	3300	
	M28TSW12-3	12/16/96	1/13/97	3030	

1 psi = 0.00690 MPa

Table 3.7 Masonry Grout Specimen Tests
(a) 28-Day Tests of Moist-Cured Specimens

Batch No.	Shear Wall No.	Specimen Designation	Date Cast	Date Tested	Compression Strength (psi)	
					individual	average
1	2	1G28DM-1	6/26/96	7/24/96	3820	3780
		1G28DM-2	6/26/96	7/24/96	3720	
		1G28DM-3	6/26/96	7/24/96	3790	
2	6	2G28DM-1	6/27/96	7/25/96	4210	4230
		2G28DM-2	6/27/96	7/25/96	4110	
		2G28DM-3	6/27/96	7/25/96	4370	
3	4	3G28DM-1	6/27/96	7/25/96	4220	4260
		3G28DM-2	6/27/96	7/25/96	4260	
		3G28DM-3	6/27/96	7/25/96	4290	
5	12	5G28DM-1	6/27/96	7/25/96	3940	4000
		5G28DM-2	6/27/96	7/25/96	3980	
		5G28DM-3	6/27/96	7/25/96	4080	
6	10	6G28DM-1	6/27/96	7/25/96	4430	4310
		6G28DM-2	6/27/96	7/25/96	4280	
		6G28DM-3	6/27/96	7/25/96	4220	
7	8	7G28DM-1	6/27/96	7/25/96	4460	4430
		7G28DM-2	6/27/96	7/25/96	4400	
		7G28DM-3	6/27/96	7/25/96	4430	

1 psi = 0.00690 MPa

Table 3.7 Masonry Grout Specimen Tests
(b) Tests of Air-Cured Specimens at Various Ages

Batch No.	Age (days)	Specimen Designation	Date Cast	Date Tested	Compression Strength (psi)	
					individual	average
1	7	1G7DA-1	6/26/96	7/3/96	3240	3120
		1G7DA-2	6/26/96	7/3/96	3000	
	28	1G28DA-1	6/26/96	7/24/96	3540	3630
		1G28DA-2	6/26/96	7/24/96	3730	
	56	1G56DA-1	6/26/96	8/21/96	3670	3740
		1G56DA-2	6/26/96	8/21/96	3810	

1 psi = 0.00690 MPa

Table 3.8 Cube Tests of Anchorage Plug Grout
(a) 7-Day Tests of Moist-Cured Header Beam Grout

Shear Wall	Specimen Designation	Date Cast	Date Tested	Compression Strength (psi)	
				individual	average
2	G7TSW2-1	7/25/96	8/1/96	8880	8750
	G7TSW2-2	7/25/96	8/1/96	8700	
	G7TSW2-3	7/25/96	8/1/96	8570	
4	G7TSW4-1	8/26/96	9/3/96	9120	9200
	G7TSW4-2	8/26/96	9/3/96	9160	
	G7TSW4-3	8/26/96	9/3/96	9320	
6	G7TSW6-1	8/28/96	9/4/96	9170	9060
	G7TSW6-2	8/28/96	9/4/96	8980	
	G7TSW6-3	8/28/96	9/4/96	9040	
8	G7TSW8-1	10/8/96	10/15/96	7890	7670
	G7TSW8-2	10/8/96	10/15/96	7500	
	G7TSW8-3	10/8/96	10/15/96	7610	
10	G7TSW10-1	10/18/96	10/25/96	7650	7750
	G7TSW10-2	10/18/96	10/25/96	7710	
	G7TSW10-3	10/18/96	10/25/96	7890	
12	G7TSW12-1	12/17/96	12/24/96	9240	9370
	G7TSW12-2	12/17/96	12/24/96	9390	
	G7TSW12-3	12/17/96	12/24/96	9480	

1 psi = 0.00690 MPa

Table 3.8 Cube Tests of Anchorage Plug Grout
(b) 7-Day Tests of Moist-Cured Footer Beam Grout

Shear Wall	Specimen Designation	Date Cast	Date Tested	Compression Strength (psi)	
				individual	average
2	G7BSW2-1	7/24/96	7/31/96	8250	8260
	G7BSW2-2	7/24/96	7/31/96	8230	
	G7BSW2-3	7/24/96	7/31/96	8320	
4	G7BSW4-1	8/23/96	8/30/96	8720	8590
	G7BSW4-2	8/23/96	8/30/96	8210	
	G7BSW4-3	8/23/96	8/30/96	8820	
6	G7BSW6-1	8/28/96	9/4/96	9170	9060
	G7BSW6-2	8/28/96	9/4/96	8980	
	G7BSW6-3	8/28/96	9/4/96	9040	
8	G7BSW8-1	10/7/96	10/15/96	6090	6650
	G7BSW8-2	10/7/96	10/15/96	6860	
	G7BSW8-3	10/7/96	10/15/96	7010	
10	G7BSW10-1	10/17/96	12/24/96	8620	8720
	G7BSW10-2	10/17/96	12/24/96	8700	
	G7BSW10-3	10/17/96	12/24/96	8830	
12	G7BSW12-1	12/16/96	12/23/96	8510	8510
	G7BSW12-2	12/16/96	12/23/96	8820	
	G7BSW12-3	12/16/96	12/23/96	8200	

1 psi = 0.00690 MPa

Table 3.8 Cube Tests of Anchorage Plug Grout
(c) 28-Day Tests of Moist-Cured Header Beam Grout

Shear Wall	Specimen Designation	Date Cast	Date Tested	Compression Strength (psi)	
				individual	average
2	G28TSW2-1	7/25/96	8/22/96	8800	9350
	G28TSW2-2	7/25/96	8/22/96	9540	
	G28TSW2-3	7/25/96	8/22/96	9720	
4	G28TSW4-1	8/26/96	9/23/96	10,450	10,490
	G28TSW4-2	8/26/96	9/23/96	10,590	
	G28TSW4-3	8/26/96	9/23/96	10,430	
6	G28TSW6-1	8/28/96	9/25/96	10,760	10,890
	G28TSW6-2	8/28/96	9/25/96	10,940	
	G28TSW6-3	8/28/96	9/25/96	10,970	
8	G28TSW8-1	10/8/96	11/5/96	9540	9390
	G28TSW8-2	10/8/96	11/5/96	9470	
	G28TSW8-3	10/8/96	11/5/96	9150	
10	G28TSW10-1	10/18/96	11/15/96	9520	9550
	G28TSW10-2	10/18/96	11/15/96	9470	
	G28TSW10-3	10/18/96	11/15/96	9670	
12	G28TSW12-1	12/17/96	1/14/97	10,060	10,500
	G28TSW12-2	12/17/96	1/14/97	10,800	
	G28TSW12-3	12/17/96	1/14/97	10,650	

1 psi = 0.00690 MPa

Table 3.8 Cube Tests of Anchorage Plug Grout
(d) 28-Day Tests of Moist-Cured Footer Beam Grout

Shear Wall	Specimen Designation	Date Cast	Date Tested	Compression Strength (psi)	
				individual	average
2	G7BSW2-1	7/24/96	8/21/96	8980	9120
	G7BSW2-2	7/24/96	8/21/96	8870	
	G7BSW2-3	7/24/96	8/21/96	9520	
4	G7BSW4-1	8/23/96	9/20/96	10,460	10,530
	G7BSW4-2	8/23/96	9/2096	10,490	
	G7BSW4-3	8/23/96	9/20/96	10,650	
6	G7BSW6-1	8/28/96	9/25/96	10,760	10,890
	G7BSW6-2	8/28/96	9/25/96	10,940	
	G7BSW6-3	8/28/96	9/25/96	10,970	
8	G7BSW8-1	10/7/96	11/4/96	8050	7630
	G7BSW8-2	10/7/96	11/4/96	7200	
	G7BSW8-3	10/7/96	11/4/96	7630	
10	G7BSW10-1	10/17/96	11/14/96	10,460	10,140
	G7BSW10-2	10/17/96	11/14/96	10,150	
	G7BSW10-3	10/17/96	11/14/96	9820	
12	G7BSW12-1	12/16/96	1/13/97	9670	9670
	G7BSW12-2	12/16/96	1/13/97	9660	
	G7BSW12-3	12/16/96	1/13/97	9690	

1 psi = 0.00690 MPa

Table 3.9 Concrete Masonry Unit Tests

Specimen Designation	Date Tested	Compression Strength (psi)	
		individual	average
CMU-1	9/22/97	3040	3380
CMU-2	9/22/97	3980	
CMU-3	9/22/97	3240	
CMU-4	9/22/97	3260	

1 psi = 0.00690 MPa

Table 3.10 Tension Test Results for Vertical Reinforcing Bars

Bar Size	Sample No.	Stress (ksi)		Strain (in./in.)			Modulus of Elasticity (ksi)
		Yield	Ultimate	Yield	Strain Hardening	Ultimate	
6	1	64.57	105.93	0.00241	0.00543	0.1000	26,760
	2	65.18	107.49	0.00245	0.00514	0.1293	26,580
	3	63.99	107.08	0.00226	0.00446	0.1027	28,340
	average	*64.58*	*106.83*	*0.00237*	*0.00501*	*0.1107*	*27,230*

1 ksi = 6.90 MPa

Table 3.11 Tension Test Results for Longitudinal Wires in Horizontal Reinforcing Grids

Shear Wall No.	Sample No.	Wire Diameter[1] (in.)		Stress (ksi)[2]		Strain (in./in.)		Modulus of Elasticity[2] (ksi)
		Longitudinal	Transverse	Yield[3]	Ultimate	Yield[3,4]	Ultimate	
2	1	0.148	0.148	100.37	106.97	-----	0.04200	-----
	2			104.26	108.42	0.00306	0.03050	34,080
4	1			99.17	102.90	0.00375	0.02980	26,450
	2			98.33	103.39	0.00315	0.06954	31,220
6	1			98.13	102.88	0.00329	0.03052	29,800
	2			104.17	108.12	0.00351	0.05787	29,690
average for 9 Ga. wire				*100.74*	*105.45*	*0.00335*	*0.04337*	*30,250*
8	1	0.207	0.148	83.70	89.95	0.00275	0.03563	30,450
	2			91.76	95.36	-----	0.03881	-----
	3			88.68	93.70	0.00305	0.09288	29,070
	4			80.19	87.28	0.00326	0.05740	24,580
10	1			75.56	82.36	0.00272	0.06505	27,770
	2			76.39	83.11	0.00256	0.06697	29,870
	3			80.09	85.44	0.00277	0.05315	28,950
	4			79.63	85.44	-----	0.07341	-----
average for 5 Ga. wire				*82.00*	*87.83*	*0.00285*	*0.06041*	*28,450*

[1]1 in. = 25.4 mm
[2]1 ksi = 6.90 MPa
[3]0.2% offset yield
[4]Ratio of yield stress to modulus of elasticity

Table 4.1 Vertical (Axial) Load Variation During Tests

Shear Wall No.	Specimen Designation	Length, mm (in.)	Aspect Ratio, H/L	Vertical Load, kN (kips)		
				Nominal	Measured	
					Mean	Std. Dev.
2	CO-R05-J05-Q10	2845 (112)	0.5	266.9 (60)	265.0 (59.58)	11.3 (2.55)
4	CO-R07-J05-Q10	2032 (80)	0.7	186.8 (42)	185.4 (41.69)	8.4 (1.88)
6	CO-R10-J05-Q10	1422 (56)	1	133.4 (30)	130.2 (29.27)	5.9 (1.32)
8	CO-R05-J12-Q10	2845 (112)	0.5	266.9 (60)	265.5 (59.70)	4.9 (1.11)
10	CO-R07-J12-Q10	2032 (80)	0.7	186.8 (42)	187.6 (42.17)	5.6 (1.26)
12	CO-R10-J12-Q10	1422 (56)	1	133.4 (30)	133.2 (29.95)	4.5 (1.02)

1 in. = 25.4 mm; 1 kN = 0.225

Table 4.2 Location of LST Transducers

Instrument	Orientation	Dimensions (in.)[1]					
		Wall 2	Wall 4	Wall 6	Wall 8	Wall 10	Wall 12
Alpha	V	24.0	24.0	24.0	24.0	24.0	23.88
	H	-52.25	-36.19	-24.19	-52.19	-36.19	-24.19
Beta	V	0.0	0.0	0.0	0.0	0.0	0.0
	H	-52.25	-36.19	-24.19	-52.13	-36.13	-24.19
Cathy	V	-24.0	-24.0	-24.0	-24.0	-24.0	-24.19
	H	-52.25	-36.19	-24.19	-52.13	-36.13	-24.19
Dog	V	8.25	9.50	9.38	8.94	9.13	9.25
	H	-18.25	-14.50	-9.63	-19.31	-13.69	-9.25
Ed	V	6.5	7.50	6.50	7.19	6.88	6.44
	H	-14.75	-11.50	-6.81	-15.69	-10.31	-6.44
Fox	V	-8.25	-7.50	-9.38	-8.75	-9.31	-9.44
	H	-18.25	-14.50	-9.63	-18.81	-13.75	-9.75
George	V	-6.25	-9.50	-6.50	-7.13	-7.0	-6.63
	H	-14.75	-11.63	-6.81	-15.25	-10.44	-7.0
Opal[2]	V	----	0.0	0.0	0.0	0.0	0.0
	H	----	-2.0	-0.25	-2.19	-2.0	-0.19
Jane	V	8.25	9.50	9.63	8.38	9.06	9.19
	H	18.25	14.38	9.63	18.0	14.13	9.44
King	V	6.5	7.50	6.63	7.06	6.88	6.88
	H	14.75	11.25	6.75	15.13	10.81	6.63
Ivan	V	-6.5	-7.50	-6.38	-7.19	-7.13	-6.75
	H	14.75	11.63	-6.88	15.75	10.94	7.19
Paul[3]	V	-8.25	-9.50	-9.25	-8.88	-9.31	-9.56
	H	18.25	-14.63	9.63	19.38	14.25	9.88
Love	V	24.0	24.0	24.0	24.0	24.0	24.0
	H	52.25	36.19	24.19	52.13	36.19	24.19
Mark	V	0.0	0.0	0.0	0.0	0.0	0.0
	H	52.25	36.19	24.19	52.13	36.19	24.19
Neal	V	-24.0	-24.0	-24.0	-24.0	-24.0	-24.19
	H	52.25	36.19	24.19	52.13	36.19	24.19
θ (°)		26.5	35.0	45.0	26.5	35.0	45.0

1 in. = 25.4 mm [1]Vertical (V) or horizontal (H) dimension from center of wall.
[2]Not used in Wall Specimen 2. [3]"Harry" in Wall Specimen 2.

Table 5.1 Timeline for Test of Wall Specimen 2

Point	Cycle Group	Cycle No.	Disp. (in.)	Force (kips)	Comments
1	E1	1	0.0014	-0.958	Begin first day of testing.
4	E1	1	0.0107	5.164	Positive peak.
10	E1	1	-0.0087	-8.231	Negative peak.
13	E1	1	0.0004	-0.250	End of cycle.
16	E1	2	0.0104	5.576	Positive peak.
22	E1	2	-0.0086	-8.355	Negative peak.
25	E1	2	0.0006	-0.431	End of cycle.
28	E1	3	0.0105	5.4060	Positive peak.
43	E1	3	-0.0090	-7.797	Negative peak.
46	E1	3	0.0007	-0.487	End of cycle.
49	E2	1	0.0148	9.687	Positive peak.
55	E2	1	-0.0125	-13.101	Negative peak.
58	E2	1	0.0007	-0.479	End of cycle.
61	E2	2	0.0149	9.501	Positive peak.
67	E2	2	-0.0128	-12.769	Negative peak.
70	E2	2	0.0008	-0.518	End of cycle.
73	E2	3	0.0149	9.516	Positive peak.
79	E2	3	-0.0127	-12.852	Negative peak.
82	E2	3	0.0008	-0.518	End of cycle.
85	E3	1	0.0189	14.130	Positive peak.
91	E3	1	-0.0166	-17.631	Negative peak.
94	E3	1	0.0007	-0.500	End of cycle.
97	E3	2	0.0189	14.090	Positive peak.
103	E3	2	-0.0166	-17.737	Negative peak.
106	E3	2	0.0007	-0.503	End of cycle.

1 in. = 25.4 mm; 1 kip = 4.45 kN

Table 5.1 (Cont'd)

Point	Cycle Group	Cycle No.	Disp. (in.)	Force (kips)	Comments
109	E3	3	0.0189	14.050	Positive peak.
115	E3	3	-0.0165	-17.835	Negative peak.
118	E3	3	0.0007	-0.503	End of cycle.
122	E4	1	0.0229	18.709	Positive peak.
130	E4	1	-0.0203	-22.788	Negative peak.
134	E4	1	0.0007	-0.502	End of cycle.
137	E4	2	0.0230	18.580	Positive peak.
143	E4	2	-0.0203	-22.726	Negative peak.
146	E4	2	0.0007	-0.505	End of cycle.
149	E4	3	0.0231	18.494	Positive peak.
155	E4	3	-0.0202	-22.952	Negative peak.
158	E4	3	0.0007	-0.498	End of cycle.
162	E5	1	0.0273	22.739	Positive peak.
170	E5	1	-0.0243	-27.388	Negative peak.
173	E5	1	0.0007	-0.495	End of cycle.
176	E5	2	0.0274	22.699	Positive peak.
182	E5	2	-0.0243	-27.358	Negative peak.
185	E5	2	0.0008	-0.507	End of cycle.
188	E5	3	0.0274	22.558	Positive peak.
194	E5	3	-0.0243	-27.433	Negative peak.
197	E5	3	0.0008	-0.512	End of cycle.
201	E6	1	0.0317	26.834	Positive peak.
209	E6	1	-0.0279	-32.671	Negative peak.
213	E6	1	0.0007	-0.460	End of cycle.
217	E6	2	0.0316	26.929	Positive peak.

1 in. = 25.4 mm; 1 kip = 4.45 kN

Table 5.1 (Cont'd)

Point	Cycle Group	Cycle No.	Disp. (in.)	Force (kips)	Comments
225	E6	2	-0.0280	-32.546	Negative peak.
229	E6	2	0.0007	-0.476	End of cycle.
233	E6	3	0.0317	26.767	Positive peak.
241	E6	3	-0.0280	-32.615	Negative peak.
245	E6	3	0.0007	-0.469	End of cycle.
250	E7	1	0.0360	31.005	Positive peak.
260	E7	1	-0.0319	-37.402	Negative peak.
265	E7	1	0.0006	-0.419	End of cycle.
270	E7	2	0.0360	31.048	Positive peak.
280	E7	2	-0.0320	-37.223	Negative peak.
285	E7	2	0.0007	-0.444	End of cycle.
290	E7	3	0.0362	30.719	Positive peak.
300	E7	3	-0.0320	-37.203	Negative peak.
305	E7	3	0.0007	-0.449	End of cycle.
310	E8	1	0.0401	35.449	Positive peak.
320	E8	1	-0.0365	-41.136	Negative peak.
325	E8	1	0.0006	-0.380	End of cycle.
330	E8	2	0.0402	35.407	Positive peak.
340	E8	2	-0.0364	-41.196	Negative peak.
345	E8	2	0.0006	-0.388	End of cycle.
350	E8	3	0.0404	35.053	Positive peak.
360	E8	3	-0.0361	-41.642	Negative peak.
365	E8	3	0.0006	-0.395	End of cycle.
370	E9	1	0.0448	39.028	Positive peak.
380	E9	1	-0.0404	-45.946	Negative peak.

1 in. = 25.4 mm; 1 kip = 4.45 kN

Table 5.1 (Cont'd)

Point	Cycle Group	Cycle No.	Disp. (in.)	Force (kips)	Comments
385	E9	1	0.0005	-0.349	End of cycle.
390	E9	2	0.0447	39.193	Positive peak.
400	E9	2	-0.0406	-45.633	Negative peak.
405	E9	2	0.0005	-0.355	End of cycle.
410	E9	3	0.0445	39.522	Positive peak.
420	E9	3	-0.0408	-45.199	Negative peak.
425	E9	3	0.0005	-0.366	End of cycle.
430	E10	1	0.0491	43.310	Positive peak.
440	E10	1	-0.0451	-49.485	Negative peak.
445	E10	1	0.0004	-0.240	End of cycle.
450	E10	2	0.0490	43.391	Positive peak.
460	E10	2	-0.0451	-49.510	Negative peak.
465	E10	2	0.0004	-0.252	End of cycle.
470	E10	3	0.0491	43.215	Positive peak.
480	E10	3	-0.0453	-49.128	Negative peak.
485	E10	3	0.0002	-0.123	End of cycle. End first day of testing.
486	E11	1	-0.0006	0.375	Begin second day of testing.
491	E11	1	0.0518	49.967	Positive peak.
501	E11	1	-0.0515	-50.321	Negative peak.
506	E11	1	-0.0025	1.684	End of cycle.
511	E11	2	0.0543	46.014	Positive peak.
521	E11	2	-0.0527	-48.446	Negative peak.
526	E11	2	-0.0032	2.139	End of cycle.
531	E11	3	0.0559	43.504	Positive peak.
541	E11	3	-0.0536	-47.194	Negative peak.

1 in. = 25.4 mm; 1 kip = 4.45 kN

Table 5.1 (Cont'd)

Point	Cycle Group	Cycle No.	Disp. (in.)	Force (kips)	Comments
546	E11	3	-0.0035	2.357	End of cycle.
551	$1.0D_c$	D1	0.0643	42.803	Positive peak. Vertical cracks top course, east and west jambs.
561	$1.0D_c$	D1	-0.0612	-46.125	Negative peak. Vertical cracks, bottom and middle courses, east jambs.
566	$1.0D_c$	D1	-0.0050	7.712	End of cycle.
570	$1.0D_c$	D2	0.0469	33.147	Positive peak.
578	$1.0D_c$	D2	-0.0443	-37.223	Negative peak.
582	$1.0D_c$	D2	-0.0035	2.339	End of cycle.
585	$1.0D_c$	D3	0.0283	26.658	Positive peak.
591	$1.0D_c$	D3	-0.0285	-26.304	Negative peak.
594	$1.0D_c$	D3	-0.0016	1.093	End of cycle.
599	$1.0D_c$	S1	0.0638	42.133	Positive peak.
609	$1.0D_c$	S1	-0.0611	-46.316	Negative peak.
614	$1.0D_c$	S1	-0.0046	7.066	End of cycle.
619	$1.0D_c$	S2	0.0643	41.402	Positive peak.
629	$1.0D_c$	S2	-0.0621	-44.796	Negative peak.
634	$1.0D_c$	S2	-0.0054	8.343	End of cycle.
639	$1.5D_c$	D1	0.1060	47.232	Positive peak. Inclined and vertical cracks, top course, west jamb.
650	$1.5D_c$	D1	-0.1043	-49.875	Negative peak. Vertical cracks bottom and middle courses, east jambs.
656	$1.5D_c$	D1	-0.0162	25.065	End of cycle.
661	$1.5D_c$	D2	0.0773	38.942	Positive peak.
671	$1.5D_c$	D2	-0.0770	-39.443	Negative peak.
676	$1.5D_c$	D2	-0.0127	19.707	End of cycle.
680	$1.5D_c$	D3	0.0475	32.231	Positive peak.
688	$1.5D_c$	D3	-0.0494	-29.314	Negative peak.
692	$1.5D_c$	D3	-0.0065	10.034	End of cycle.

1 in. = 25.4 mm; 1 kip = 4.45 kN

Table 5.1 (Cont'd)

Point	Cycle Group	Cycle No.	Disp. (in.)	Force (kips)	Comments
698	$1.5D_c$	S1	0.1062	46.995	Positive peak.
710	$1.5D_c$	S1	-0.1038	-50.652	Negative peak.
716	$1.5D_c$	S1	-0.0156	24.229	End of cycle.
722	$1.5D_c$	S2	0.1072	45.386	Positive peak.
734	$1.5D_c$	S2	-0.1042	-49.997	Negative peak.
740	$1.5D_c$	S2	-0.0148	22.985	End of cycle.
750	$2.0D_c$	D1	0.1485	51.888	Positive peak. Inclined cracks, bottom course, west jamb.
770	$2.0D_c$	D1	-0.1462	-55.542	Negative peak. Vertical cracks, top course, east jamb.
780	$2.0D_c$	D1	-0.0161	24.921	End of cycle.
786	$2.0D_c$	D2	0.1100	41.030	Positive peak.
797	$2.0D_c$	D2	-0.1091	-42.425	Negative peak.
803	$2.0D_c$	D2	-0.0153	23.695	End of cycle.
807	$2.0D_c$	D3	0.0698	32.868	Positive peak.
815	$2.0D_c$	D3	-0.0707	-31.514	Negative peak.
819	$2.0D_c$	D3	-0.0123	19.142	End of cycle.
827	$2.0D_c$	S1	0.1511	47.972	Positive peak.
843	$2.0D_c$	S1	-0.1470	-54.289	Negative peak.
851	$2.0D_c$	S1	-0.0163	25.297	End of cycle.
859	$2.0D_c$	S2	0.1518	46.740	Positive peak.
875	$2.0D_c$	S2	-0.1491	-51.063	Negative peak. Inclined cracks/mortar crush., top course/joint, east jamb.
883	$2.0D_c$	S2	-0.0102	15.810	End of cycle. End second day of testing. Crack width ~ 4 mm.
884	$3.0D_c$	D1	-0.0057	3.834	Begin third day of testing.
890	$3.0D_c$	D1	0.1087	43.143	Loud "crack".
894	$3.0D_c$	D1	0.1734	48.588	Loud "bang".
898	$3.0D_c$	D1	0.2398	51.503	Positive peak. Inclined cracks, top/bottom courses, west jamb.

1 in. = 25.4 mm; 1 kip = 4.45 kN

Table 5.1 (Cont'd)

Point	Cycle Group	Cycle No.	Disp. (in.)	Force (kips)	Comments
928	$3.0D_c$	D1	-0.2332	-61.680	Negative peak. Inclined cracks/mortar crush., top course/joint, east jamb.
948	$3.0D_c$	D1	-0.0078	12.115	End of cycle.
963	$3.0D_c$	D2	0.1780	41.495	Positive peak.
992	$3.0D_c$	D2	-0.1750	-46.235	Negative peak.
1007	$3.0D_c$	D2	-0.0024	1.616	End of cycle.
1015	$3.0D_c$	D3	0.1179	28.804	Positive peak.
1027	$3.0D_c$	D3	-0.1136	-35.555	Negative peak.
1033	$3.0D_c$	D3	0.0	-0.044	End of cycle.
1045	$3.0D_c$	S1	0.2428	46.859	Positive peak. Inclined cracks/mortar crush., top course/joint, west jamb.
1060	$3.0D_c$	S1	-0.0463	-34.083	Loud "bang". Crack width ~ 6 mm.
1068	$3.0D_c$	S1	-0.2232	-42.000	Three loud "snaps".
1069	$3.0D_c$	S1	-0.2459	-41.963	Negative peak. Inclined cracks, east jamb. Mortar spalling.
1081	$3.0D_c$	S1	-0.0054	8.447	End of cycle.
1092	$3.0D_c$	S2	0.2219	44.020	Loud "bang".
1093	$3.0D_c$	S2	0.2437	45.486	Positive peak.
1112	$3.0D_c$	S2	-0.1405	-29.158	Loud "bang".
1116	$3.0D_c$	S2	-0.1833	-33.277	Loud "snap". Mortar spalling.
1119	$3.0D_c$	S2	-0.2441	-44.850	Negative peak.
1131	$3.0D_c$	S2	-0.0102	15.754	End of cycle.
1152	$4.0D_c$	D1	0.3305	51.912	Positive peak. Crushing damage, 4th and 6th courses.
1182	$4.0D_c$	D1	-0.1600	-34.219	Loud "bang".
1183	$4.0D_c$	D1	-0.1811	-36.736	Loud "bang".
1187	$4.0D_c$	D1	-0.2567	-42.924	Loud "bang".
1192	$4.0D_c$	D1	-0.3108	-47.229	Negative peak. Mortar/face-shell spalling damage, 4th course.
1215	$4.0D_c$	D1	0.0013	33.259	End of cycle.

1 in. = 25.4 mm; 1 kip = 4.45 kN

Table 5.1 (Cont'd)

Point	Cycle Group	Cycle No.	Disp. (in.)	Force (kips)	Comments
1219	$4.0D_c$	D2	0.0910	35.298	Loud "snap".
1226	$4.0D_c$	D2	0.2473	39.829	Positive peak. Loud "snap".
1250	$4.0D_c$	D2	-0.2475	-39.455	Negative peak.
1262	$4.0D_c$	D2	-0.0138	21.320	End of cycle. Face-shell spalling, 4th and 6th courses.
1271	$4.0D_c$	D3	0.1631	29.226	Positive peak.
1289	$4.0D_c$	D3	-0.1631	-29.358	Negative peak.
1298	$4.0D_c$	D3	-0.0122	18.941	End of cycle.
1314	$4.0D_c$	S1	0.3061	42.708	Loud "bang".
1316	$4.0D_c$	S1	0.3360	43.379	Positive peak.
1355	$4.0D_c$	S1	-0.3322	-49.347	Negative peak.
1371	$4.0D_c$	S1	-0.0128	19.830	End of cycle. End third day of testing.
1372	$4.0D_c$	S2	-0.0036	5.6070	Begin fourth day of testing.
1388	$4.0D_c$	S2	0.2802	35.846	Loud "snap". Crack width ~ 10 mm.
1392	$4.0D_c$	S2	0.3385	39.504	Positive peak.
1429	$4.0D_c$	S2	-0.3337	-46.967	Negative peak.
1450	$4.0D_c$	S2	-0.0173	26.788	End of cycle. End fourth day of testing.
1451	$5.0D_c$	D1	-0.0059	3.9710	Begin fifth day of testing.
1473	$5.0D_c$	D1	0.3573	38.667	Loud "bang".
1481	$5.0D_c$	D1	0.4297	39.222	Positive peak. Crushing damage, bottom joint and 6th course, west side.
1546	$5.0D_c$	D1	-0.4220	-51.074	Negative peak. Extensive crushing/spalling. Crack width ~ 12 mm.
1576	$5.0D_c$	D1	-0.0017	26.360	End of cycle.
1596	$5.0D_c$	D2	0.3207	31.875	Positive peak.
1636	$5.0D_c$	D2	-0.3170	-37.608	Negative peak.
1656	$5.0D_c$	D2	-0.0208	32.315	End of cycle.
1671	$5.0D_c$	D3	0.2072	31.531	Positive peak.

1 in. = 25.4 mm; 1 kip = 4.45 kN

Table 5.1 (Cont'd)

Point	Cycle Group	Cycle No.	Disp. (in.)	Force (kips)	Comments
1701	$5.0D_c$	D3	-0.2054	-34.312	Negative peak.
1716	$5.0D_c$	D3	-0.0189	29.439	End of cycle.
1746	$5.0D_c$	S1	0.4285	41.108	Positive peak.
1806	$5.0D_c$	S1	-0.4226	-50.297	Negative peak.
1835	$5.0D_c$	S1	-0.0200	31.075	End of cycle.
1863	$5.0D_c$	S2	0.4120	38.460	Loud "bang". Crushing/spalling damage.
1865	$5.0D_c$	S2	0.4301	38.529	Positive peak.
1925	$5.0D_c$	S2	-0.4232	-49.235	Negative peak.
1955	$5.0D_c$	S2	-0.0029	32.760	End of cycle.
1988	$6.0D_c$	D1	0.5177	43.942	Positive peak.
2058	$6.0D_c$	D1	-0.5120	-52.644	Negative peak.
2093	$6.0D_c$	D1	-0.0227	35.132	End of cycle.
2118	$6.0D_c$	D2	0.3865	35.692	Positive peak.
2168	$6.0D_c$	D2	-0.3814	-43.513	Negative peak.
2194	$6.0D_c$	D2	-0.0215	33.337	End of cycle.
2208	$6.0D_c$	D3	0.2506	34.660	Positive peak. Falling debris from upper west.
2238	$6.0D_c$	D3	-0.2479	-38.858	Negative peak. Loud "thuds", wall sliding.
2253	$6.0D_c$	D3	-0.0227	35.184	Loud "thuds", wall sliding.
2254	$6.0D_c$	D3	-0.0043	35.184	End of cycle.
2283	$6.0D_c$	S1	0.5164	45.851	Positive peak.
2343	$6.0D_c$	S1	-0.5136	-50.145	Negative peak.
2374	$6.0D_c$	S1	-0.0034	33.518	End of cycle.
2403	$6.0D_c$	S2	0.5182	43.153	Positive peak.
2463	$6.0D_c$	S2	-0.5136	-50.179	Negative peak.
2483	$6.0D_c$	S2	-0.0235	36.353	End of cycle. End of fifth day of testing.

1 in. = 25.4 mm; 1 kip = 4.45 kN

Table 5.1 (Cont'd)

Point	Cycle Group	Cycle No.	Disp. (in.)	Force (kips)	Comments
2484	$8.0D_c$	D1	-0.0056	8.735	Begin sixth day of testing.
2529	$8.0D_c$	D1	0.6968	48.429	Positive peak.
2629	$8.0D_c$	D1	-0.6942	-52.428	Negative peak.
2678	$8.0D_c$	D1	-0.0081	40.806	End of cycle.
2707	$8.0D_c$	D2	0.5201	40.107	Positive peak.
2777	$8.0D_c$	D2	-0.5239	-34.324	Negative peak.
2814	$8.0D_c$	D2	-0.0086	13.347	End of cycle.
2834	$8.0D_c$	D3	0.3584	8.756	Positive peak.
2874	$8.0D_c$	D3	-0.3592	-7.405	Negative peak.
2894	$8.0D_c$	D3	-0.0031	4.878	End of cycle.
2895	$8.0D_c$	S1	0.0150	4.929	Loud "crack". Falling debris, explosive unit failure, top course, west end.
2934	$8.0D_c$	S1	0.7185	14.796	Positive peak.
2971	$8.0D_c$	S1	0.0056	-8.698	Loud "crack", falling debris.
3011	$8.0D_c$	S1	-0.7169	-17.222	Negative peak.
3054	$8.0D_c$	S1	-0.0095	14.753	End of cycle. End of sixth day of testing.

1 in. = 25.4 mm; 1 kip = 4.45 kN

Table 5.2 Timeline for Test of Wall Specimen 4

Point	Cycle Group	Cycle No.	Disp. (in.)	Force (kips)	Comments
1	E1	1	-0.0035	2.381	Begin first day of testing.
4	E1	1	0.0086	9.855	Positive peak.
10	E1	1	-0.0100	-3.344	Negative peak.
13	E1	1	-0.0035	2.318	End of cycle.
16	E1	2	0.0084	10.234	Positive peak.
22	E1	2	-0.0101	-3.329	Negative peak.
25	E1	2	-0.0035	2.338	End of cycle.
28	E1	3	0.0084	10.192	Positive peak.
34	E1	3	-0.0102	-3.239	Negative peak.
37	E1	3	-0.0034	2.315	End of cycle.
40	E2	1	0.0131	14.609	Positive peak.
46	E2	1	-0.0185	-6.165	Negative peak.
49	E2	1	-0.0034	2.301	End of cycle.
52	E2	2	0.0134	14.060	Positive peak.
58	E2	2	-0.0186	-6.108	Negative peak.
61	E2	2	-0.0034	2.273	End of cycle.
64	E2	3	0.0135	13.997	Positive peak.
70	E2	3	-0.0186	-6.066	Negative peak.
73	E2	3	-0.0034	2.279	End of cycle.
76	E3	1	0.0185	17.819	Positive peak.
82	E3	1	-0.0231	-10.670	Negative peak.
85	E3	1	-0.0034	2.285	End of cycle.
88	E3	2	0.0185	17.836	Positive peak.
94	E3	2	-0.0230	-10.789	Negative peak.
97	E3	2	-0.0034	2.283	End of cycle.

1 in. = 25.4 mm; 1 kip = 4.45 kN

Table 5.2 (Cont'd)

Point	Cycle Group	Cycle No.	Disp. (in.)	Force (kips)	Comments
100	E3	3	0.0187	17.589	Positive peak.
106	E3	3	-0.0232	-10.576	Negative peak.
109	E3	3	-0.0035	2.330	End of cycle.
112	E4	1	0.0232	21.588	Positive peak.
118	E4	1	-0.0280	-14.758	Negative peak.
121	E4	1	-0.0035	2.338	End of cycle.
124	E4	2	0.0236	21.473	Positive peak.
130	E4	2	-0.0278	-15.014	Negative peak.
133	E4	2	-0.0033	2.220	End of cycle.
136	E4	3	0.0237	21.361	Positive peak.
142	E4	3	-0.0277	-15.168	Negative peak.
145	E4	3	-0.0034	2.317	End of cycle.
148	E5	1	0.0287	25.232	Positive peak.
154	E5	1	-0.0331	-18.411	Negative peak.
157	E5	1	-0.0034	2.324	End of cycle.
160	E5	2	0.0288	25.104	Positive peak.
166	E5	2	-0.0327	-19.016	Negative peak.
169	E5	2	-0.0034	2.323	End of cycle.
172	E5	3	0.0289	25.011	Positive peak.
178	E5	3	-0.0327	-19.003	Negative peak.
181	E5	3	-0.0033	2.220	End of cycle.
184	E6	1	0.0335	29.418	Positive peak.
190	E6	1	-0.0378	-22.862	Negative peak.
193	E6	1	-0.0032	2.154	End of cycle.
196	E6	2	0.0339	28.815	Positive peak.

1 in. = 25.4 mm; 1 kip = 4.45 kN

Table 5.2 (Cont'd)

Point	Cycle Group	Cycle No.	Disp. (in.)	Force (kips)	Comments
202	E6	2	-0.0378	-22.814	Negative peak.
205	E6	2	-0.0034	2.262	End of cycle.
208	E6	3	0.0340	28.687	Positive peak.
214	E6	3	-0.0380	-22.507	Negative peak.
217	E6	3	-0.0034	2.289	End of cycle.
220	E7	1	0.0388	32.889	Positive peak.
226	E7	1	-0.0428	-26.618	Negative peak.
229	E7	1	-0.0035	2.347	End of cycle.
232	E7	2	0.0390	32.546	Positive peak.
238	E7	2	-0.0426	-26.956	Negative peak.
241	E7	2	-0.0034	2.315	End of cycle.
244	E7	3	0.0390	32.568	Positive peak.
250	E7	3	-0.0427	-26.843	Negative peak. Short hairline crack top course, west jamb.
253	E7	3	-0.0035	2.366	End of cycle.
256	E7	1	0.0440	36.427	Positive peak.
262	E8	1	-0.0476	-30.794	Negative peak.
265	E8	1	-0.0036	2.418	End of cycle.
268	E8	2	0.0442	36.123	Positive peak.
274	E8	2	-0.0479	-30.359	Negative peak.
277	E8	2	-0.0036	2.394	End of cycle.
280	E8	3	0.0442	36.049	Positive peak.
286	E8	3	-0.0478	-30.512	Negative peak.
289	E8	3	-0.0035	2.391	End of cycle.
292	E9	1	0.0495	39.507	Positive peak.
298	E9	1	-0.0530	-34.059	Negative peak.

1 in. = 25.4 mm; 1 kip = 4.45 kN

Table 5.2 (Cont'd)

Point	Cycle Group	Cycle No.	Disp. (in.)	Force (kips)	Comments
301	E9	1	-0.0039	2.601	End of cycle.
304	E9	2	0.0497	39.139	Positive peak.
310	E9	2	-0.0532	-33.722	Negative peak.
313	E9	2	-0.0037	2.510	End of cycle.
316	E9	3	0.0499	38.885	Positive peak.
322	E9	3	-0.0532	-33.766	Negative peak.
325	E9	3	-0.0036	2.444	End of cycle. End first day of testing.
326	E10	1	-0.0040	2.668	Begin second day of testing.
330	E10	1	0.0545	43.443	Positive peak.
337	E10	1	-0.0601	-34.782	Negative peak.
340	E10	1	-0.0028	4.282	End of cycle.
343	E10	2	0.0549	42.747	Positive peak.
349	E10	2	-0.0603	-34.336	Negative peak.
352	E10	2	-0.0027	4.123	End of cycle.
355	E10	3	0.0552	42.311	Positive peak.
361	E10	3	-0.0602	-34.618	Negative peak.
364	E10	3	-0.0030	4.586	End of cycle.
367	E11	1	0.0612	44.707	Positive peak.
373	E11	1	-0.0654	-38.148	Negative peak.
376	E11	1	-0.0035	5.383	End of cycle.
379	E11	2	0.0618	43.649	Positive peak.
385	E11	2	-0.0657	-37.645	Negative peak.
388	E11	2	-0.0035	5.444	End of cycle.
391	E11	3	0.0627	42.347	Positive peak.
397	E11	3	-0.0658	-37.583	Negative peak.

1 in. = 25.4 mm; 1 kip = 4.45 kN

Table 5.2 (Cont'd)

Point	Cycle Group	Cycle No.	Disp. (in.)	Force (kips)	Comments
400	E11	3	-0.0038	5.843	End of cycle.
403	E12	1	0.0691	44.067	Positive peak.
411	E12	1	-0.0723	-39.112	Negative peak.
415	E12	1	-0.0053	8.150	End of cycle.
417	E12	2	0.0703	42.146	Positive peak.
423	E12	2	-0.0733	-37.570	Negative peak.
426	E12	2	-0.0056	8.722	End of cycle.
429	E12	3	0.0710	41.136	Positive peak.
434	E12	3	-0.0736	-37.052	Negative peak.
437	E12	3	-0.0062	9.683	End of cycle.
441	$1.0D_c$	D1	0.0783	46.332	Positive peak. Vertical crack, top course, west jamb.
451	$1.0D_c$	D1	-0.0813	-36.698	Negative peak. Vertical crack, top course, east jamb.
456	$1.0D_c$	D1	-0.0085	13.249	End of cycle.
460	$1.0D_c$	D2	0.0584	31.507	Positive peak.
468	$1.0D_c$	D2	-0.0614	-26.854	Negative peak.
472	$1.0D_c$	D2	-0.0060	9.347	End of cycle.
475	$1.0D_c$	D3	0.0373	23.626	Positive peak.
481	$1.0D_c$	D3	-0.0395	-20.080	Negative peak.
483	$1.0D_c$	D3	-0.0036	2.433	End of cycle.
487	$1.0D_c$	S1	0.0796	39.437	Positive peak.
497	$1.0D_c$	S1	-0.0815	-36.450	Negative peak.
502	$1.0D_c$	S1	-0.0089	13.778	End of cycle.
506	$1.0D_c$	S2	0.0805	37.997	Positive peak.
516	$1.0D_c$	S2	-0.0821	-35.474	Negative peak.
521	$1.0D_c$	S2	-0.0091	14.053	End of cycle.

1 in. = 25.4 mm; 1 kip = 4.45 kN

Table 5.2 (Cont'd)

Point	Cycle Group	Cycle No.	Disp. (in.)	Force (kips)	Comments
527	$1.5D_c$	D1	0.1301	42.534	Positive peak.
545	$1.5D_c$	D1	-0.1317	-40.030	Negative peak. Vertical and horizontal cracks, top joint/course.
552	$1.5D_c$	D1	-0.0137	21.270	End of cycle.
557	$1.5D_c$	D2	0.0966	33.308	Positive peak.
567	$1.5D_c$	D2	-0.0983	-30.691	Negative peak.
572	$1.5D_c$	D2	-0.0118	18.239	End of cycle.
576	$1.5D_c$	D3	0.0626	24.938	Positive peak.
586	$1.5D_c$	D3	-0.0635	-23.674	Negative peak.
590	$1.5D_c$	D3	-0.0075	11.591	End of cycle.
597	$1.5D_c$	S1	0.1320	39.581	Positive peak.
611	$1.5D_c$	S1	-0.1326	-38.563	Negative peak.
618	$1.5D_c$	S1	-0.0134	20.770	End of cycle.
625	$1.5D_c$	S2	0.1326	38.539	Positive peak. Crack width ~ 2 mm, top course, west end.
639	$1.5D_c$	S2	-0.1328	-38.224	Negative peak.
646	$1.5D_c$	S2	-0.0130	20.075	End of cycle.
655	$2.0D_c$	D1	0.1831	41.654	Positive peak. Crack width ~ 4 mm, top course, west end.
672	$2.0D_c$	D1	-44.253	-0.1639	Soft "bang".
673	$2.0D_c$	D1	-0.1806	-45.516	Negative peak. Crack width ~1 mm, top course, east end.
682	$2.0D_c$	D1	-0.0119	18.517	End of cycle.
688	$2.0D_c$	D2	0.1375	31.020	Positive peak
700	$2.0D_c$	D2	-0.1359	-33.528	Negative peak.
706	$2.0D_c$	D2	-0.0112	17.420	End of cycle.
709	$2.0D_c$	D3	0.0906	22.358	Positive peak.
715	$2.0D_c$	D3	-0.0886	-25.460	Negative peak.
717	$2.0D_c$	D3	-0.0107	16.516	End of cycle. End second day of testing.

1 in. = 25.4 mm; 1 kip = 4.45 kN

Table 5.2 (Cont'd)

Point	Cycle Group	Cycle No.	Disp. (in.)	Force (kips)	Comments
718	$2.0D_c$	S1	-0.0053	8.145	Begin third day of testing.
723	$2.0D_c$	S1	0.1863	36.702	Positive peak.
735	$2.0D_c$	S1	-0.1827	-42.308	Negative peak.
740	$2.0D_c$	S1	-0.0119	18.467	End of cycle.
745	$2.0D_c$	S2	0.1872	35.324	Positive peak. Crack width ~ 5 mm, top course, west end.
758	$2.0D_c$	S2	-0.1826	-42.422	Negative peak. Crack width ~ 1 mm, top course, east end.
763	$2.0D_c$	S2	-0.0124	19.221	End of cycle.
779	$3.0D_c$	D1	0.2830	49.660	Positive peak.
811	$3.0D_c$	D1	-0.2800	-54.191	Negative peak.
825	$3.0D_c$	D1	-0.0135	20.949	End of cycle.
837	$3.0D_c$	D2	0.2110	39.200	Positive peak.
854	$3.0D_c$	D2	-0.2100	-40.722	Negative peak.
861	$3.0D_c$	D2	-0.0120	18.597	End of cycle.
867	$3.0D_c$	D3	0.1385	29.409	Positive peak.
877	$3.0D_c$	D3	-0.1378	-30.585	Negative peak.
883	$3.0D_c$	D3	-0.0117	18.206	End of cycle.
891	$3.0D_c$	S1	0.2824	50.499	Positive peak.
913	$3.0D_c$	S1	-0.2814	-52.071	Negative peak.
932	$3.0D_c$	S1	-0.0138	21.393	End of cycle.
941	$3.0D_c$	S2	0.2816	51.719	Positive peak.
967	$3.0D_c$	S2	-0.2694	-43.515	Negative peak. Spalling at west end of top joint.
977	$3.0D_c$	S2	-0.0132	20.499	End of cycle. End third day of testing.
978	$4.0D_c$	D1	-0.0071	10.955	Begin fourth day of testing.
1001	$4.0D_c$	D1	0.3840	55.844	Positive peak. Crack width ~ 7 mm, top course, west end.
1061	$4.0D_c$	D1	-0.3841	-55.643	Negative peak.

1 in. = 25.4 mm; 1 kip = 4.45 kN

Table 5.2 (Cont'd)

Point	Cycle Group	Cycle No.	Disp. (in.)	Force (kips)	Comments
1089	$4.0D_c$	D1	-0.0143	22.167	End of cycle.
1107	$4.0D_c$	D2	0.2868	43.715	Positive peak.
1148	$4.0D_c$	D2	-0.2871	-43.216	Negative peak.
1167	$4.0D_c$	D2	-0.0052	8.129	End of cycle.
1178	$4.0D_c$	D3	0.1876	34.741	Positive peak.
1202	$4.0D_c$	D3	-0.1894	-31.872	Negative peak.
1214	$4.0D_c$	D3	-0.0057	3.881	End of cycle.
1238	$4.0D_c$	S1	0.3337	52.435	Loud "snap".
1240	$4.0D_c$	S1	0.3824	58.338	Positive peak.
1287	$4.0D_c$	S1	-0.3198	-33.239	Loud "snap".
1292	$4.0D_c$	S1	-0.3834	-36.414	Loud "snap".
1293	$4.0D_c$	S1	-0.3968	-35.933	Negative peak.
1320	$4.0D_c$	S1	-0.0176	27.344	End of cycle.
1334	$4.0D_c$	S2	0.2081	43.622	Loud "bang".
1348	$4.0D_c$	S2	0.3879	49.768	Positive peak. Extensive crushing and spalling damage.
1401	$4.0D_c$	S2	-0.3988	-32.901	Negative peak.
1428	$4.0D_c$	S2	-0.0133	20.623	End of cycle. End fourth day of testing.
1429	$5.0D_c$	D1	-0.0118	18.338	Begin fifth day of testing.
1448	$5.0D_c$	D1	0.2756	40.785	Loud "snap".
1449	$5.0D_c$	D1	0.2888	40.566	Loud "snap".
1460	$5.0D_c$	D1	0.4355	42.174	Loud "snap".
1463	$5.0D_c$	D1	0.4713	42.513	Loud "snap".
1465	$5.0D_c$	D1	0.4973	42.916	Positive peak.
1532	$5.0D_c$	D1	-0.4641	-33.427	Loud "snap".
1535	$5.0D_c$	D1	-0.5027	-34.567	Negative peak.

1 in. = 25.4 mm; 1 kip = 4.45 kN

Table 5.2 (Cont'd)

Point	Cycle Group	Cycle No.	Disp. (in.)	Force (kips)	Comments
1571	$5.0D_c$	D1	-0.0075	11.632	End of cycle.
1591	$5.0D_c$	D2	0.3097	28.584	Loud "snap".
1596	$5.0D_c$	D2	0.3609	30.679	Two loud "snaps".
1598	$5.0D_c$	D2	0.3747	29.678	Positive peak.
1649	$5.0D_c$	D2	-0.3802	-21.118	Negative peak.
1677	$5.0D_c$	D2	-0.0043	6.611	End of cycle.
1691	$5.0D_c$	D3	0.2487	21.396	Positive peak.
1721	$5.0D_c$	D3	-0.2544	-12.544	Negative peak.
1737	$5.0D_c$	D3	-0.0054	3.626	End of cycle.
1768	$5.0D_c$	S1	0.5045	31.840	Positive peak.
1834	$5.0D_c$	S1	-0.5086	-25.476	Negative peak.
1868	$5.0D_c$	S1	-0.0033	5.099	End of cycle.
1898	$5.0D_c$	S2	0.5073	27.481	Positive peak. Horizontal (west) and vertical (east) cracks.
1966	$5.0D_c$	S2	-0.5106	-22.363	Negative peak.
1999	$5.0D_c$	S2	-0.0048	3.244	End of cycle. End fifth day of testing.
2000	$6.0D_c$	D1	-0.0003	0.1790	Begin sixth day of testing.
2029	$6.0D_c$	D1	0.6132	25.999	Positive peak. Crack width ~ 8 mm.
2080	$6.0D_c$	D1	-0.6144	-24.179	Negative peak.
2106	$6.0D_c$	D1	-0.0006	2.399	End of cycle.
2126	$6.0D_c$	D2	0.4623	15.839	Positive peak.
2162	$6.0D_c$	D2	-0.4640	-13.198	Negative peak.
2179	$6.0D_c$	D2	-0.0080	0.541	End of cycle.
2191	$6.0D_c$	D3	0.3098	7.991	Positive peak.
2211	$6.0D_c$	D3	-0.3101	-7.577	Negative peak.
2222	$6.0D_c$	D3	0.0	0.150	End of cycle.

1 in. = 25.4 mm; 1 kip = 4.45 kN

Table 5.2 (Cont'd)

Point	Cycle Group	Cycle No.	Disp. (in.)	Force (kips)	Comments
2245	$6.0D_c$	S1	0.6173	19.626	Positive peak.
2298	$6.0D_c$	S1	-0.6177	-18.990	Negative peak.
2325	$6.0D_c$	S1	-0.0014	0.9290	End of cycle. End sixth day of testing.

1 in. = 25.4 mm; 1 kip = 4.45 kN

Table 5.3 Timeline for Test of Wall Specimen 6

Point	Cycle Group	Cycle No.	Disp. (in.)	Force (kips)	Comments
1	E1	1	-0.0014	0.961	Begin first day of testing.
4	E1	1	0.0133	5.783	Positive peak.
10	E1	1	-0.0143	-4.198	Negative peak.
13	E1	1	-0.0020	1.325	End of cycle.
16	E1	2	0.0134	5.615	Positive peak.
22	E1	2	-0.0111	-3.949	Negative peak.
25	E1	2	-0.0019	1.300	End of cycle.
28	E1	3	0.0132	5.870	Positive peak.
34	E1	3	-0.0142	-4.330	Negative peak.
37	E1	3	-0.0019	1.301	End of cycle.
40	E2	1	0.0197	8.968	Positive peak.
46	E2	1	-0.0209	-7.103	Negative peak.
49	E2	1	-0.0021	1.430	End of cycle.
52	E2	2	0.0198	8.831	Positive peak.
58	E2	2	-0.0209	-7.107	Negative peak.
61	E2	2	-0.0021	1.391	End of cycle.
64	E2	3	0.0198	8.759	Positive peak.
70	E2	3	-0.0209	-7.123	Negative peak.
73	E2	3	-0.0021	1.397	End of cycle.
76	E3	1	0.0264	11.748	Positive peak.
82	E3	1	-0.0273	-10.337	Negative peak.
85	E3	1	-0.0023	1.554	End of cycle.
88	E3	2	0.0265	11.702	Positive peak.
94	E3	2	-0.0273	-10.337	Negative peak.
97	E3	2	-0.0019	1.255	End of cycle.

1 in. = 25.4 mm; 1 kip = 4.45 kN

Table 5.3 (Cont'd)

Point	Cycle Group	Cycle No.	Disp. (in.)	Force (kips)	Comments
100	E3	3	0.0264	11.716	Positive peak.
106	E3	3	-0.0273	-10.412	Negative peak.
109	E3	3	-0.0021	1.430	End of cycle.
112	E4	1	0.0332	14.439	Positive peak.
118	E4	1	-0.0340	-13.120	Negative peak.
121	E4	1	-0.0024	1.630	End of cycle.
124	E4	2	0.0333	14.265	Positive peak.
130	E4	2	-0.0342	-12.942	Negative peak.
133	E4	2	-0.0022	1.486	End of cycle.
136	E4	3	0.0334	14.127	Positive peak.
142	E4	3	-0.0341	-13.093	Negative peak.
145	E4	3	-0.0024	1.619	End of cycle.
148	E5	1	0.0404	16.425	Positive peak.
154	E5	1	-0.0411	-15.378	Negative peak.
157	E5	1	-0.0033	2.254	End of cycle.
160	E5	2	0.0408	15.826	Positive peak.
166	E5	2	-0.0414	-14.825	Negative peak.
169	E5	2	-0.0032	2.137	End of cycle.
172	E5	3	0.0410	15.537	Positive peak.
178	E5	3	-0.0413	-15.025	Negative peak.
181	E5	3	-0.0033	2.230	End of cycle.
184	E6	1	0.0482	17.508	Positive peak.
190	E6	1	-0.0487	-16.792	Negative peak.
193	E6	1	-0.0044	2.981	End of cycle.
196	E6	2	0.0486	16.902	Positive peak.

1 in. = 25.4 mm; 1 kip = 4.45 kN

Table 5.3 (Cont'd)

Point	Cycle Group	Cycle No.	Disp. (in.)	Force (kips)	Comments
202	E6	2	-0.0489	-16.409	Negative peak.
205	E6	2	-0.0045	3.020	End of cycle.
208	E6	3	0.0485	17.021	Positive peak.
214	E6	3	-0.0488	-16.612	Negative peak.
217	E6	3	-0.0045	3.052	End of cycle.
220	E7	1	0.0561	18.472	Positive peak.
226	E7	1	-0.0561	-18.453	Negative peak.
229	E7	1	-0.0029	4.565	End of cycle.
232	E7	2	0.0563	18.200	Positive peak.
238	E7	2	-0.0565	-17.898	Negative peak.
241	E7	2	-0.0030	4.596	End of cycle.
244	E7	3	0.0563	18.097	Positive peak.
250	E7	3	-0.0564	-18.051	Negative peak.
253	E7	3	-0.0029	4.444	End of cycle.
256	E8	1	0.0637	19.904	Positive peak.
260	E8	1	-0.0637	-19.823	Negative peak.
263	E8	1	-0.0037	5.755	End of cycle.
266	E8	2	0.0639	-19.590	Positive peak.
272	E8	2	-0.0639	-19.538	Negative peak.
275	E8	2	-0.0037	5.806	End of cycle.
278	E8	3	0.0641	19.202	Positive peak.
283	E8	3	-0.0640	-19.411	Negative peak.
286	E8	3	-0.0037	5.808	End of cycle.
289	E9	1	0.0712	21.419	Positive peak.
295	E9	1	-0.0713	-21.286	Negative peak.

1 in. = 25.4 mm; 1 kip = 4.45 kN

Table 5.3 (Cont'd)

Point	Cycle Group	Cycle No.	Disp. (in.)	Force (kips)	Comments
298	E9	1	-0.0042	6.468	End of cycle.
301	E9	2	0.0718	20.458	Positive peak.
307	E9	2	-0.0717	-20.640	Negative peak.
310	E9	2	-0.0043	6.664	End of.cycle.
313	E9	3	0.0720	20.140	Positive peak.
319	E9	3	-0.0718	-20.386	Negative peak.
322	E9	3	-0.0045	6.919	End of cycle.
324	E10	1	0.0794	21.803	Positive peak.
329	E10	1	-0.0796	-21.549	Negative peak.
332	E10	1	-0.0049	7.618	End of cycle.
335	E10	2	0.0797	21.313	Positive peak.
340	E10	2	-0.0799	-21.118	Negative peak.
343	E10	2	-0.0051	7.962	End of cycle.
346	E10	3	0.0799	21.107	Positive peak.
352	E10	3	-0.0802	-20.691	Negative peak.
355	E10	3	-0.0052	8.050	End of cycle. End first day of testing.
356	E11	1	-0.0040	2.691	Begin second day of testing.
360	E11	1	0.0872	22.931	Positive peak. Short, vertical hairline crack, top course, west end.
374	E11	1	-0.0885	-20.960	Negative peak.
381	E11	1	-0.0055	8.571	End of cycle.
386	E11	2	0.0879	21.918	Positive peak.
398	E11	2	-0.0890	-20.105	Negative peak.
403	E11	2	-0.0055	8.592	End of cycle.
408	$1.0D_c$	D1	0.0880	21.725	Positive peak. Hairline vertical crack, top course, west end.
419	$1.0D_c$	D1	-0.0887	-20.543	Negative peak.

1 in. = 25.4 mm; 1 kip = 4.45 kN

Table 5.3 (Cont'd)

Point	Cycle Group	Cycle No.	Disp. (in.)	Force (kips)	Comments
425	$1.0D_c$	D1	-0.0057	8.776	End of cycle.
429	$1.0D_c$	D2	0.0665	15.549	Positive peak.
435	$1.0D_c$	D2	-0.0670	-14.673	Negative peak.
439	$1.0D_c$	D2	-0.0054	8.336	End of cycle.
442	$1.0D_c$	D3	0.0433	11.981	Positive peak.
447	$1.0D_c$	D3	-0.0435	-11.655	Negative peak.
450	$1.0D_c$	D3	-0.0055	3.713	End of cycle.
456	$1.0D_c$	S1	0.0880	21.743	Positive peak.
467	$1.0D_c$	S1	-0.0889	-20.249	Negative peak.
472	$1.0D_c$	S1	-0.0059	9.077	End of cycle.
478	$1.0D_c$	S2	0.0879	21.843	Positive peak.
489	$1.0D_c$	S2	-0.0893	-19.744	Negative peak. Cracking top joint, west end.
494	$1.0D_c$	S2	-0.0057	8.845	End of cycle.
503	$1.5D_c$	D1	0.1344	28.839	Positive peak.
518	$1.5D_c$	D1	-0.1378	23.523	Negative peak.
524	$1.5D_c$	D1	-0.0072	11.118	End of cycle.
531	$1.5D_c$	D2	0.1008	21.726	Positive peak.
543	$1.5D_c$	D2	-0.1040	-16.680	Negative peak.
550	$1.5D_c$	D2	-0.0066	10.198	End of cycle.
554	$1.5D_c$	D3	0.0665	15.562	Positive peak.
560	$1.5D_c$	D3	-0.0685	-12.734	Negative peak.
564	$1.5D_c$	D3	-0.0061	9.427	End of cycle.
572	$1.5D_c$	S1	0.1358	26.585	Positive peak.
587	$1.5D_c$	S1	-0.1396	-20.844	Negative peak
593	$1.5D_c$	S1	-0.0070	10.835	End of cycle.

1 in. = 25.4 mm; 1 kip = 4.45 kN

Table 5.3 (Cont'd)

Point	Cycle Group	Cycle No.	Disp. (in.)	Force (kips)	Comments
601	$1.5D_c$	S2	0.1364	25.758	Positive peak.
619	$1.5D_c$	S2	-0.1400	-20.098	Negative peak.
626	$1.5D_c$	S2	-0.0070	10.916	End of cycle.
639	$2.0D_c$	D1	0.1859	28.070	Positive peak.
660	$2.0D_c$	D1	-0.1860	-27.844	Negative peak.
671	$2.0D_c$	D1	-0.0077	12.0	End of cycle.
679	$2.0D_c$	D2	0.1396	20.824	Positive peak.
696	$2.0D_c$	D2	-0.1405	-19.360	Negative peak.
704	$2.0D_c$	D2	-0.0069	10.622	End of cycle.
710	$2.0D_c$	D3	0.0929	14.180	Positive peak.
721	$2.0D_c$	D3	-0.0933	-13.453	Negative peak
727	$2.0D_c$	D3	-0.0066	10.183	End of cycle.
738	$2.0D_c$	S1	0.1859	28.069	Positive peak.
761	$2.0D_c$	S1	-0.1865	-27.167	Negative peak.
773	$2.0D_c$	S1	-0.0070	10.841	End of cycle.
784	$2.0D_c$	S2	0.1859	28.120	Positive peak. Abrasion damage from sliding along top joint.
807	$2.0D_c$	S2	-0.1876	-25.487	Negative peak.
819	$2.0D_c$	S2	-0.0073	11.258	End of cycle.
840	$3.0D_c$	D1	0.2841	33.917	Positive peak. Extensive, well-developed crack pattern.
873	$3.0D_c$	D1	-0.2841	-34.001	Negative peak.
889	$3.0D_c$	D1	-0.0084	12.969	End of cycle. End second day of testing.
890	$3.0D_c$	D2	-0.0037	5.673	Begin third day of testing.
903	$3.0D_c$	D2	0.2118	27.358	Positive peak.
932	$3.0D_c$	D2	-0.2135	-24.832	Negative peak.
944	$3.0D_c$	D2	-0.0083	12.829	End of cycle.

1 in. = 25.4 mm; 1 kip = 4.45 kN

Table 5.3 (Cont'd)

Point	Cycle Group	Cycle No.	Disp. (in.)	Force (kips)	Comments
951	$3.0D_c$	D3	0.1399	20.249	Positive peak.
966	$3.0D_c$	D3	-0.1420	-17.087	Negative peak.
974	$3.0D_c$	D3	-0.0081	12.611	End of cycle.
990	$3.0D_c$	S1	0.2835	34.846	Positive peak.
1023	$3.0D_c$	S1	-0.2847	-33.022	Negative peak.
1042	$3.0D_c$	S1	-0.0076	11.793	End of cycle.
1058	$3.0D_c$	S2	0.2836	34.691	Positive peak.
1087	$3.0D_c$	S2	-0.2851	-32.424	Negative peak. Splitting/spalling top course, east end.
1101	$3.0D_c$	S2	-0.0089	13.837	End of cycle.
1125	$4.0D_c$	D1	0.3813	41.391	Positive peak.
1177	$4.0D_c$	D1	-0.3837	-37.693	Negative peak.
1203	$4.0D_c$	D1	-0.0101	15.722	End of cycle.
1220	$4.0D_c$	D2	0.2851	32.369	Positive peak.
1253	$4.0D_c$	D2	-0.2879	-28.106	Negative peak.
1269	$4.0D_c$	D2	-0.0104	16.082	End of cycle.
1280	$4.0D_c$	D3	0.1859	28.060	Positive peak.
1305	$4.0D_c$	D3	-0.1926	-17.620	Negative peak.
1318	$4.0D_c$	D3	-0.0080	12.427	End of cycle.
1348	$4.0D_c$	S1	0.3846	36.196	Positive peak. Loud "bang".
1401	$4.0D_c$	S1	-0.3843	-36.774	Negative peak.
1425	$4.0D_c$	S1	-0.0070	10.890	End of cycle. End third day of testing.
1426	$4.0D_c$	S2	-0.0036	5.638	Begin fourth day of testing.
1451	$4.0D_c$	S2	0.3874	31.870	Positive peak.
1496	$4.0D_c$	S2	-0.3753	-30.931	Soft "bang".
1497	$4.0D_c$	S2	-0.3873	-32.109	Negative peak.

1 in. = 25.4 mm; 1 kip = 4.45 kN

Table 5.3 (Cont'd)

Point	Cycle Group	Cycle No.	Disp. (in.)	Force (kips)	Comments
1521	$4.0D_c$	S2	-0.0057	8.847	End of cycle.
1553	$5.0D_c$	D1	0.4921	27.759	Positive peak. Extensive spalling damage, 5th and 7th courses.
1617	$5.0D_c$	D1	-0.4887	-33.034	Negative peak. Extensive spalling damage, top three courses.
1641	$5.0D_c$	D1	-0.0043	6.661	End of cycle.
1665	$5.0D_c$	D2	0.3701	19.165	Positive peak.
1684	$5.0D_c$	D2	0.0049	-3.279	Extensive spalling damage throughout panel.
1704	$5.0D_c$	D2	-0.3685	-21.765	Negative peak.
1724	$5.0D_c$	D2	-0.0027	4.115	End of cycle.
1739	$5.0D_c$	D3	0.2473	11.867	Positive peak.
1754	$5.0D_c$	D3	0.0016	-1.080	Further spalling damage throughout panel.
1769	$5.0D_c$	D3	-0.2477	-11.255	Negative peak.
1784	$5.0D_c$	D3	-0.0045	3.004	End of cycle.
1810	$5.0D_c$	S1	0.4317	19.894	Loud "bang".
1812	$5.0D_c$	S1	0.4973	19.760	Positive peak.
1868	$5.0D_c$	S1	-0.4918	-28.216	Negative peak.
1897	$5.0D_c$	S1	-0.0028	4.297	End of cycle.
1925	$5.0D_c$	S2	0.4989	17.207	Positive peak.
1981	$5.0D_c$	S2	-0.4816	-24.279	Loud "bang".
1982	$5.0D_c$	S2	-0.4940	-24.865	Negative peak.
2011	$5.0D_c$	S2	-0.0030	4.668	End of cycle. End fourth day of testing.
2012	$6.0D_c$	D1	-0.0035	2.342	Begin fifth day of testing.
2042	$6.0D_c$	D1	0.5261	14.531	Loud "bang".
2044	$6.0D_c$	D1	0.5518	14.326	Loud "bang".
2048	$6.0D_c$	D1	0.6026	14.566	Positive peak.
2100	$6.0D_c$	D1	-0.3552	-14.051	Loud "bang".

1 in. = 25.4 mm; 1 kip = 4.45 kN

Table 5.3 (Cont'd)

Point	Cycle Group	Cycle No.	Disp. (in.)	Force (kips)	Comments
2107	$6.0D_c$	D1	-0.4540	-19.004	Loud "bang".
2157	$6.0D_c$	D1	-0.0037	5.795	End of cycle.
2121	$6.0D_c$	D1	-0.5984	-21.157	Negative peak.
2180	$6.0D_c$	D2	0.4516	11.413	Positive peak
2225	$6.0D_c$	D2	-0.4512	-12.085	Negative peak.
2250	$6.0D_c$	D2	-0.0036	2.443	End of cycle.
2264	$6.0D_c$	D3	0.3021	6.082	Positive peak.
2293	$6.0D_c$	D3	-0.3023	-5.682	Negative peak.
2308	$6.0D_c$	D3	-0.0017	1.150	End of cycle.
2343	$6.0D_c$	S1	0.6047	11.350	Positive peak.
2414	$6.0D_c$	S1	-0.6011	-16.953	Negative peak.
2449	$6.0D_c$	S1	-0.0034	2.288	End of cycle.
2484	$6.0D_c$	S2	0.6063	8.877	Positive peak.
2554	$6.0D_c$	S2	-0.6030	-14.003	Negative peak.
2589	$6.0D_c$	S2	-0.0026	1.745	End of cycle. End of fifth day of testing.

1 in. = 25.4 mm; 1 kip = 4.45 kN

Table 5.4 Timeline for Test of Wall Specimen 8

Point	Cycle Group	Cycle No.	Disp. (in.)	Force (kips)	Comments
1	E1	1	0.0010	-0.690	Begin first day of testing.
4	E1	1	0.0103	5.786	Positive peak.
10	E1	1	-0.0097	-6.728	Negative peak.
13	E1	1	-0.0011	0.709	End of cycle.
16	E1	2	0.0099	6.378	Positive peak.
22	E1	2	-0.0102	-5.927	Negative peak.
25	E1	2	-0.0013	0.902	End of cycle.
28	E1	3	0.0099	6.399	Positive peak.
34	E1	3	-0.0099	-6.424	Negative peak.
37	E1	3	-0.0014	0.948	End of cycle.
40	E2	1	0.0139	10.996	Positive peak.
46	E2	1	-0.0144	-10.297	Negative peak.
49	E2	1	-0.0013	0.896	End of cycle.
52	E2	2	0.0141	10.675	Positive peak.
58	E2	2	-0.0141	-10.708	Negative peak.
61	E2	2	-0.0012	0.801	End of cycle.
64	E2	3	0.0141	10.675	Positive peak.
70	E2	3	-0.0141	-10.660	Negative peak.
73	E2	3	-0.0013	0.876	End of cycle.
76	E3	1	0.0180	15.434	Positive peak.
82	E3	1	-0.0179	-15.608	Negative peak.
85	E3	1	-0.0016	1.049	End of cycle.
88	E3	2	0.0180	15.431	Positive peak.
94	E3	2	-0.081	-15.393	Negative peak.
97	E3	2	-0.0014	0.968	End of cycle.

1 in. = 25.4 mm; 1 kip = 4.45 kN

Table 5.4 (Cont'd)

Point	Cycle Group	Cycle No.	Disp. (in.)	Force (kips)	Comments
100	E3	3	0.0181	15.318	Positive peak.
106	E3	3	-0.0181	-15.396	Negative peak.
109	E3	3	-0.0014	0.959	End of cycle.
112	E4	1	0.0220	20.080	Positive peak.
118	E4	1	-0.0219	-20.307	Negative peak.
121	E4	1	-0.0016	1.111	End of cycle.
124	E4	2	0.0221	20.057	Positive peak.
130	E4	2	-0.0220	-20.185	Negative peak.
133	E4	2	-0.0015	1.015	End of cycle.
136	E4	3	0.0221	20.011	Positive peak.
142	E4	3	-0.0219	-20.251	Negative peak.
145	E4	3	-0.0015	1.005	End of cycle.
148	E5	1	0.0264	24.221	Positive peak.
154	E5	1	-0.0262	-24.491	Negative peak.
157	E5	1	-0.0017	1.145	End of cycle.
160	E5	2	0.0264	24.188	Positive peak.
166	E5	2	-0.0262	-24.486	Negative peak.
169	E5	2	-0.0015	1.017	End of cycle.
172	E5	3	0.0264	24.224	Positive peak.
178	E5	3	-0.0262	-24.521	Negative peak.
181	E5	3	-0.0015	0.981	End of cycle.
184	E6	1	0.0305	28.710	Positive peak.
190	E6	1	-0.0301	-29.257	Negative peak.
193	E6	1	-0.0017	1.157	End of cycle.
196	E6	2	0.0305	28.636	Positive peak.

1 in. = 25.4 mm; 1 kip = 4.45 kN

Table 5.4 (Cont'd)

Point	Cycle Group	Cycle No.	Disp. (in.)	Force (kips)	Comments
202	E6	2	-0.0302	-29.194	Negative peak.
205	E6	2	-0.0015	1.037	End of cycle.
208	E6	3	0.0306	28.483	Positive peak.
214	E6	3	-0.0302	-29.148	Negative peak.
217	E6	3	-0.0016	1.071	End of cycle.
220	E7	1	0.0346	33.093	Positive peak.
226	E7	1	-0.0342	-33.782	Negative peak.
229	E7	1	-0.0018	1.186	End of cycle.
232	E7	2	0.0348	32.937	Positive peak.
240	E7	2	-0.0342	-33.829	Negative peak
243	E7	2	-0.0013	0.888	End of cycle.
246	E7	3	0.0352	32.186	Positive peak.
252	E7	3	-0.0342	-33.788	Negative peak.
255	E7	3	-0.0011	0.724	End of cycle.
258	E8	1	0.0394	36.641	Positive peak.
264	E8	1	-0.0385	-37.981	Negative peak.
267	E8	1	-0.0014	0.955	End of cycle.
270	E8	2	0.0394	36.564	Positive peak.
276	E8	2	-0.0385	-37.971	Negative peak.
279	E8	2	-0.0013	0.883	End of cycle.
282	E8	3	0.0395	36.494	Positive peak.
288	E8	3	-0.0385	-38.013	Negative peak.
291	E8	3	-0.0013	0.871	End of cycle.
294	E9	1	0.0441	40.129	Positive peak.
300	E9	1	-0.0426	-42.490	Negative peak.

1 in. = 25.4 mm; 1 kip = 4.45 kN

Table 5.4 (Cont'd)

Point	Cycle Group	Cycle No.	Disp. (in.)	Force (kips)	Comments
302	E9	1	-0.0016	1.054	End of cycle.
304	E9	2	0.0442	39.952	Positive peak.
310	E9	2	-0.0429	-41.959	Negative peak.
313	E9	2	-0.0016	1.053	End of cycle.
316	E9	3	0.0443	39.909	Positive peak.
322	E9	3	-0.0428	-42.184	Negative peak.
325	E9	3	-0.0016	1.095	End of cycle.
328	E10	1	0.0491	43.235	Positive peak.
334	E10	1	-0.0447	-45.352	Negative peak.
337	E10	1	-0.0025	1.663	End of cycle.
340	E10	2	0.0490	43.356	Positive peak.
346	E10	2	-0.0482	-44.609	Negative peak.
349	E10	2	-0.0023	1.570	End of cycle.
352	E10	3	0.0492	43.110	Positive peak.
355	E10	3	0.0036	-2.456	End of cycle.
358	E10	3	-0.0482	-44.601	Negative peak.
364	$1.0D_c$	D1	0.0541	46.276	Positive peak. Vertical crack, top course, both end.
370	$1.0D_c$	D1	-0.0531	-47.958	Negative peak. Vertical crack, top course, east end.
373	$1.0D_c$	D1	-0.0031	2.081	End of cycle.
376	$1.0D_c$	D2	0.0407	34.544	Positive peak.
382	$1.0D_c$	D2	-0.0396	-36.339	Negative peak.
385	$1.0D_c$	D2	-0.0020	1.356	End of cycle.
388	$1.0D_c$	D3	0.0273	22.826	Positive peak.
394	$1.0D_c$	D3	-0.0262	-24.542	Negative peak.
397	$1.0D_c$	D3	-0.0013	0.900	End of cycle.

1 in. = 25.4 mm; 1 kip = 4.45 kN

Table 5.4 (Cont'd)

Point	Cycle Group	Cycle No.	Disp. (in.)	Force (kips)	Comments
400	$1.0D_c$	S1	0.0545	45.731	Positive peak.
406	$1.0D_c$	S1	-0.0531	-47.894	Negative peak.
403	$1.0D_c$	S1	0.0050	-3.406	End of cycle.
410	$1.0D_c$	S2	0.0549	45.124	Positive peak.
416	$1.0D_c$	S2	-0.0533	-47.581	Negative peak.
419	$1.0D_c$	S2	-0.0030	2.023	End of cycle.
427	$1.5D_c$	D1	0.0914	53.704	Positive peak. Vertical crack, mid-height, west jamb.
441	$1.5D_c$	D1	-0.0903	-55.341	Negative peak. Vertical crack, mid-height, east jamb.
448	$1.5D_c$	D1	-0.0064	9.859	End of cycle.
452	$1.5D_c$	D2	0.0672	42.479	Positive peak.
464	$1.5D_c$	D2	-0.0669	-42.782	Negative peak.
470	$1.5D_c$	D2	-0.0040	6.136	End of cycle.
473	$1.5D_c$	D3	0.0427	31.421	Positive peak.
479	$1.5D_c$	D3	-0.0437	-29.885	Negative peak.
482	$1.5D_c$	D3	-0.0058	3.903	End of cycle. End first day of testing.
483	$1.5D_c$	S1	-0.0032	2.165	Begin second day of testing.
490	$1.5D_c$	S1	0.0929	51.240	Positive peak.
502	$1.5D_c$	S1	-0.0920	-52.760	Negative peak.
509	$1.5D_c$	S1	-0.0066	10.723	End of cycle.
516	$1.5D_c$	S2	0.0940	49.574	Positive peak.
530	$1.5D_c$	S2	-0.0932	-52.194	Negative peak.
537	$1.5D_c$	S2	-0.0066	10.157	End of cycle.
547	$2.0D_c$	D1	0.1331	54.073	Positive peak. Crack along bottom mortar joint.
567	$2.0D_c$	D1	-0.1333	-53.308	Negative peak. Cracks, top course, both ends. Crack width ~ 1.5 mm.
576	$2.0D_c$	D1	-0.0095	14.660	End of cycle.

1 in. = 25.4 mm; 1 kip = 4.45 kN

Table 5.4 (Cont'd)

Point	Cycle Group	Cycle No.	Disp. (in.)	Force (kips)	Comments
583	$2.0D_c$	D2	0.0990	41.779	Positive peak.
596	$2.0D_c$	D2	-0.0989	-42.058	Negative peak.
603	$2.0D_c$	D2	-0.0056	8.653	End of cycle.
607	$2.0D_c$	D3	0.0629	32.738	Positive peak.
615	$2.0D_c$	D3	-0.0650	-29.480	Negative peak.
619	$2.0D_c$	D3	-0.0051	7.882	End of cycle.
628	$2.0D_c$	S1	0.1361	49.409	Positive peak.
648	$2.0D_c$	S1	-0.1361	-49.518	Negative peak.
658	$2.0D_c$	S1	-0.0072	11.142	End of cycle.
666	$2.0D_c$	S2	0.1382	46.234	Positive peak.
682	$2.0D_c$	S2	-0.1379	-46.643	Negative peak.
690	$2.0D_c$	S2	-0.0068	10.475	End of cycle.
704	$3.0D_c$	D1	0.2205	48.861	Positive peak. Vertical/inclined cracks, top 3 courses, west jamb.
733	$3.0D_c$	D1	-0.2229	-45.064	Negative peak. Vertical/inclined cracks, top 3 courses, east jamb.
747	$3.0D_c$	D1	-0.0110	17.074	End of cycle.
758	$3.0D_c$	D2	0.1635	39.452	Positive peak. Crack width ~ 5 mm.
778	$3.0D_c$	D2	-0.1643	-38.827	Negative peak.
789	$3.0D_c$	D2	-0.0105	16.228	End of cycle.
796	$3.0D_c$	D3	0.1061	30.804	Positive peak.
810	$3.0D_c$	D3	-0.1080	-27.902	Negative peak.
817	$3.0D_c$	D3	-0.0101	15.592	End of cycle.
833	$3.0D_c$	S1	0.2181	36.345	Positive peak.
861	$3.0D_c$	S1	-0.2229	-45.137	Negative peak. Vertical crack extension, top 3 courses, east jamb.
877	$3.0D_c$	S1	-0.0121	18.769	End of cycle.
889	$3.0D_c$	S2	0.2266	39.341	Positive peak. Vertical crack extension, top 3 courses, west jamb.

1 in. = 25.4 mm; 1 kip = 4.45 kN

Table 5.4 (Cont'd)

Point	Cycle Group	Cycle No.	Disp. (in.)	Force (kips)	Comments
911	$3.0D_c$	S2	-0.2244	-42.709	Negative peak. Crack width ~ 7.5 mm.
923	$3.0D_c$	S2	-0.0129	19.928	End of cycle. End second day of testing.
924	$4.0D_c$	D1	-0.0042	6.465	Begin third day of testing.
938	$4.0D_c$	D1	0.2563	36.776	Loud "snap".
941	$4.0D_c$	D1	0.3116	37.885	Positive peak. Spalling damage, 6th course, west end.
974	$4.0D_c$	D1	-0.3069	-45.050	Negative peak. Crushing, top course/joint. Crack width ~ 10 mm.
991	$4.0D_c$	D1	-0.0144	22.340	End of cycle.
1000	$4.0D_c$	D2	0.2117	29.982	Loud "bang".
1001	$4.0D_c$	D2	0.2322	30.616	Positive peak.
1022	$4.0D_c$	D2	-0.2285	-36.488	Negative peak.
1034	$4.0D_c$	D2	-0.0156	24.151	End of cycle.
1041	$4.0D_c$	D3	0.1487	29.919	Positive peak.
1056	$4.0D_c$	D3	-0.1479	-31.117	Negative peak.
1064	$4.0D_c$	D3	-0.0161	24.911	End of cycle.
1084	$4.0D_c$	S1	0.3123	36.771	Positive peak.
1119	$4.0D_c$	S1	-0.3096	-40.905	Negative peak.
1135	$4.0D_c$	S1	-0.0163	25.250	End of cycle.
1150	$4.0D_c$	S2	0.3126	36.248	Positive peak.
1180	$4.0D_c$	S2	-0.3107	-39.232	Negative peak. Spalling/splitting of face-shells, top four courses.
1194	$4.0D_c$	S2	-0.0178	27.529	End of cycle.
1216	$5.0D_c$	D1	0.3943	39.836	Positive peak. Crushing damage, top joint.
1260	$5.0D_c$	D1	-0.3924	-42.787	Negative peak. Extensive spalling, both ends of top two courses.
1278	$5.0D_c$	D1	-0.0183	28.384	End of cycle.
1294	$5.0D_c$	D2	0.2923	35.208	Positive peak.
1324	$5.0D_c$	D2	-0.2910	-37.137	Negative peak.

1 in. = 25.4 mm; 1 kip = 4.45 kN

Table 5.4 (Cont'd)

Point	Cycle Group	Cycle No.	Disp. (in.)	Force (kips)	Comments
1339	$5.0D_c$	D2	-0.0182	28.153	End of cycle.
1351	$5.0D_c$	D3	0.1890	32.539	Positive peak.
1370	$5.0D_c$	D3	-0.1889	-32.753	Negative peak.
1379	$5.0D_c$	D3	-0.0187	29.024	End of cycle.
1402	$5.0D_c$	S1	0.3943	39.765	Positive peak.
1429	$5.0D_c$	S1	-0.1484	-30.321	Interruption of third day of testing.
1430	$5.0D_c$	S1	-0.1487	-29.905	Continuation of third day of testing.
1444	$5.0D_c$	S1	-0.3929	-42.060	Negative peak.
1463	$5.0D_c$	S1	-0.0191	29.603	End of cycle. End third day of testing.
1464	$5.0D_c$	S2	-0.0037	5.678	Begin fourth day of testing.
1484	$5.0D_c$	S2	0.3938	40.566	Positive peak.
1523	$5.0D_c$	S2	-0.3920	-43.427	Negative peak.
1543	$5.0D_c$	S2	-0.0194	30.079	End of cycle.
1569	$6.0D_c$	D1	0.4766	42.403	Positive peak.
1617	$6.0D_c$	D1	-0.4752	-44.594	Negative peak.
1643	$6.0D_c$	D1	-0.0197	30.600	End of cycle. Loud "thuds" from wall sliding.
1663	$6.0D_c$	D2	0.3549	35.825	Positive peak.
1701	$6.0D_c$	D2	-0.3535	-37.942	Negative peak.
1720	$6.0D_c$	D2	-0.0190	29.473	End of cycle.
1732	$6.0D_c$	D3	0.2306	33.109	Positive peak.
1756	$6.0D_c$	D3	-0.2307	-32.997	Negative peak.
1766	$6.0D_c$	D3	-0.0196	30.390	End of cycle. Loud "thuds" from wall sliding.
1792	$6.0D_c$	S1	0.4776	40.896	Positive peak. Falling debris, top course, west end. Wall sliding.
1842	$6.0D_c$	S1	-0.4761	-43.316	Negative peak. Loud "thuds" from wall sliding.
1864	$6.0D_c$	S1	-0.0193	29.950	End of cycle.

1 in. = 25.4 mm; 1 kip = 4.45 kN

Table 5.4 (Cont'd)

Point	Cycle Group	Cycle No.	Disp. (in.)	Force (kips)	Comments
1888	$6.0D_c$	S2	0.4776	40.889	Positive peak. Loud "thuds" from wall sliding.
1934	$6.0D_c$	S2	-0.4764	-42.807	Negative peak.
1956	$6.0D_c$	S2	-0.0195	30.181	End of cycle. End fourth day of testing.
1957	$8.0D_c$	D1	-0.0038	5.921	Begin fifth day of testing.
1995	$8.0D_c$	D1	0.6425	45.779	Positive peak.
2063	$8.0D_c$	D1	-0.6404	-49.029	Negative peak.
2097	$8.0D_c$	D1	-0.0193	29.845	End of cycle.
2121	$8.0D_c$	D2	0.4797	37.674	Positive peak.
2167	$8.0D_c$	D2	-0.4777	-40.823	Negative peak.
2191	$8.0D_c$	D2	-0.0190	29.414	End of cycle.
2207	$8.0D_c$	D3	0.3146	33.206	Positive peak.
2238	$8.0D_c$	D3	-0.3135	-34.829	Negative peak.
2253	$8.0D_c$	D3	-0.0190	29.596	End of cycle.
2285	$8.0D_c$	S1	0.6440	43.400	Positive peak.
2347	$8.0D_c$	S1	-0.6415	-47.339	Negative peak.
2379	$8.0D_c$	S1	-0.0190	29.477	End of cycle.
2411	$8.0D_c$	S2	0.6443	42.874	Positive peak.
2475	$8.0D_c$	S2	-0.6432	-44.677	Negative peak.
2505	$8.0D_c$	S2	-0.0188	29.106	End of cycle.
2545	$10.0D_c$	D1	0.8098	46.805	Positive peak.
2623	$10.0D_c$	D1	-0.8080	-49.573	Negative peak.
2663	$10.0D_c$	D1	-0.0189	29.347	End of cycle.
2694	$10.0D_c$	D2	0.6058	37.530	Positive peak.
2753	$10.0D_c$	D2	-0.6046	-39.392	Negative peak.
2781	$10.0D_c$	D2	-0.0185	28.724	End of cycle.

1 in. = 25.4 mm; 1 kip = 4.45 kN

Table 5.4 (Cont'd)

Point	Cycle Group	Cycle No.	Disp. (in.)	Force (kips)	Comments
2801	$10.0D_c$	D3	0.3994	31.873	Positive peak.
2840	$10.0D_c$	D3	-0.3996	-31.685	Negative peak.
2856	$10.0D_c$	D3	-0.0176	27.260	End of cycle. End fifth day of testing.
2857	$10.0D_c$	S1	-0.0038	5.947	Begin sixth day of testing.
2885	$10.0D_c$	S1	0.8121	43.233	Positive peak.
2943	$10.0D_c$	S1	-0.8111	-44.721	Negative peak.
2970	$10.0D_c$	S1	-0.0177	27.449	End of cycle.
3000	$10.0D_c$	S2	0.8139	40.386	Positive peak.
3055	$10.0D_c$	S2	-0.8146	-39.386	Negative peak.
3084	$10.0D_c$	S2	-0.0155	23.972	End of cycle.
3126	$12.0D_c$	D1	0.9863	33.586	Positive peak.
3210	$12.0D_c$	D1	-0.9944	-21.085	Negative peak.
3249	$12.0D_c$	D1	-0.0036	2.400	End of cycle.
3276	$12.0D_c$	D2	0.7510	7.816	Positive peak.
3332	$12.0D_c$	D2	-0.7502	-9.018	Negative peak.
3360	$12.0D_c$	D2	-0.0039	2.657	End of cycle.
3377	$12.0D_c$	D3	0.4987	8.144	Positive peak.
3412	$12.0D_c$	D3	-0.4968	-11.204	Negative peak.
3430	$12.0D_c$	D3	-0.0059	9.135	End of cycle.
3466	$12.0D_c$	S1	0.9953	19.706	Positive peak.
3536	$12.0D_c$	S1	-0.9933	-22.788	Negative peak.
3569	$12.0D_c$	S1	-0.0143	22.120	End of cycle. End sixth day of testing.

1 in. = 25.4 mm; 1 kip = 4.45 kN

Table 5.5 Timeline for Test of Wall Specimen 10

Point	Cycle Group	Cycle No.	Disp. (in.)	Force (kips)	Comments
1	E1	1	-0.0005	0.323	Begin first day of testing.
4	E1	1	0.0109	6.368	Positive peak.
10	E1	1	-0.0119	-4.798	Negative peak.
13	E1	1	-0.0021	1.448	End of cycle.
16	E1	2	0.0110	6.275	Positive peak.
22	E1	2	-0.0121	-4.533	Negative peak.
25	E1	2	-0.0021	1.393	End of cycle.
28	E1	3	0.0110	6.152	Positive peak.
33	E1	3	-0.0119	-4.874	Negative peak.
36	E1	3	-0.0021	1.401	End of cycle.
39	E2	1	0.0158	10.399	Positive peak.
45	E2	1	-0.0168	-8.818	Negative peak.
48	E2	1	-0.0023	1.526	End of cycle.
51	E2	2	0.0160	10.100	Positive peak.
57	E2	2	-0.0169	-8.735	Negative peak.
60	E2	2	-0.0023	1.535	End of cycle.
63	E2	3	0.0160	10.142	Positive peak.
69	E2	3	-0.0168	-8.804	Negative peak.
72	E2	3	-0.0020	1.351	End of cycle.
75	E3	1	0.0209	14.155	Positive peak.
81	E3	1	-0.0220	-12.403	Negative peak.
84	E3	1	-0.0018	1.210	End of cycle.
87	E3	2	0.0211	13.774	Positive peak.
93	E3	2	-0.0221	-12.319	Negative peak.
96	E3	2	-0.0021	1.342	End of cycle.

1 in. = 25.4 mm; 1 kip = 4.45 kN

Table 5.5 (Cont'd)

Point	Cycle Group	Cycle No.	Disp. (in.)	Force (kips)	Comments
99	E3	3	0.0209	14.162	Positive peak.
105	E3	3	-0.0220	-12.432	Negative peak.
108	E3	3	-0.0021	1.423	End of cycle.
111	E4	1	0.0261	17.709	Positive peak.
117	E4	1	-0.0271	-16.160	Negative peak.
120	E4	1	-0.0022	1.517	End of cycle.
123	E4	2	0.0261	17.635	Positive peak.
129	E4	2	-0.0272	-15.941	Negative peak.
132	E4	2	-0.0025	1.673	End of cycle.
135	E4	3	0.0261	17.629	Positive peak.
141	E4	3	-0.0272	-16.003	Negative peak.
144	E4	3	-0.0022	1.501	End of cycle.
147	E5	1	0.0313	21.192	Positive peak.
153	E5	1	-0.0321	-20.025	Negative peak.
155	E5	1	-0.0024	1.601	End of cycle.
158	E5	2	0.0314	21.038	Positive peak.
164	E5	2	-0.0323	-19.673	Negative peak.
167	E5	2	-0.0026	1.284	End of cycle.
170	E5	3	0.0315	20.964	Positive peak.
176	E5	3	-0.0325	-19.332	Negative peak.
179	E5	3	-0.0023	1.652	End of cycle.
182	E6	1	0.0364	24.945	Positive peak.
188	E6	1	-0.0375	-23.320	Negative peak.
191	E6	1	-0.0024	1.618	End of cycle.
194	E6	2	0.0365	24.753	Positive peak.

1 in. = 25.4 mm; 1 kip = 4.45 kN

Table 5.5 (Cont'd)

Point	Cycle Group	Cycle No.	Disp. (in.)	Force (kips)	Comments
200	E6	2	-0.374	-23.531	Negative peak.
203	E6	2	-0.0026	1.752	End of cycle.
206	E6	3	0.0366	24.586	Positive peak.
212	E6	3	-0.0373	-23.489	Negative peak.
215	E6	3	-0.0023	1.549	End of cycle.
218	E7	1	0.0418	28.143	Positive peak.
224	E7	1	-0.0426	-26.975	Negative peak.
227	E7	1	-0.0023	1.576	End of cycle.
230	E7	2	0.0420	27.950	Positive peak.
236	E7	2	-0.0426	-27.027	Negative peak.
239	E7	2	-0.0027	1.835	End of cycle.
242	E7	3	0.0421	27.771	Positive peak.
248	E7	3	-0.0425	-27.174	Negative peak.
251	E7	3	-0.0026	1.770	End of cycle.
253	E8	1	0.0474	31.279	Positive peak.
259	E8	1	-0.0477	-30.767	Negative peak.
262	E8	1	-0.0027	1.818	End of cycle.
265	E8	2	0.0474	31.126	Positive peak.
271	E8	2	-0.0476	-30.876	Negative peak.
274	E8	2	-0.0026	1.758	End of cycle.
277	E8	3	0.0475	31.058	Positive peak.
283	E8	3	-0.0478	-30.491	Negative peak.
286	E8	3	-0.0028	1.877	End of cycle.
289	E9	1	0.0531	33.891	Positive peak.
295	E9	1	-0.0532	-33.766	Negative peak.

1 in. = 25.4 mm; 1 kip = 4.45 kN

Table 5.5 (Cont'd)

Point	Cycle Group	Cycle No.	Disp. (in.)	Force (kips)	Comments
298	E9	1	-0.0032	2.153	End of cycle.
301	E9	2	0.0531	33.987	Positive peak.
307	E9	2	-0.0532	-33.846	Negative peak.
310	E9	2	-0.0030	2.048	End of cycle.
313	E9	3	0.0532	33.759	Positive peak.
319	E9	3	-0.0532	-33.826	Negative peak.
322	E9	3	-0.0024	1.597	End of cycle.
325	E10	1	0.0590	36.412	Positive peak.
331	E10	1	-0.0589	-36.647	Negative peak.
335	E10	1	-0.0033	2.254	End of cycle.
339	E10	2	0.0590	36.364	Positive peak.
345	E10	2	-0.0590	-36.439	Negative peak.
349	E10	2	-0.0035	2.335	End of cycle.
353	E10	3	0.0589	36.595	Positive peak.
360	E10	3	-0.0590	-36.468	Negative peak.
364	E10	3	-0.0037	2.464	End of cycle.
368	$1.0D_c$	D1	0.0650	38.795	Positive peak. Vertical cracks, top course, east/west ends.
376	$1.0D_c$	D1	-0.0644	-39.609	Negative peak. Vertical cracks. Cracks along bottom joint.
380	$1.0D_c$	D1	-0.0040	2.686	End of cycle.
384	$1.0D_c$	D2	0.0489	28.891	Positive peak.
392	$1.0D_c$	D2	-0.0486	-29.319	Negative peak.
396	$1.0D_c$	D2	-0.0034	2.299	End of cycle.
400	$1.0D_c$	D3	0.0325	19.356	Positive peak.
408	$1.0D_c$	D3	-0.0328	-18.944	Negative peak.
412	$1.0D_c$	D3	-0.0026	1.734	End of cycle.

1 in. = 25.4 mm; 1 kip = 4.45 kN

Table 5.5 (Cont'd)

Point	Cycle Group	Cycle No.	Disp. (in.)	Force (kips)	Comments
416	$1.0D_c$	S1	0.0649	38.830	Positive peak.
424	$1.0D_c$	S1	-0.0648	-39.125	Negative peak.
428	$1.0D_c$	S1	-0.0040	2.694	End of cycle.
434	$1.0D_c$	S2	0.0655	38.026	Positive peak.
446	$1.0D_c$	S2	-0.0650	-38.699	Negative peak.
452	$1.0D_c$	S2	-0.0041	2.751	End of cycle.
459	$1.5D_c$	D1	0.1057	45.425	Positive peak. Vertical cracks, 6th course, west end.
476	$1.5D_c$	D1	-0.1033	-49.142	Negative peak. Vertical cracks, 6th course, east end.
485	$1.5D_c$	D1	-0.0061	9.472	End of cycle.
493	$1.5D_c$	D2	0.0794	34.018	Positive peak.
511	$1.5D_c$	D2	-0.0733	-37.154	Negative peak.
520	$1.5D_c$	D2	-0.0049	7.554	End of cycle.
525	$1.5D_c$	D3	0.0514	24.957	Positive peak.
535	$1.5D_c$	D3	-0.0504	-26.568	Negative peak.
540	$1.5D_c$	D3	-0.0041	2.748	End of cycle.
549	$1.5D_c$	S1	0.1066	44.044	Positive peak.
567	$1.5D_c$	S1	-0.1035	-48.774	Negative peak.
576	$1.5D_c$	S1	-0.0062	9.598	End of cycle.
585	$1.5D_c$	S2	0.1074	42.718	Positive peak.
603	$1.5D_c$	S2	-0.1045	-47.271	Negative peak.
612	$1.5D_c$	S2	-0.0067	10.317	End of cycle. End first day of testing.
613	$2.0D_c$	D1	-0.0040	6.221	Begin second day of testing.
625	$2.0D_c$	D1	0.1513	44.413	Positive peak. Vertical crack, courses 3-5, west jamb.
647	$2.0D_c$	D1	-0.1497	-46.978	Negative peak.Vertical crack, courses 4 and 5, east jamb.
658	$2.0D_c$	D1	-0.0101	15.672	End of cycle.

1 in. = 25.4 mm; 1 kip = 4.45 kN

Table 5.5 (Cont'd)

Point	Cycle Group	Cycle No.	Disp. (in.)	Force (kips)	Comments
667	$2.0D_c$	D2	0.1131	33.926	Positive peak.
682	$2.0D_c$	D2	-0.1121	-35.476	Negative peak.
688	$2.0D_c$	D2	-0.0097	15.058	End of cycle.
694	$2.0D_c$	D3	0.0726	27.002	Positive peak.
704	$2.0D_c$	D3	-0.0723	-27.475	Negative peak.
710	$2.0D_c$	D3	-0.0065	10.056	End of cycle.
722	$2.0D_c$	S1	0.1526	42.405	Positive peak.
744	$2.0D_c$	S1	-0.1519	-43.604	Negative peak. Crack width ~ 1 mm.
754	$2.0D_c$	S1	-0.0103	16.019	End of cycle.
766	$2.0D_c$	S2	0.1526	42.479	Positive peak. Crack width ~ 1 mm.
790	$2.0D_c$	S2	-0.1522	-43.080	Negative peak.
801	$2.0D_c$	S2	-0.0107	16.588	End of cycle.
819	$3.0D_c$	D1	0.2369	51.247	Positive peak. Splitting damage top course, west. Crack width ~ 3 mm.
853	$3.0D_c$	D1	-0.2347	-54.731	Negative peak. Stairstep, inclined cracks in middle of panel.
872	$3.0D_c$	D1	-0.0123	19.123	End of cycle.
887	$3.0D_c$	D2	0.1764	40.383	Positive peak.
918	$3.0D_c$	D2	-0.1757	-41.463	Negative peak.
933	$3.0D_c$	D2	-0.0122	18.842	End of cycle.
942	$3.0D_c$	D3	0.1152	30.751	Positive peak.
958	$3.0D_c$	D3	-0.1146	-31.653	Negative peak.
967	$3.0D_c$	D3	-0.0111	17.263	End of cycle.
983	$3.0D_c$	S1	0.2382	49.230	Positive peak.
1019	$3.0D_c$	S1	-0.2366	-51.701	Negative peak.
1037	$3.0D_c$	S1	-0.0124	19.163	End of cycle.
1055	$3.0D_c$	S2	0.2390	48.068	Positive peak.

1 in. = 25.4 mm; 1 kip = 4.45 kN

Table 5.5 (Cont'd)

Point	Cycle Group	Cycle No.	Disp. (in.)	Force (kips)	Comments
1091	$3.0D_c$	S2	-0.2372	-50.805	Negative peak.
1108	$3.0D_c$	S2	-0.0119	18.395	End of cycle. End second day of testing.
1109	$4.0D_c$	D1	-0.0048	7.370	Begin third day of testing.
1131	$4.0D_c$	D1	0.3234	56.75	Positive peak. Splitting damage, top two courses, west.
1178	$4.0D_c$	D1	-0.3225	-58.156	Negative peak. Spalling damage, courses 2-6. Crack width ~ 5 mm.
1202	$4.0D_c$	D1	-0.0137	21.284	End of cycle.
1220	$4.0D_c$	D2	0.2414	44.334	Positive peak.
1253	$4.0D_c$	D2	-0.2412	-44.620	Negative peak.
1271	$4.0D_c$	D2	-0.0124	19.246	End of cycle.
1283	$4.0D_c$	D3	0.1576	34.774	Positive peak.
1305	$4.0D_c$	D3	-0.1585	-33.375	Negative peak.
1317	$4.0D_c$	D3	-0.0118	18.308	End of cycle.
1341	$4.0D_c$	S1	0.3243	55.295	Positive peak.
1388	$4.0D_c$	S1	-0.3235	-56.553	Negative peak.
1411	$4.0D_c$	S1	-0.0133	20.610	End of cycle.
1435	$4.0D_c$	S2	0.3247	54.781	Positive peak.
1482	$4.0D_c$	S2	-0.3245	-54.998	Negative peak. Splitting damage, top course, east.
1505	$4.0D_c$	S2	-0.0129	19.988	End of cycle.
1535	$5.0D_c$	D1	0.4099	62.209	Positive peak. Inclined crack from top center to lower east corner.
1591	$5.0D_c$	D1	-0.4117	-59.355	Negative peak.
1621	$5.0D_c$	D1	-0.0136	21.091	End of cycle.
1644	$5.0D_c$	D2	0.3062	48.448	Positive peak.
1691	$5.0D_c$	D2	-0.3082	-45.551	Negative peak.
1713	$5.0D_c$	D2	-0.0120	18.618	End of cycle.
1728	$5.0D_c$	D3	0.2017	36.131	Positive peak.

1 in. = 25.4 mm; 1 kip = 4.45 kN

Table 5.5 (Cont'd)

Point	Cycle Group	Cycle No.	Disp. (in.)	Force (kips)	Comments
1758	$5.0D_c$	D3	-0.2033	-33.683	Negative peak.
1773	$5.0D_c$	D3	-0.0108	16.764	End of cycle. End third day of testing.
1774	$5.0D_c$	S1	-0.0054	8.314	Begin fourth day of testing.
1802	$5.0D_c$	S1	0.4105	61.238	Positive peak.
1860	$5.0D_c$	S1	-0.4178	-49.938	Negative peak.
1891	$5.0D_c$	S1	-0.0133	20.692	End of cycle.
1918	$5.0D_c$	S2	0.4122	58.533	Positive peak.
1978	$5.0D_c$	S2	-0.4209	-45.174	Negative peak.
2005	$5.0D_c$	S2	-0.0141	21.872	End of cycle.
2039	$6.0D_c$	D1	0.5042	55.423	Positive peak.
2107	$6.0D_c$	D1	-0.5139	-40.532	Negative peak. Inclined crack from top center to lower west corner.
2142	$6.0D_c$	D1	-0.0158	24.486	End of cycle.
2145	$6.0D_c$	D2	0.0276	26.990	Loud "snap".
2168	$6.0D_c$	D2	0.3790	40.265	Positive peak.
2222	$6.0D_c$	D2	-0.3866	-28.589	Negative peak.
2250	$6.0D_c$	D2	-0.0089	13.854	End of cycle.
2268	$6.0D_c$	D3	0.2493	32.021	Positive peak.
2304	$6.0D_c$	D3	-0.2587	-17.481	Negative peak.
2322	$6.0D_c$	D3	-0.0052	8.034	End of cycle. End fourth day of testing.
2323	$6.0D_c$	D3	-0.0055	3.732	Begin fourth day of testing.
2359	$6.0D_c$	S1	0.5114	44.358	Positive peak.
2420	$6.0D_c$	S1	-0.4323	-27.440	Loud "snap".
2426	$6.0D_c$	S1	-0.5224	-27.232	Negative peak.
2458	$6.0D_c$	S1	-0.0080	12.405	End of cycle.
2487	$6.0D_c$	S2	0.5143	39.765	Positive peak.

1 in. = 25.4 mm; 1 kip = 4.45 kN

Table 5.5 (Cont'd)

Point	Cycle Group	Cycle No.	Disp. (in.)	Force (kips)	Comments
2548	$6.0D_c$	S2	-0.5263	-21.216	Negative peak.
2578	$6.0D_c$	S2	-0.0068	10.552	End of cycle.
2605	$8.0D_c$	D1	0.5024	30.383	Loud "snap".
2618	$8.0D_c$	D1	0.6991	32.403	Positive peak. Extensive spalling/crushing damage throughout panel.
2698	$8.0D_c$	D1	-0.7078	-18.900	Negative peak. Extensive spalling/crushing damage throughout panel.
2714	$8.0D_c$	D1	-0.4196	3.762	Interruption of fourth day of testing.
2715	$8.0D_c$	D1	-0.0932	5.032	Continuation of fourth day of testing.
2716	$8.0D_c$	D1	-0.0754	5.244	End of cycle.
2750	$8.0D_c$	D2	0.5290	17.009	Positive peak.
2812	$8.0D_c$	D2	-0.5335	-10.148	Negative peak.
2843	$8.0D_c$	D2	-0.0059	3.990	End of cycle.
2863	$8.0D_c$	D3	0.3540	9.260	Positive peak.
2913	$8.0D_c$	D3	-0.3543	-3.817	Negative peak.
2932	$8.0D_c$	D3	-0.0044	2.983	End of cycle. End of fourth day of testing.

1 in. = 25.4 mm; 1 kip = 4.45 kN

Table 5.6 Timeline for Test of Wall Specimen 12

Point	Cycle Group	Cycle No.	Disp. (in.)	Force (kips)	Comments
1	E1	1	-0.0032	2.167	Begin first day of testing.
4	E1	1	0.0113	8.798	Positive peak.
10	E1	1	-0.0119	-3.452	Negative peak.
13	E1	1	-0.0034	2.307	End of cycle.
16	E1	2	0.0114	8.749	Positive peak.
22	E1	2	-0.0115	-3.717	Negative peak.
25	E1	2	-0.0033	2.246	End of cycle.
28	E1	3	0.0114	8.630	Positive peak.
34	E1	3	-0.0114	-3.770	Negative peak.
37	E1	3	-0.0033	2.201	End of cycle.
40	E2	1	0.0178	11.993	Positive peak.
46	E2	1	-0.0212	-6.702	Negative peak.
49	E2	1	-0.0032	2.147	End of cycle.
52	E2	2	0.0179	11.795	Positive peak.
58	E2	2	-0.0211	-6.796	Negative peak.
61	E2	2	-0.0031	2.124	End of cycle.
64	E2	3	0.0179	11.705	Positive peak.
70	E2	3	-0.0211	-6.873	Negative peak.
73	E2	3	-0.0032	2.189	End of cycle.
76	E3	1	0.0243	15.084	Positive peak.
82	E3	1	-0.0270	-10.817	Negative peak.
85	E3	1	-0.0031	2.081	End of cycle.
88	E3	2	0.0245	14.796	Positive peak.
94	E3	2	-0.0269	-10.946	Negative peak.
97	E3	2	-0.0030	2.045	End of cycle.

1 in. = 25.4 mm; 1 kip = 4.45 kN

Table 5.6 (Cont'd)

Point	Cycle Group	Cycle No.	Disp. (in.)	Force (kips)	Comments
100	E3	3	0.0245	14.725	Positive peak.
105	E3	3	-0.0269	-10.982	Negative peak.
108	E3	3	-0.0033	2.224	End of cycle.
111	E4	1	0.0308	18.150	Positive peak.
117	E4	1	-0.0334	-14.099	Negative peak.
120	E4	1	-0.0035	2.331	End of cycles.
123	E4	2	0.0306	18.396	Positive peak.
129	E4	2	-0.0335	-13.951	Negative peak.
132	E4	2	-0.0035	2.350	End of cycles.
135	E4	3	0.0307	18.214	Positive peak.
141	E4	3	-0.0335	-14.013	Negative peak.
144	E4	3	-0.0033	2.208	End of cycles.
148	E5	1	0.0375	20.890	Positive peak.
156	E5	1	-0.0397	-17.494	Negative peak.
160	E5	1	-0.0036	2.413	End of cycles.
163	E5	2	0.0380	20.093	Positive peak.
170	E5	2	-0.0395	-17.883	Negative peak.
174	E5	2	-0.0035	2.352	End of cycles.
177	E5	3	0.0383	19.743	Positive peak.
184	E5	3	-0.0393	-18.083	Negative peak.
188	E5	3	-0.0033	2.255	End of cycles.
193	E6	1	0.0455	21.733	Positive peak.
204	E6	1	-0.0456	-21.503	Negative peak.
210	E6	1	-0.0036	2.411	End of cycles.
216	E6	2	0.0454	21.822	Positive peak.

1 in. = 25.4 mm; 1 kip = 4.45 kN

Table 5.6 (Cont'd)

Point	Cycle Group	Cycle No.	Disp. (in.)	Force (kips)	Comments
228	E6	2	-0.0455	-21.723	Negative peak.
234	E6	2	-0.0034	2.294	End of cycles.
240	E6	3	0.0455	21.691	Positive peak.
252	E6	3	-0.0457	-21.320	Negative peak.
258	E6	3	-0.0035	2.331	End of cycles.
264	E7	1	0.0520	24.752	Positive peak.
276	E7	1	-0.0521	-24.568	Negative peak.
282	E7	1	-0.0036	2.438	End of cycles.
288	E7	2	0.0522	24.535	Positive peak.
300	E7	2	-0.0527	-23.638	Negative peak.
306	E7	2	-0.0037	2.477	End of cycles.
312	E7	3	0.0522	24.476	Positive peak.
324	E7	3	-0.0527	-23.737	Negative peak.
330	E7	3	-0.0037	2.478	End of cycles.
336	E8	1	0.0587	27.542	Positive peak.
348	E8	1	-0.0593	-26.598	Negative peak.
354	E8	1	-0.0046	3.098	End of cycles.
360	E8	2	0.0590	27.052	Positive peak.
372	E8	2	-0.0597	-26.024	Negative peak.
378	E8	2	-0.0044	2.994	End of cycles.
383	E8	3	0.0591	26.931	Positive peak.
394	E8	3	-0.0579	-25.775	Negative peak.
400	E8	3	-0.0050	3.369	End of cycles.
406	E9	1	0.0659	29.673	Positive peak.
416	E9	1	-0.0668	-28.166	Negative peak.

1 in. = 25.4 mm; 1 kip = 4.45 kN

Table 5.6 (Cont'd)

Point	Cycle Group	Cycle No.	Disp. (in.)	Force (kips)	Comments
422	E9	1	-0.0028	4.269	End of cycle.
427	E9	2	0.0660	29.375	Positive peak.
437	E9	2	-0.0673	-27.382	Negative peak.
442	E9	2	-0.0028	4.353	End of cycle.
448	E9	3	0.0662	29.193	Positive peak.
458	E9	3	-0.0672	-27.555	Negative peak.
463	E9	3	-0.0029	4.534	End of cycle. End first day of testing.
464	E10	1	-0.0029	4.472	Begin second day of testing.
470	E10	1	0.0723	32.823	Positive peak.
482	E10	1	-0.0755	-27.974	Negative peak.
488	E10	1	-0.0042	6.587	End of cycle.
494	E10	2	0.0729	31.900	Positive peak.
506	E10	2	-0.0753	-28.198	Negative peak.
512	E10	2	-0.0042	6.440	End of cycle.
518	E10	3	0.0733	31.381	Positive peak.
530	E10	3	-0.0754	-28.085	Negative peak.
536	E10	3	-0.0039	6.086	End of cycle.
542	$1.0D_c$	D1	0.0804	33.531	Positive peak. Vertical crack, top course, both ends.
554	$1.0D_c$	D1	-0.0821	-30.829	Negative peak. Stairstep inclined crack, 2nd and 3rd courses.
560	$1.0D_c$	D1	-0.0044	6.745	End of cycle.
566	$1.0D_c$	D2	0.0606	24.642	Positive peak.
578	$1.0D_c$	D2	-0.0623	-21.987	Negative peak.
584	$1.0D_c$	D2	-0.0038	5.892	End of cycle.
587	$1.0D_c$	D3	0.0401	16.932	Positive peak.
593	$1.0D_c$	D3	-0.411	-15.293	Negative peak.

1 in. = 25.4 mm; 1 kip = 4.45 kN

Table 5.6 (Cont'd)

Point	Cycle Group	Cycle No.	Disp. (in.)	Force (kips)	Comments
596	$1.0D_c$	D3	-0.0042	2.830	End of cycle.
602	$1.0D_c$	S1	0.0807	32.976	Positive peak.
614	$1.0D_c$	S1	-0.0823	-30.511	Negative peak.
620	$1.0D_c$	S1	-0.0043	6.596	End of cycle.
626	$1.0D_c$	S2	0.0810	32.511	Positive peak.
638	$1.0D_c$	S2	-0.0825	-30.213	Negative peak.
644	$1.0D_c$	S2	-0.0045	7.025	End of cycle.
653	$1.5D_c$	D1	0.1275	39.465	Positive peak.
671	$1.5D_c$	D1	-0.1316	-33.097	Negative peak. Diagonal crack from upper east to lower west corners.
681	$1.5D_c$	D1	-0.0067	10.439	End of cycle.
690	$1.5D_c$	D2	0.0962	28.835	Positive peak.
708	$1.5D_c$	D2	-0.0989	-24.681	Negative peak.
716	$1.5D_c$	D2	-0.0061	9.447	End of cycle.
722	$1.5D_c$	D3	0.0634	20.257	Positive peak.
734	$1.5D_c$	D3	-0.0657	-16.734	Negative peak.
740	$1.5D_c$	D3	-0.0054	8.430	End of cycle.
749	$1.5D_c$	S1	0.1290	37.154	Positive peak.
766	$1.5D_c$	S1	-0.1329	-31.089	Negative peak.
774	$1.5D_c$	S1	-0.0065	10.004	End of cycle.
783	$1.5D_c$	S2	0.1293	36.658	Positive peak.
800	$1.5D_c$	S2	-0.1336	-30.042	Negative peak.
809	$1.5D_c$	S2	-0.0065	10.144	End of cycle.
821	$2.0D_c$	D1	0.1749	45.046	Positive peak. Diagonal crack from upper west to lower east corners
843	$2.0D_c$	D1	-0.1839	-31.214	Negative peak. Inclined crack from top middle to lower west corner.
855	$2.0D_c$	D1	-0.0078	12.027	End of cycle.

1 in. = 25.4 mm; 1 kip = 4.45 kN

Table 5.6 (Cont'd)

Point	Cycle Group	Cycle No.	Disp. (in.)	Force (kips)	Comments
864	$2.0D_c$	D2	0.1326	31.682	Positive peak.
881	$2.0D_c$	D2	-0.1369	-24.941	Negative peak.
890	$2.0D_c$	D2	-0.0070	10.926	End of cycle.
896	$2.0D_c$	D3	0.0877	22.238	Positive peak.
907	$2.0D_c$	D3	-0.0908	-17.362	Negative peak.
913	$2.0D_c$	D3	-0.0066	10.302	End of cycle.
925	$2.0D_c$	S1	0.1772	41.598	Positive peak.
947	$2.0D_c$	S1	-0.1830	-32.561	Negative peak.
959	$2.0D_c$	S1	-0.0074	11.423	End of cycle.
971	$2.0D_c$	S2	0.1779	40.472	Positive peak.
993	$2.0D_c$	S2	-0.1833	-32.098	Negative peak.
1005	$2.0D_c$	S2	-0.0072	11.165	End of cycle. End second day of testing.
1006	$3.0D_c$	D1	-0.0035	5.420	Begin third day of testing.
1025	$3.0D_c$	D1	0.2772	44.606	Positive peak. Bed joint cracks in courses 5 and 6. Crack width ~ 1 mm.
1061	$3.0D_c$	D1	-0.2796	-40.939	Negative peak. Sliding along base of wall.
1079	$3.0D_c$	D1	-0.0077	11.995	End of cycle.
1095	$3.0D_c$	D2	0.2082	33.061	Positive peak.
1143	$3.0D_c$	D2	-0.0069	10.653	End of cycle.
1127	$3.0D_c$	D2	-0.2107	-29.200	Negative peak.
1152	$3.0D_c$	D3	0.1380	23.282	Positive peak.
1170	$3.0D_c$	D3	-0.1399	-20.353	Negative peak.
1179	$3.0D_c$	D3	-0.0070	10.828	End of cycle.
1197	$3.0D_c$	S1	0.2785	42.571	Positive peak.
1233	$3.0D_c$	S1	-0.2812	-38.454	Negative peak.
1251	$3.0D_c$	S1	-0.0075	11.652	End of cycle.

1 in. = 25.4 mm; 1 kip = 4.45 kN

Table 5.6 (Cont'd)

Point	Cycle Group	Cycle No.	Disp. (in.)	Force (kips)	Comments
1269	$3.0D_c$	S2	0.2794	41.200	Positive peak.
1305	$3.0D_c$	S2	-0.2916	-37.879	Negative peak.
1325	$3.0D_c$	S2	-0.0077	12.006	End of cycle.
1337	$4.0D_c$	D1	0.1868	26.708	Interruption of third day of testing.
1338	$4.0D_c$	D1	0.1872	26.100	Continuation of third day of testing.
1343	$4.0D_c$	D1	0.3785	45.800	Positive peak. Diagonal crack from upper west to lower east corners.
1358	$4.0D_c$	D1	-0.3788	-45.200	Negative peak. Crushing of bed joints in courses 1-3.
1367	$4.0D_c$	D1	-0.0074	11.500	End of cycle.
1373	$4.0D_c$	D2	0.2852	32.300	Positive peak.
1385	$4.0D_c$	D2	-0.2866	-30.100	Negative peak.
1391	$4.0D_c$	D2	-0.0070	10.900	End of cycle.
1395	$4.0D_c$	D3	0.1893	22.800	Positive peak.
1403	$4.0D_c$	D3	-0.1903	-21.300	Negative peak.
1407	$4.0D_c$	D3	-0.0071	11.000	End of cycle.
1415	$4.0D_c$	S1	0.3803	42.900	Positive peak.
1431	$4.0D_c$	S1	-0.3814	-41.200	Negative peak.
1439	$4.0D_c$	S1	-0.0075	11.700	End of cycle.
1447	$4.0D_c$	S2	0.3810	41.800	Positive peak.
1463	$4.0D_c$	S2	-0.3825	-39.600	Negative peak.
1471	$4.0D_c$	S2	-0.0076	11.800	End of cycle. End third day of testing.
1472	$5.0D_c$	D1	-0.0030	4.643	Begin fourth day of testing.
1501	$5.0D_c$	D1	0.4791	47.861	Positive peak.
1561	$5.0D_c$	D1	-0.4812	-44.677	Negative peak. Crushing/spalling damage throughout panel.
1591	$5.0D_c$	D1	-0.0084	13.079	End of cycle.
1615	$5.0D_c$	D2	0.3608	33.768	Positive peak.

1 in. = 25.4 mm; 1 kip = 4.45 kN

Table 5.6 (Cont'd)

Point	Cycle Group	Cycle No.	Disp. (in.)	Force (kips)	Comments
1663	$5.0D_c$	D2	-0.3631	-30.086	Negative peak.
1687	$5.0D_c$	D2	-0.0070	10.778	End of cycle.
1702	$5.0D_c$	D3	0.2398	23.503	Positive peak.
1731	$5.0D_c$	D3	-0.2418	-20.470	Negative peak.
1745	$5.0D_c$	D3	-0.0065	10.008	End of cycle.
1775	$5.0D_c$	S1	0.4813	44.424	Positive peak.
1835	$5.0D_c$	S1	-0.4834	-41.185	Negative peak.
1865	$5.0D_c$	S1	-0.0083	12.894	End of cycle.
1895	$5.0D_c$	S2	0.4824	42.751	Positive peak.
1954	$5.0D_c$	S2	-0.4842	-39.930	Negative peak.
1984	$5.0D_c$	S2	-0.0080	12.379	End of cycle. End fourth day of testing.
1985	$6.0D_c$	D1	-0.0049	7.542	Begin fifth day of testing.
2020	$6.0D_c$	D1	0.5817	46.901	Positive peak. Crack width ~ 5-6 mm.
2092	$6.0D_c$	D1	-0.5835	-44.160	Negative peak.
2128	$6.0D_c$	D1	-0.0090	13.995	End of cycle.
2152	$6.0D_c$	D2	0.3892	29.168	Soft "bang".
2155	$6.0D_c$	D2	0.4382	32.269	Positive peak
2207	$6.0D_c$	D2	-0.4400	-29.460	Negative peak. Crushing/spalling damage throughout panel.
2234	$6.0D_c$	D2	-0.0097	14.972	End of cycle.
2252	$6.0D_c$	D3	0.2911	23.081	Positive peak.
2288	$6.0D_c$	D3	-0.2935	-19.386	Negative peak.
2306	$6.0D_c$	D3	-0.0092	14.206	End of cycle.
2341	$6.0D_c$	S1	0.5831	44.807	Positive peak.
2413	$6.0D_c$	S1	-0.5858	-40.602	Negative peak.

1 in. = 25.4 mm; 1 kip = 4.45 kN

Table 5.6 (Cont'd)

Point	Cycle Group	Cycle No.	Disp. (in.)	Force (kips)	Comments
2449	$6.0D_c$	S1	-0.0124	19.160	End of cycle. End fifth day of testing.
2450	$6.0D_c$	S2	-0.0124	10.062	Begin sixth day of testing.
2483	$6.0D_c$	S2	0.5847	42.246	Positive peak. Spalling damage of top course, west end.
2555	$6.0D_c$	S2	-0.5863	-39.910	Negative peak.
2591	$6.0D_c$	S2	-0.0116	17.971	End of cycle.
2632	$8.0D_c$	D1	0.7862	46.166	Positive peak. Crushing damage of top course, east end.
2727	$8.0D_c$	D1	-0.7856	-47.165	Negative peak. Spalling damage of top two courses, west end.
2773	$8.0D_c$	D1	-0.0120	18.602	End of cycle.
2798	$8.0D_c$	D2	0.4057	29.986	Loud "bang".
2808	$8.0D_c$	D2	0.5900	34.159	Positive peak.
2876	$8.0D_c$	D2	-0.5417	-29.855	Loud "bang".
2879	$8.0D_c$	D2	-0.5917	-31.396	Negative peak.
2915	$8.0D_c$	D2	-0.0068	10.580	End of cycle. End sixth day of testing.
2916	$8.0D_c$	D3	-0.0059	3.981	Begin seventh day of testing.
2937	$8.0D_c$	D3	0.3940	21.656	Positive peak.
2985	$8.0D_c$	D3	-0.3961	-18.428	Negative peak.
3009	$8.0D_c$	D3	-0.0030	4.699	End of cycle.
3053	$8.0D_c$	S1	0.7961	30.870	Positive peak.
3148	$8.0D_c$	S1	-0.7933	-35.122	Negative peak.
3196	$8.0D_c$	S1	-0.0045	7.048	End of scale.
3243	$8.0D_c$	S2	0.7999	24.950	Positive peak.
3336	$8.0D_c$	S2	-0.7976	-28.494	Negative peak.
3384	$8.0D_c$	S2	-0.0053	3.550	End of cycle.
3443	$10.0D_c$	D1	1.0054	22.614	Positive peak
3528	$10.0D_c$	D1	-0.4153	-15.036	Loud "bang".

1 in. = 25.4 mm; 1 kip = 4.45 kN

Table 5.6 (Cont'd)

Point	Cycle Group	Cycle No.	Disp. (in.)	Force (kips)	Comments
3561	$10.0D_c$	D1	-1.0039	-24.958	Negative peak.
3619	$10.0D_c$	D1	-0.0034	2.268	End of cycle. End seventh day of testing.
3620	$10.0D_c$	D2	-0.0011	0.775	Begin eighth day of testing.
3659	$10.0D_c$	D2	0.7569	12.630	Positive peak.
3747	$10.0D_c$	D2	-0.7584	-10.272	Negative peak. Extensive crushing/spalling damage throughout panel.
3789	$10.0D_c$	D2	-0.0005	0.365	End of cycle.
3819	$10.0D_c$	D3	0.5066	5.264	Positive peak.
3879	$10.0D_c$	D3	-0.5043	-3.865	Negative peak.
3909	$10.0D_c$	D3	-0.0001	0.0930	End of cycle.
3965	$10.0D_c$	S1	1.0107	14.346	Positive peak.
4084	$10.0D_c$	S1	-1.0105	-14.726	Negative peak.
4144	$10.0D_c$	S1	-0.0015	1.011	End of cycle. End eighth day of testing.

1 in. = 25.4 mm; 1 kip = 4.45 kN

Table 6.1.1 Positive Peak Lateral Displacement During the Simulated Seismic Drift Tests

Wall No.	Point	Peak Displacement, Δ_{max}		Drift Ratio, Δ_{max}/H	Shear at Peak Disp., $V_{\Delta,max}$†		$V_{\Delta,max}/V_{max}$‡
		(mm)	(in.)	(%)	(kN)	(kips)	
2	2934	18.25	0.719	1.283	65.81	14.796	0.276
4	2245	15.68	0.617	1.102	87.30	19.626	0.336
6	2484	15.40	0.606	1.083	39.48	8.877	0.214
8	3466	25.28	0.995	1.777	87.65	19.706	0.364
10	2618	26.10	0.699	1.248	144.13	32.403	0.521
12	3965	25.67	1.011	1.805	63.81	14.346	0.300

†Shear force at instant of peak positive displacement
‡Positive peak shear force

Table 6.1.2 Negative Peak Lateral Displacement During the Simulated Seismic Drift Tests

Wall No.	Point	Peak Displacement, Δ_{max}		Drift Ratio, Δ_{max}/H	Shear at Peak Disp., $V_{\Delta,max}$†		$V_{\Delta,max}/V_{max}$‡
		(mm)	(in.)	(%)	(kN)	(kips)	
2	3011	18.21	0.717	1.280	76.6	17.22	0.270
4	2298	15.69	0.618	1.103	84.5	18.99	0.341
6	2554	15.32	0.603	1.077	62.3	14.00	0.372
8	3210	25.26	0.994	1.776	93.8	21.09	0.381
10	2698	17.98	0.708	1.264	84.1	18.90	0.318
12	4084	25.67	1.011	1.804	65.5	14.73	0.312

†Shear force at instant of peak negative displacement
‡Negative peak shear force

Table 6.1.3 Average Peak Lateral Displacement During the Simulated Seismic Drift Tests

Wall No.	Peak Displacement, Δ_{max}		Drift Ratio, Δ_{max}/H	Shear at Peak Disp., $V_{\Delta,max}$†		$V_{\Delta,max}/V_{max}$‡
	(mm)	(in.)	(%)	(kN)	(kips)	
2	18.23	0.718	1.282	71.2	16.01	0.273
4	15.68	0.618	1.103	85.9	19.31	0.339
6	16.27	0.605	1.080	50.9	11.44	0.289
8	25.27	0.995	1.777	90.7	20.40	0.373
10	17.87	0.704	1.256	114.1	25.65	0.422
12	25.67	1.011	1.805	64.7	14.54	0.306

†Shear force at instant of peak average displacement
‡Average peak shear force

Table 6.2.1 Positive Peak Shear Force During the Simulated Seismic Drift Tests

Wall No.	Point	Peak Shear Force, V_{max}		Displacement @ Peak Force, $\Delta_{V,max}$		Drift Ratio, $\Delta_{V,max}/H$
		(kN)	(kips)	(mm)	(in.)	(%)
2	896	238.5	53.63	6.06	0.238	0.426
4	1240	259.5	58.34	9.71	0.382	0.683
6	1125	184.1	41.39	9.69	0.381	0.681
8	547	240.5	54.07	3.38	0.133	0.238
10	1535	276.7	62.21	10.41	0.410	0.732
12	1501	212.9	47.86	12.17	0.479	0.856

Table 6.2.2 Negative Peak Shear Force During the Simulated Seismic Drift Tests

Wall No.	Point	Peak Shear Force, V_{max}		Displacement @ Peak Force, $\Delta_{V,max}$		Drift Ratio, $\Delta_{V,max}/H$
		(kN)	(kips)	(mm)	(in.)	(%)
2	924	284.1	63.87	5.39	0.212	0.379
4	1061	247.5	55.64	9.76	0.384	0.686
6	1177	167.7	37.69	9.75	0.384	0.685
8	441	246.2	55.34	2.29	0.090	0.161
10	1591	264.0	59.36	10.46	0.412	0.735
12	2727	209.8	47.17	19.95	0.786	1.403

Table 6.2.3 Average Peak Shear Force During the Simulated Seismic Drift Tests

Wall No.	Peak Shear Force, V_{max}		Displacement @ Peak Force, $\Delta_{V,max}$		Drift Ratio, $\Delta_{V,max}/H$
	(kN)	(kips)	(mm)	(in.)	(%)
2	261.3	58.75	5.72	0.225	0.402
4	253.5	56.99	9.74	0.383	0.684
6	175.9	39.54	9.72	0.383	0.683
8	243.3	54.71	2.84	0.112	0.199
10	270.4	60.78	10.43	0.411	0.734
12	211.3	47.51	16.06	0.632	1.129

Table 6.3.1 Deformation Capacities

Shear Wall No.	Displacement Capacity Δ_u, mm (in.)			Drift Capacity, %		
	Positive	Negative	Average	Positive	Negative	Average
2	18.25 (0.719)	16.95 (0.667)	17.60 (0.693)	1.283	1.192	1.237
4	11.97 (0.471)	10.17 (0.401)	11.07 (0.436)	0.842	0.715	0.778
6	11.86 (0.467)	12.62 (0.497)	12.24 (0.482)	0.833	0.887	0.860
8	20.80 (0.819)	20.52 (0.808)	20.66 (0.814)	1.463	1.443	1.453
10	13.06 (0.514)	11.93 (0.470)	12.50 (0.492)	0.918	0.839	0.879
12	20.22 (0.796)	20.34 (0.801)	20.28 (0.798)	1.422	1.430	1.426

Table 6.4.1 Shear Force and In-Plane Lateral Displacement at First Visible Cracking

Shear Wall No.	Point @ Cracking		Shear Force, kN (kips)			Displacement, mm (in.)		
	Positive	Negative	Positive	Negative	Average	Positive	Negative	Average
2	551	561	190.4 (42.80)	205.2 (46.13)	197.8 (44.46)	1.633 (0.0643)	1.554 (0.0612)	1.594 (0.0628)
4	441	451	183.8 (41.33)	163.2 (36.70)	173.5 (39.01)	1.989 (0.0783)	2.065 (0.0813)	2.027 (0.0798)
6	360	374	102.0 (22.93)	93.2 (20.96)	97.6 (21.94)	2.215 (0.0872)	2.248 (0.0885)	2.232 (0.0879)
8	364	370	205.8 (46.28)	213.3 (47.96)	209.6 (47.12)	1.374 (0.0541)	1.349 (0.0531)	1.361 (0.0536)
10	368	376	172.6 (38.80)	176.2 (39.61)	174.4 (39.20)	1.651 (0.0650)	1.636 (0.0644)	1.644 (0.0647)
12	542	554	149.1 (33.53)	137.1 (30.83)	143.1 (32.18)	2.042 (0.0804)	2.085 (0.0821)	2.063 (0.0812)

Table 6.4.2 Shear Force and In-Plane Lateral Displacement at Proportional Limit

Shear Wall No.	Shear Force, kN (kips)			Displacement, mm (in.)		
	Positive	Negative	Average	Positive	Negative	Average
2	201 (45.1)	208 (46.7)	204 (45.9)	1.60 (0.063)	1.14 (0.045)	1.37 (0.054)
4	188 (42.2)	163 (36.7)	176 (39.5)	1.40 (0.055)	1.65 (0.065)	1.52 (0.060)
6	110 (24.8)	91 (20.4)	101 (22.6)	2.24 (0.088)	1.83 (0.072)	2.03 (0.080)
8	214 (48.0)	221 (49.6)	217 (48.8)	1.37 (0.054)	1.35 (0.053)	1.36 (0.054)
10	178 (40.0)	190 (42.8)	184 (41.4)	1.70 (0.067)	1.68 (0.066)	1.69 (0.067)
12	155 (34.8)	136 (30.6)	145 (32.7)	2.03 (0.080)	2.08 (0.082)	2.06 (0.081)

Table 6.4.3 Shear Force and In-Plane Lateral Displacement at Stiffness Change

Shear Wall No.	Shear Force, kN (kips)			Displacement, mm (in.)		
	Positive	Negative	Average	Positive	Negative	Average
2	181 (40.8)	205 (46.2)	193 (43.5)	1.22 (0.048)	1.07 (0.042)	1.14 (0.045)
4	178 (40.0)	152 (34.2)	165 (37.1)	1.27 (0.050)	1.45 (0.057)	1.36 (0.054)
6	110 (24.8)	88 (19.8)	99 (22.3)	2.29 (0.090)	1.63 (0.064)	1.96 (0.077)
8	214 (48.1)	219 (49.3)	217 (48.7)	1.40 (0.055)	1.35 (0.053)	1.37 (0.054)
10	167 (37.5)	188 (42.3)	177 (39.9)	1.52 (0.060)	1.65 (0.065)	1.59 (0.063)
12	157 (35.3)	125 (28.1)	141 (31.7)	2.08 (0.082)	1.70 (0.067)	1.89 (0.074)

Table 6.5.1 Initial Stiffnesses Inferred from Experimental Data

Shear Wall No.	Points	Cycles	Peak Shear Force V, kN (kips)		Peak Displacement Δ_o, mm (in.)		Cycle Effective Slope K_o	Initial Stiffness $K^\dagger$
			Positive	Negative	Positive	Negative	kN/mm (kips/in.)	
2	1-158	E1-E4	82.8 (18.61)	101.5 (22.82)	0.135 (0.00531)	0.181 (0.00713)	583.2 (3330)	501.5 (2864)
4	1-145	E1-E4	95.4 (21.44)	67.3 (15.14)	0.248 (0.00975)	0.279 (0.01098)	309.1 (1765)	265.8 (1518)
6	1-109	E1-E3	51.9 (11.67)	45.7 (10.28)	0.229 (0.00902)	0.300 (0.01180)	184.6 (1054)	158.8 (907)
8	1-181	E1-E5	89.0 (20.0)	90.2 (20.28)	0.154 (0.00605)	0.166 (0.00654)	560.2 (3199)	481.7 (2751)
10	1-108	E1-E3	79.1 (17.78)	71.7 (16.11)	0.208 (0.00820)	0.260 (0.01025)	321.7 (1837)	276.7 (1580)
12	1-108	E1-E3	66.6 (14.98)	53.0 (11.92)	0.246 (0.00967)	0.256 (0.01008)	238.4 (1362)	205.0 (1171)

$^\dagger K = 0.86K_o$

Table 6.6.1 Energy Dissipation Indices

Shear Wall No.	Aspect Ratio, H/L	Reinf. Ratio, ρ_h (%)	Drift Ratio, Δ/H (%)						
			0.25	0.50	0.75	1.0	1.25	1.5	Δ_{max}/H^*
2	0.5	0.056	21	64	115	281	308	---	350
4	0.7	0.056	24	47	99	134	---	---	143
6	1.0	0.056	21	49	106	132	---	---	144
8	0.5	0.110	20	47	157	251	370	512	568
10	0.7	0.110	11	46	82	149	156	---	160
12	1.0	0.110	13	26	63	103	141	183	199

*Drift ratio at maximum lateral displacement ($\Delta=\Delta_{max}$)

Table 7.1.1 Summary of Vertical Reinforcement Strains[1] for Wall Specimen 2

Strain Gage	First Yield[2]		Peak Response			Limit of Reliability	
	Point	Drift[3] (%)	Strain (in/in)	Point	Drift[3] (%)	Point	Drift[3] (%)
VTWO	650	0.186	0.00475	770	0.261	*NA*	*NA*
VTWI	770	0.261	0.00295	843	0.262/0.262	*NA*	*NA*
VBWO	*NA*	*NA*	-0.00058	1481	0.767	*NA*	*NA*
VBWI	*NA*	*NA*	0.00088	1316	0.595/0.595	*NA*	*NA*
VTEO	749	0.235	0.00393	859	0.270/0.270	*NA*	*NA*
VTEI	827	0.268/0.268	0.00351	893	0.307	*NA*	*NA*
VBEO	2841	0.429/1.244	-0.00245	2913	0.611/1.244	*NA*	*NA*
VBEI	*NA*	*NA*	0.00061	1083	0.064/0.434	2992	0.670/1.240

[1]*NA* denotes that strain never achieved the indicated condition.
[2]Strain (tension or compression) first exceeds nominal yield (0.00237).
[3]First value is current drift, second value is previous peak drift.

Table 7.1.2 Summary of Vertical Reinforcement Strains[1] for Wall Specimen 4

Strain Gage	First Yield[2]		Peak Response			Limit of Reliability	
	Point	Drift[3] (%)	Strain (in/in)	Point	Drift[3] (%)	Point	Drift[3] (%)
VTWO	1000	0.663	0.00295	1465	0.888	*NA*	*NA*
VTWI	735	0.325/0.325	0.00456	808	0.477	*NA*	*NA*
VBWO	*NA*	*NA*	0.00119	2268	0.101/1.102	*NA*	*NA*
VBWI	891	0.504/0.504	0.00287	941	0.504/0.504	*NA*	*NA*
VTEO	655	0.327	0.00530	745	0.334/0.334	*NA*	*NA*
VTEI	654	0.297	0.00525	723	0.330/0.330	*NA*	*NA*
VBEO[4]	----	----	----	----	----	----	----
VBEI	*NA*	*NA*	----	2080	1.097	*NA*	*NA*

[1]*NA* denotes that strain never achieved the indicated condition.
[2]Strain (tension or compression) first exceeds nominal yield (0.00237).
[3]First value is current drift, second value is previous peak drift.
[4]Gage was not functional throughout test.

Table 7.1.3 Summary of Vertical Reinforcement Strains[1] for Wall Specimen 6

Strain Gage	First Yield[2]		Peak Response			Limit[2]	
	Point	Drift[3] (%)	Strain (in/in)	Point	Drift[3] (%)	Point	Drift[3] (%)
VTWO	866	0.378/	0.00444	1177	0.685	*NA*	*NA*
VTWI	*NA*	*NA*	0.00099	585	0.186/0.246	*NA*	*NA*
VBWO	*NA*	*NA*	-0.00134	1544	0.672	*NA*	*NA*
VBWI[4]	----	----	----	----	----	----	----
VTEO	531	0.180/0.240	0.00587	601	0.244/0.244	637	0.332
VTEI	500	0.223	0.00367	501	0.239	*NA*	*NA*
VBEO	*NA*	*NA*	0.00219	1547	0.739	*NA*	*NA*
VBEI	*NA*	*NA*	-0.00179	2554	1.075/1.075	*NA*	*NA*

[1]*NA* denotes that strain never achieved the indicated condition.
[2]Strain (tension or compression) first exceeds nominal yield (0.00237).
[3]First value is current drift, second value is previous peak drift.
[4]Gage was not functional throughout test.

Table 7.1.4 Summary of Vertical Reinforcement Strains[1] for Wall Specimen 8

Strain Gage	First Yield[2]		Peak Response			Limit of Reliability	
	Point	Drift[3] (%)	Strain (in/in)	Point	Drift[3] (%)	Point	Drift[3] (%)
VTWO	566	0.213	0.01263	941	0.556	*NA*	*NA*
VTWI	643	0.134/0.238	0.00488	682	0.245/0.245	2383	0.116/1.150
VBWO	*NA*	*NA*	-0.00040	938	0.458	*NA*	*NA*
VBWI	*NA*	*NA*	0.00044	2623	1.443	*NA*	*NA*
VTEO	547	0.238	0.00447	1119	0.550/0.550	2152	0.301/1.144
VTEI	490	0.166/0.166	0.00407	547	0.238	3368	0.444/1.761
VBEO	*NA*	*NA*	0.00037	2545	1.446	*NA*	*NA*
VBEI	*NA*	*NA*	-0.00024	3315	0.645/1.776	*NA*	*NA*

[1]*NA* denotes that strain never achieved the indicated condition.
[2]Strain (tension or compression) first exceeds nominal yield (0.00237).
[3]First value is current drift, second value is previous peak drift.

Table 7.1.5 Summary of Vertical Reinforcement Strains[1] for Wall Specimen 10

Strain Gage	First Yield[2]		Peak Response			Limit of Reliability	
	Point	Drift[3] (%)	Strain (in/in)	Point	Drift[3] (%)	Point	Drift[3] (%)
VTWO	646	0.237	0.00452	647	0.267	*NA*	*NA*
VTWI	1171	0.400/0.424	0.00655	2851	0.251/1.248	*NA*	*NA*
VBWO	*NA*	*NA*	0.00135	2618	1.248	*NA*	*NA*
VBWI	*NA*	*NA*	-0.00054	2817	0.827/1.264	*NA*	*NA*
VTEO	625	0.270	0.00875	1999	0.181/0.752	1759	0.343/0.735
VTEI	623	0.218	0.00429	625	0.270	*NA*	*NA*
VBEO	1898	0.157/0.733	0.00387	2039	0.900	2540	0.687/0.933
VBEI	*NA*	*NA*	0.00195	2039	0.900	*NA*	*NA*

[1]*NA* denotes that strain never achieved the indicated condition.
[2]Strain (tension or compression) first exceeds nominal yield (0.00237).
[3]First value is current drift, second value is previous peak drift.

Table 7.1.6 Summary of Vertical Reinforcement Strains[1] for Wall Specimen 12

Strain Gage	First Yield[2]		Peak Response			Limit of Reliability	
	Point	Drift[3] (%)	Strain (in/in)	Point	Drift[3] (%)	Point	Drift[3] (%)
VTWO	1883	0.516/0.860	0.00807	3411	0.806/1.428	*NA*	*NA*
VTWI	*NA*	*NA*	0.00098	1305	0.503/0.503	*NA*	*NA*
VBWO	1431	0.680/0.680	-0.00587	3109	0.227/1.403	*NA*	*NA*
VBWI	*NA*	*NA*	0.00236	3831	0.546/1.795	*NA*	*NA*
VTEO	1024	0.495	0.00357	1269	0.498/0.498	1406	0.099/0.676
VTEI	821	0.312	0.00332	1019	0.345/----	*NA*	*NA*
VBEO	1427	0.339/0.676	0.00625	3068	0.996/1.422	*NA*	*NA*
VBEI	1418	0.449/0.679	0.00700	3014	0.142/1.404	*NA*	*NA*

[1]*NA* denotes that strain never achieved the indicated condition.
[2]Strain (tension or compression) first exceeds nominal yield (0.00237).
[3]First value is current drift, second value is previous peak drift.

Table 7.2.1 Summary of Horizontal Reinforcement Strains[1] for Wall Specimen 2

Strain Gage	Tension Threshold[2]		First Yield[3]		Peak Strain (in./in.)	Limit of Reliability	
	Point	Drift[4] (%)	Point	Drift[4] (%)		Point	Drift[4] (%)
6NW	551	0.113	661	0.138/0.189	0.00287	696	0.119/0.189
6SW	551	0.113	*NA*	*NA*	0.00266	661	0.138/0.189
1NE	874	0.230/0.263	*NA*	*NA*	0.00263	1193	0.575
1SE	874	0.230/0.263	*NA*	*NA*	0.00239	1193	0.575
2NE	870	0.085/0.263	921	0.345	0.00459	1183	0.323
2SE	869	0.048/0.263	*NA*	*NA*	0.00240	1066	0.315/0.416
3NE	27	0.010/0.019	873	0.194/0.263	0.00305	1064	0.238/0.416
3SE	841	0.192/0.261	1061	0.121/0.416	0.00306	1064	0.238/0.416
3NEC	876	0.245/0.266	915	0.148/0.266	0.00376	1184	0.363
3SEC	*NA*	*NA*	*NA*	*NA*	-0.00008	1194	0.595
3NC	875	0.266	916	0.184/0.266	0.00362	1350	0.465/0.555
3SC	*NA*	*NA*	*NA*	*NA*	-0.00004	1118	0.399/0.439
4NE	770	0.261	871	0.121/0.263	0.00361	1063	0.197/0.439
4SE	770	0.261	872	0.158/0.263	0.00342	1064	0.238/0.439
4SEC	873	0.194/0.263	913	0.077/0.266	0.00390	1191	0.535/0.555
4NEC	872	0.158/0.263	913	0.077/0.266	0.00403	1065	0.276/0.439
5NE	650	0.186	843	0.263	0.00303	869	0.048/0.263
5SE	650	0.186	843	0.263	0.00418	872	0.158/0.263
6NE	770	0.261	*NA*	*NA*	0.00239	*NA*	*NA*
6SE	770	0.261	*NA*	*NA*	0.00244	*NA*	*NA*
1NW	660	0.106/0.189	1226	0.442/0.590	0.00520	1473	0.638
1SW	662	0.119/0.189	1310	0.445/0.590	0.00513	*NA*	*NA*
2NW	660	0.106/0.189	1045	0.434/0.434	0.00444	1224	0.364/0.590
2SW	660	0.106/0.189	896	0.426	0.00445	1223	0.325/0.590
3NW	620	0.099/0.114	749	0.235	0.00341	896	0.426
3SW	600	0.097/0.115	827	0.270/0.270	0.00473	1149	0.532
3NWC	1149	0.532	*NA*	*NA*	0.00122	*NA*	*NA*
3SWC	*NA*	*NA*	*NA*	*NA*	0.00016	*NA*	*NA*
4NW	551	0.113	661	0.138/0.189	0.00337	750	0.265
4SW	551	0.113	748	0.206	0.00320	853	0.049/0.270
4NWC	*NA*	*NA*	*NA*	*NA*	0.00010	855	0.125/0.270
4SWC	*NA*	*NA*	*NA*	*NA*	0.00005	893	0.307
4NC	*NA*	*NA*	*NA*	*NA*	-0.00002	750	0.265
4SC	*NA*	*NA*	*NA*	*NA*	-0.00004	859	0.271/0.271
5NW	551	0.113	661	0.138/0.189	0.00384	881	0.089/0.266
5SW	531	0.100/0.100	661	0.138/0.189	0.00481	749	0.235

[1]*NA* denotes that strain never achieved the indicated condition.
[2]Grid tension strain first exceeds 0.0002.
[3]Strain (tension or compression) first exceeds nominal yield (0.00280).
[4]If two values are shown, the first value is current drift, second value is previous peak drift.

Table 7.2.2 Summary of Horizontal Reinforcement Strains[1] for Wall Specimen 4

Strain Gage	Tension Threshold[2]		First Yield[3]		Peak Strain (in./in.)	Limit of Reliability	
	Point	Drift[4] (%)	Point	Drift[4] (%)		Point	Drift[4] (%)
6NW	525	0.172	*NA*	*NA*	0.00247	649	0.154/0.237
6SW	526	0.203	*NA*	*NA*	0.00271	649	0.154/0.237
1NE	801	0.327	*NA*	*NA*	0.00240	*NA*	*NA*
1SE	801	0.327	*NA*	*NA*	0.00194	*NA*	*NA*
2NE	806	0.433	*NA*	*NA*	0.00274	*NA*	*NA*
2SE	806	0.433	1526	0.692/0.712	0.00307	*NA*	*NA*
3NE	314	0.029/0.089	996	0.572	0.00462	*NA*	*NA*
3SE	673	0.323	*NA*	*NA*	0.00217	*NA*	*NA*
3NEC	801	0.327	1055	0.548	0.00287	*NA*	*NA*
3SEC	801	0.327	1061	0.686	0.00286	*NA*	*NA*
4NE	673	0.323	1286	0.478	0.00379	*NA*	*NA*
4SE	543	0.234	1146	0.467/0.686	0.00340	*NA*	*NA*
4SEC	768	0.278/0.334	1058	0.618	0.00310	*NA*	*NA*
4NEC	746	0.295/0.334	1058	0.618	0.00314	*NA*	*NA*
3NW	526	0.203	653	0.268	0.00318	*NA*	*NA*
5NE	541	0.175	*NA*	*NA*	0.00236	1287	0.571
5SE	541	0.175	*NA*	*NA*	0.00270	1148	0.513/0.686
6NE	542	0.205	*NA*	*NA*	0.00191	892	0.460/0.505
6SE	542	0.205	*NA*	*NA*	0.00217	1286	0.478
1NW	650	0.183/0.237	1240	0.683	0.00490	1591	0.553/0.888
1SW	649	0.154/0.237	1240	0.683	0.01167	*NA*	*NA*
2NW	598	0.217/0.236	997	0.595	0.00339	*NA*	*NA*
2SW	598	0.217/0.236	941	0.504/0.504	0.00323	1335	0.394/0.683
3SW	526	0.203	654	0.297	0.00312	1337	0.440/0.686
3NWC	769	0.334	1238	0.596/0.686	0.00352	1646	0.645/0.898
3SWC	769	0.334	1236	0.551/0.686	0.00297	*NA*	*NA*
4NW[5]	----	----	----	----	----	----	----
4SW	526	0.203	649	0.154/0.237	0.00309	723	0.330/0.330
4NWC	769	0.334	1001	0.686	0.00284	1007	0.559/0.686
4SWC	769	0.334	941	0.503/0.503	0.00327	1128	0.023/0.686
5NW	454	0.073/0.145	597	0.236/0.271	0.00429	650	0.183/0.237
5SW	525	0.172	596	0.207/0.271	0.00353	649	0.154/0.237

[1]*NA* denotes that strain never achieved the indicated condition.
[2]Grid tension strain first exceeds 0.0002.
[3]Strain (tension or compression) first exceeds nominal yield (0.00280).
[4]First value is current drift, second value is previous peak drift.
[5]Gage was not functional throughout test.

Table 7.2.3 Summary of Horizontal Reinforcement Strains[1] for Wall Specimen 6

Strain Gage	Tension Threshold[2]		First Yield[3]		Peak Strain (in./in.)	Limit of Reliability	
	Point	Drift[4] (%)	Point	Drift[4] (%)		Point	Drift[4] (%)
6NW	500	0.223	*NA*	*NA*	0.00232	1632	0.511/0.873
6SW	500	0.223	1549	0.833	0.00290	2114	0.977
1NE	867	0.409	*NA*	*NA*	0.00231	1606	0.630/0.873
1SE	867	0.409	*NA*	*NA*	0.00236	1494	0.627/0.686
2NE	832	0.406	1391	0.447/0.685	0.00404	2112	0.931
2SE	869	0.478	1395	0.556/0.685	0.00416	*NA*	*NA*
3NE	1126	0.665/0.681	*NA*	*NA*	0.00179	1859	0.702/0.873
3SE	1217	0.411/0.681	*NA*	*NA*	0.00189	1546	0.717
3NC	866	0.378	1121	0.593	0.00388	1869	0.860/0.878
3SC	838	0.506	1119	0.550	0.00385	1547	0.739
5NE	761	0.333/0.333	*NA*	*NA*	0.00249	1121	0.593
5SE	833	0.441	*NA*	*NA*	0.00265	1121	0.593
4NE	1114	0.413/0.506	*NA*	*NA*	0.00268	*NA*	*NA*
4SE	994	0.335/0.506	1338	0.456/0.681	0.00355	*NA*	*NA*
6SE	761	0.333/0.333	*NA*	*NA*	0.00187	1345	0.620/0.681
6NE	601	0.244/0.244	*NA*	*NA*	0.00122	1496	0.670/0.686
1NW	834	0.463	1123	0.637	0.00364	1754	0.003/0.879
1SW	637	0.332	1122	0.615	0.00453	*NA*	*NA*
2NW	833	0.441	*NA*	*NA*	0.00249	1121	0.593
2SW	833	0.441	1058	0.506/0.506	0.00315	1122	0.615
3SW	562	0.071/0.246	1337	0.431/0.681	0.00385	*NA*	*NA*
3NW	835	0.484	1337	0.431/0.681	0.00350	*NA*	*NA*
4NW	1122	0.615	*NA*	*NA*	0.00176	*NA*	*NA*
4SW	1338	0.456/0.681	*NA*	*NA*	0.00231	*NA*	*NA*
4NC	833	0.441	987	0.412/0.525	0.00395	1349	0.671/0.687
4SC	833	0.441	903	0.378/0.525	0.00357	1058	0.506/0.506
5NW	867	0.409	1346	0.642/0.681	0.00333	*NA*	*NA*
5SW	869	0.478	1393	0.513/0.685	0.00357	*NA*	*NA*

[1]*NA* denotes that strain never achieved the indicated condition.
[2]Grid tension strain first exceeds 0.0002.
[3]Strain (tension or compression) first exceeds nominal yield (0.00280).
[4]First value is current drift, second value is previous peak drift.

Table 7.2.4 Summary of Horizontal Reinforcement Strains[1] for Wall Specimen 8

Strain Gage	Tension Threshold[2]		First Yield[3]		Peak Strain (in./in.)	Limit of Reliability	
	Point	Drift[4] (%)	Point	Drift[4] (%)		Point	Drift[4] (%)
6NW	425	0.140	*NA*	*NA*	0.00247	704	0.394
6SW	425	0.140	*NA*	*NA*	0.00167	583	0.177/0.238
1NE	663	0.148/0.243	*NA*	*NA*	0.00131	*NA*	*NA*
1SE	629	0.231/0.243	*NA*	*NA*	0.00145	*NA*	*NA*
2NE	567	0.238	*NA*	*NA*	0.00145	*NA*	*NA*
2SE	568	0.225/0.238	*NA*	*NA*	0.00166	*NA*	*NA*
3NE	441	0.161	*NA*	*NA*	0.00230	*NA*	*NA*
3SE	441	0.161	*NA*	*NA*	0.00226	*NA*	*NA*
3NEC	*NA*	*NA*	*NA*	*NA*	0.00009	*NA*	*NA*
3SEC	*NA*	*NA*	*NA*	*NA*	-0.00007	*NA*	*NA*
3NC	*NA*	*NA*	*NA*	*NA*	0.00006	*NA*	*NA*
3SC	*NA*	*NA*	*NA*	*NA*	-0.00016	*NA*	*NA*
4NE	439	0.116	567	0.238	0.00300	682	0.246/0.246
4SE	440	0.139	646	0.198/0.238	0.00470	*NA*	*NA*
4SEC	*NA*	*NA*	*NA*	*NA*	0.00009	*NA*	*NA*
4NEC	647	0.220/0.238	*NA*	*NA*	0.00058	*NA*	*NA*
3NW	425	0.140	*NA*	*NA*	0.00221	*NA*	*NA*
5NE	439	0.116	722	0.114/0.246	0.00311	729	0.321
5SE	439	0.116	*NA*	*NA*	0.00227	567	0.238
6NE	499	0.104/0.161	*NA*	*NA*	0.00227	723	0.147/0.246
6SE	440	0.139	730	0.347	0.00331	732	0.398
1NW	679	0.149/0.243	*NA*	*NA*	0.00116	*NA*	*NA*
1SW	679	0.149/0.243	*NA*	*NA*	0.00085	*NA*	*NA*
2NW	547	0.238	*NA*	*NA*	0.00173	*NA*	*NA*
2SW	582	0.154/0.238	*NA*	*NA*	0.00171	*NA*	*NA*
3SW	426	0.152	831	0.382/0.394	0.00281	*NA*	*NA*
3NWC	*NA*	*NA*	*NA*	*NA*	0.00008	*NA*	*NA*
3SWC	3157	0.818/1.453	*NA*	*NA*	0.00021	*NA*	*NA*
4NW	425	0.140	*NA*	*NA*	0.00250	667	0.226/0.243
4SW	425	0.140	*NA*	*NA*	0.00211	699	0.272
4NWC	890	0.383/0.405	*NA*	*NA*	0.00011	890	0.383/0.394
4SWC	41	0.018/0.025	*NA*	*NA*	-0.00060	754	0.223/0.394
4NC	668	0.200/0.243	*NA*	*NA*	0.00030	938	0.458
4SC	829	0.346/0.394	*NA*	*NA*	-0.00003	829	0.346/0.394
5NW	292	0.029	545	0.191	0.00594	629	0.231/0.242
5SW	424	0.118	703	0.368	0.00636	*NA*	*NA*

[1]*NA* denotes that strain never achieved the indicated condition.
[2]Grid tension strain first exceeds 0.0002.
[3]Strain (tension or compression) first exceeds nominal yield (0.00270).
[4]First value is current drift, second value is previous peak drift.

Table 7.2.5 Summary of Horizontal Reinforcement Strains[1] for Wall Specimen 10

Strain Gage	Tension Threshold[2]		First Yield[3]		Peak Strain (in./in.)	Limit of Reliability	
	Point	Drift[4] (%)	Point	Drift[4] (%)		Point	Drift[4] (%)
6NW	459	0.189	*NA*	*NA*	0.00185	888	0.306/0.423
6SW	368	0.116	*NA*	*NA*	0.00147	816	0.345
1NE	819	0.423	*NA*	*NA*	0.00218	2000	0.156/0.752
1SE	849	0.323	*NA*	*NA*	0.00147	2140	0.080/0.900
2NE	1091	0.424/0.424	*NA*	*NA*	0.00260	2096	0.569/0.752
2SE	1176	0.525	*NA*	*NA*	0.00155	2101	0.699/0.752
3NE	847	0.272/0.272	*NA*	*NA*	0.00157	2103	0.752
3SE	848	0.298	*NA*	*NA*	0.00143	2037	0.848
3SEC	815	0.321	1534	0.700	0.00274	1589	0.700
3NEC	815	0.321	1587	0.632	0.00350	1978	0.752
4NE	647	0.267	*NA*	*NA*	0.00217	1916	0.687/0.733
4SE	646	0.237	*NA*	*NA*	0.00234	2038	0.874
4SEC	827	0.220/0.423	*NA*	*NA*	0.00253	*NA*	*NA*
4NEC	855	0.390/0.419	1591	0.735	0.00293	*NA*	*NA*
3NW	626	0.255/0.270	*NA*	*NA*	0.00217	*NA*	*NA*
5NE	476	0.184	*NA*	*NA*	0.00179	1115	0.131/0.427
5SE	476	0.184	*NA*	*NA*	0.00170	1191	0.301/0.576
6NE	425	0.090/0.115	*NA*	*NA*	0.00256	853	0.419
6SE	476	0.184	*NA*	*NA*	0.00223	1085	0.279/0.423
1NW	820	0.408/0.423	*NA*	*NA*	0.00258	2482	0.787/0.913
1SW	819	0.423	*NA*	*NA*	0.00242	2179	0.422/0.900
2NW	820	0.408/0.423	*NA*	*NA*	0.00211	2040	0.883/0.900
2SW	1148	0.175/0.578	*NA*	*NA*	0.00222	2464	0.173/0.913
3SW	189	0.047/0.067	*NA*	*NA*	0.00140	*NA*	*NA*
3NWC	850	0.346	1533	0.681	0.00307	2689	0.976
3SWC	850	0.346	1859	0.718/0.735	0.00344	*NA*	*NA*
4NW	622	0.193	*NA*	*NA*	0.00198	1861	0.713/0.746
4SW	625	0.270	*NA*	*NA*	0.00175	1692	0.541/0.735
4NWC	852	0.395	1589	0.683	0.00297	1973	0.621/0.746
4SWC	853	0.419	*NA*	*NA*	0.00199	1536	0.714/0.732
5NW	459	0.189	819	0.423	0.00294	1589	0.683
5SW	459	0.189	1055	0.426/0.426	0.00270	1389	0.559/0.578

[1]*NA* denotes that strain never achieved the indicated condition.
[2]Grid tension strain first exceeds 0.0002.
[3]Strain (tension or compression) first exceeds nominal yield (0.00270).
[4]First value is current drift, second value is previous peak drift.

Table 7.2.6 Summary of Horizontal Reinforcement Strains[1] for Wall Specimen 12

Strain Gage	Tension Threshold[2]		First Yield[3]		Peak Strain (in./in.)	Limit of Reliability	
	Point	Drift[4] (%)	Point	Drift[4] (%)		Point	Drift[4] (%)
6NW	844	0.308/0.328	*NA*	*NA*	0.00148	1359	0.676
6SW	542	0.144	*NA*	*NA*	0.00166	1373	0.509
1NE	116	0.041/0.048	*NA*	*NA*	0.01169	2587	0.138/1.047
1SE	614	0.147	*NA*	*NA*	0.01269	2590	0.050/1.047
2NE	968	0.239/0.316	*NA*	*NA*	0.00238	*NA*	*NA*
2SE	975	0.222/0.318	*NA*	*NA*	0.00265	1535	0.105/0.683
3NE	650	0.146	*NA*	*NA*	0.00107	2497	0.665/1.044
3SE	542	0.144	*NA*	*NA*	0.00118	2497	0.665/1.044
3SC	653	0.228	1882	0.487/0.860	0.00502	2917	0.023/1.403
4NE	820	0.285	2660	0.585/1.402	0.00371	2675	0.134/1.404
4SE	653	0.228	2497	0.665/1.044	0.01692	*NA*	*NA*
3NC	653	0.228	1879	0.399/0.860	0.00680	3067	1.024/1.422
3NW	843	0.328	1884	0.545/0.860	0.00319	2939	0.651/1.404
5NE	653	0.228	*NA*	*NA*	0.00154	1880	0.428/0.860
5SE	653	0.228	*NA*	*NA*	0.00132	1762	0.487/0.856
6NE	614	0.147	*NA*	*NA*	0.00205	2746	0.827/1.403
6SE	652	0.199	*NA*	*NA*	0.00265	2495	0.723/1.044
1NW	668	0.147/0.147	*NA*	*NA*	0.00238	1426	0.253/0.676
1SW	109	0.018/0.044	*NA*	*NA*	0.00242	1469	0.191/0.683
2NW	670	0.205	*NA*	*NA*	0.00219	1533	0.046/0.683
2SW	670	0.205	*NA*	*NA*	0.00226	1542	0.311/0.683
3SW	2	0.0	2496	0.691/1.044	0.00275	2652	0.828/1.404
4NW	1275	0.349/0.499	*NA*	*NA*	-0.00220	1896	0.839/0.861
4SW	1221	0.162/0.499	1535	0.105/0.683	-0.00539	2041	0.465/1.039
4NC	843	0.328	1426	0.253/0.676	0.00277	1535	0.105/0.683
4SC	843	0.328	*NA*	*NA*	0.00237	1535	0.105/0.683
5NW	154	0.037/0.060	*NA*	*NA*	0.00265	1535	0.105/0.683
5SW	119	0.024/0.060	*NA*	*NA*	0.00225	1535	0.105/0.683

[1]*NA* denotes that strain never achieved the indicated condition. [2]Grid tension strain first exceeds 0.0002. [3]Strain (tension or compression) first exceeds nominal yield (0.00270). [4]First value is current drift, second value is previous peak drift.

Table 7.2.7 Composite Drift Indices for Horizontal Reinforcement Strains

Wall Specimen	Number of Gages			Composite Drift Index (%)			
				Gross[1]		Net[2]	
	total functional	tension threshold	first yield	tension threshold	first yield	tension threshold	first yield
2	36	29	30	0.166	0.293	0.206	0.330
4	31	30	27	0.257	0.438	0.265	0.502
6	28	28	25	0.428	0.598	0.428	0.669
8	36	30	17	0.189	0.147	0.226	0.311
10	32	32	29	0.305	0.620	0.305	0.684
12	28	27	27	0.217	0.819	0.225	0.849

[1]Based on total number of functional gages.
[2]Based on number of gages meeting the limiting condition indicated.

Table 7.3.1 Summary of Masonry Surface (LST) Strains[1] in Wall Specimen 2

Gage Name	Tension Threshold[2]		Compression Threshold[3]		Limit of Reliability		Peak Strain (in./in.)	
	Point	Drift[4] (%)	Point	Drift[4] (%)	Point	Drift[4] (%)	Tension	Comp.
Alpha	924	0.379	*NA*	*NA*	2880	0.492/1.240	0.02435	0.00015
Beta	*NA*	*NA*	*NA*	*NA*	*NA*	*NA*	0.00001	0.00117
Cathy	*NA*	*NA*	*NA*	*NA*	*NA*	*NA*	0.00004	0.00118
Dog	2652	0.863/1.240	*NA*	*NA*	*NA*	*NA*	0.00015	0.00036
Ed	460	0.081/0.081	*NA*	*NA*	*NA*	*NA*	0.00021	0.00082
Fox	*NA*	*NA*	*NA*	*NA*	*NA*	*NA*	0.00004	0.00119
George	*NA*	*NA*	*NA*	*NA*	*NA*	*NA*	0.00003	0.00018
Harry	1206	0.345/0.555	*NA*	*NA*	*NA*	*NA*	0.00100	0.00019
Ivan	2489	0.219/0.925	*NA*	*NA*	*NA*	*NA*	0.00100	0.00008
Jane	2030	0.188/0.756	*NA*	*NA*	*NA*	*NA*	0.00025	0.00013
King	1148	0.512	*NA*	*NA*	*NA*	*NA*	0.00391	0.00021
Love	896	0.426	*NA*	*NA*	*NA*	*NA*	0.00361	0.00023
Mark	*NA*	*NA*	*NA*	*NA*	*NA*	*NA*	0.00004	0.00021
Neal	916	0.184/0.266	2059	0.905/0.914	*NA*	*NA*	0.00486	0.00595

[1]*NA* denotes that surface strain never achieved the indicated condition.
[2]Surface tension strain magnitude first exceeds 0.0001.
[3]Surface compression strain magnitude first exceeds 0.002.
[4]If two values are shown, the first value is current drift, second value is previous peak drift.

Table 7.3.2 Summary of Masonry Surface (LST) Strains[1] in Wall Specimen 4

Gage Name	Tension Threshold[2]		Compression Threshold[3]		Limit of Reliability		Peak Strain (in./in.)	
	Point	Drift[4] (%)	Point	Drift[4] (%)	Point	Drift[4] (%)	Tension	Comp.
Alpha	*NA*	*NA*	*NA*	*NA*	*NA*	*NA*	0.00001	0.00123
Beta	*NA*	*NA*	*NA*	*NA*	*NA*	*NA*	0.00002	0.00062
Cathy	*NA*	*NA*	*NA*	*NA*	*NA*	*NA*	0.00002	0.00087
Dog	*NA*	*NA*	*NA*	*NA*	*NA*	*NA*	0.00033	0.00033
Ed	*NA*	*NA*	2071	0.868/0.912	*NA*	*NA*	0.03305	0.00258
Fox	1627	0.040/0.898	*NA*	*NA*	1898	0.901/0.906	0.00004	0.00165
George	1953	0.615/0.908	*NA*	*NA*	*NA*	*NA*	0.00047	0.00039
Ivan	670	0.236/0.237	*NA*	*NA*	*NA*	*NA*	0.01212	0.00019
Jane	202	0.068/0.068	1644	0.611/0.898	*NA*	*NA*	0.00118	0.00307
King	525	0.172	*NA*	*NA*	*NA*	*NA*	0.00132	0.00033
Love	*NA*	*NA*	*NA*	*NA*	*NA*	*NA*	0.00009	0.00034
Mark	810	0.500	*NA*	*NA*	*NA*	*NA*	0.00010	0.00040
Neal	*NA*	*NA*	1993	0.257/0.908	*NA*	*NA*	0.00001	0.00206
Opal	322	0.095/0.095	*NA*	*NA*	*NA*	*NA*	0.00048	0.00002
Paul	914	0.459/0.503	*NA*	*NA*	*NA*	*NA*	0.01671	0.00066

[1]*NA* denotes that surface strain never achieved the indicated condition.
[2]Surface tension strain magnitude first exceeds 0.0001.
[3]Surface compression strain magnitude first exceeds 0.002.
[4]First value is current drift, second value is previous peak drift.

Table 7.3.3 Summary of Masonry Surface (LST) Strains[1] in Wall Specimen 6

Gage Name	Tension Threshold[2]		Compression Threshold[3]		Limit of Reliability		Peak Strain (in./in.)	
	Point	Drift[4] (%)	Point	Drift[4] (%)	Point	Drift[4] (%)	Tension	Comp.
Alpha	868	0.441	2056	0.879/1.076	*NA*	*NA*	0.02554	0.00204
Beta	*NA*	*NA*	*NA*	*NA*	*NA*	*NA*	0.0	0.00033
Cathy	*NA*	*NA*	*NA*	*NA*	*NA*	*NA*	0.00004	0.00067
Dog	867	0.410	*NA*	*NA*	*NA*	*NA*	0.03215	0.00027
Ed	352	0.143/0.143	*NA*	*NA*	*NA*	*NA*	0.02626	0.00069
Fox	2097	0.559/0.882	*NA*	*NA*	*NA*	*NA*	0.00032	0.00064
George	346	0.143/0.143	*NA*	*NA*	*NA*	*NA*	0.00034	0.00027
Ivan	865	0.345	*NA*	*NA*	*NA*	*NA*	0.00010	0.00036
Jane	130	0.061/0.061	*NA*	*NA*	*NA*	*NA*	0.00039	0.00058
King	832	0.406	*NA*	*NA*	1618	0.856/0.873	0.05568	0.00032
Love	532	0.129/0.240	*NA*	*NA*	*NA*	*NA*	0.00057	0.00009
Mark	869	0.478	*NA*	*NA*	*NA*	*NA*	0.00034	0.00001
Neal	895	0.183/0.507	*NA*	*NA*	*NA*	*NA*	0.00011	0.00162
Opal	836	0.492	1595	0.322/0.692	*NA*	*NA*	0.03614	0.00337
Paul	1602	0.542/0.692	*NA*	*NA*	*NA*	*NA*	0.01160	0.00027

[1]*NA* denotes that surface strain never achieved the indicated condition.
[2]Surface tension strain magnitude first exceeds 0.0001.
[3]Surface compression strain magnitude first exceeds 0.002.
[4]First value is current drift, second value is previous peak drift.

Table 7.3.4 Summary of Masonry Surface (LST) Strains[1] in Wall Specimen 8

Gage Name	Tension Threshold[2]		Compression Threshold[3]		Limit of Reliability		Peak Strain (in./in.)	
	Point	Drift[4] (%)	Point	Drift[4] (%)	Point	Drift[4] (%)	Tension	Comp.
Alpha	413	0.010/0.098	*NA*	*NA*	1261	0.687/0.701	0.00056	0.00057
Beta	*NA*	*NA*	*NA*	*NA*	3214	1.708/1.776	0.00001	0.00075
Cathy	*NA*	*NA*	329	0.063/0.088	3214	1.708/1.776	0.00001	0.00433
Dog	2072	0.965/1.144	*NA*	*NA*	*NA*	*NA*	0.00033	0.00022
Ed	1119	0.550/0.550	3050	1.063/1.448	*NA*	*NA*	0.00013	0.00704
Fox	*NA*	*NA*	*NA*	*NA*	*NA*	*NA*	0.00006	0.00050
George	3024	0.230/0.453	*NA*	*NA*	*NA*	*NA*	0.00020	0.00014
Ivan	*NA*	*NA*	*NA*	*NA*	*NA*	*NA*	0.00007	0.00026
Jane	1187	0.293/0.555	*NA*	*NA*	*NA*	*NA*	0.00036	0.00017
King	1257	0.627	*NA*	*NA*	*NA*	*NA*	0.00904	0.00035
Love	*NA*	*NA*	*NA*	*NA*	3214	1.708/1.776	0.00055	0.00042
Mark	1215	0.680	*NA*	*NA*	3214	1.708/1.776	0.00014	0.00033
Neal	*NA*	*NA*	*NA*	*NA*	3214	1.708/1.776	0.00006	0.00036
Opal	449	0.075/0.163	*NA*	*NA*	*NA*	*NA*	0.00034	0.00001
Paul	975	0.534/0.548	*NA*	*NA*	*NA*	*NA*	0.00062	0.00028

[1]*NA* denotes that surface strain never achieved the indicated condition.
[2]Surface tension strain magnitude first exceeds 0.0001.
[3]Surface compression strain magnitude first exceeds 0.002.
[4]First value is current drift, second value is previous peak drift.

Table 7.3.5 Summary of Masonry Surface (LST) Strains[1] in Wall Specimen 10

Gage Name	Tension Threshold[2]		Compression Threshold[3]		Limit of Reliability		Peak Strain (in./in.)	
	Point	Drift[4] (%)	Point	Drift[4] (%)	Point	Drift[4] (%)	Tension	Comp.
Alpha	568	0.169/0.185	*NA*	*NA*	2725	0.152/1.248	0.00027	0.00028
Beta	*NA*	*NA*	*NA*	*NA*	*NA*	*NA*	0.00003	0.00021
Cathy	2316	0.170/0.918	*NA*	*NA*	*NA*	*NA*	0.00028	0.00104
Dog	1181	0.518/0.576	*NA*	*NA*	*NA*	*NA*	0.00367	0.00030
Ed	2584	0.176/0.918	2359	0.910/0.910	2619	1.229/1.248	0.02219	0.01233
Fox	*NA*	*NA*	*NA*	*NA*	*NA*	*NA*	0.00009	0.00073
George	817	0.370	*NA*	*NA*	*NA*	*NA*	0.00016	0.00016
Ivan	851	0.370	*NA*	*NA*	*NA*	*NA*	0.01256	0.00027
Jane	424	0.115/0.115	*NA*	*NA*	*NA*	*NA*	0.00045	0.00015
King	449	0.064/0.116	*NA*	*NA*	1287	0.198/0.578	0.14959	0.00012
Love	1055	0.426/0.426	817	0.370	*NA*	*NA*	0.03088	0.00243
Mark	2739	0.597/1.248	*NA*	*NA*	*NA*	*NA*	0.00016	0.00013
Neal	1926	0.560/0.736	*NA*	*NA*	*NA*	*NA*	0.00022	0.00063
Opal	*NA*	*NA*	*NA*	*NA*	*NA*	*NA*	0.00002	0.00126
Paul	325	0.105	*NA*	*NA*	*NA*	*NA*	0.00145	0.00041

[1]*NA* denotes that surface strain never achieved the indicated condition.
[2]Surface tension strain magnitude first exceeds 0.0001.
[3]Surface compression strain magnitude first exceeds 0.002.
[4]First value is current drift, second value is previous peak drift.

Table 7.3.6 Summary of Masonry Surface (LST) Strains[1] in Wall Specimen 12

Gage Name	Tension Threshold[2]		Compression Threshold[3]		Limit of Reliability		Peak Strain (in./in.)	
	Point	Drift[4] (%)	Point	Drift[4] (%)	Point	Drift[4] (%)	Tension	Comp.
Alpha[5]	715	0.038/0.235	1487	0.456/0.680	2350	0.806/1.041	0.02347	0.01228
Beta[5]	1413	0.509/0.676	*NA*	*NA*	*NA*	*NA*	0.00021	0.00009
Cathy[5]	114	0.001/0.055	1808	0.078/0.859	*NA*	*NA*	0.02477	0.03812
Dog	470	0.129	*NA*	*NA*	*NA*	*NA*	0.00031	0.00088
Ed	204	0.081/0.081	2594	0.078/1.044	*NA*	*NA*	0.00027	0.00451
Fox	116	0.041/0.048	*NA*	*NA*	*NA*	*NA*	0.00013	0.00111
George	111	0.055/0.055	*NA*	*NA*	3254	1.113/1.404	0.02671	0.00081
Ivan	416	0.119	*NA*	*NA*	2977	0.472/1.403	0.03599	0.00029
Jane	669	0.173	*NA*	*NA*	*NA*	*NA*	0.00148	0.00081
King	263	0.081/0.081	*NA*	*NA*	2699	0.580/1.047	0.10194	0.00021
Love	394	0.105/0.105	*NA*	*NA*	2350	0.806/1.041	0.02690	0.00003
Mark	654	0.208/0.228	*NA*	*NA*	*NA*	*NA*	0.00039	0.00006
Neal	*NA*	*NA*	*NA*	*NA*	*NA*	*NA*	0.00009	0.00187
Opal	653	0.228	*NA*	*NA*	*NA*	*NA*	0.00022	0.00030
Paul	3019	0.290/1.404	*NA*	*NA*	*NA*	*NA*	0.00483	0.00141

[1]*NA* denotes that surface strain never achieved the indicated condition.
[2]Surface tension strain magnitude first exceeds 0.0001.
[3]Surface compression strain magnitude first exceeds 0.002.
[4]First value is current drift, second value is previous peak drift.
[5]Single spike of electrical noise at Point 1535.

Table 7.3.7 Composite Drift Indices for Masonry Surface Strains at Tension Threshold

Wall Specimen	Number of Gages				Composite Drift Index (%)			
	total functional		tension threshold		Gross[1]		Net[2]	
	diag.	trans.	diag.	trans.	diag.	trans.	diag.	trans.
2	4	4	3	3	0.638	0.380	0.850	0.506
4	4	4	3	3	0.167	0.329	0.223	0.439
6	4	4	4	4	0.511	0.259	0.511	0.259
8	4	4	3	3	0.562	0.408	0.749	0.543
10	4	4	3	4	0.199	0.444	0.265	0.444
12	4	4	4	4	0.439	0.084	0.439	0.084

[1]Based on total number of functional gages.
[2]Based on number of gages meeting the tension threshold condition.

Table 7.4.1 Summary of Gross (LVDT) Strains[1] in Wall Specimen 2

LVDT Channel	Gage Length (in.)	Threshold[2]		Peak Strain (in./in.)	Limit of Reliability	
		Point	Drift[3] (%)		Point	Drift[3] (%)
ETBWD	114.31	769	0.230/0.186	0.01312	*NA*	*NA*
WTBED	114.04	551	0.115	0.00679	2327	0.409/0.914
WVTFTG	4.12	61	0.027/0.026	0.00247	*NA*	*NA*
WVTBOT	16.25	659	0.073/0.189	0.00033	*NA*	*NA*
WVTMID	16.0	659	0.073/0.189	0.0105	*NA*	*NA*
WVTTOP	15.88	780	0.029/0.265	-0.01123	2895	0.027/1.244
EVTFTG	4.62	91	0.030	-0.00160	2327	0.409/0.914
EVTBOT	15.50	841	0.192/0.261	0.00173	2327	0.409/0.914
EVTMID	16.50	52	0.004/0.026	-0.00207	*NA*	*NA*
EVTTOP	15.75	561	0.109	-0.00459	*NA*	*NA*

[1]*NA* denotes that gross strain never achieved the indicated condition.
[2]Gross strain first exceeds 0.0001.
[3]If two values are shown, the first value is current drift, second value is previous peak drift.

Table 7.4.2 Summary of Gross (LVDT) Strains[1] in Wall Specimen 4

LVDT Channel	Gage Length (in.)	Threshold[2]		Peak Strain (in./in.)	Limit of Reliability	
		Point	Drift[3] (%)		Point	Drift[3] (%)
ETBWD	86.46	542	0.205	0.01636	2030	1.025/1.095
WTBED	86.46	525	0.172	0.00891	*NA*	*NA*
WVTFTG	4.37	3	0.009	-0.00919	1428	0.024/0.693
WVTBOT	16.0	557	0.173/0.232	0.00619	1991	0.301/0.912
WVTMID	16.0	669	0.209/0.237	0.00101	*NA*	*NA*
WVTTOP	16.0	611	0.236/0.236	-0.00080	*NA*	*NA*
EVTFTG	4.37	4	0.015	0.00442	*NA*	*NA*
EVTBOT	16.0	423	0.130/0.130	0.00042	*NA*	*NA*
EVTMID	16.0	182	0.019/0.052	0.00116	*NA*	*NA*
EVTTOP	16.0	787	0.401/0.557	-0.00560	2163	0.808/1.097

[1]*NA* denotes that gross strain never achieved the indicated condition.
[2]Gross strain first exceeds 0.0001.
[3]First value is current drift, second value is previous peak drift.

Table 7.4.3 Summary of Gross (LVDT) Strains[1] in Wall Specimen 6

LVDT Channel	Gage Length (in.)	Threshold[2]		Peak Strain (in./in.)	Limit of Reliability	
		Point	Drift[3] (%)		Point	Drift[3] (%)
ETBWD	67.97	499	0.176	0.00722	*NA*	*NA*
WTBED	67.97	501	-0.239	0.00819	*NA*	*NA*
WVTFTG	4.37	3	0.010	-0.00290	*NA*	*NA*
WVTBOT	16.0	869	0.478	0.00069	*NA*	*NA*
WVTMID	16.0	835	0.484	0.00080	*NA*	*NA*
WVTTOP	16.0	303	0.052/0.128	0.00463	2415	1.051/1.073
EVTFTG	4.37	3	0.010	0.00373	*NA*	*NA*
EVTBOT	16.0	239	0.101/0.101	0.00066	*NA*	*NA*
EVTMID	16.0	76	0.047	-0.00055	1450	0.670/0.687
EVTTOP	16.0	357	0.034/0.143	0.02077	2394	0.565/0.540

[1]*NA* denotes that gross strain never achieved the indicated condition.
[2]Gross strain first exceeds 0.0001.
[3]First value is current drift, second value is previous peak drift.

Table 7.4.4 Summary of Gross (LVDT) Strains[1] in Wall Specimen 8

LVDT Channel	Gage Length (in.)	Threshold[2]		Peak Strain (in./in.)	Limit of Reliability	
		Point	Drift[3] (%)		Point	Drift[3] (%)
ETBWD	114.43	424	0.118	0.02538	2971	0.018/1.450
WTBED	114.43	425	0.140	0.00724	1485	0.682/0.703
WVTFTG	4.37	44	0.004/0.018	0.00200	*NA*	*NA*
WVTBOT	16.0	494	0.099/0.166	0.00067	*NA*	*NA*
WVTMID	16.0	516	0.166/0.166	0.00028	*NA*	*NA*
WVTTOP	16.0	292	0.029/0.071	0.01479	1190	0.181/0.555
EVTFTG	4.37	76	0.032	0.00221	*NA*	*NA*
EVTBOT	16.0	705	0.381/0.394	0.00034	*NA*	*NA*
EVTMID	16.0	202	0.054/0.054	0.00095	2990	0.962/1.450
EVTTOP	16.0	491	0.154/0.166	0.00551	1453	0.520/0.702

[1]*NA* denotes that gross strain never achieved the indicated condition.
[2]Gross strain first exceeds 0.0001.
[3]First value is current drift, second value is previous peak drift.

Table 7.4.5 Summary of Gross (LVDT) Strains[1] in Wall Specimen 10

LVDT Channel	Gage Length (in.)	Threshold[2]		Peak Strain (in./in.)	Limit of Reliability	
		Point	Drift[3] (%)		Point	Drift[3] (%)
ETBWD	86.46	475	0.138	0.00353	1791	0.460/0.732
WTBED	86.46	459	0.189	0.00492	1860	0.746
WVTFTG	4.25	5	0.010/0.020	0.00421	*NA*	*NA*
WVTBOT	16.09	646	0.237	0.00059	*NA*	*NA*
WVTMID	15.94	724	0.237/0.273	-0.00078	*NA*	*NA*
WVTTOP	16.0	296	0.068/0.095	-0.00194	1840	0.233/0.735
EVTFTG	4.25	2	0.002	0.01812	*NA*	*NA*
EVTBOT	16.0	459	0.189	-0.00127	*NA*	*NA*
EVTMID	16.13	676	0.032/0.267	0.00092	2487	0.916/0.916
EVTTOP	16.0	862	0.259/0.419	-0.00252	1791	0.460/0.732

[1]*NA* denotes that gross strain never achieved the indicated condition.
[2]Gross strain first exceeds 0.0001.
[3]First value is current drift, second value is previous peak drift.

Table 7.4.6 Summary of Gross (LVDT) Strains[1] in Wall Specimen 12

LVDT Channel	Gage Length (in.)	Threshold[2]		Peak Strain (in./in.)	Limit of Reliability	
		Point	Drift[3] (%)		Point	Drift[3] (%)
ETBWD[4]	67.88	264	0.093	0.03144	*NA*	*NA*
WTBED[4]	67.88	506	0.135/0.135	0.01672	*NA*	*NA*
WVTFTG	4.63	3	0.013	0.01423	3206	0.322/1.422
WVTBOT	16.31	189	0.016/0.068	0.00241	3632	0.355/1.795
WVTMID	15.75	819	0.258	0.00080	*NA*	*NA*
WVTTOP	16.06	189	0.016/0.068	0.01046	*NA*	*NA*
EVTFTG	4.0	3	0.013	0.00955	*NA*	*NA*
EVTBOT	16.25	652	0.199	0.00164	*NA*	*NA*
EVTMID	16.13	146	0.033/0.055	0.00044	1306	0.480/0.521
EVTTOP	15.75	217	0.075/0.081	-0.00042	975	0.222/0.318

[1]*NA* denotes that gross strain never achieved the indicated condition.
[2]Gross strain first exceeds 0.0001.
[3]First value is current drift, second value is previous peak drift.
[4]Single spike of electrical noise at point 1669 was ignored.

Table 7.5.1 Wall Displacement Profiles (LVDT) for Wall Specimen 2

Point	Cycle Group	Peak Positive Lateral Drift Ratio Along Wall Height* (%)					
		BASHOR	BOTHOR	MIDHOR	TOPHOR	SPACER	EWDISP
551	$1.0D_c$	0.0166	0.0279	0.0383	0.0514	0.0874	0.113
750	$2.0D_c$	0.0210	0.0356	0.0478	0.0657	0.228	0.265
898	$3.0D_c$	0.0254	0.0399	0.0059	0.0252	0.369	0.428
1152	$4.0D_c$	0.0222	-0.154	-0.202	-0.0950	0.518	0.590
1481	$5.0D_c$	0.0308	-1.015	-0.564	-0.249	0.639	0.767
1988	$6.0D_c$	0.0333	-1.061	-0.680	-0.251	0.784	0.925
2529	$8.0D_c$	0.0475	-1.605	-0.798	-0.256	1.048	1.244

*During the D1 cycles.

Table 7.5.2 Wall Displacement Profiles (LVDT) for Wall Specimen 4

Point	Cycle Group	Peak Positive Lateral Drift Ratio Along Wall Height* (%)					
		BASHOR	BOTHOR	MIDHOR	TOPHOR	SPACER	EWDISP
441	$1.0D_c$	0.0170	0.0319	0.0479	0.0663	0.111	0.140
655	$2.0D_c$	0.0175	0.0360	0.0497	0.0665	0.294	0.327
779	$3.0D_c$	0.0262	0.0478	0.0667	0.126	0.451	0.505
1001	$4.0D_c$	0.0307	0.0489	0.0685	0.160	0.601	0.686
1465	$5.0D_c$	0.0245	-0.0025	-0.0173	0.0588	0.786	0.888
2029	$6.0D_c$	0.0165	-0.0404	-0.171	-0.0694	0.970	1.095

*During the D1 cycles.

Table 7.5.3 Wall Displacement Profiles (LVDT) for Wall Specimen 6

Point	Cycle Group	Peak Positive Lateral Drift Ratio Along Wall Height* (%)					
		BASHOR	BOTHOR	MIDHOR	TOPHOR	SPACER	EWDISP
408	$1.0D_c$	0.0104	0.0353	0.0573	0.0829	0.120	0.157
639	$2.0D_c$	0.0134	0.0568	0.0839	0.129	0.281	0.332
840	$3.0D_c$	0.0163	0.0742	0.1081	0.219	0.449	0.507
1125	$4.0D_c$	0.0235	0.0729	0.1434	0.362	0.604	0.681
1553	$5.0D_c$	0.0177	-0.0189	0.0314	0.364	0.784	0.879
2048	$6.0D_c$	0.0115	-0.0459	-0.0731	0.236	0.963	1.076

*During the D1 cycles.

Table 7.5.4 Wall Displacement Profiles (LVDT) for Wall Specimen 8

Point	Cycle Group	Peak Positive Lateral Drift Ratio Along Wall Height* (%)					
		BASHOR	BOTHOR	MIDHOR	TOPHOR	SPACER	EWDISP
376	$1.0D_c$	0.0148	0.0247	0.0337	0.0447	0.0543	0.0727
547	$2.0D_c$	0.0265	0.0549	0.0572	0.0714	0.203	0.238
704	$3.0D_c$	0.0247	0.0555	0.0468	0.0552	0.351	0.394
941	$4.0D_c$	0.0261	0.0443	0.0252	-0.0540	0.499	0.556
1216	$5.0D_c$	0.0249	0.0299	-0.0230	-0.275	0.640	0.704
1569	$6.0D_c$	0.0398	0.0494	0.0057	-0.449	0.750	0.851
1995	$8.0D_c$	0.0553	0.0706	0.0365	-0.444	1.003	1.147
2545	$10.0D_c$	0.0560	0.0715	0.0358	-0.595	1.282	1.446
3126	$12.0D_c$	0.0645	0.0702	0.0404	-1.316	1.565	1.761

*During the D1 cycles.

Table 7.5.5 Wall Displacement Profiles (LVDT) for Wall Specimen 10

Point	Cycle Group	Peak Positive Lateral Drift Ratio Along Wall Height* (%)					
		BASHOR	BOTHOR	MIDHOR	TOPHOR	SPACER	EWDISP
368	$1.0D_c$	0.0177	0.0362	0.0551	0.0734	0.0809	0.116
625	$2.0D_c$	0.0217	0.0764	0.0536	0.0985	0.216	0.270
819	$3.0D_c$	0.0254	0.0681	0.0949	0.144	0.365	0.423
1131	$4.0D_c$	0.0330	0.0709	0.110	0.194	0.494	0.578
1535	$5.0D_c$	0.0356	0.0759	0.136	0.270	0.640	0.732
2039	$6.0D_c$	0.0356	0.0575	-0.116	0.393	0.794	0.900
2618	$8.0D_c$	0.0224	-0.803	-0.353	0.482	1.119	1.248

*During the D1 cycles.

Table 7.5.6 Wall Displacement Profiles (LVDT) for Wall Specimen 12

Point	Cycle Group	Peak Positive Lateral Drift Ratio Along Wall Height[1] (%)					
		BASHOR	BOTHOR	MIDHOR	TOPHOR	SPACER	EWDISP
542	$1.0D_c$	0.0139	0.0461	0.0734	0.0960	0.103	0.144
821	$2.0D_c$	0.0194	0.0716	0.145	0.223	0.258	0.312
1025	$3.0D_c$	0.0224	0.0567	0.161	0.294	0.426	0.495
1343	$4.0D_c$	-----[2]	-----[2]	-----[2]	-----[2]	-----[2]	0.676
1501	$5.0D_c$	0.0279	0.0956	0.246	0.426	0.761	0.856
2020	$6.0D_c$	0.0304	0.0757	0.258	0.482	0.923	1.039
2632	$8.0D_c$	0.0350	-0.0081	0.262	0.652	1.250	1.404
3443	$10.0D_c$	0.0259	-0.256	-0.0782	0.672	1.607	1.795

[1]During the D1 cycles.
[2]LVDT data was not recovered for this segment.

Table 7.5.7 Linear Correlation of Displacements for Wall Specimens[1]

Wall Specimen	Vertical Intercept, M_0 mm (in.)	Slope, M_1	Correlation Coefficient, R
2	-1.0554 (-0.04155)	0.9407	0.9922
4	-0.5961 (-0.02347)	0.9409	0.9969
6	-0.5784 (-0.02277)	0.9191	0.9926
8	-1.1206 (-0.04412)	0.9558	0.9931
10	-0.5987 (-0.02357)	0.9369	0.9976
12	-0.8087 (-0.03184)	0.9323	0.9951

1 in. = 25.4 mm

[1]Spacer beam relative deflection = $M_0 + M_1$*TTF displacement

Table 8.1 Initial Stiffness Estimates

Shear Wall No.	Aspect Ratio, *H/L*	Initial Stiffness, kN/mm (kip/in.)		Inferred-to-Calculated Stiffness Ratio
		Inferred	Calculated	
2	0.5	501.5 (2864)	451.5 (2578)	1.111
4	0.7	265.8 (1518)	300.3 (1715)	0.885
6	1.0	158.8 (907)	183.3 (1047)	0.866
8	0.5	481.9 (2752)	451.5 (2578)	1.067
10	0.7	276.7 (1580)	300.3 (1715)	0.921
12	1.0	205.1 (1171)	183.3 (1047)	1.118

Table 8.2.1 Cracking Shear Strength from Shing's Formula

Specimen No.	Length, L mm (in.)	Cracking Strength, V_c kN (kips)		Calculated /Measured
		Measured	Calculated	
2	2845 (112)	197.8 (44.46)	250.1 (56.12)	1.262
4	2032 (80)	173.5 (39.01)	178.6 (40.09)	1.028
6	1422 (56)	97.6 (21.94)	125.0 (28.06)	1.279
8	2845 (112)	209.6 (47.12)	250.1 (56.12)	1.191
10	2032 (80)	174.4 (39.20)	178.6 (40.09)	1.023
12	1422 (56)	143.1 (32.18)	125.0 (28.06)	0.872
mean				*1.109*
standard deviation				*0.161*

Table 8.2.2 Cracking Shear Strength from Proposed Formula

Specimen No.	Length, L mm (in.)	Vertical Load, P_v kN (kips)	Cracking Strength, V_c kN (kips)		Calculated /Measured
			Measured	Calculated	
2	2845 (112)	265.0 (59.58)	197.8 (44.46)	208.3 (46.84)	1.054
4	2032 (80)	185.4 (41.69)	173.5 (39.01)	160.6 (36.10)	0.926
6	1422 (56)	130.2 (29.27)	97.6 (21.94)	127.4 (28.65)	1.306
8	2845 (112)	265.5 (59.70)	209.6 (47.12)	208.7 (46.90)	0.996
10	2032 (80)	187.6 (42.17)	174.4 (39.20)	161.9 (36.39)	0.928
12	1422 (56)	133.2 (29.95)	143.1 (32.18)	129.3 (29.06)	0.903
mean					*1.019*
standard deviation					*0.151*

Table 8.3.1 Average Net and Gross Area Shear Stresses

(a) Series 1

Shear Wall No.	Length, mm (in.)	Aspect Ratio, *H/L*	Horizontal Reinforcement Ratio ρ_h, %		Shear Strength V_u, kN (kips)	Shear Stress v_u, MPa (psi)	
			gross[1]	net[2]		net	gross
1	2845 (112)	0.5	0.0512	0.148	186.8 (42.00)	0.9720 (141.0)	0.3371 (48.89)
3	2032 (80)	0.7	0.0512	0.148	245.1 (55.10)	1.7852 (258.9)	0.6191 (89.80)
5	1422 (56)	1.0	0.0512	0.148	133.0 (29.90)	1.3839 (200.7)	0.4799 (69.61)
7	2845 (112)	0.5	0.119	0.342	240.2 (54.00)	1.2497 (181.3)	0.4334 (62.86)
9	2032 (80)	0.7	0.119	0.342	192.2 (43.20)	1.3996 (203.0)	0.4854 (70.40)
11	1422 (56)	1.0	0.119	0.342	153.9 (34.60)	1.6014 (232.3)	0.5554 (80.56)

[1] t_g = 194.8 mm (7.67 in.)

[2] t_f = 33.8 mm (1.33 in.)

Table 8.3.1 Average Net and Gross Area Shear Stresses

(b) Series 2

Shear Wall No.	Length, mm (in.)	Aspect Ratio, *H/L*	Horizontal Reinforcement Ratio ρ_h, %		Shear Strength V_u, kN (kips)	Shear Stress v_u, MPa (psi)	
			gross[1]	net[2]		net	gross
1	2845 (112)	0.5	0.0560	0.162	261.3 (58.75)	1.3596 (197.2)	0.4715 (68.39)
3	2032 (80)	0.7	0.0560	0.162	253.5 (56.99)	1.8464 (267.8)	0.6403 (92.88)
5	1422 (56)	1.0	0.0560	0.162	175.9 (39.54)	1.8301 (265.4)	0.6347 (92.06)
7	2845 (112)	0.5	0.110	0.316	243.4 (54.71)	1.2661 (183.6)	0.4391 (63.69)
9	2032 (80)	0.7	0.110	0.316	270.3 (60.78)	1.9692 (285.6)	0.6829 (99.05)
11	1422 (56)	1.0	0.110	0.316	211.3 (47.51)	2.1989 (318.9)	0.7626 (110.61)

[1] t_g = 194.8 mm (7.67 in.)

[2] t_f = 33.8 mm (1.33 in.)

Table 8.3.2 Material Properties for Shear Strength Estimates

parameter	Series 1		Series 2	
	nominal	actual	nominal	actual
f'_m, MPa (psi)	13.8 (2000)	17.24 (2500)	13.8 (2000)	17.24 (2500)
f_{yv}, MPa (ksi)	413.7 (60)	445.3 (64.6)	413.7 (60)	445.3 (64.6)
f_{yh}[1], MPa (ksi)	413.7 (60)	409.7 (59.4)	413.7 (60)	715.2 (103.7)
f_{yh}[2], MPa (ksi)	413.7 (60)	433.4 (62.9)	413.7 (60)	593.2 (86.0)
t_g,mm (in.)	194.8 (7.67)	194.8 (7.67)	194.8 (7.67)	194.8 (7.67)

[1]#3 rebar for Series 1 (Walls 1, 3 and 5), and No. 9 Ga wire for Series 2 (Walls 2, 4 and 6).

[2]Weighted average for #4 and #5 rebar in Series (Walls 7, 9, and 11), and No. 5 Ga wire for Series 2 (Walls 8, 10 and 12).

Table 8.3.3 Calculated Average Ultimate (Gross Area) Shear Stresses for Nominal Properties and Original Matsumura-Fattal Formula

(a) Series 1

Shear Wall No.	Aspect Ratio, H/L	Reinforcement (Gross) Ratio (%)		Average Ultimate Shear Stresses, MPa (psi)					Ratio, v_n/v_u
				Calculated				Test, v_u	
		ρ_v	ρ_h	v_m	v_s	v_a	v_n		
1	0.5	0.205	0.0512	0.1602 (23.23)	0.2086 (30.25)	0.1365 (19.80)	0.5053 (73.29)	0.3371 (48.89)	1.499
3	0.7	0.287	0.0512	0.1843 (26.73)	0.2086 (30.25)	0.1365 (19.80)	0.5294 (76.79)	0.6191 (89.80)	0.855
5	1.0	0.410	0.0512	0.2110 (30.60)	0.2086 (30.25)	0.1365 (19.80)	0.5561 (80.66)	0.4799 (69.61)	1.159
7	0.5	0.205	0.119	0.1602 (23.23)	0.2707 (39.26)	0.1365 (19.80)	0.5674 (82.30)	0.4334 (62.86)	1.309
9	0.7	0.287	0.119	0.1843 (26.73)	0.2707 (39.26)	0.1365 (19.80)	0.5915 (85.79)	0.4854 (70.40)	1.219
11	1.0	0.410	0.119	0.2110 (30.60)	0.2707 (39.26)	0.1365 (19.80)	0.6182 (89.66)	0.5554 (80.56)	1.113
mean									1.192
std. dev.									0.214

t_g = 193.5 mm (7.62 in.); t_f = 31.8 mm (1.25 in.)

f'_m = 13.79 MPa (2000 psi)

f_{yv} = 413.7 MPa (60 ksi)

f_{yh} = 413.7 MPa (60 ksi)

Table 8.3.3 Calculated Average Ultimate (Gross Area) Shear Stresses for Nominal Properties and Original Matsumura-Fattal Formula

(b) Series 2

Shear Wall No.	Aspect Ratio, *H/L*	Reinforcement (Gross) Ratio (%)		Average Ultimate Shear Stresses, MPa (psi)					Ratio, v_n/v_u
				Calculated				Test, v_u	
		ρ_v	ρ_h	v_m	v_s	v_a	v_n		
2	0.5	0.205	0.0560	0.1602 (23.23)	0.2145 (31.11)	0.1365 (19.80)	0.5112 (74.14)	0.4715 (68.39)	1.084
4	0.7	0.287	0.0560	0.1843 (26.73)	0.2145 (31.11)	0.1365 (19.80)	0.5353 (77.64)	0.6403 (92.88)	0.836
6	1.0	0.410	0.0560	0.2110 (30.60)	0.2145 (31.11)	0.1365 (19.80)	0.5620 (81.51)	0.6347 (92.06)	0.885
8	0.5	0.205	0.110	0.1602 (23.23)	0.2641 (38.30)	0.1365 (19.80)	0.5608 (81.34)	0.4391 (63.69)	1.277
10	0.7	0.287	0.110	0.1843 (26.73)	0.2641 (38.30)	0.1365 (19.80)	0.5849 (84.83)	0.6829 (99.05)	0.856
12	1.0	0.410	0.110	0.2110 (30.60)	0.2641 (38.30)	0.1365 (19.80)	0.6116 (88.70)	0.7626 (110.6)	0.802
mean									0.957
std. dev.									0.186

t_g = 193.5 mm (7.62 in.); t_f = 31.8 mm (1.25 in.)

f'_m = 13.79 MPa (2000 psi)

f_{yv} = 413.7 MPa (60 ksi)

f_{yh} = 413.7 MPa (60 ksi)

Table 8.3.4 Calculated Average Ultimate (Gross Area) Shear Stresses for Actual Properties and Original Matsumura-Fattal Formula

(a) Series 1

Shear Wall No.	Aspect Ratio, *H/L*	Reinforcement (Gross) Ratio (%)		Average Ultimate Shear Stresses, MPa (psi)					Ratio, v_n/v_u
				Calculated				Test, v_u	
		ρ_v	ρ_h	v_m	v_s	v_a	v_n		
1[1]	0.5	0.205	0.0512	0.1858 (26.95)	0.2066 (29.96)	0.1469 (21.30)	0.5392 (78.21)	0.3371 (48.89)	1.600
3[1]	0.7	0.287	0.0512	0.2138 (31.01)	0.2066 (29.96)	0.1469 (21.30)	0.5672 (82.27)	0.6191 (89.80)	0.916
5[1]	1.0	0.410	0.0512	0.2447 (35.50)	0.2066 (29.96)	0.1469 (21.30)	0.5981 (86.76)	0.4799 (69.61)	1.246
7[2]	0.5	0.205	0.119	0.1858 (26.95)	0.2836 (41.13)	0.1469 (21.30)	0.6162 (89.38)	0.4334 (62.86)	1.422
9[2]	0.7	0.287	0.119	0.2138 (31.01)	0.2836 (41.13)	0.1469 (21.30)	0.6442 (93.44)	0.4854 (70.40)	1.327
11[2]	1.0	0.410	0.119	0.2447 (35.50)	0.2836 (41.13)	0.1469 (21.30)	0.6752 (97.93)	0.5554 (80.56)	1.216
mean									1.288
std. dev.									0.229

t_g = 194.8 mm (7.67 in.); t_f = 33.8 mm (1.33 in.)

f'_m = 17.24 MPa (2500 psi)

f_{yv} = 445.3 MPa (64.58 ksi)

$^1f_{yh}$ = 409.7 MPa (59.42 ksi)

$^2f_{yh}$ = 433.4 MPa (62.86 ksi)

Table 8.3.4 Calculated Average Ultimate (Gross Area) Shear Stresses for Actual Properties and Original Matsumura-Fattal Formula

(b) Series 2

Shear Wall No.	Aspect Ratio, H/L	Reinforcement (Gross) Ratio (%)		Average Ultimate Shear Stresses, MPa (psi)					Ratio, v_n/v_u
				Calculated				Test, v_u	
		ρ_v	ρ_h	v_m	v_s	v_a	v_n		
2^1	0.5	0.205	0.0560	0.2175 (31.55)	0.3708 (53.78)	0.1660 (24.08)	0.7544 (109.4)	0.4715 (68.39)	1.600
4^1	0.7	0.287	0.0560	0.2503 (36.31)	0.3708 (53.78)	0.1660 (24.08)	0.7871 (114.2)	0.6403 (92.88)	1.229
6^1	1.0	0.410	0.0560	0.2865 (41.56)	0.3708 (53.78)	0.1660 (24.08)	0.8233 (119.4)	0.6347 (92.06)	1.297
8^2	0.5	0.205	0.110	0.2175 (31.55)	0.3787 (54.92)	0.1660 (24.08)	0.7622 (110.6)	0.4391 (63.69)	1.736
10^2	0.7	0.287	0.110	0.2503 (36.31)	0.3787 (54.92)	0.1660 (24.08)	0.7950 (115.3)	0.6829 (99.05)	1.164
12^2	1.0	0.410	0.110	0.2865 (41.56)	0.3787 (54.92)	0.1660 (24.08)	0.8312 (120.6)	0.7626 (110.6)	1.090
mean									1.353
std. dev.									0.257

t_g = 194.8 mm (7.67 in.); t_f = 33.8 mm (1.33 in.)

f'_m = 14.48 MPa (2100 psi)

f_{yv} = 445.3 MPa (64.58 ksi)

$^1f_{yh}$ = 715.2 MPa (103.73 ksi)

$^2f_{yh}$ = 593.2 MPa (86.04 ksi)

Table 8.3.5 Calculated Average Ultimate (Gross Area) Shear Stresses Using Actual Properties and Modified Matsumura-Fattal Formula

(a) Series 1

Shear Wall No.	Aspect Ratio, H/L	Reinforcement (Gross) Ratio (%)		Average Ultimate Shear Stresses, MPa (psi)					Ratio, v_n/v_u
				Calculated				Test, v_u	
		ρ_v	ρ_h	v_m	v_s	v_a	v_n		
1^1	0.5	0.205	0.0512	0.1371 (19.89)	0.1525 (22.11)	0.1333 (19.34)	0.4229 (61.34)	0.3371 (48.89)	1.255
3^1	0.7	0.287	0.0512	0.1578 (22.89)	0.1525 (22.11)	0.1333 (19.34)	0.4436 (64.34)	0.6191 (89.80)	0.717
5^1	1.0	0.410	0.0512	0.1806 (26.20)	0.1525 (22.11)	0.1333 (19.34)	0.4664 (67.65)	0.4799 (69.61)	0.972
7^2	0.5	0.205	0.119	0.1371 (19.89)	0.2093 (30.36)	0.1333 (19.34)	0.4979 (69.59)	0.4334 (62.86)	1.107
9^2	0.7	0.287	0.119	0.1578 (22.89)	0.2093 (30.36)	0.1333 (19.34)	0.5004 (72.59)	0.4854 (70.40)	1.031
11^2	1.0	0.410	0.119	0.1806 (26.20)	0.2093 (30.36)	0.1333 (19.34)	0.5233 (75.90)	0.5554 (80.56)	0.942
mean									1.004
std. dev.									0.180

t_g = 194.8 mm (7.67 in.); t_f = 33.8 mm (1.33 in.)

f'_m = 17.24 MPa (2500 psi)

f_{yv} = 445.3 MPa (64.58 ksi)

$^1f_{yh}$ = 409.7 MPa (59.42 ksi)

$^2f_{yh}$ = 433.4 MPa (62.86 ksi)

Table 8.3.5 Calculated Average Ultimate (Gross Area) Shear Stresses Using Actual Properties and Modified Matsumura-Fattal Formula

(b) Series 2

Shear Wall No.	Aspect Ratio, H/L	Reinforcement (Gross) Ratio (%)		Average Ultimate Shear Stresses, MPa (psi)					Ratio, v_n/v_u
				Calculated				Test, v_u	
		ρ_v	ρ_h	v_m	v_s	v_a	v_n		
2^1	0.5	0.205	0.0560	0.1606 (23.29)	0.2737 (39.70)	0.1475 (21.39)	0.5817 (84.38)	0.4715 (68.39)	1.234
4^1	0.7	0.287	0.0560	0.1933 (28.04)	0.2863 (41.53)	0.1499 (21.74)	0.6295 (91.31)	0.6403 (92.88)	0.983
6^1	1.0	0.410	0.0560	0.2359 (34.22)	0.3053 (44.28)	0.1535 (22.27)	0.6948 (100.8)	0.6347 (92.06)	1.095
8^2	0.5	0.205	0.110	0.1606 (23.29)	0.2795 (40.54)	0.1475 (21.39)	0.5875 (85.22)	0.4391 (63.69)	1.338
10^2	0.7	0.287	0.110	0.1933 (28.04)	0.2924 (42.41)	0.1499 (21.74)	0.6356 (92.19)	0.6829 (99.05)	0.931
12^2	1.0	0.410	0.110	0.2359 (34.22)	0.3118 (45.22)	0.1535 (22.27)	0.7013 (101.7)	0.7626 (110.6)	0.920
mean									1.083
std. dev.									0.172

t_g = 194.8 mm (7.67 in.); t_f = 33.8 mm (1.33 in.)

f'_m = 14.48 MPa (2100 psi)

f_{yv} = 445.3 MPa (64.58 ksi)

$^1f_{yh}$ = 715.2 MPa (103.73 ksi)

$^2f_{yh}$ = 593.2 MPa (86.04 ksi)

Table 8.4.1 Calculated Shear Strength at Ultimate Using Actual Properties and Modified Matsumura-Fattal Formula

(a) Series 1

Shear Wall No.	Aspect Ratio, H/L	Reinforcement (Gross) Ratio, %		A_g, cm^2 (in^2)	Shear Strength at Ultimate, kN (kips)				V_n/V_u
		ρ_v	ρ_h		V_m	V_s	V_a	V_n	
1[1]	0.5	0.205	0.0512	5,542 (859.0)	76.0 (17.09)	84.5 (19.00)	73.9 (16.61)	234.4 (52.70)	1.255
3[1]	0.7	0.287	0.0512	3,959 (613.6)	62.5 (14.04)	60.3 (13.57)	52.8 (11.87)	175.6 (39.48)	0.717
5[1]	1.0	0.410	0.0512	2,771 (429.5)	50.1 (11.25)	42.2 (9.50)	36.9 (8.31)	129.2 (29.06)	0.972
7[2]	0.5	0.205	0.119	5,542 (859.0)	76.0 (17.09)	116.0 (26.08)	73.9 (16.61)	265.9 (59.78)	1.107
9[2]	0.7	0.287	0.119	3,959 (613.6)	62.5 (14.04)	82.8 (18.63)	52.8 (11.87)	198.1 (44.54)	1.031
11[2]	1.0	0.410	0.119	2,771 (429.5)	50.1 (11.25)	58.0 (13.04)	36.9 (8.31)	145.0 (32.60)	0.942
mean									1.004
std. dev.									0.180

t_g = 194.8 mm (7.67 in.); t_f = 33.8 mm (1.33 in.)

f'_m = 17.24 MPa (2500 psi)

f_{yv} = 445.3 MPa (64.58 ksi)

[1]f_{yh} = 409.7 MPa (59.42 ksi)

[2]f_{yh} = 433.4 MPa (62.86 ksi)

Table 8.4.1 Calculated Shear Strength at Ultimate Using Actual Properties and Modified Matsumura-Fattal Formula

(b) Series 2

Shear Wall No.	Aspect Ratio, H/L	Reinforcement (Gross) Ratio, %		A_g, cm^2 (in^2)	Shear Strength at Ultimate, kN (kips)				V_n/V_u
		ρ_v	ρ_h		V_m	V_s	V_a	V_n	
2[1]	0.5	0.205	0.0560	5,542 (859.0)	89.0 (20.01)	151.7 (34.10)	81.7 (18.37)	322.4 (72.48)	1.234
4[1]	0.7	0.287	0.0560	3,959 (613.6)	76.5 (17.20)	113.4 (25.48)	59.3 (13.34)	249.2 (56.02)	0.983
6[1]	1.0	0.410	0.0560	2,771 (429.5)	65.4 (14.70)	84.6 (19.02)	42.5 (9.56)	192.5 (43.28)	1.095
8[2]	0.5	0.205	0.110	5,542 (859.0)	89.0 (20.01)	154.9 (34.82)	81.7 (18.38)	325.6 (73.21)	1.338
10[2]	0.7	0.287	0.110	3,959 (613.6)	76.5 (17.20)	115.8 (26.03)	59.3 (13.34)	251.6 (56.57)	0.931
12[2]	1.0	0.410	0.110	2,771 (429.5)	65.4 (14.70)	86.4 (19.43)	42.5 (9.56)	194.3 (43.69)	0.920
mean									1.083
std. dev.									0.172

t_g = 194.8 mm (7.67 in.); t_f = 33.8 mm (1.33 in.)

f'_m = 14.48 MPa (2100 psi)

f_{yv} = 445.3 MPa (64.58 ksi)

[1]f_{yh} = 715.2 MPa (103.73 ksi)

[2]f_{yh} = 593.2 MPa (86.04 ksi)

Table 8.4.2 Calculated Shear Strength at Ultimate Using Actual Properties and Shing's Formula

(a) Series 1

Shear Wall No.	Length, mm (in.)	A_n, cm^2 (in^2)	ρ_v, % gross (net)	A_b, mm^2 (in^2)	Shear Strength at Ultimate, kN (kips)			V_n/V_u
					V_m	V_s	V_n	
1[1]	2845 (112)	1,922 (297.9)	0.591 (0.205)	142 (0.22)	201.9 (45.38)	157.8 (35.48)	359.7 (80.86)	1.925
3[1]	2032 (80)	1,373 (212.8)	0.827 (0.287)	142 (0.22)	157.2 (35.34)	91.4 (20.54)	248.6 (55.88)	1.014
5[1]	1422 (56)	961 (149.0)	1.182 (0.410)	142 (0.22)	123.7 (27.80)	41.5 (9.34)	165.2 (37.14)	1.242
7[2]	2845 (112)	1,922 (297.9)	0.591 (0.205)	329 (0.51)	201.9 (45.38)	387.0 (87.02)	588.9 (132.4)	2.452
9[2]	2032 (80)	1,373 (212.8)	0.827 (0.287)	329 (0.51)	157.2 (35.34)	224.1 (50.38)	381.3 (85.72)	1.984
11[2]	1422 (56)	961 (149.0)	1.182 (0.410)	329 (0.51)	123.6 (27.81)	101.9 (22.90)	225.5 (50.71)	1.466
mean								1.681
std. dev.								0.535

t_g = 194.8 mm (7.67 in.); t_f = 33.8 mm (1.33 in.)

bar spacing, s = 711 mm (28.0 in.)

f'_m = 17.24 MPa (2500 psi)

f_{yv} = 445.3 MPa (64.58 ksi)

$^1f_{yh}$ = 409.7 MPa (59.42 ksi)

$^2f_{yh}$ = 433.4 MPa (62.86 ksi)

Table 8.4.2 Calculated Shear Strength at Ultimate Using Actual Properties and Shing's Formula

(b) Series 2

Shear Wall No.	Length, mm (in.)	A_n, cm^2 (in^2)	ρ_v, % gross (net)	A_b, mm^2 (in^2)	Shear Strength at Ultimate, kN (kips)			V_n/V_u
					V_m	V_s	V_n	
2[1]	2845 (112)	1,922 (297.9)	0.591 (0.205)	22.2 (0.0344)	182.0 (40.93)	190.4 (42.80)	372.4 (83.73)	1.994
4[1]	2032 (80)	1,373 (212.8)	0.827 (0.287)	22.2 (0.0344)	141.1 (31.72)	126.9 (28.53)	268.0 (60.25)	1.094
6[1]	1422 (56)	961 (149.0)	1.182 (0.410)	22.2 (0.0344)	110.4 (24.82)	79.3 (17.83)	189.7 (42.65)	1.427
8[2]	2845 (112)	1,922 (297.9)	0.591 (0.205)	43.4 (0.0673)	182.0 (40.93)	308.9 (69.45)	490.9 (110.4)	2.044
10[2]	2032 (80)	1,373 (212.8)	0.827 (0.287)	43.4 (0.0673)	141.1 (31.72)	205.9 (46.30)	347.0 (78.02)	1.806
12[2]	1422 (56)	961 (149.0)	1.182 (0.410)	43.4 (0.0673)	110.4 (24.82)	128.7 (28.93)	239.1 (53.75)	1.554
mean								1.653
std. dev.								0.365

t_g = 194.8 mm (7.67 in.); t_f = 33.8 mm (1.33 in.)

bar spacing, s = 203 mm (8.0 in.)

f'_m = 14.48 MPa (2100 psi)

f_{yv} = 445.3 MPa (64.58 ksi)

$^1f_{yh}$ = 715.2 MPa (103.73 ksi)

$^2f_{yh}$ = 593.2 MPa (86.04 ksi)

Table 8.4.3 Calculated Shear Strength at Ultimate Using Actual Properties and UBC Formula

(a) Series 1

Shear Wall No.	M/Vd (C_d)	ρ_h, % gross (net)	A_n, cm^2 (in^2)	Shear Strength at Ultimate, kN (kips)					V_n/V_u
				V_m	V_s	$V_{lim,1}$	$V_{lim,2}$	V_n	
1[1]	0.2593 (2.385)	0.0512 (0.148)	1,922 (297.9)	158.0 (35.53)	116.3 (26.14)	395.9 (89.01)	501.4 (112.7)	274.3 (61.67)	1.468
3[1]	0.3684 (2.211)	0.0512 (0.148)	1,373 (212.8)	104.6 (23.52)	83.1 (18.67)	269.0 (60.48)	340.3 (76.50)	187.7 (42.19)	0.766
5[1]	0.5385 (1.938)	0.0512 (0.148)	961 (149.0)	64.2 (14.44)	58.1 (13.07)	173.3 (38.96)	218.6 (49.16)	122.4 (27.51)	0.920
7[2]	0.2593 (2.385)	0.119 (0.342)	1,922 (297.9)	158.0 (35.53)	285.2 (64.12)	395.9 (89.01)	501.4 (112.7)	395.9 (89.01)	1.648
9[2]	0.3684 (2.211)	0.119 (0.342)	1,373 (212.8)	104.6 (23.52)	203.7 (45.80)	269.0 (60.48)	340.3 (76.50)	269.0 (60.48)	1.400
11[2]	0.5385 (1.938)	0.119 (0.342)	961 (149.0)	64.2 (14.44)	142.6 (32.06)	173.3 (38.96)	218.6 (49.16)	173.3 (38.96)	1.126
mean									1.221
std. dev.									0.341

t_g = 194.8 mm (7.67 in.); t_f = 33.8 mm (1.33 in.)

f'_m = 17.24 MPa (2500 psi)

f_{yv} = 445.3 MPa (64.58 ksi)

$^1f_{yh}$ = 409.7 MPa (59.42 ksi)

$^2f_{yh}$ = 433.4 MPa (62.86 ksi)

Table 8.4.3 Calculated Shear Strength at Ultimate for Series 2 Using Actual Properties and UBC Formula

(b) Series 2

Shear Wall No.	M/Vd (C_d)	ρ_h, % gross (net)	A_n, cm² (in²)	Shear Strength at Ultimate, kN (kips)					V_n/V_u
				V_m	V_s	$V_{lim,1}$	$V_{lim,2}$	V_n	
2[1]	0.2593 (2.385)	0.0560 (0.162)	1,922 (297.9)	144.8 (32.56)	222.1 (49.93)	362.9 (81.58)	501.4 (112.7)	362.9 (81.58)	1.389
4[1]	0.3684 (2.211)	0.0560 (0.162)	1,373 (212.8)	95.9 (21.56)	158.7 (35.67)	246.6 (55.43)	340.3 (76.50)	246.6 (55.43)	0.973
6[1]	0.5385 (1.938)	0.0560 (0.162)	961 (149.0)	58.9 (13.23)	111.1 (24.97)	158.8 (35.71)	218.6 (49.16)	158.8 (35.71)	0.903
8[2]	0.2593 (2.385)	0.110 (0.316)	1,922 (297.9)	144.8 (32.56)	360.4 (81.02)	362.9 (81.58)	501.4 (112.7)	362.9 (81.58)	1.491
10[2]	0.3684 (2.211)	0.110 (0.316)	1,373 (212.8)	95.9 (21.56)	257.4 (57.87)	246.6 (55.43)	340.3 (76.50)	246.6 (55.43)	0.912
12[2]	0.5385 (1.938)	0.110 (0.316)	961 (149.0)	58.9 (13.23)	180.2 (40.51)	158.8 (35.71)	218.6 (49.16)	158.8 (35.71)	0.752
mean									1.070
std. dev.									0.298

t_g = 194.8 mm (7.67 in.); t_f = 33.8 mm (1.33 in.)

f'_m = 14.48 MPa (2100 psi)

f_{yv} = 445.3 MPa (64.58 ksi)

[1]f_{yh} = 715.2 MPa (103.73 ksi)

[2]f_{yh} = 593.2 MPa (86.04 ksi)

Table 8.4.4 Calculated Shear Strength at Ultimate Using Actual Properties and NEHRP Formula

(a) Series 1

Shear Wall No.	M/Vd	Reinforcement Ratio, ρ_h (%)		A_n, cm^2 (in^2)	Shear Strength at Ultimate, kN (kips)				V_n/V_u
		gross	net		V_m	V_s	V_a	V_n	
1[1]	0.2593	0.0512	0.148	1,922 (297.9)	235.0 (52.82)	58.1 (13.07)	66.2 (14.90)	359.3 (80.79)	1.924
3[1]	0.3684	0.0512	0.148	1,373 (212.8)	158.8 (35.70)	41.5 (9.34)	47.3 (10.64)	247.6 (55.68)	1.011
5[1]	0.5385	0.0512	0.148	961 (149.0)	101.3 (22.77)	29.1 (6.54)	33.1 (7.45)	163.5 (36.76)	1.229
7[2]	0.2593	0.119	0.342	1,922 (297.9)	235.0 (52.82)	142.6 (32.06)	66.2 (14.90)	443.8 (99.78)	1.848
9[2]	0.3684	0.119	0.342	1,373 (212.8)	158.8 (35.70)	101.9 (22.90)	47.3 (10.64)	308.0 (69.24)	1.603
11[2]	0.5385	0.119	0.342	961 (149.0)	101.3 (22.77)	71.3 (16.03)	33.1 (7.45)	205.7 (46.25)	1.337
mean									1.492
std. dev.									0.361

t_g = 194.8 mm (7.67 in.); t_f = 33.8 mm (1.33 in.)

f'_m = 17.24 MPa (2500 psi)

f_{yv} = 445.3 MPa (64.58 ksi)

[1]f_{yh} = 409.7 MPa (59.42 ksi)

[2]f_{yh} = 433.4 MPa (62.86 ksi)

Table 8.4.4 Calculated Shear Strength at Ultimate Using Actual Properties and NEHRP Formula

(b) Series 2

Shear Wall No.	M/Vd	Reinforcement Ratio, ρ_h (%)		A_n, cm^2 (in^2)	Shear Strength at Ultimate, kN (kips)				V_n/V_u
		gross	net		V_m	V_s	V_a	V_n	
2[1]	0.2593	0.0560	0.162	1,922 (297.9)	215.3 (48.41)	111.1 (24.97)	66.3 (14.90)	392.7 (88.28)	1.503
4[1]	0.3684	0.0560	0.162	1,373 (212.8)	145.5 (32.72)	79.3 (17.83)	47.3 (10.64)	272.1 (61.19)	1.074
6[1]	0.5385	0.0560	0.162	961 (149.0)	92.8 (20.87)	55.5 (12.48)	33.1 (7.45)	181.4 (40.80)	1.032
8[2]	0.2593	0.110	0.316	1,922 (297.9)	215.3 (48.41)	180.2 (40.51)	66.3 (14.90)	461.8 (103.82)	1.898
10[2]	0.3684	0.110	0.316	1,373 (212.8)	145.5 (32.72)	128.7 (28.94)	47.3 (10.64)	321.5 (72.30)	1.190
12[2]	0.5385	0.110	0.316	961 (149.0)	92.8 (20.87)	90.1 (20.26)	33.1 (7.45)	216.0 (48.58)	1.023
mean									1.286
std. dev.									0.349

t_g = 194.8 mm (7.67 in.); t_f = 33.8 mm (1.33 in.)

f'_m = 14.48 MPa (2100 psi)

f_{yv} = 445.3 MPa (64.58 ksi)

$^1f_{yh}$ = 715.2 MPa (103.73 ksi)

$^2f_{yh}$ = 593.2 MPa (86.04 ksi)

Table 8.5 Updated Minimum Horizontal Reinforcement Ratios for Phase 2 Specimens

Specimen		f'_m, MPa (psi)	f_{yh}, MPa (ksi)	σ_v, MPa (psi)	L, mm (in.)	minimum ρ_h (%)	
No.	Designation					Strength	Energy
2	CO-R05-J05-Q10	15.72 (2280)	715.2 (103.7)	1.38 (200)	2845 (112)	0.0372	0.0768
4	CO-R07-J05-Q10	16.90 (2450)	715.2 (103.7)	1.35 (196)	2032 (80)	0.0381	0.0607
6	CO-R10-J05-Q10	18.55 (2690)	715.2 (103.7)	1.36 (197)	1422 (56)	0.0400	0.0479
8	CO-R05-J12-Q10	17.24 (2500)	595.9 (86.4)	1.38 (200)	2845 (112)	0.0468	0.0769
10	CO-R07-J12-Q10	17.17 (2490)	595.9 (86.4)	1.37 (198)	2032 (80)	0.0464	0.0611
12	CO-R10-J12-Q10	18.34 (2660)	595.9 (86.4)	1.39 (201)	1422 (56)	0.0484	0.0486

a) $H/L = 0.5$

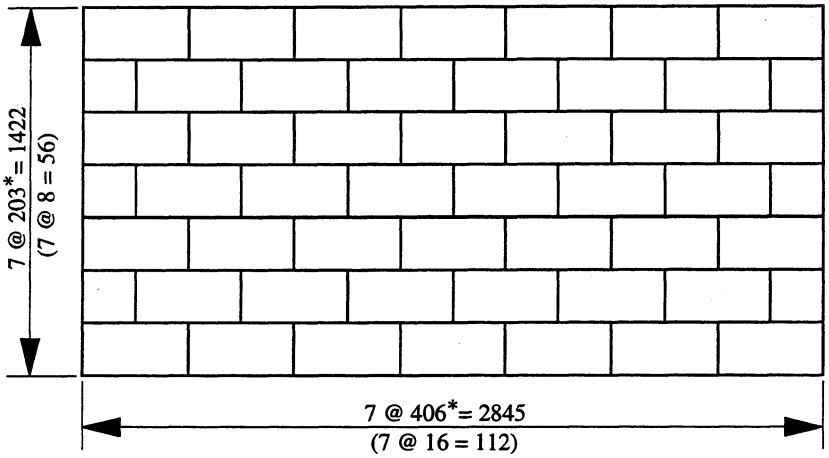

b) $H/L = 0.7$

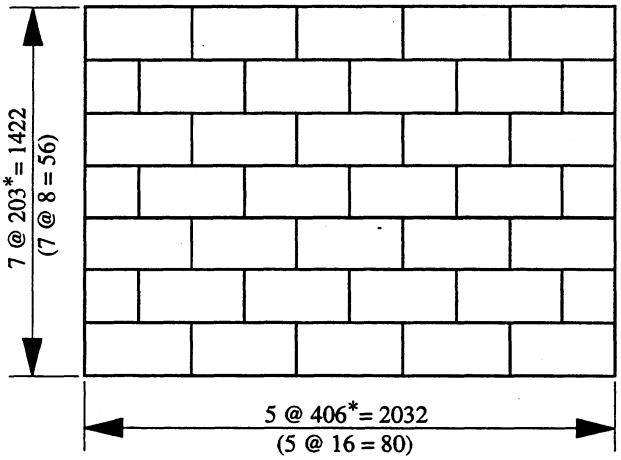

c) $H/L = 1.0$

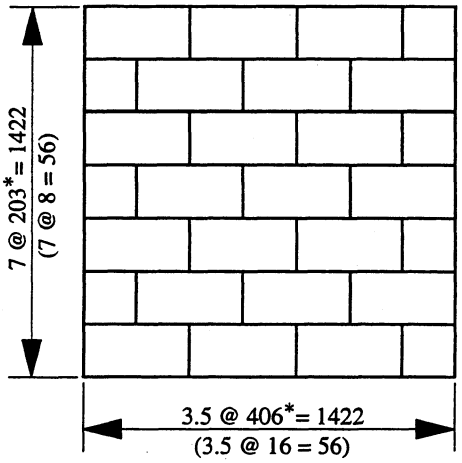

*Masonry unit plus one bed joint and one head joint is 203 mm (8 in.) tall and 406 mm (16 in.) long.

Fig. 3.1 Masonry Wall Panel Configurations

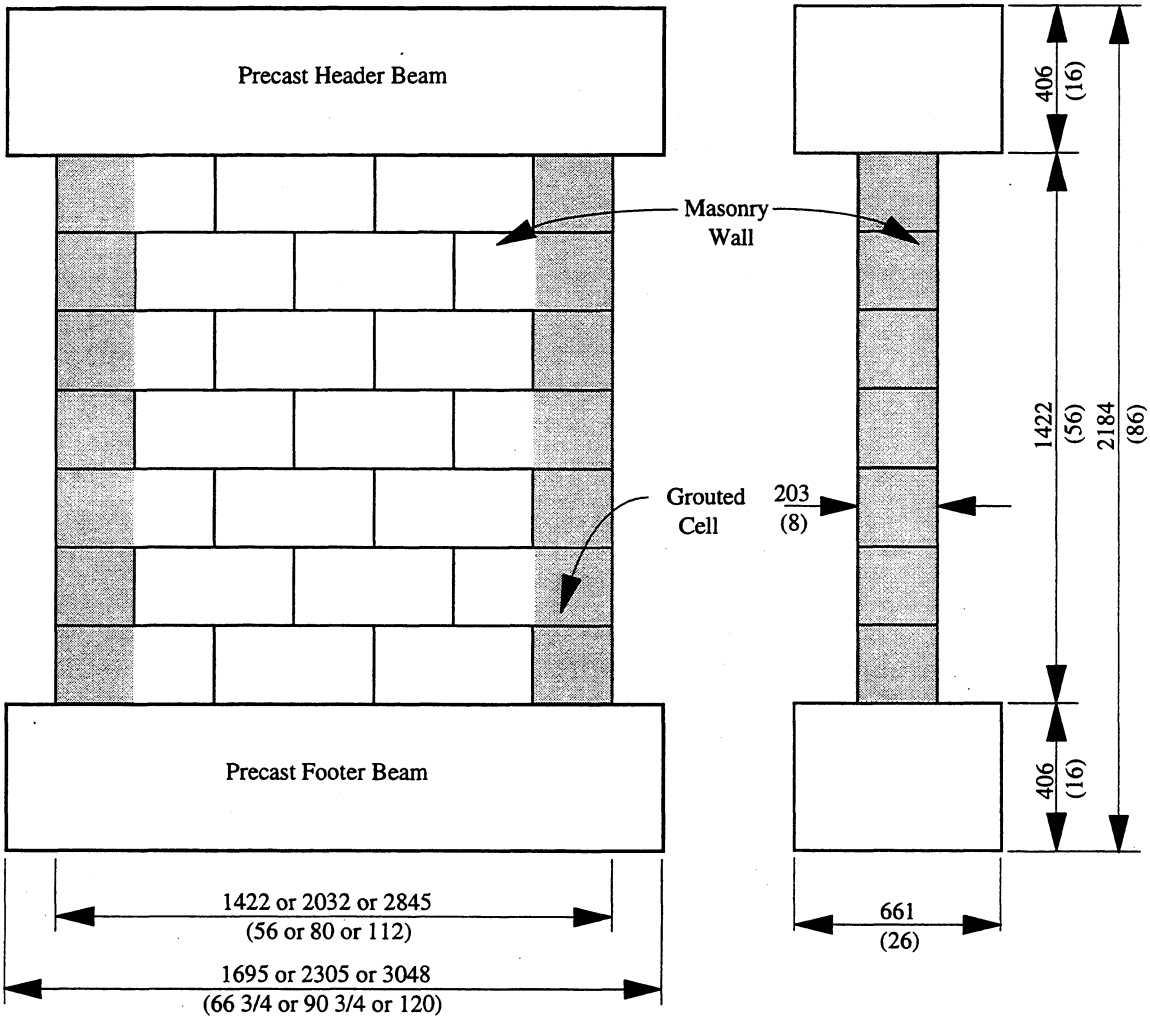

Shaded areas represent grouted, reinforced elements.
Dimensions are in mm (in.).

a) Elevation

b) Side View

Fig. 3.2 Test Specimen Configuration

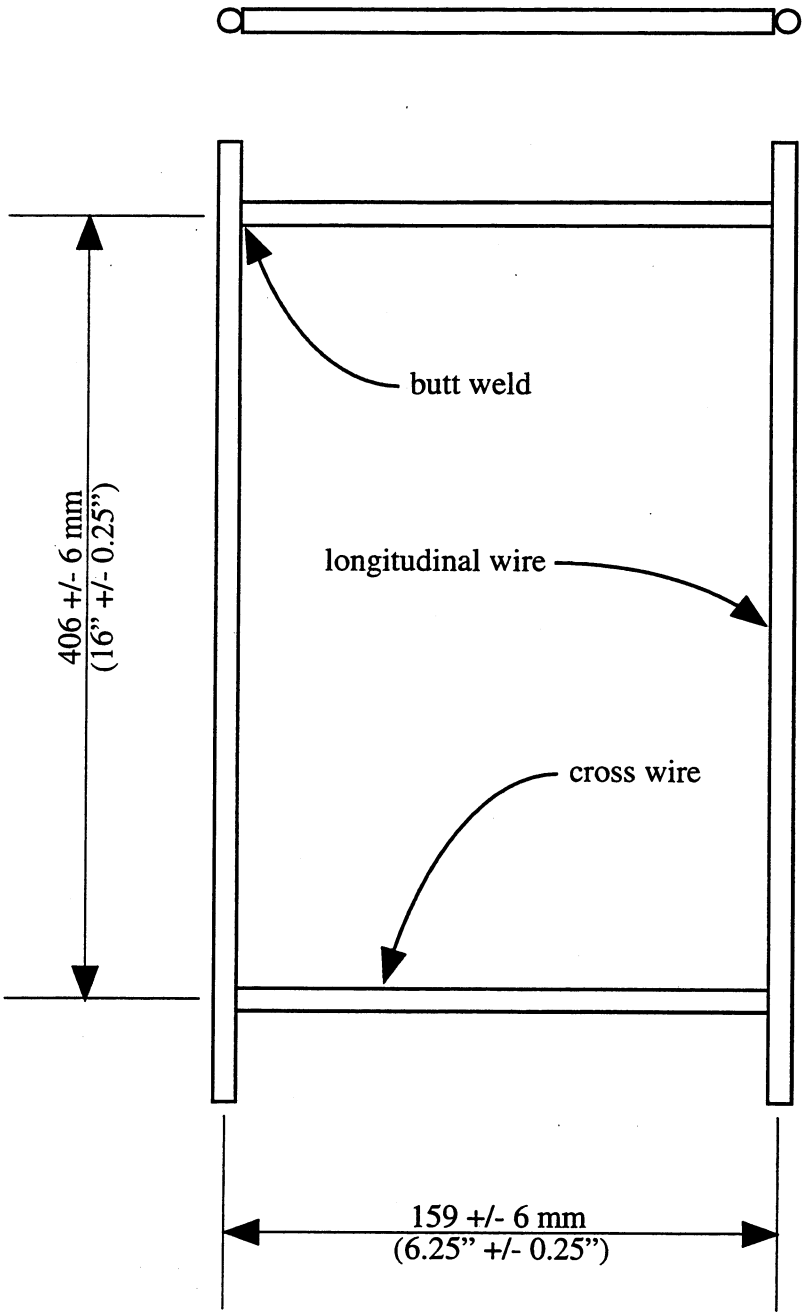

Dimensions are in mm (in.)

Fig. 3.3 Welded Wire Grid Configuration

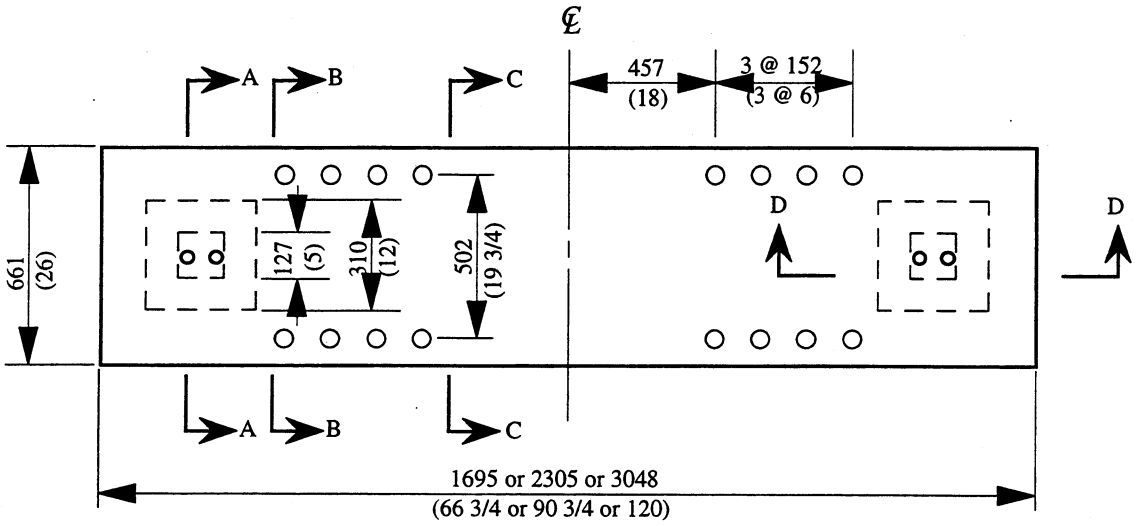

a) Plan

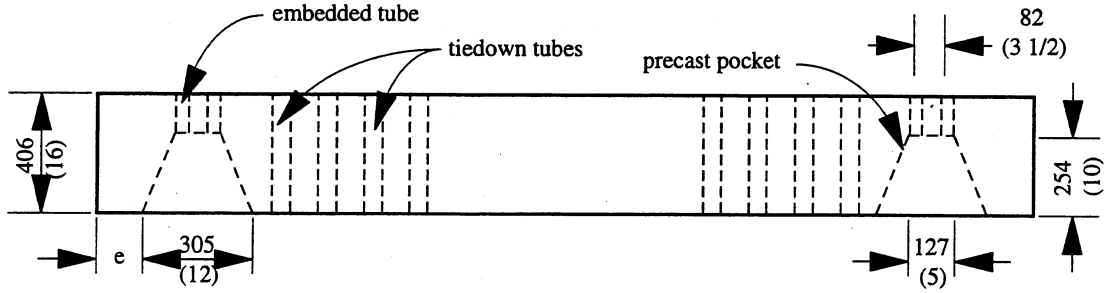

e = 68 (2 11/16) for H/L = 0.5; e = 86 mm (3 3/8) for H/L = 0.7 and 1.0.
Dimensions are in mm (in.)

b) Elevation

Fig. 3.4 Precast Concrete Header/Footer Beams

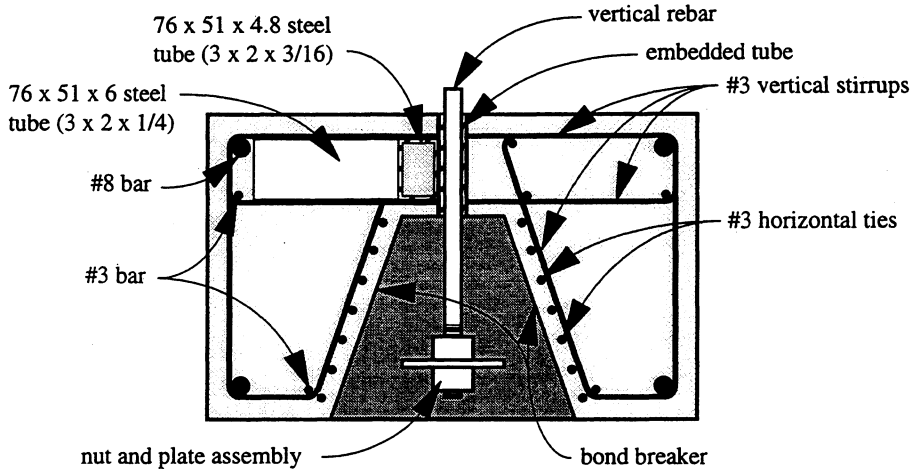

a) Section A-A

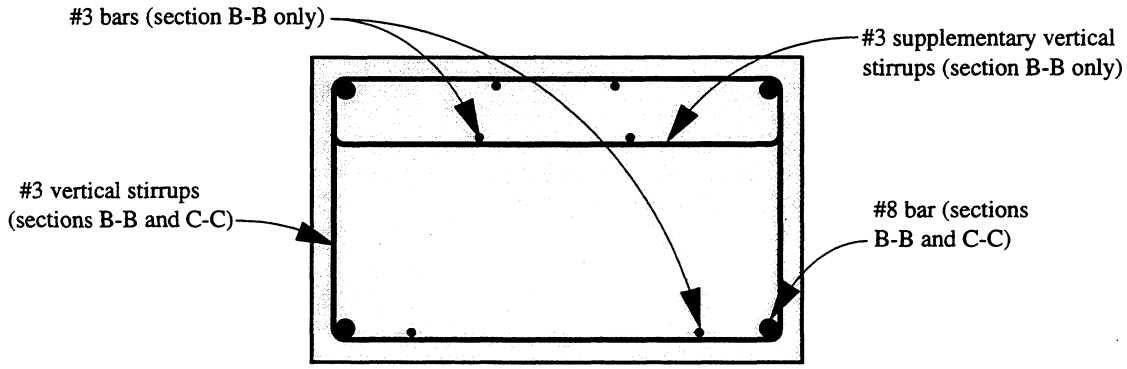

b) Sections B-B and C-C

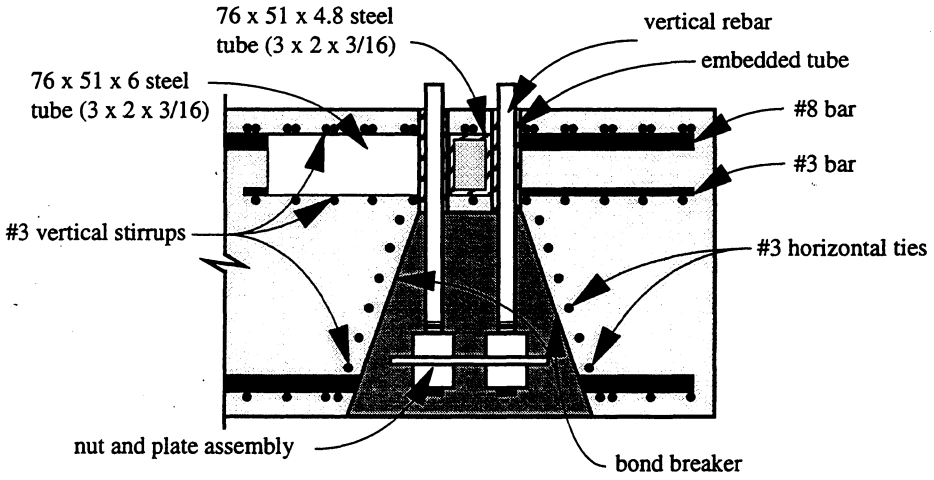

c) Section D-D

Dimensions in mm (in.).

Fig. 3.5 Precast Concrete Header/Footer Beam Sections

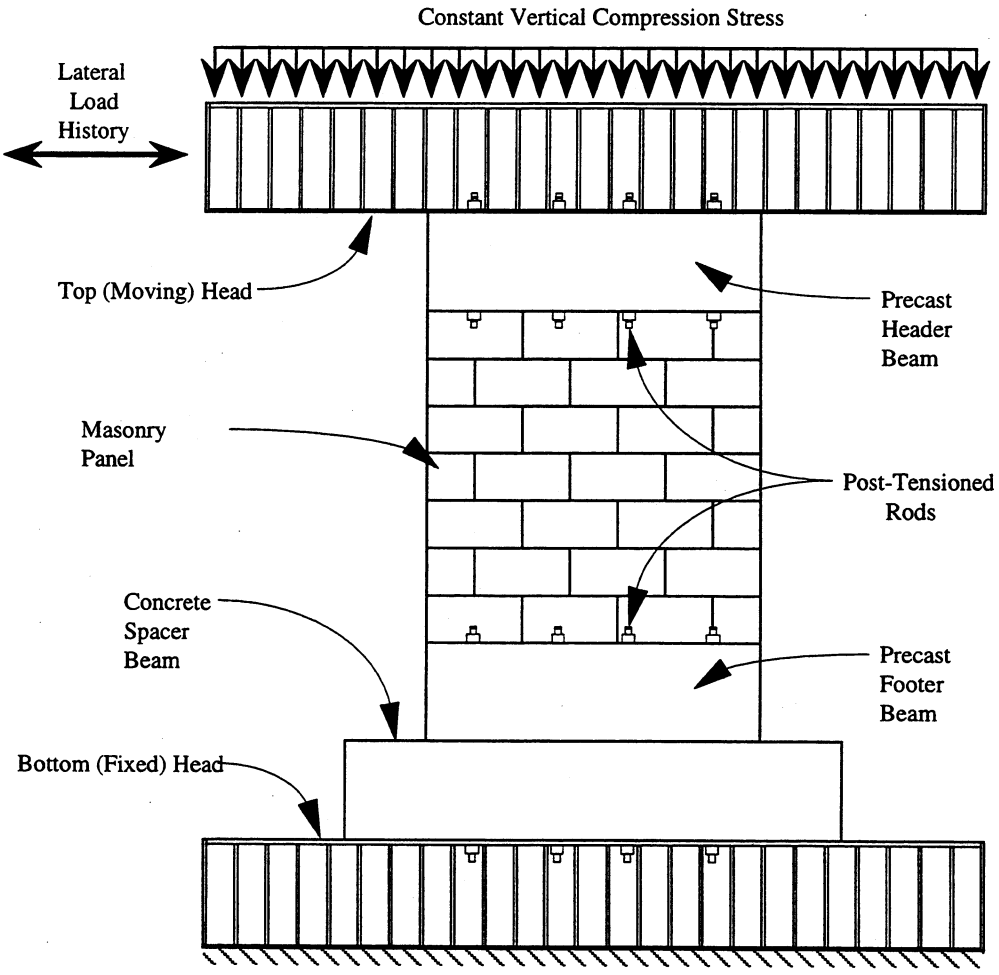

Fig. 4.1 Test Setup

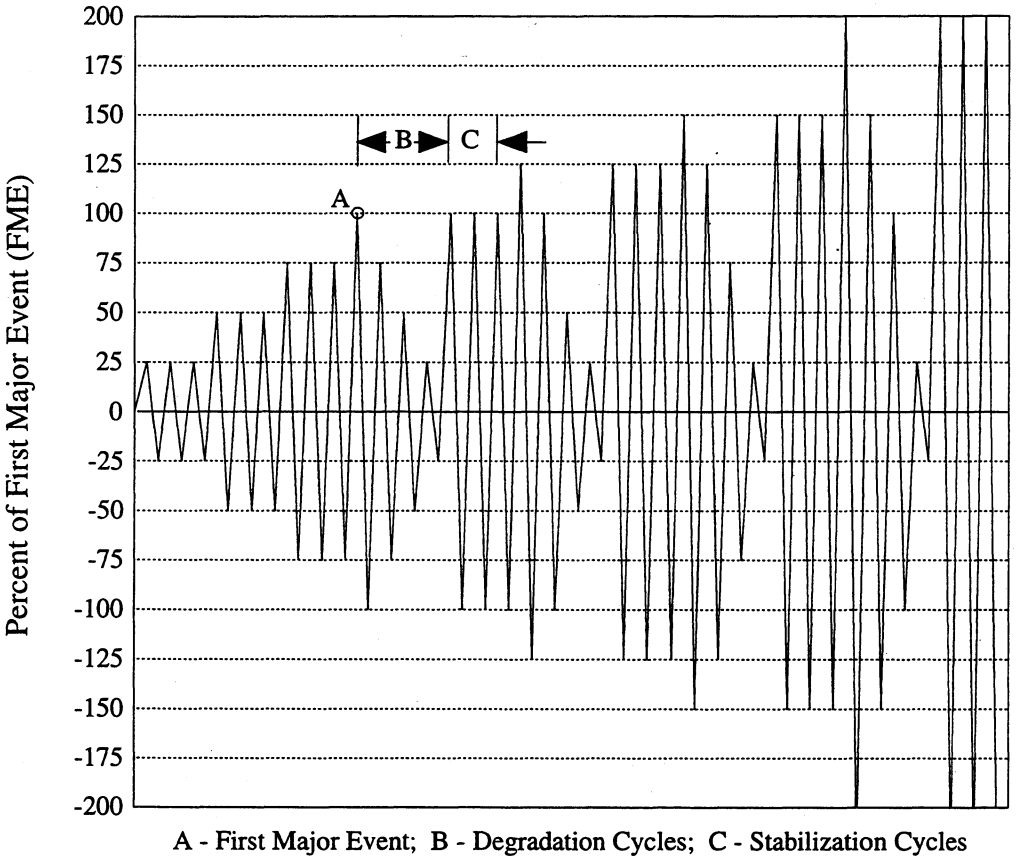

Fig. 4.2 In-Plane Displacement History

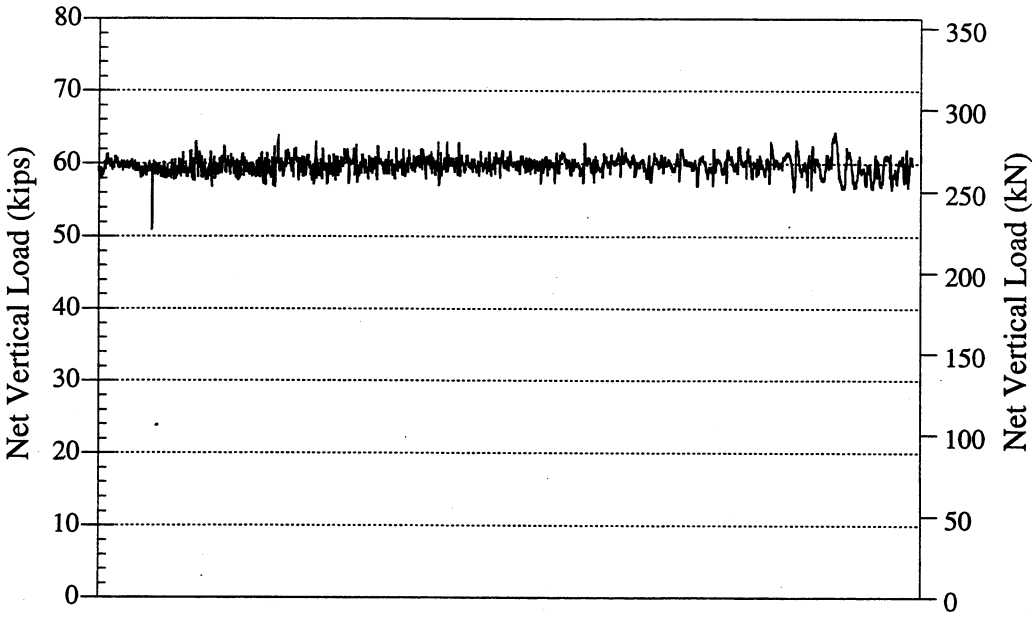

Fig. 4.3 Vertical Load Variation for Shear Wall No. 8

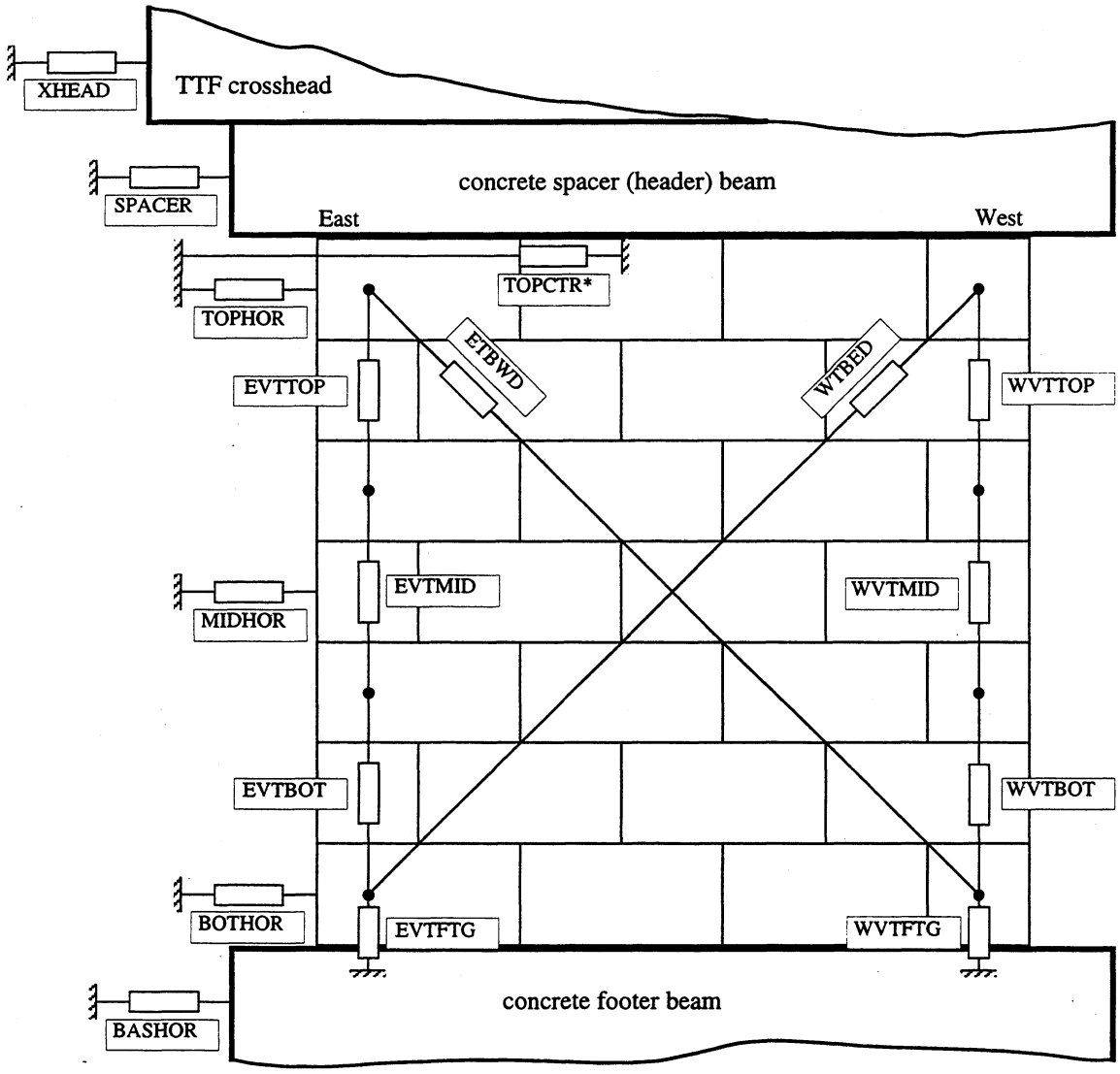

*On Wall Specimens 10 and12

Fig. 4.4 Location and Designation of LVDT Transducers

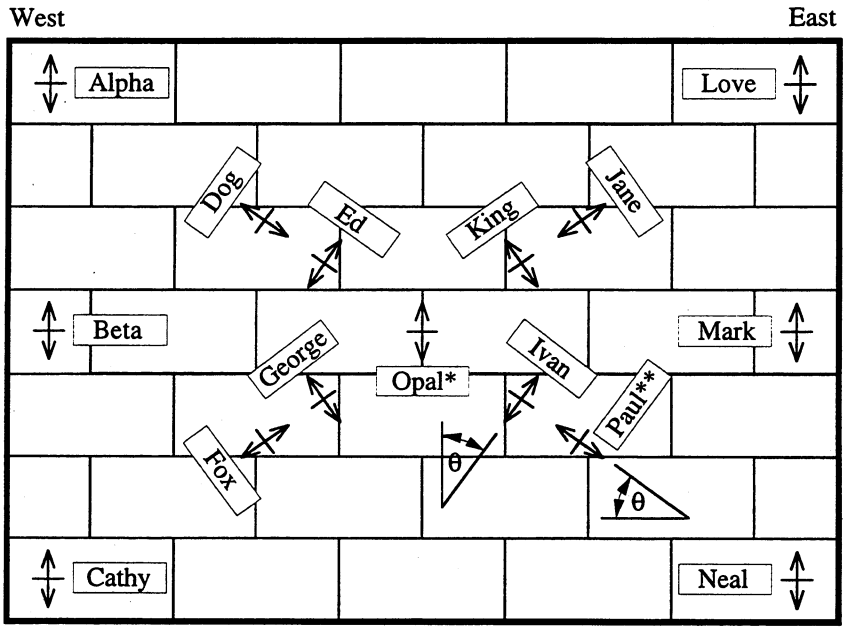

Fig. 4.5 Location and Designation of LST Transducers

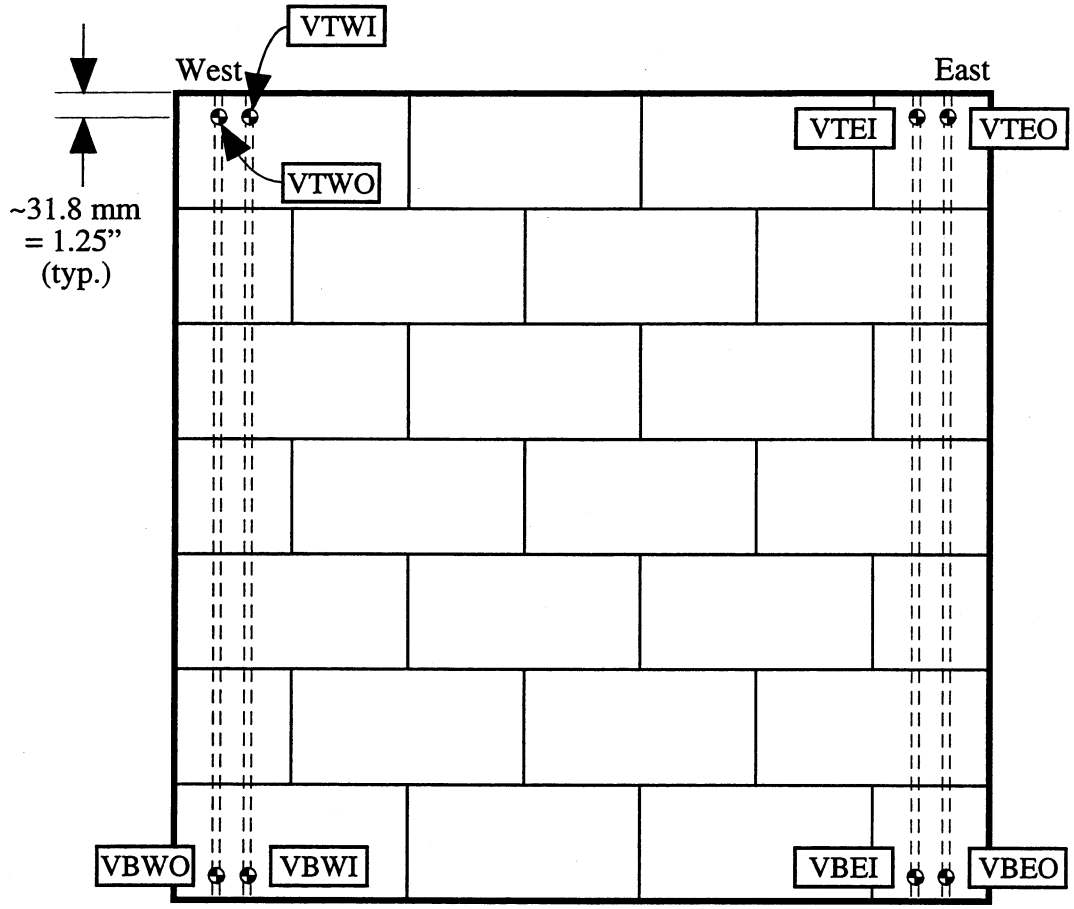

Fig. 4.6 Location and Designation of Strain Gages on Vertical Reinforcement

a) Walls 2 and 8

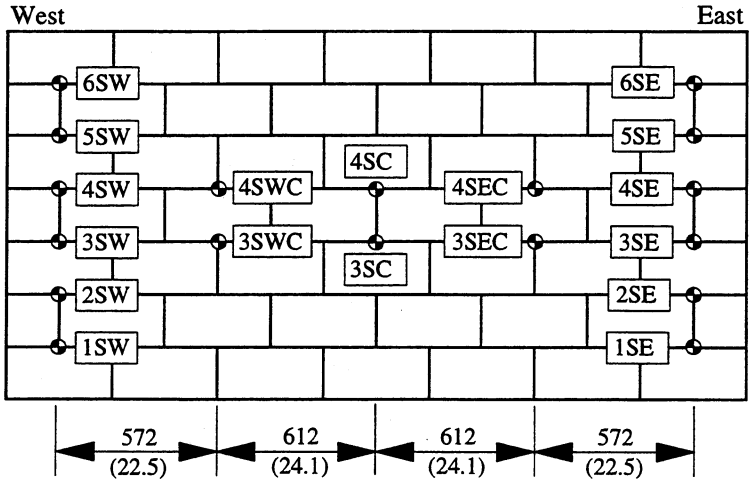

b) Walls 4 and 10

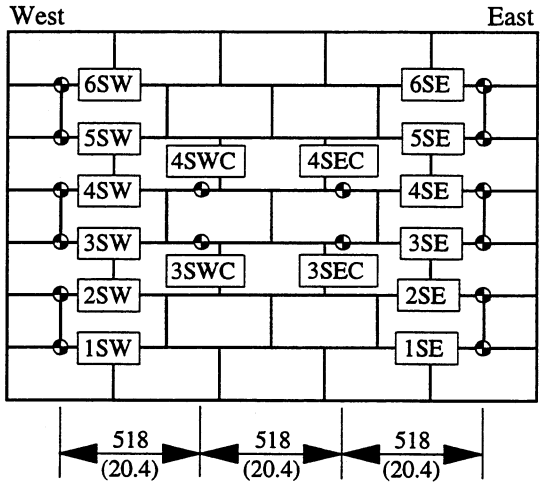

c) Walls 6 and 12

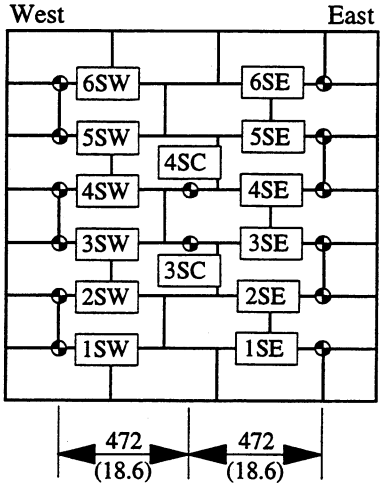

Dimensions in mm (in.)

Fig. 4.7 Location and Designation of Strain Gages on Horizontal Reinforcement

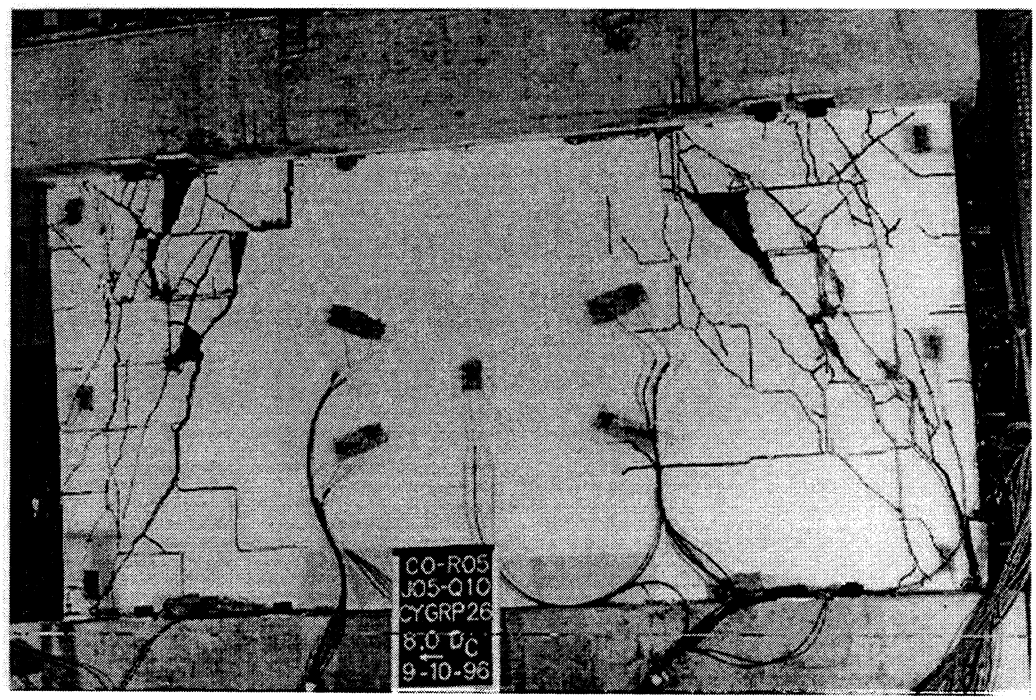

Fig. 5.1 Photograph of Wall Specimen 2 at End of Test

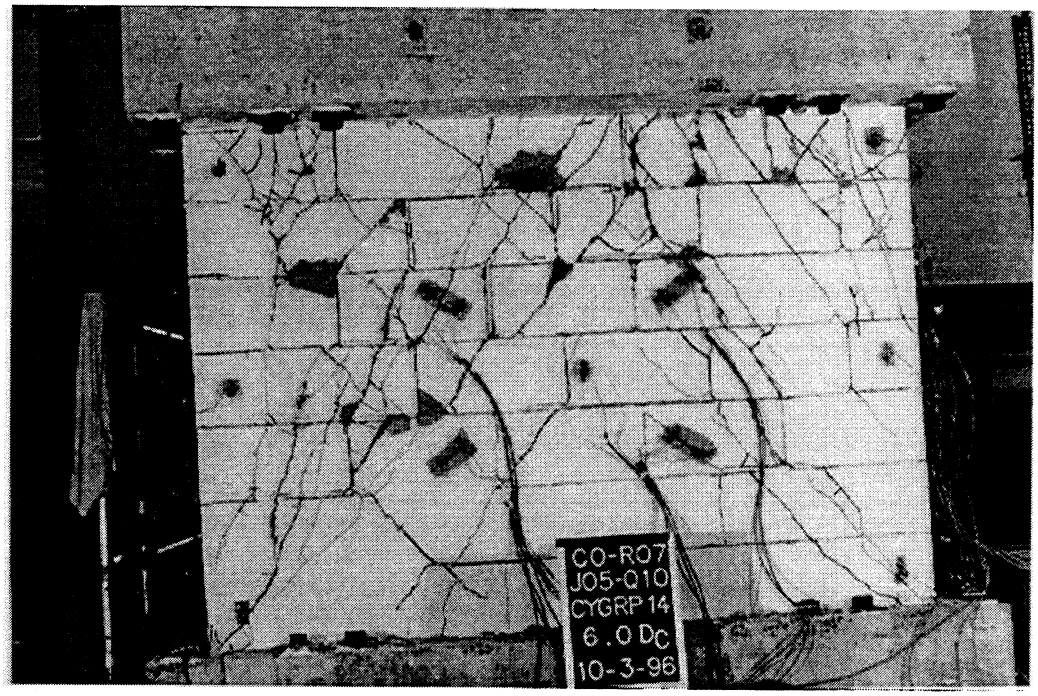

Fig. 5.2 Photograph of Wall Specimen 4 at End of Test

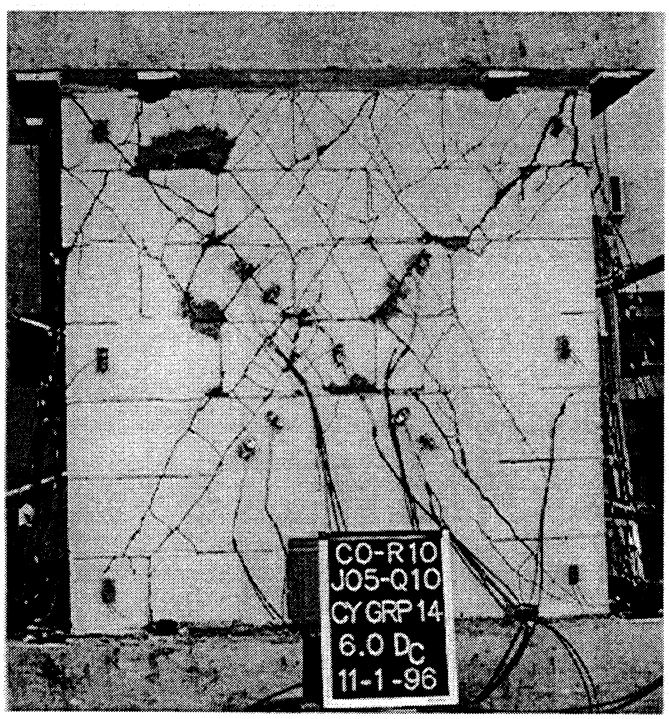

Fig. 5.3 Photograph of Wall Specimen 6 at End of Test

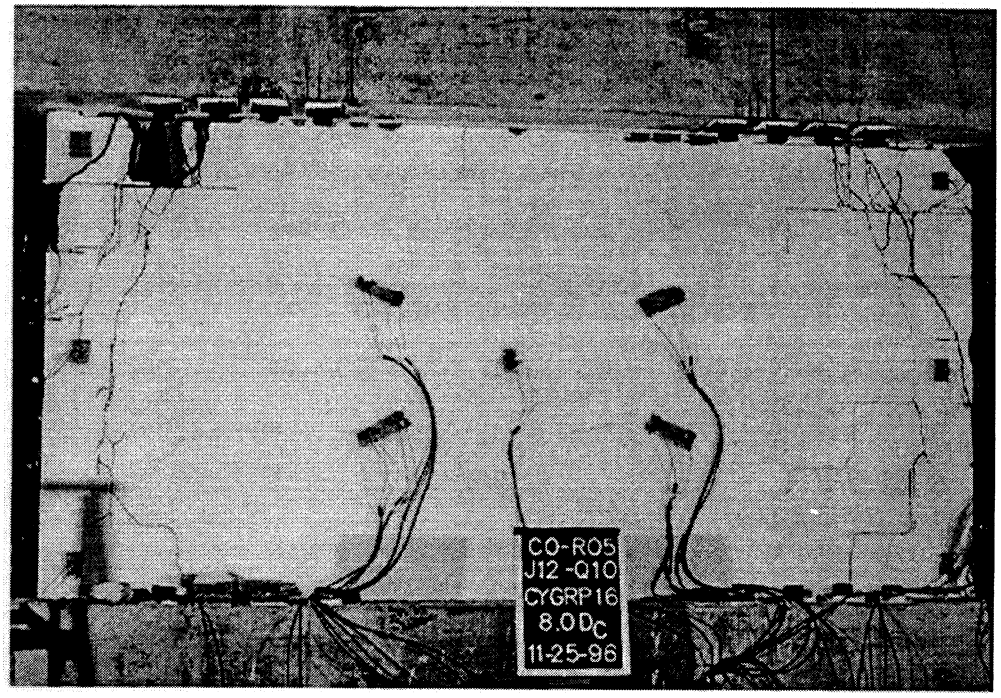

Fig. 5.4 Photograph of Wall Specimen 8 at End of Test

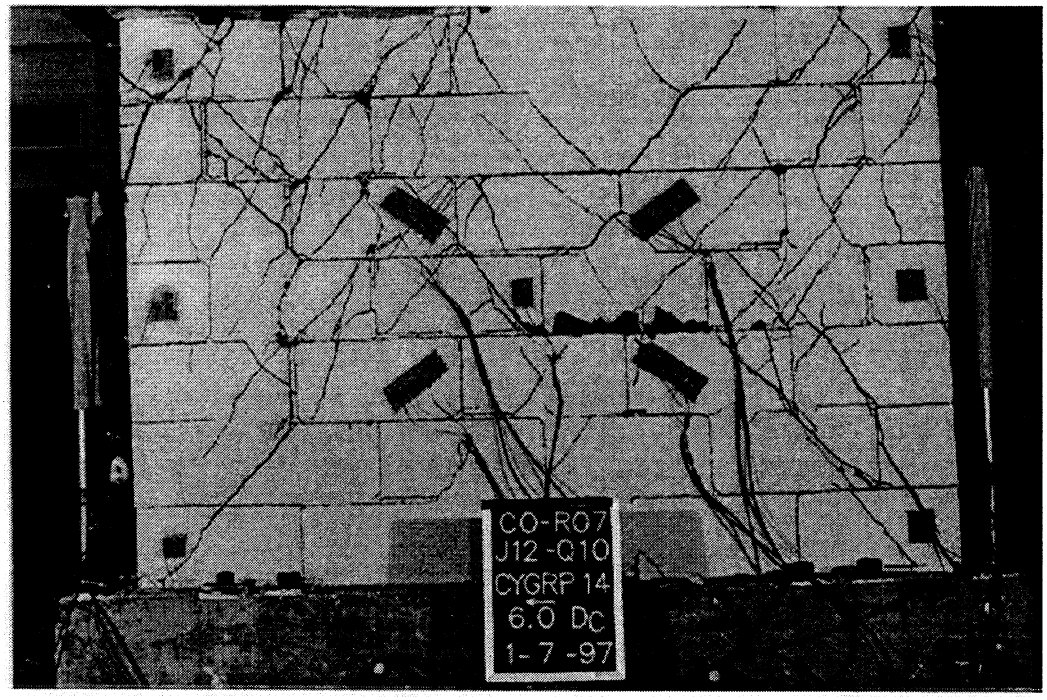

Fig. 5.5 Photograph of Wall Specimen 10 at End of Test

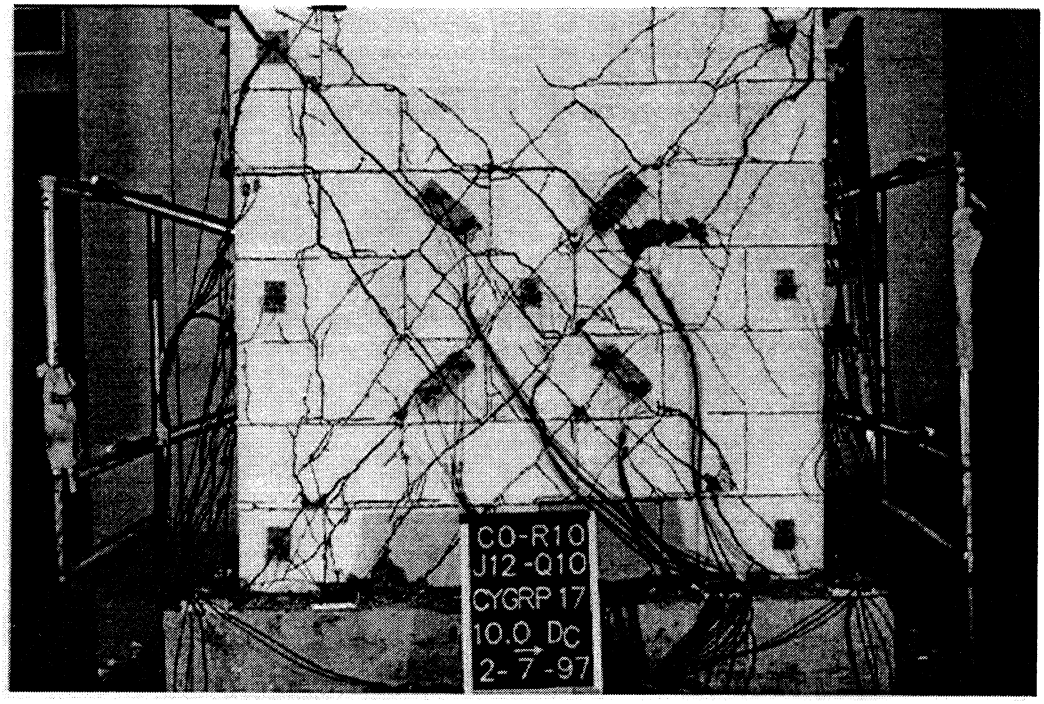

Fig. 5.6 Photograph of Wall Specimen 12 at End of Test

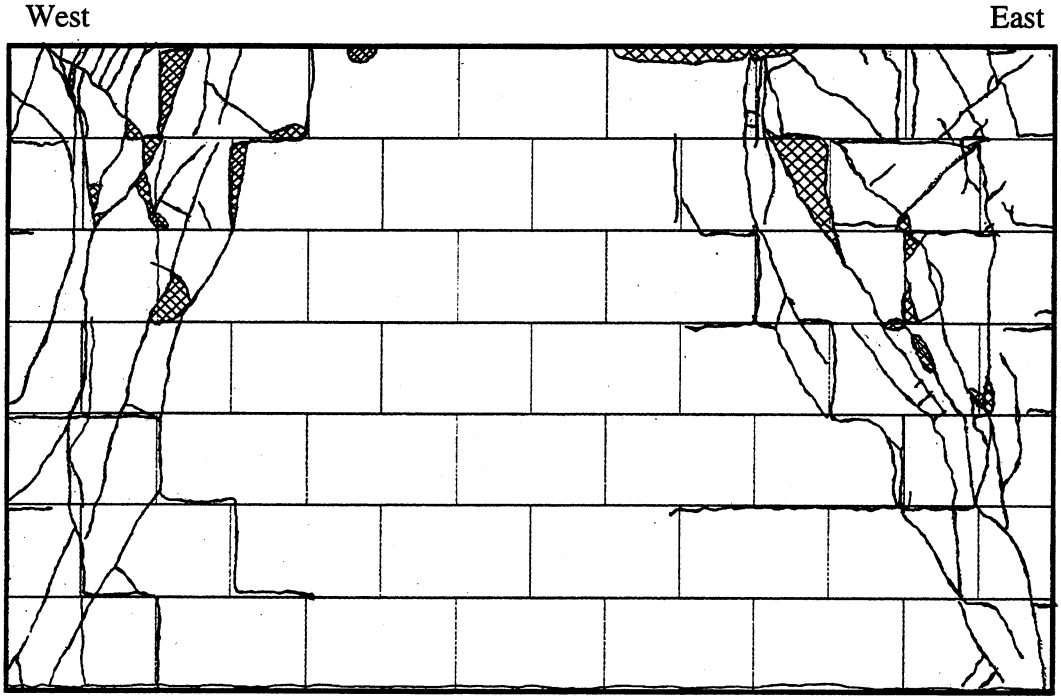

Fig. 5.7 Final Crack Pattern for South Face of Wall Specimen 2

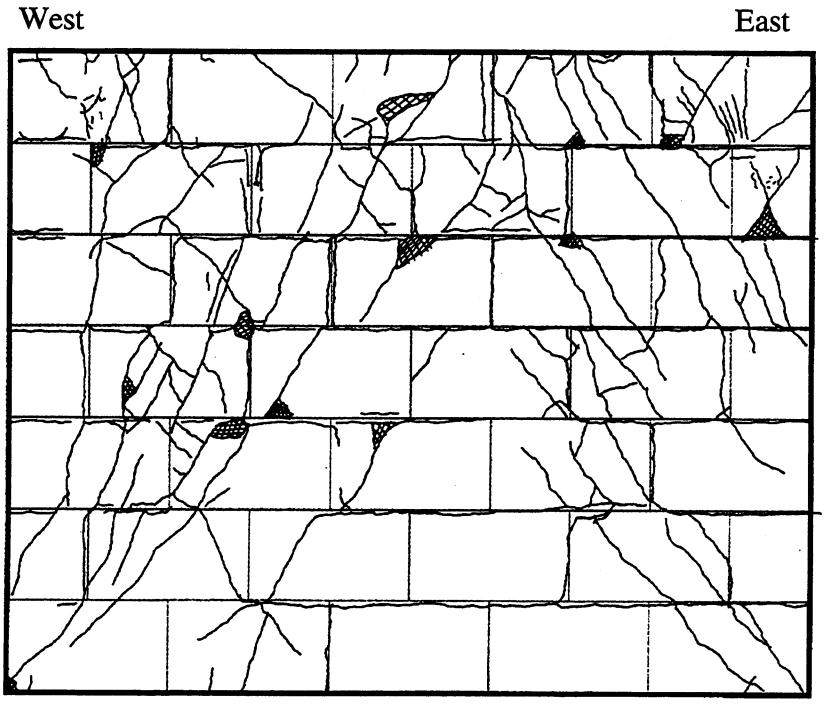

Fig. 5.8 Final Crack Pattern for South Face of Wall Specimen 4

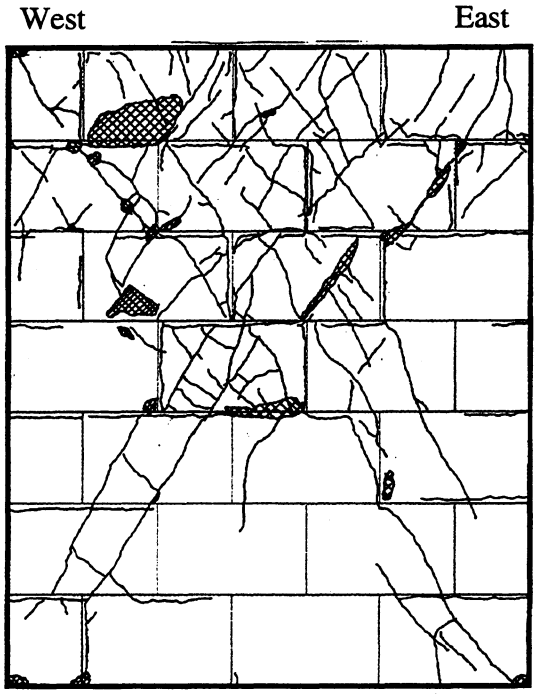

Fig. 5.9 Final Crack Pattern for South Face of Wall Specimen 6

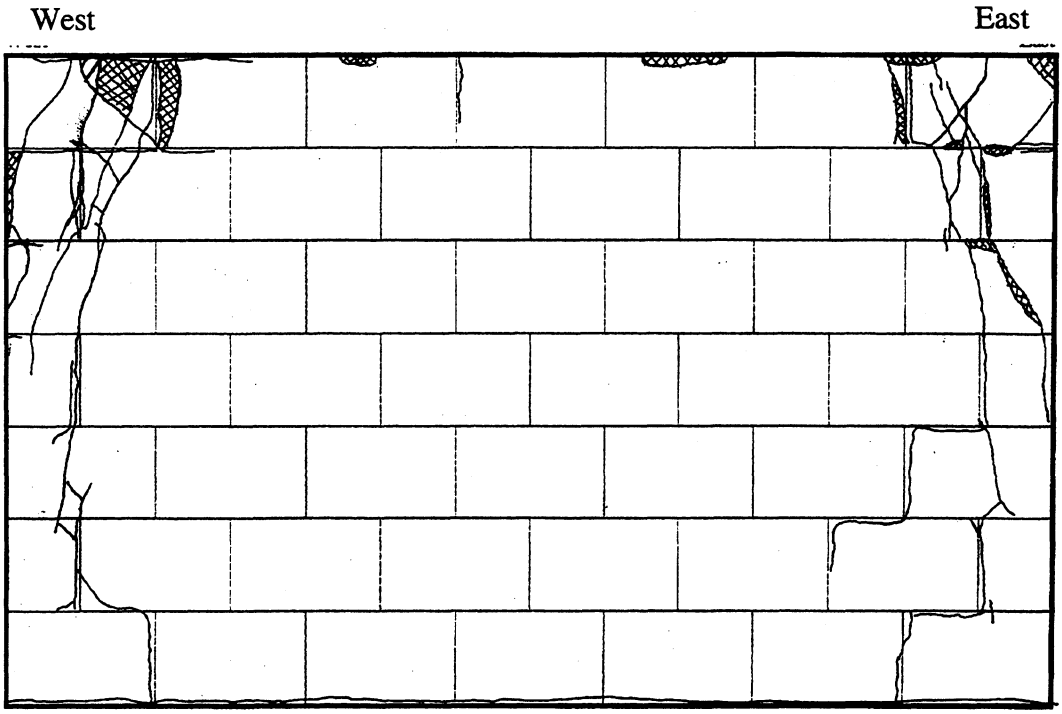

Fig. 5.10 Final Crack Pattern for South Face of Wall Specimen 8

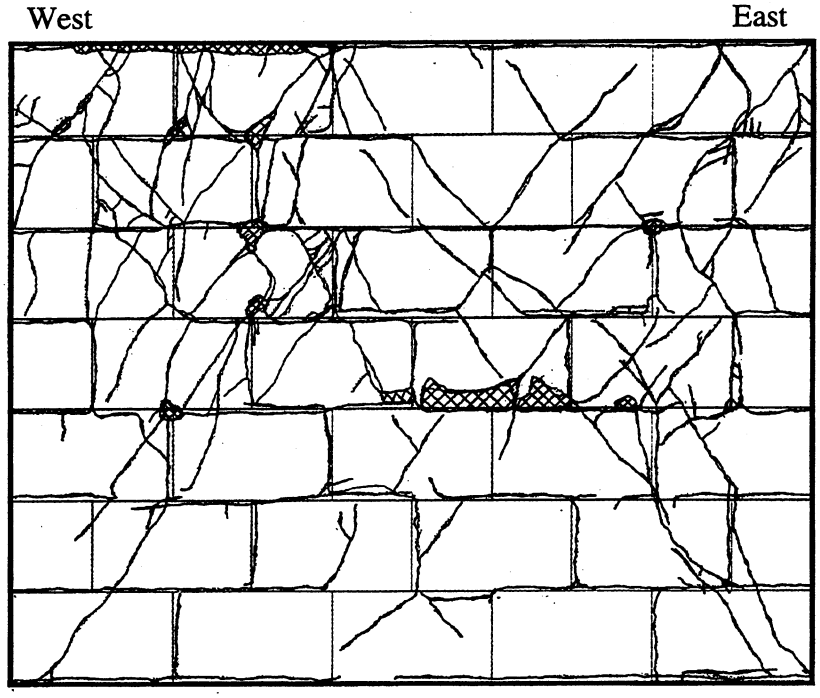

Fig. 5.11 Final Crack Pattern for South Face of Wall Specimen 10

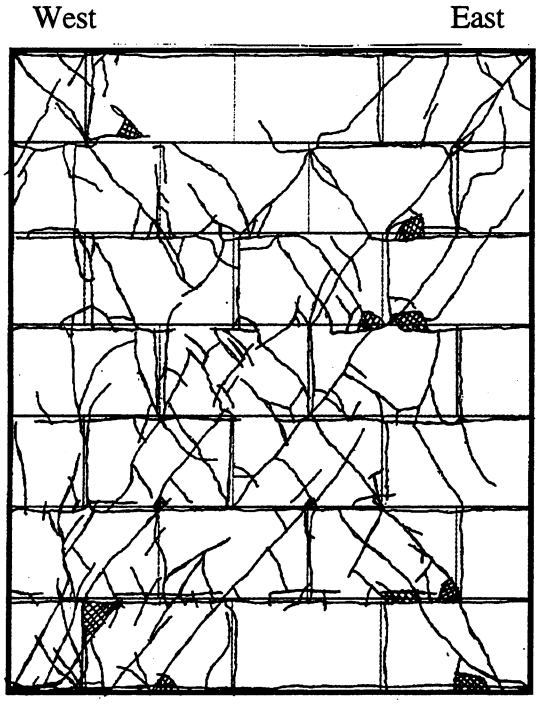

Fig. 5.12 Final Crack Pattern for South Face of Wall Specimen 12

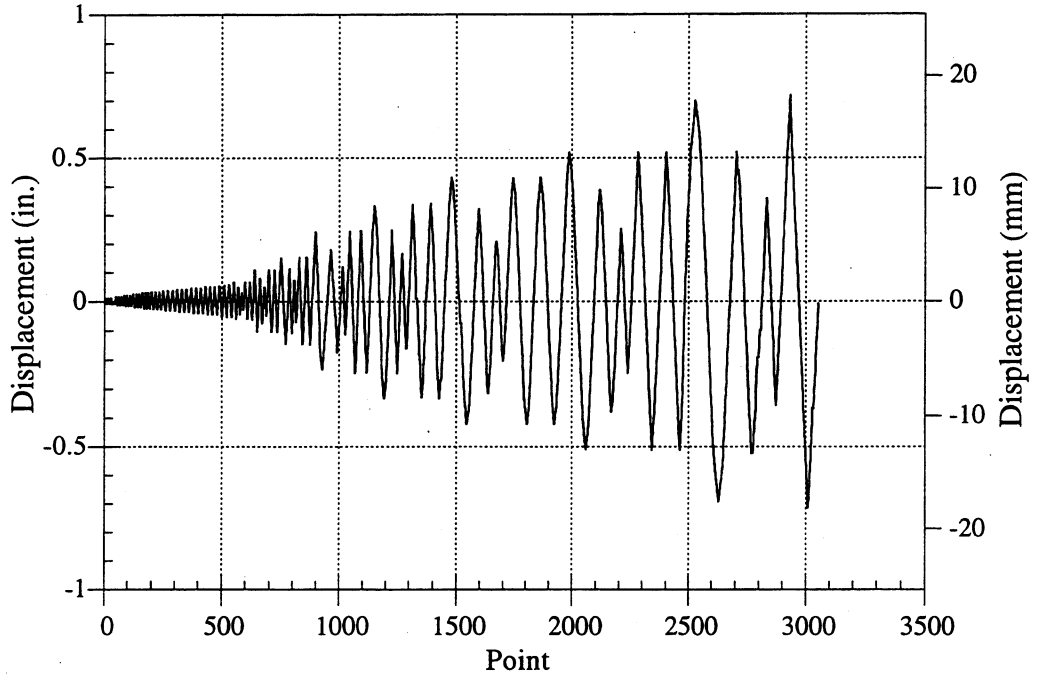

Fig. 6.1.1 In-Plane Lateral Displacement History for Wall Specimen 2

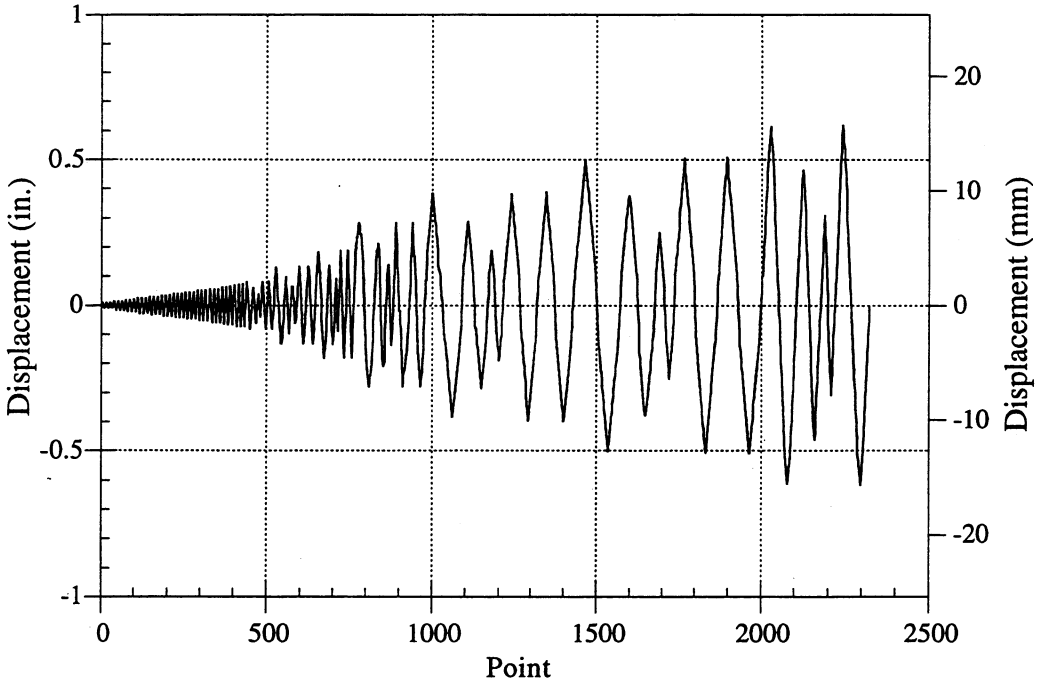

Fig. 6.1.2 In-Plane Lateral Displacement History for Wall Specimen 4

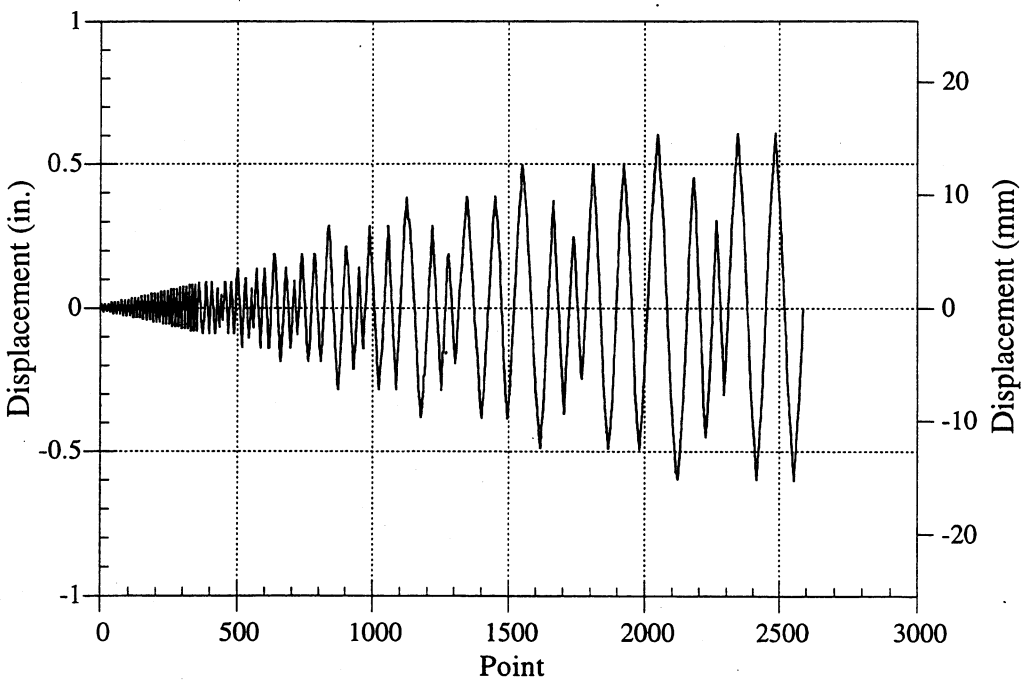

Fig. 6.1.3 In-Plane Lateral Displacement History for Wall Specimen 6

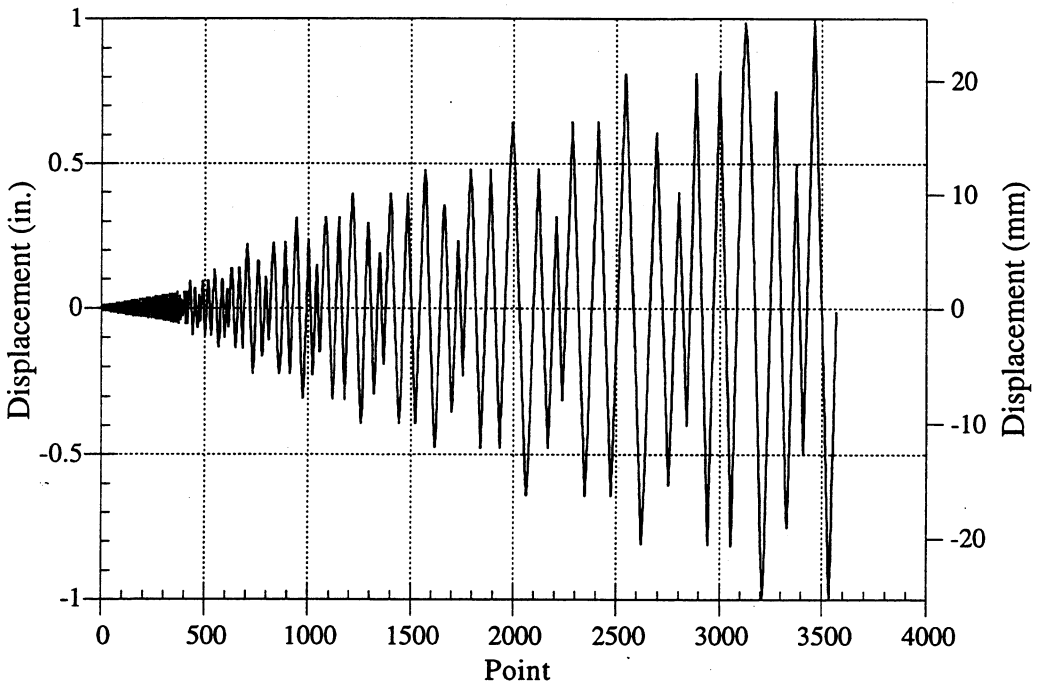

Fig. 6.1.4 In-Plane Lateral Displacement History for Wall Specimen 8

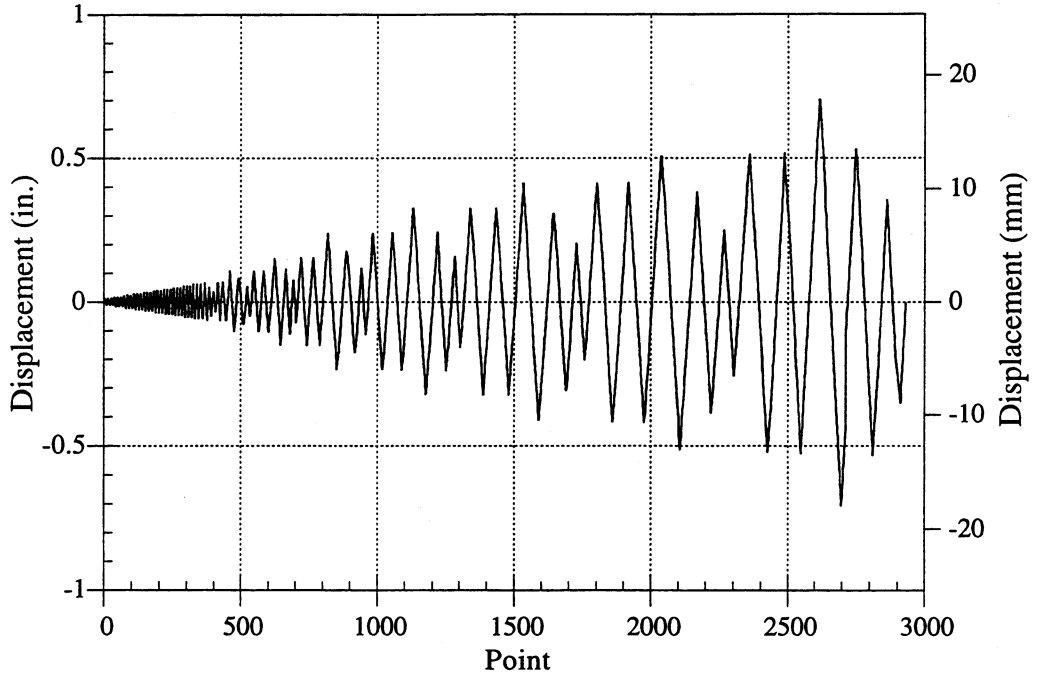

Fig. 6.1.5 In-Plane Lateral Displacement History for Wall Specimen 10

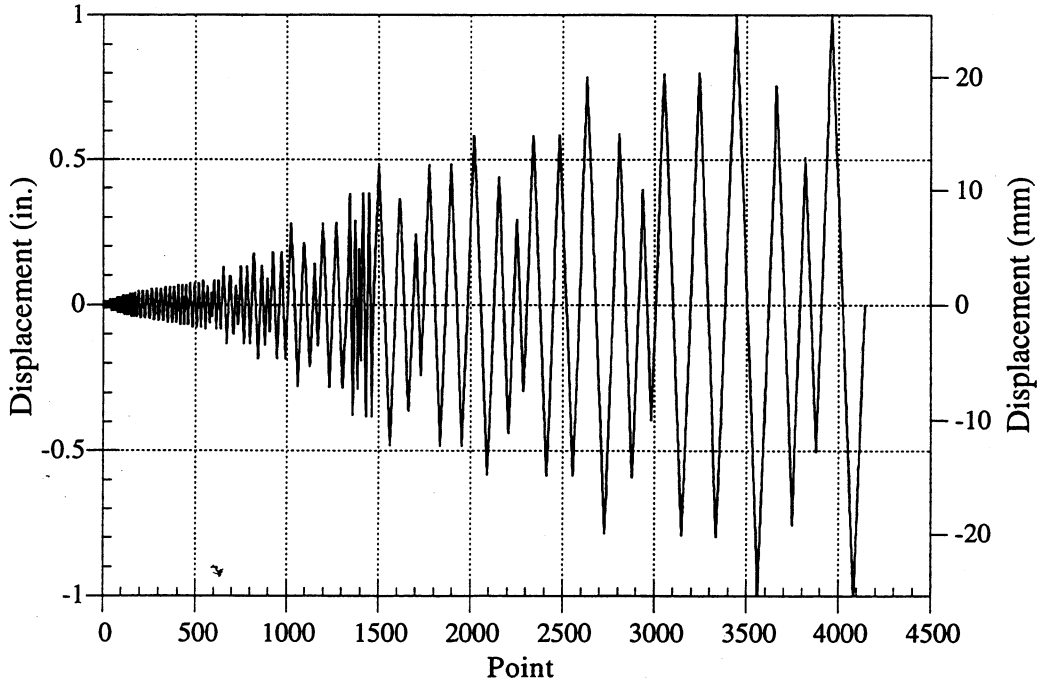

Fig. 6.1.6 In-Plane Lateral Displacement History for Wall Specimen 12

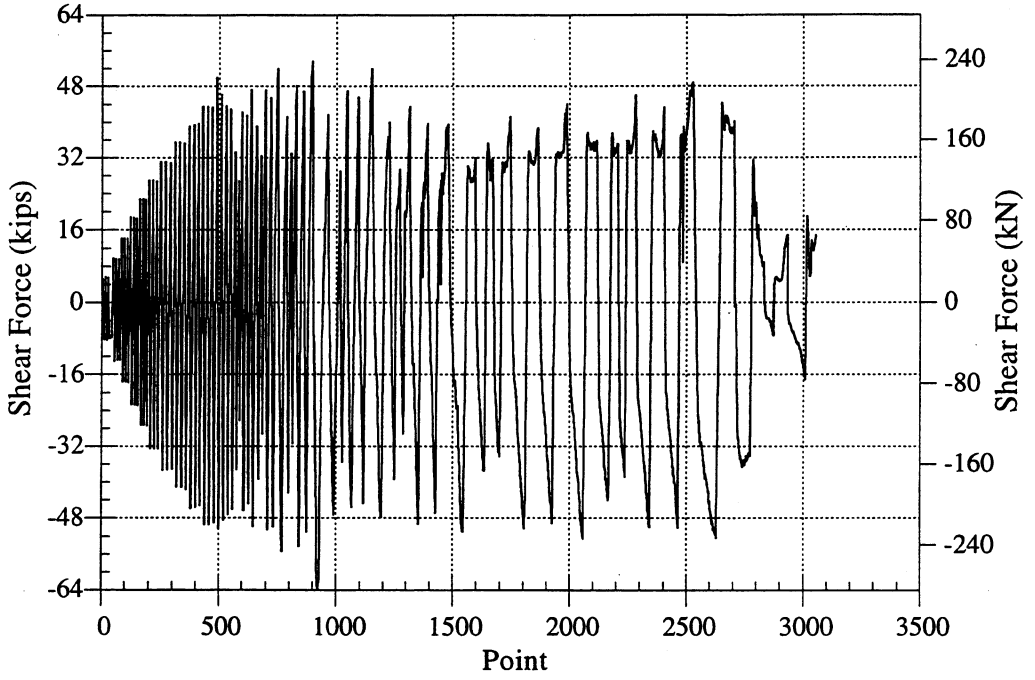

Fig. 6.2.1 Shear Force History for Wall Specimen 2

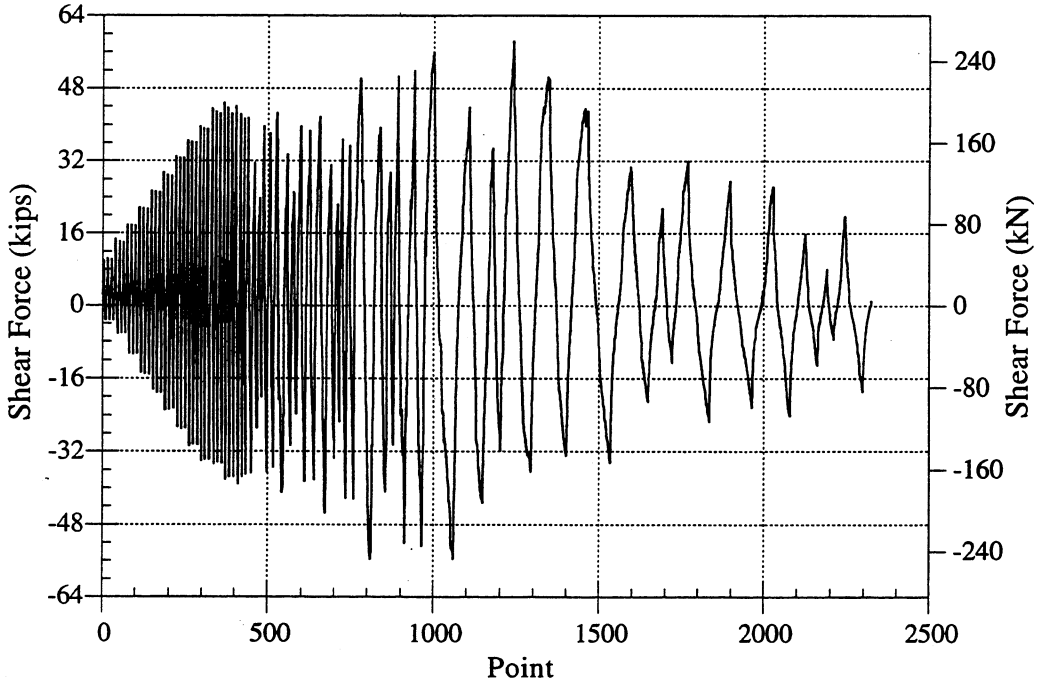

Fig. 6.2.2 Shear Force History for Wall Specimen 4

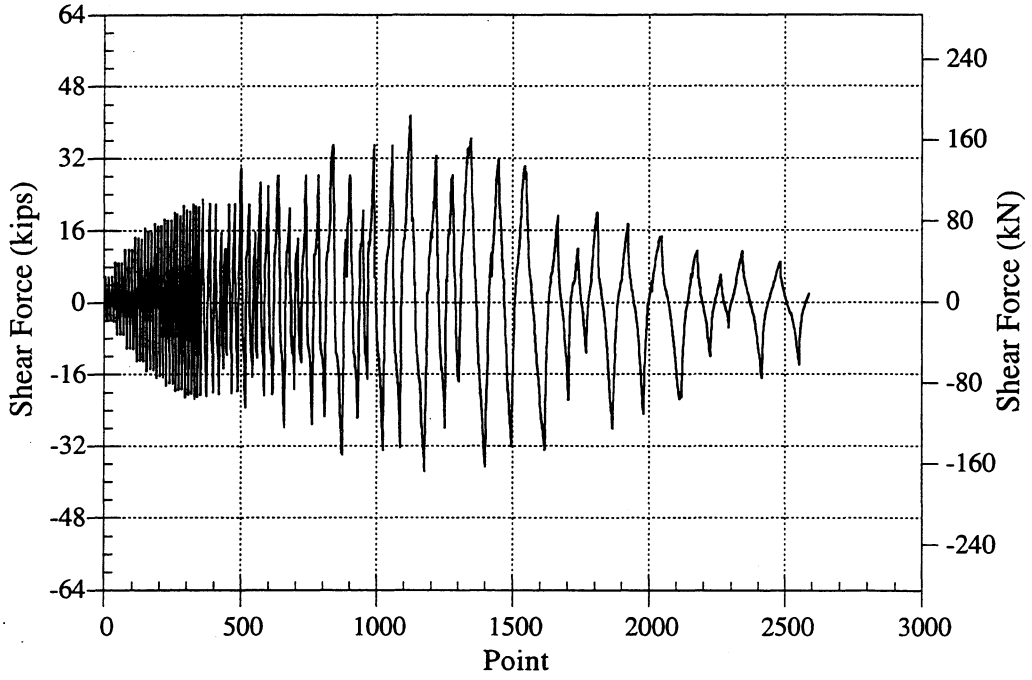

Fig. 6.2.3 Shear Force History for Wall Specimen 6

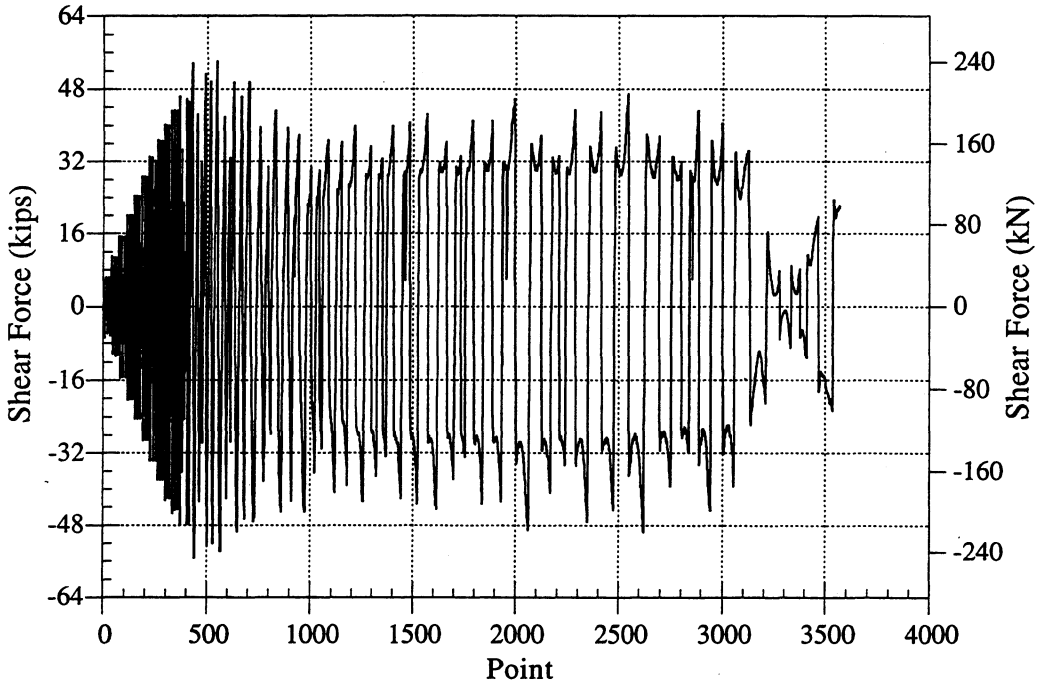

Fig. 6.2.4 Shear Force History for Wall Specimen 8

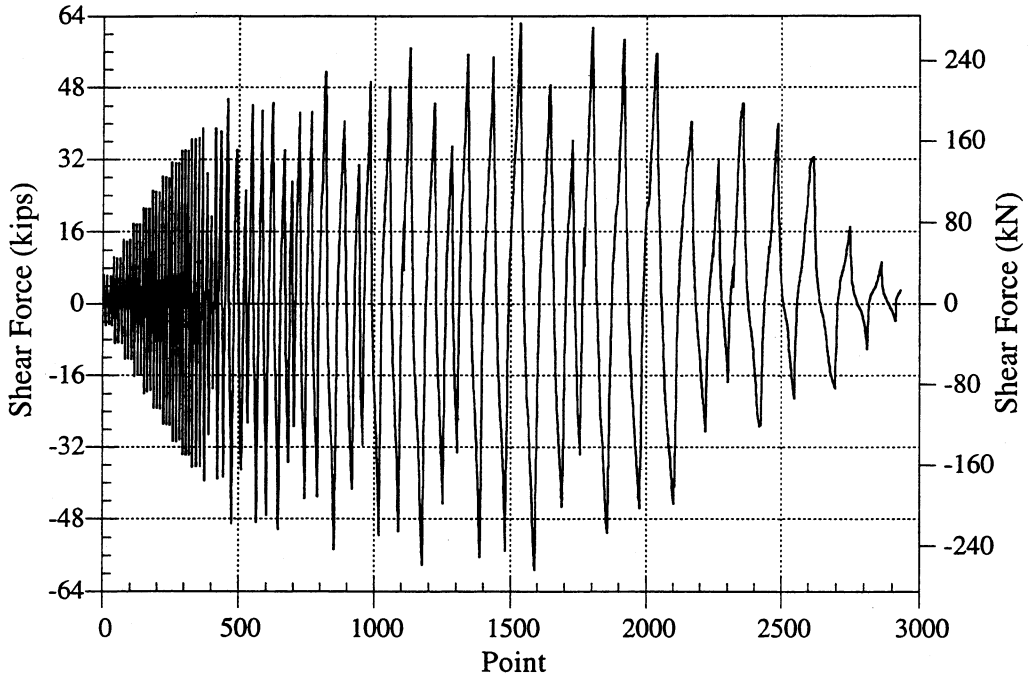

Fig. 6.2.5 Shear Force History for Wall Specimen 10

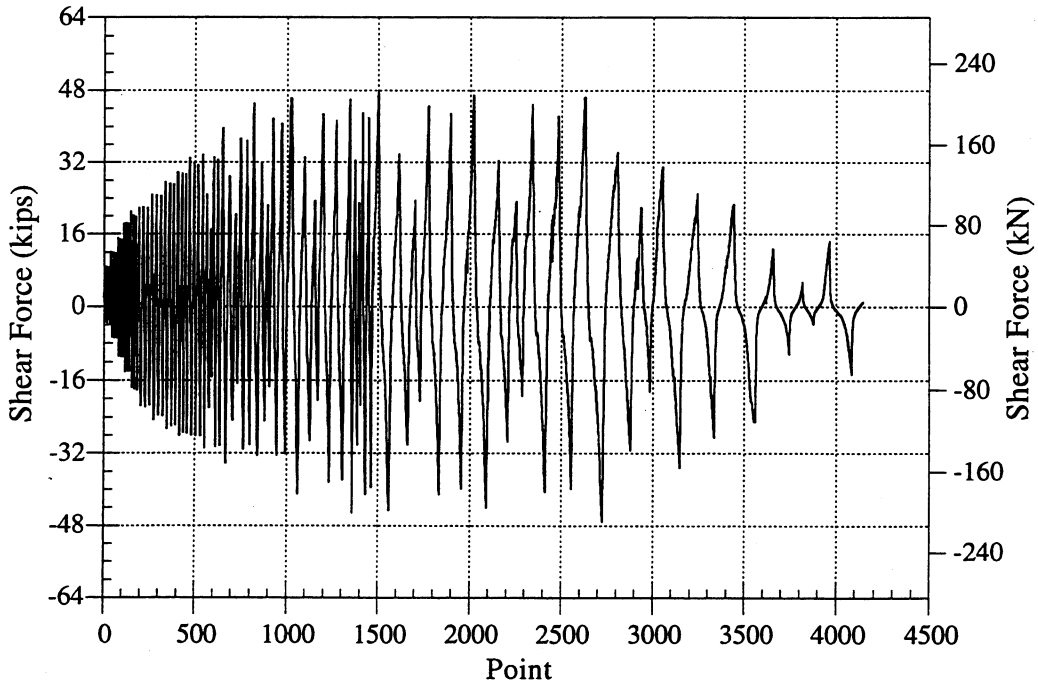

Fig. 6.2.6 Shear Force History for Wall Specimen 12

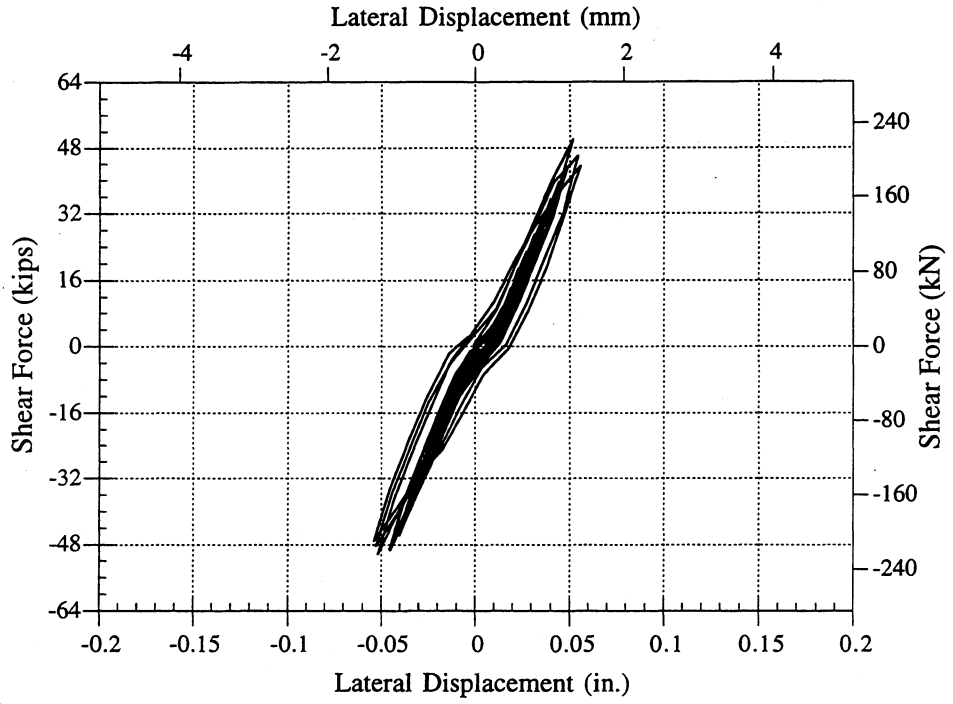

a) Elastic Cycles (Points 1-546)

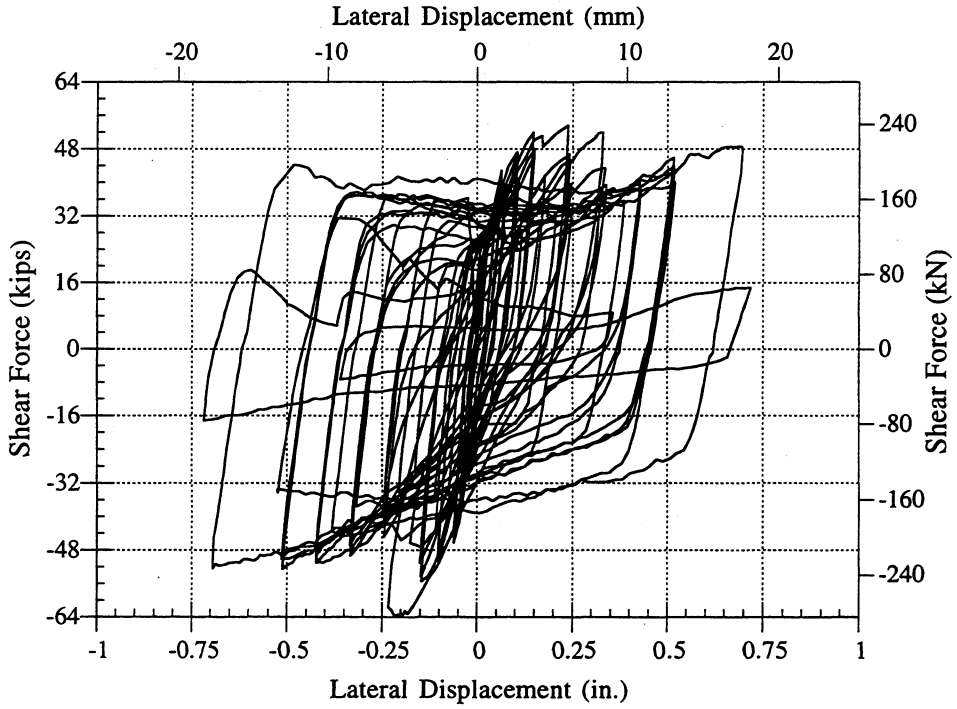

b) Inelastic Cycles (Points 546-3054)

Fig. 6.2.7 Force-Displacement Relations for Wall Specimen 2

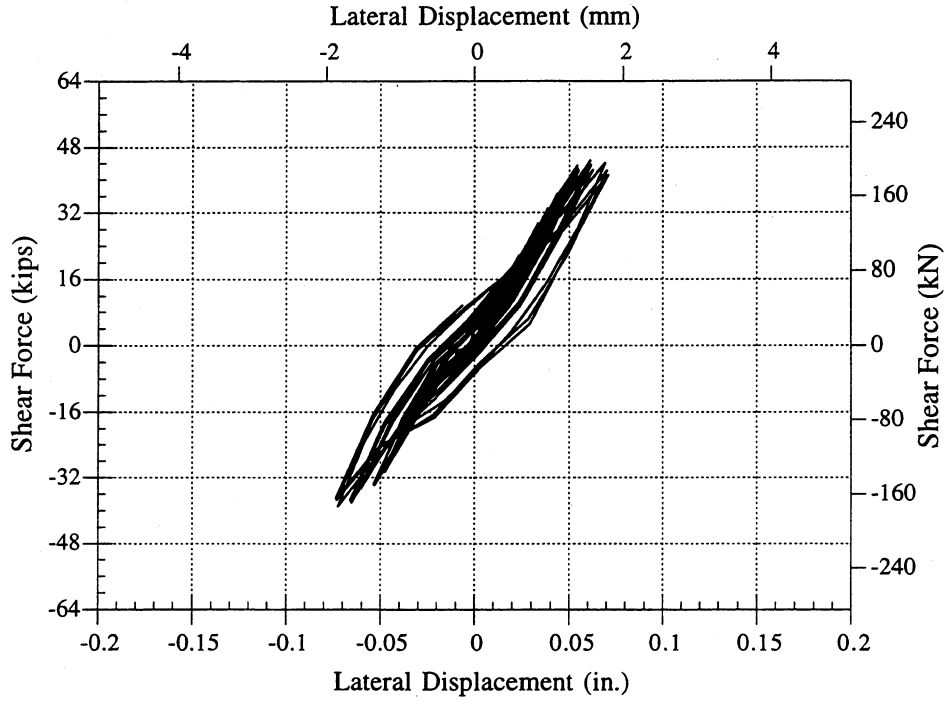

a) Elastic Cycles (Points 1-437)

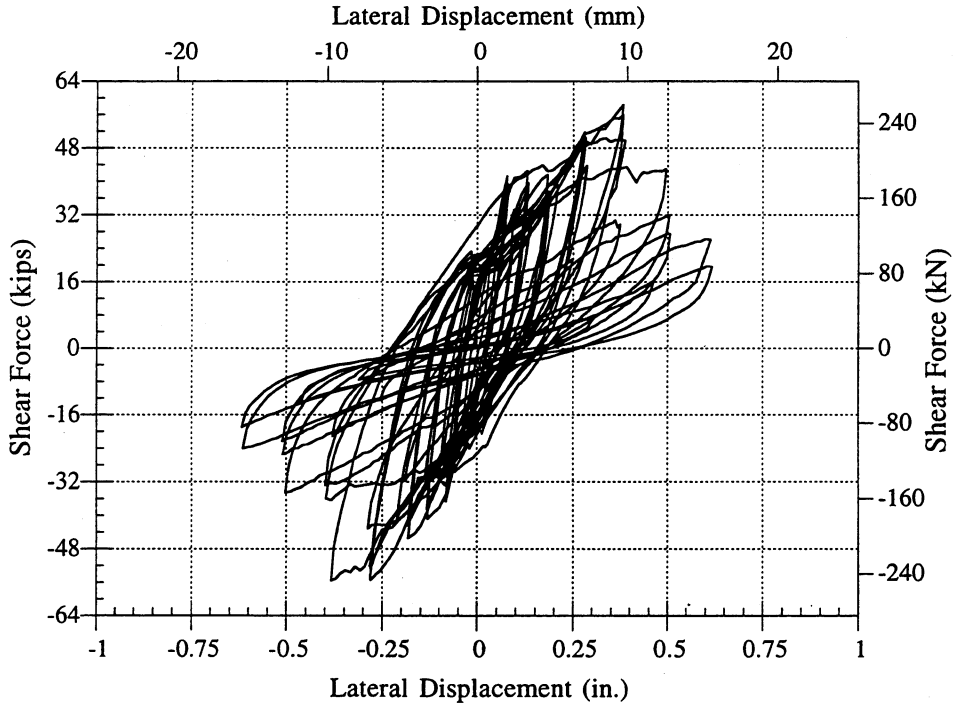

b) Inelastic Cycles (Points 437-2325)

Fig. 6.2.8 Force-Displacement Relations for Wall Specimen 4

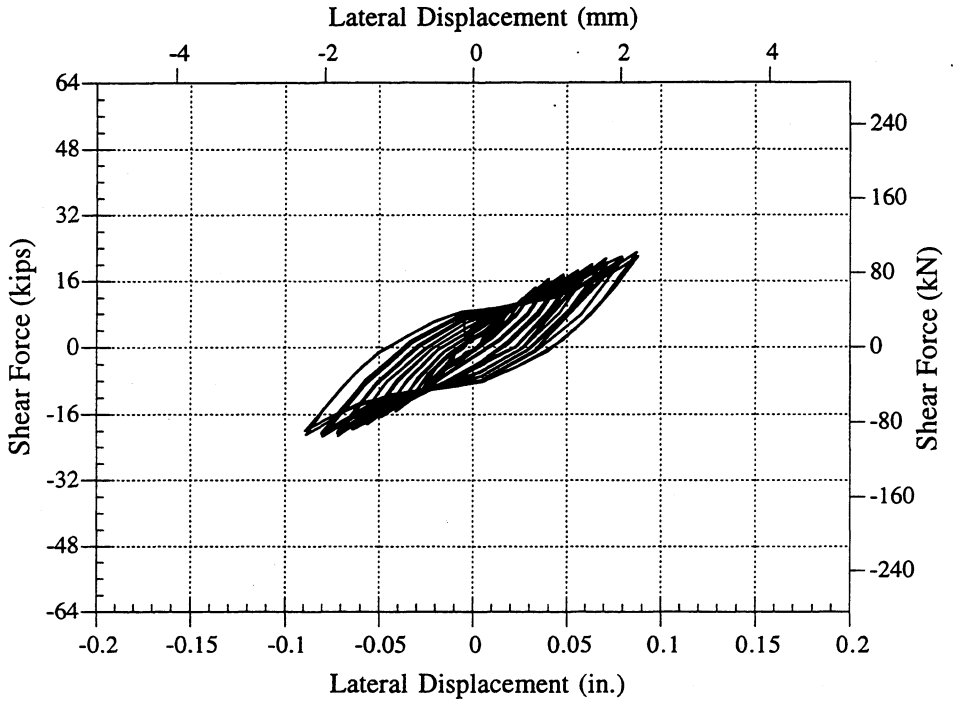

a) Elastic Cycles (Points 1-403)

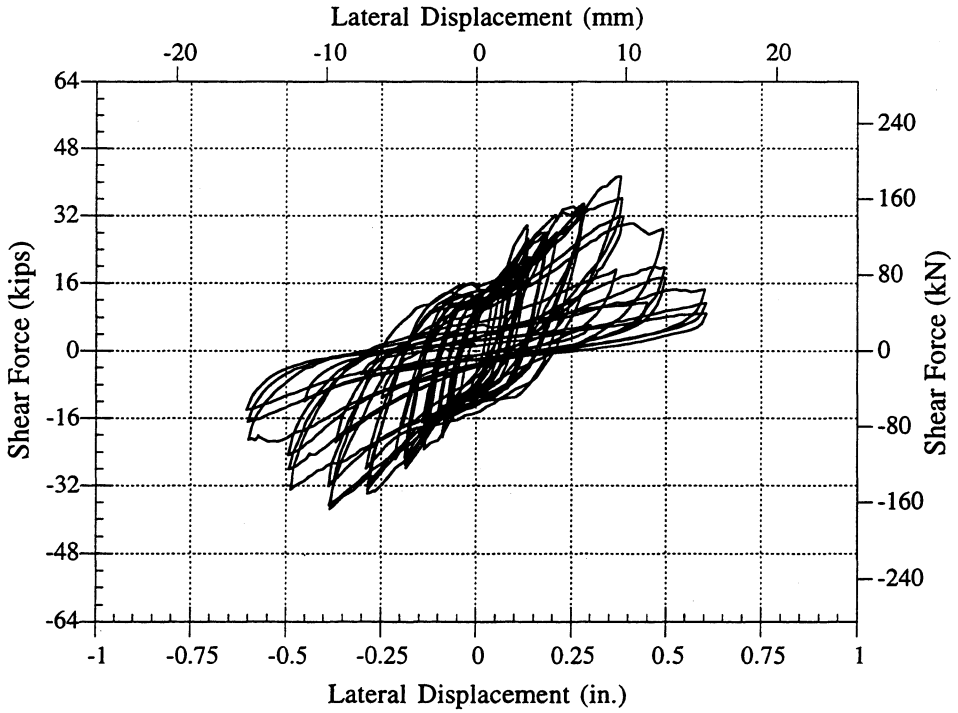

b) Inelastic Cycles (Points 403-2589)

Fig. 6.2.9 Force-Displacement Relations for Wall Specimen 6

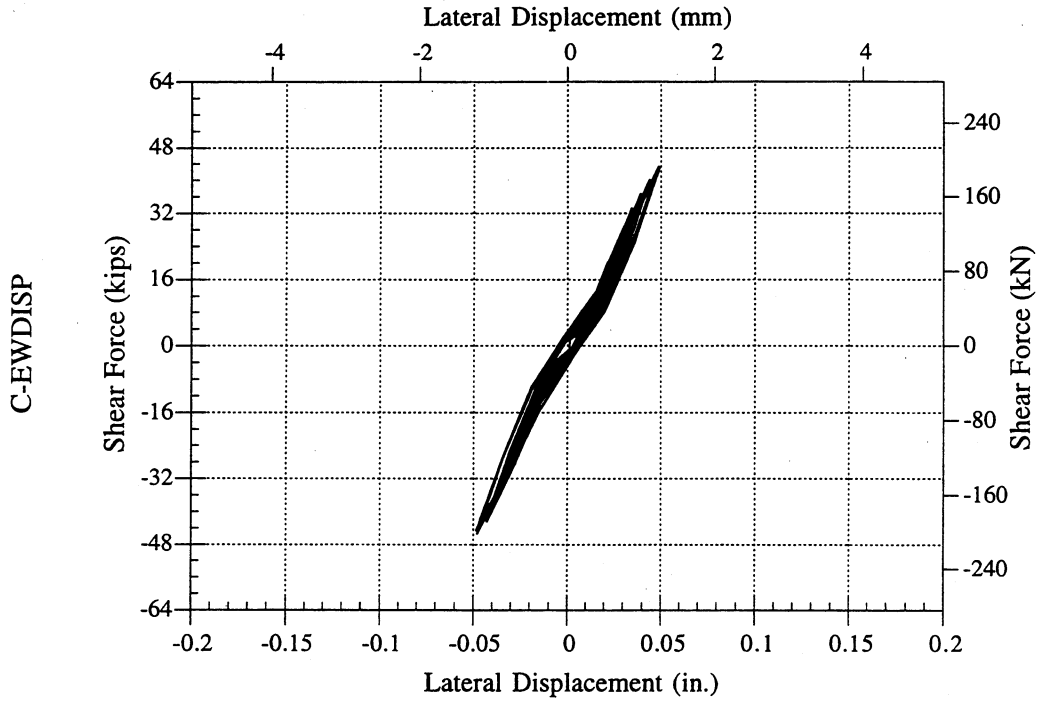

a) Elastic Cycles (Points 1-361)

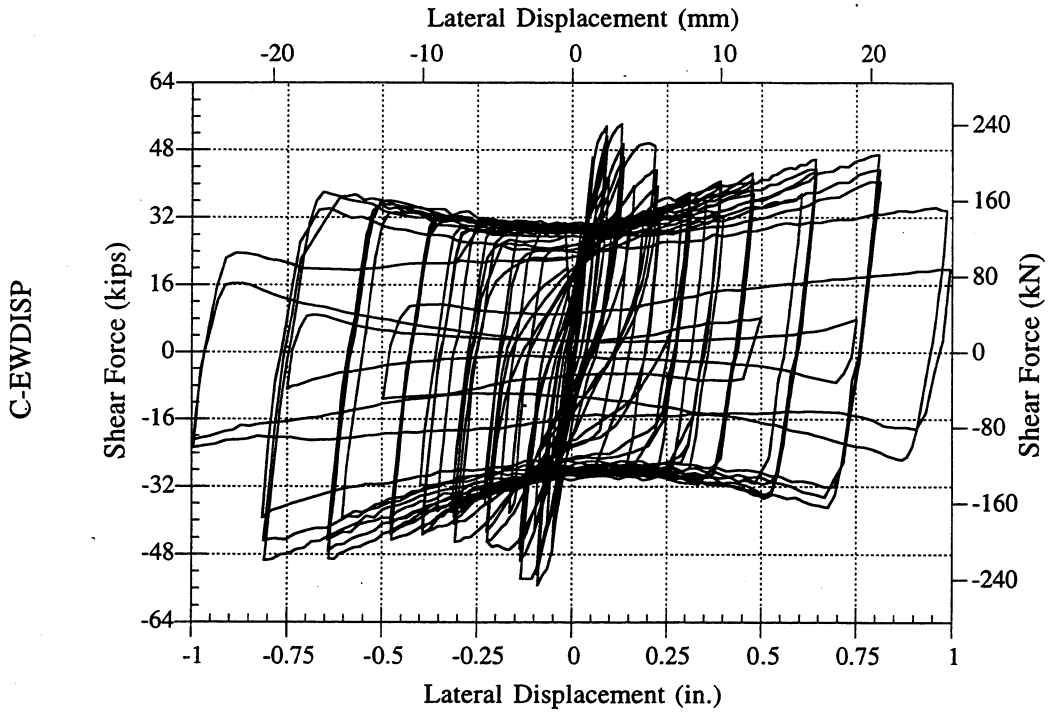

b) Inelastic Cycles (Points 361-3569)

Fig. 6.2.10 Force-Displacement Relations for Wall Specimen 8

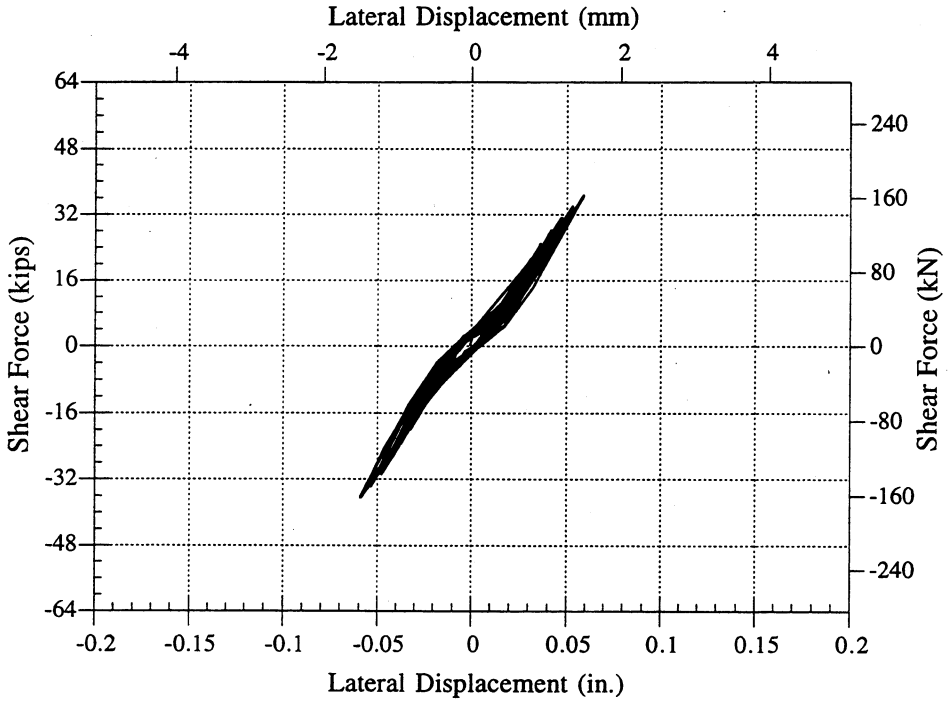

a) Elastic Cycles (Points 1-364)

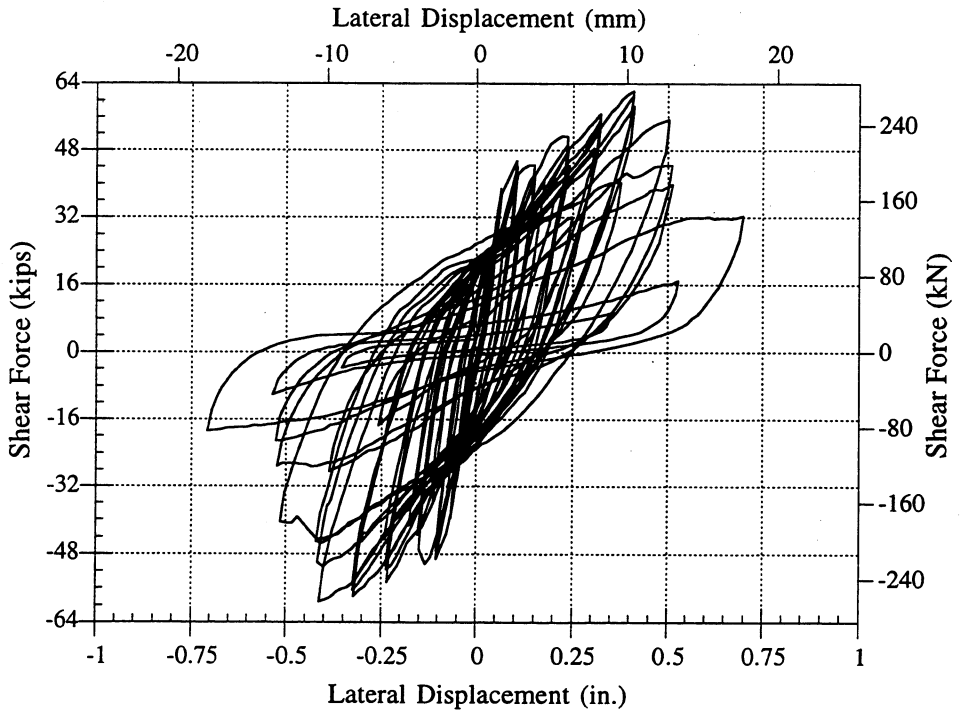

b) Inelastic Cycles (Points 364-2932)

Fig. 6.2.11 Force-Displacement Relations for Wall Specimen 10

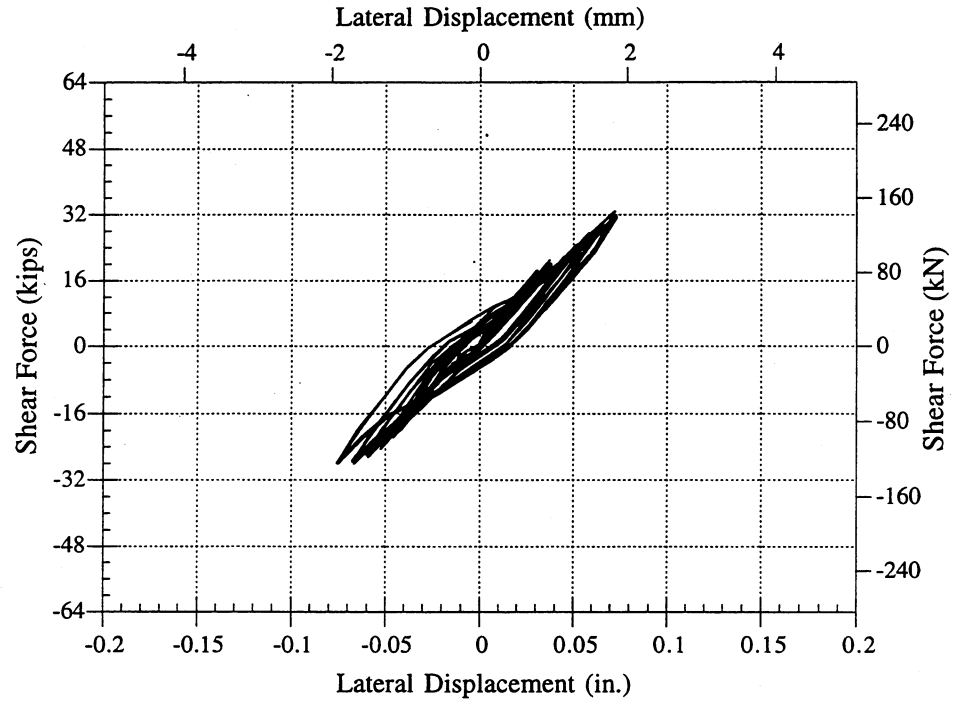

a) Elastic Cycles (Points 1-536)

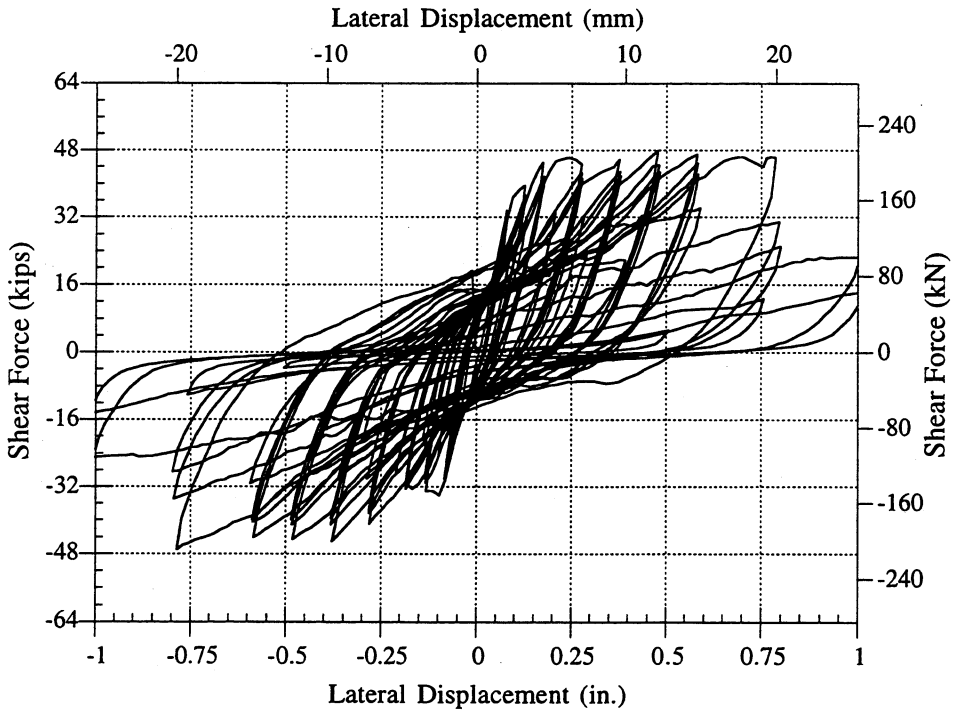

b) Inelastic Cycles (Points 536-4144)

Fig. 6.2.12 Force-Displacement Relations for Wall Specimen 12

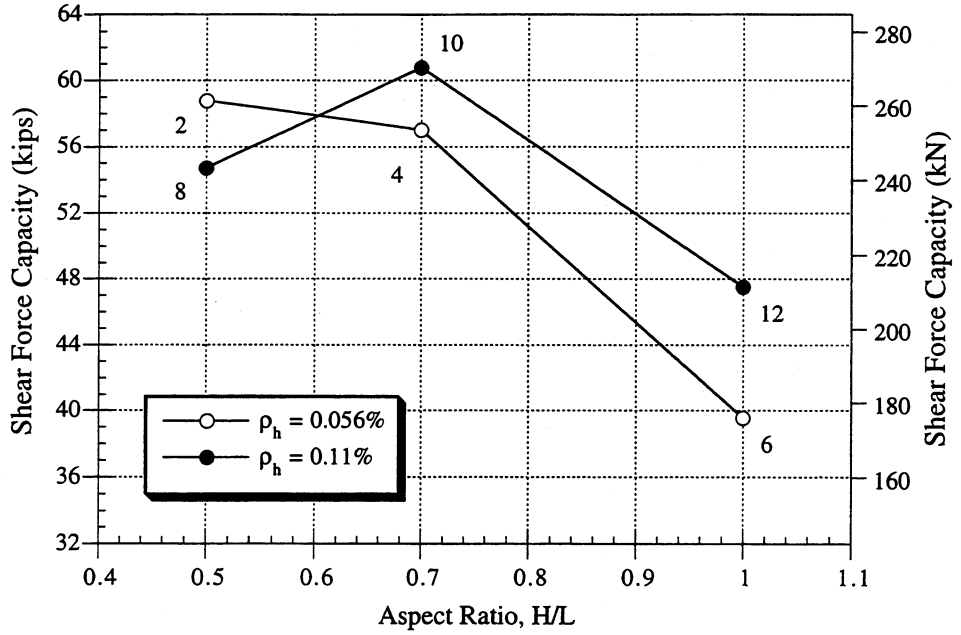

Fig. 6.2.13 Shear Force Capacity vs. Aspect Ratio

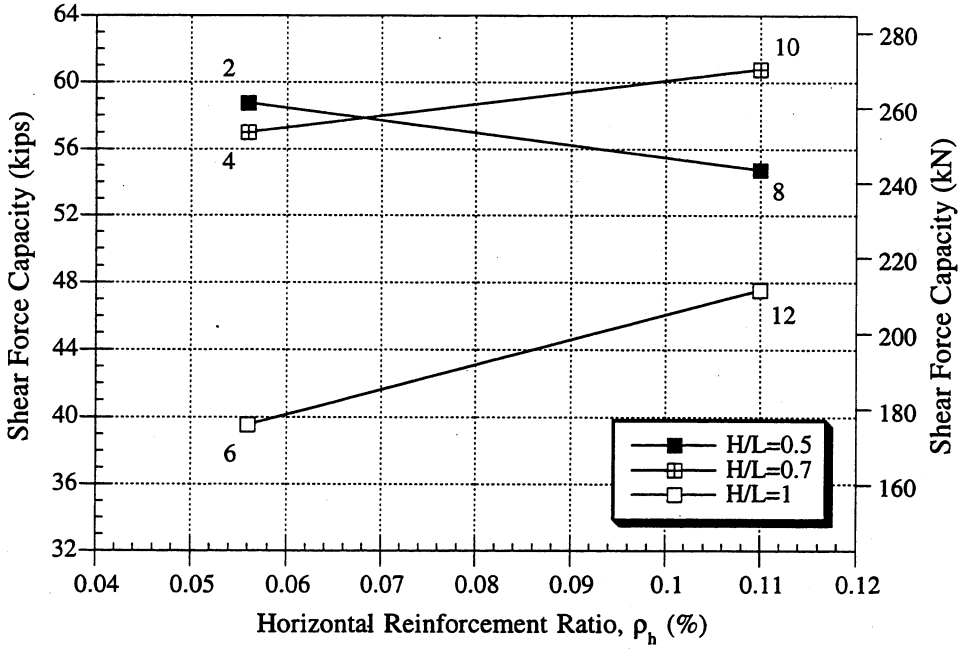

Fig. 6.2.14 Shear Force Capacity vs. Horizontal Reinforcement Ratio

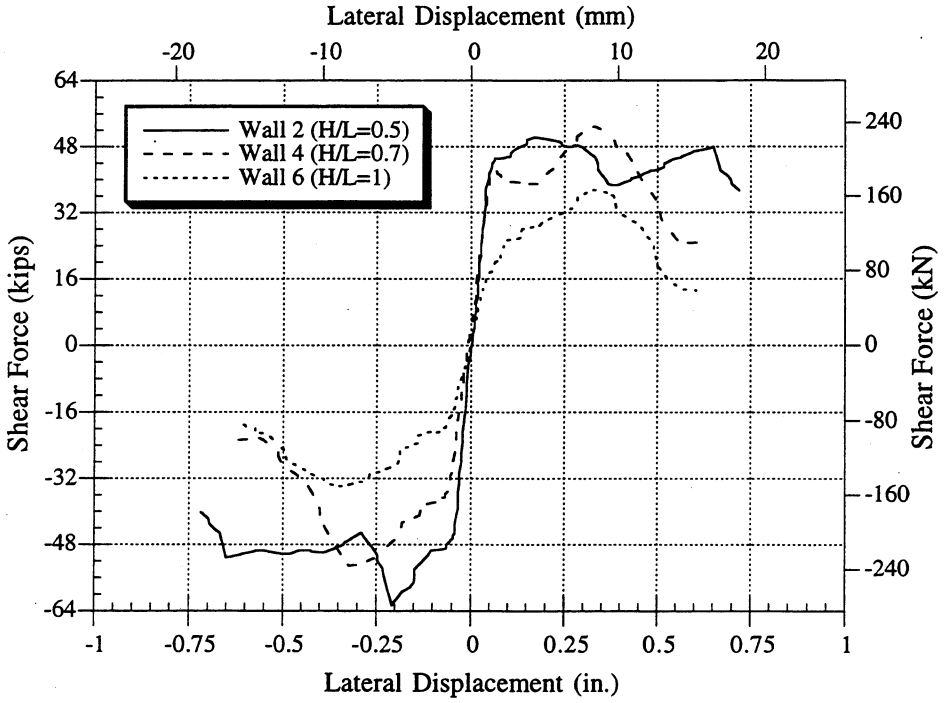

Fig. 6.3.1 Force-Displacement Envelopes for Walls with ρ_h= 0.056%

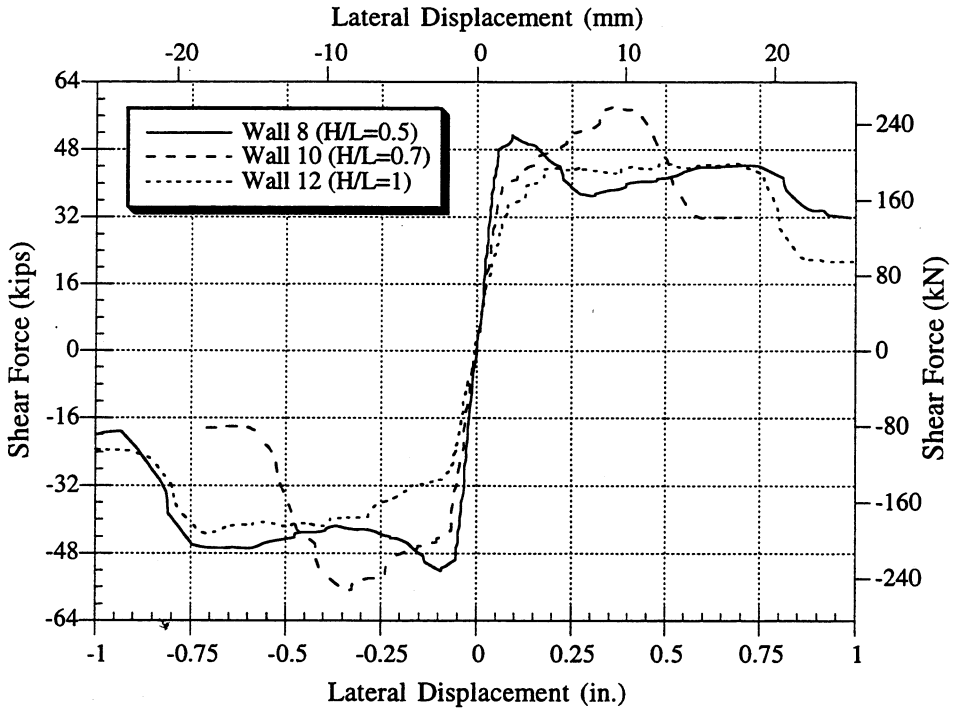

Fig. 6.3.2 Force-Displacement Envelopes for Walls with ρ_h= 0.11%

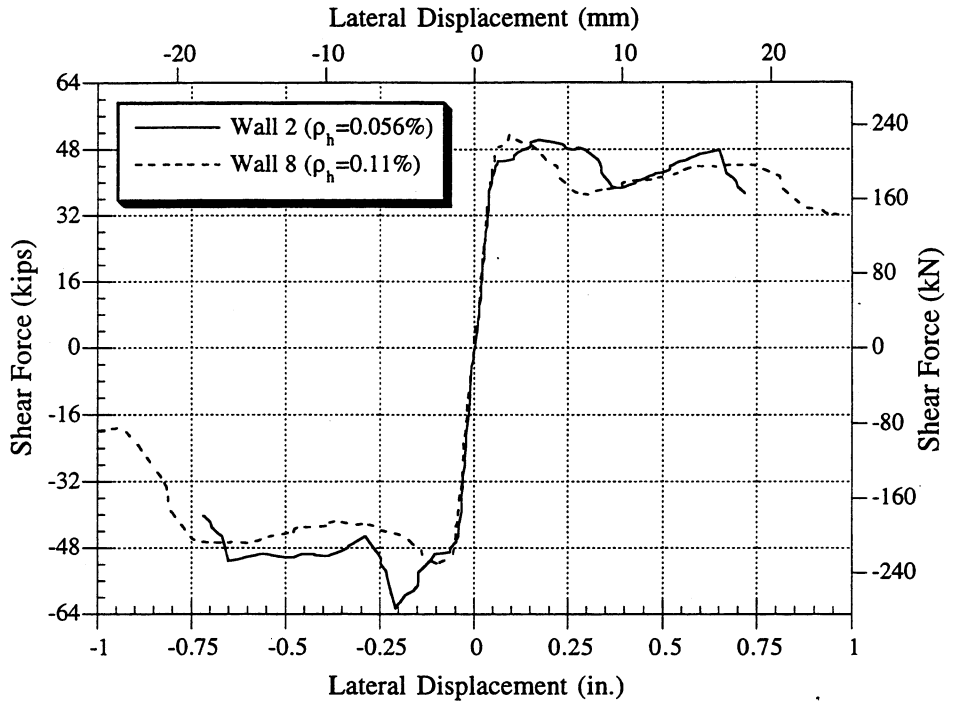

Fig. 6.3.3 Force-Displacement Envelopes for Walls with H/L = 0.5

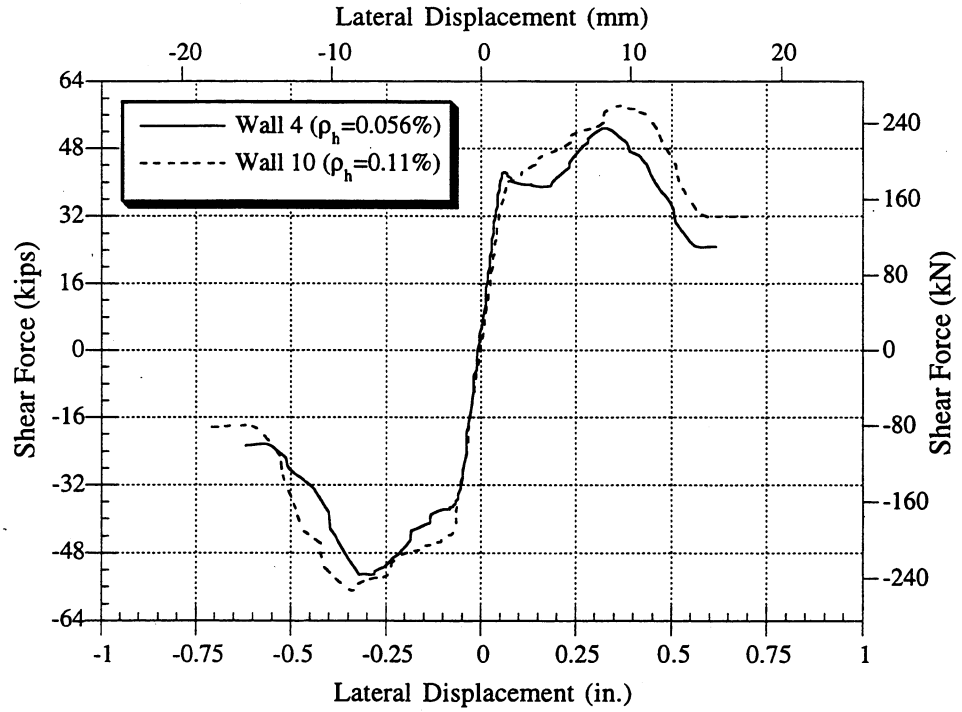

Fig. 6.3.4 Force-Displacement Envelopes for Walls with H/L = 0.7

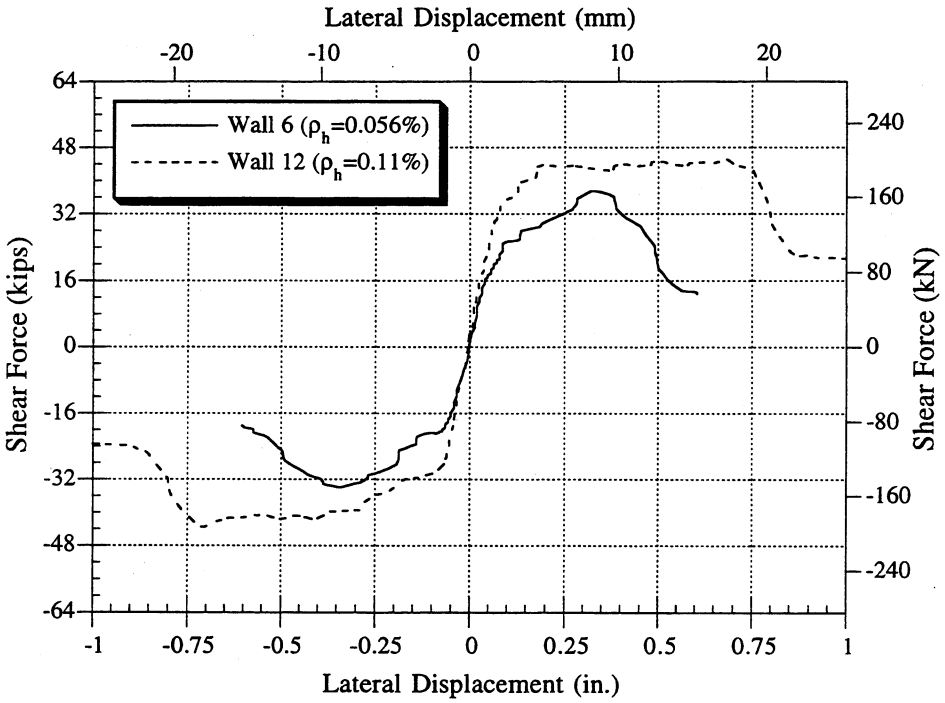

Fig. 6.3.5 Force-Displacement Envelopes for Walls with H/L = 1

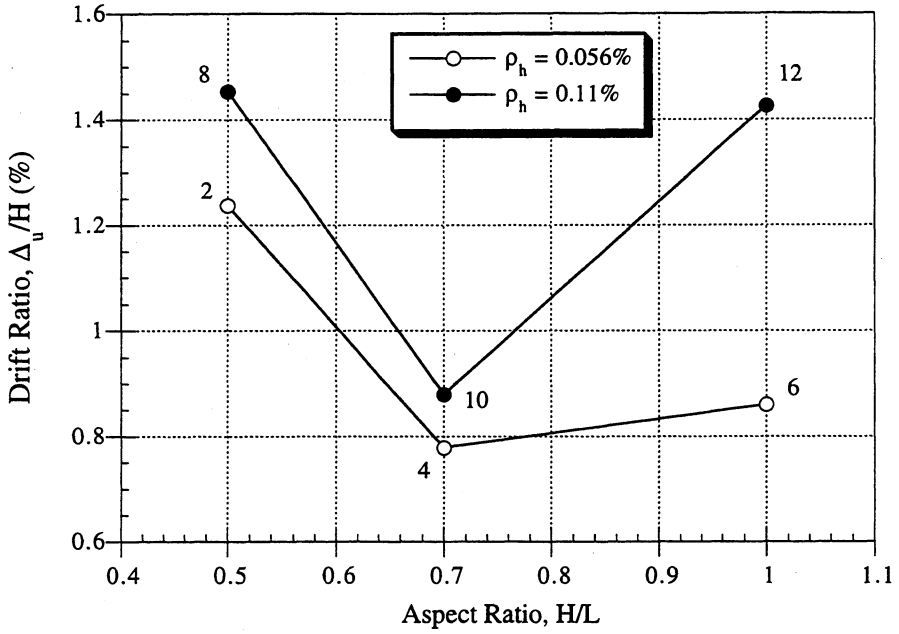

Fig. 6.3.6 Deformation Capacity vs. Aspect Ratio

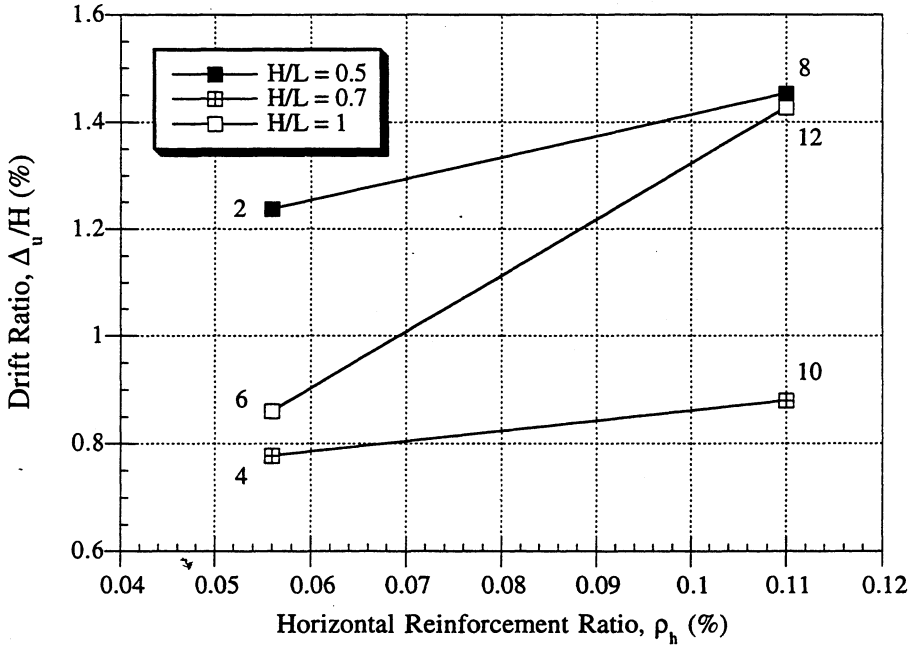

Fig. 6.3.7 Deformation Capacity vs. Horizontal Reinforcement Ratio

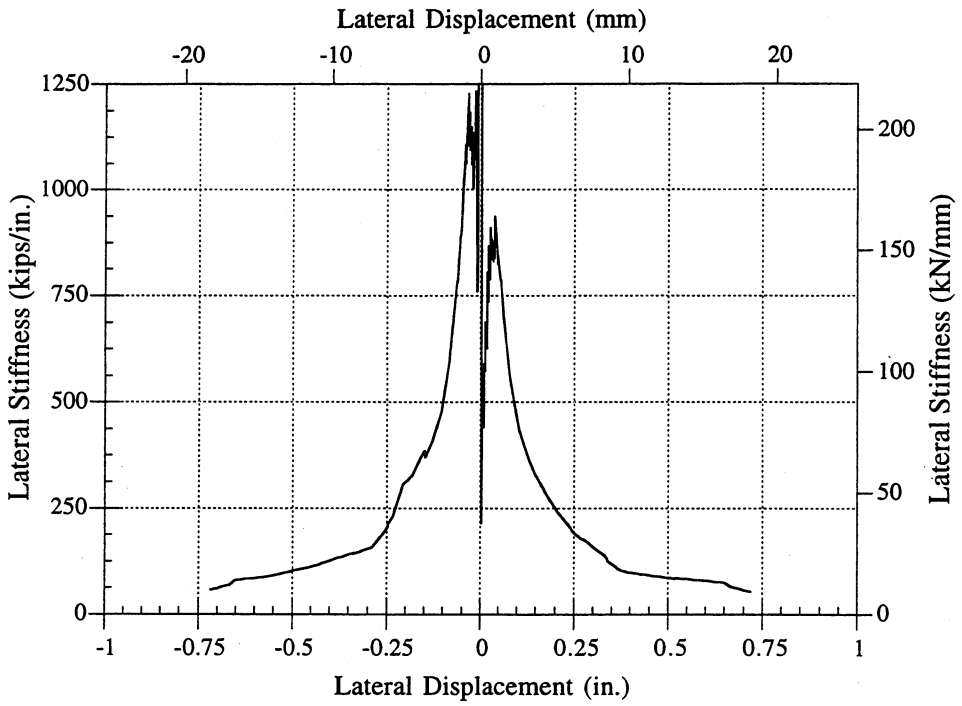

Fig. 6.4.1 Lateral Stiffness Envelope for Wall Specimen 2

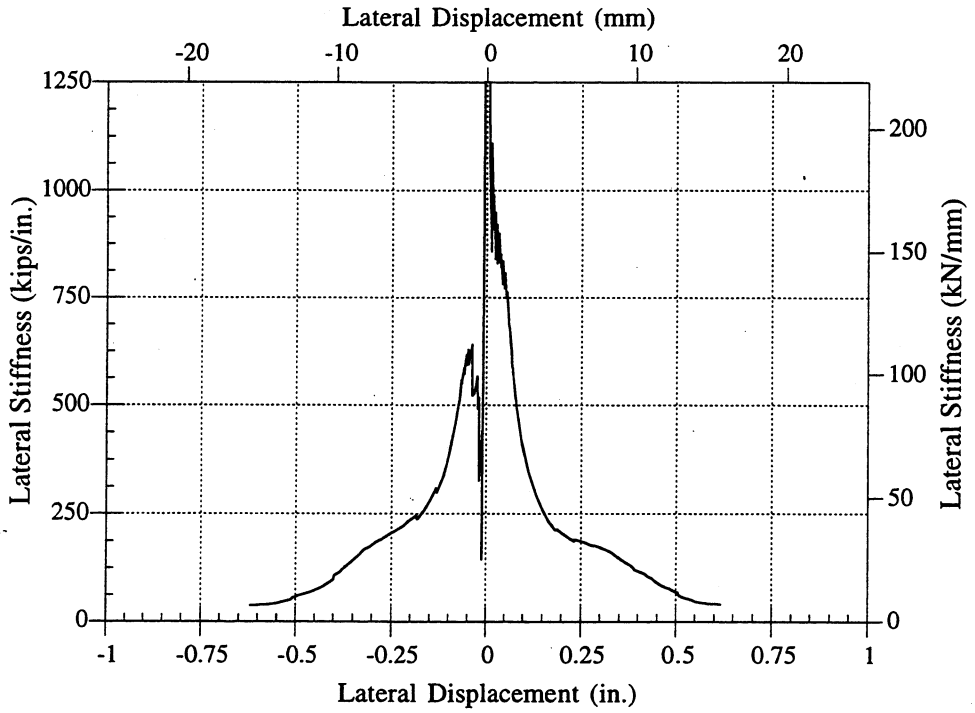

Fig. 6.4.2 Lateral Stiffness Envelope for Wall Specimen 4

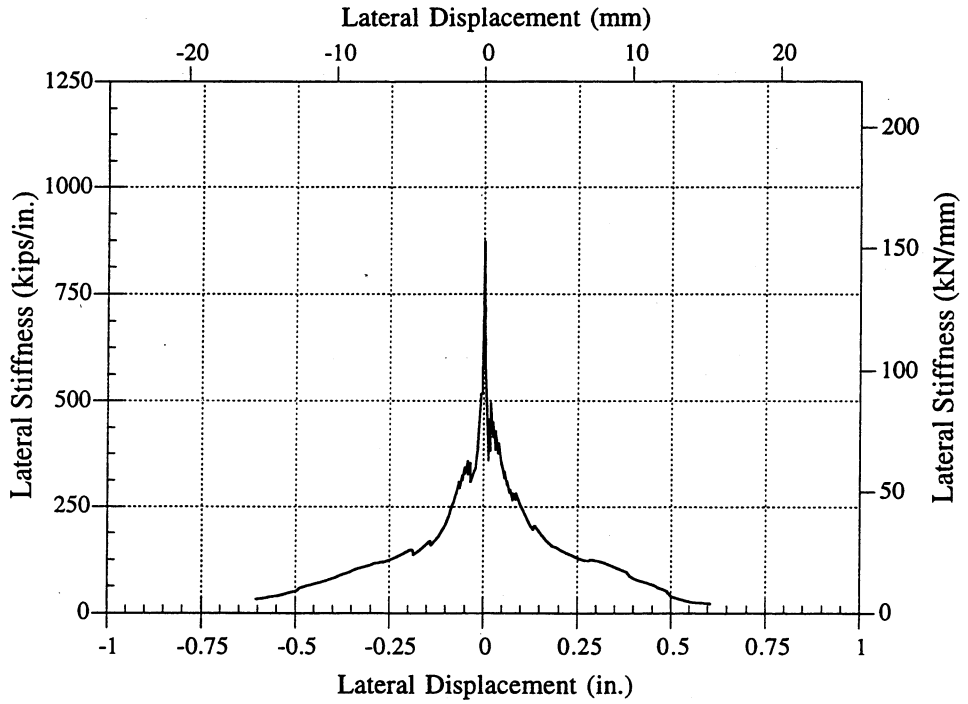

Fig. 6.4.3 Lateral Stiffness Envelope for Wall Specimen 6

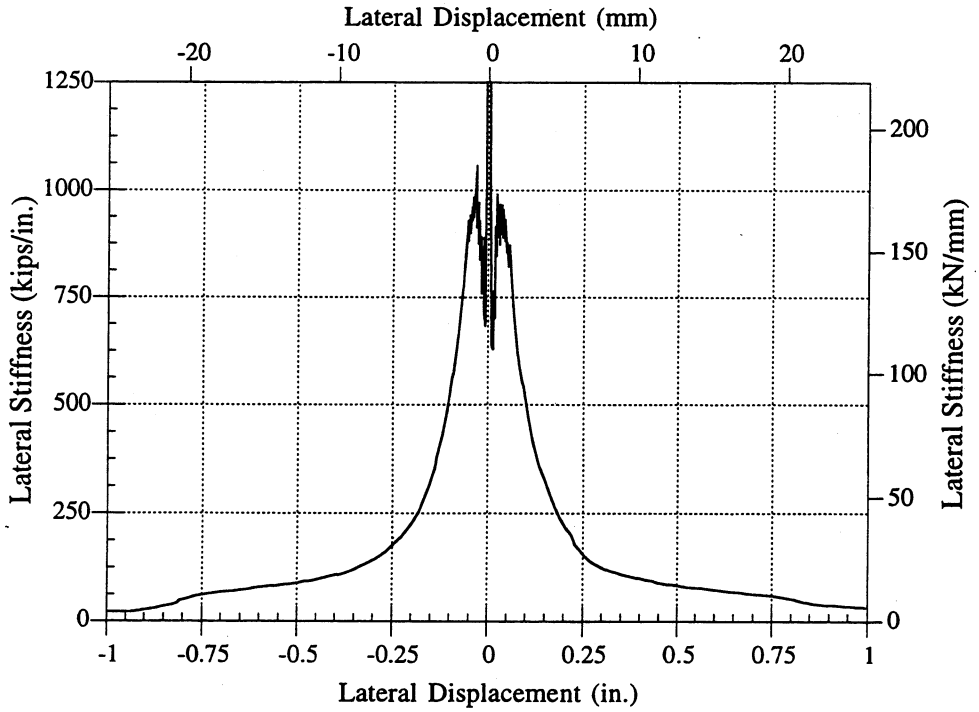

Fig. 6.4.4 Lateral Stiffness Envelope for Wall Specimen 8

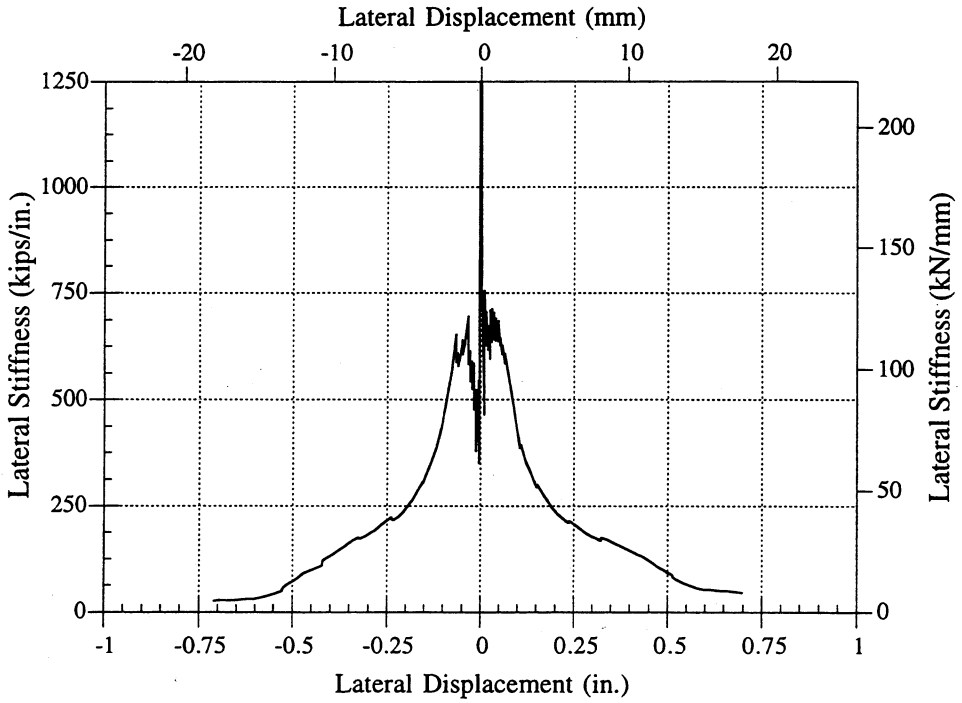

Fig. 6.4.5 Lateral Stiffness Envelope for Wall Specimen 10

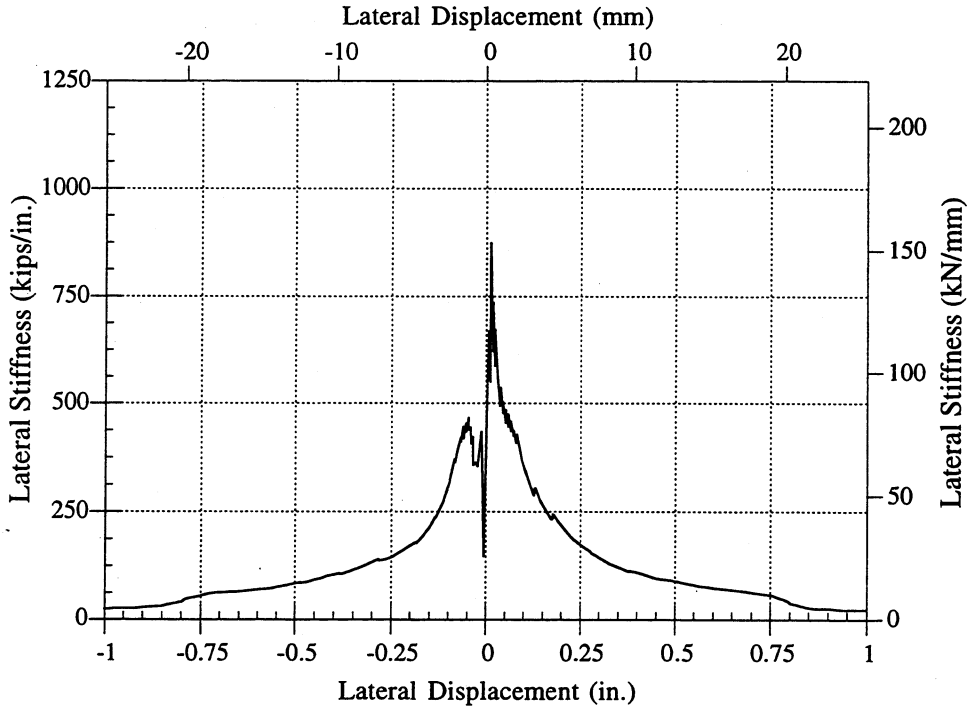

Fig. 6.4.6 Lateral Stiffness Envelope for Wall Specimen 12

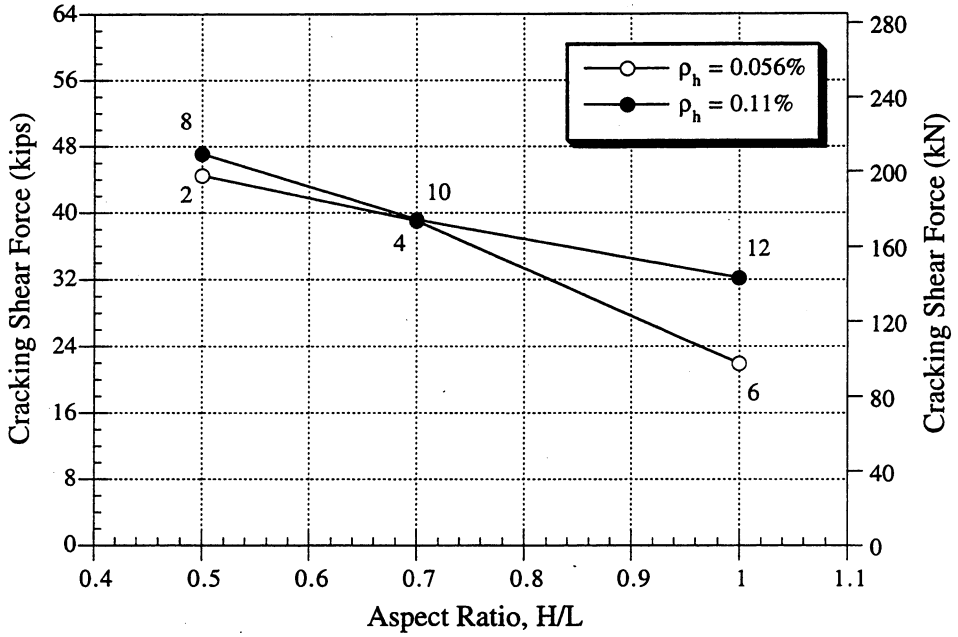

Fig. 6.4.7 Average Shear Force at First Cracking vs. Aspect Ratio

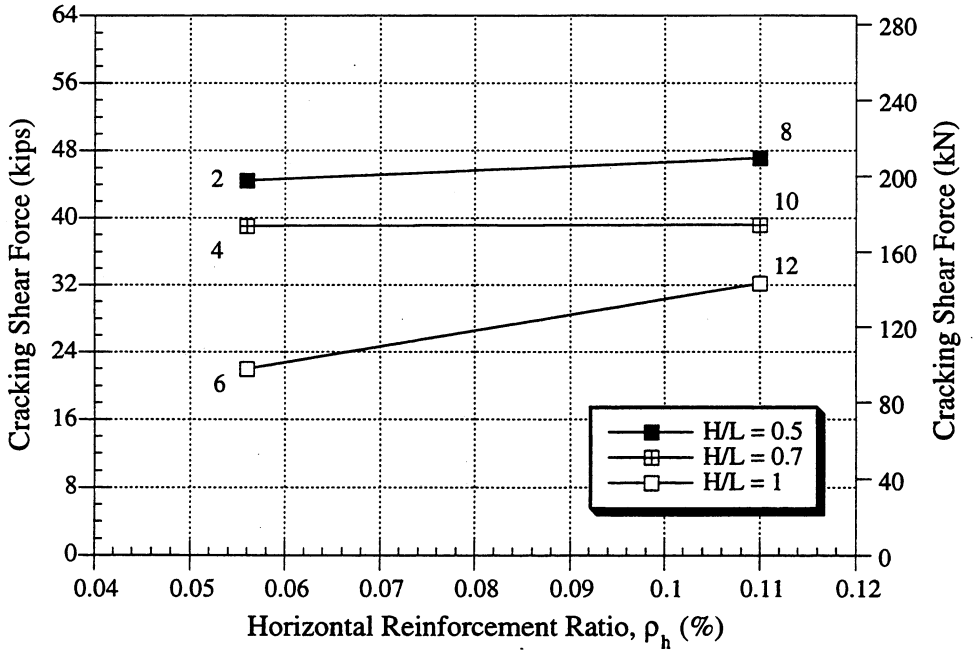

Fig. 6.4.8 Average Shear Force at First Cracking vs. Reinforcement Ratio

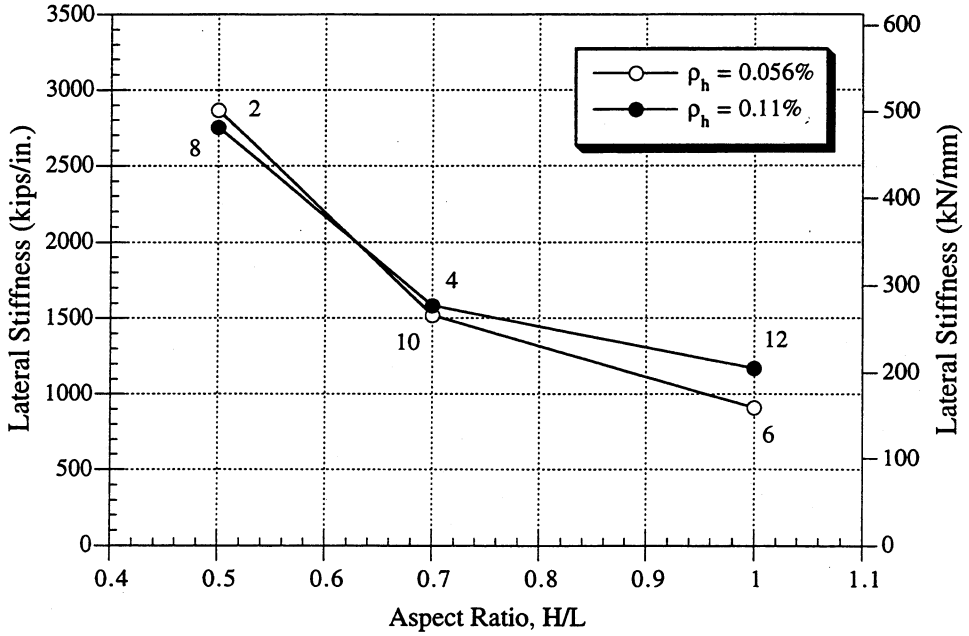

Fig. 6.5.1 Initial Stiffnesses vs. Aspect Ratio

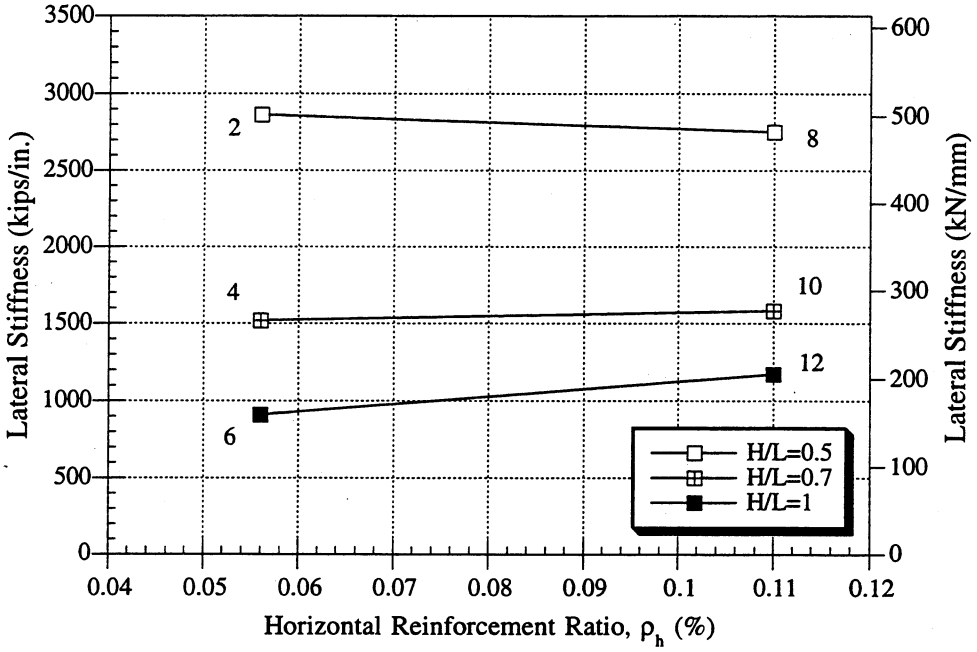

Fig. 6.5.2 Initial Stiffnesses vs. Horizontal Reinforcement Ratio

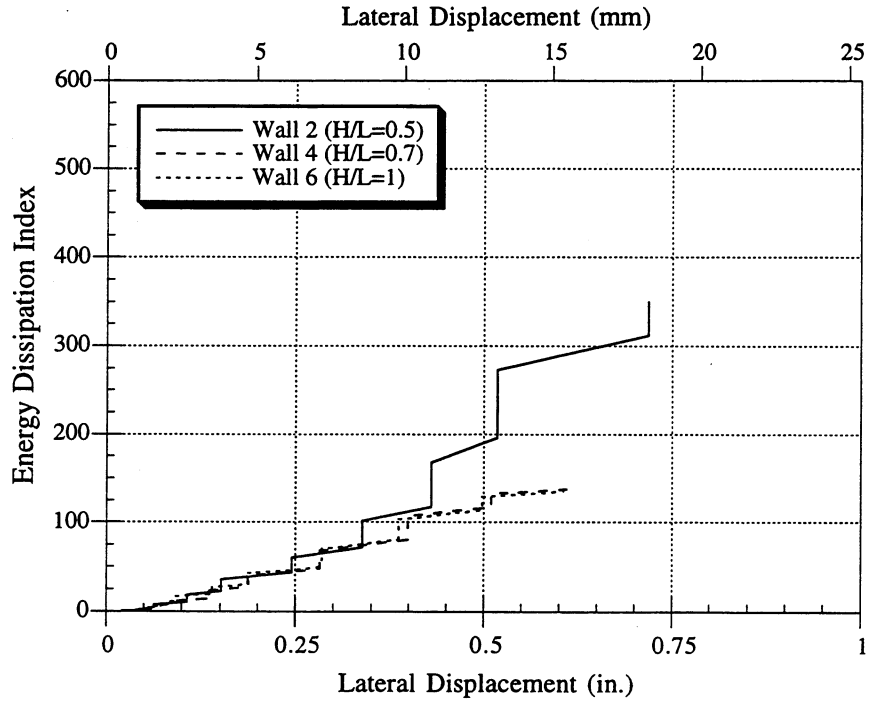

Fig. 6.6.1 Energy Dissipation for Walls with ρ_h= 0.056%

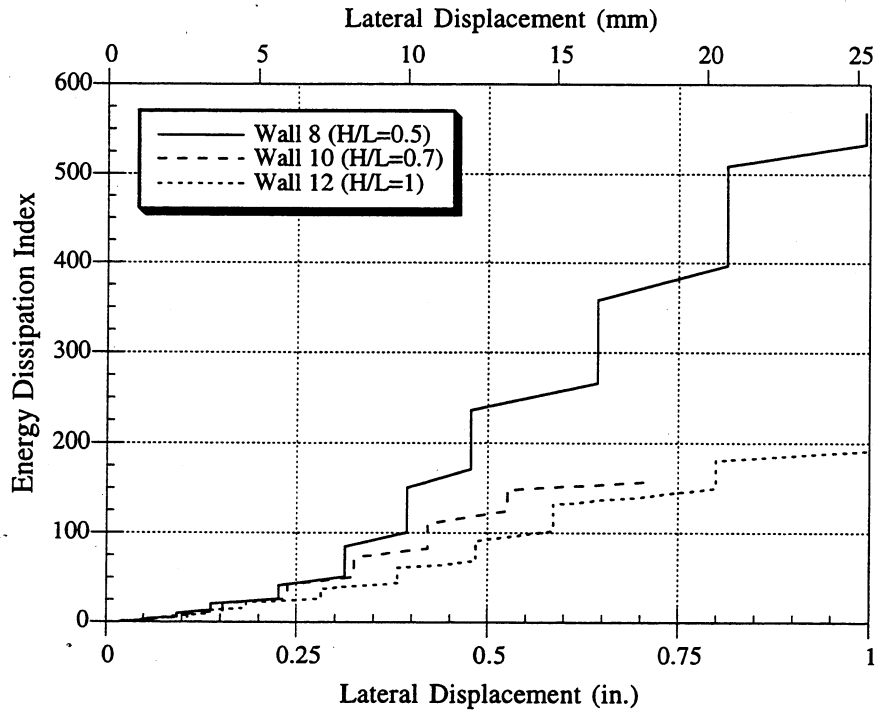

Fig. 6.6.2 Energy Dissipation for Walls with ρ_h= 0.11%

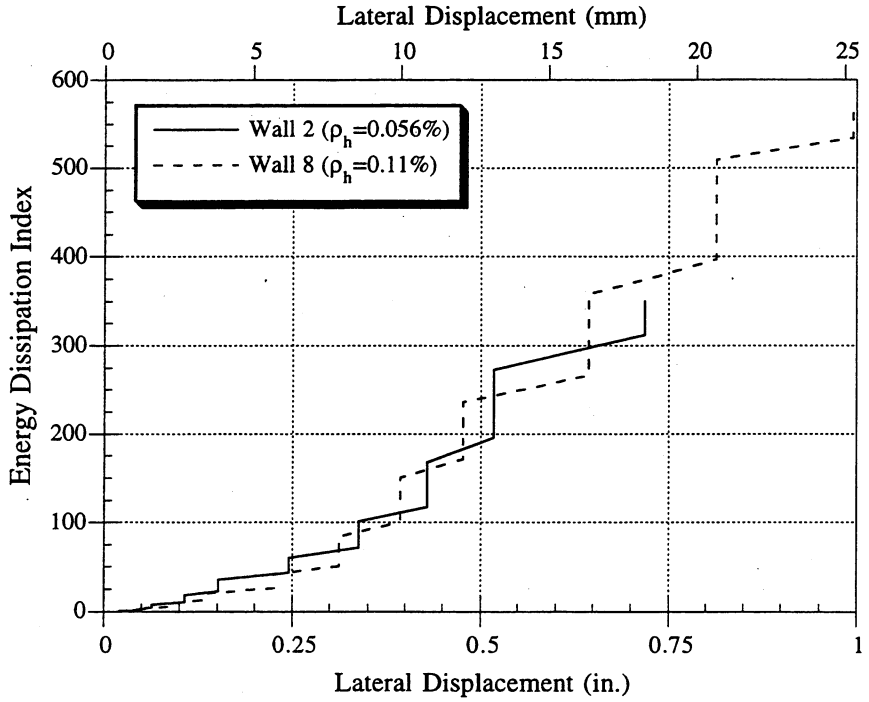

Fig. 6.6.3 Energy Dissipation for Walls with H/L= 0.5

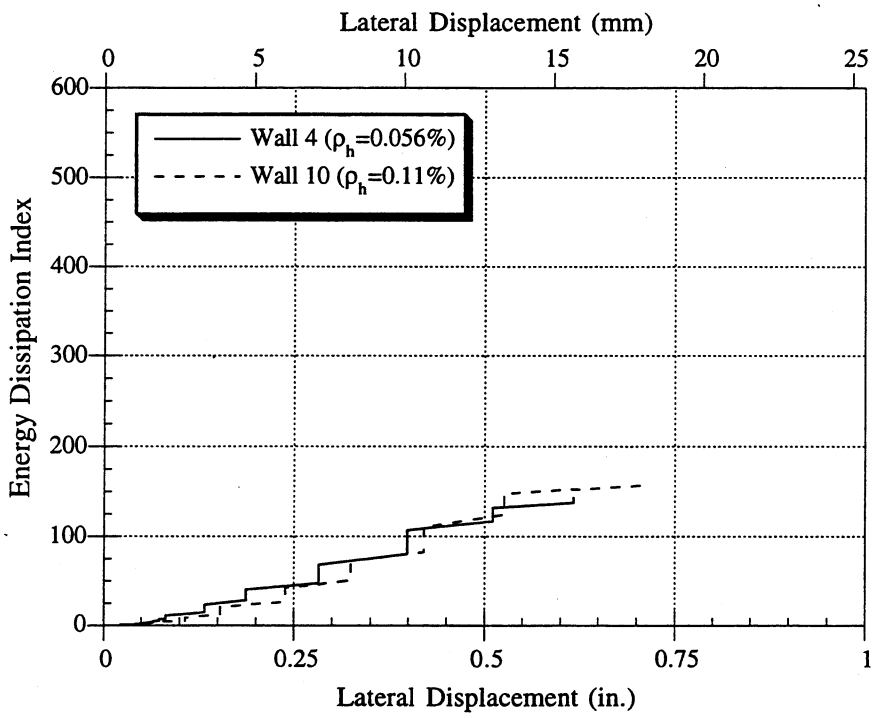

Fig. 6.6.4 Energy Dissipation for Walls with H/L=0.7

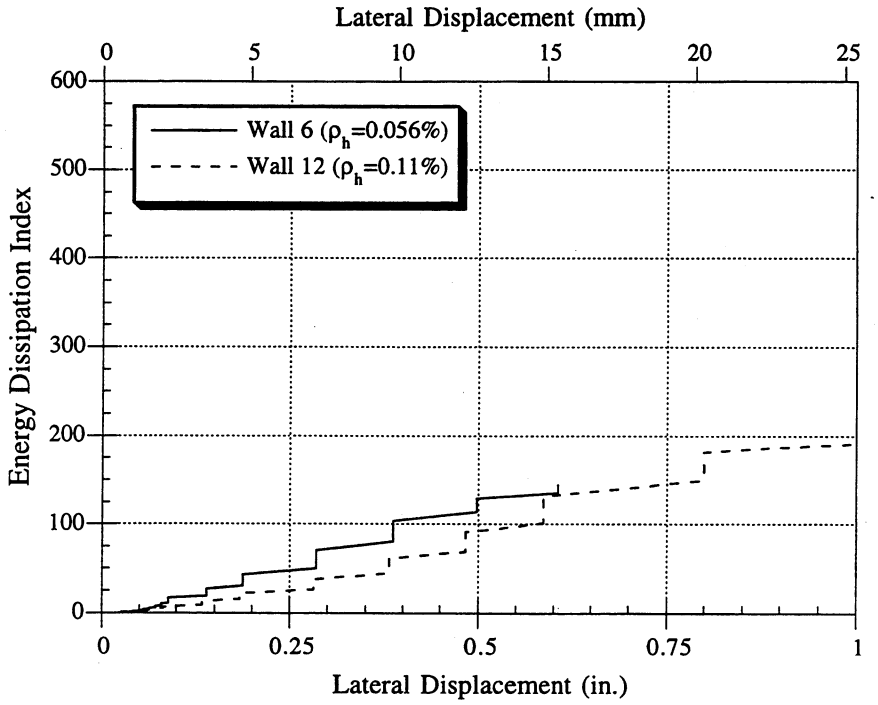

Fig. 6.6.5 Energy Dissipation for Walls with H/L= 1

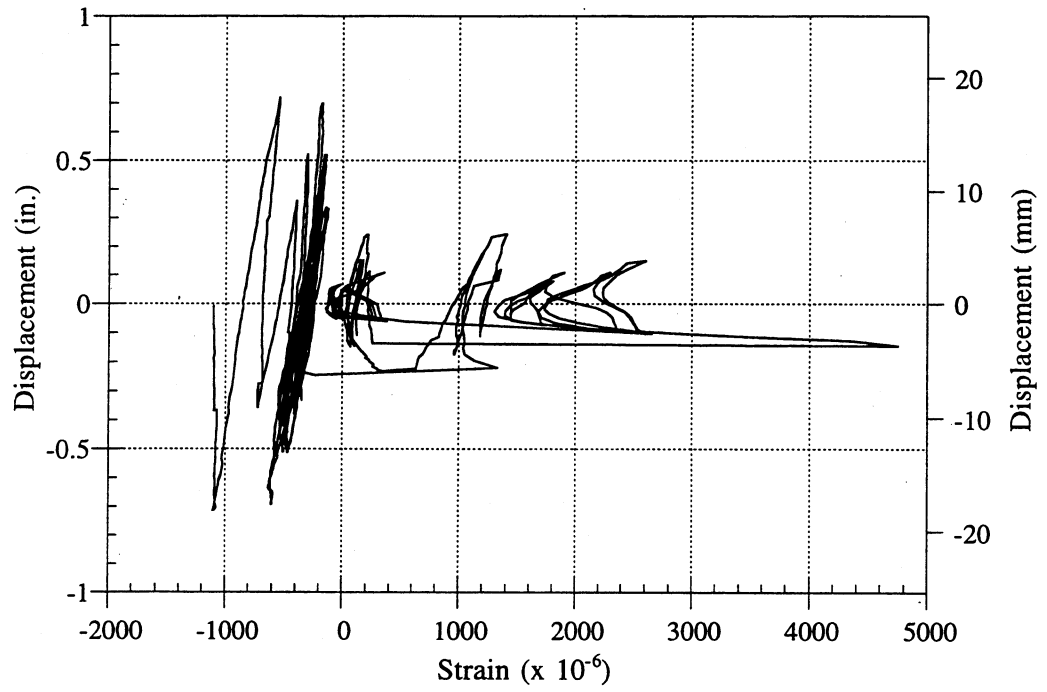

a) Gage VTWO

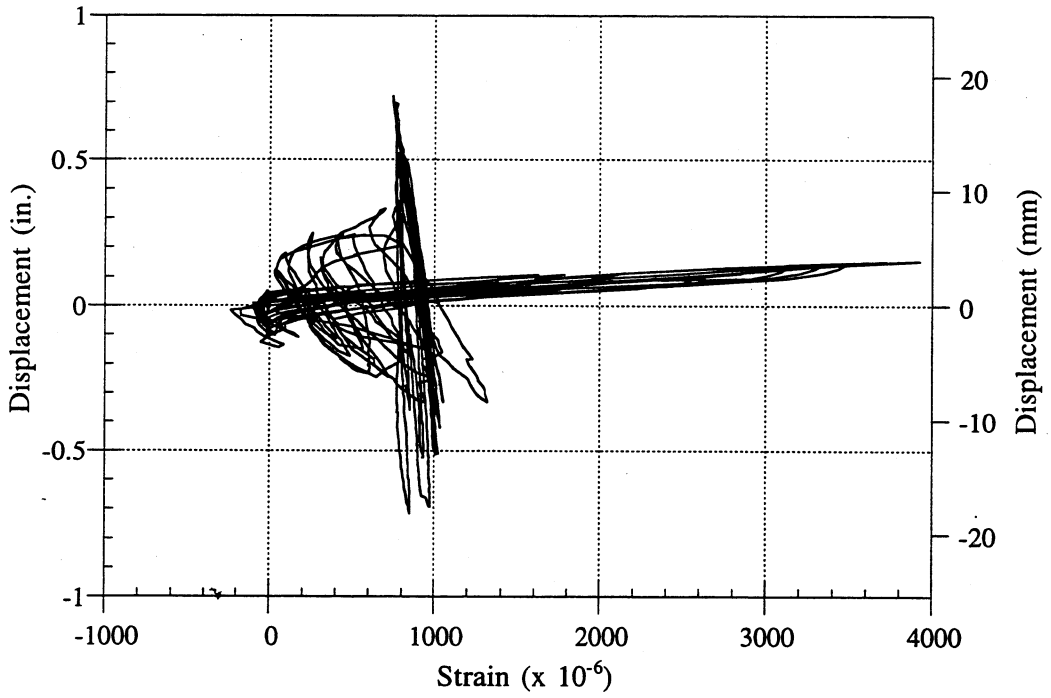

b) Gage VTEO

Fig. 7.1.1 Strains in Vertical Rebars vs. Lateral Drift in Wall Specimen 2

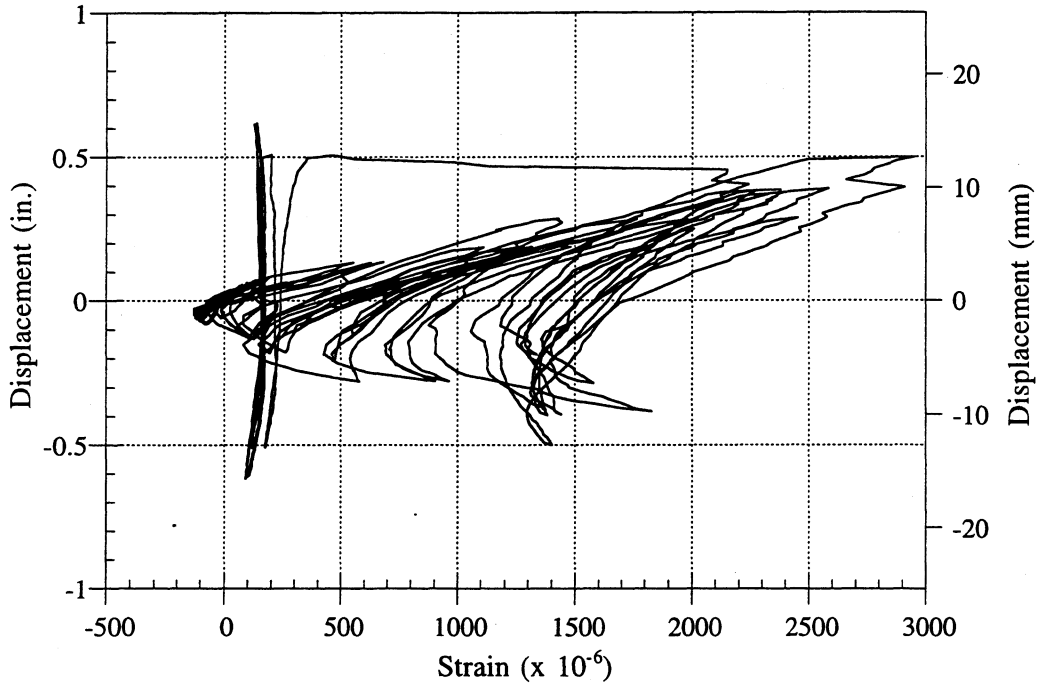

a) Gage VTWO

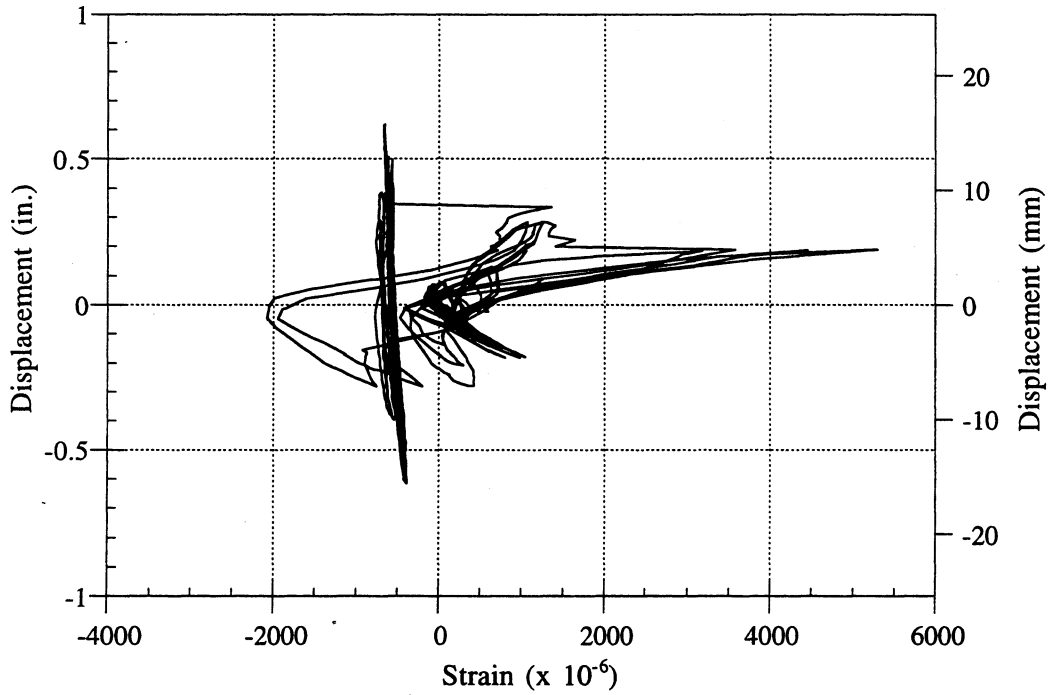

b) Gage VTEO

Fig. 7.1.2 Strains in Vertical Rebars vs. Lateral Drift in Wall Specimen 4

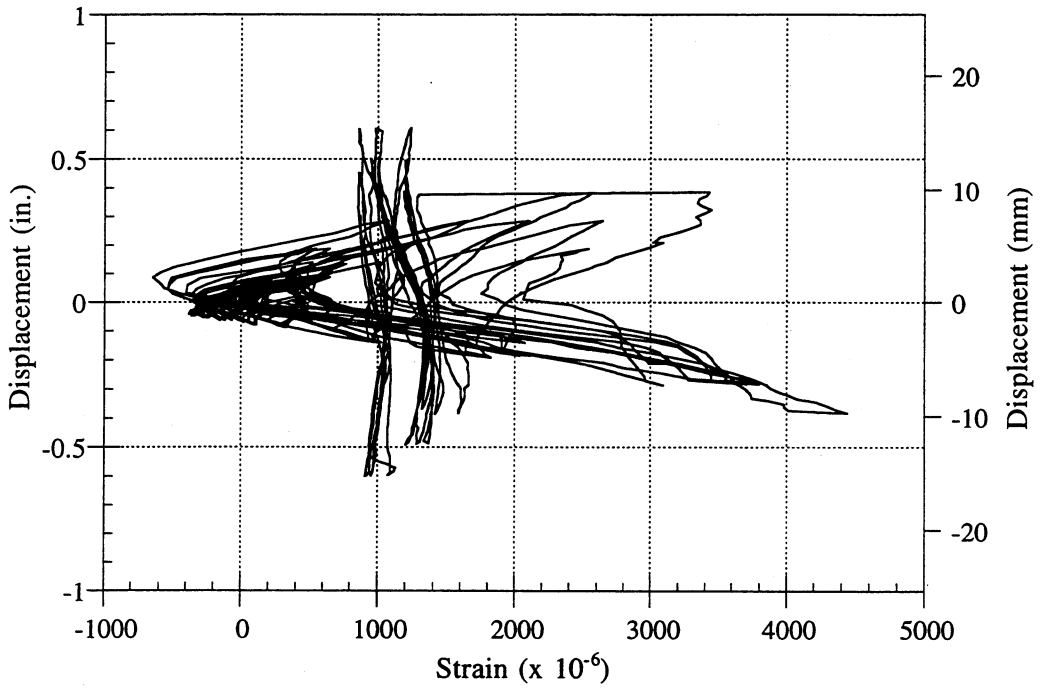

a) Gage VTWO

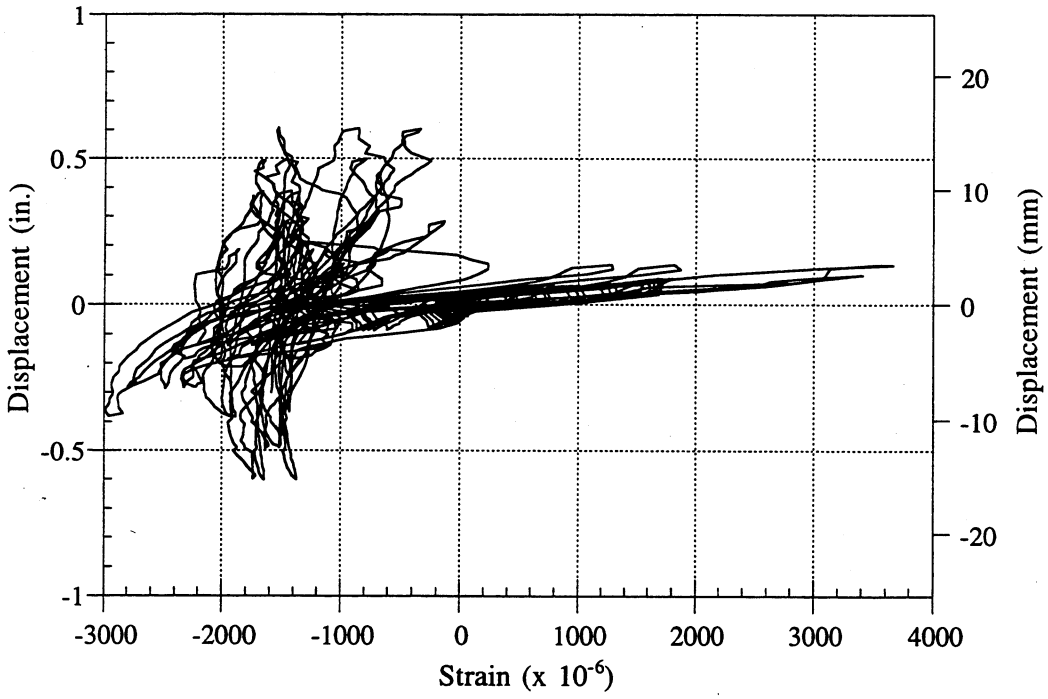

b) Gage VTEI

Fig. 7.1.3 Strains in Vertical Rebars vs. Lateral Drift in Wall Specimen 6

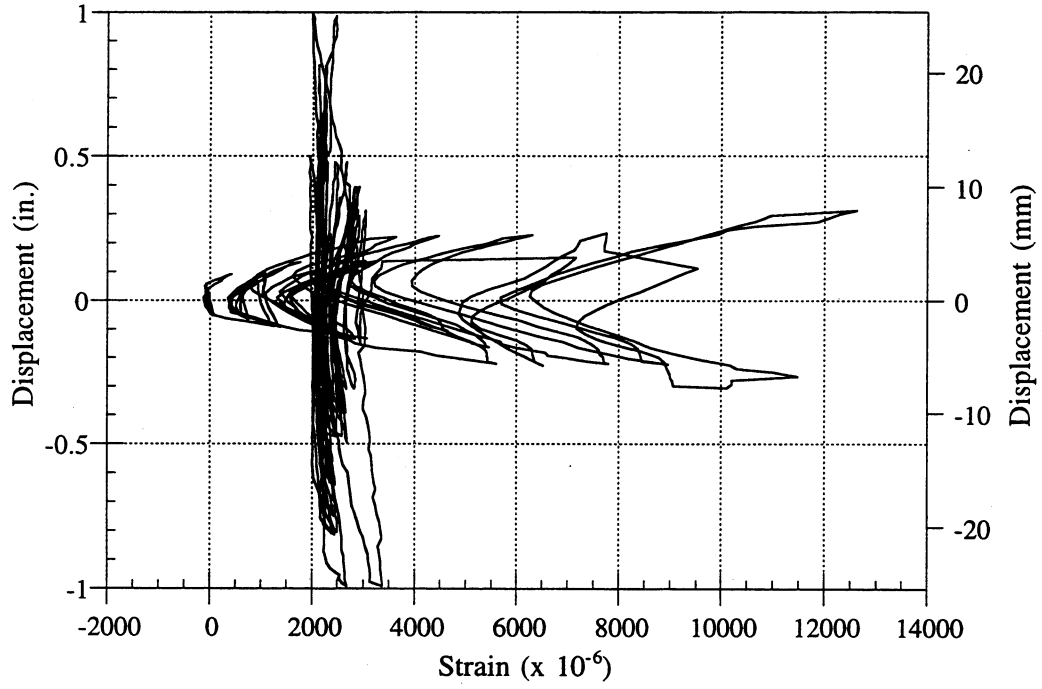

a) Gage VTWO

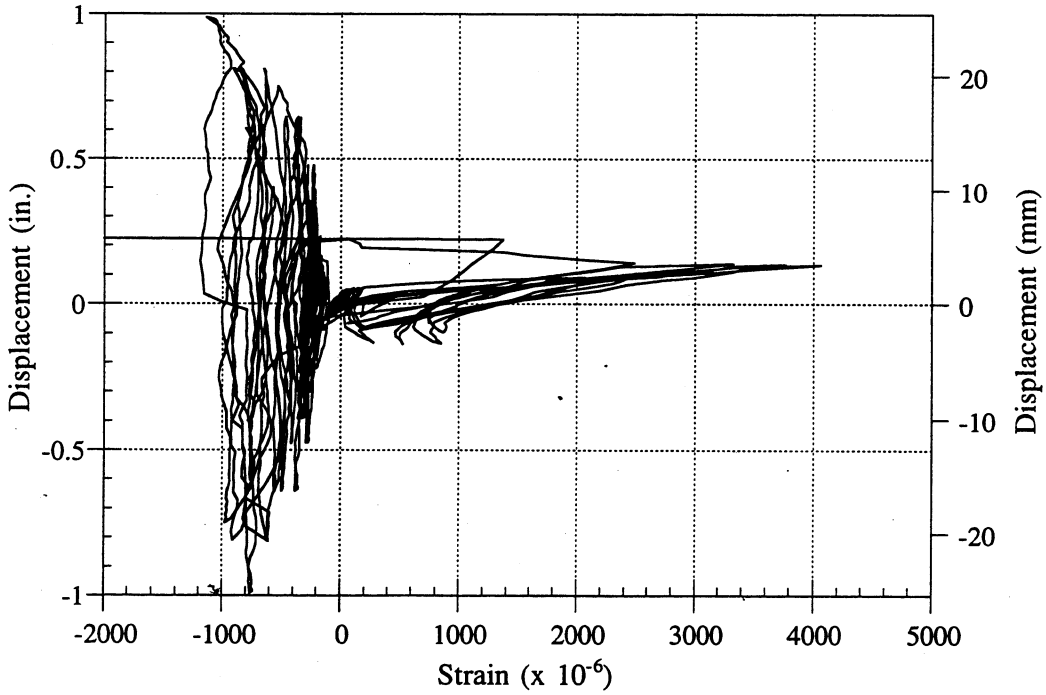

b) Gage VTEI

Fig. 7.1.4 Strains in Vertical Rebars vs. Lateral Drift in Wall Specimen 8

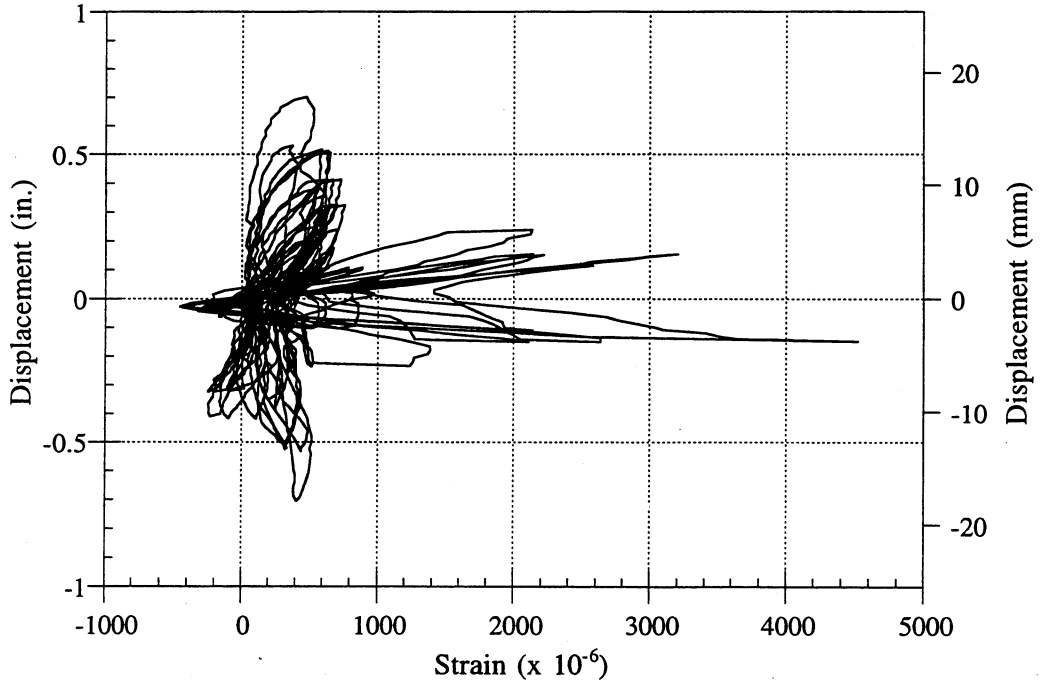

a) Gage VTWO

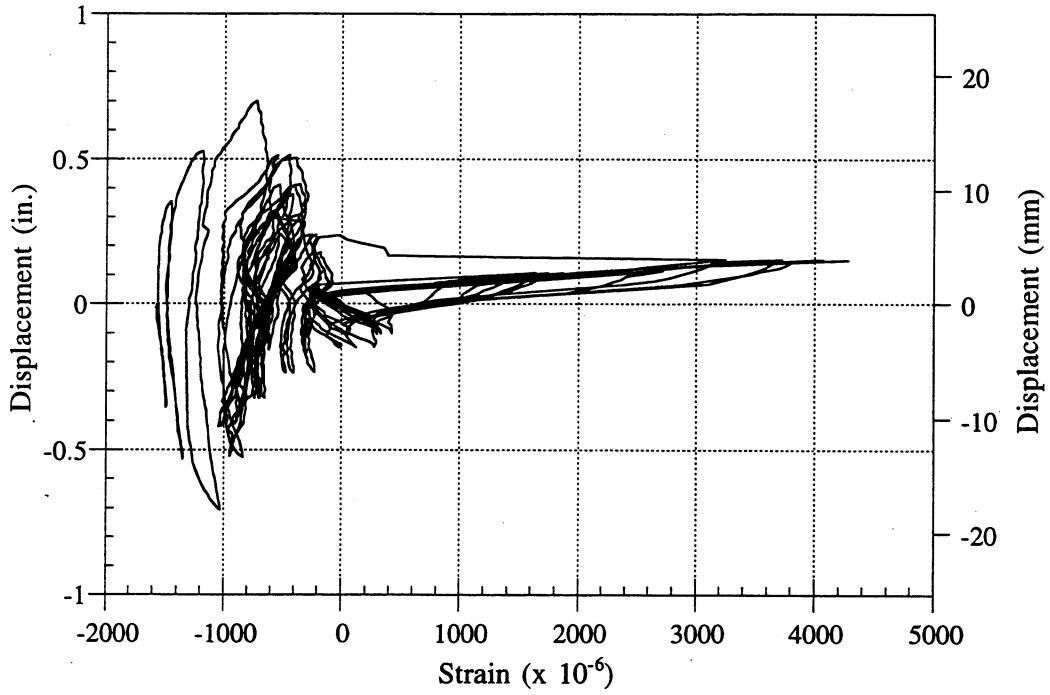

b) Gage VTEI

Fig. 7.1.5 Strains in Vertical Rebars vs. Lateral Drift in Wall Specimen 10

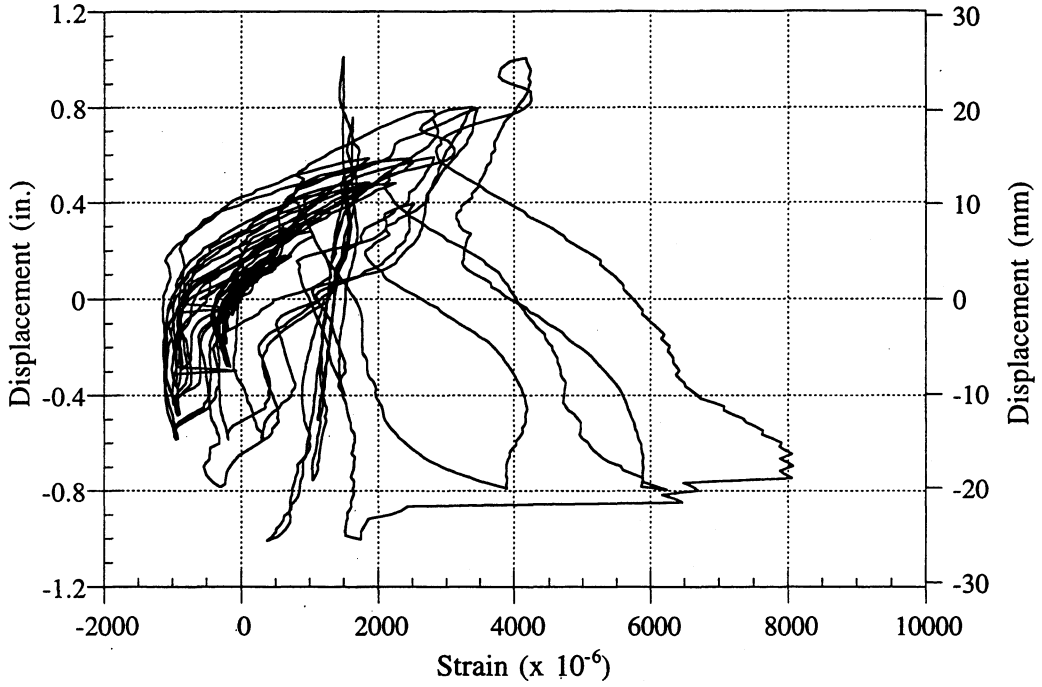

a) Gage VTWO

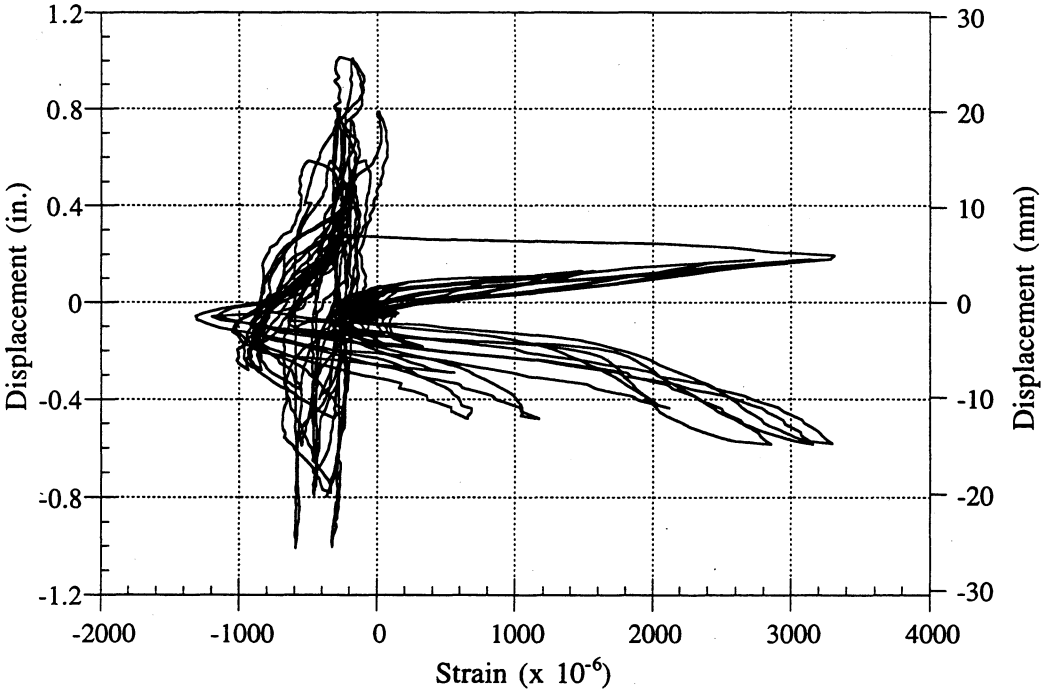

b) Gage VTEI

Fig. 7.1.6 Strains in Vertical Rebars vs. Lateral Drift in Wall Specimen 12

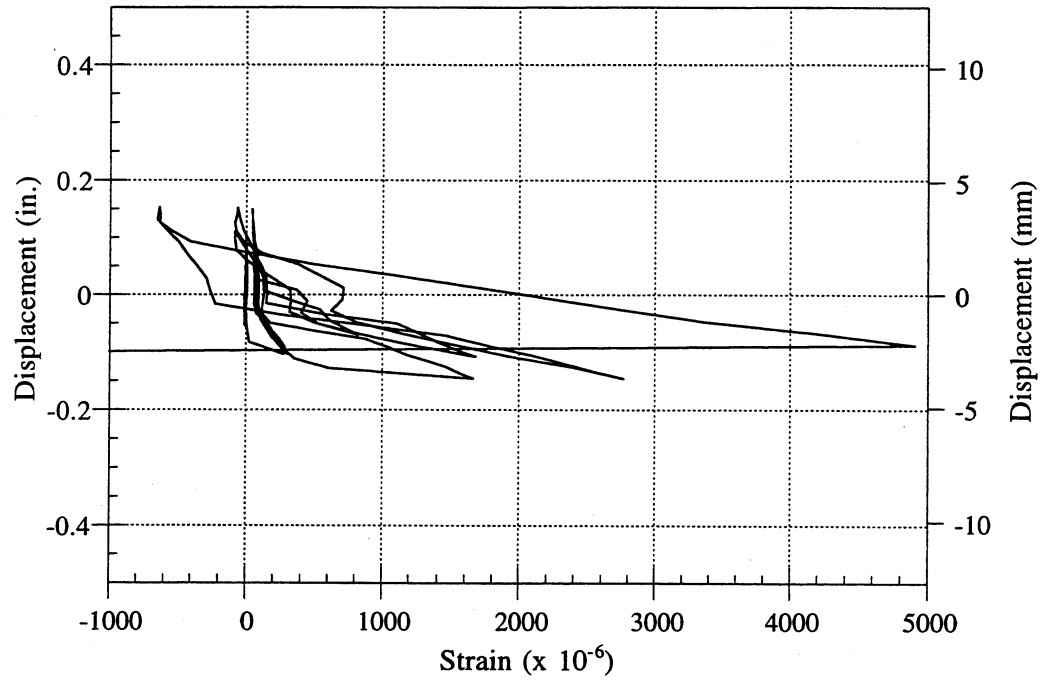

a) Gage 5SE

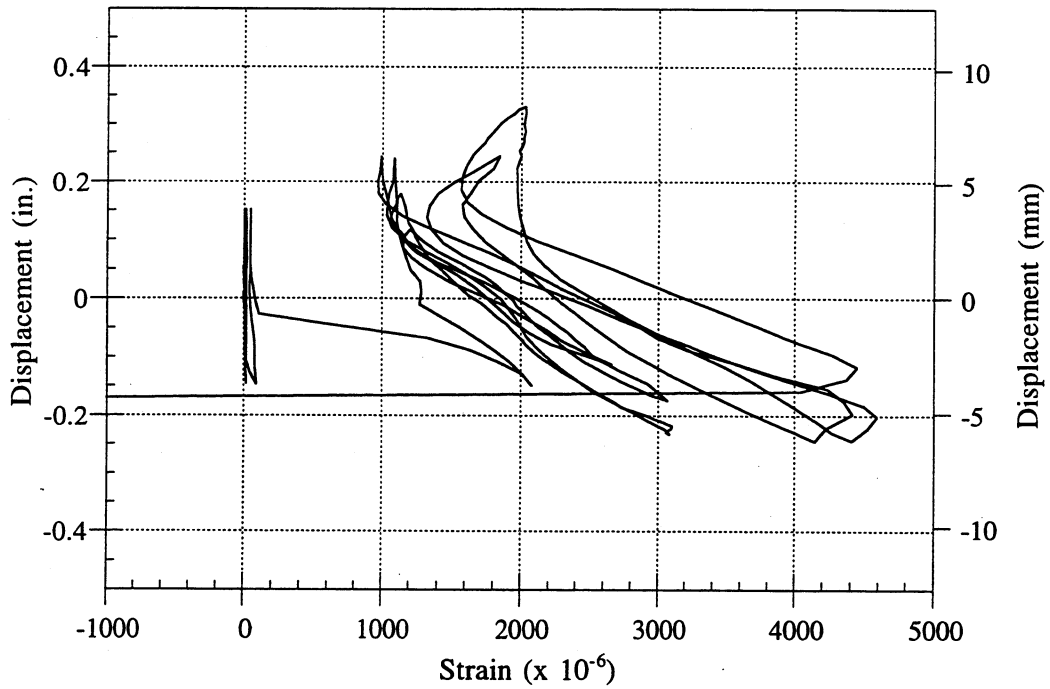

b) Gage 2NE

Fig. 7.2.1 Strains in Horizontal Grids vs. Lateral Drift in Wall Specimen 2

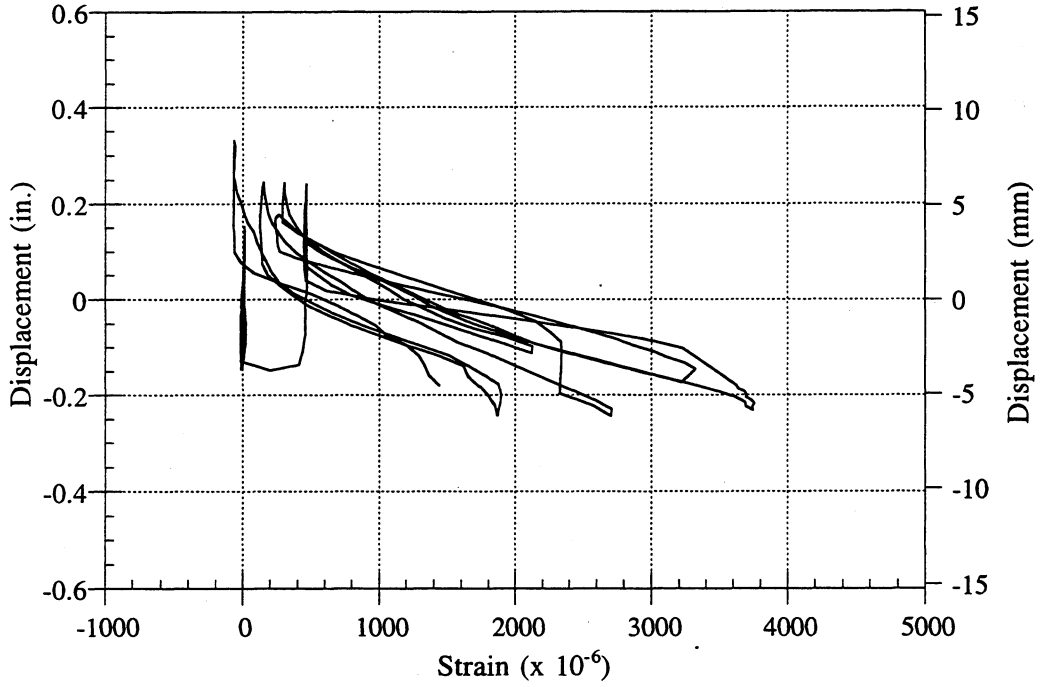

c) Gage 3NEC

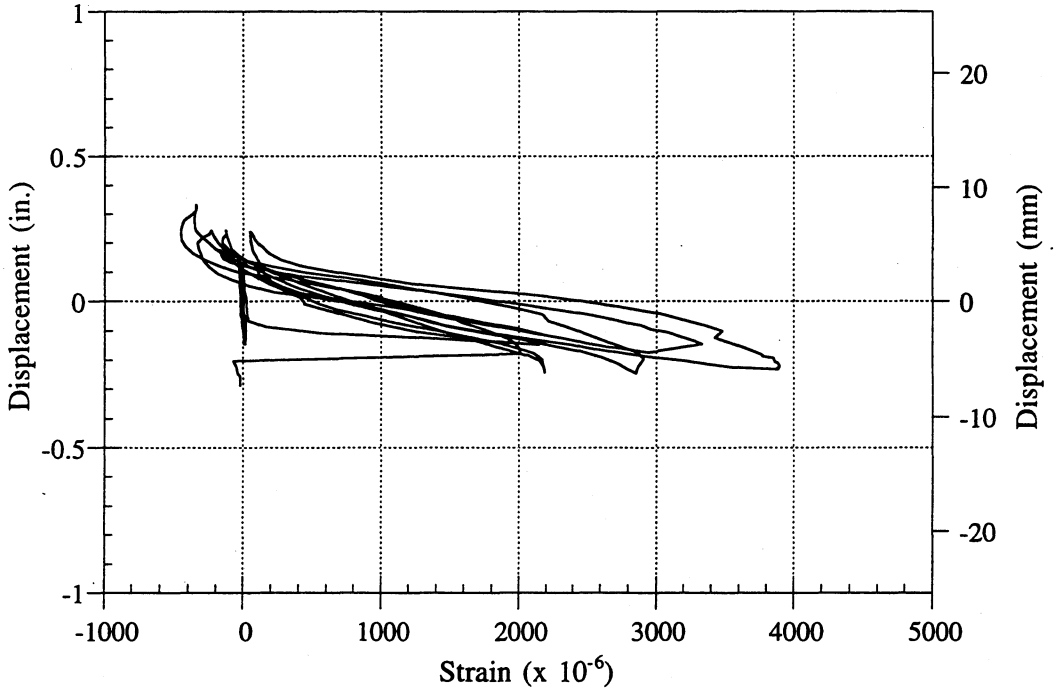

d) Gage 4SEC

Fig. 7.2.1 (Cont'd)

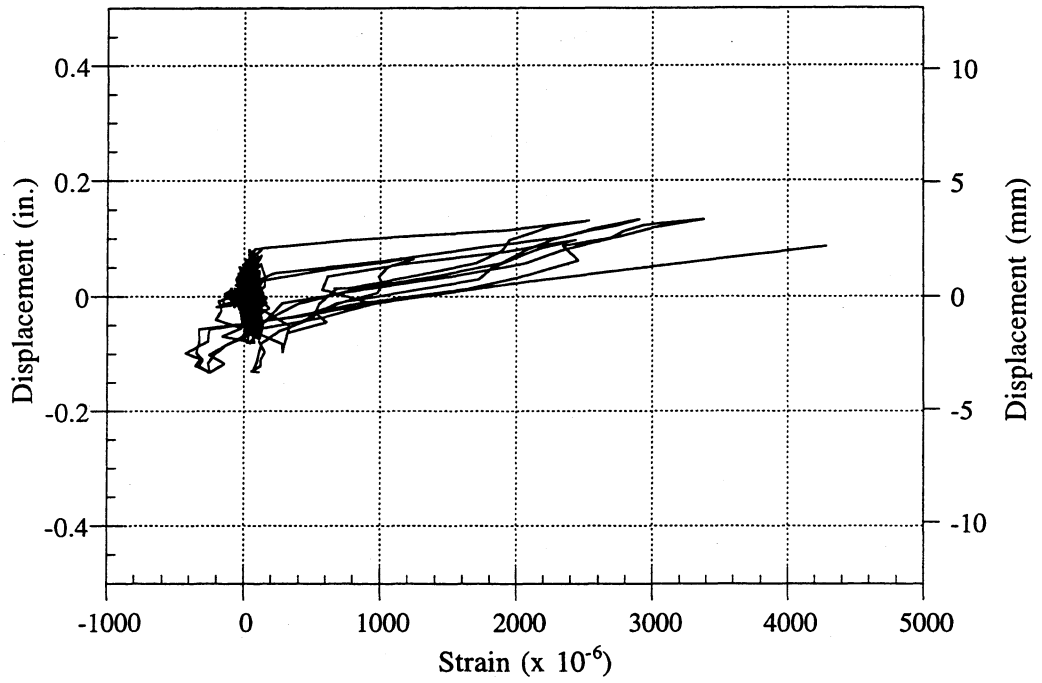

a) Gage 5NW

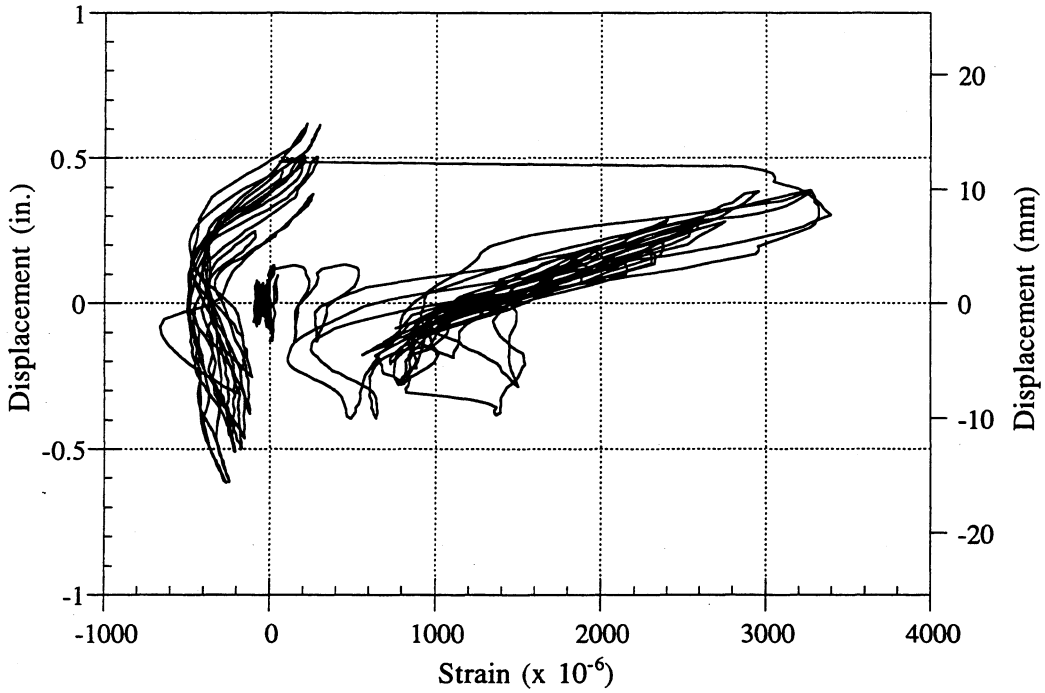

b) Gage 2NW

Fig. 7.2.2 Strains in Horizontal Grids vs. Lateral Drift in Wall Specimen 4

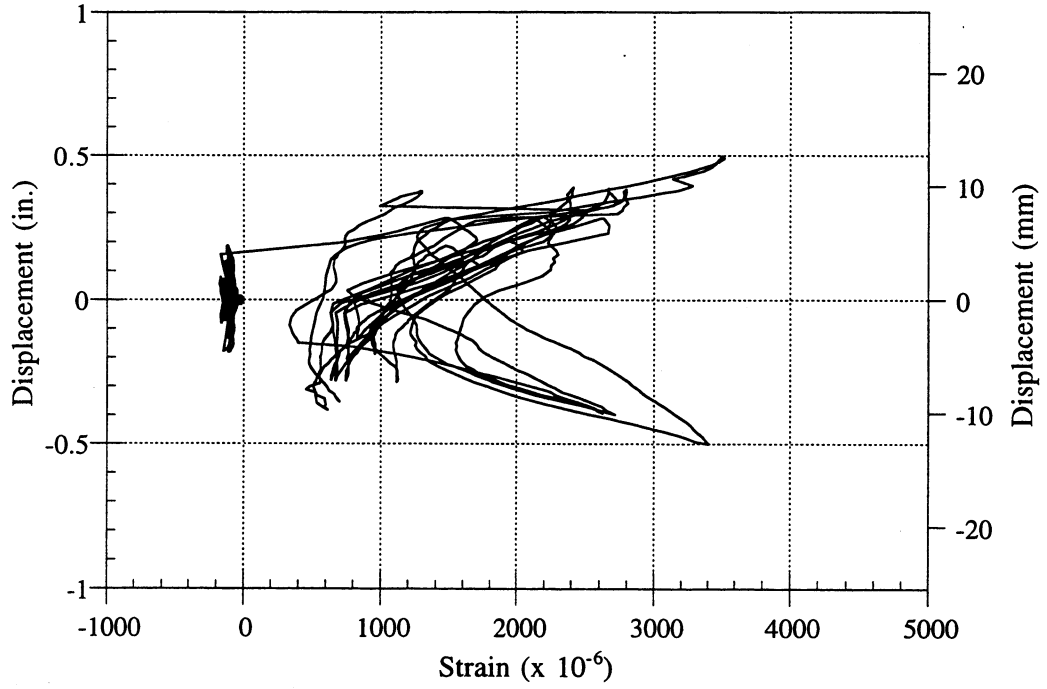

c) Gage 3NWC

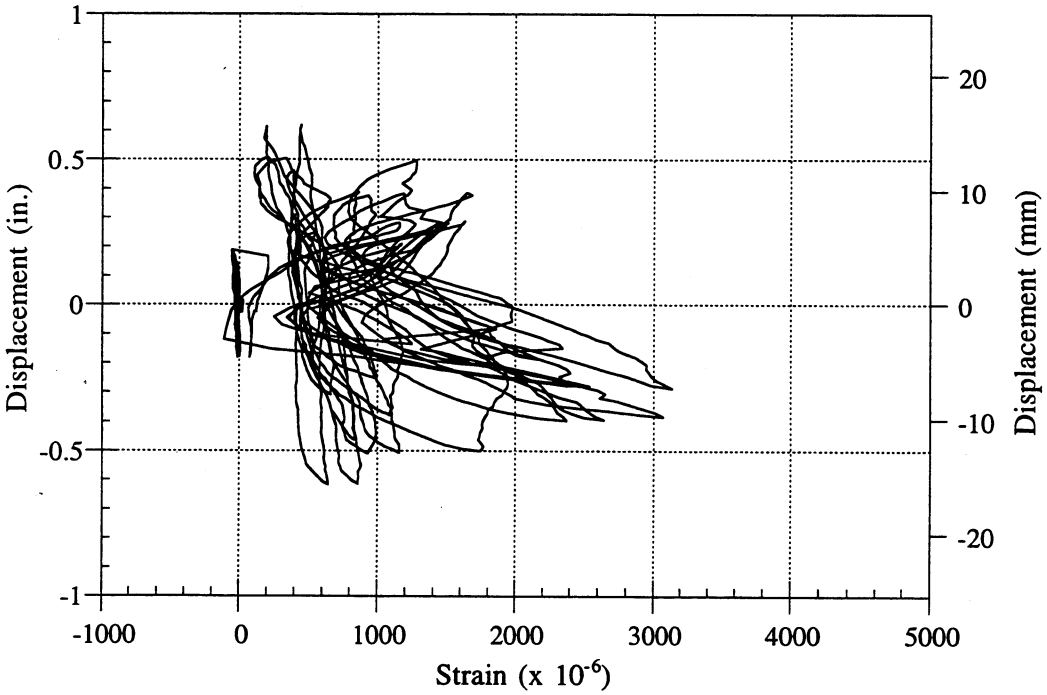

d) Gage 4NEC

Fig. 7.2.2 (Cont'd)

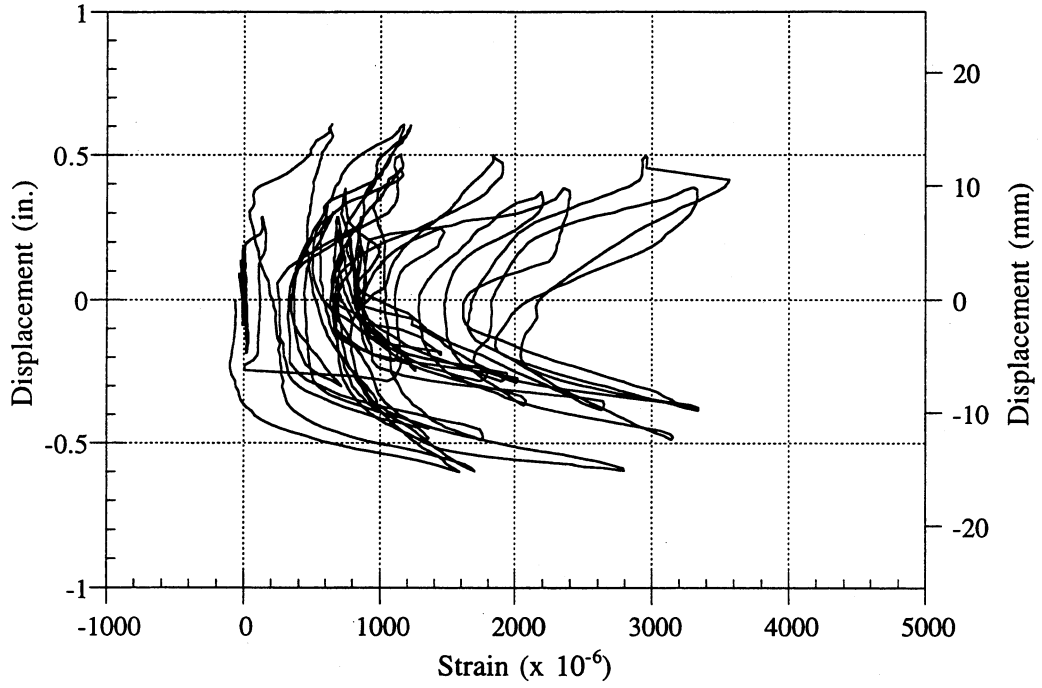

a) Gage 5SW

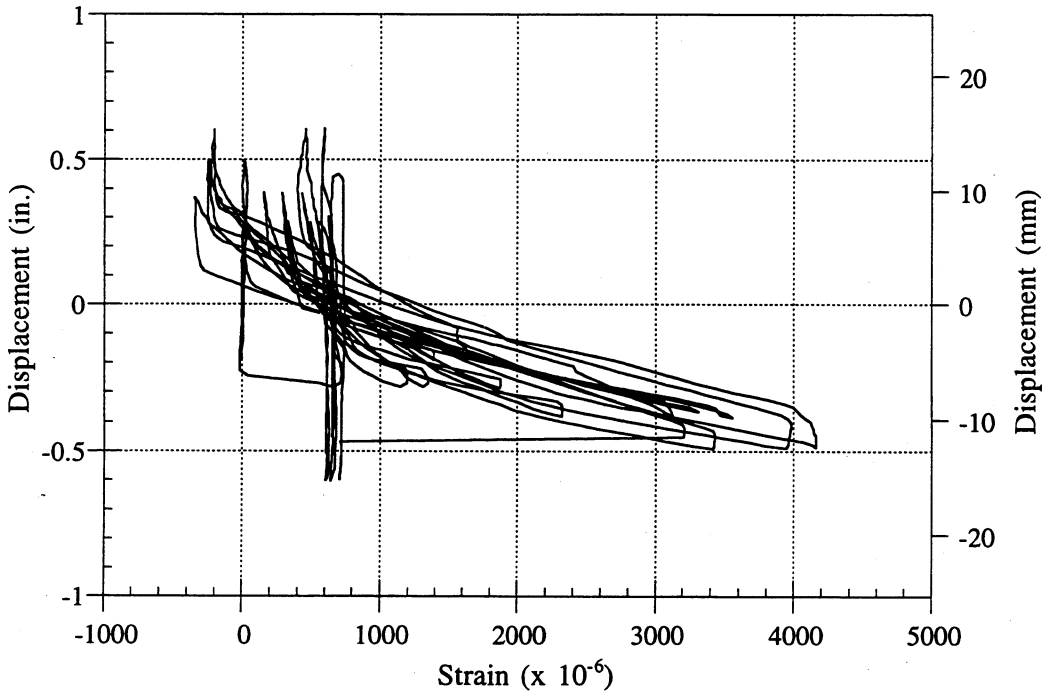

b) Gage 2SE

Fig. 7.2.3 Strains in Horizontal Grids vs. Lateral Drift in Wall Specimen 6

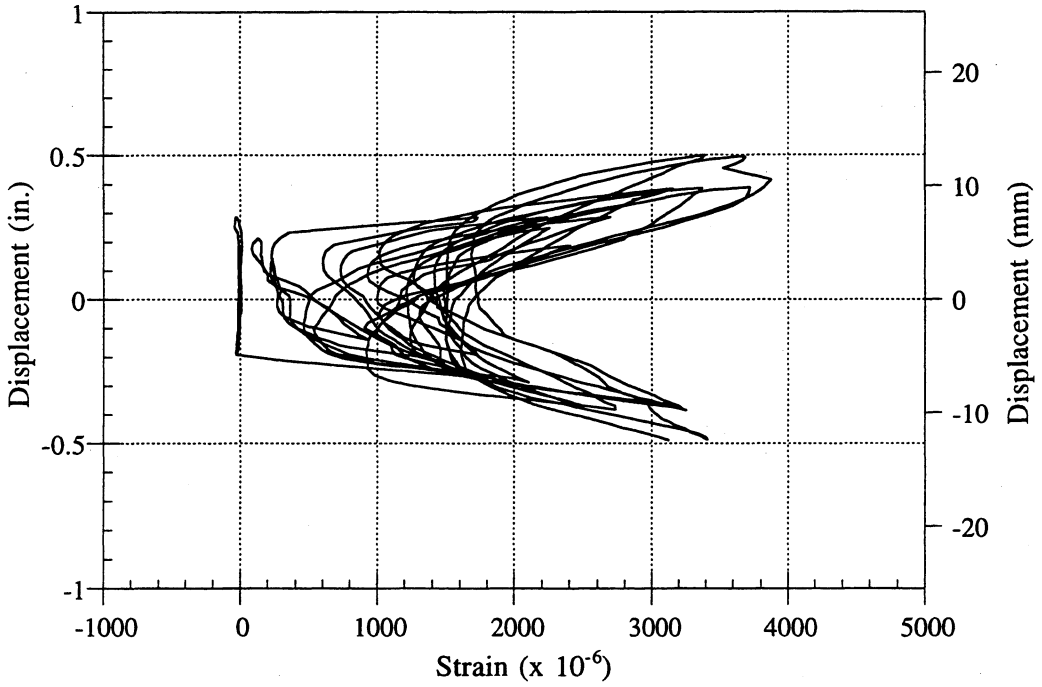

c) Gage 3NC

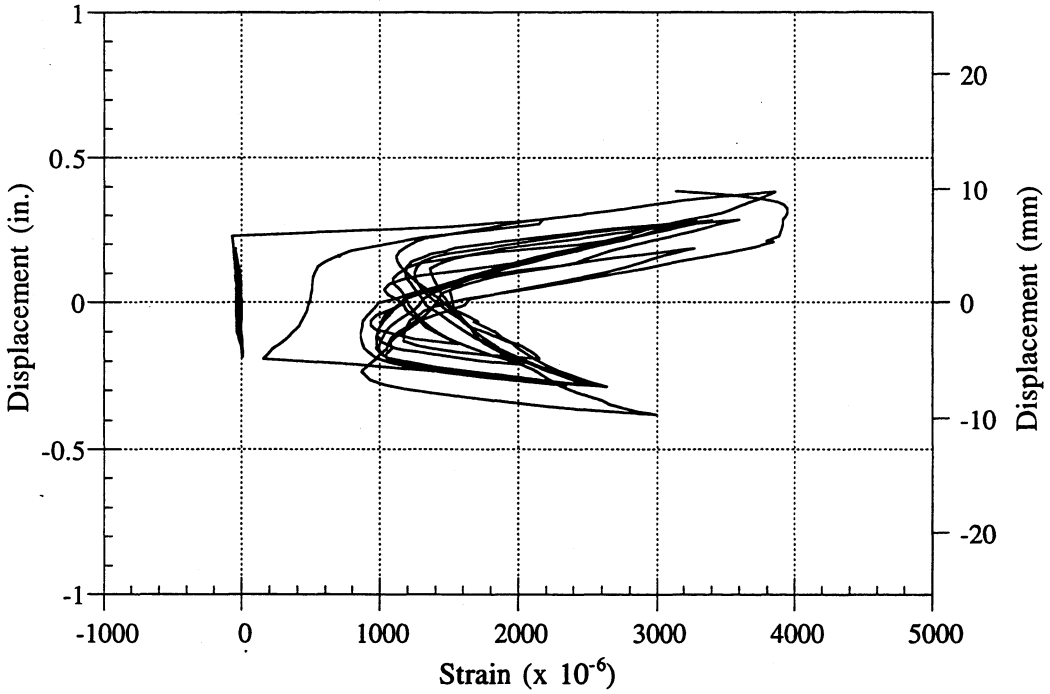

d) Gage 4NC

Fig. 7.2.3 (Cont'd)

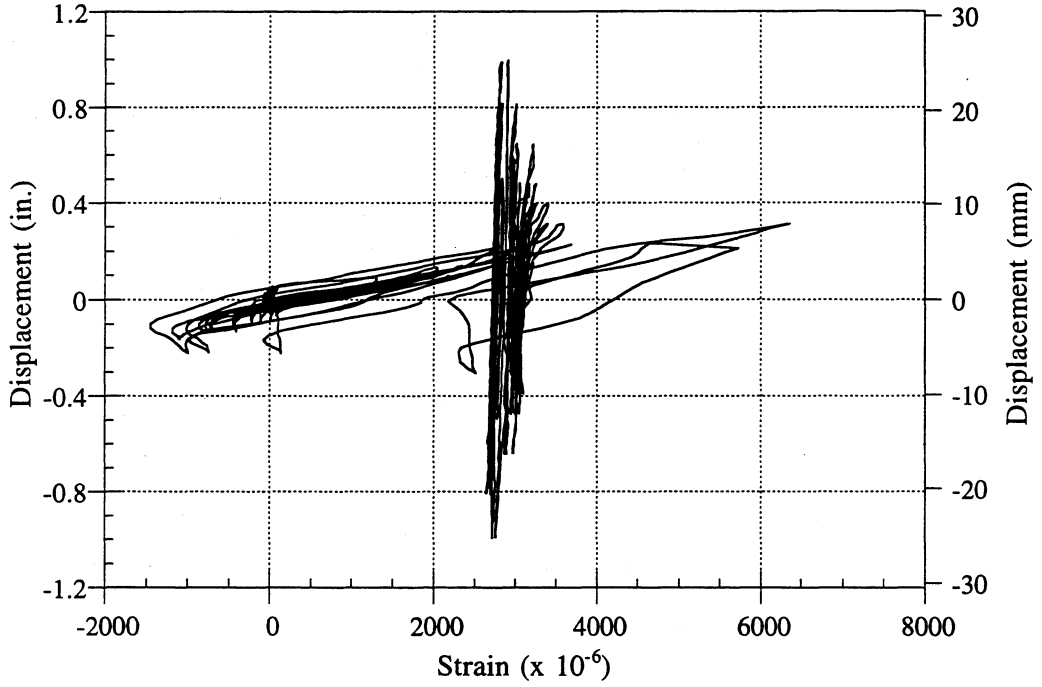

a) Gage 5SW

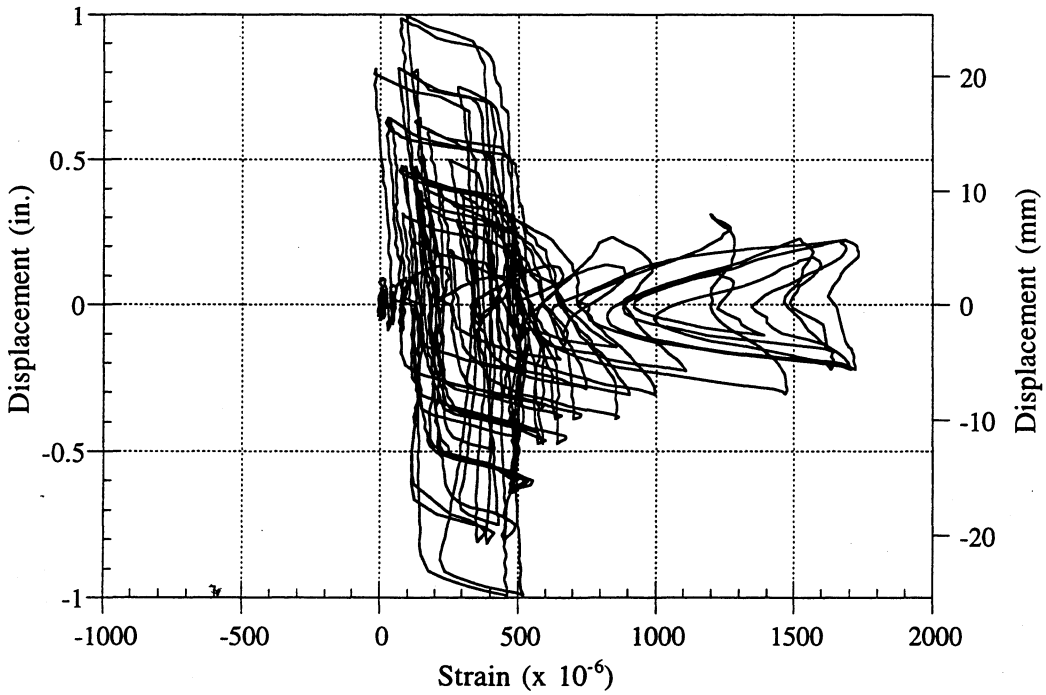

b) Gage 2NW

Fig. 7.2.4 Strains in Horizontal Grids vs. Lateral Drift in Wall Specimen 8

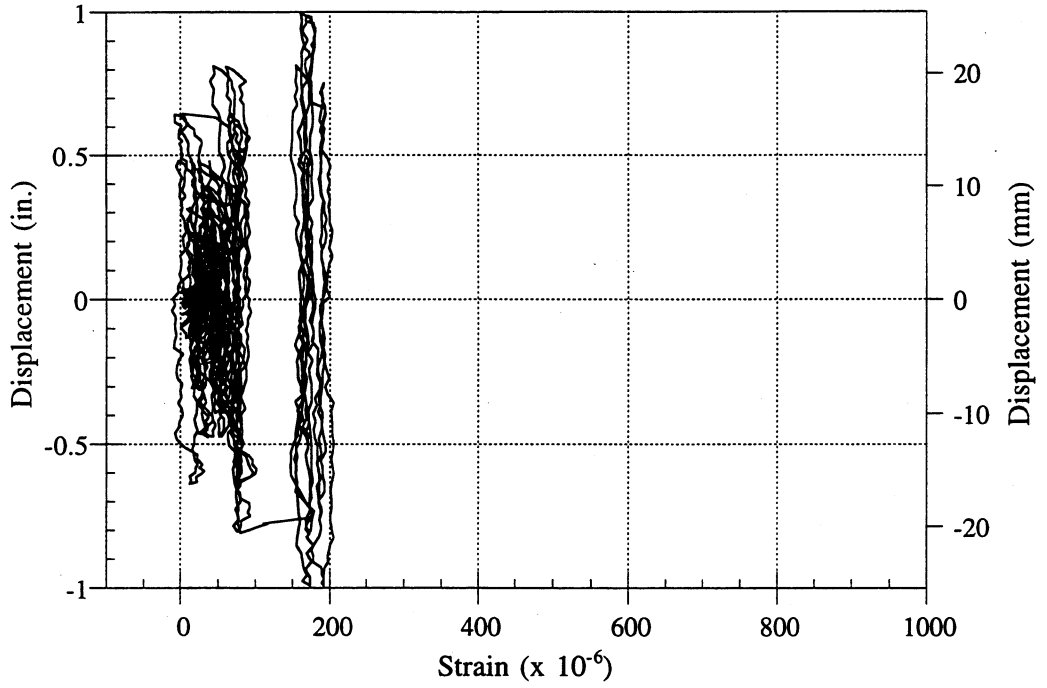

c) Gage 3SWC

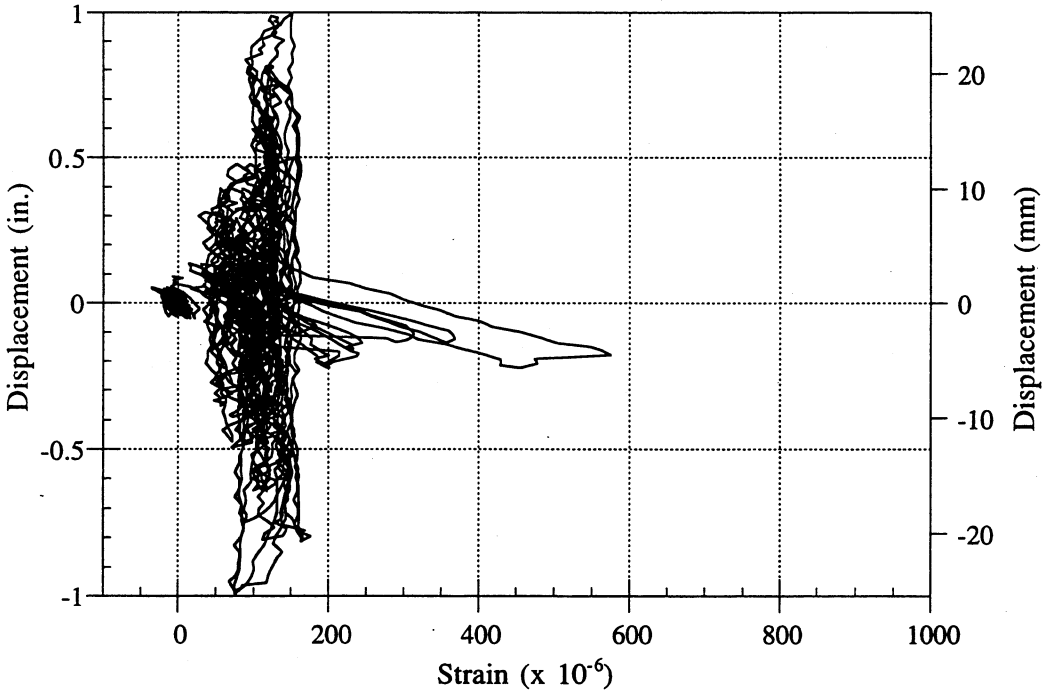

d) Gage 4NEC

Fig. 7.2.4 (Cont'd)

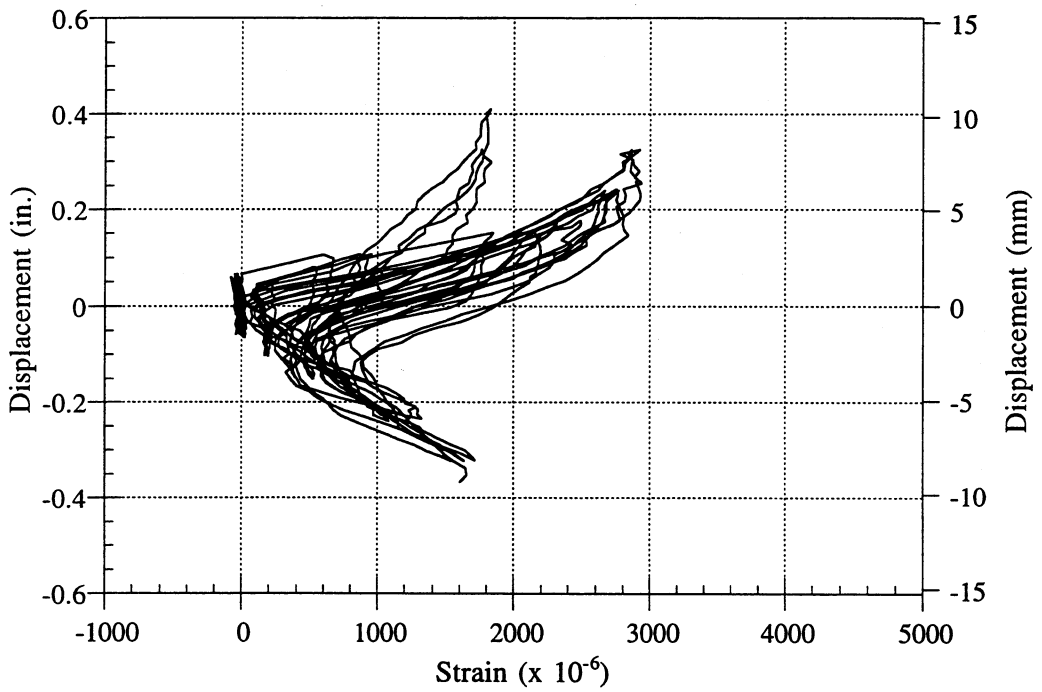

a) Gage 5NW

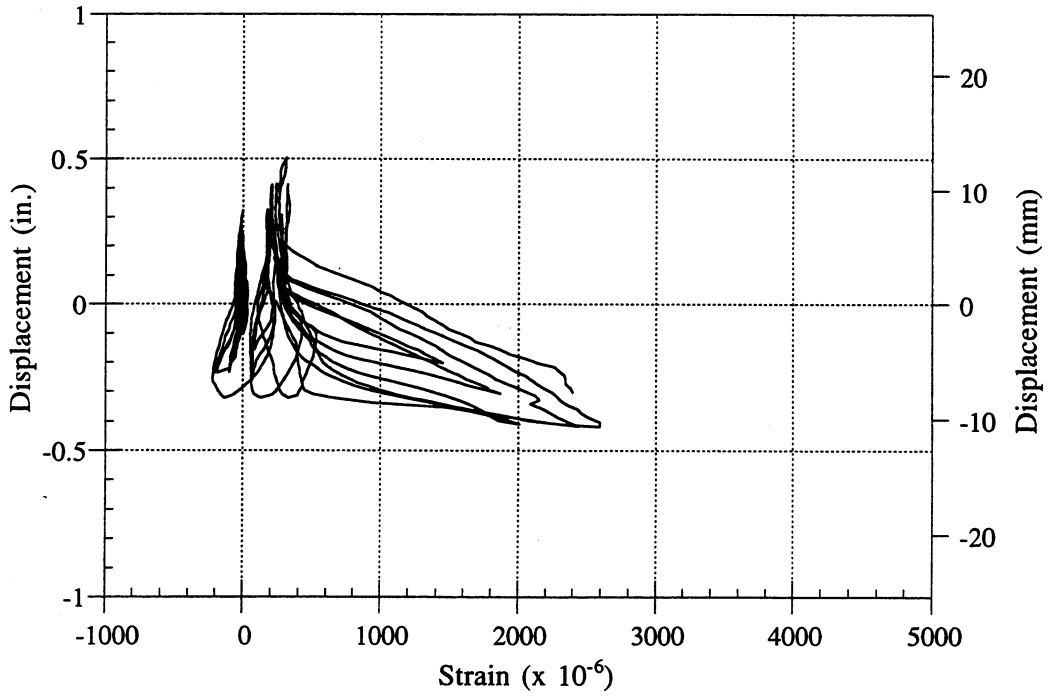

b) Gage 2NE

Fig. 7.2.5 Strains in Horizontal Grids vs. Lateral Drift in Wall Specimen 10

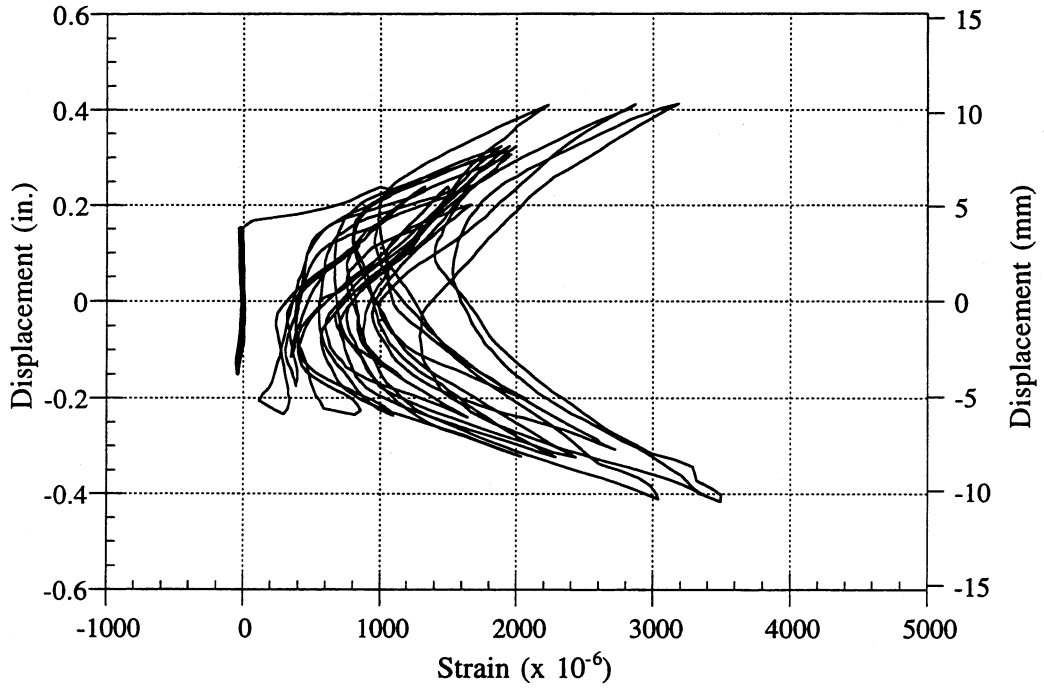

c) Gage 3NEC

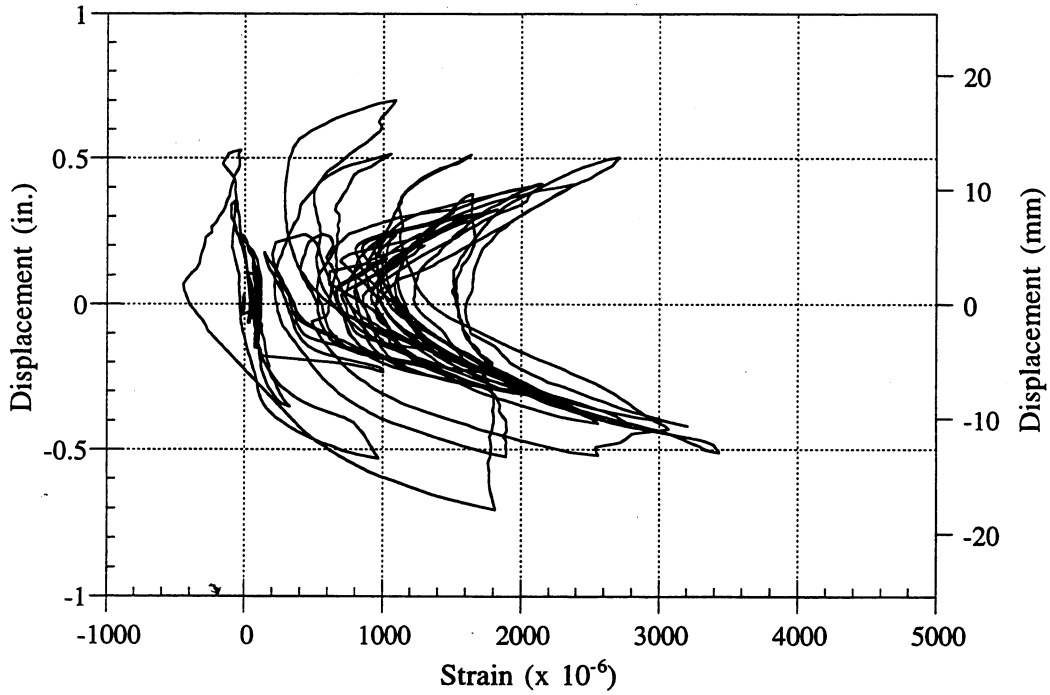

d) Gage 3SWC

Fig. 7.2.5 (Cont'd)

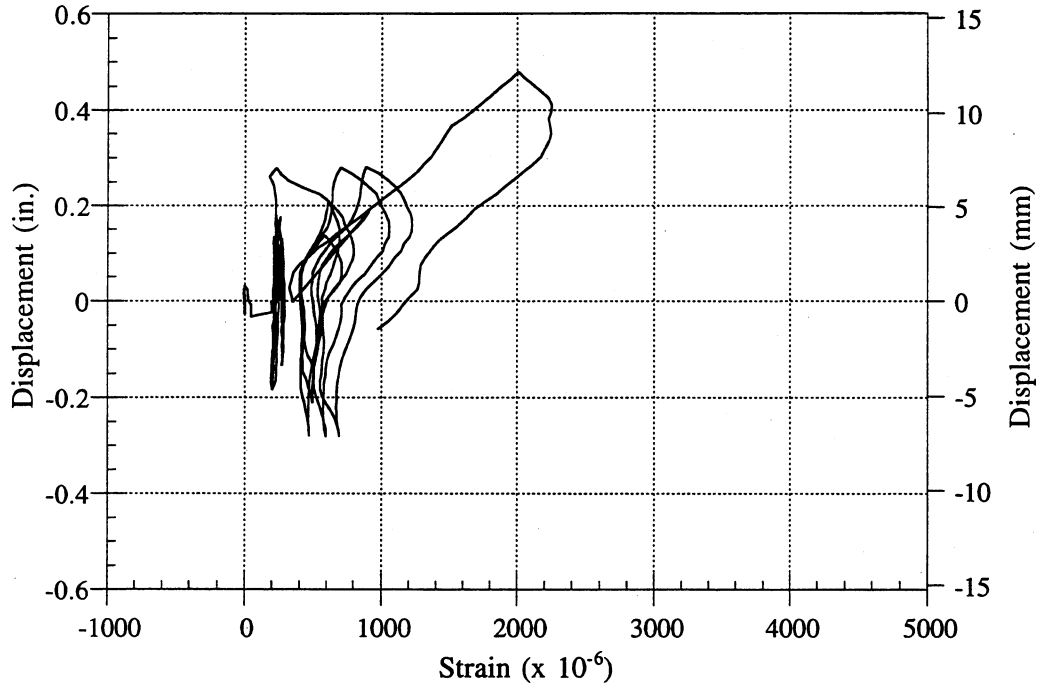

a) Gage 5NW

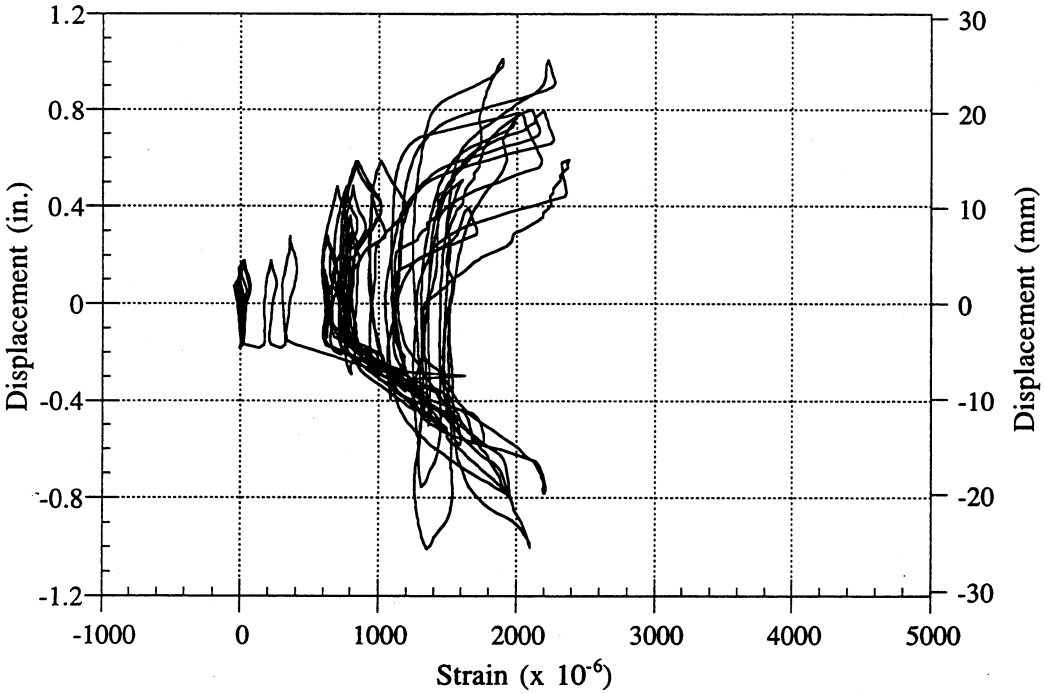

b) Gage 2NE

Fig. 7.2.6 Strains in Horizontal Grids vs. Lateral Drift in Wall Specimen 12

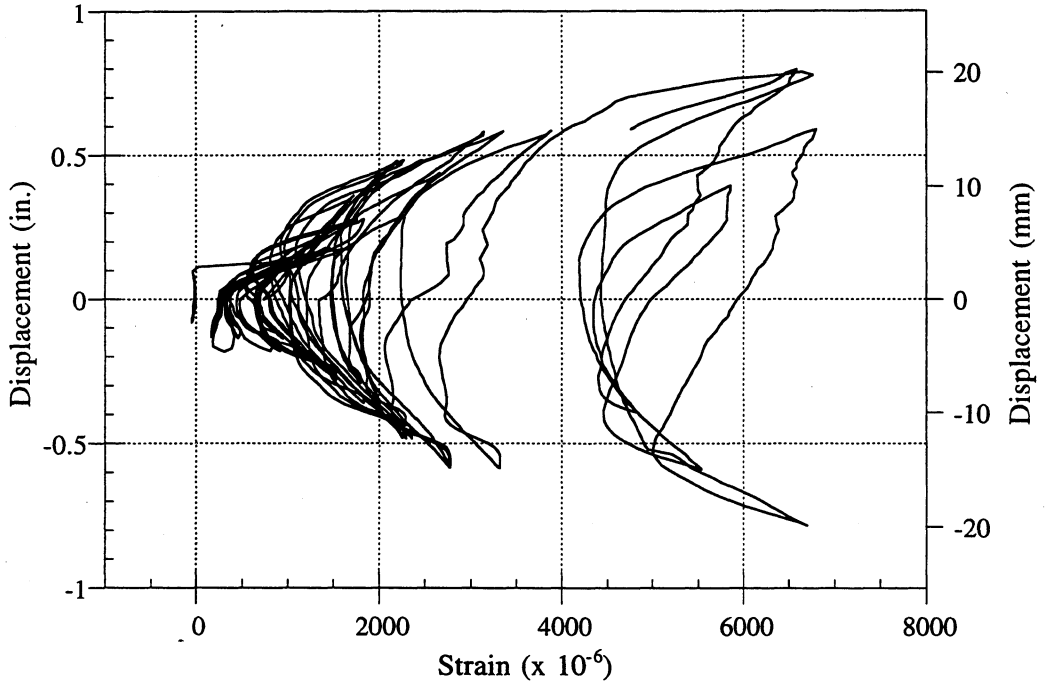

c) Gage 3NC

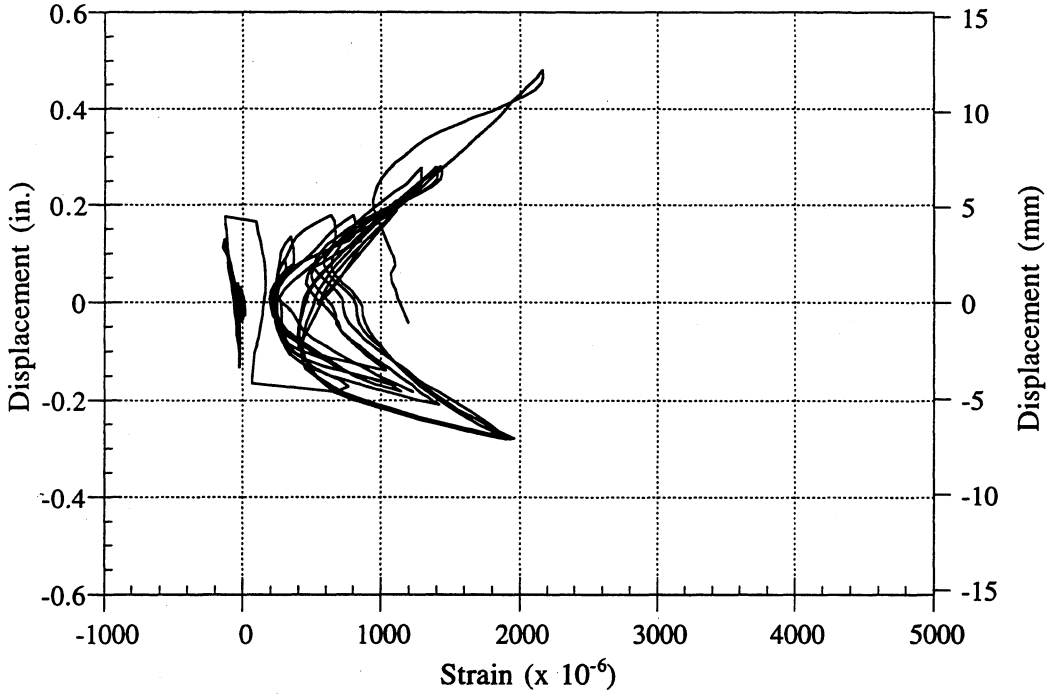

d) Gage 4NC

Fig. 7.2.6 (Cont'd)

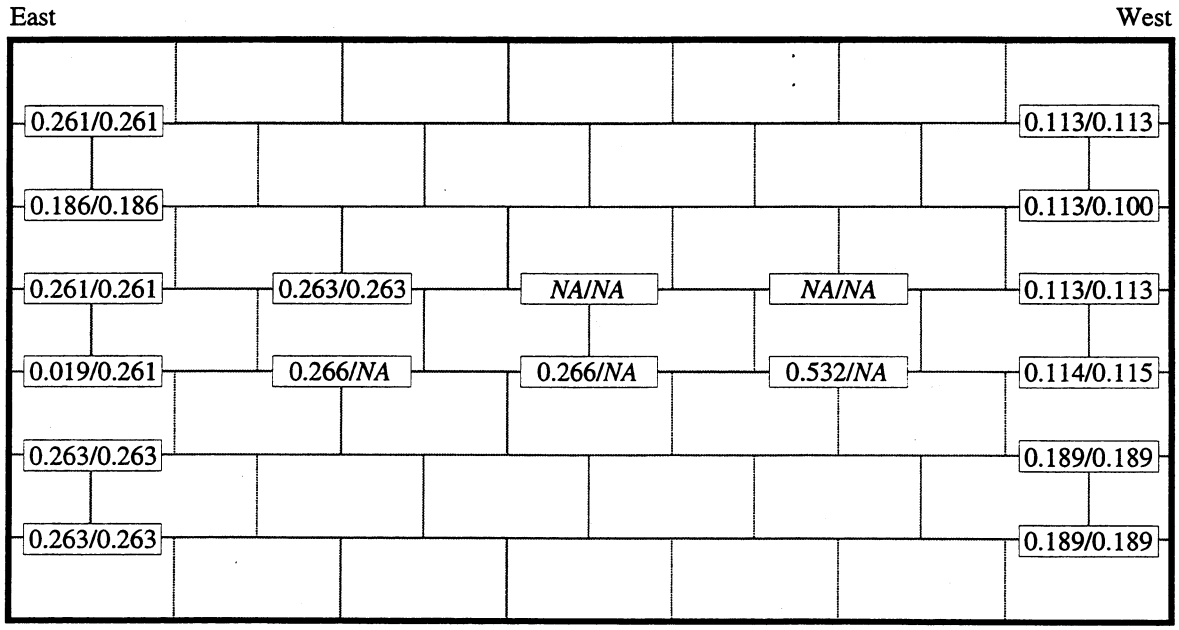

a) At tension threshold

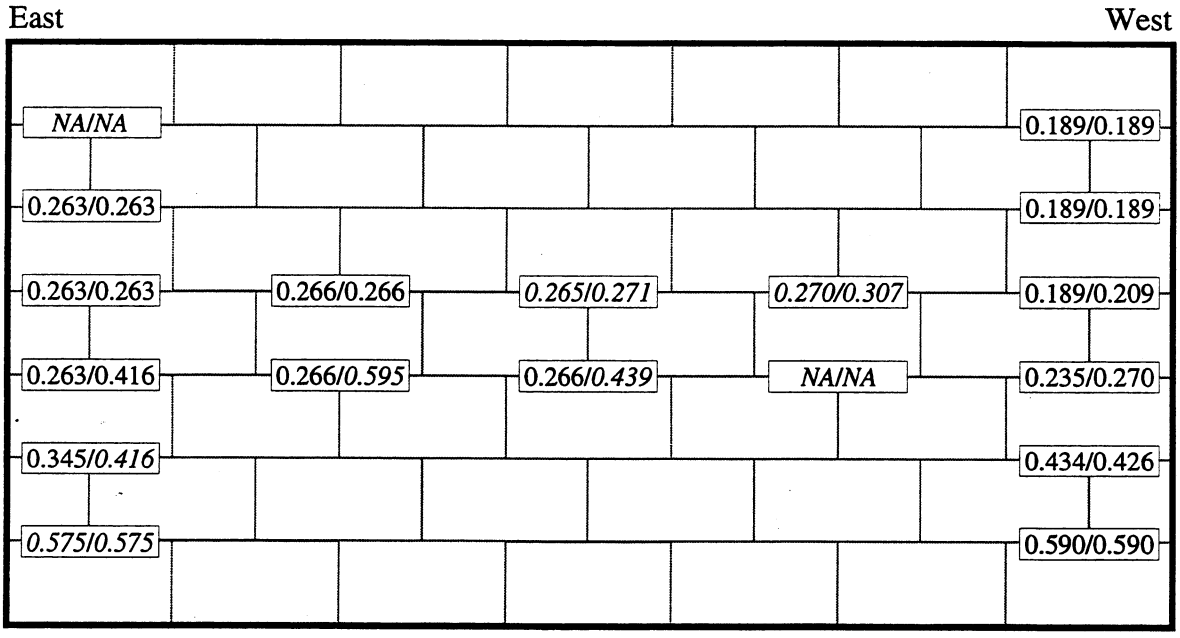

b) At first yield

Fig. 7.2.7 Drift Ratios (%) at Target Horizontal Reinforcement Strains for Wall Specimen 2

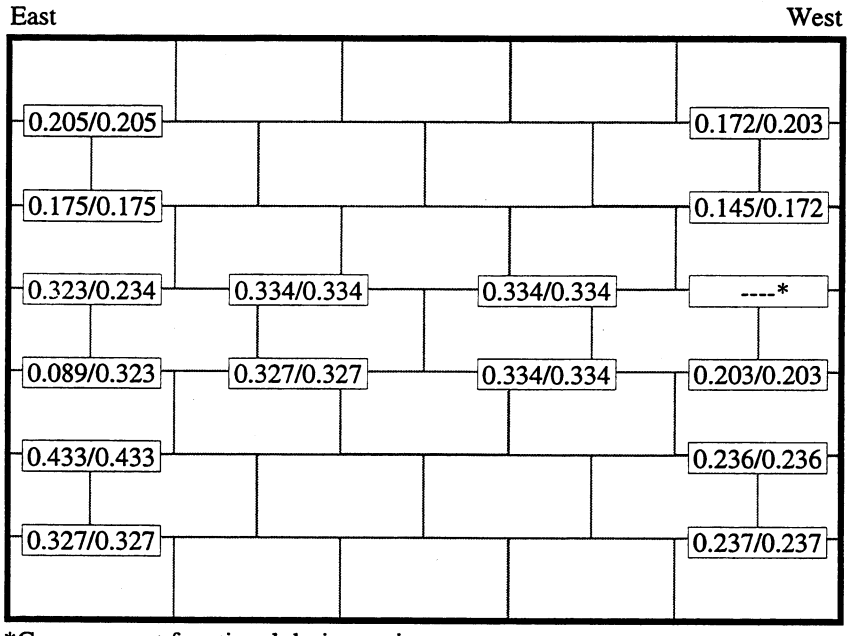

*Gage was not functional during entire test.

a) At tension threshold

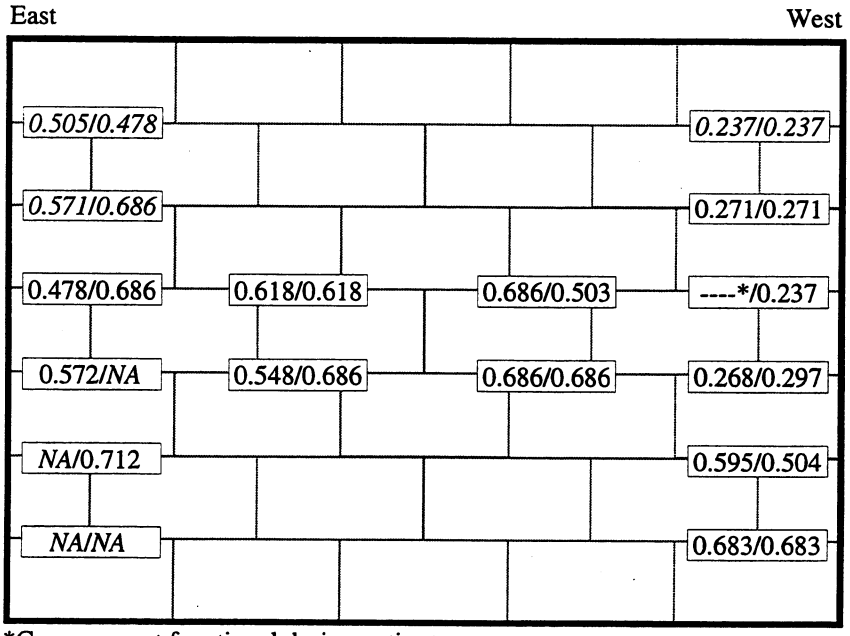

*Gage was not functional during entire test.

b) At first yield

Fig. 7.2.8 Drift Ratios (%) at Target Horizontal Reinforcement Strains for Wall Specimen 4

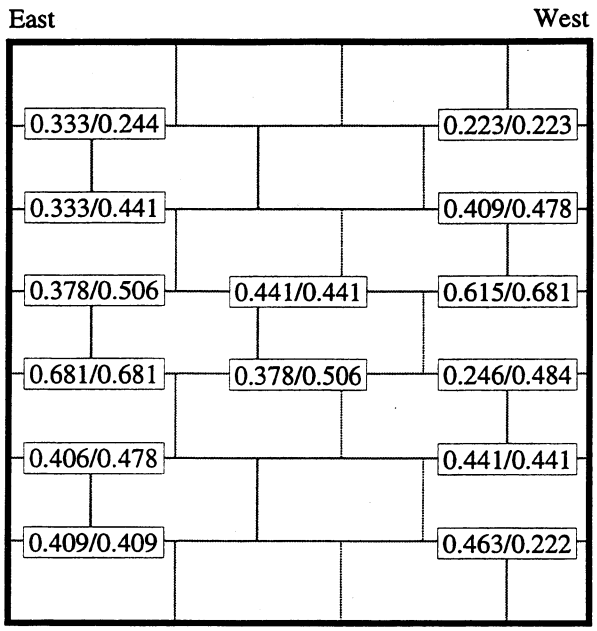

a) At tension threshold

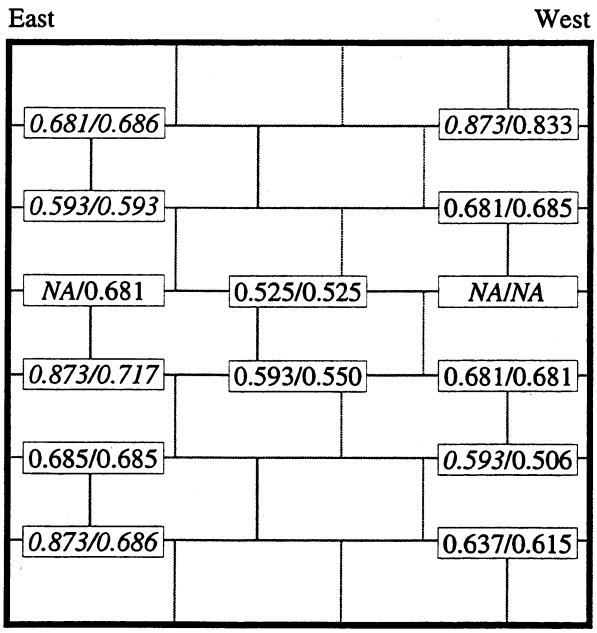

b) At first yield

Fig. 7.2.9 Drift Ratios (%) at Target Horizontal Reinforcement Strains for Wall Specimen 6

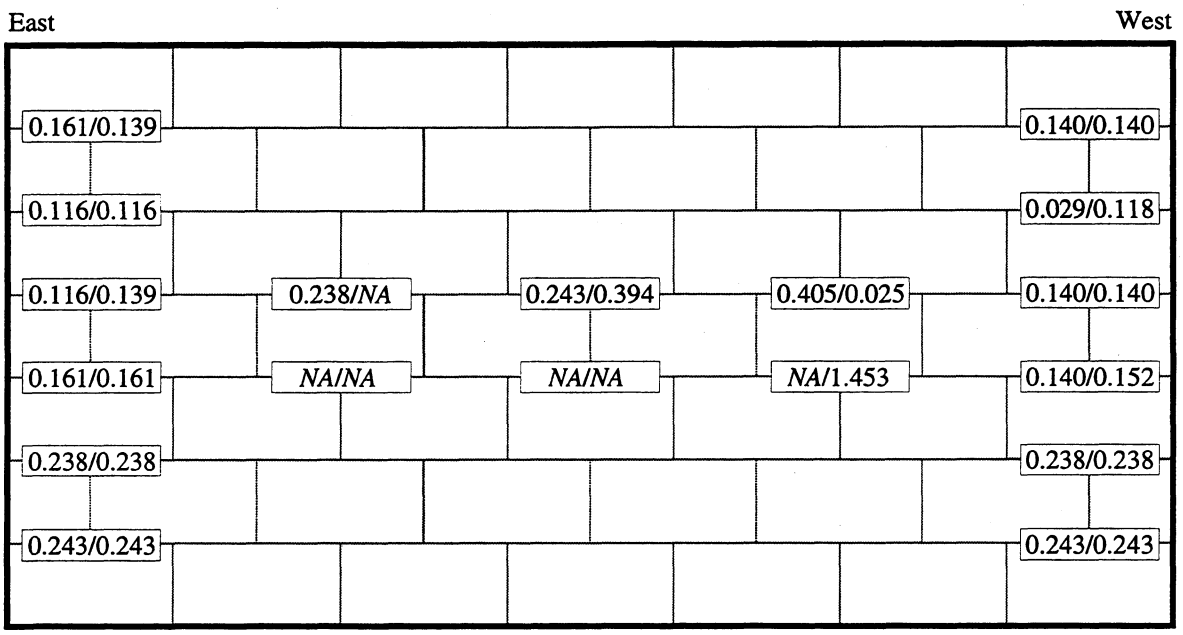

a) At tension threshold

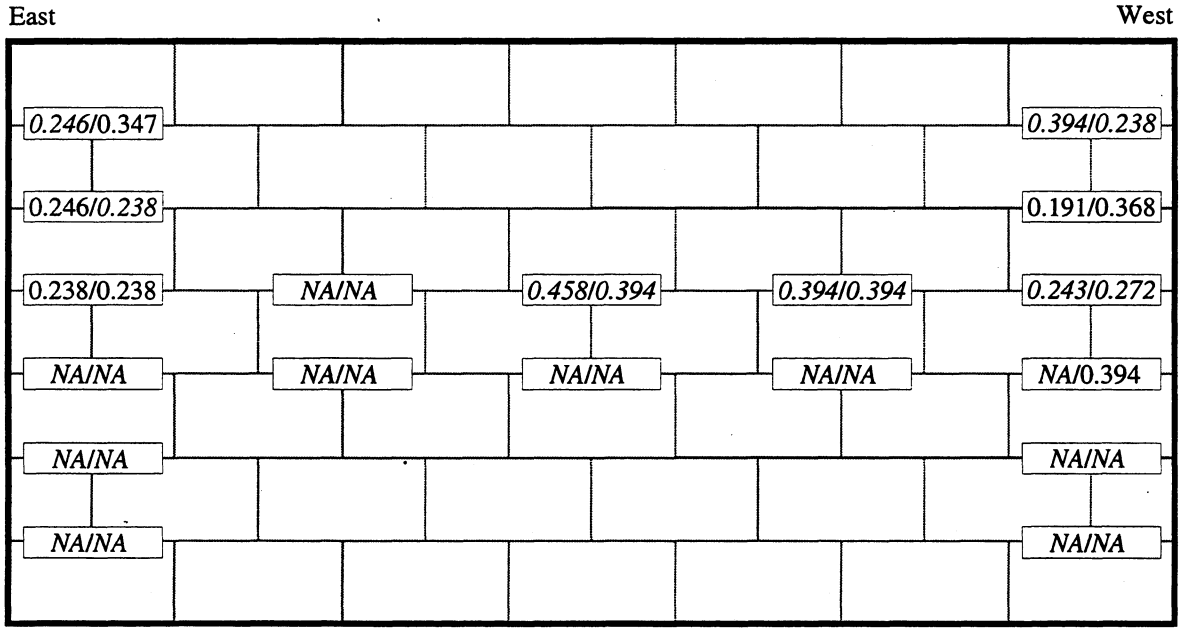

b) At first yield

Fig. 7.2.10 Drift Ratios (%) at Target Horizontal Reinforcement Strains for Wall Specimen 8

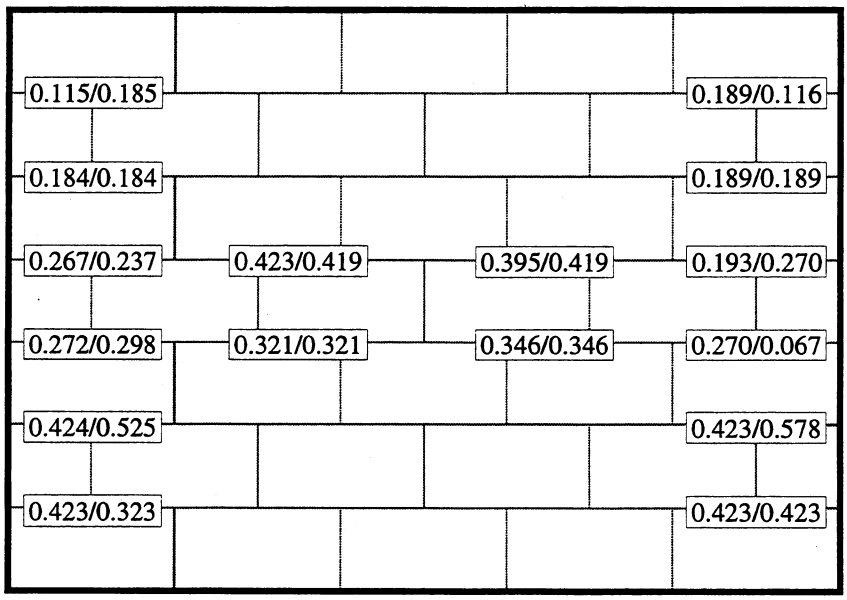

a) At tension threshold

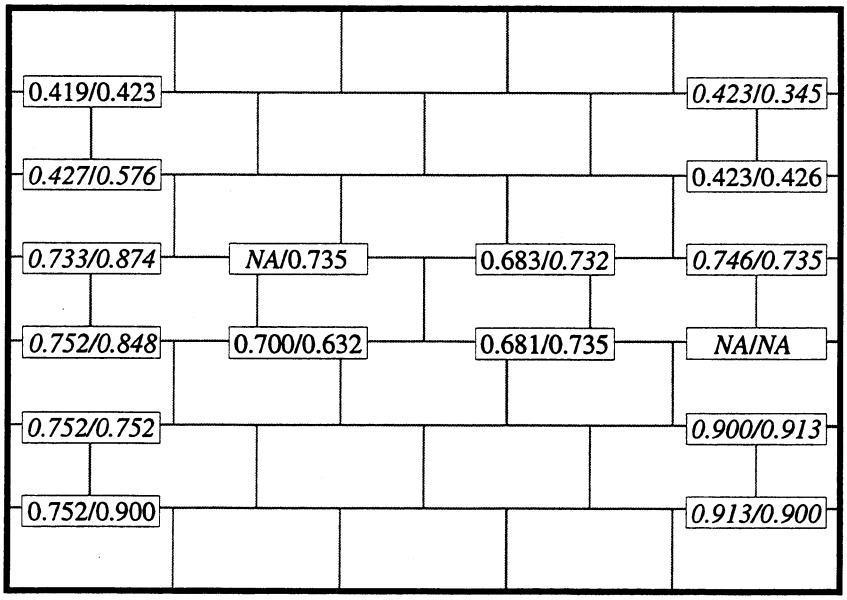

b) At first yield

Fig. 7.2.11 Drift Ratios (%) at Target Horizontal Reinforcement Strains for Wall Specimen 10

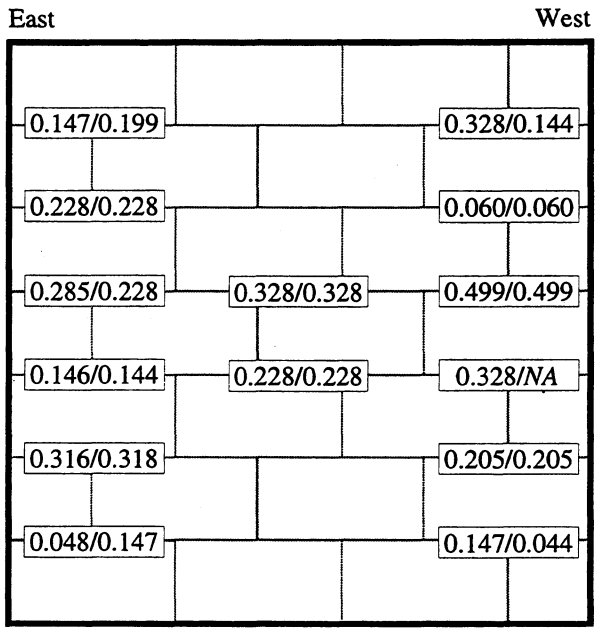

a) At tension threshold

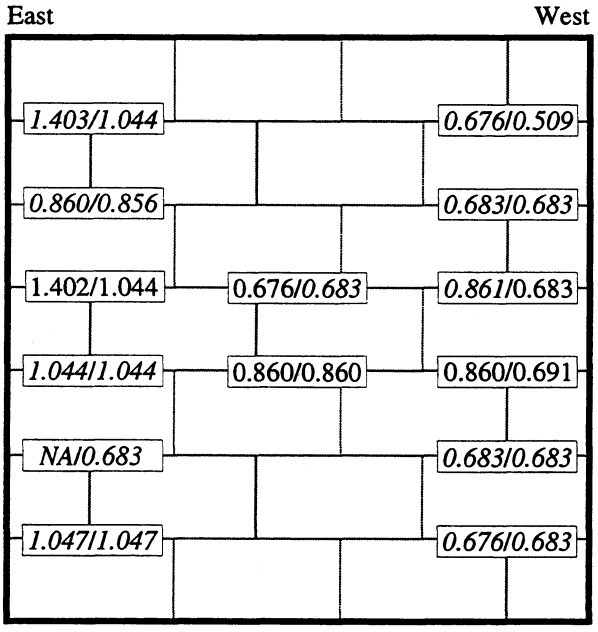

b) At first yield

Fig. 7.2.12 Drift Ratios (%) at Target Horizontal Reinforcement Strains for Wall Specimen 12

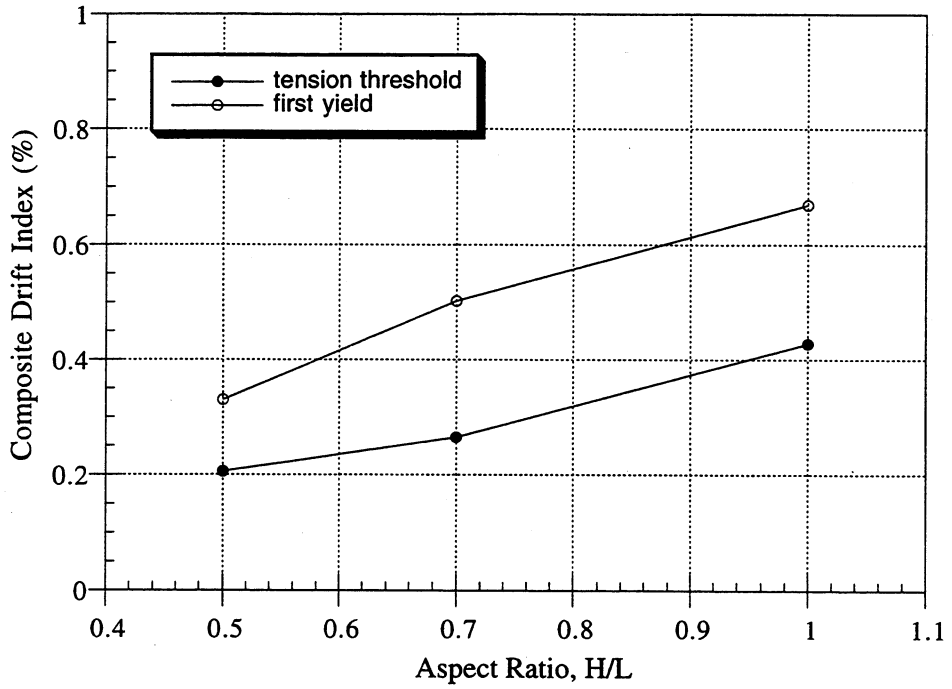

a) $\rho_h = 0.05\%$

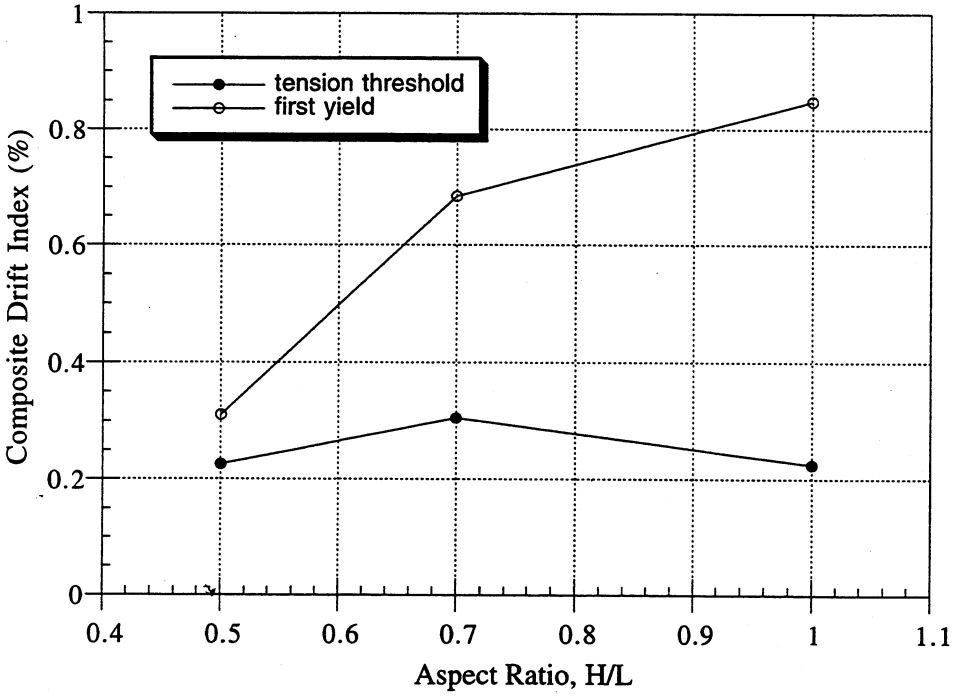

b) $\rho_h = 0.12\%$

Fig. 7.2.13 Influence of Aspect Ratio on Net Composite Drift Indices for Horizontal Reinforcement Strains

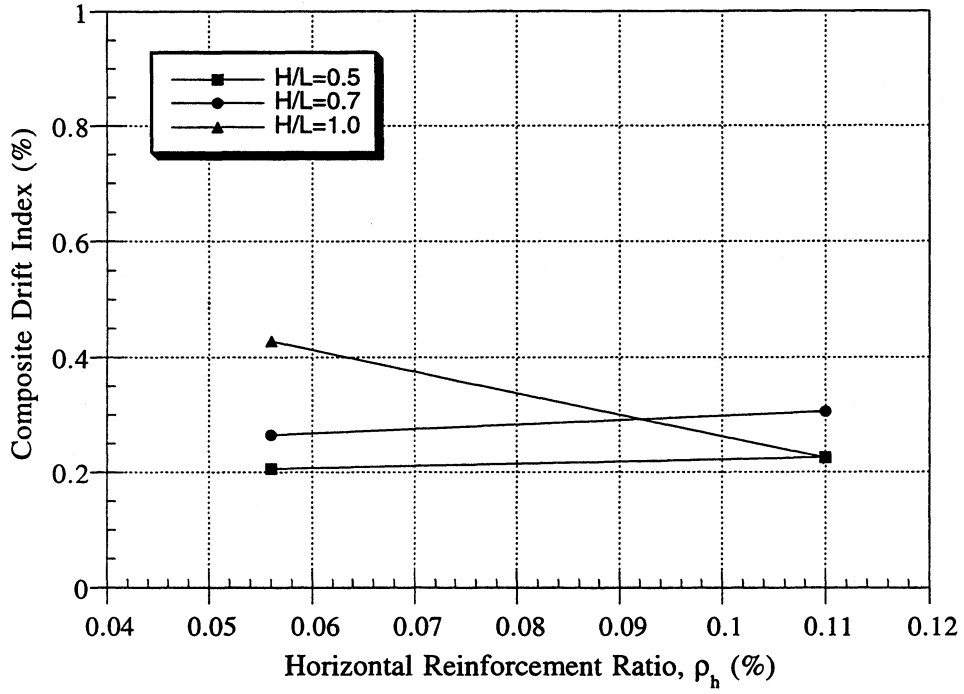

a) Tension Threshold

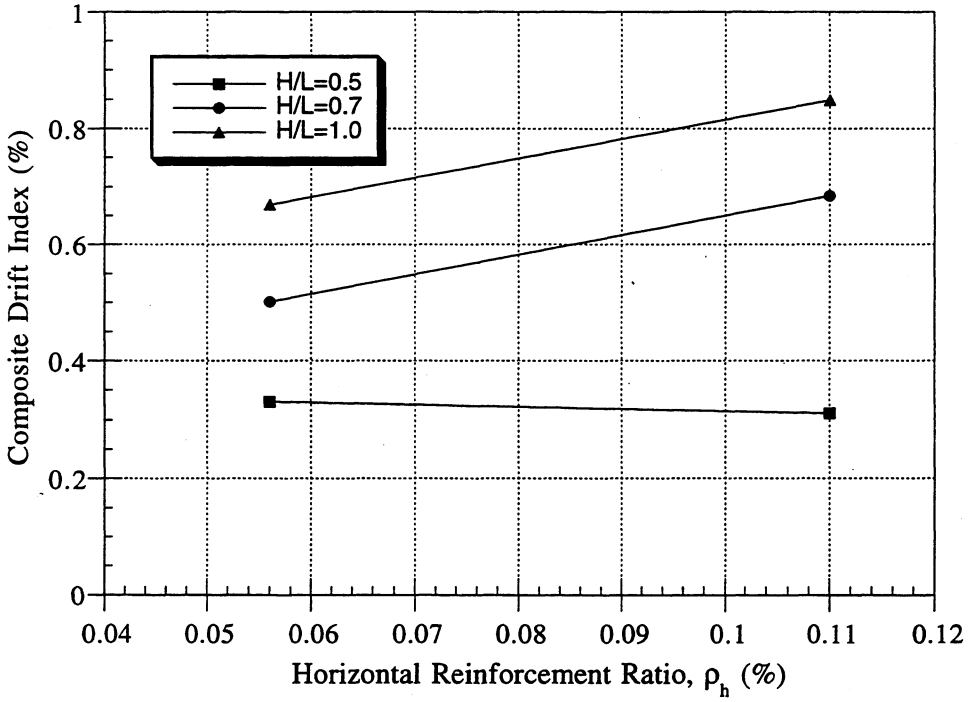

b) First Yield

Fig. 7.2.14 Influence of Reinforcement Ratio on Net Composite Drift Indices for Horizontal Reinforcement Strains

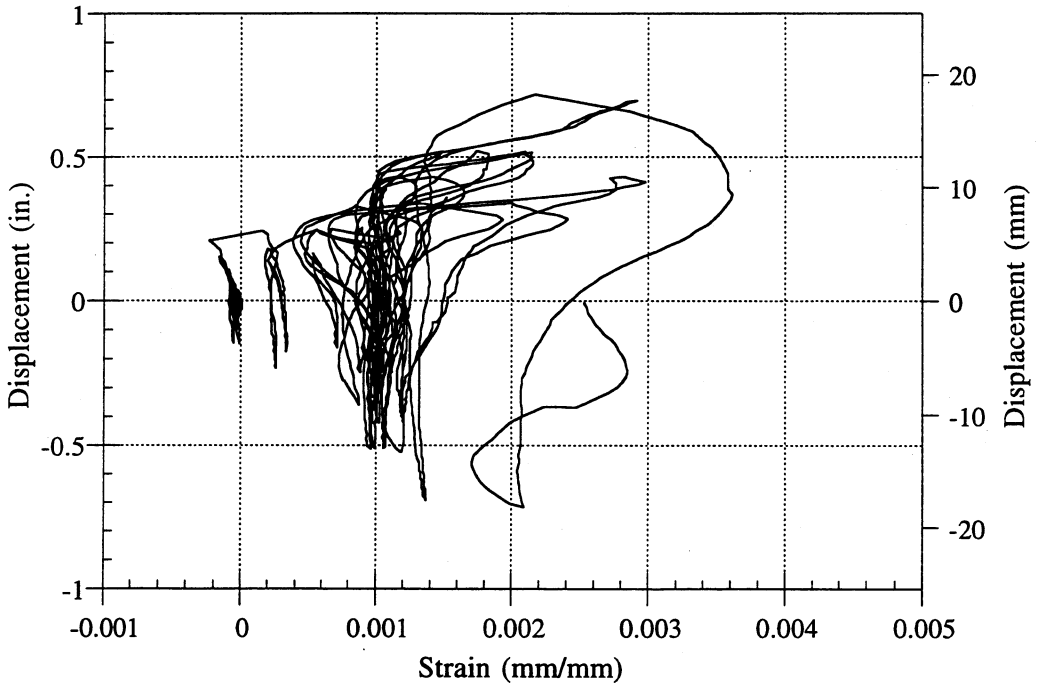

a) Transducer LOVE

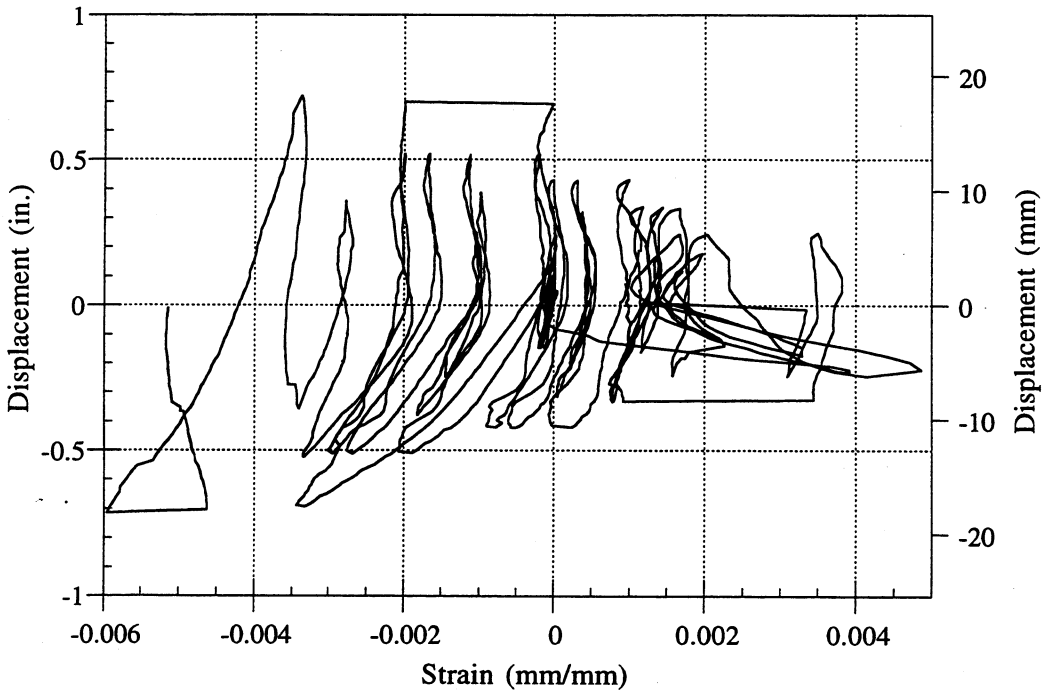

b) Transducer NEAL

Fig. 7.3.1 Masonry Surface Strains vs. Lateral Drift in Wall Specimen 2

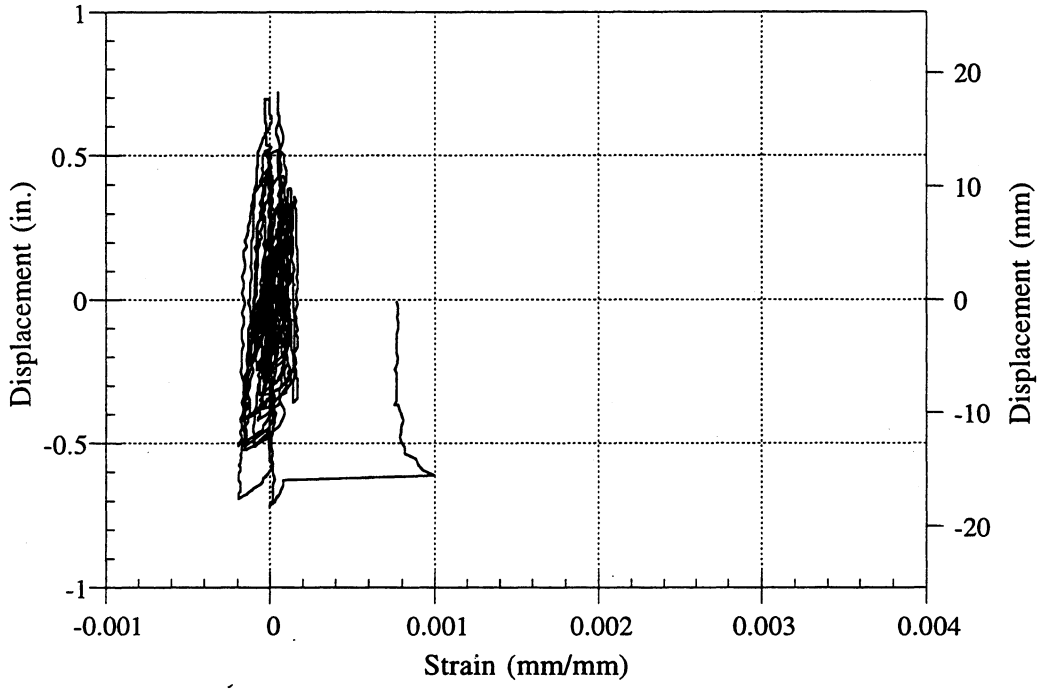

c) Transducer HARRY

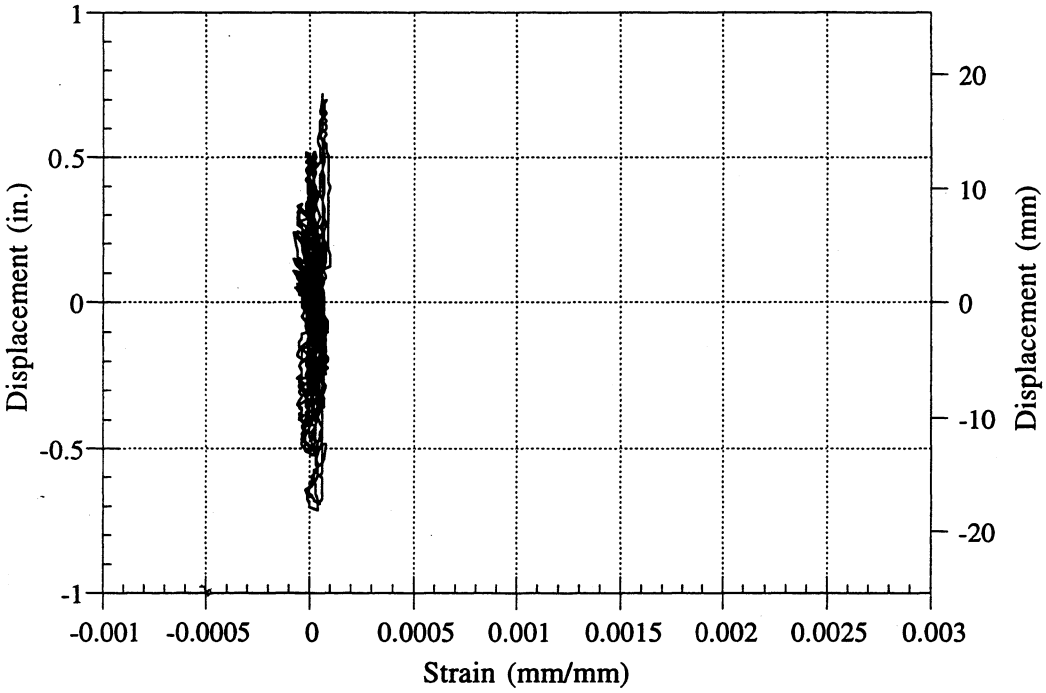

d) Transducer IVAN

Fig. 7.3.1 (Cont'd)

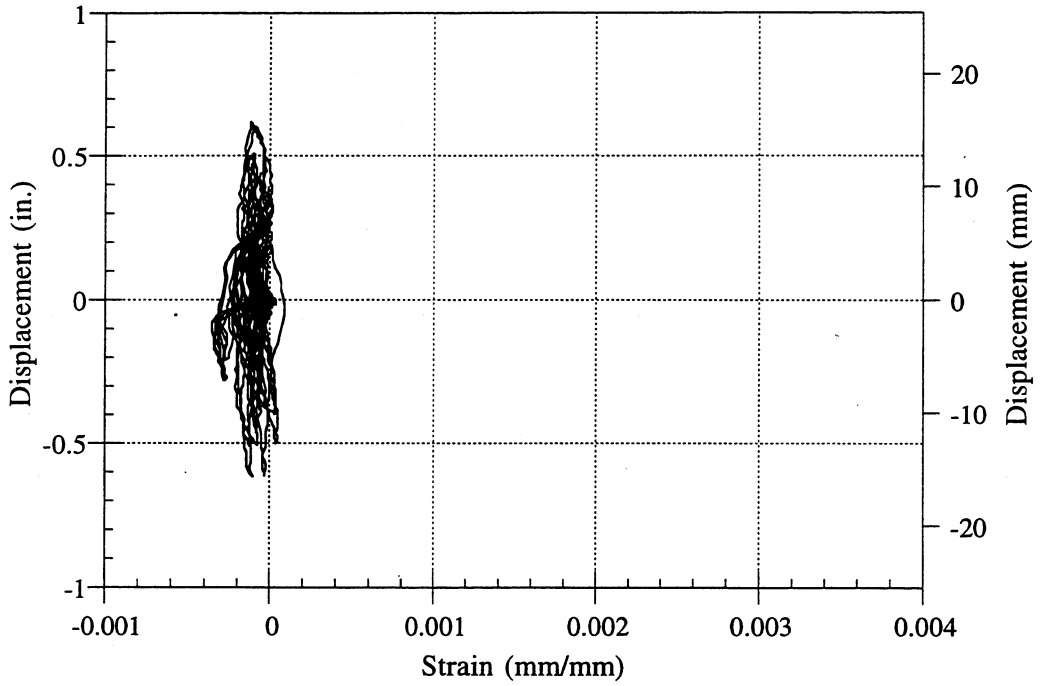

a) Transducer LOVE

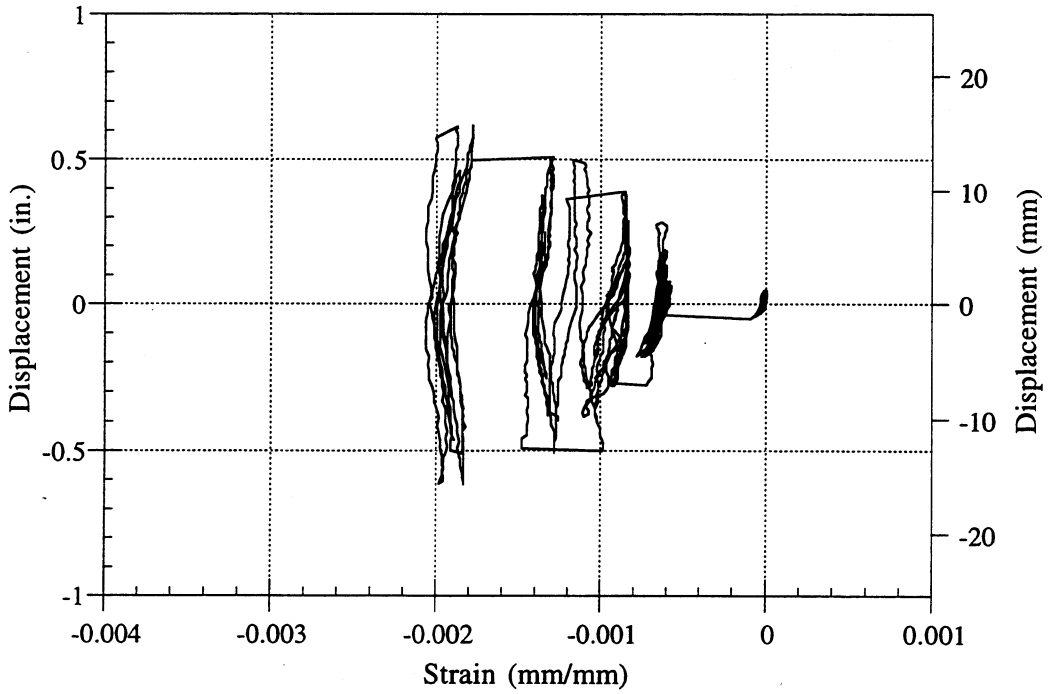

b) Transducer NEAL

Fig. 7.3.2 Masonry Surface Strains vs. Lateral Drift in Wall Specimen 4

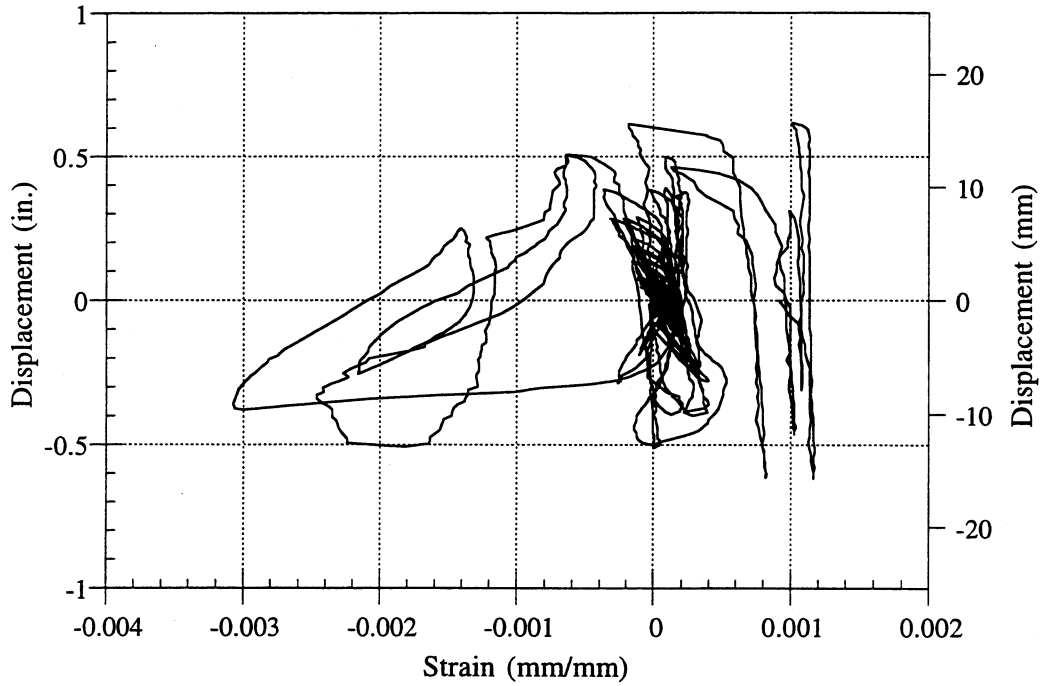

c) Transducer JANE

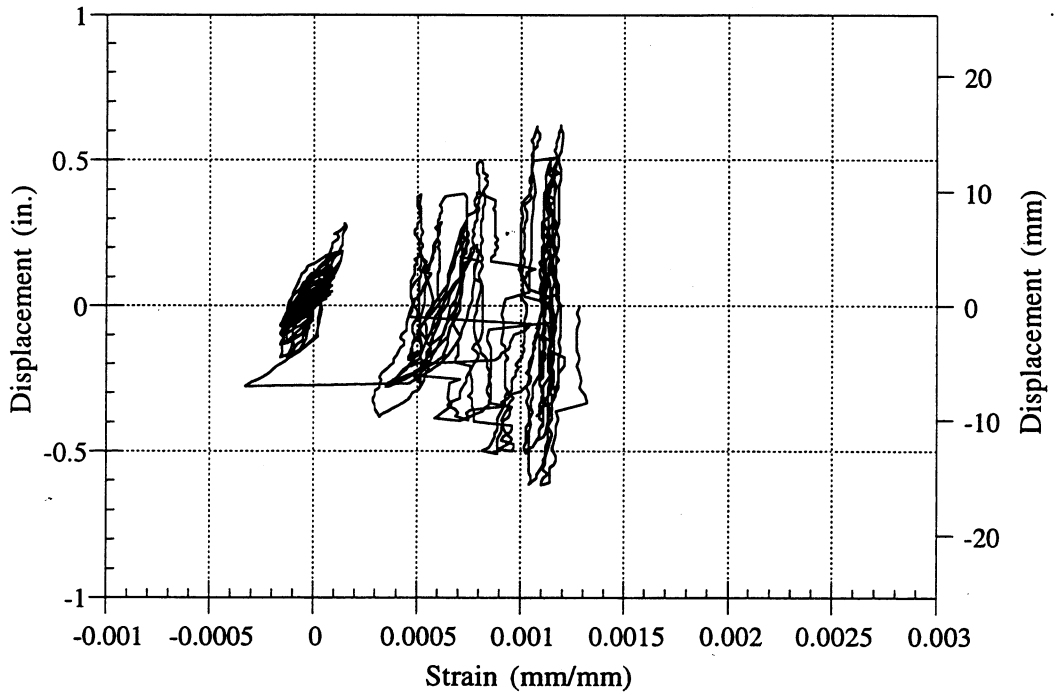

d) Transducer KING

Fig. 7.3.2 (Cont'd)

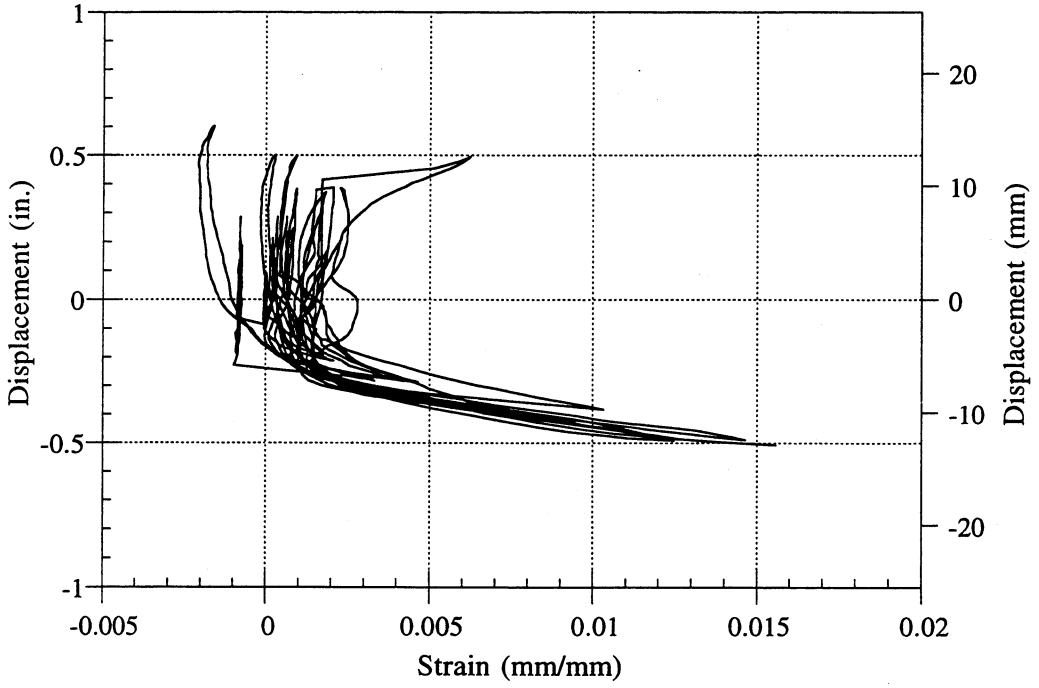

a) Transducer ALPHA

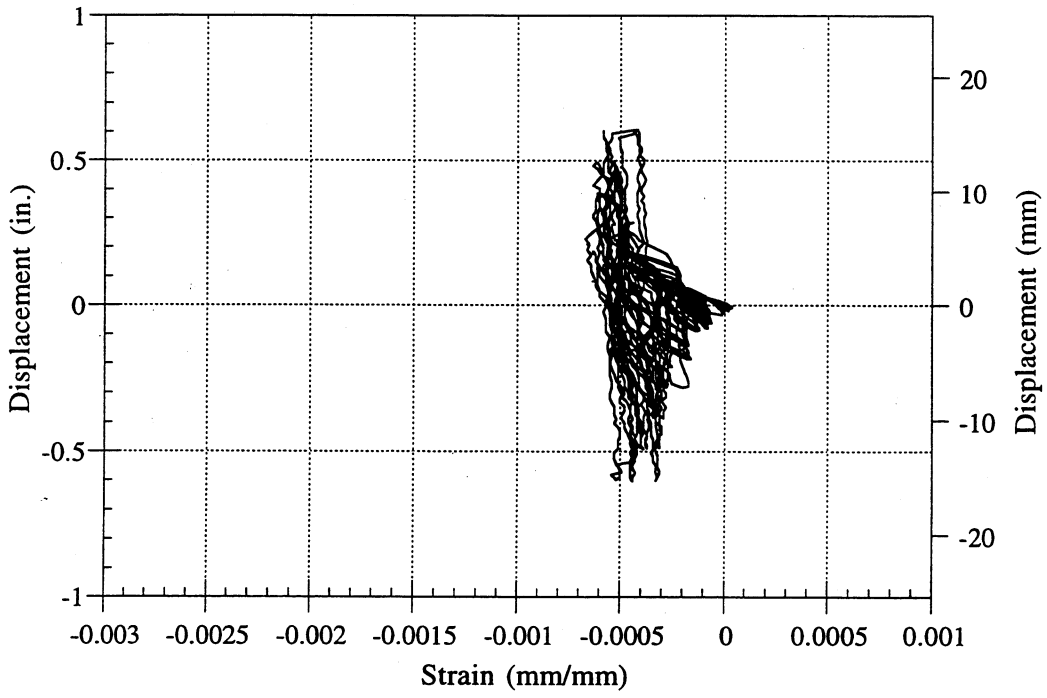

b) Transducer CATHY

Fig. 7.3.3 Masonry Surface Strains vs. Lateral Drift in Wall Specimen 6

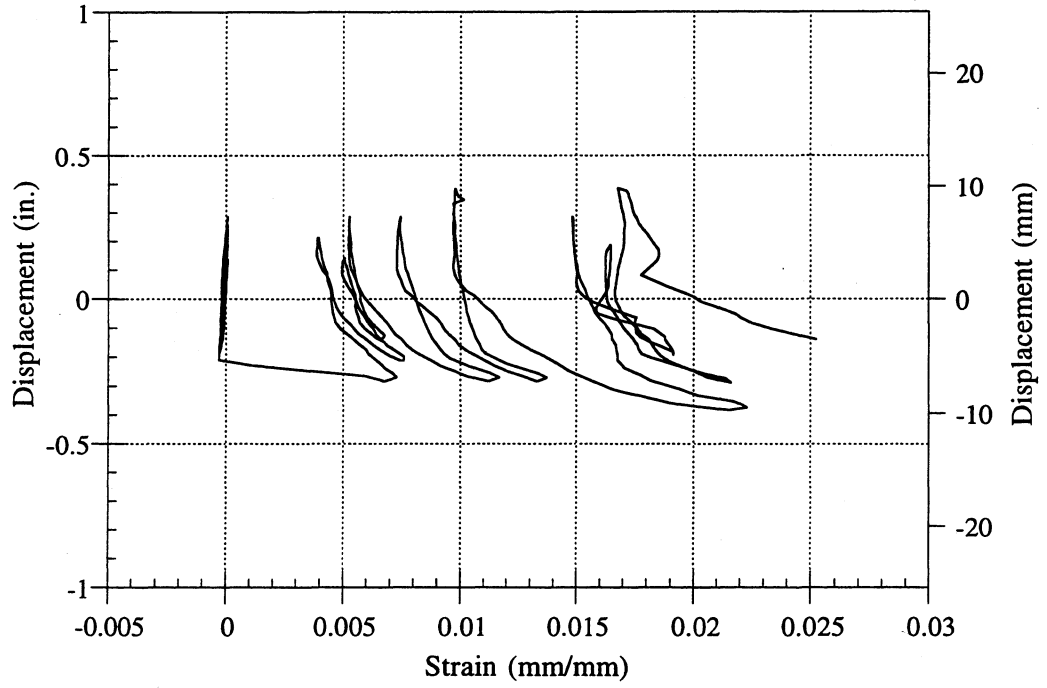

c) Transducer DOG

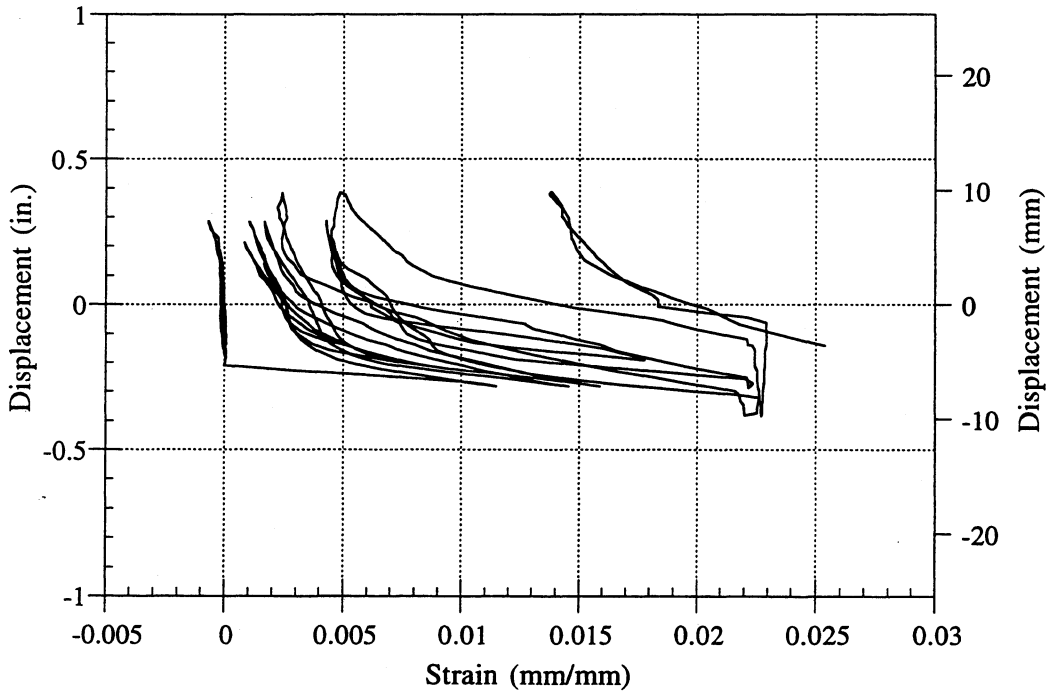

d) Transducer ED

Fig. 7.3.3 (Cont'd)

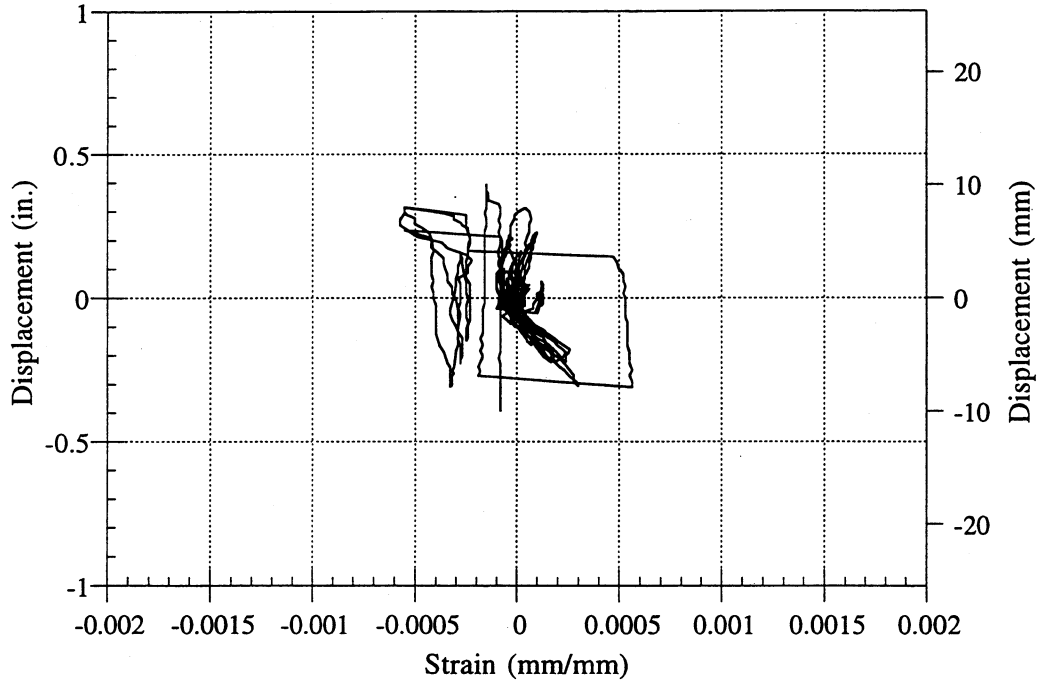

a) Transducer ALPHA

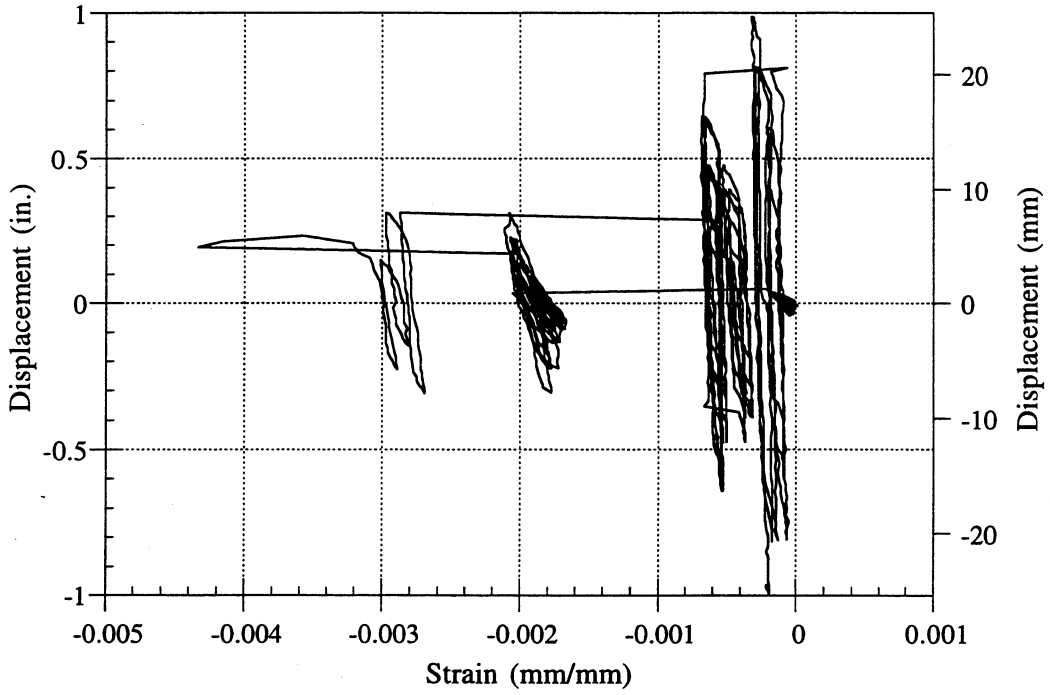

b) Transducer CATHY

Fig. 7.3.4 Masonry Surface Strains vs. Lateral Drift in Wall Specimen 8

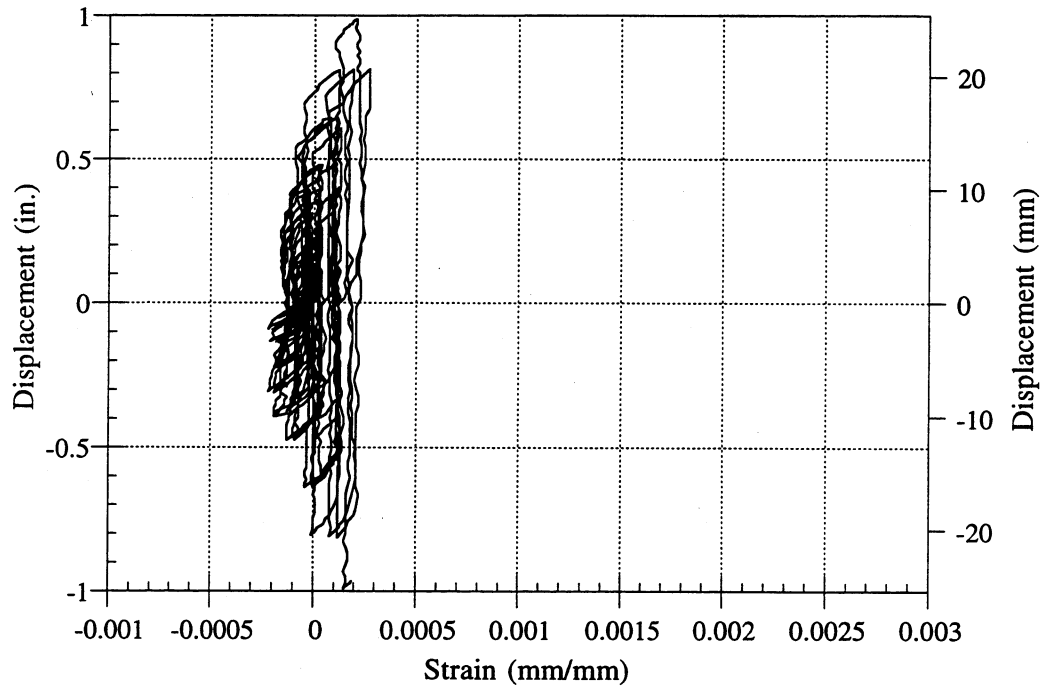

c) Transducer DOG

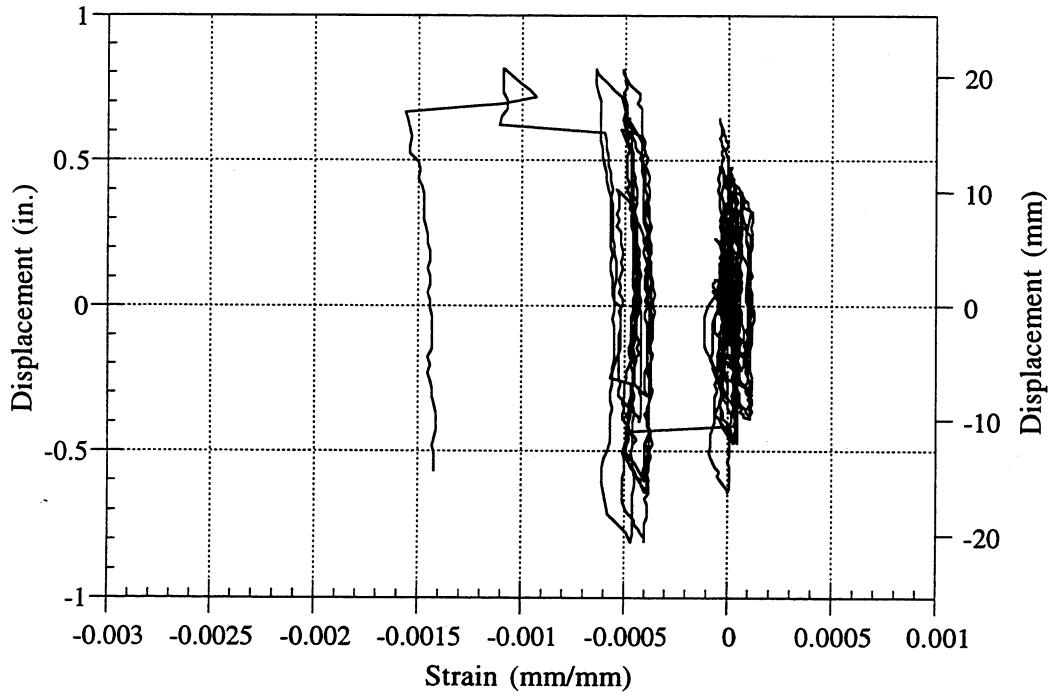

d) Transducer ED

Fig. 7.3.4 (Cont'd)

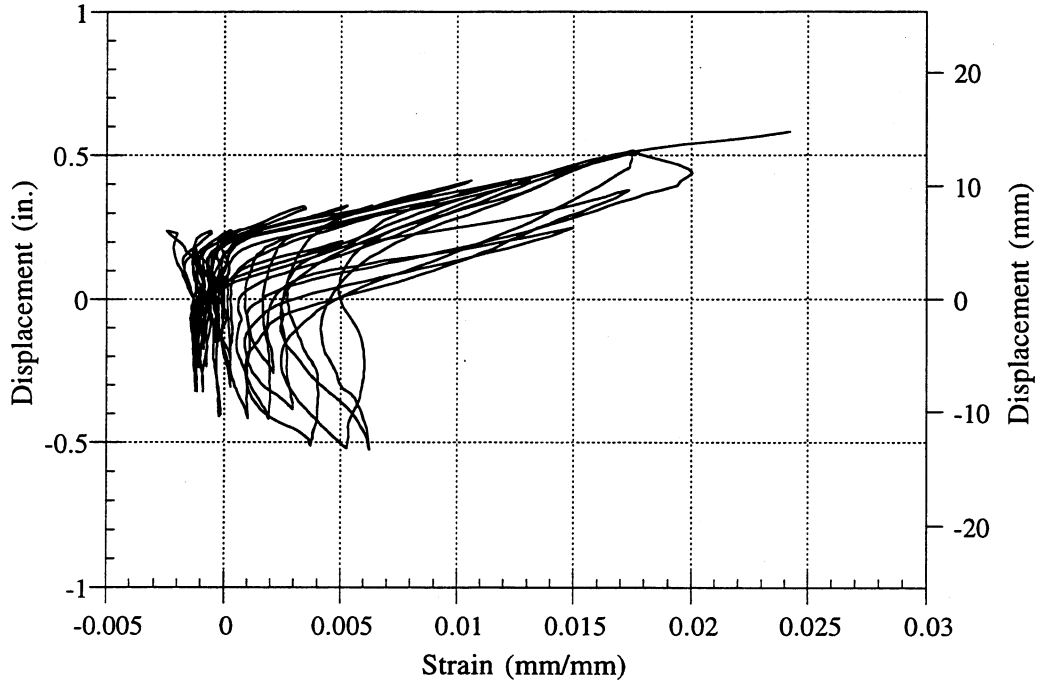

a) Transducer LOVE

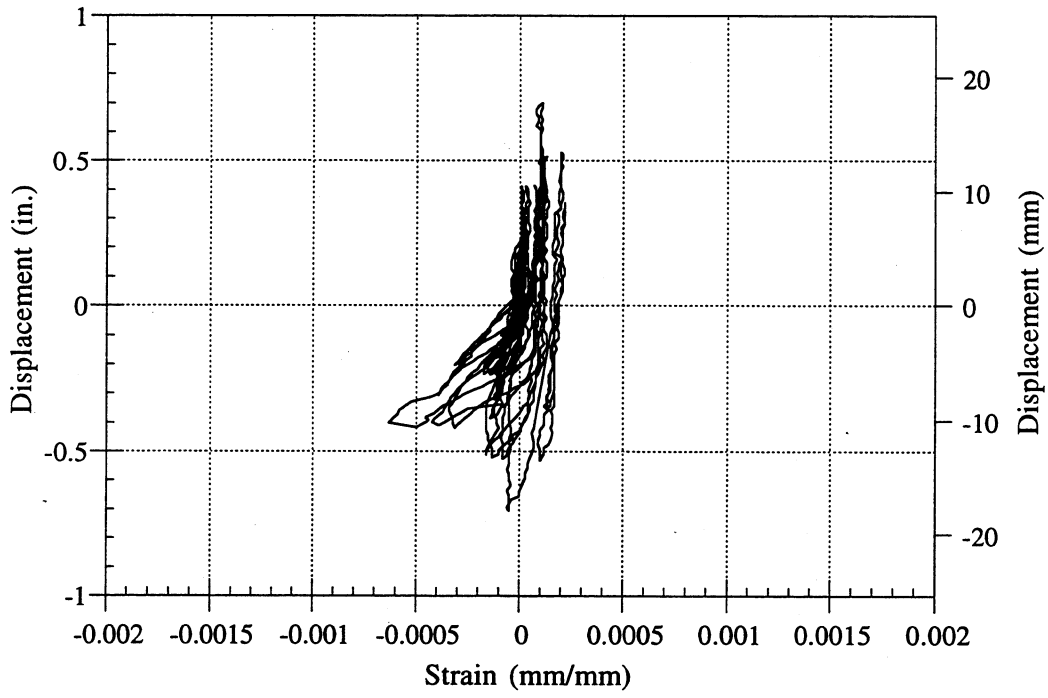

b) Transducer NEAL

Fig. 7.3.5 Masonry Surface Strains vs. Lateral Drift in Wall Specimen 10

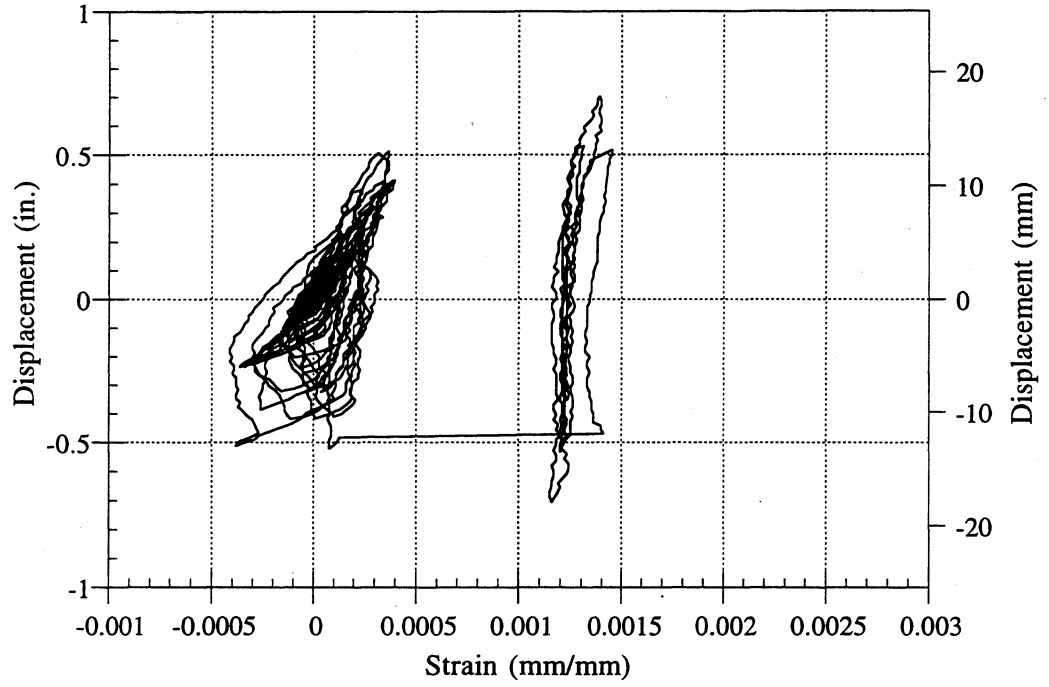

c) Transducer PAUL

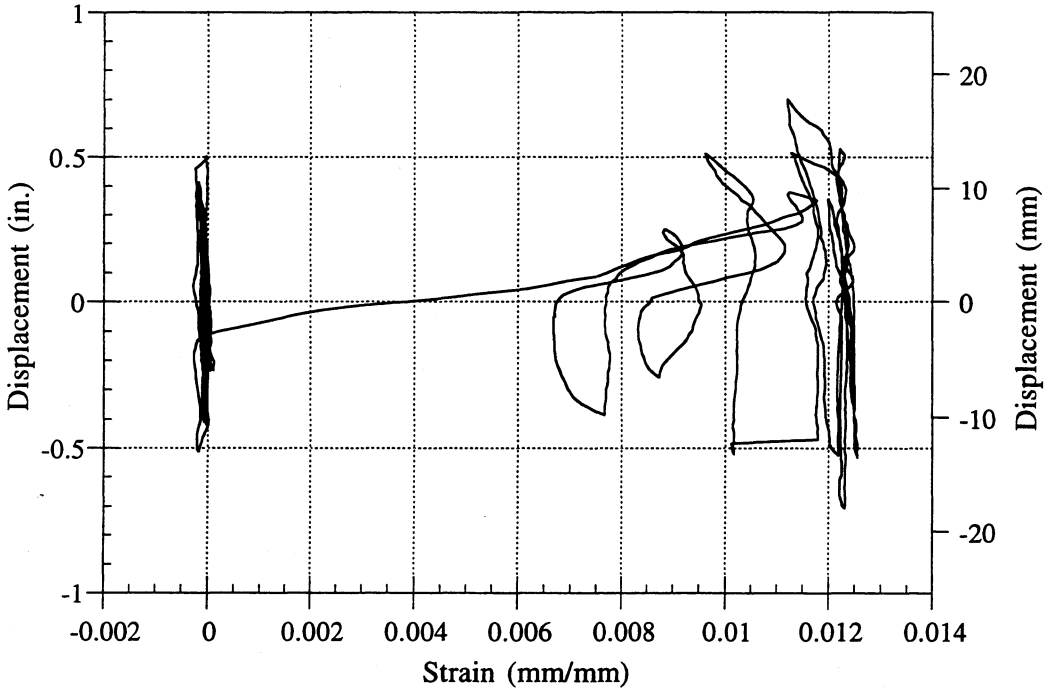

d) Transducer IVAN

Fig. 7.3.5 (Cont'd)

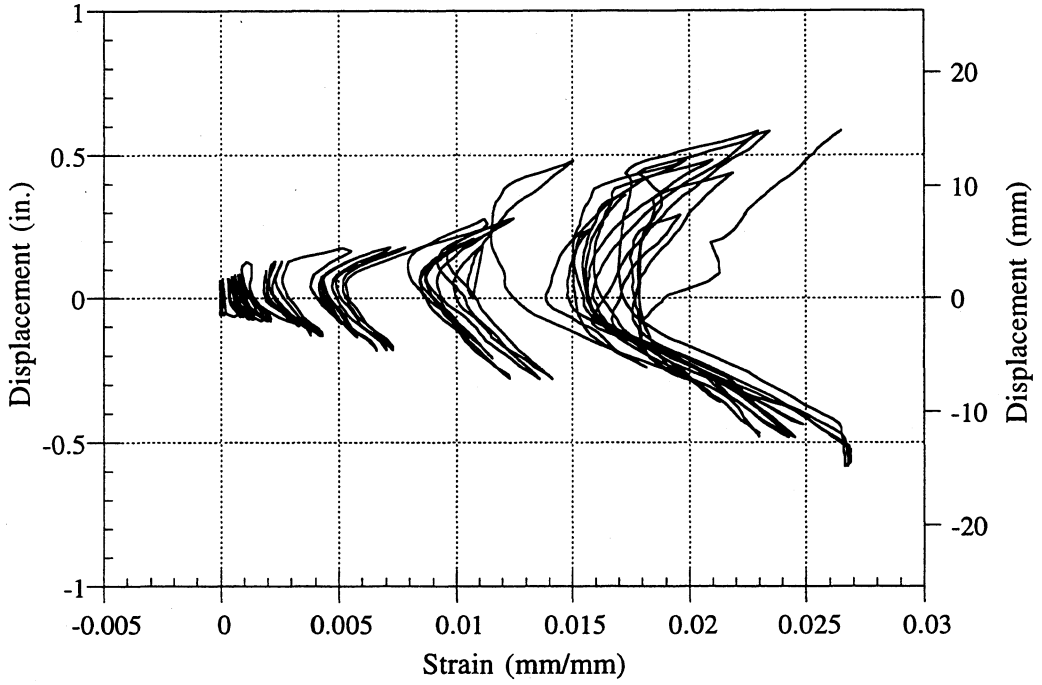

a) Transducer LOVE

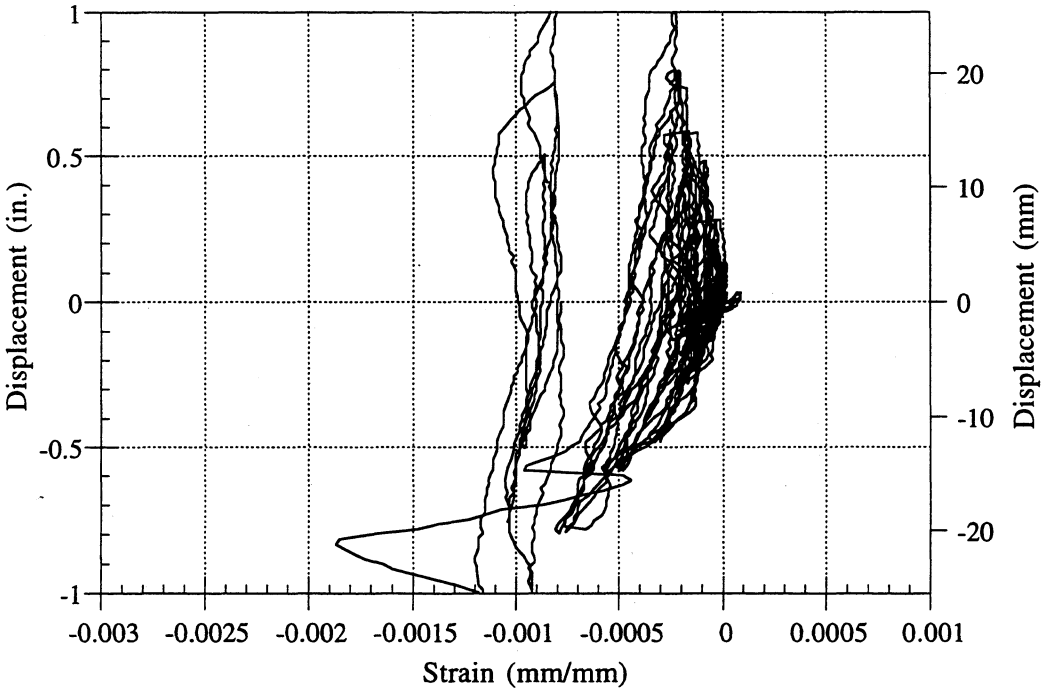

b) Transducer NEAL

Fig. 7.3.6 Masonry Surface Strains vs. Lateral Drift in Wall Specimen 12

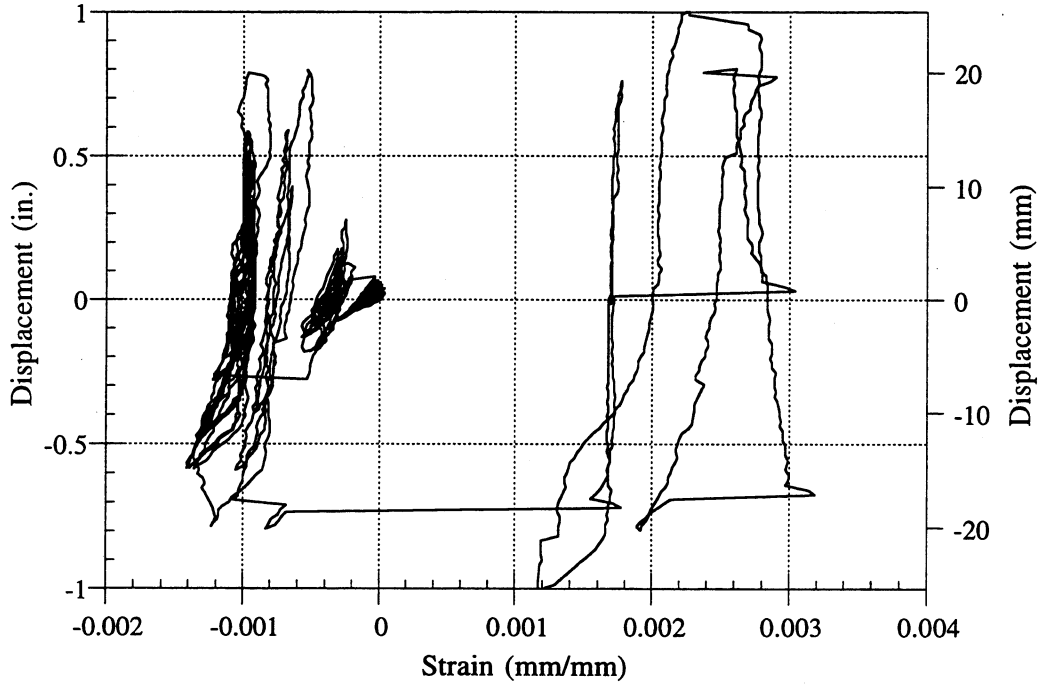

c) Transducer PAUL

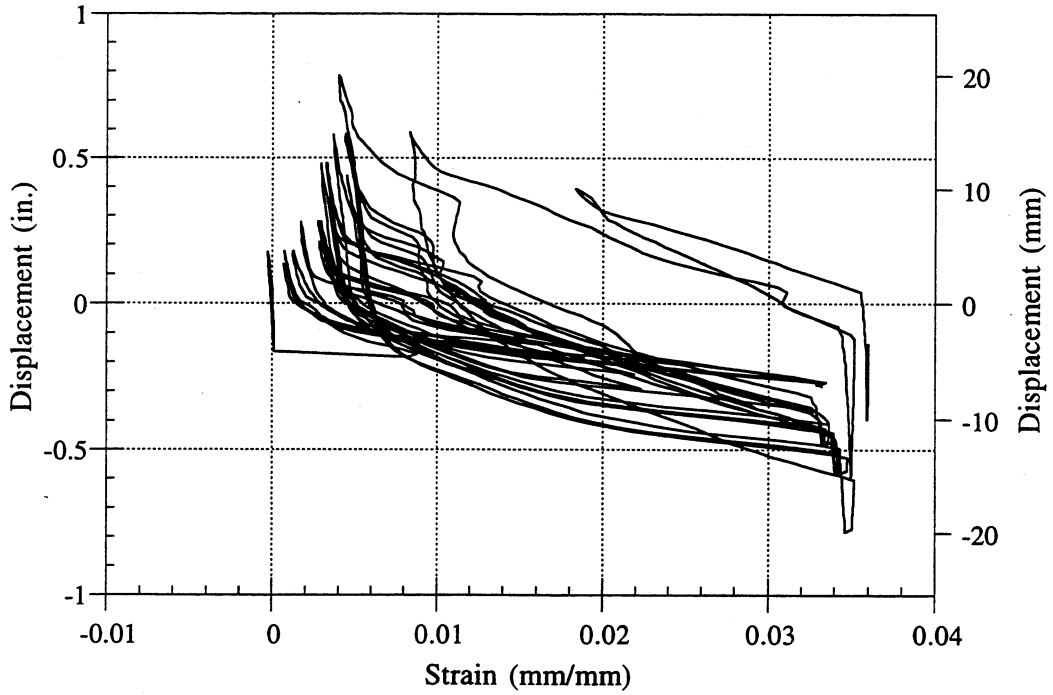

d) Transducer IVAN

Fig. 7.3.6 (Cont'd)

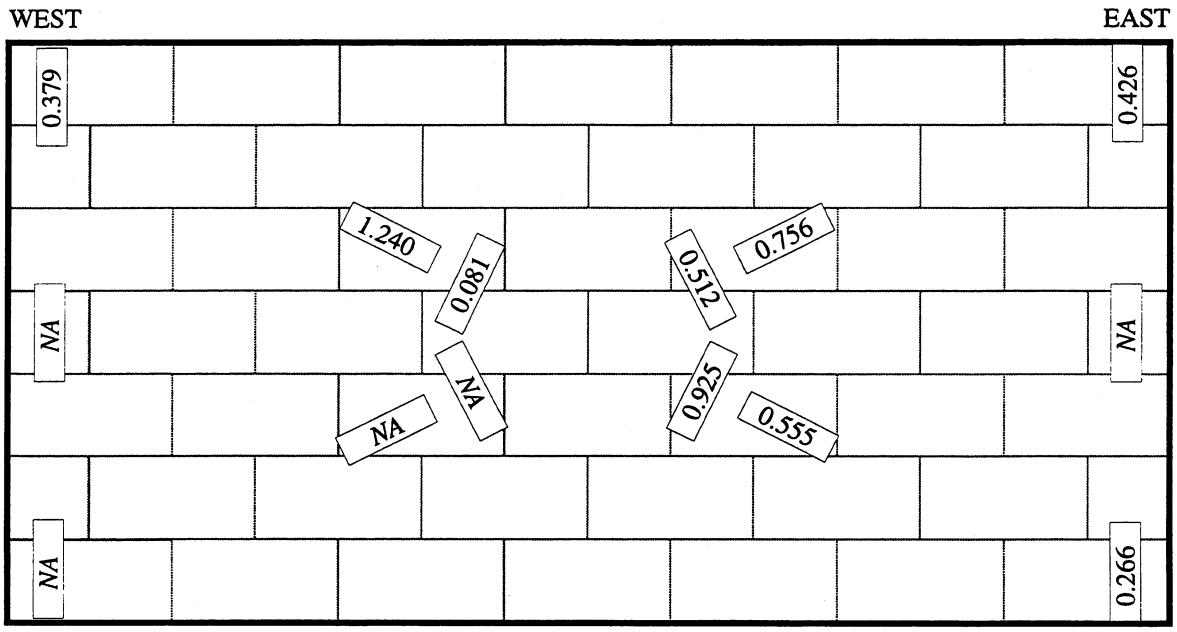

a) Drift Ratios (%) at Tension Threshold

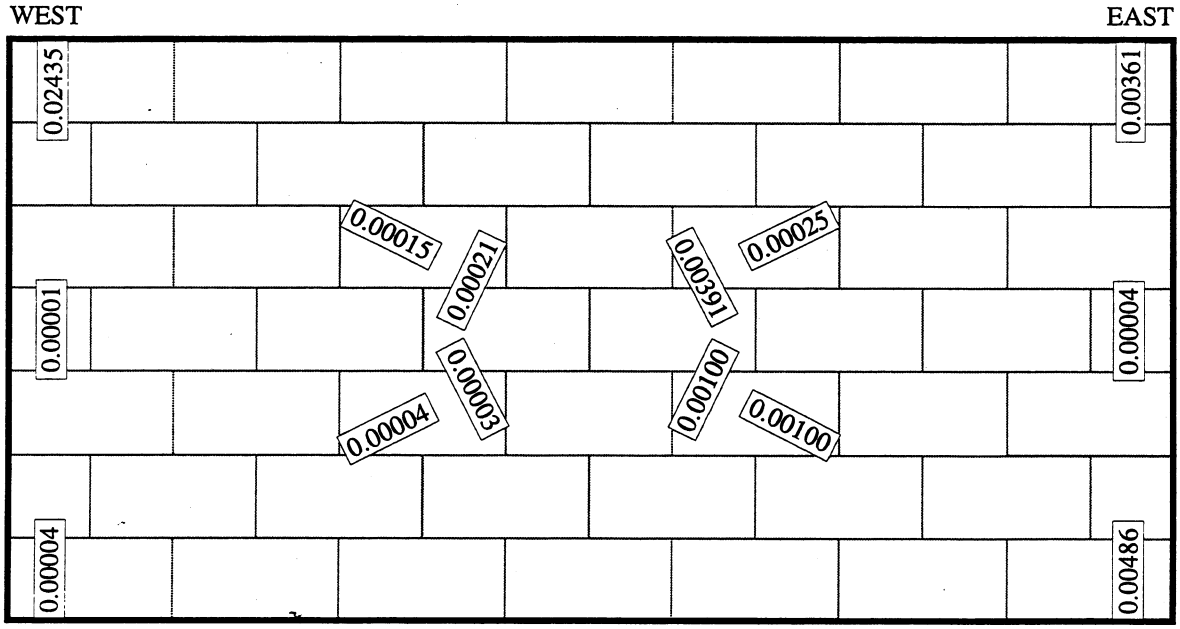

b) Peak Tension Strain Response

Fig. 7.3.7 Masonry Surface Tension Strain Response (LST) for Wall Specimen 2

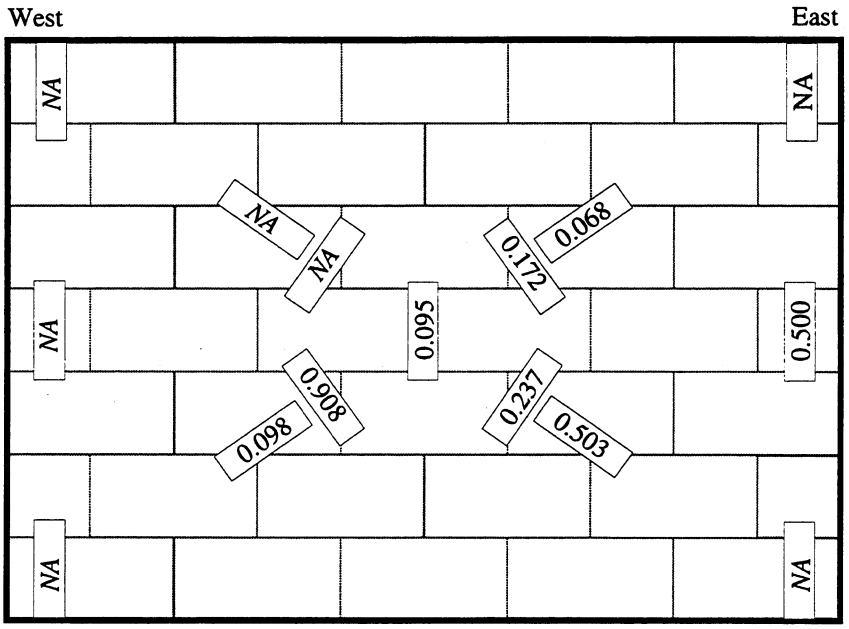

a) Drift Ratios (%) at Tension Threshold

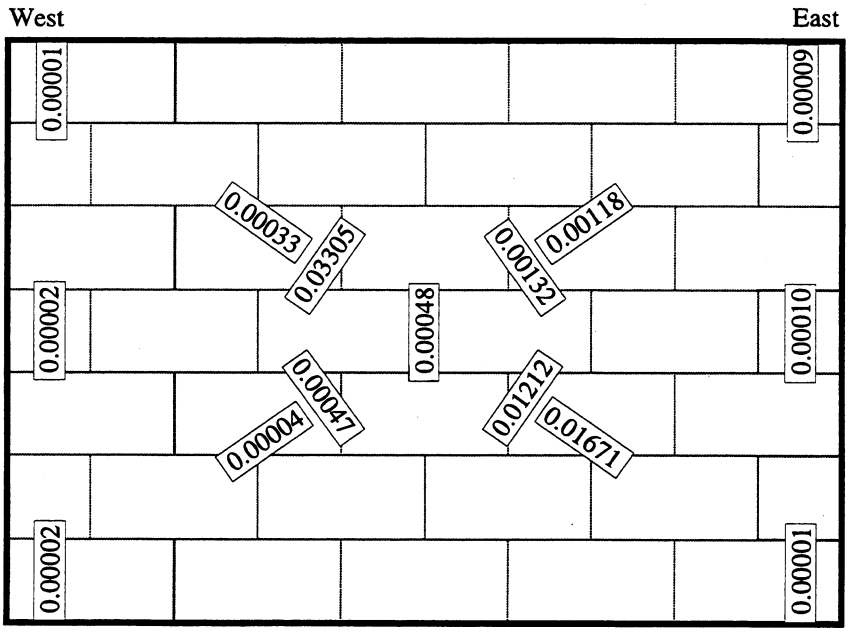

b) Peak Tension Strain Response (mm/mm)

Fig. 7.3.8 Masonry Surface Tension Strain Response (LST) for Wall Specimen 4

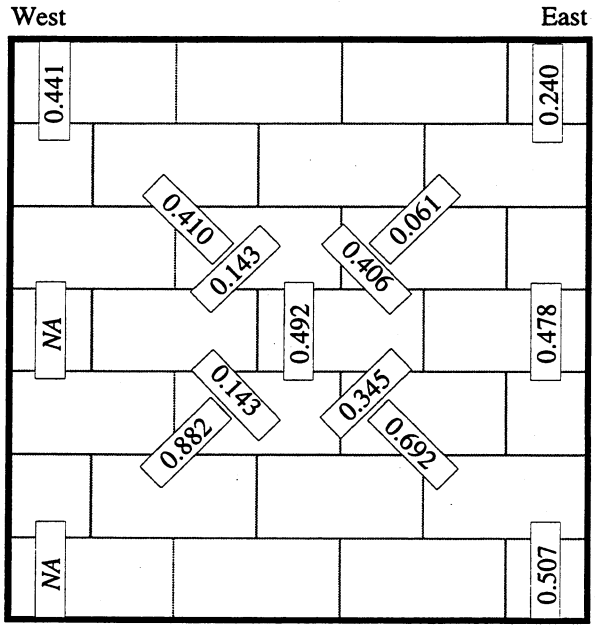

a) Drift Ratios (%) at Tension Threshold

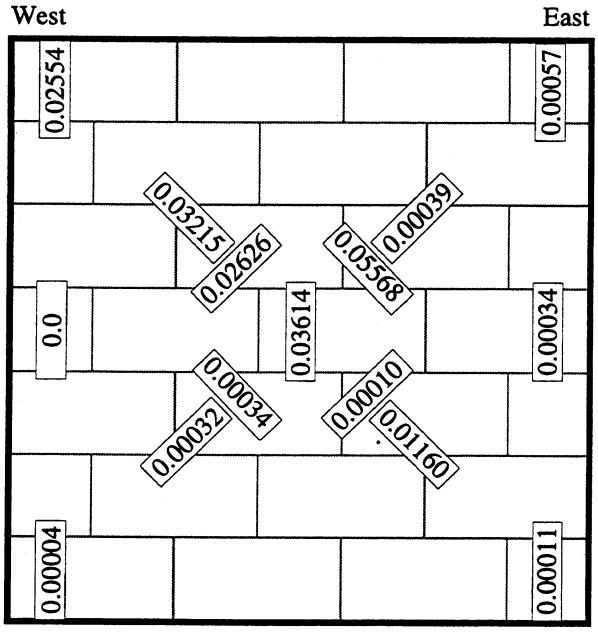

b) Peak Tension Strain Response (mm/mm)

Fig. 7.3.9 Masonry Surface Tension Strain Response (LST) for Wall Specimen 6

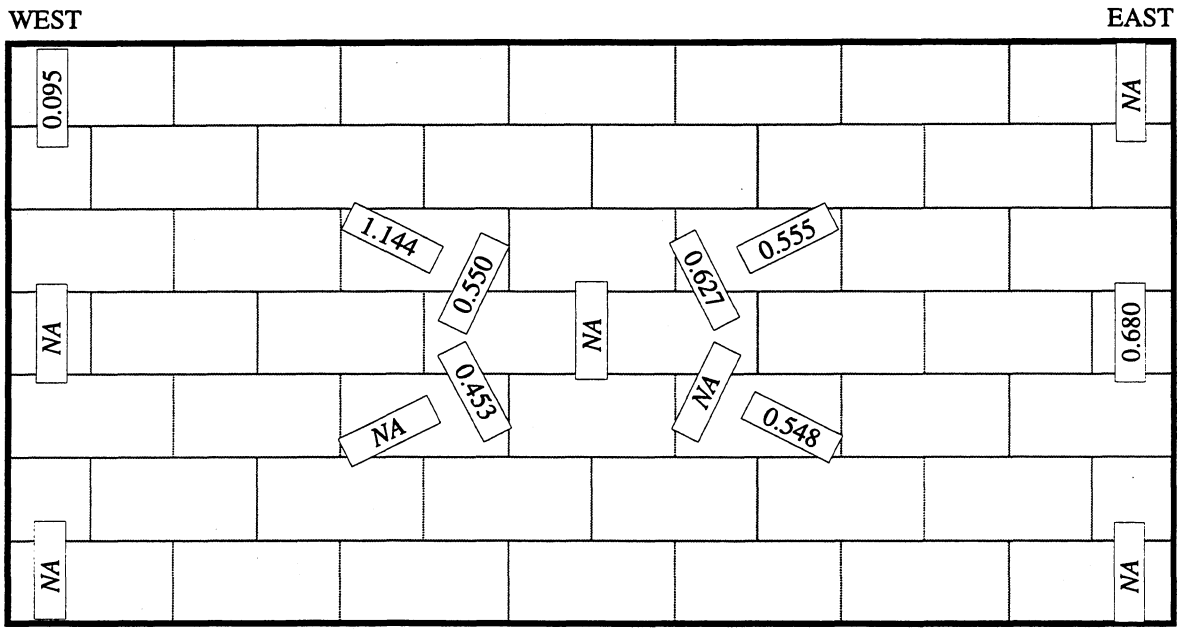

a) Drift Ratios (%) at Tension Threshold

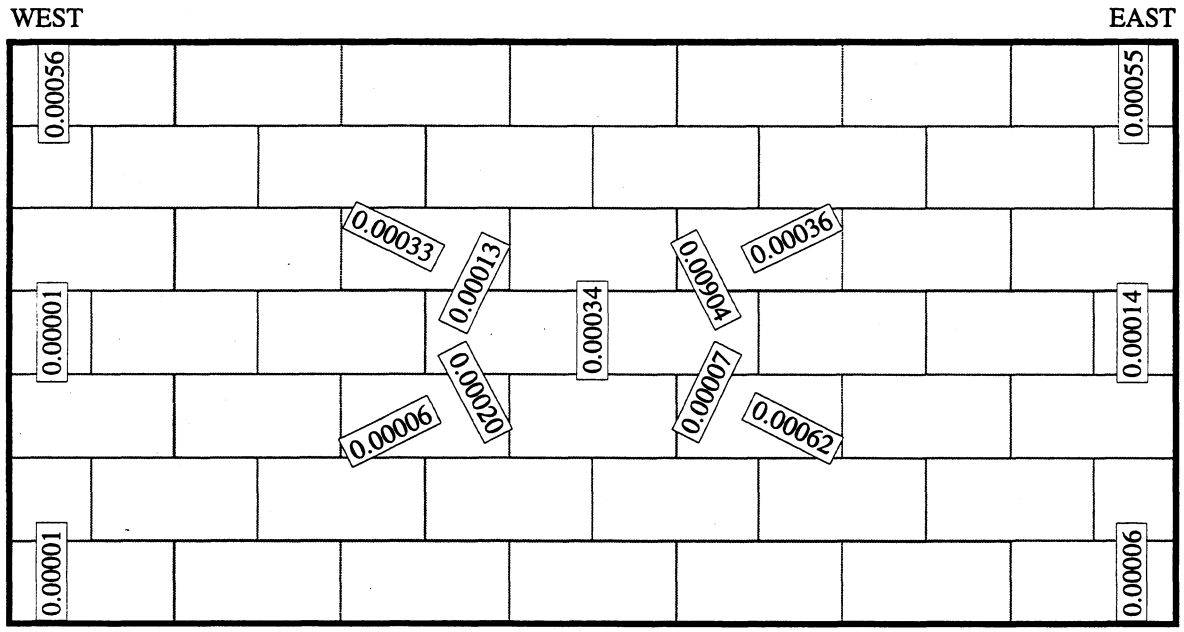

b) Peak Tension Strain Response (mm/mm)

Fig. 7.3.10 Masonry Surface Tension Strain Response (LST) for Wall Specimen 8

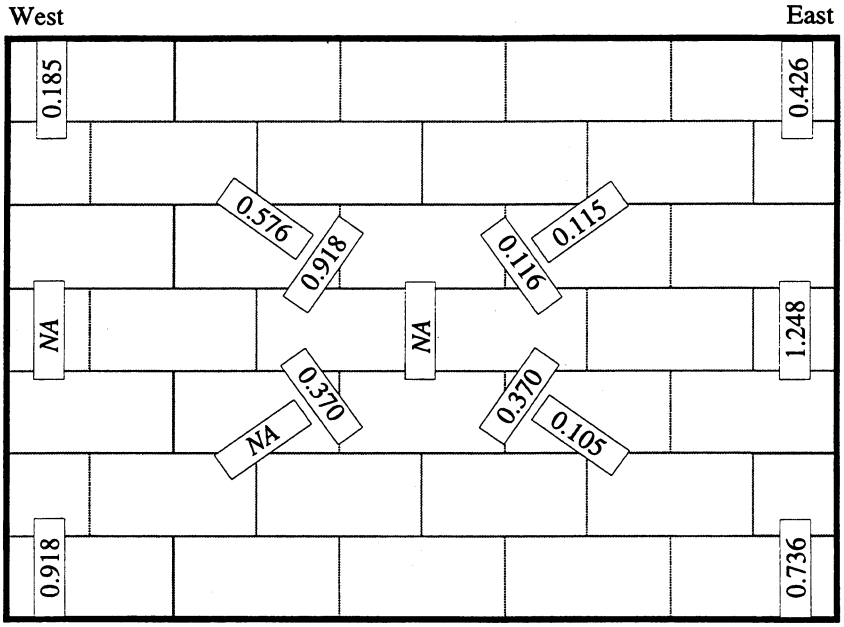

a) Drift Ratios (%) at Tension Threshold

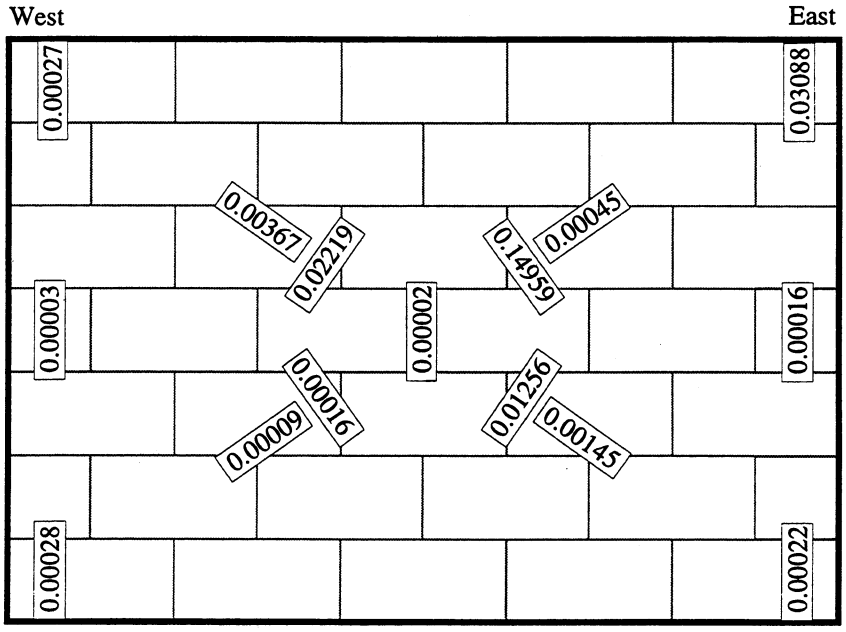

b) Peak Tension Strain Response (mm/mm)

Fig. 7.3.11 Masonry Surface Tension Strain Response (LST) for Wall Specimen 10

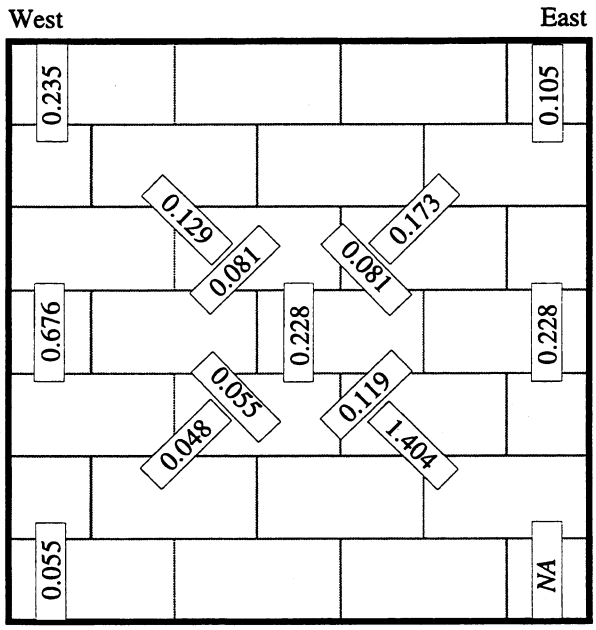

a) Drift Ratios (%) at Tension Threshold

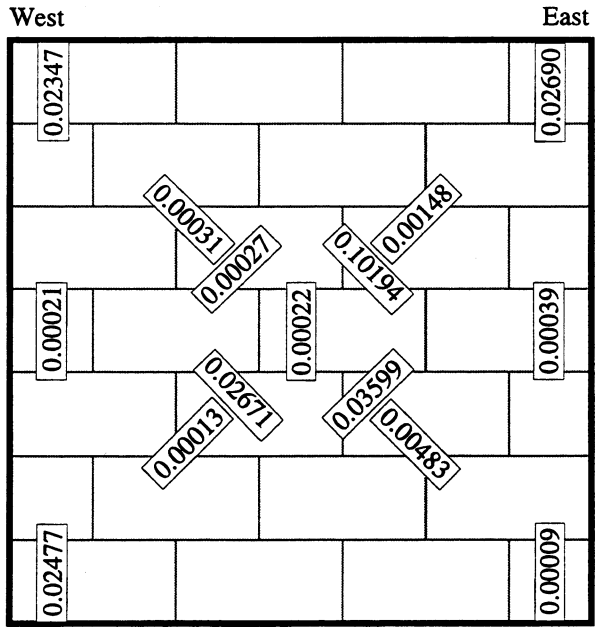

b) Peak Tension Strain Response (mm/mm)

Fig. 7.3.12 Masonry Surface Tension Strain Response (LST) for Wall Specimen 12

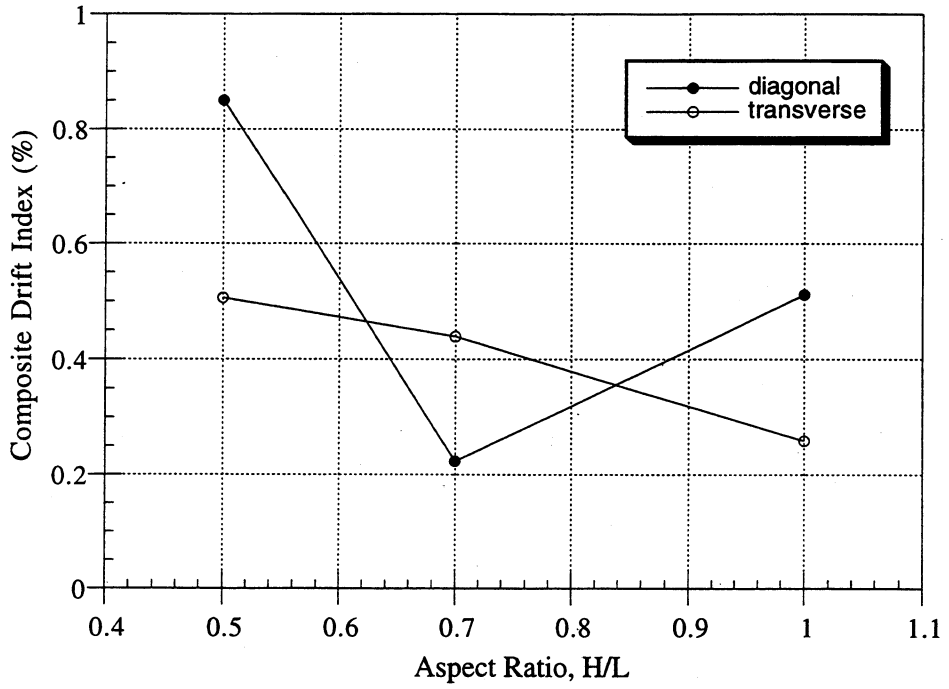

a) $\rho_h = 0.05\%$

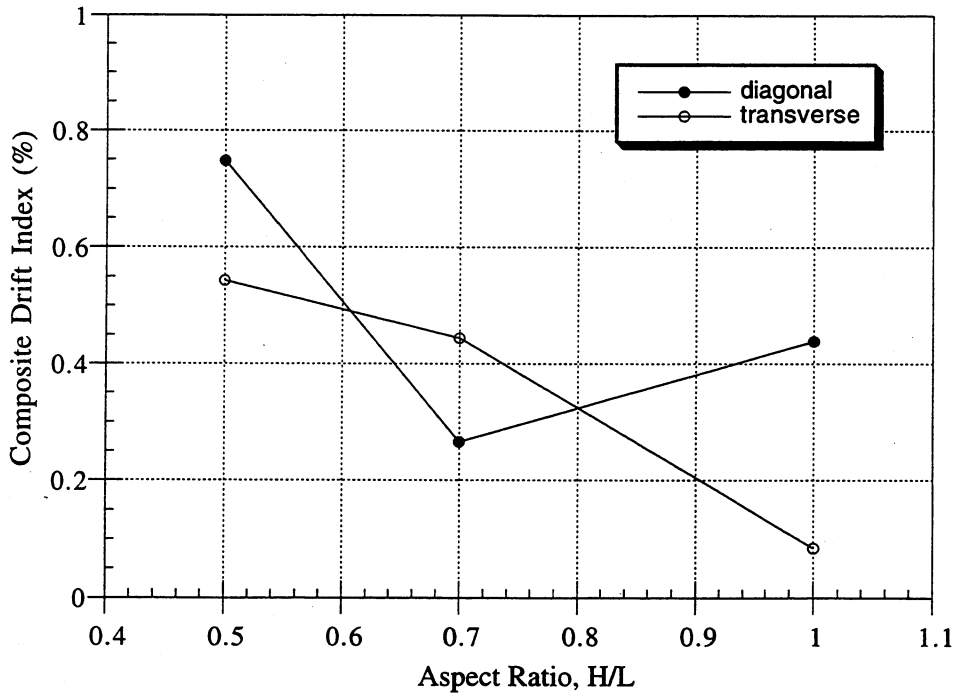

b) $\rho_h = 0.12\%$

Fig. 7.3.13 Influence of Aspect Ratio on Net Composite Drift Indices for Masonry Surface Strains

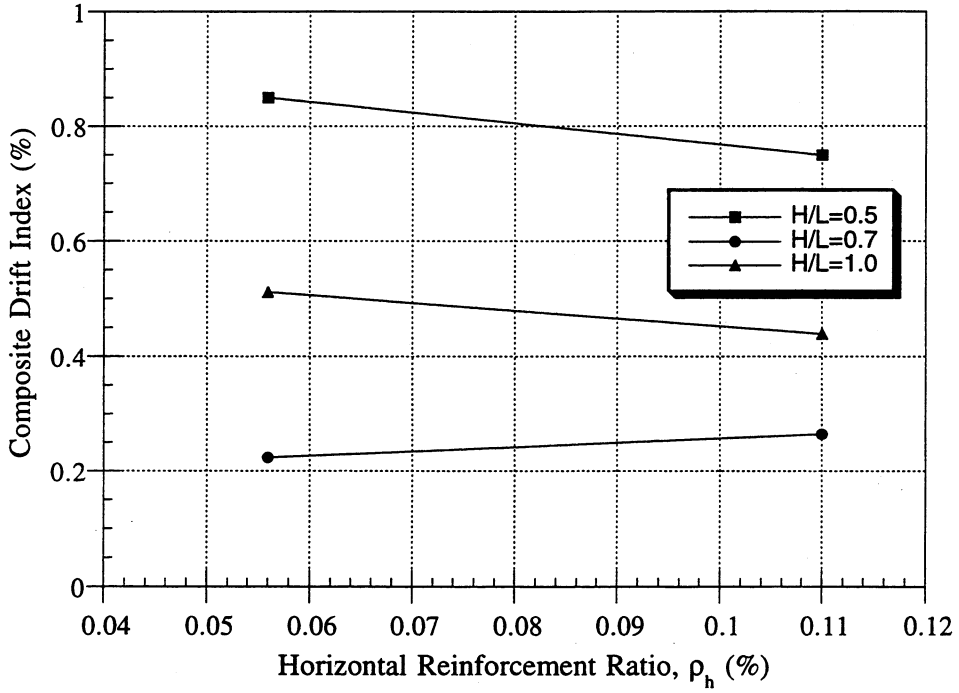

a) Diagonal

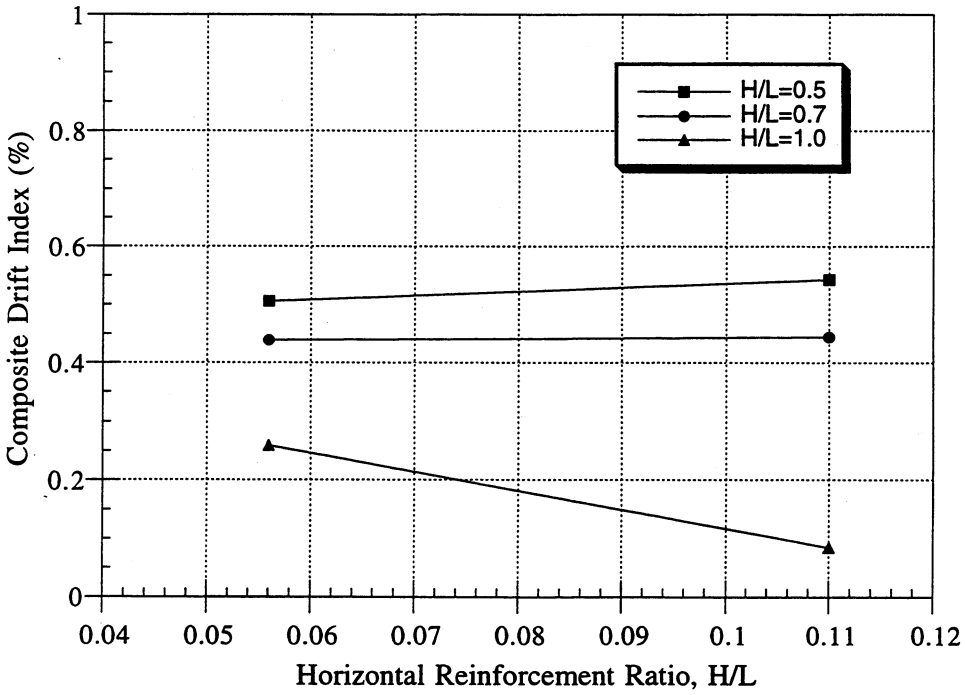

b) Transverse

Fig. 7.3.14 Influence of Reinforcement Ratio on Net Composite Drift Indices for Masonry Surface Strains

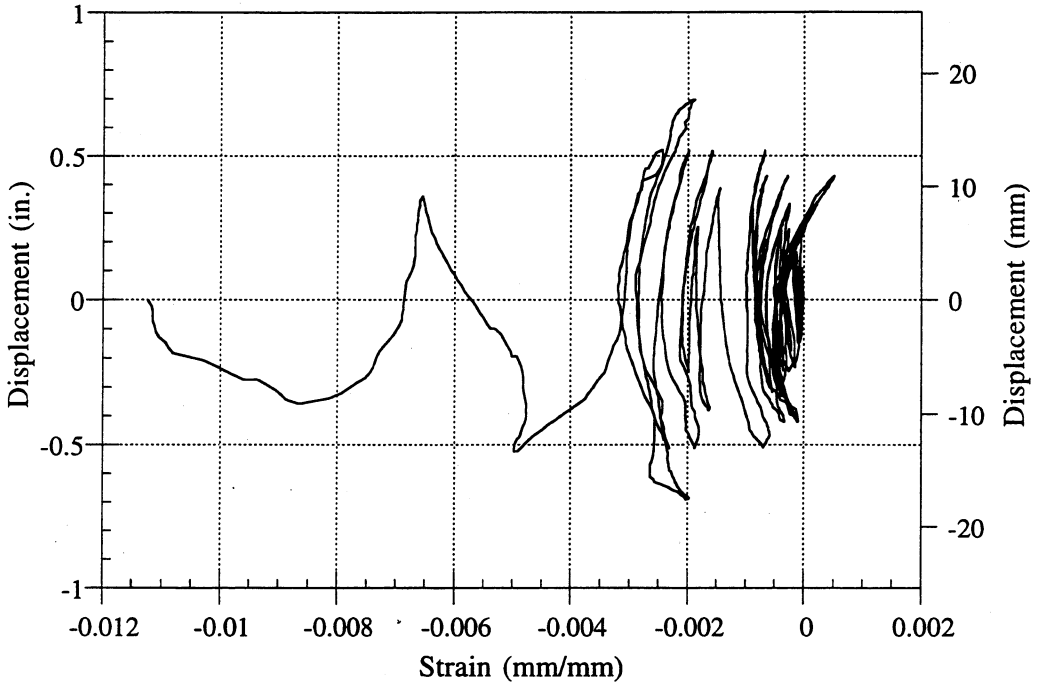

a) Transducer WVTTOP

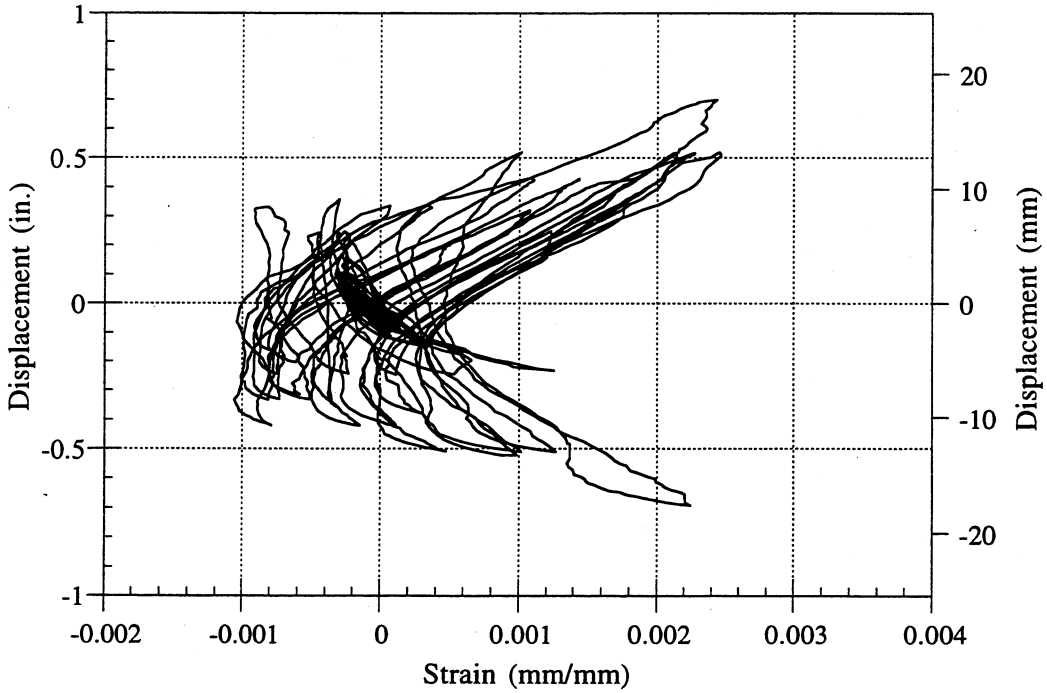

b) Transducer WVTFTG

Fig. 7.4.1 Gross (LVDT) Strains vs. Lateral Drift in Wall Specimen 2

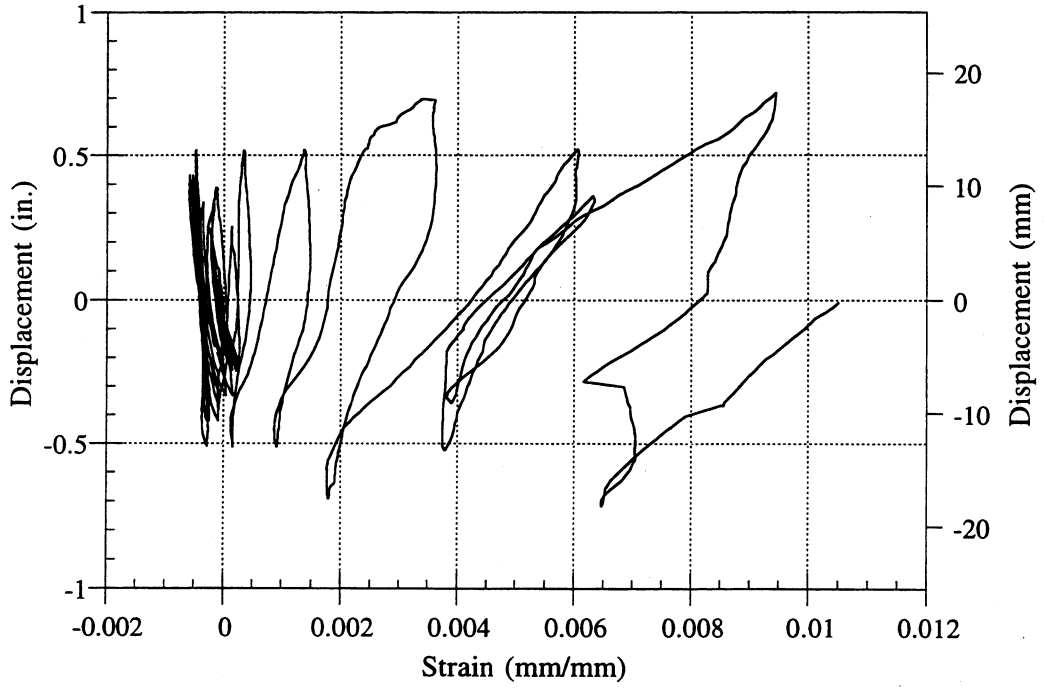

c) Transducer WVTMID

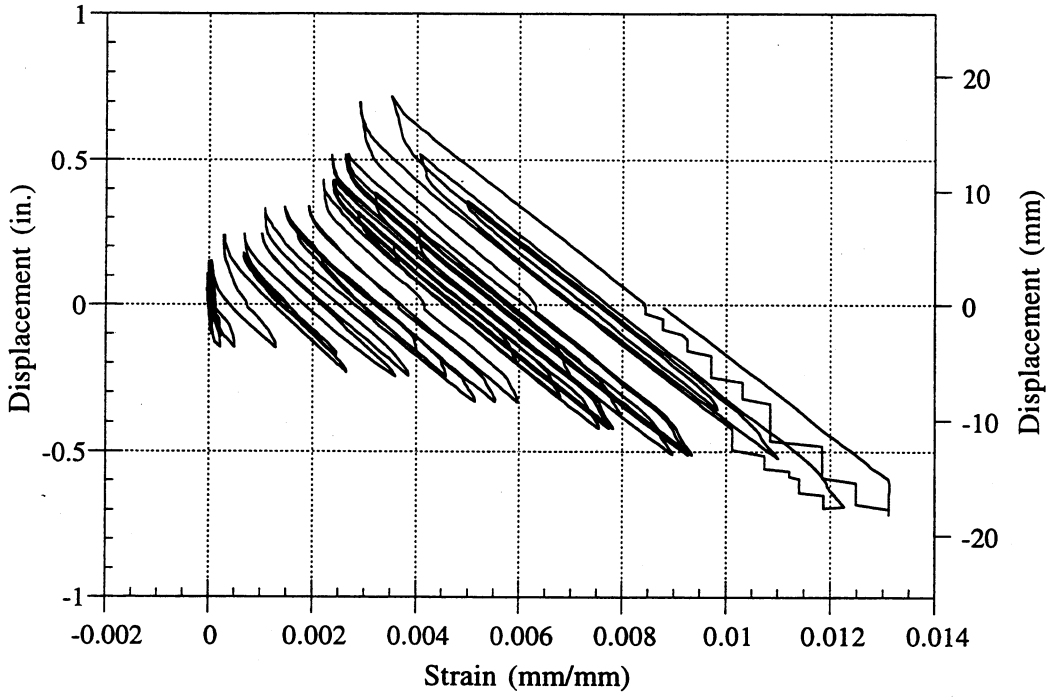

d) Transducer ETWBD

Fig. 7.4.1 (Cont'd)

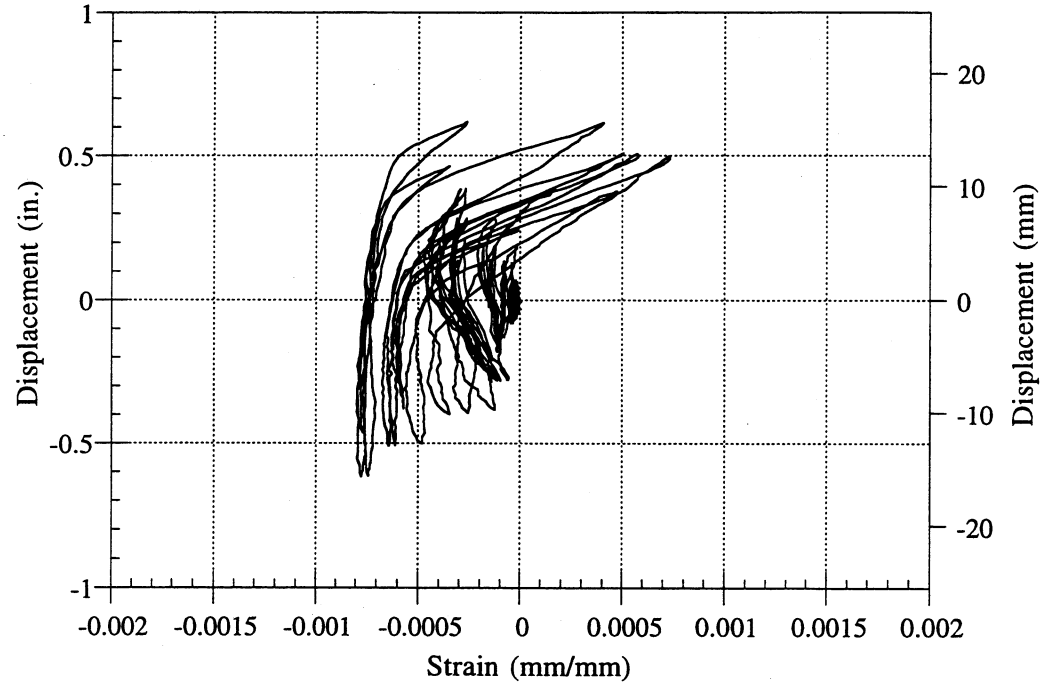

a) Transducer WVTTOP

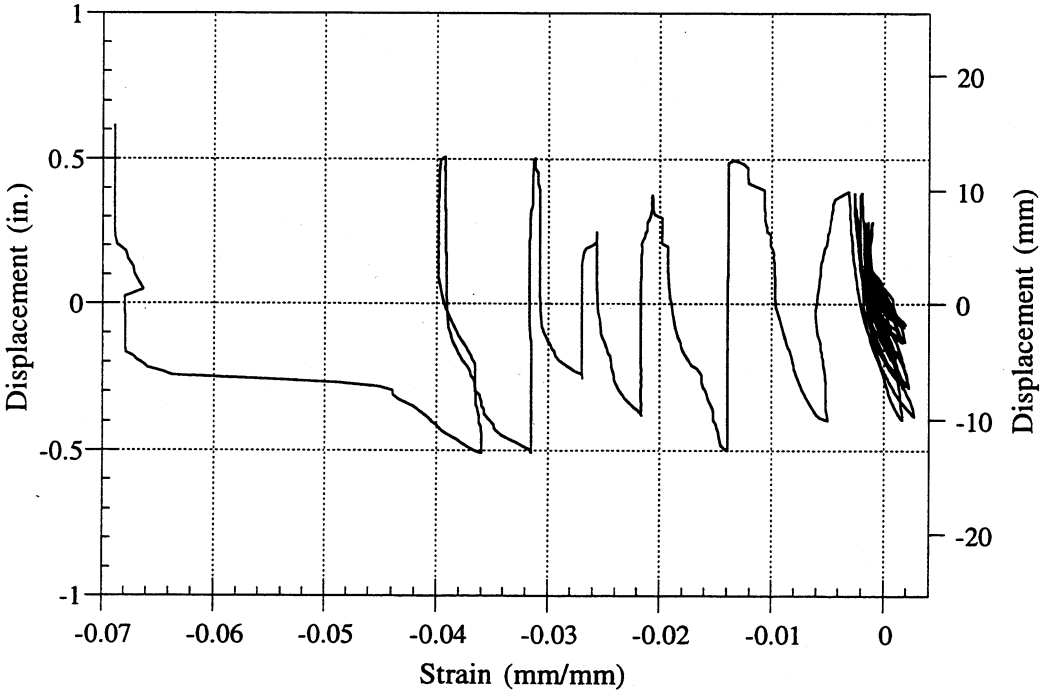

b) Transducer WVTFTG

Fig. 7.4.2 Gross (LVDT) Strains vs. Lateral Drift in Wall Specimen 4

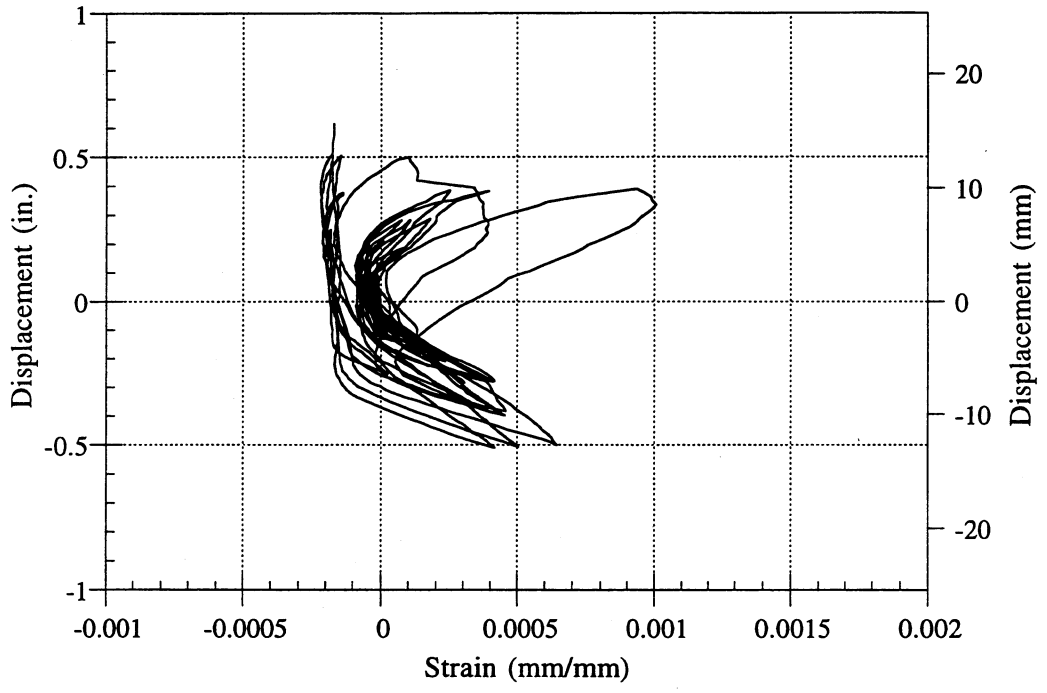

c) Transducer WVTMID

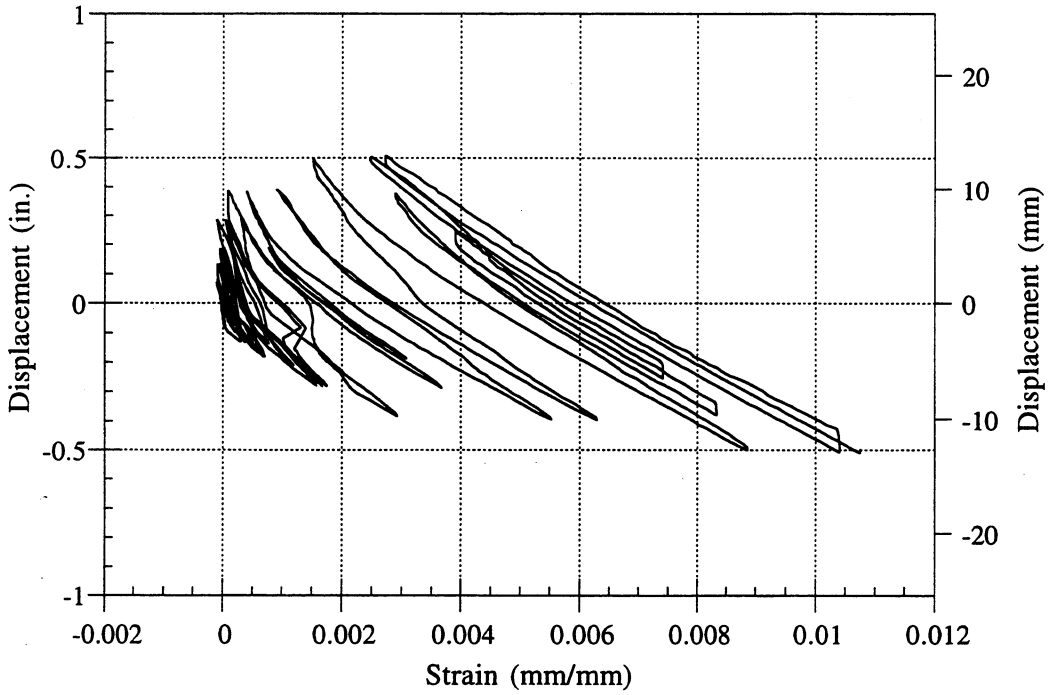

d) Transducer ETWBD

Fig. 7.4.2 (Cont'd)

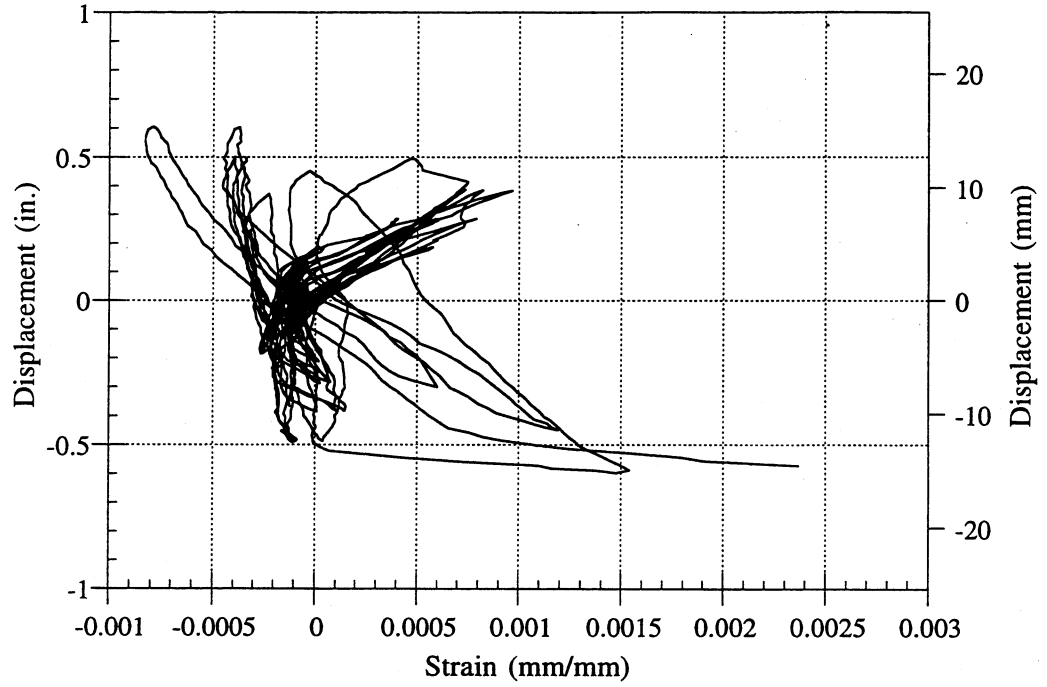

a) Transducer WVTTOP

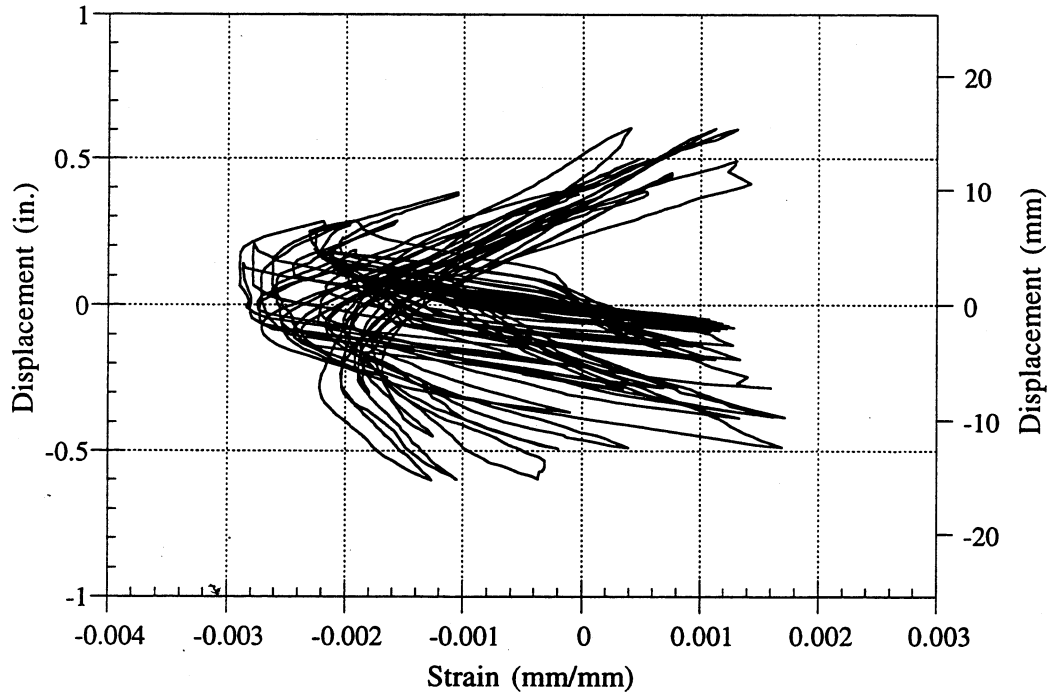

b) Transducer WVTFTG

Fig. 7.4.3 Gross (LVDT) Strains vs. Lateral Drift in Wall Specimen 6

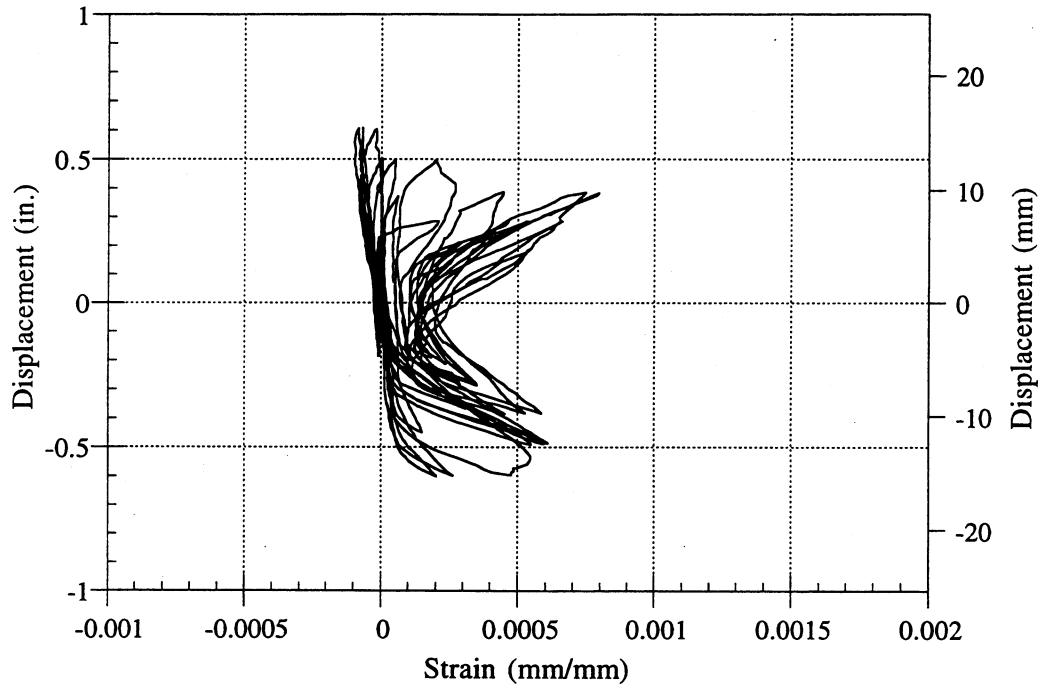

c) Transducer WVTMID

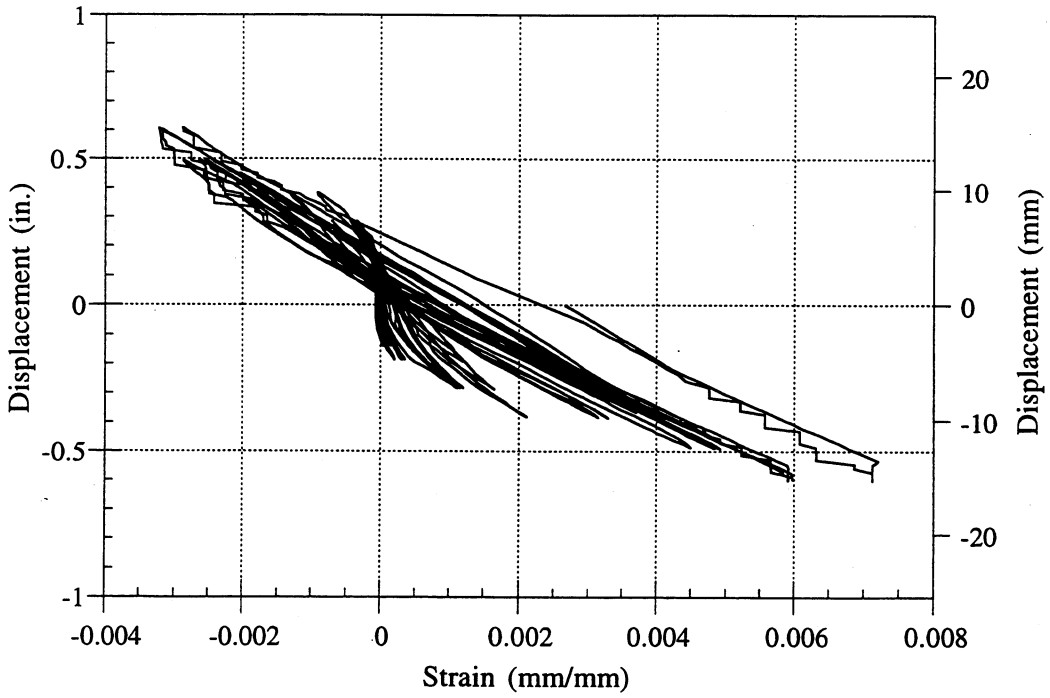

d) Transducer ETWBD

Fig. 7.4.3 (Cont'd)

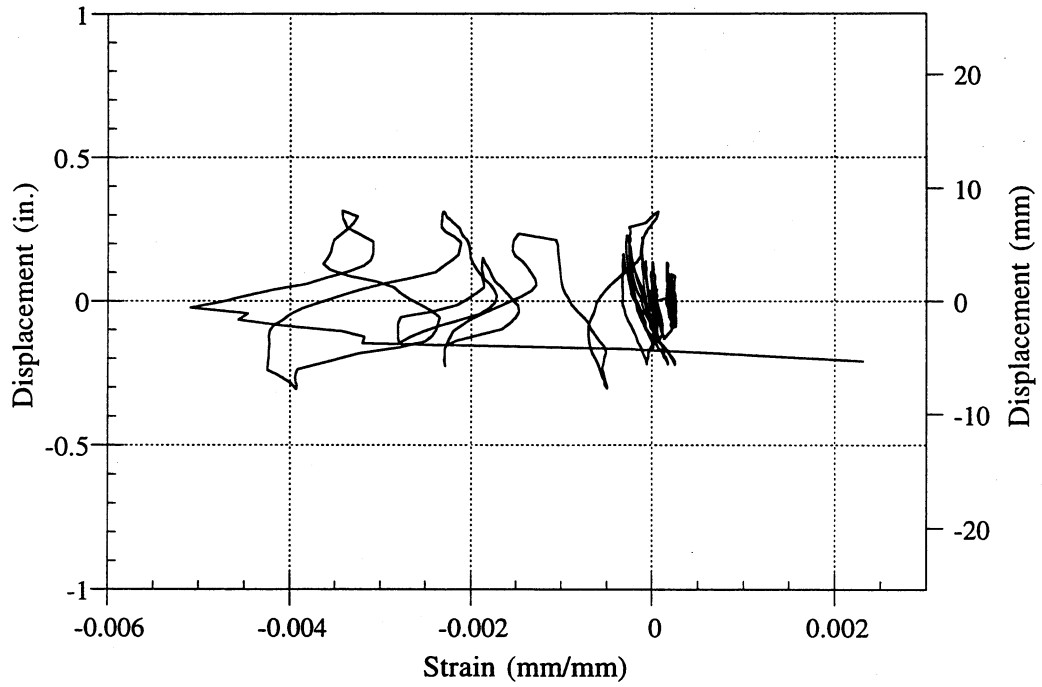

a) Transducer WVTTOP

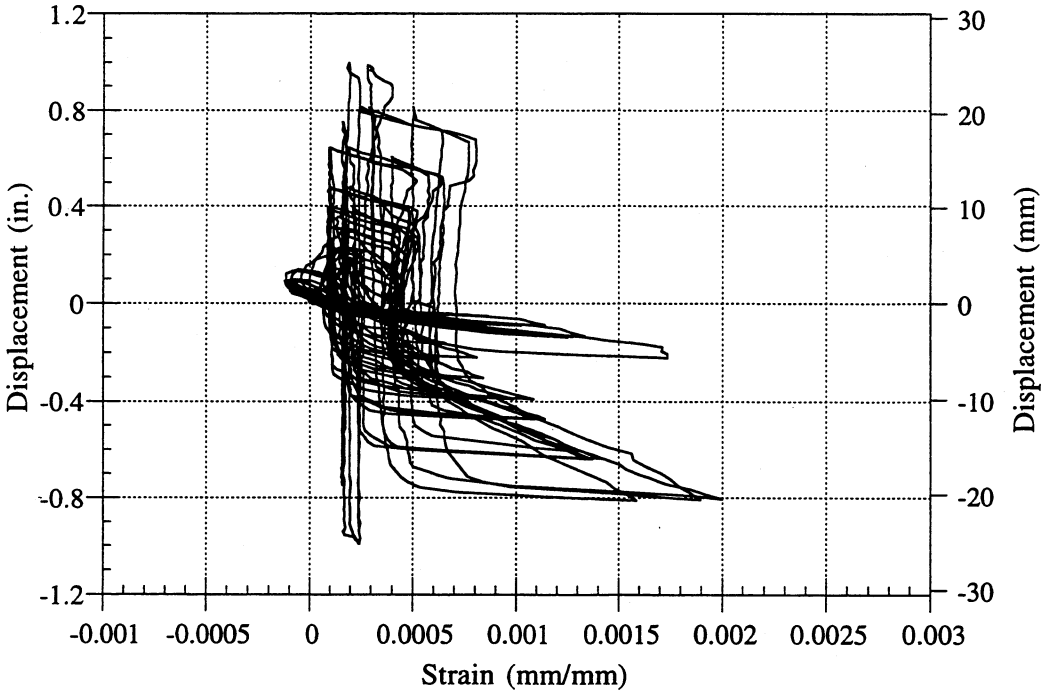

b) Transducer WVTFTG

Fig. 7.4.4 Gross (LVDT) Strains vs. Lateral Drift in Wall Specimen 8

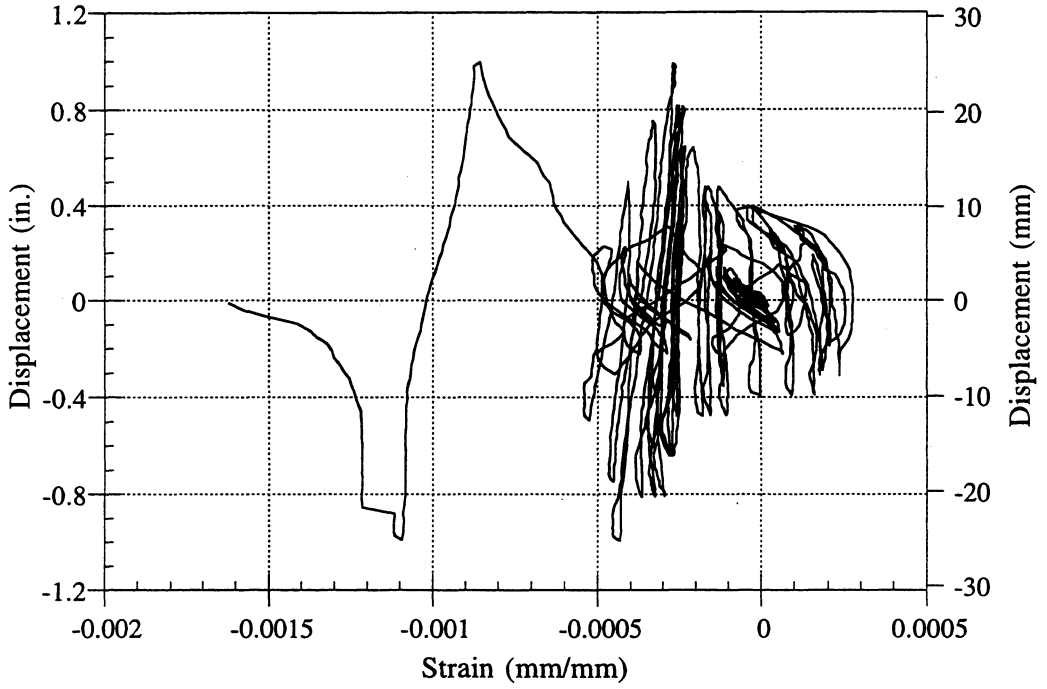

c) Transducer WVTMID

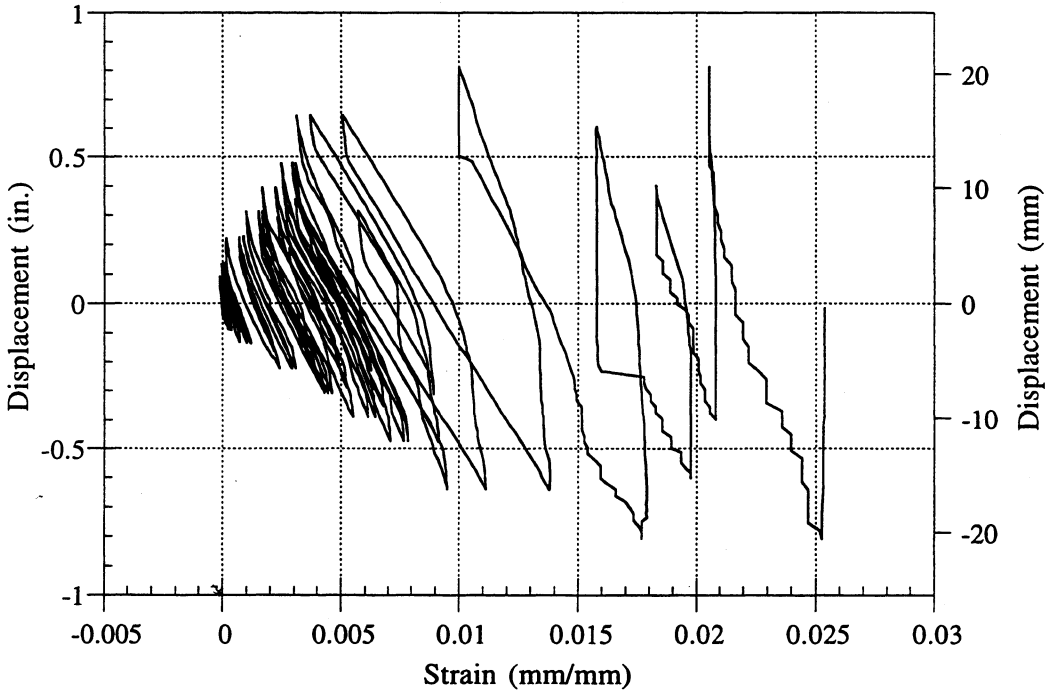

d) Transducer ETWBD

Fig. 7.4.4 (Cont'd)

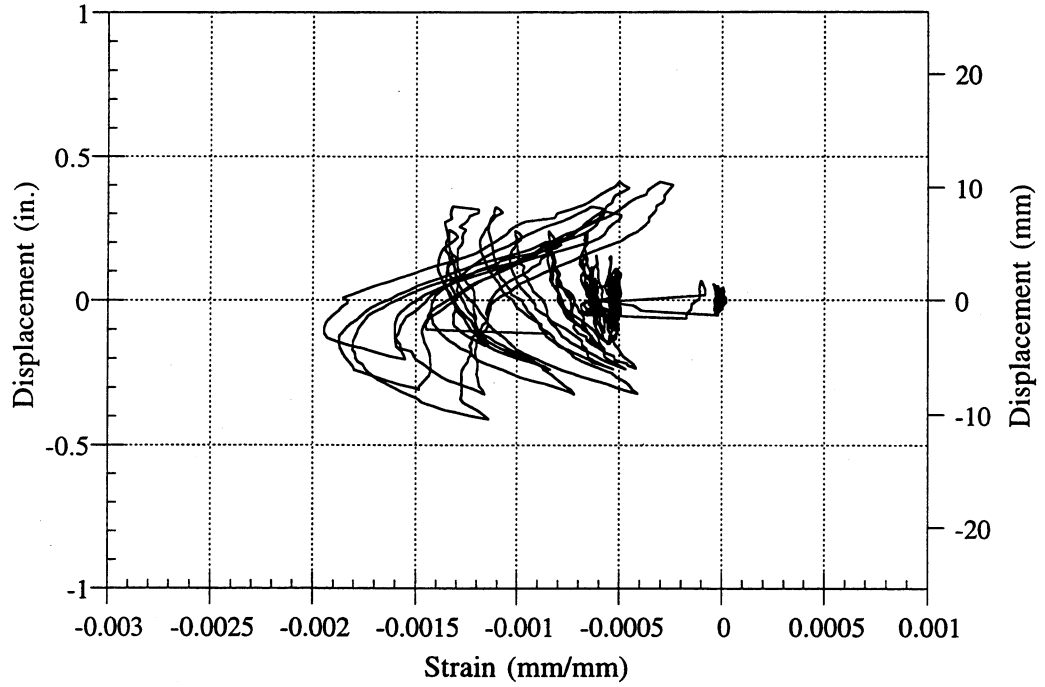

a) Transducer WVTTOP

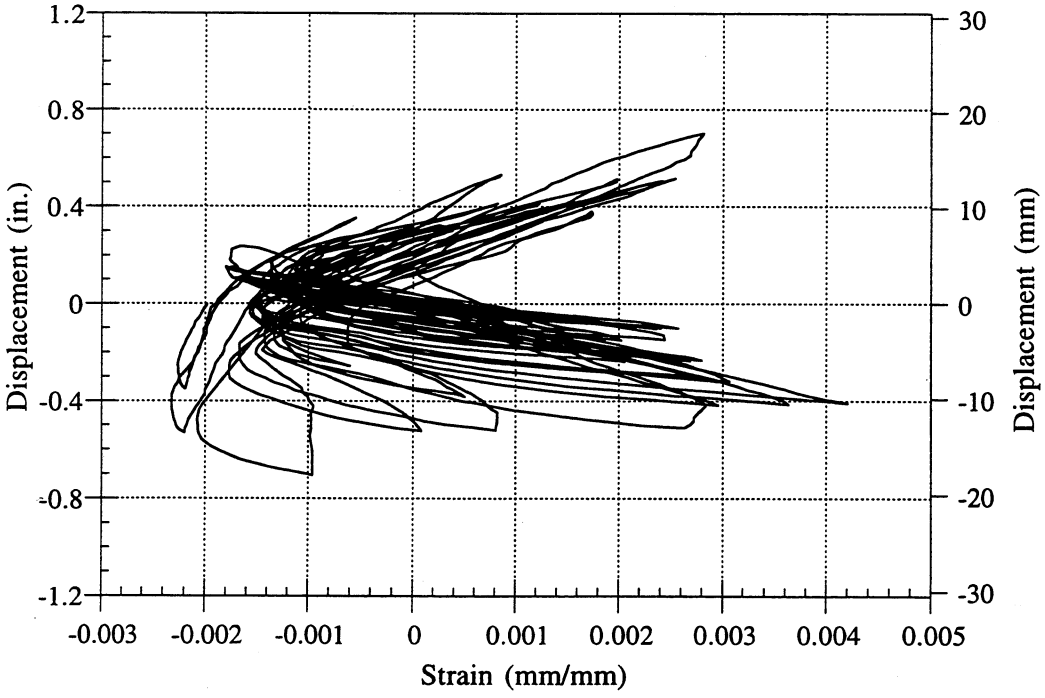

b) Transducer WVTFTG

Fig. 7.4.5 Gross (LVDT) Strains vs. Lateral Drift in Wall Specimen 10

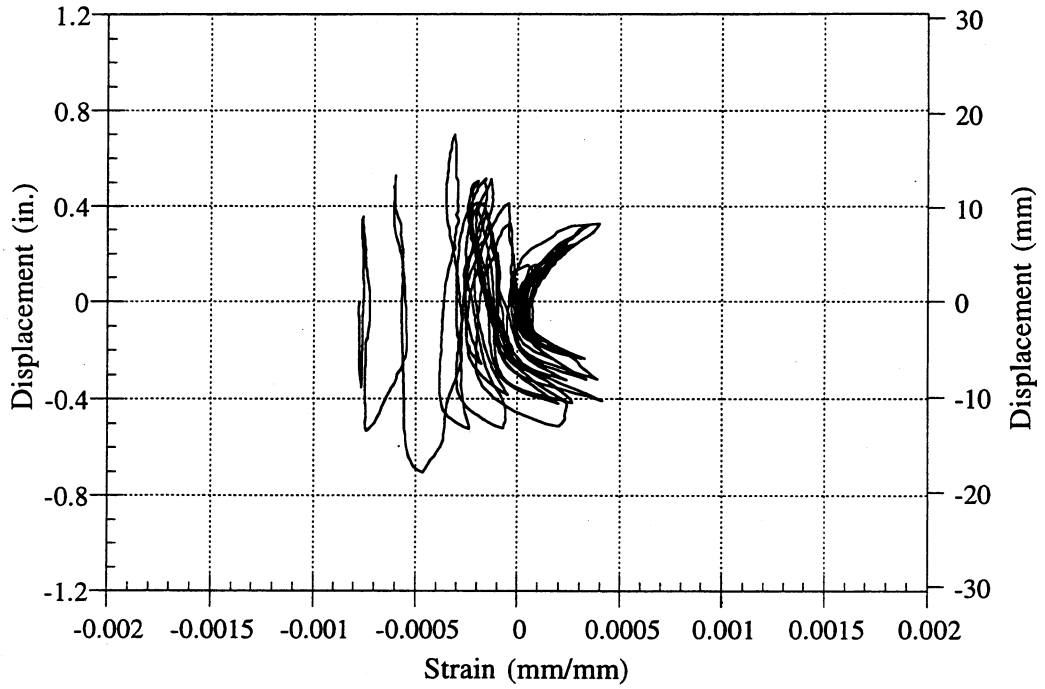

c) Transducer WVTMID

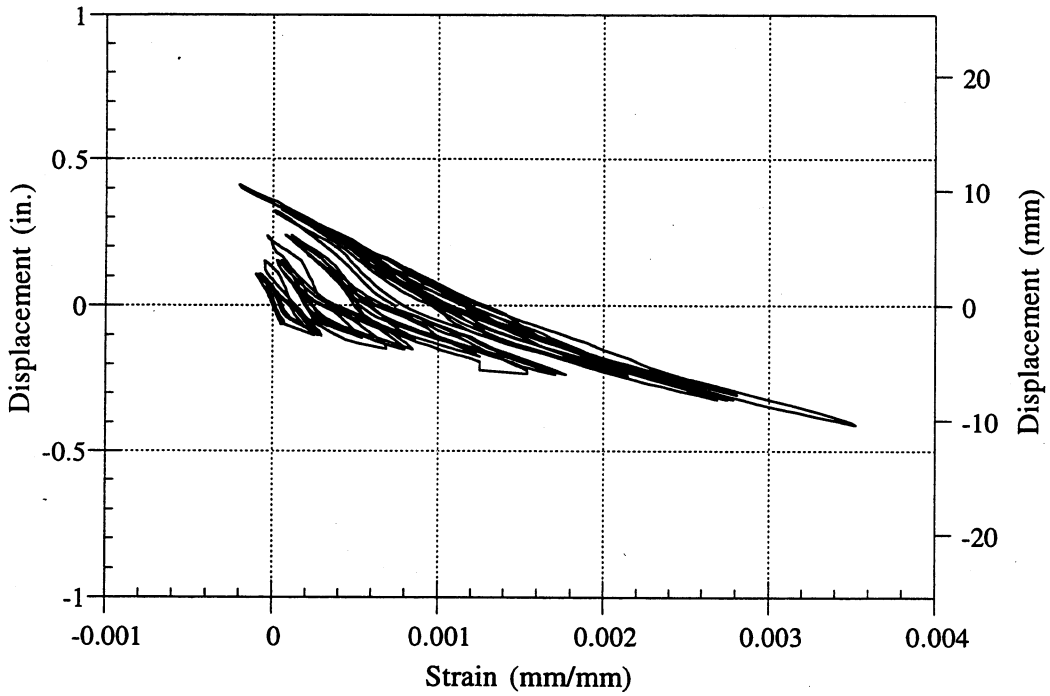

d) Transducer ETWBD

Fig. 7.4.5 (Cont'd)

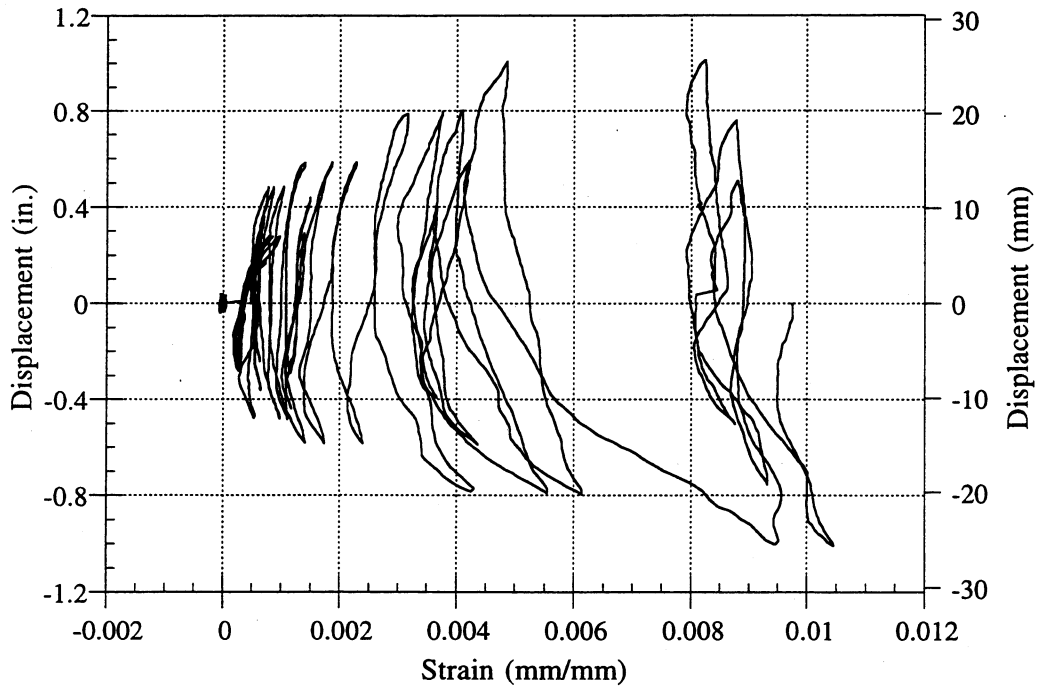

a) Transducer WVTTOP

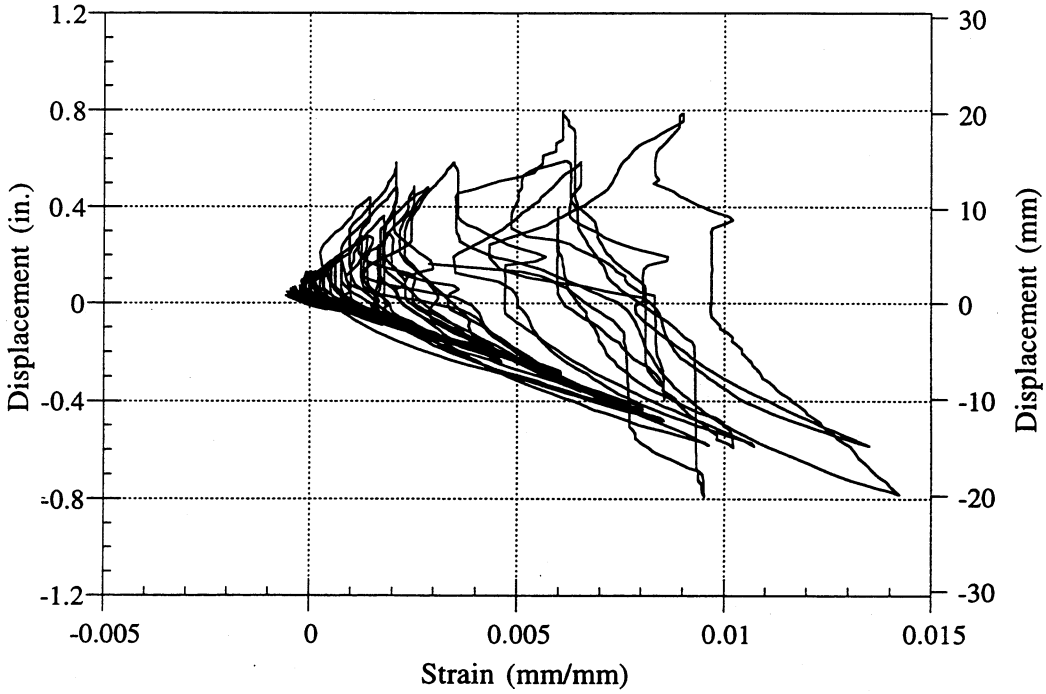

b) Transducer WVTFTG

Fig. 7.4.6 Gross (LVDT) Strains vs. Lateral Drift in Wall Specimen 12

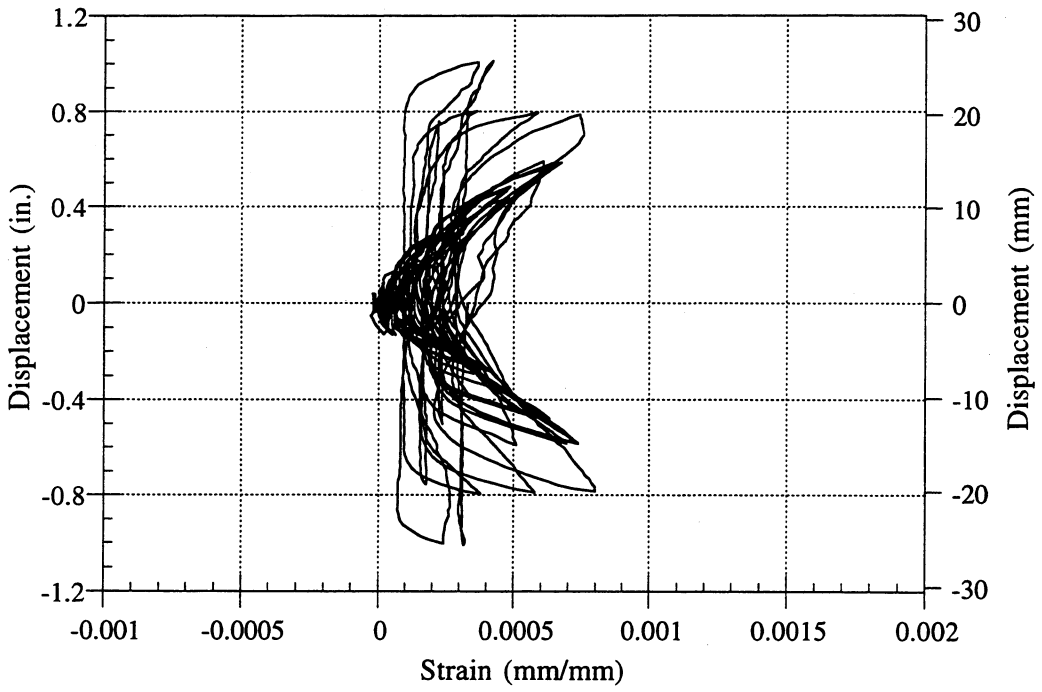

c) Transducer WVTMID

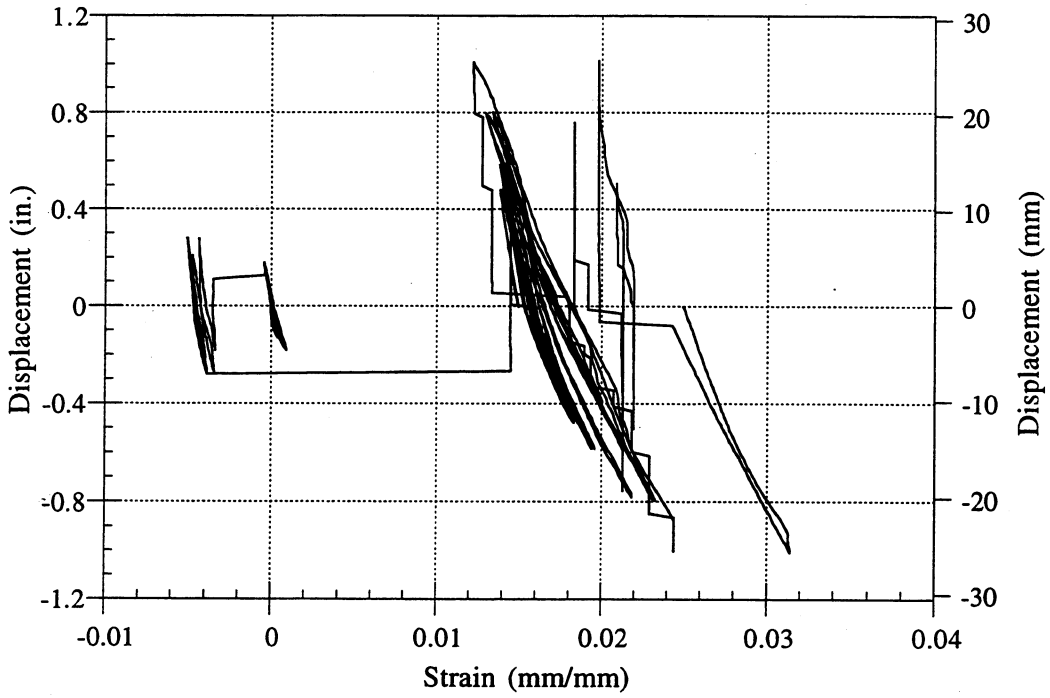

d) Transducer ETWBD

Fig. 7.4.6 (Cont'd)

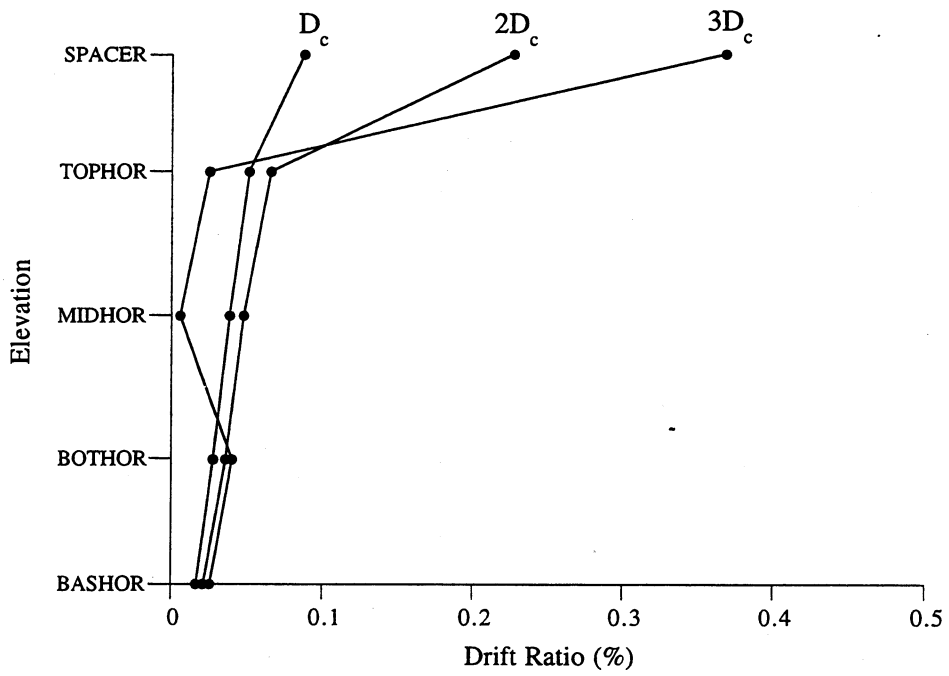

Fig. 7.5.1 Displaced Profiles for Wall Specimen 2

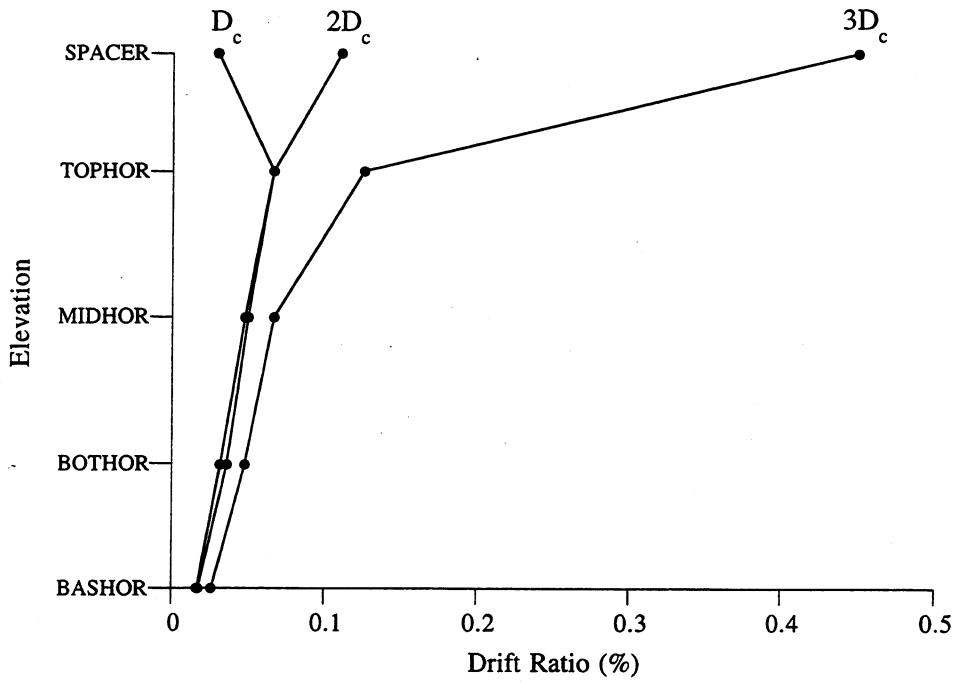

Fig. 7.5.2 Displaced Profiles for Wall Specimen 4

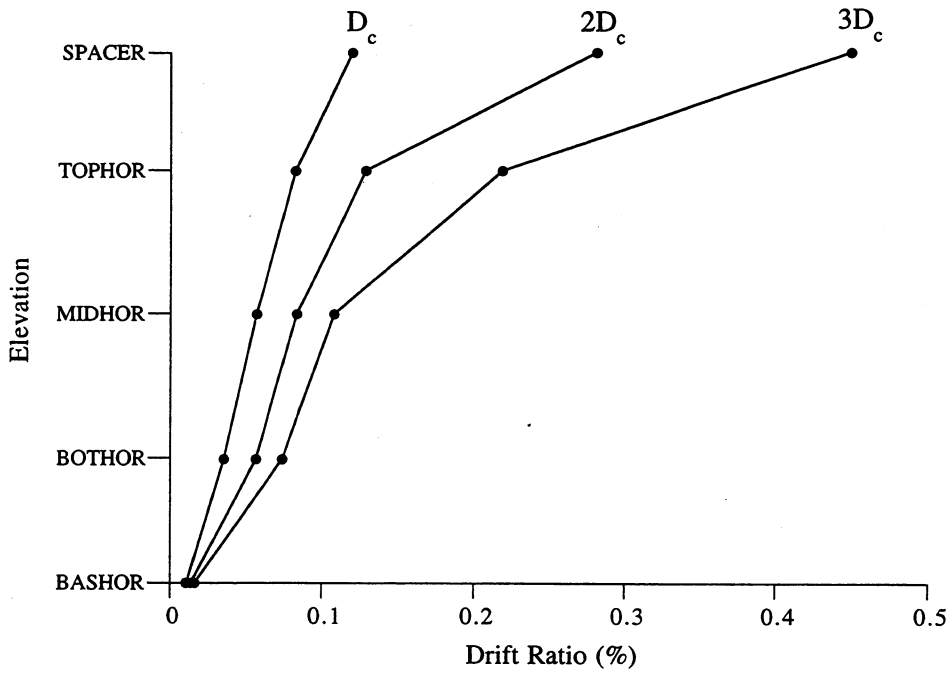

Fig. 7.5.3 Displaced Profiles for Wall Specimen 6

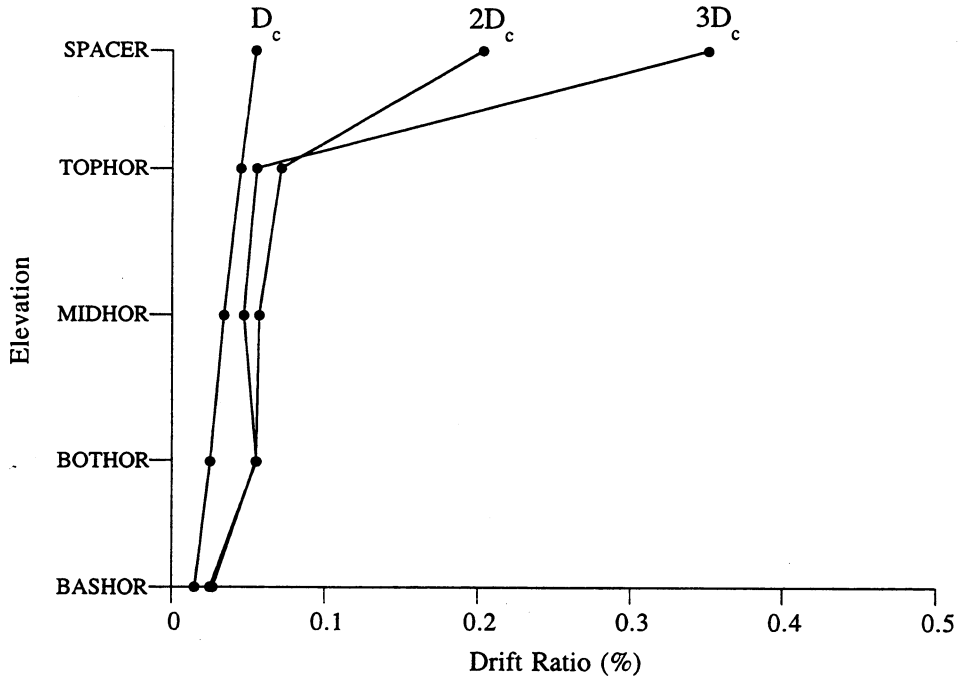

Fig. 7.5.4 Displaced Profiles for Wall Specimen 8

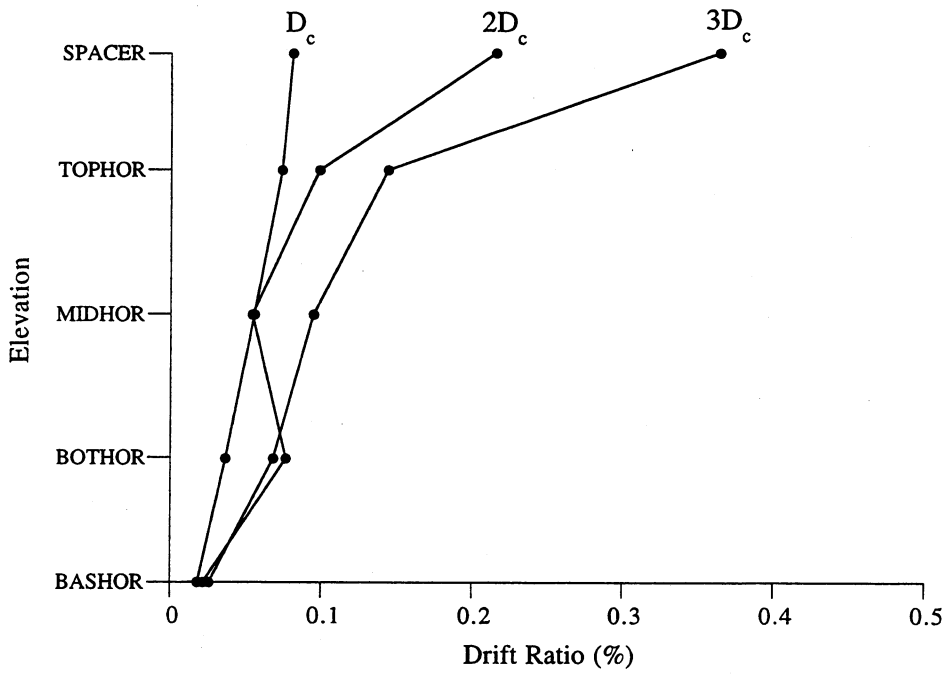

Fig. 7.5.5 Displaced Profiles for Wall Specimen 10

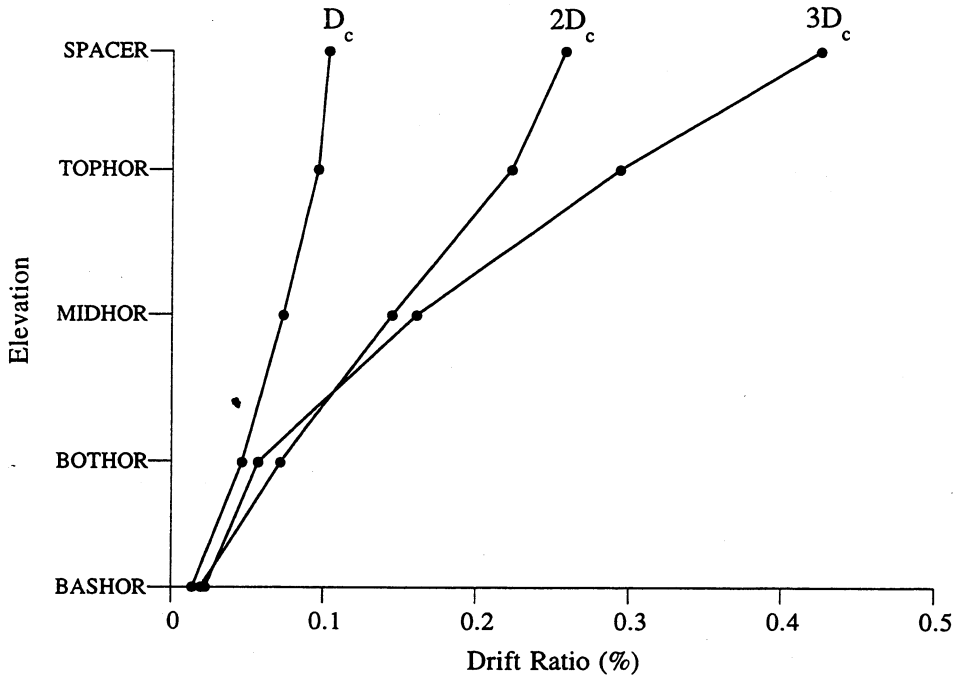

Fig. 7.5.6 Displaced Profiles for Wall Specimen 12

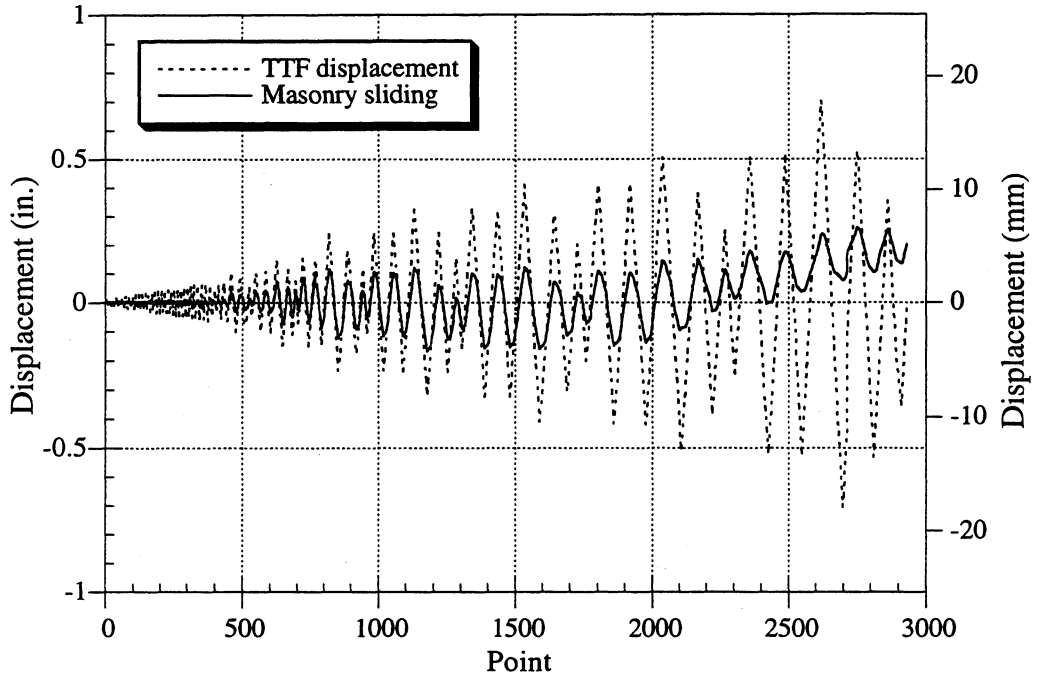

a) Along Top of Masonry

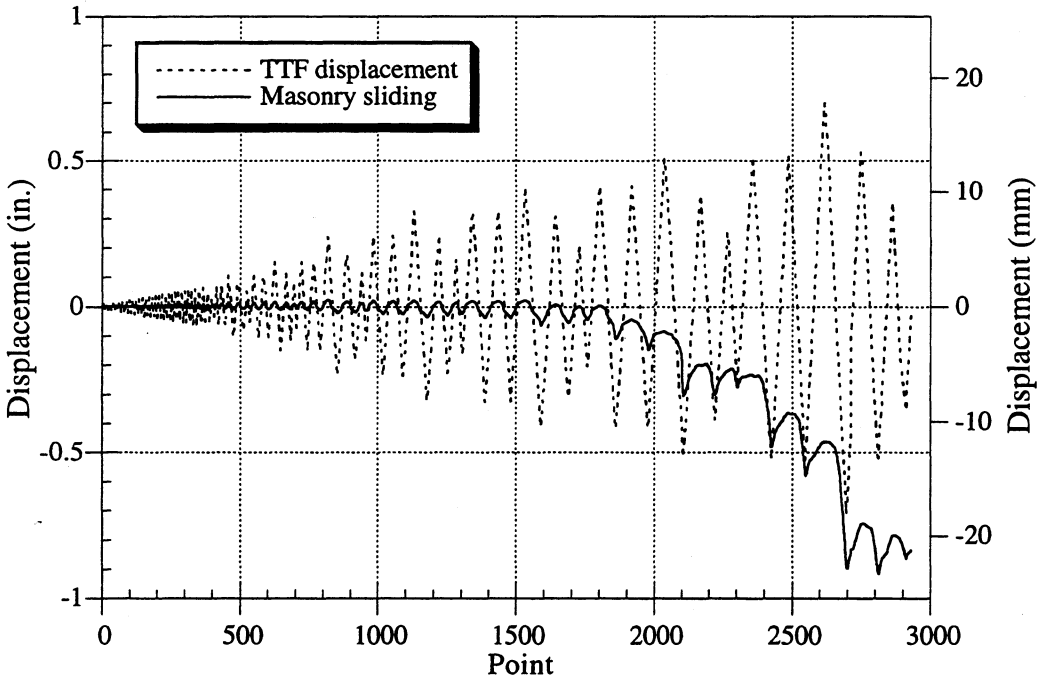

b) Along Bottom of Masonry

Fig. 7.5.7 Masonry Sliding Response in Wall Specimen 10

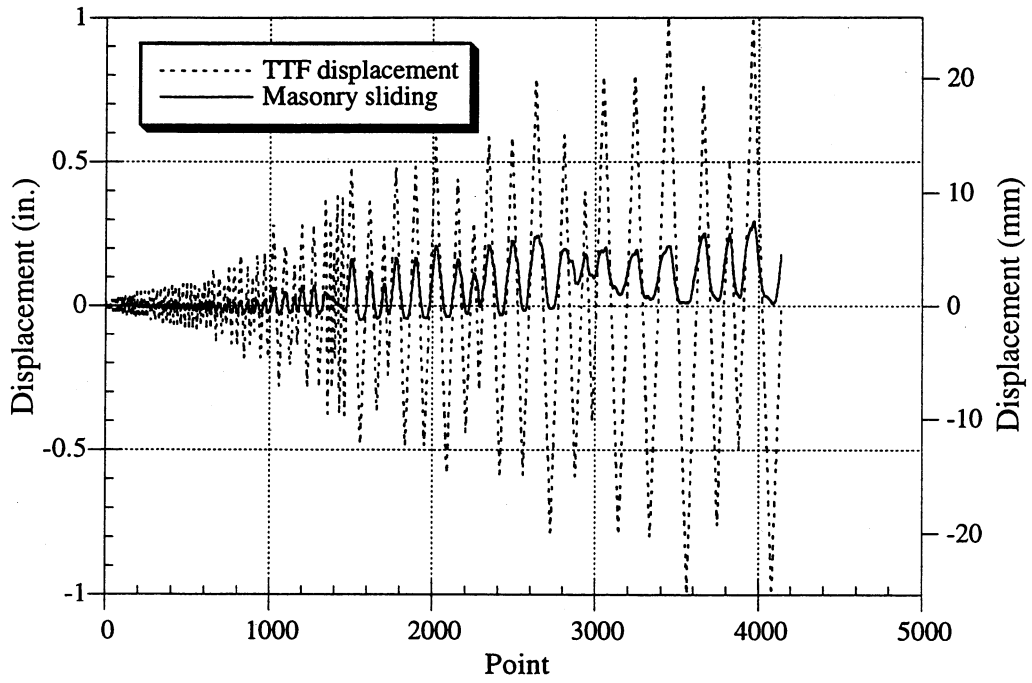

a) Along Top of Masonry

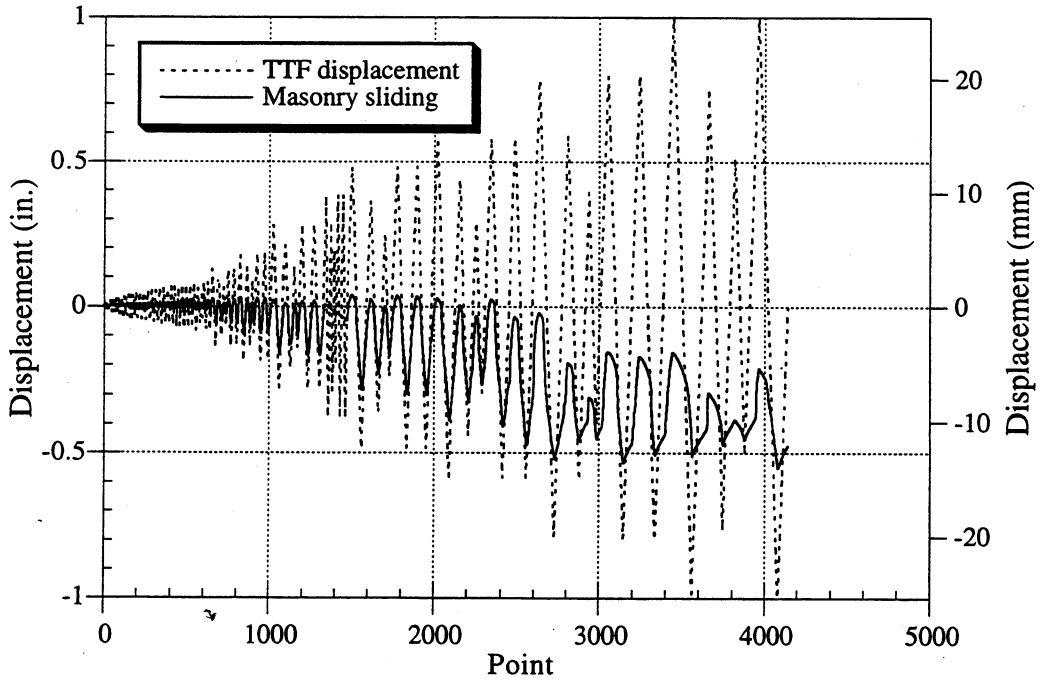

b) Along Bottom of Masonry

Fig. 7.5.8 Masonry Sliding Response in Wall Specimen 12

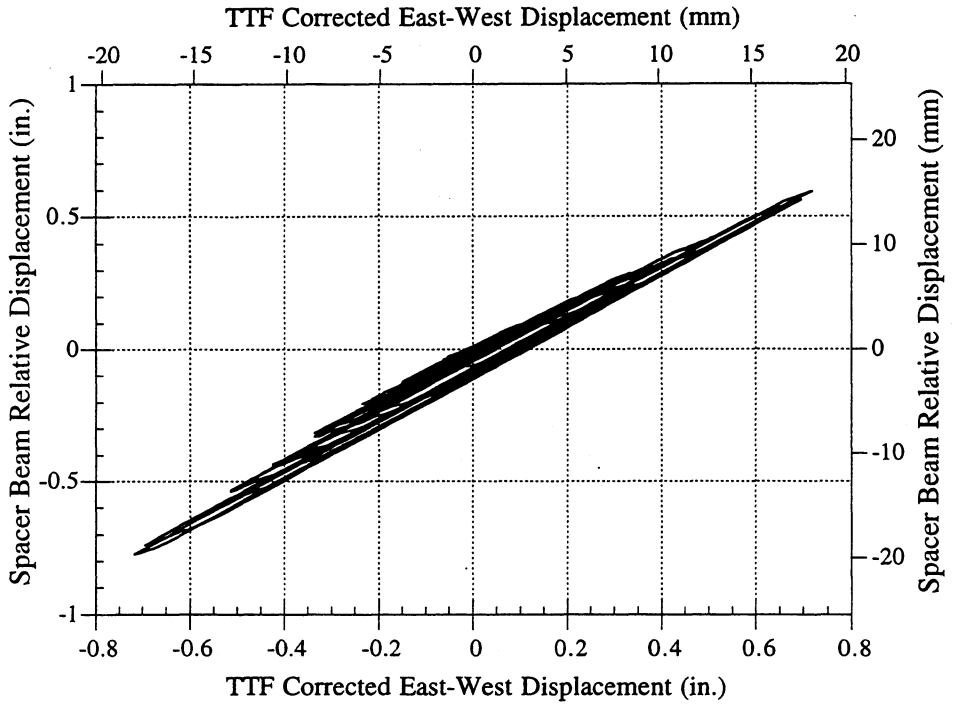

Fig. 7.5.9 Correlation Between TTF and External Displacements for Wall Specimen 2

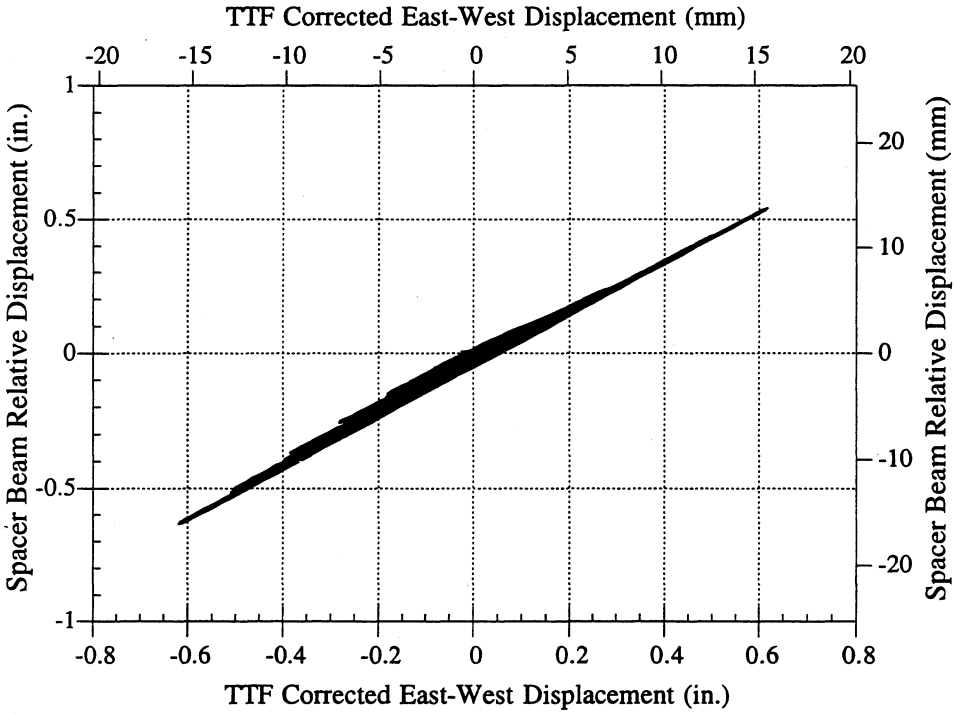

Fig. 7.5.10 Correlation Between TTF and External Displacements for Wall Specimen 4

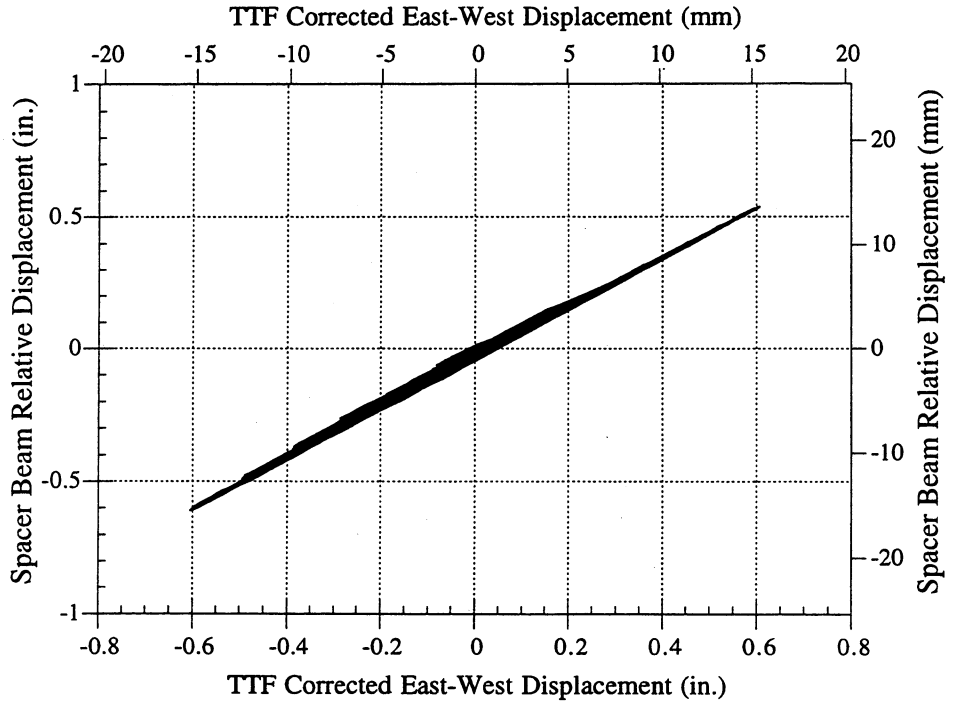

Fig. 7.5.11 Correlation Between TTF and External Displacements for Wall Specimen 6

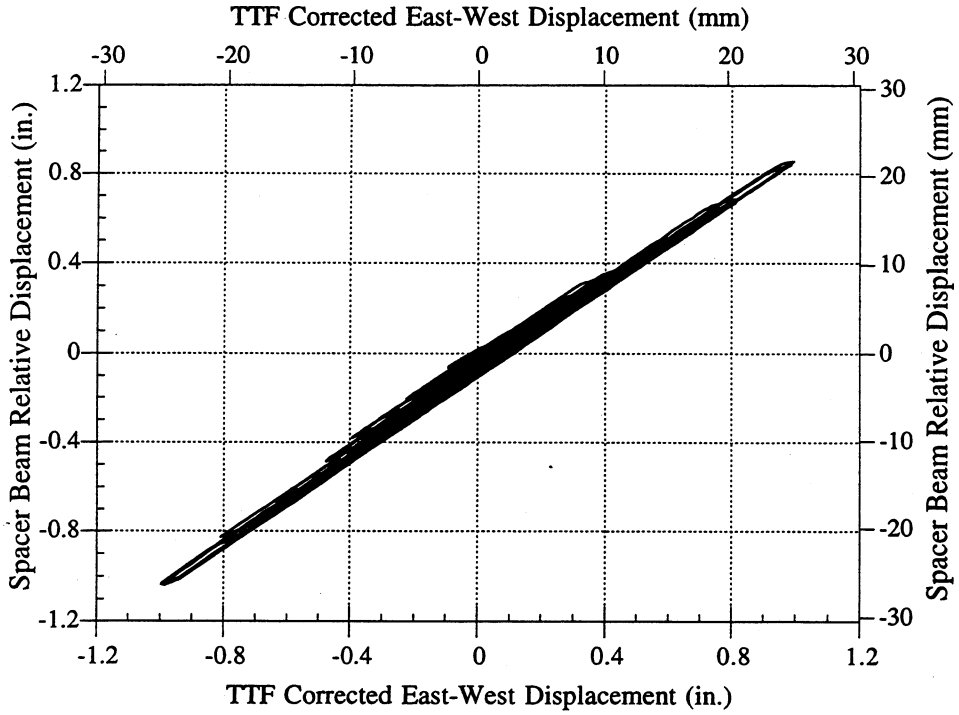

Fig. 7.5.12 Correlation Between TTF and External Displacements for Wall Specimen 8

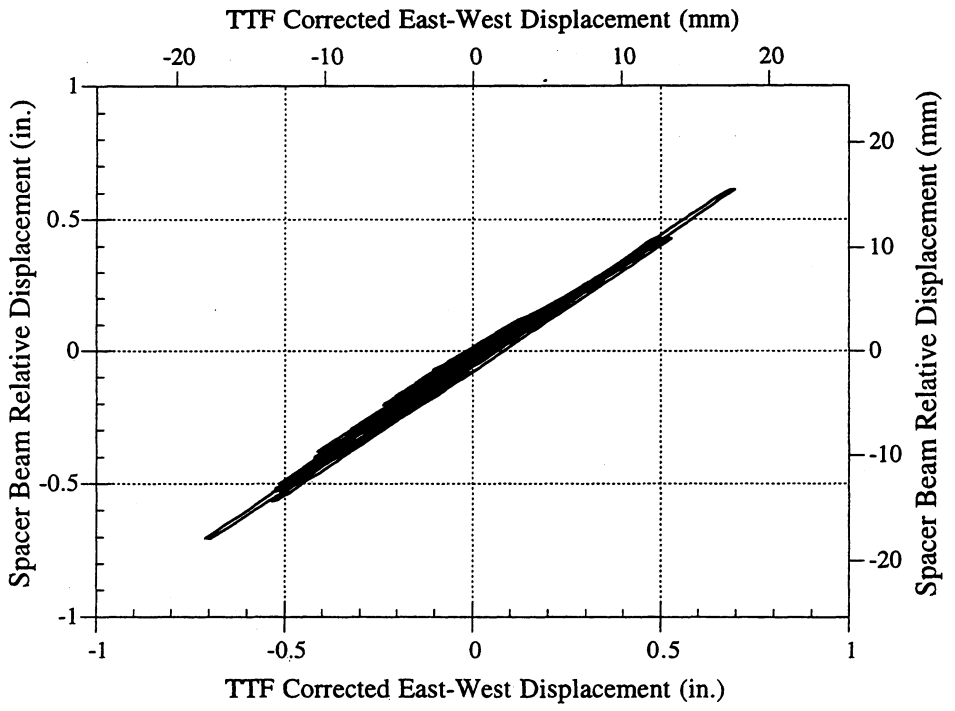

Fig. 7.5.13 Correlation Between TTF and External Displacements for Wall Specimen 10

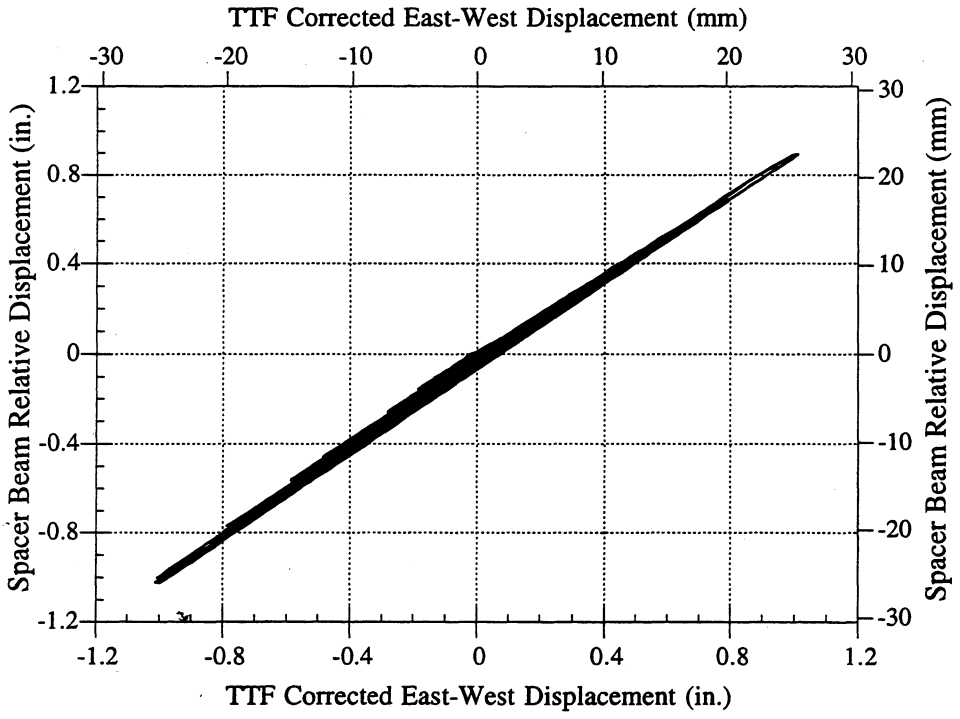

Fig. 7.5.14 Correlation Between TTF and External Displacements for Wall Specimen 12

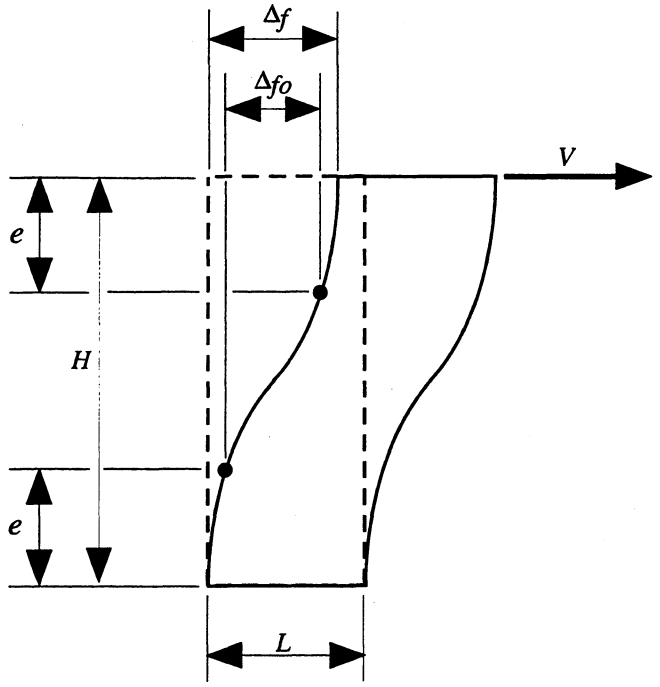

a) Pure Flexure

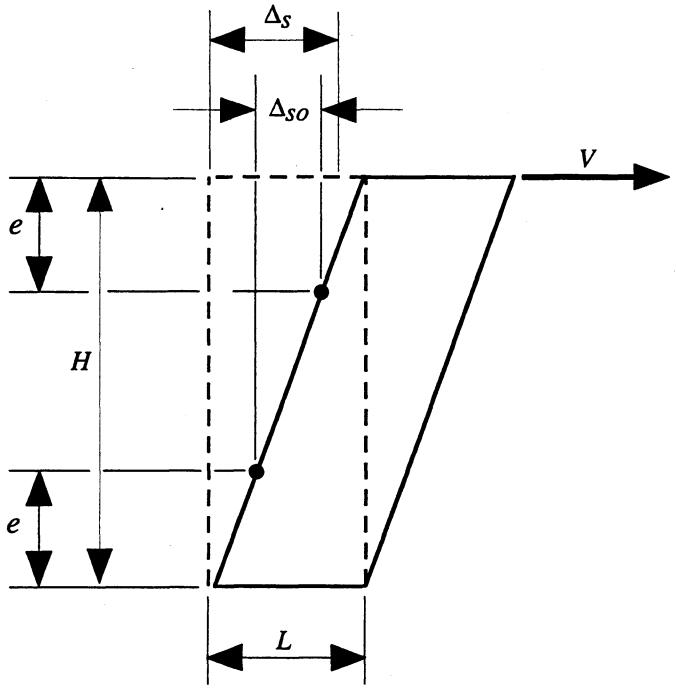

b) Pure Shear

Fig. 8.1 Shear and Flexural Deformations in Elastic Shear Walls

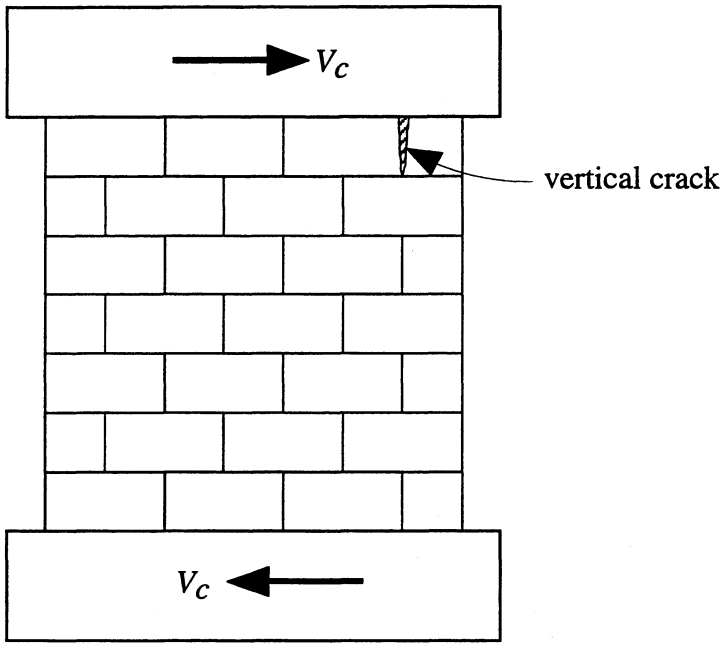

a) Cracked Wall Specimen

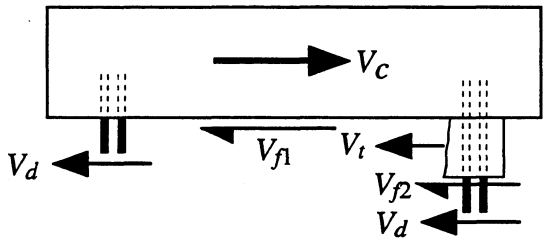

b) Forces Along Top of Masonry

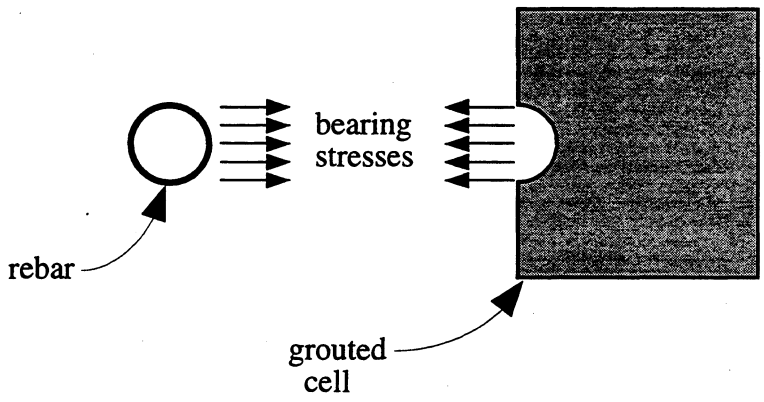

c) Dowel Action of Vertical Bars

Fig. 8.2 Shear Resistance Mechanisms at First Cracking

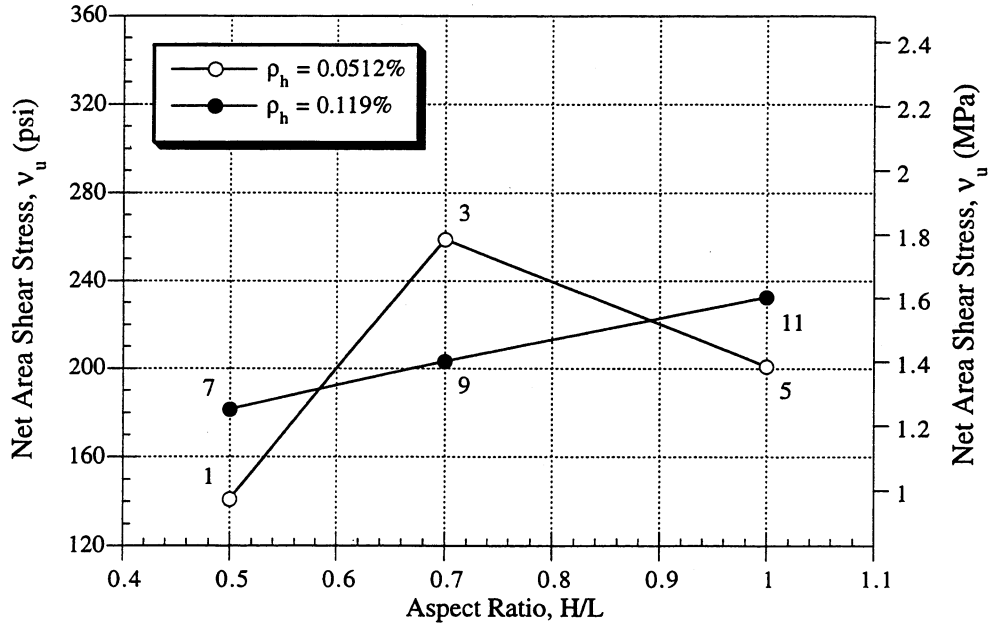

a) Series 1

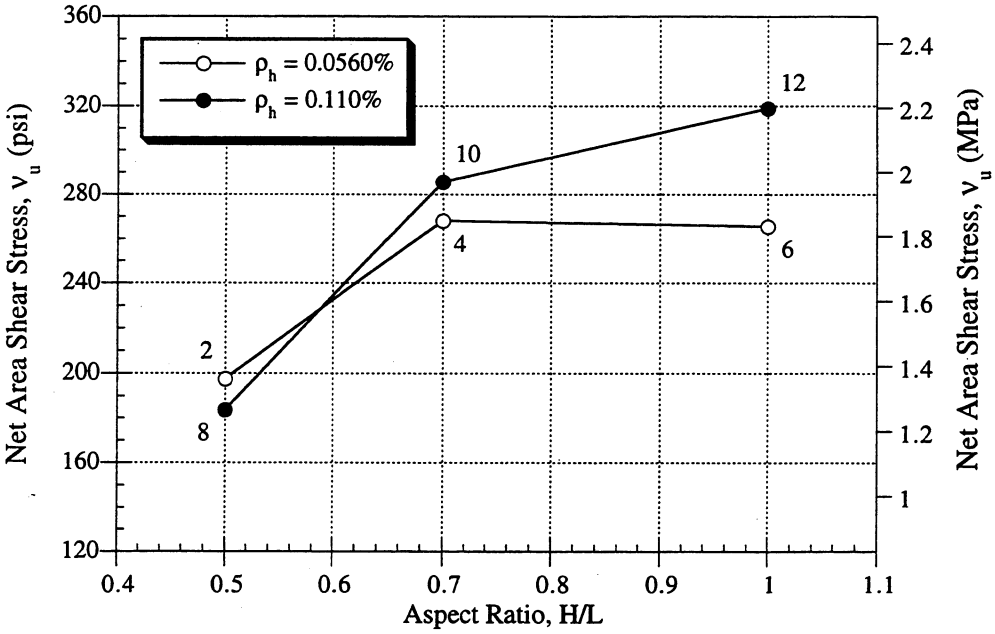

b) Series 2

Fig. 8.3.1 Dependance of Net Area Shear Stresses at Ultimate on Aspect Ratio

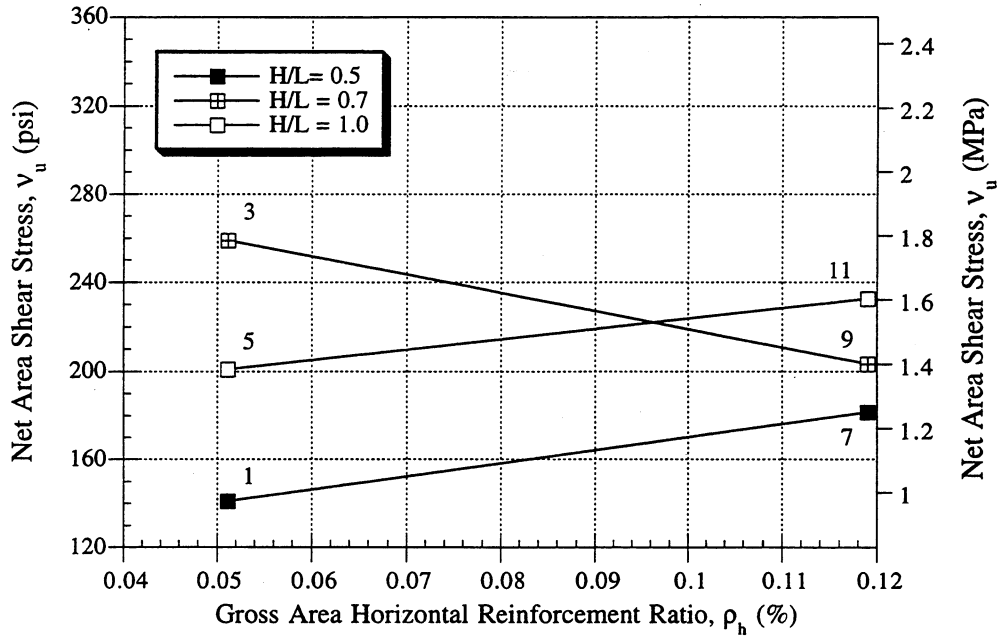

a) Series 1

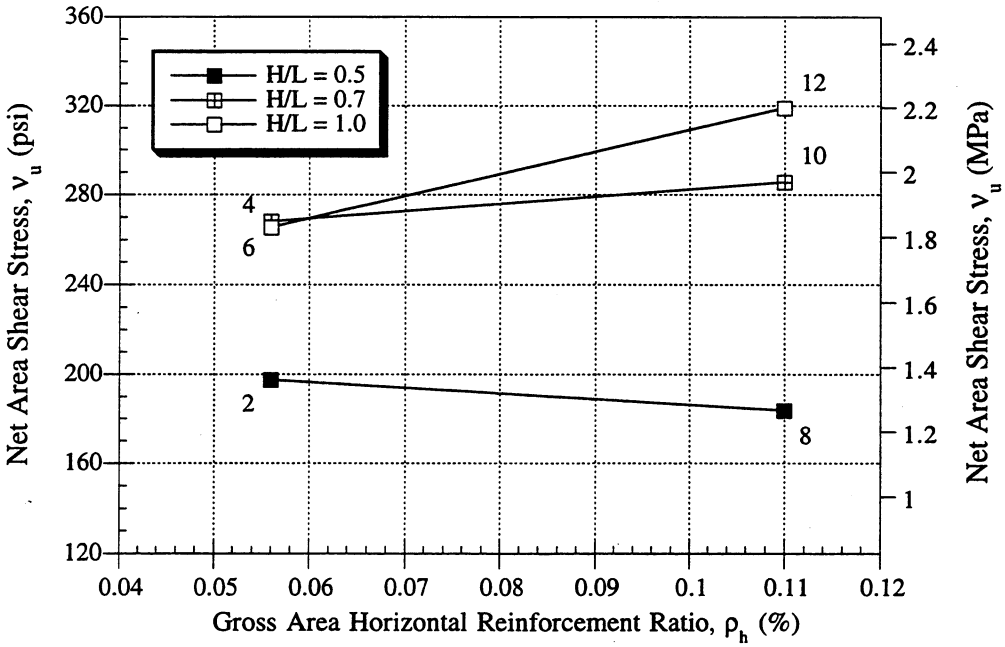

b) Series 2

Fig. 8.3.2 Dependance of Net Area Shear Stresses at Ultimate on Reinforcement Ratio

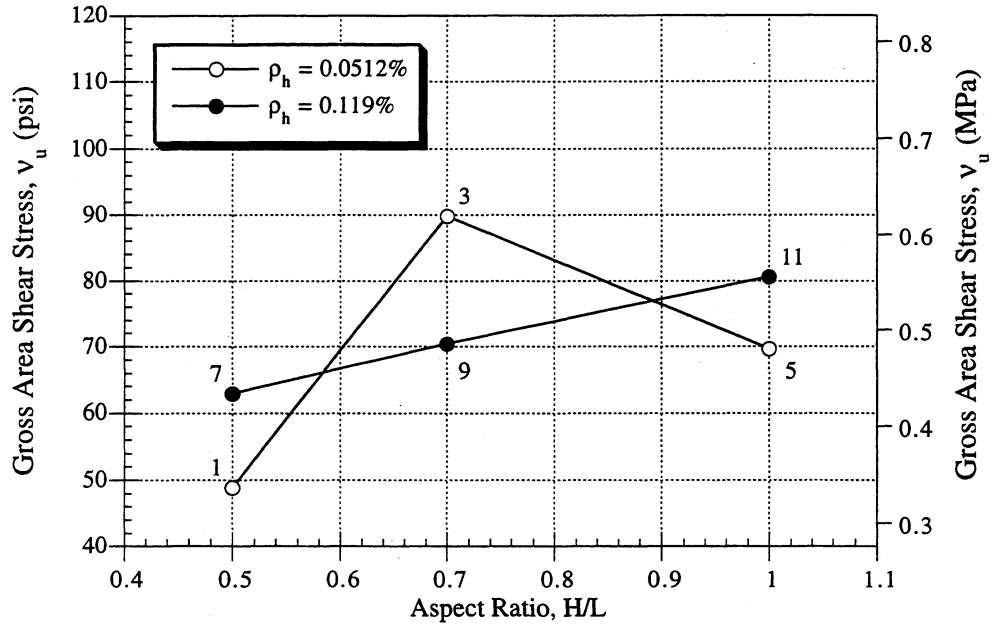

a) Series 1

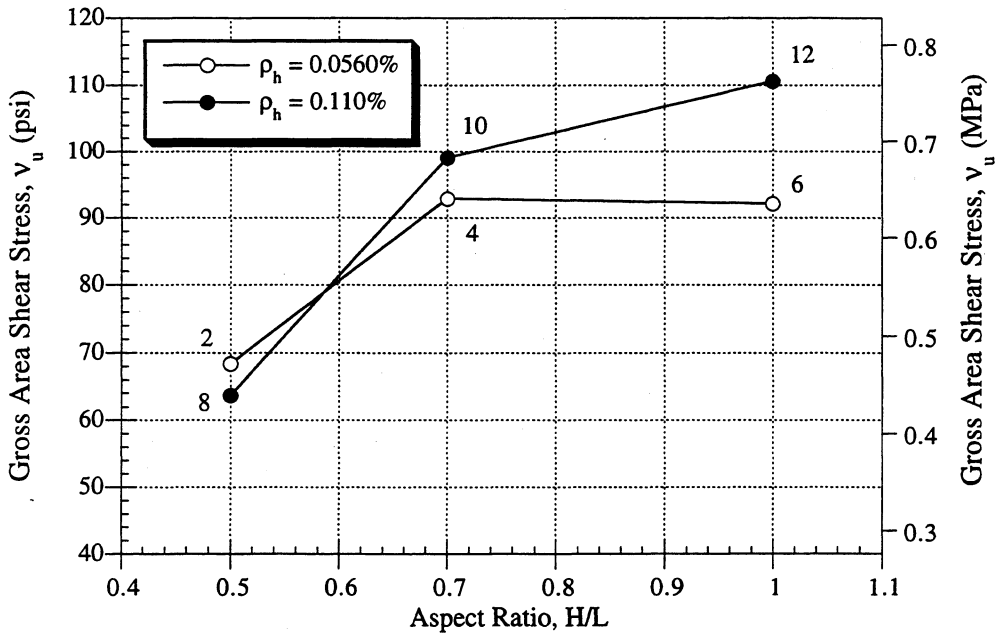

b) Series 2

Fig. 8.3.3 Dependance of Gross Area Shear Stresses at Ultimate on Aspect Ratio

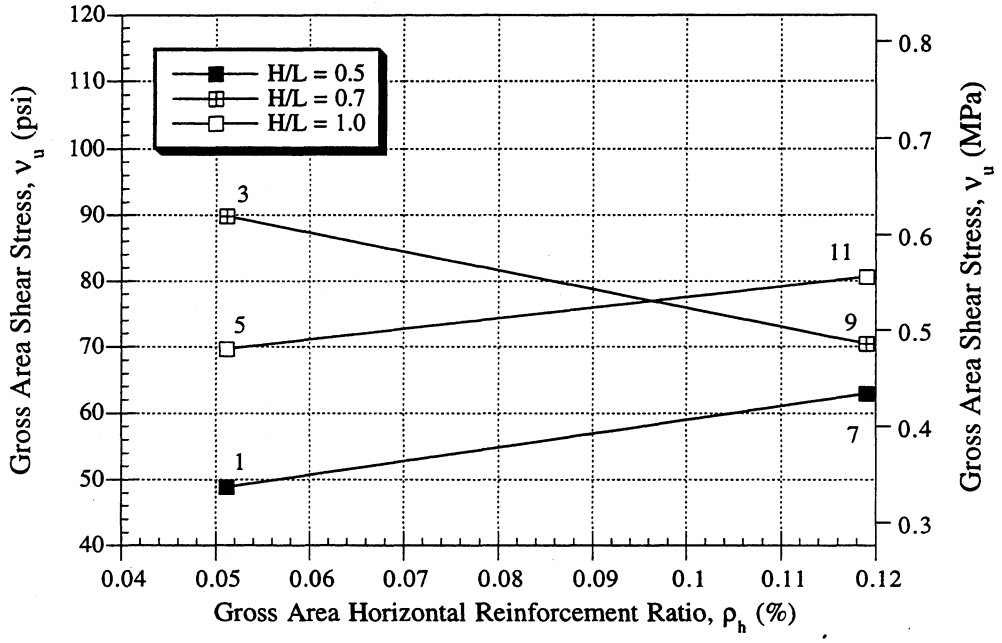

a) Series 1

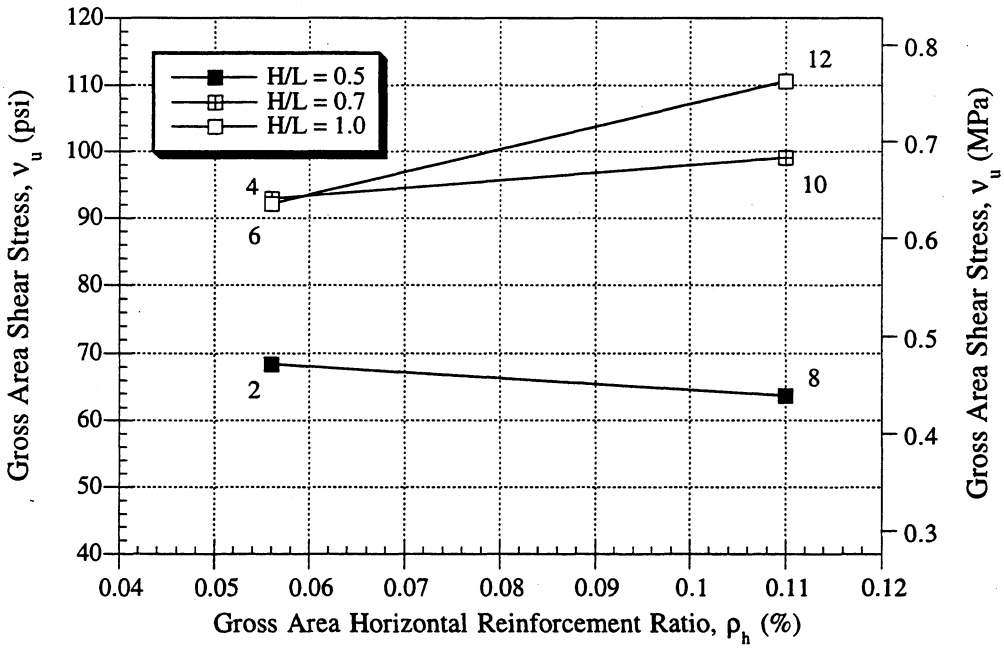

b) Series 2

Fig. 8.3.4 Dependance of Gross Area Shear Stresses at Ultimate on Reinforcement Ratio

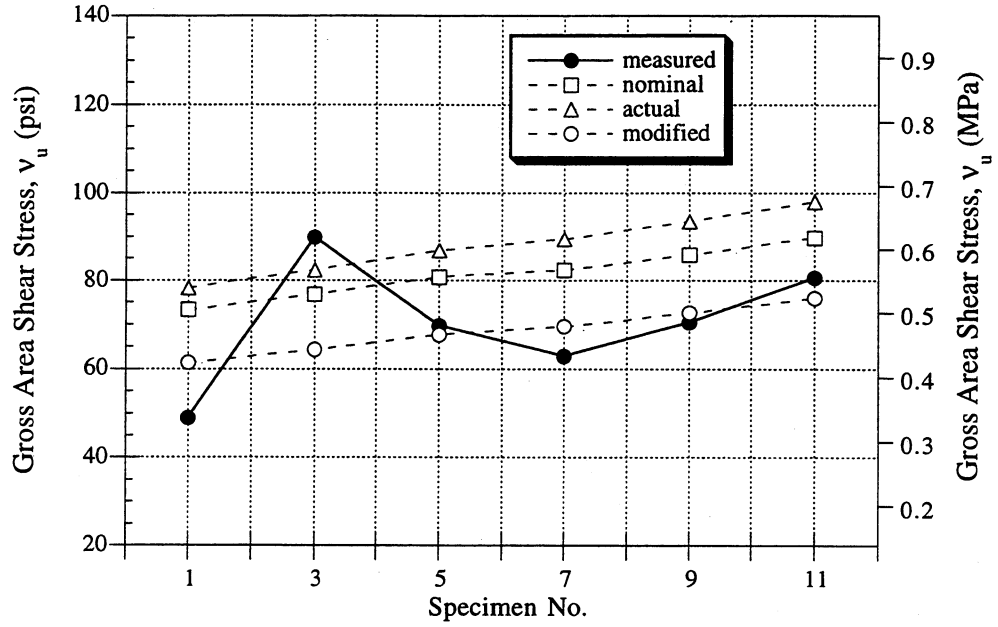

a) Series 1

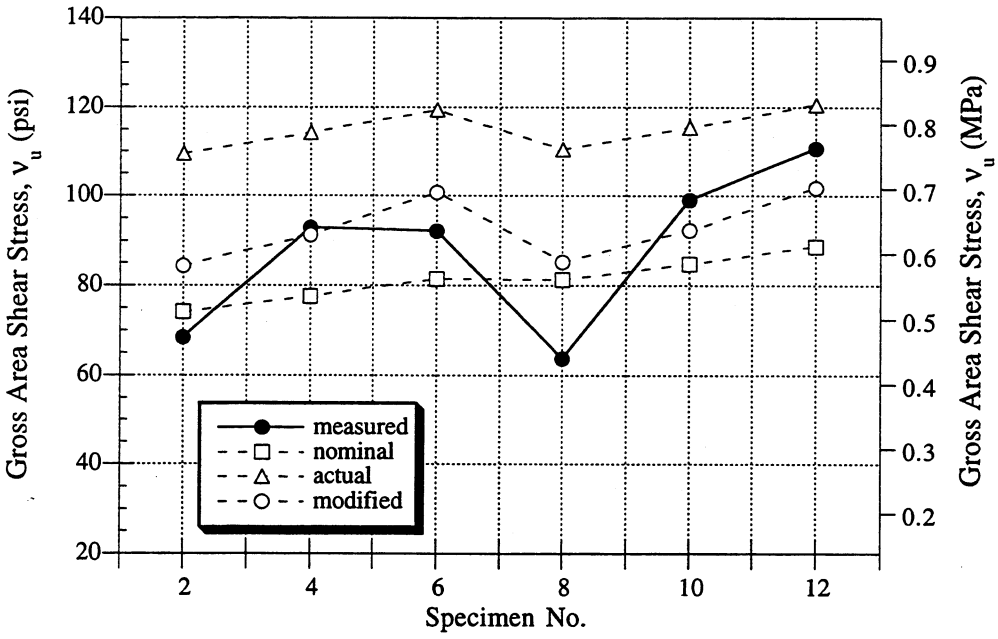

b) Series 2

Fig. 8.3.5 Calculated Gross Area Shear Stresses at Ultimate

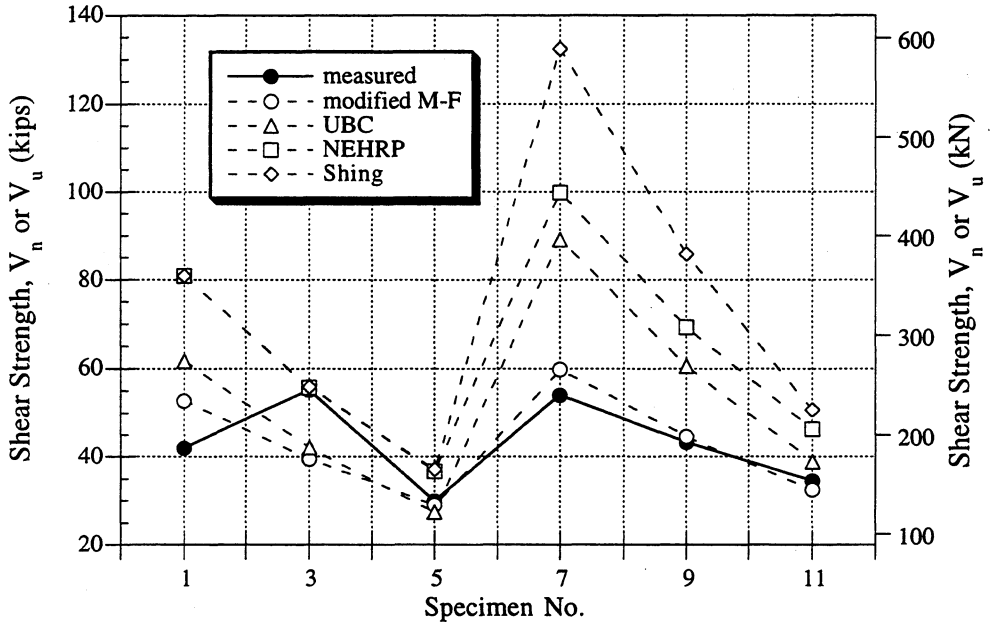

a) Series 1

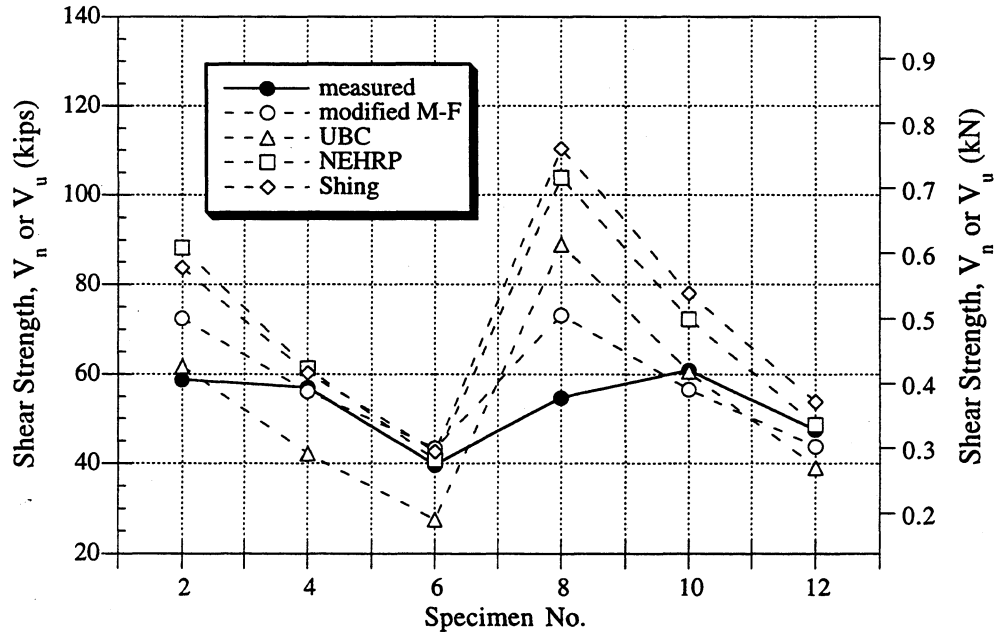

b) Series 2

Fig. 8.4.1 Calculated Shear Strengths at Ultimate

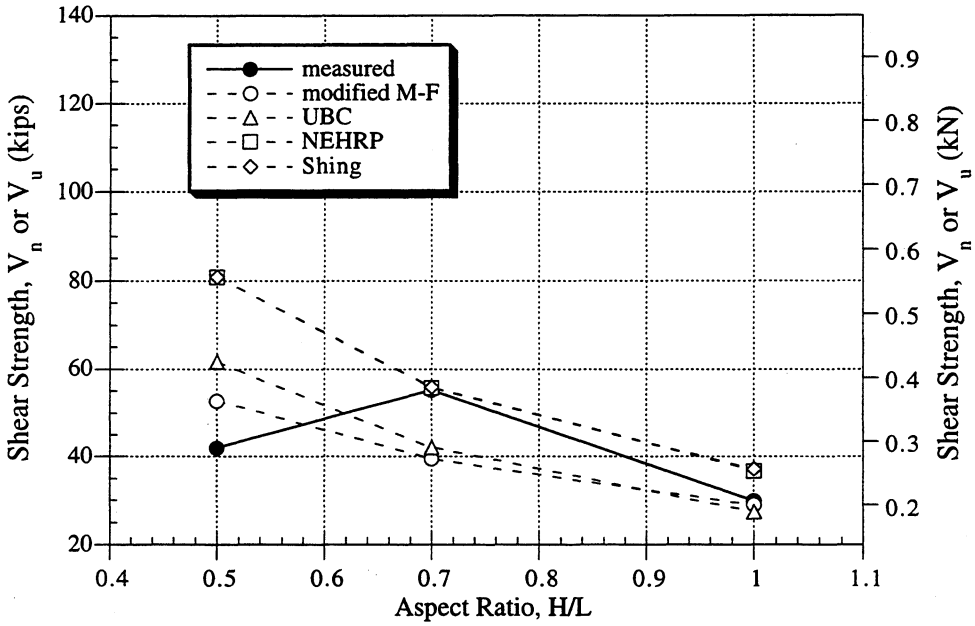

a) Series 1 (ρ_h = 0.0512%)

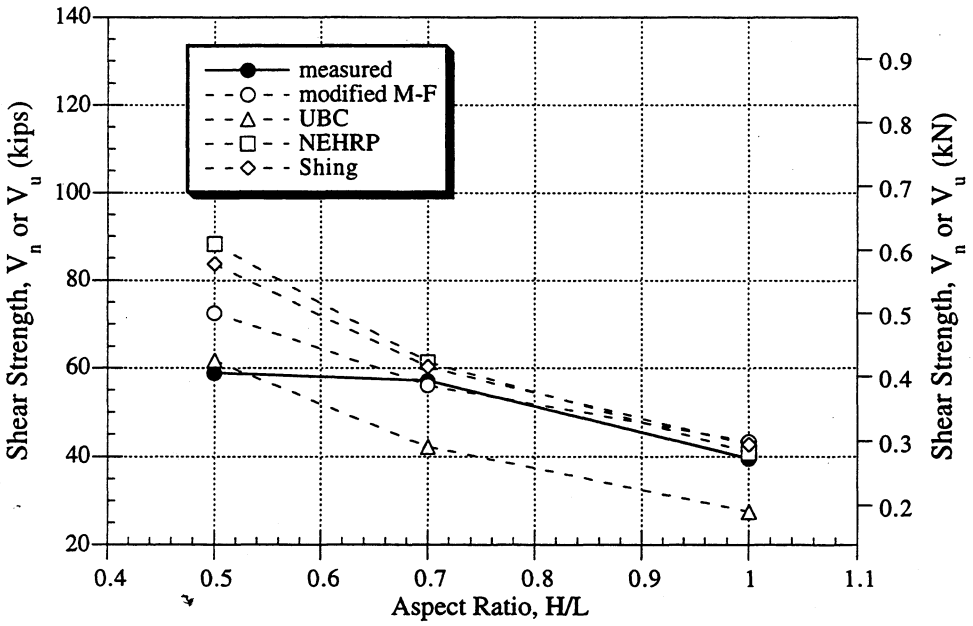

b) Series 2 (ρ_h = 0.0560%)

Fig. 8.4.2 Calculated Shear Strengths vs. Aspect Ratio for Lightly-Reinforced Specimens

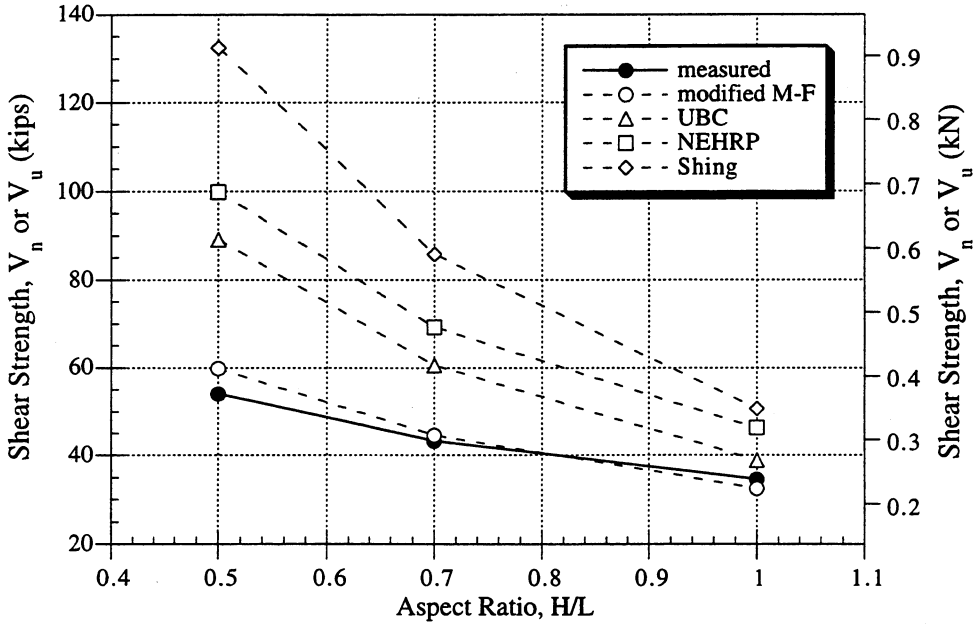

a) Series 1 (ρ_h = 0.119%)

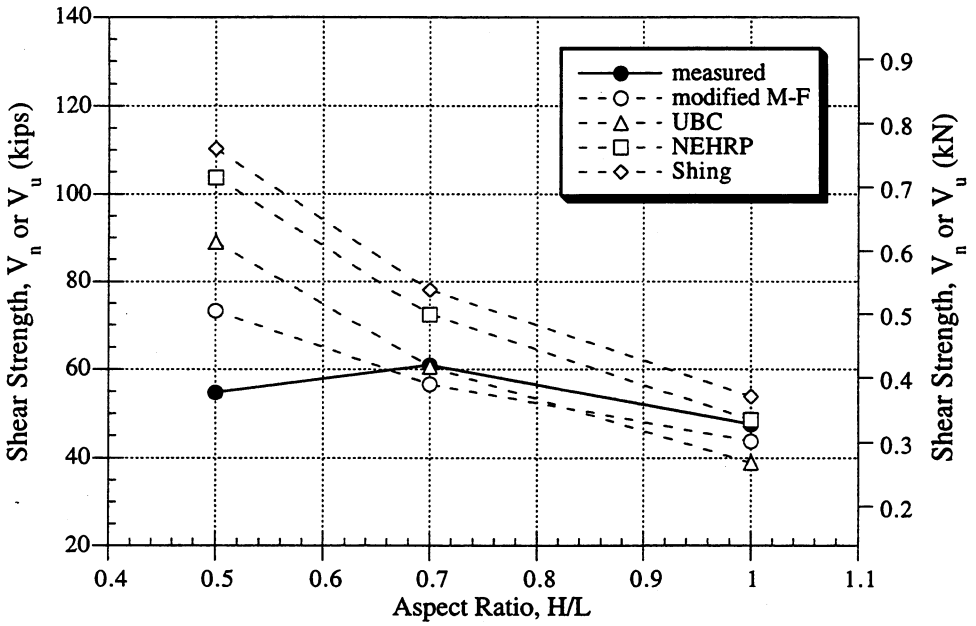

b) Series 2 (ρ_h = 0.110%)

Fig. 8.4.3 Calculated Shear Strengths vs. Aspect Ratio for Heavily-Reinforced Specimens

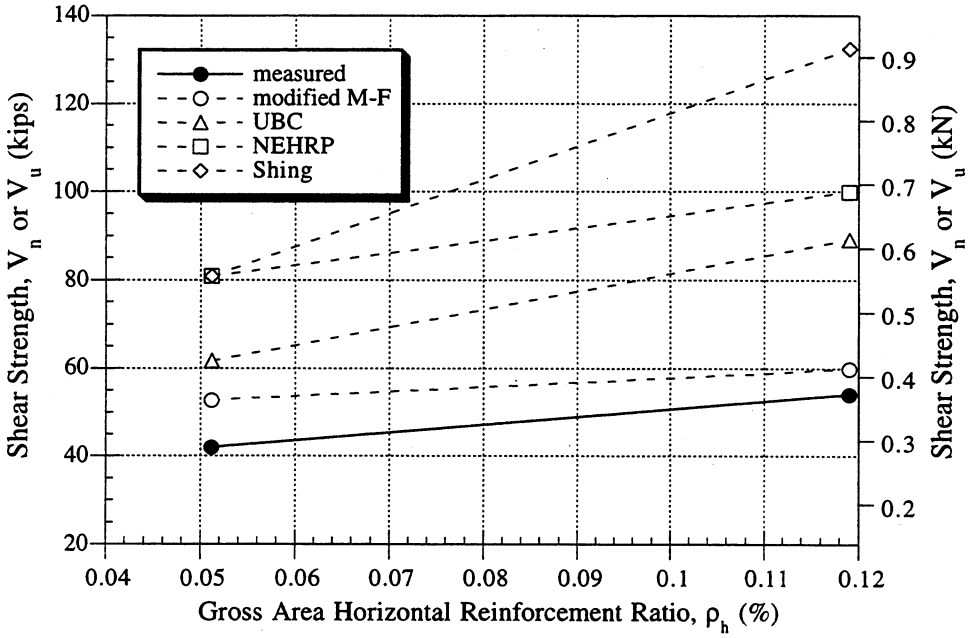

a) Series 1 (H/L = 0.5)

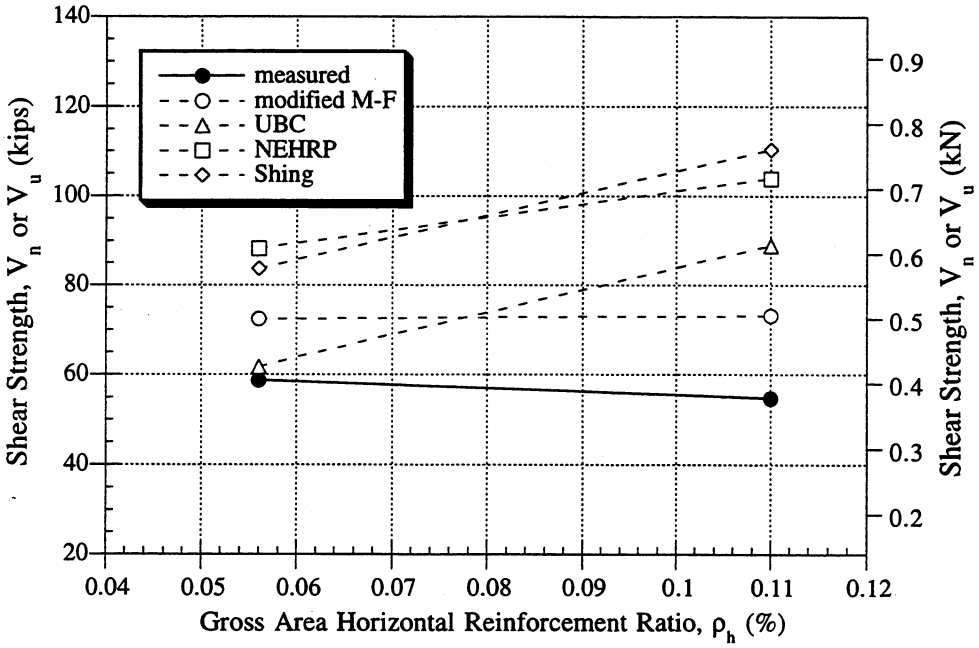

b) Series 2 (H/L = 0.5)

Fig. 8.4.4 Calculated Shear Strengths vs. Reinforcement Ratio for Stocky Specimens

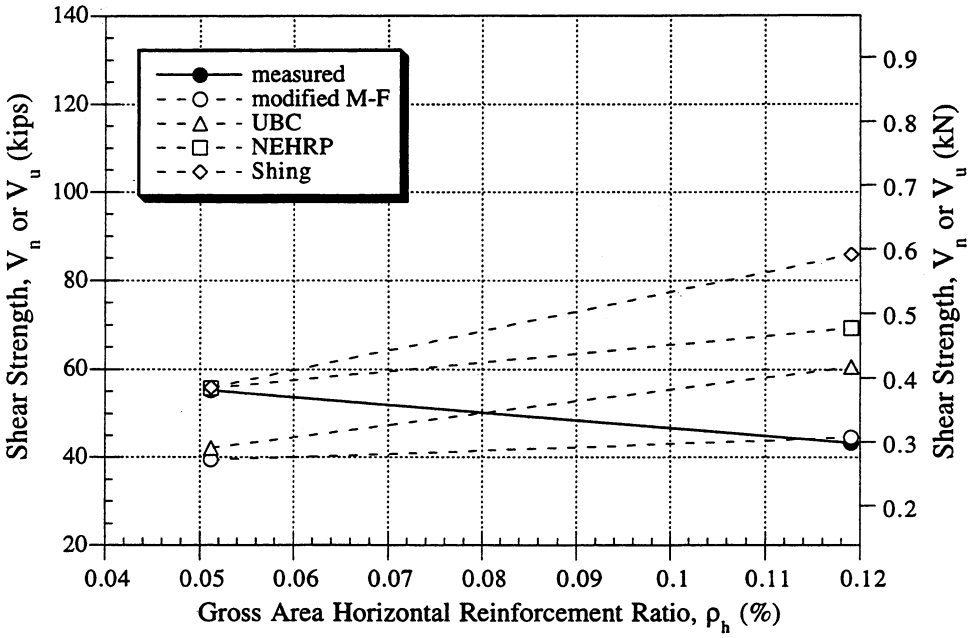

a) Series 1 (H/L = 0.7)

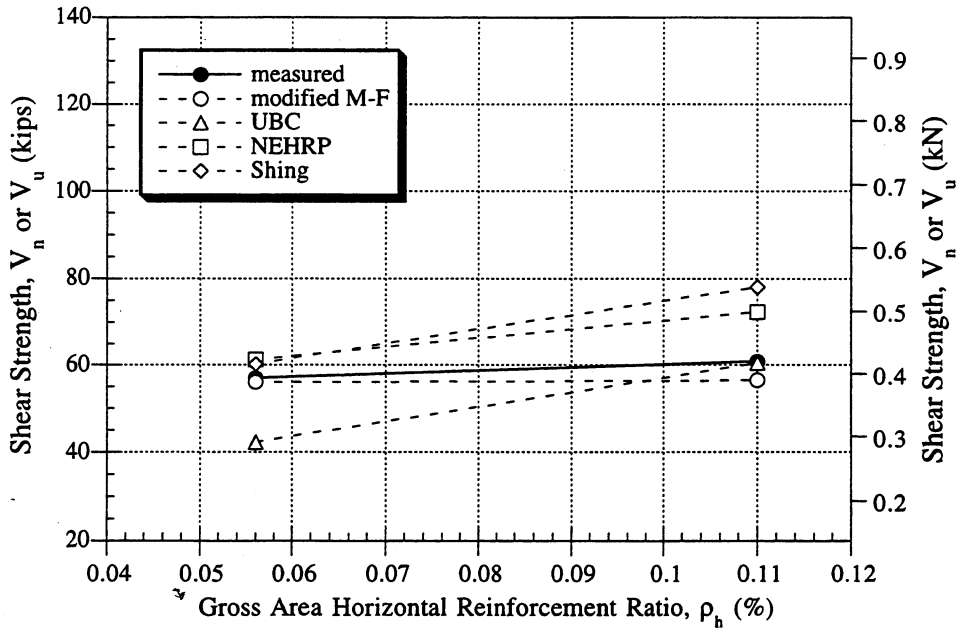

b) Series 2 (H/L = 0.7)

Fig. 8.4.5 Calculated Shear Strengths vs. Reinforcement Ratio for Intermediate Specimens

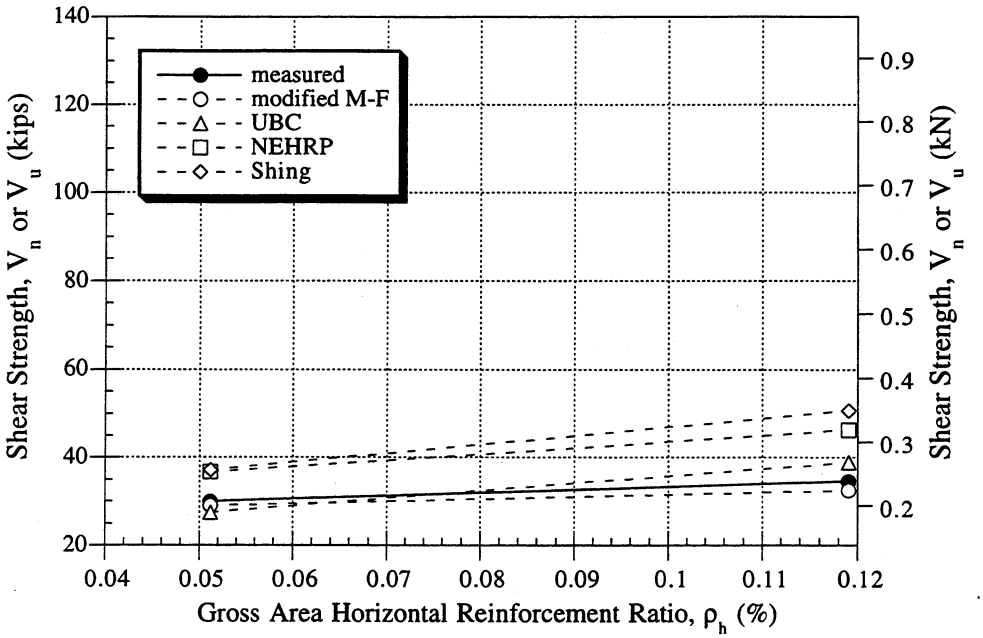

a) Series 1 (H/L = 1.0)

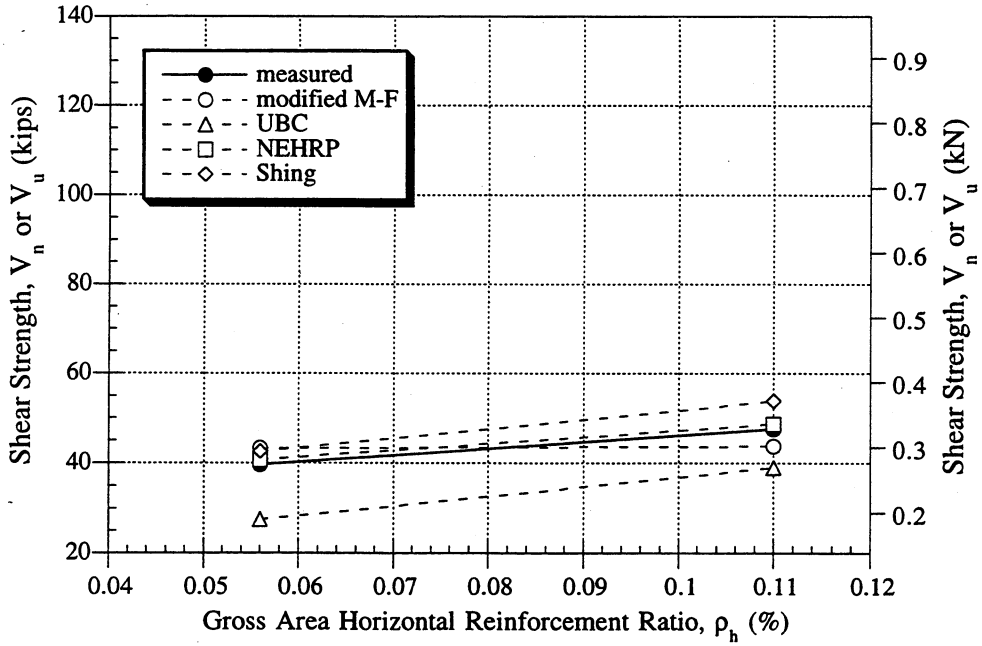

b) Series 2 (H/L = 1.0)

Fig. 8.4.6 Calculated Shear Strengths vs. Reinforcement Ratio for Slender Specimens

APPENDIX. SHEAR WALL SPECIMEN 14

A.1 Introduction

A seventh shear wall specimen was fabricated and tested as an extension of Series 2. This specimen, Shear Wall 14, is not identified in Priority I (Table 2.2), nor in any part of the NIST Masonry Research Program (Table 2.2). It was added to the research program to explore the use of welded wire grids that serve not only as horizontal reinforcement, but also as confining reinforcement for grouted vertical cells. Confinement is achieved by providing close spacing of the transverse wires in the welded grids, such that the axial stiffness of these wires prevents the out-of-plane lateral deformation of the grouted cells. Lateral deformation (i.e., dilatation) of the grouted cell under vertical compression, particularly from overturning due to lateral loading, generates tension in the transverse wires which serves to confine the grouted masonry. Confinement of the grouted cells is desirable because it leads to tougher walls with more reliable lateral resistance characteristics.

The objective of building and testing Shear Wall 14 was to verify the confinement mechanism mobilized by welded wire grids with closely-spaced transverse wires. To this end, the specimen was configured to be identical to one of the six specimens in Series 2 in every respect, except for the spacing of the transverse wires in the welded horizontal reinforcement grids. Shear Wall 12 was selected as the most suitable target in Series 2 for two reasons. Wall 12 has both the most slender profile in Series 2 ($r = H/L = 1$), as well as the highest horizontal reinforcement ratio ($\rho_h = 0.110$ %). The former increases axial compression demands on the grouted vertical cells from overturning, while the latter endows the wall with ample shear strength and drift capacity to mobilize the confinement mechanism. This combination provides the best opportunity to observe if the confinement afforded by close transverse wire spacing can lead to observable results.

Finally, a note regarding the relative effectiveness of confining partially-grouted and fully-grouted masonry walls is in order. A fully-grouted wall should benefit more from the confinement provided by closely-spaced, welded wire grids than a partially-grouted wall because there is more grouted masonry present in a fully-grouted section. However, if

partially-grouted masonry shear walls can be shown to benefit from such confinement, then fully-grouted masonry walls are certain to enjoy these benefits as well. The inverse, however, is not necessarily true. Thus, a partially-grouted masonry shear wall test is viewed as a stricter criterion than the test of a fully-grouted wall.

A.2 Welded Wire Confining Reinforcement Grids

The welded wire grids used as horizontal reinforcement in Shear Wall 14 (Fig. A.1) are very similar to those used for Wall No.s 8, 10 and 12 in Series 2 (Fig. 3.3). Cold-drawn No. 5 Gage steel wire with a 5.26-mm (0.207-in.) diameter was used for both the longitudinal and the transverse (cross) wires, and these were butt-welded at the intersections. The only difference in the specifications for the wire grids in Wall 14 is the spacing of the cross wires (102 mm or 4 in.) which were placed at one-fourth the spacing used for the grids in Walls 8, 10 and 12 (406 mm or 16 in.). A smaller cross-wire spacing was deemed necessary if the welded grids in Wall 14 were to provide adequate confining pressure to the grouted cells.

The primary structural action for the wire grids used in Series 2 is cyclic tension along the principal axis of the longitudinal wires. This behavior was clearly evident during the tests of Walls 2, 4, 6, 8, 10, and 12, culminating with ductile fracture of wire, usually away from the welded intersections. However, the confining stresses that the type of grids in Shear Wall 14 are expected to develop introduce loading along the axis of the cross-wires, with direct stress being applied to the butt welds. This loading is of concern because butt welds in steel wire products are usually not as strong as lap welds. Upon attaining the axial capacity of the butt welds, the confinement mechanism in Wall 14 will be effectively terminated regardless of the stress state in the cross wires.

A.3 Fabrication and Testing of Wall Specimen 14

Shear Wall 14 was built at the same time as the Walls in Series 2, using the same personnel and fabrication procedure. Nominal dimensions for Wall 14 were identical to those for Wall 12 (Fig. 3.1c). Masonry units from the same batch (Table 3.1) were used for Wall 14, as were the mortar mix (Table 3.2a) and grout mix (Table 3.2b). Masonry compression strengths for

Wall 14 (Table A.1) were comparable to those for the other walls (Table 3.5), and tensile strength results for the wire grids with a 102-mm (4-in.) cross-wire spacing (Table A.2) were nearly identical to those for the wire grids with a 5.26-mm (0.207-in.) diameter and 406-mm (16-in.) cross-wire spacing (Table 3.11).

The lateral loading history for Wall 14 was carried out by displacing the top of the wall, without allowing rotation, using the same drift history that was used for the other walls in Series 2 (Fig. 4.2). As in previous tests, vertical load was maintained approximately constant during the lateral loading history. The magnitude of vertical load variation that was sufficiently small to be considered nearly constant (e.g., see Fig. 4.3). The target value for vertical load was 133.4 kN (30 kips), and the mean value of measured vertical load history was equal to 131.3 kN (29.53 kips) with a standard deviation equal to 6.2 kN (1.40 kips).

Shear Wall 14 was instrumented with strain gages, LVDT's and LST's employing the same sensor and transducer placement schemes used in Series 2 (Fig. 4.4-4.7). Precise locations of the LST's in Wall 14 are given in Table A.3. Data from these instruments was recorded, processed and analyzed using the procedures outlined in Chapters 5-7.

The final crack pattern for Wall 14 is shown in a sketch in Fig. A.2. The crack pattern is very similar to that recorded for Wall 12 (Fig. 5.12), except that Wall 14 displays a slightly less-developed inclined crack formation. Many of the inclined cracks in Wall 14 are essentially discontinued in the vicinity of the center of the wall. In addition, there is more compression damage, including spalling, along the vertical edges (i.e., jambs) of Wall 14 than in Wall 12.

A.4 Force-Displacement Response

The in-plane, lateral displacement history for Wall 14, measured between top and bottom crossheads, is shown in Fig. A.3. The history is quite similar to that for Wall 12 (Fig. 6.1.6), except that Wall 12 was loaded to a larger peak lateral displacement than was Wall 14. The shear force history for Wall 14 is given in Fig. A.4, and a strong resemblance to the shear force history for Wall 12 (Fig. 6.2.6) is also noted. However, lateral shear strength decayed faster for Wall 14 than for Wall 12, and this observation indicates more deterioration of the

former at earlier stages of the loading history than for the latter. Finally, shear forces and lateral displacements at all positive and negative peaks for the loading history of Wall 14 are summarized in Table A.4.

Force-dispacement response for Wall 14 during the initial elastic cycles (Fig. A.5a) are very similar to those obtained for Wall 12 (Fig. 6.2.12a), except that the response of Wall 14 is slightly more stable. This feature can be observed as a lesser amount of stiffness deterioration in Wall 14. However, for the inelastic cycles, Wall 14 illustrates a force-displacement response (Fig. A.5b) with inferior toughness characteristics to that displayed by Wall 12 (Fig. 6.12.12b). Even though peak lateral shear force for Wall 14 is larger than for Wall 12, the former exhibits more strength degradation than the latter at displacements exceeding 15 mm (0.6 in.). Furthermore, the force-displacement hysteresis loops for Wall 14 encompass less area (i.e., dissipated energy) than do those for Wall 12.

Peak lateral displacements measured during the test of Wall 14 are listed in Table A.5, along with the corresponding shear forces. These values compare well with those for Wall 12 (Tables 6.1.1-6.1.3), with the exception of a more symmetric force-displacement response for Wall 14. Peak shear forces measured using the test of Wall 14 are listed in Table A.6 along with the corresponding lateral displacements. Wall 14 is seen to generate approximately 12% more shear force than Wall 12 (Tables 6.2.1-6.2.3).

The force-displacement envelope of the load cycles for the test of Wall 14 is plotted in Fig. A.6 along with that for Wall 12. Wall 14 is seen to develop greater shear forces in both loading directions than Wall 12, but Wall 12 displays a more stable envelope with a flatter post-peak branch and larger displacements at shear force decreases substantially. Deformation capacity is defined from the force-deformation envelope as the largest displacement at which shear force decreases permanently below a value equal to 75% of the previous peak shear force in that loading direction. Deformation capacities for Wall 14 are tabulated in Table A.7, and the average value for both loading directions is only 78% of that for Wall 12 (Table 6.3.1). This reiterates the previous observation regarding the onset of deterioration of lateral resistance in Wall 14 compared to that for Wall 12.

A.5 Global Behavior

The first major event (FME) for Wall 14 was observed to comprise vertical cracking in the top course of masonry in the interface between grouted and ungrouted masonry. Forces and displacements at the FME were defined for Wall 14 on the basis of the force-displacement cycles and envelope using the three techniques described in Section 6.4 (Visible Cracking, Proportional Limit and Stiffness Change), and these values are listed in Table A.8. They are similar to those obtained from the data for Wall 12 (Tables 6.4.1-6.4.3).

Effective (secant) stiffnesses calculated from the cyclic test data (Fig. A.7) indicate that Wall 14 was initially stiffer than Wall 12 (Fig. 6.4.6), but it decayed at a faster rate for the former. Initial stiffness was inferred from early elastic cycles as the secant stiffness for this displacement range, and is listed in Table A.9. This value of initial stiffness for Wall 14 is equal to 66% and 85% of the inferred initial stiffnesses for Walls 12 and 6, respectively. The initial stiffnesses for these three walls should be comparable because the horizontal reinforcement is not expected to contribute much to the lateral resistance mechanism in this range of loading.

Energy dissipation capacity was obtained from the cyclic test data as the cumulative area encapsulated by the force-displacement hysteresis curves. This energy was expressed as a fraction of one-half of the product of shear force and lateral displacement at the FME. The history of Energy Dissipation Index is plotted in Fig. A.8 for Walls 12 and 14, and values at various drift ratios are listed for Wall 14 in Table A.10. Initially, both of these walls dissipated comparable amounts of energy, but by the time they had displaced to a drift ratio equal to 1.5%, Wall 12 had absorbed 37% more energy than Wall 14.

The slight but systematic difference in the inelastic behavior of Wall 14 when compared to that for Wall 12 can be understood in the context of the horizontal reinforcement. The larger number of cross-wires at a smaller spacing in Wall 14, relative to that for Wall 12, provide better anchorage for the longitudinal wires. In the process, the length of longitudinal wires that yield and undergo plastic deformation between masonry cracks and welded intersections (the longitudinal wires are assumed to be anchored) is likely to be shorter for the grids in Wall 14 than for those in Wall 12. Thus, longitudinal and transverse wires for the grids in Wall 14 are

likely to have been deformed to larger plastic strains than the corresponding wires in Wall 12. Consequently, fracture of longitudinal wires and welded intersections is assumed to have occurred earlier in the loading history for Wall 14 than for Wall 12.

A.6 Local Response

Strain data for the vertical reinforcing bars in Wall 14 (Table A.11), sample histories of which are shown in Fig. A.9, indicate that first yield occurred in these bars at a later stage of the loading history than for Wall 12 (Table 7.16). This observation can be seen clearly upon comparing the sample point numbers or drifts at first yield for the vertical bars. However, peak strain responses for the vertical bars were generally larger (approximately 25%) for Wall 14 than Wall 12. These larger strains indicate larger overturning effects in Wall 14, which follows from the larger peak shear force exhibited by Wall 14. And, Wall 14 exhibits a larger shear force capacity than Wall 12 because, presumably, the wire grids in the former were better developed by the more numerous welded intersections arising from the smaller cross-wire spacing than in the latter.

Measured strains in the longitudinal wires of the horizontal reinforcing grids are in agreement with the comparative description of lateral load resistance mechanisms given in the preceding paragraph for Walls 12 and 14. The grid strains for Wall 14 (Table A.12) indicate that the tension threshold of the gages were reached at slightly later stages in the loading history than those for Wall 12 (Table 7.2.6). However, more grids are seen to attain the nominal yield strain in Wall 14 than in Wall 12. Composite drift indices (CDI) for horizontal reinforcement strains corroborate these observations, with the tension threshold being attained, on the average, at a larger drift in Wall 14 (Table A.13) than in Wall 12 (Table 7.2.7), but with first yield being reached at smaller drifts for the former. Drift ratios at target reinforcement strains for Wall 14 are summarized in Fig. A.11. Table A.13 also indicates that peak strains in the grids of Wall 14 were an average of 22% larger than those for Wall 12 (Table 7.2.6). Sample strain histories for the grids in Wall 14 (Fig. A.10) illustrate this last observation.

Masonry surface strains are summarized in Table A.14 for Wall 14 indicate that both the tension and compression thresholds were generally attained at later drifts than in Wall 12 (Table

7.3.6). Composite drift indices (CDI) for masonry surface strains in Walls 12 and 14 are reported in Tables 7.3.7 and A.15, respectively. Furthermore, with only a few exceptions, the LST's recorded smaller peak surface strains in Wall 14 than in Wall 12. Sample LST strain histories for Wall 14 (Fig. A.12) and Wall 12 (Fig. 7.3.6) illustrate this observation. The LST data suggest that the masonry face shell in Wall 14 (Fig. A.13) was not required to carry as much stress as that in Wall 12 (Fig. 7.3.12). This observation may be explained by the larger contribution of the horizontal reinforcement grids to lateral load resistance in Wall 14.

Gross masonry strains measured using LVDT's are summarized in Table A.16 for Wall 14, and sample histories are shown in Fig. A.14. The LVDT strain data for Wall 14 and Wall 12 (Table 7.4.6 and Fig. 7.4.6) corroborate the observations made in the preceding paragraph on the basis of the LST strain data. The masonry in Wall 14 was not called upon to resist stresses as large as those in the face shell of Wall 12.

Lateral displacement profiles for Wall 14 are listed in Table A.17 and are shown in Fig. A.15. These profiles are similar to those for Wall 12 (Table 7.5.6 and Fig. 7.5.6), except that the former displays a slightly larger amount of distortion (i.e., whiplash) than the latter for large drifts (in excess of 1%). This may be due to larger sliding displacements between the top of the masonry and the header beam in Wall 14 than in Wall 12. The sliding displacement histories for Wall 14 (Fig. A.16) and Wall 12 (Fig. 7.5.7) corroborate this observation. As was noted for the other walls in Series 2, sliding displacements in Wall 14 did not assume a dominant role until the end of the test (i.e., sample point 2900 and larger) when peak drifts exceeded deformation capacity. Furthermore, Fig. A.17 indicates a good correlation between TTF displacement and external displacements measured at the top and bottom cross-heads.

A.7 Shear Strength Calculations

Shear stresses at ultimate (v_n) were calculated for Wall 14 using the Matsumura-Fattal (M-F) formula with nominal properties, the M-F formula with actual (measured) properties, and the modified M-F formula with actual properties, as was done in Chapter 8 for the walls in Series 1 and 2. The results of these calculations are summarized in Table A.18, along with the values assumed for the nominal and actual properties. The latter includes the 28-day compression

strength (f'_m) of ungrouted masonry prisms that were cured under high humidity conditions (i.e., moist-cured). However, because Wall 14 was the last one tested, the masonry had gained higher strength than in the other walls. A discrepancy was noted between the 28-day strength of ungrouted, moist-cured prisms (f'_m = 14.48 Mpa = 2100 psi), and the strength of ungrouted, companion prisms that were cured in laboratory air and tested on the same day as the wall (f_m = 16.89 Mpa = 2450 psi). Thus, two more rows were added to Table A.18, one for the M-F formula with actual properties and companion prism strength (CMP), and another for the modified M-F formula with actual properties and companion prism strength.

An noteworthy observation regarding Table A.18 concerns the M-F shear strength formula. The original Matsumura-Fattal formula (i.e., unmodified) provides a better estimate of the average shear strength for Wall 14 than does the modified version. A possible explanation for this observation rests on the improved anchorage provided by the closely-spaced cross-ties in Wall 14, while the modified M-F formula was explicitly calibrated to six shear wall tests which featured cross-ties with a much larger spacing and, consequently, inferior anchorage of the longitudinal wires. The improved anchorage of the grids in Wall 14 forced the longitudinal wires to carry larger forces, thus increasing their contribution to overall shear strength of Wall 14 relative to that predicted by the modified M-F formula. The compression strength obtained from ungrouted, companion prism tests is also seen to improve prediction accuracy.

Shear strengths at ultimate (V_n) were calculated for Wall 14 using the MF. Modified M-F, NEHRP, UBC and Shing formulas that were described in Chapter 8 (Table A.19). Actual geometry and material properties were used, including compression strengths (f_m) determined from ungrouted, companion prism tests. Thus UBC formula is observed to provide the least accurate estimate, while the M-F, NEHRP and Shing formulas providing equally accurate values. The modified M-F formula provides a conservative estimate (15% below capacity) of the shear strength of Wall 14.

A.8 Concluding Remarks

Shear Wall Specimen 14 was built using horizontal reinforcement in the form of welded wire grids, but with closer spacing of transverse wires (102 mm or 4 in.) than the other walls in

Series 2 (406 mm or 16 in.). Lateral load resistance characteristics for Wall 14 were observed to compare well with those for Wall 12, except for two notable exceptions. First, Wall 14 developed 12% more shear strength than did Wall 12. Second, Wall 14 proved to be less tough than Wall 12. Toughness was quantified in terms of deformation capacity and energy dissipation capacity, for which 22% and 37% reductions, respectively, were observed for Wall 14. Initial stiffness of Wall 14 (i.e., prior to the FME) was also found to be inferior to that for Wall 12. Nonetheless, the overall behavior of Wall 14 is deemed to be acceptable for seismic design of masonry structures.

The differences in the behavior exhibited by Walls 12 and 14 are attributed primarily to the change in anchorage conditions for the horizontal reinforcement as a consequence of the tighter spacing of transverse wires in Wall 14. This feature allowed larger, localized post-yield strains in the longitudinal wire of the grids in Wall 14, leading to larger horizontal force resistance from this wall relative to that for Wall 12. However, the larger horizontal reinforcement strains in Wall 14 also led to earlier fracture of these wires during the lateral load test, and these fractures generated premature deterioration of lateral strength and stiffness for Wall 14. Localized masonry surface strains, measured with LST's, and gross masonry strains, measured with LVDT's, indicated slightly lower stress and strain demands for Wall 14, relative to Wall 12. Apparently, when the reinforcement carried larger stresses in Wall 14, the masonry was subjected to lower stress/strain demands.

The tighter cross-wire spacing in the grids of Wall 14 had some negative repercussions on overall wall behavior. However, the magnitude of these effects were not sufficiently large to render the cyclic load response of Wall 14 unacceptable. Nonetheless, it is desirable to specify requirements for "confining" grids which provide compression damage mitigation along the jambs without the observed repercussions to wall toughness (i.e., reductions in deformation and energy dissipation capacities). A minimum elongation of 8%, or even 10%, should be required for confining grids (i.e., with tight spacing of cross-wires) instead of the 6% minimum elongation which worked well for the walls with large cross-wire spacing.

Finally, only a limited amount of local strain data was acquired to demonstrate the superior confining ability of the grids in Wall 14 relative to that for the grids in Wall 12. The data,

including local (LST) and global (LVDT) masonry strains, crack patterns and measured shear force, suggest that the confining grids did achieve, to some extent, the goals that had been identified for Wall 14. This conclusion follows from the greater compression damage visible in the final crack pattern for Wall 14 relative to that for Wall 12, while masonry compression strain demands were lower and lateral force capacity higher in the former. This phenomenon can only have occurred if the jambs in Wall 14 were toughened by the confining grids.

Table A.1 Masonry Material Compression Tests
a) Masonry and Mortar

Specimen Description	Specimen Designation	Date Cast	Date Tested	Compression Strength[1] (psi)	
				individual	average
air-cured, companion, grouted masonry prisms	PGSW14-1	6/18/96[2]	12/6/96	2280	2250
	PGSW14-2	6/18/96[2]	12/6/96	2240	
	PGSW14-3	6/18/96[2]	12/6/96	2230	
air-cured, companion, ungrouted masonry prisms	PUSW14-1	6/18/96	12/6/96	2410	2450
	PUSW14-2	6/18/96	12/6/96	2450	
	PUSW14-3	6/18/96	12/6/96	2500	
28-day, moist-cured mortar cubes[3] for masonry mortar batch 9	9M28DM-1	6/18/96	7/16/96	3490	3450
	9M28DM-2	6/18/96	7/16/96	3500	
	9M28DM-3	6/18/96	7/16/96	3370	
7-day, moist-cured masonry mortar cubes[3] for top joint of shear wall	M7TSW14-1	11/13/96	11/20/96	2660	2630
	M7TSW14-2	11/13/96	11/20/96	2630	
	M7TSW14-3	11/13/96	11/20/96	2590	
7-day, moist-cured masonry mortar cubes[3] for bottom joint of shear wall	M7BSW14-1	11/6/96	11/13/96	2730	2780
	M7BSW14-2	11/6/96	11/13/96	2800	
	M7BSW14-3	11/6/96	11/13/96	2820	
28-day, moist-cured masonry mortar cubes[3] for top joint of shear wall	M28TSW14-1	11/12/96	12/11/96	3390	3470
	M28TSW14-2	11/12/96	12/11/96	3420	
	M28TSW14-3	11/12/96	12/11/96	3590	
28-day, moist-cured masonry mortar cubes[3] for bottom joint of shear wall	M28BSW14-1	11/6/96	12/4/96	3680	3570
	M28BSW14-2	11/6/96	12/4/96	3470	
	M28BSW14-3	11/6/96	12/4/96	3560	

[1] 1 psi = 0.00690 MPa
[2] Grouted 6/27/96
[3] 50 x 50 x 50 mm (2 x 2 x 2 in.)

Table A.1 Masonry Material Compression Tests
b) Grout

Specimen Description	Specimen Designation	Date Cast	Date Tested	Compression Strength[1] (psi)	
				individual	average
28-day, moist-cured grout specimens[2] for masonry grout batch 9	4G28DM-1	6/27/96	7/25/96	4,010	3,940
	4G28DM-2	6/27/96	7/25/96	3,970	
	4G28DM-3	6/27/96	7/25/96	3,840	
7-day, moist-cured, high-strength grout cubes[3] for header plugs in Wall 14	G7TSW14-1	11/13/96	11/20/96	8,520	8,580
	G7TSW14-2	11/13/96	11/20/96	8,670	
	G7TSW14-3	11/13/96	11/20/96	8,540	
7-day, moist-cured, high-strength grout cubes[3] for footer plugs in Wall 14	G7BSW14-1	11/7/96	11/14/96	8,380	8,280
	G7BSW14-2	11/7/96	11/14/96	8,230	
	G7BSW14-3	11/7/96	11/14/96	8,220	
28-day, moist-cured, high-strength grout cubes[3] for header plugs in Wall 14	G28TSW14-1	11/13/96	12/11/96	9,300	9,450
	G28TSW14-2	11/13/96	12/11/96	9,520	
	G28TSW14-3	11/13/96	12/11/96	9,540	
28-day, moist-cured, high-strength grout cubes[3] for footer plugs in Wall 14	G28BSW14-1	11/9/96	12/5/96	10,360	10,210
	G28BSW14-2	11/9/96	12/5/96	10,000	
	G28BSW14-3	11/9/96	12/5/96	10,280	

[1] 1 psi = 0.00690 MPa
[2] 90 x 90 x 150 mm (3.5 x 3.5 x 6 in.)
[3] 50 x 50 x 50 mm (2 x 2 x 2 in.)

Table A.2 Tension Test Results for Horizontal Reinforcing Grids in Wall Specimen 14

Sample No.	Wire Diameter[1] (in.)		Stress[1] (ksi)		Strain (in./in.)		Modulus of Elasticity (ksi)
	Longitudinal	Transverse	Yield[3]	Ultimate	Yield[4]	Ultimate	
1	0.207	0.209	82.13	89.77	0.00270	0.08634	30,430
2			89.81	95.78	0.00322	0.05102	27,890
3			84.17	90.57	0.00266	0.03952	31,690
4			84.26	91.61	0.00282	0.07461	29,880
average			*85.09*	*91.93*	*0.00285*	*0.06287*	*29,970*

[1]1 in. = 25.4 mm
[2]1 ksi = 6.90 MPa
[3]0.2% offset yield
[4]Ratio of yield stress to modulus of elasticity

Table A.3 Location of LST Transducers for Wall Specimen 14

Instrument	Orientation[1]	Dimension[2] (in.)	Instrument	Orientation[1]	Dimension[2] (in.)
Alpha	V	24.0	Jane	V	9.44
	H	-24.19		H	9.38
Beta	V	0.0	King	V	6.56
	H	-24.19		H	6.56
Cathy	V	-24.0	Ivan	V	-6.75
	H	-24.19		H	6.94
Dog	V	9.44	Paul	V	-9.56
	H	-9.50		H	9.75
Ed	V	6.63	Love	V	24.06
	H	-6.63		H	24.13
Fox	V	-9.56	Mark	V	0.0
	H	-9.94		H	24.06
George	V	-6.75	Neal	V	-24.0
	H	-7.13		H	24.06
Opal	V	0.0	θ (°)		45.0
	H	-0.13			

[1]Vertical (V) or horizontal (H) dimension from center of wall.
[2]1 in. = 25.4 mm

Table A.4 Timeline for Test of Wall Specimen 14

Point	Cycle Group	Cycle No.	Disp. (in.)	Force (kips)	Comments
1	E1	1	-0.0019	1.307	Begin first day of testing.
4	E1	1	0.0119	7.976	Positive peak.
10	E1	1	-0.0111	-3.951	Negative peak.
12	E1	1	-0.0033	2.196	End of cycle.
15	E1	2	0.0119	7.963	Positive peak.
21	E1	2	-0.0111	-3.992	Negative peak.
24	E1	2	-0.0032	2.158	End of cycle.
27	E1	3	0.0119	7.925	Positive peak.
33	E1	3	-0.0113	-3.855	Negative peak.
36	E1	3	-0.0032	2.165	End of cycle.
39	E2	1	0.0180	11.647	Positive peak.
45	E2	1	-0.0205	-7.746	Negative peak.
48	E2	1	-0.0031	2.122	End of cycle.
51	E2	2	0.0180	11.629	Positive peak.
57	E2	2	-0.0205	-7.767	Negative peak.
60	E2	2	-0.0026	1.755	End of cycle.
63	E2	3	0.0180	11.645	Positive peak.
69	E2	3	-0.0205	-7.790	Negative peak.
72	E2	3	-0.0028	1.893	End of cycle.
75	E3	1	0.0235	14.688	Positive peak.
81	E3	1	-0.0261	-10.701	Negative peak.
84	E3	1	-0.0032	2.171	End of cycle.
87	E3	2	0.0236	14.612	Positive peak.
93	E3	2	-0.0258	-11.139	Negative peak.
96	E3	2	-0.0031	2.113	End of cycle.

1 in. = 25.4 mm; 1 kip = 4.45 kN

Table A.4 (Cont'd)

Point	Cycle Group	Cycle No.	Disp. (in.)	Force (kips)	Comments
99	E3	3	0.0237	14.484	Positive peak.
105	E3	3	-0.0258	-11.093	Negative peak.
108	E3	3	-0.0030	2.055	End of cycle.
111	E4	1	0.0293	17.415	Positive peak.
117	E4	1	-0.0314	-14.156	Negative peak.
120	E4	1	-0.0026	1.730	End of cycle.
123	E4	2	0.0294	17.181	Positive peak.
129	E4	2	-0.0314	-14.164	Negative peak.
132	E4	2	-0.0031	2.111	End of cycle.
135	E4	3	0.0296	16.944	Positive peak.
141	E4	3	-0.0316	-13.771	Negative peak.
144	E4	3	-0.0031	2.095	End of cycle.
147	E5	1	0.0360	20.139	Positive peak.
153	E5	1	-0.0378	-17.284	Negative peak.
156	E5	1	-0.0034	2.306	End of cycle.
159	E5	2	0.0362	19.909	Positive peak.
166	E5	2	-0.0380	-17.128	Negative peak.
170	E5	2	-0.0035	2.365	End of cycle.
173	E5	3	0.0364	19.496	Positive peak.
180	E5	3	-0.0379	-17.252	Negative peak.
184	E5	3	-0.0035	2.347	End of cycle.
189	E6	1	0.0428	22.721	Positive peak.
196	E6	1	-0.0444	-20.279	Negative peak.
200	E6	1	-0.0037	2.509	End of cycle.
203	E6	2	0.0430	22.469	Positive peak.

1 in. = 25.4 mm; 1 kip = 4.45 kN

Table A.4 (Cont'd)

Point	Cycle Group	Cycle No.	Disp. (in.)	Force (kips)	Comments
211	E6	2	-0.0445	-20.089	Negative peak.
216	E6	2	-0.0035	2.394	End of cycle.
219	E6	3	0.0431	22.325	Positive peak.
228	E6	3	-0.0445	-20.087	Negative peak.
233	E6	3	-0.0037	2.512	End of cycle.
237	E7	1	0.0497	25.230	Positive peak.
248	E7	1	-0.0515	-22.465	Negative peak.
254	E7	1	-0.0040	2.706	End of cycle.
260	E7	2	0.0500	24.867	Positive peak.
272	E7	2	-0.0516	-22.299	Negative peak.
278	E7	2	-0.0042	2.839	End of cycle.
284	E7	3	0.0499	24.932	Positive peak.
296	E7	3	-0.0517	-22.211	Negative peak.
302	E7	3	-0.0041	2.771	End of cycle.
308	E8	1	0.0569	27.290	Positive peak.
320	E8	1	-0.0585	-24.870	Negative peak.
326	E8	1	-0.0056	3.801	End of cycle.
332	E8	2	0.0571	26.968	Positive peak.
344	E8	2	-0.0587	-24.507	Negative peak.
350	E8	2	-0.0058	3.929	End of cycle.
356	E8	3	0.0573	26.729	Positive peak.
368	E8	3	-0.0590	-24.003	Negative peak.
374	E8	3	-0.0026	4.006	End of cycle.
380	E9	1	0.0639	29.680	Positive peak.
392	E9	1	-0.0656	-27.027	Negative peak.

1 in. = 25.4 mm; 1 kip = 4.45 kN

Table A.4 (Cont'd)

Point	Cycle Group	Cycle No.	Disp. (in.)	Force (kips)	Comments
398	E9	1	-0.0030	4.701	End of cycle.
404	E9	2	0.0642	29.158	Positive peak.
416	E9	2	-0.0660	-26.323	Negative peak.
422	E9	2	-0.0031	4.869	End of cycle.
428	E9	3	0.0643	29.058	Positive peak.
440	E9	3	-0.0662	-26.053	Negative peak.
446	E9	3	-0.0031	4.738	End of cycle.
452	E10	1	0.0714	31.080	Positive peak.
464	E10	1	-0.0733	-28.280	Negative peak.
470	E10	1	-0.0035	5.437	End of cycle.
476	E10	2	0.0716	30.907	Positive peak.
488	E10	2	-0.0734	-28.090	Negative peak.
494	E10	2	-0.0038	5.905	End of cycle.
500	E10	3	0.0719	30.372	Positive peak.
512	E10	3	-0.0735	-27.965	Negative peak.
518	E10	3	-0.0038	5.960	End of cycle.
524	E11	1	0.0788	32.861	Positive peak.
536	E11	1	-0.0805	-30.223	Negative peak.
541	E11	1	-0.0042	6.554	End of cycle.
547	E11	2	0.0794	31.938	Positive peak.
559	E11	2	-0.0806	-30.072	Negative peak.
565	E11	2	-0.0042	6.574	End of cycle.
571	E11	3	0.0796	31.656	Positive peak.
583	E11	3	-0.0807	-29.918	Negative peak.
589	E11	3	-0.0044	6.883	End of cycle. End first day of testing.

1 in. = 25.4 mm; 1 kip = 4.45 kN

Table A.4 (Cont'd)

Point	Cycle Group	Cycle No.	Disp. (in.)	Force (kips)	Comments
590	$1.0D_c$	D1	-0.0028	4.388	Begin second day of testing.
596	$1.0D_c$	D1	0.0868	33.559	Positive peak. Vertical crack, top course, west end.
608	$1.0D_c$	D1	-0.0879	-31.891	Negative peak. Vertical crack, bottom course, west end.
614	$1.0D_c$	D1	-0.0046	7.125	End of cycle.
618	$1.0D_c$	D2	0.0527	19.186	Positive peak.
631	$1.0D_c$	D2	-0.0667	-22.824	Negative peak.
637	$1.0D_c$	D2	-0.0043	6.686	End of cycle.
640	$1.0D_c$	D3	0.0426	18.101	Positive peak.
646	$1.0D_c$	D3	-0.0442	-15.670	Negative peak.
649	$1.0D_c$	D3	-0.0058	3.895	End of cycle.
655	$1.0D_c$	S1	0.0880	31.765	Positive peak.
667	$1.0D_c$	S1	-0.0883	-31.269	Negative peak.
673	$1.0D_c$	S1	-0.0047	7.264	End of cycle.
679	$1.0D_c$	S2	0.0885	30.931	Positive peak.
691	$1.0D_c$	S2	-0.0889	-30.401	Negative peak.
697	$1.0D_c$	S2	-0.0048	7.379	End of cycle.
706	$1.5D_c$	D1	0.1414	33.177	Positive peak. Stairstep diagonal crack, upper west to lower east corners.
723	$1.5D_c$	D1	-0.1369	-40.088	Negative peak. Stairstep diagonal crack, upper east to lower west corners.
731	$1.5D_c$	D1	-0.0062	9.541	End of cycle.
740	$1.5D_c$	D2	0.1061	24.780	Positive peak.
761	$1.5D_c$	D2	-0.1035	-28.799	Negative peak.
770	$1.5D_c$	D2	-0.0061	9.448	End of cycle.
776	$1.5D_c$	D3	0.0696	18.286	Positive peak.
788	$1.5D_c$	D3	-0.0691	-19.043	Negative peak.
794	$1.5D_c$	D3	-0.0054	8.342	End of cycle.

1 in. = 25.4 mm; 1 kip = 4.45 kN

Table A.4 (Cont'd)

Point	Cycle Group	Cycle No.	Disp. (in.)	Force (kips)	Comments
803	$1.5D_c$	S1	0.1414	33.175	Positive peak.
821	$1.5D_c$	S1	-0.1386	-37.483	Negative peak.
828	$1.5D_c$	S1	-0.0063	9.814	End of cycle.
837	$1.5D_c$	S2	0.1420	32.336	Positive peak.
855	$1.5D_c$	S2	-0.1392	-36.509	Negative peak.
864	$1.5D_c$	S2	-0.0064	9.876	End of cycle.
876	$2.0D_c$	D1	0.1913	39.777	Positive peak.
898	$2.0D_c$	D1	-0.1881	-44.757	Negative peak. Horizontal cracks in bed joints throughout the panel.
908	$2.0D_c$	D1	-0.0062	9.541	End of cycle.
917	$2.0D_c$	D2	0.1445	28.404	Positive peak.
933	$2.0D_c$	D2	-0.1422	-31.945	Negative peak.
942	$2.0D_c$	D2	-0.0061	9.448	End of cycle.
948	$2.0D_c$	D3	0.0957	19.809	Positive peak.
960	$2.0D_c$	D3	-0.0949	-21.045	Negative peak.
965	$2.0D_c$	D3	-0.0054	8.342	End of cycle.
977	$2.0D_c$	S1	0.1928	37.539	Positive peak.
998	$2.0D_c$	S1	-0.1893	-42.906	Negative peak.
1010	$2.0D_c$	S1	-0.0063	9.814	End of cycle.
1022	$2.0D_c$	S2	0.1932	36.838	Positive peak.
1045	$2.0D_c$	S2	-0.1903	-41.318	Negative peak.
1056	$2.0D_c$	S2	-0.0064	9.876	End of cycle.
1074	$3.0D_c$	D1	0.2958	46.012	Positive peak.
1109	$3.0D_c$	D1	-0.2949	-47.399	Negative peak. Inclined cracks, upper west to lower east corners.
1125	$3.0D_c$	D1	-0.0078	12.147	End of cycle.
1140	$3.0D_c$	D2	0.2231	32.483	Positive peak. Crack width ~ 1 mm.

1 in. = 25.4 mm; 1 kip = 4.45 kN

Table A.4 (Cont'd)

Point	Cycle Group	Cycle No.	Disp. (in.)	Force (kips)	Comments
1167	$3.0D_c$	D2	-0.2219	-34.401	Negative peak.
1182	$3.0D_c$	D2	-0.0075	11.616	End of cycle. End second day of testing.
1183	$3.0D_c$	D3	-0.0047	7.278	Begin third day of testing.
1192	$3.0D_c$	D3	0.1477	23.447	Positive peak.
1208	$3.0D_c$	D3	-0.1482	-22.556	Negative peak.
1217	$3.0D_c$	D3	-0.0071	10.894	End of cycle.
1235	$3.0D_c$	S1	0.2980	42.637	Positive peak.
1269	$3.0D_c$	S1	-0.2955	-46.434	Negative peak.
1286	$3.0D_c$	S1	-0.0070	10.851	End of cycle.
1304	$3.0D_c$	S2	0.2987	41.587	Positive peak.
1339	$3.0D_c$	S2	-0.2972	-43.906	Negative peak. Splitting damage in top course, both ends.
1357	$3.0D_c$	S2	-0.0073	11.377	End of cycle.
1381	$4.0D_c$	D1	0.4026	48.649	Positive peak. Mortar crushing top, west. Crack width ~ 1.5 mm.
1429	$4.0D_c$	D1	-0.4012	-50.881	Negative peak. Inclined crack, top middle to lower west corner.
1452	$4.0D_c$	D1	-0.0084	12.985	End of cycle.
1470	$4.0D_c$	D2	0.3029	35.039	Positive peak.
1503	$4.0D_c$	D2	-0.3024	-35.866	Negative peak.
1522	$4.0D_c$	D2	-0.0079	12.177	End of cycle.
1534	$4.0D_c$	D3	0.2011	24.601	Positive peak.
1556	$4.0D_c$	D3	-0.2012	-24.542	Negative peak.
1567	$4.0D_c$	D3	-0.0070	10.887	End of cycle.
1591	$4.0D_c$	S1	0.4041	46.402	Positive peak.
1636	$4.0D_c$	S1	-0.4032	-47.721	Negative peak.
1660	$4.0D_c$	S1	-0.0084	12.966	End of cycle.
1684	$4.0D_c$	S2	0.4048	45.324	Positive peak. Face-shell spalling, top course east.

1 in. = 25.4 mm; 1 kip = 4.45 kN

Table A.4 (Cont'd)

Point	Cycle Group	Cycle No.	Disp. (in.)	Force (kips)	Comments
1732	$4.0D_c$	S2	-0.4034	-47.393	Negative peak.
1756	$4.0D_c$	S2	-0.0083	12.867	End of cycle. End third day of testing.
1757	$5.0D_c$	D1	-0.0031	4.753	Begin fourth day of testing.
1787	$5.0D_c$	D1	0.5092	51.645	Positive peak. Inclined cracks, top middle to lower east corner
1842	$5.0D_c$	D1	-0.5071	-54.802	Negative peak. Inclined cracks, top middle to lower west.
1877	$5.0D_c$	D1	-0.0087	13.432	End of cycle.
1901	$5.0D_c$	D2	0.3833	36.584	Positive peak.
1949	$5.0D_c$	D2	-0.3812	-39.837	Negative peak.
1973	$5.0D_c$	D2	-0.0069	10.755	End of cycle.
1989	$5.0D_c$	D3	0.2549	25.368	Positive peak.
2018	$5.0D_c$	D3	-0.2524	-29.292	Negative peak.
2032	$5.0D_c$	D3	-0.0029	4.502	End of cycle.
2064	$5.0D_c$	S1	0.5104	49.707	Positive peak.
2130	$5.0D_c$	S1	-0.5093	-51.463	Negative peak.
2160	$5.0D_c$	S1	-0.0073	11.307	End of cycle.
2194	$5.0D_c$	S2	0.5131	45.600	Positive peak. Mortar spalling top center. Crack width ~ 2.5 mm.
2257	$5.0D_c$	S2	-0.5112	-48.500	Negative peak.
2286	$5.0D_c$	S2	-0.0054	8.377	End of cycle. End fourth day of testing.
2287	$6.0D_c$	D1	-0.0040	2.731	Begin fifth day of testing.
2322	$6.0D_c$	D1	0.6205	47.344	Positive peak. Extensive crushing/spalling damage to top course/joint.
2394	$6.0D_c$	D1	-0.6168	-53.020	Negative peak. Extensive crushing/spalling damage to top course/joint.
2428	$6.0D_c$	D1	-0.0040	6.268	End of cycle.
2452	$6.0D_c$	D2	0.4682	31.095	Positive peak.
2506	$6.0D_c$	D2	-0.4645	-36.880	Negative peak.
2530	$6.0D_c$	D2	-0.0029	1.943	End of cycle.

1 in. = 25.4 mm; 1 kip = 4.45 kN

Table A.4 (Cont'd)

Point	Cycle Group	Cycle No.	Disp. (in.)	Force (kips)	Comments
2548	$6.0D_c$	D3	0.3124	20.234	Positive peak.
2582	$6.0D_c$	D3	-0.3108	-22.771	Negative peak.
2599	$6.0D_c$	D3	-0.0009	0.640	End of cycle.
2635	$6.0D_c$	S1	0.6256	39.351	Positive peak.
2707	$6.0D_c$	S1	-0.6209	-46.635	Negative peak.
2740	$6.0D_c$	S1	-0.0048	3.217	End of cycle.
2776	$6.0D_c$	S2	0.6274	36.517	Positive peak.
2846	$6.0D_c$	S2	-0.6163	-39.852	Negative peak. Spalling top three courses, east and west.
2886	$6.0D_c$	S2	-0.0033	5.176	End of cycle. End fifth day of testing.
2887	$8.0D_c$	D1	-0.0045	3.024	Begin sixth day of testing.
2921	$8.0D_c$	D1	0.5941	32.182	Loud "bang".
2933	$8.0D_c$	D1	0.8072	38.237	Loud "bang".
2935	$8.0D_c$	D1	0.8441	37.013	Positive peak. Extensive crushing/spalling damage to 2 courses 6 and 7.
3031	$8.0D_c$	D1	-0.8550	-20.166	Negative peak.
3078	$8.0D_c$	D1	-0.0042	6.523	End of cycle.
3101	$8.0D_c$	D2	0.4091	10.649	Loud "bang".
3106	$8.0D_c$	D2	0.5173	11.010	Soft "snap".
3112	$8.0D_c$	D2	0.6441	10.685	Positive peak.
3180	$8.0D_c$	D2	-0.5938	-4.653	Soft "snap".
3183	$8.0D_c$	D2	-0.6478	-4.969	Negative peak.
3217	$8.0D_c$	D2	-0.0023	1.552	End of cycle.
3241	$8.0D_c$	D3	0.4313	4.154	Positive peak.
3285	$8.0D_c$	D3	-0.4317	1.582	Negative peak.
3309	8.0Dc	D3	-0.0014	0.956	End of cycle.

1 in. = 25.4 mm; 1 kip = 4.45 kN

Table A.4 (Cont'd)

Point	Cycle Group	Cycle No.	Disp. (in.)	Force (kips)	Comments
3357	$8.0D_c$	S1	0.8644	5.544	Positive peak.
3404	8.0Dc	S1	0.0013	-0.850	End sixth day of testing.

1 in. = 25.4 mm; 1 kip = 4.45 kN

Table A.5 Peak Lateral Displacements for Wall Specimen 14

Direction	Point	Peak Displacement, Δ_{max}		Drift Ratio, Δ_{max}/H	Shear @ Peak Displacement, $V_{\Delta,max}$†		$V_{\Delta,max}/V_{max}$‡
		(mm)	(in.)	(%)	(kN)	(kips)	
positive	3357	21.96	0.864	1.544	24.66	5.54	0.108
negative	3031	21.72	0.855	1.527	89.70	20.17	0.368
average	----	21.64	0.860	1.535	57.18	12.86	0.242

†Shear force at instant of peak displacement
‡Peak shear force

Table A.6 Peak Shear Forces for Wall Specimen 14

Loading Direction	Point	Peak Shear Force, V_{max}		Displacement @ Peak Force, $\Delta_{V,max}$		Drift Ratio, $\Delta_{V,max}/H$
		(kN)	(kips)	(mm)	(in.)	(%)
positive	1787	229.7	51.65	12.93	0.509	0.909
negative	1842	243.8	54.80	12.88	0.507	0.906
average	----	236.7	53.22	12.91	0.508	0.907

Table A.7 Deformation Capacity for Wall Specimen 14

Loading Direction	Displacement Capacity, Δ_u		Drift Capacity, %	Δ_u/Δ_{max}
	mm	in.		
positive	15.98	0.629	1.123	0.724
negative	15.71	0.619	1.105	0.725
average	15.84	0.624	1.114	0.728

Table A.8 Shear Force and Lateral Displacement at First Major Event for Wall Specimen 14

Method	Shear Force, kN (kips)			Displacement, mm (in.)		
	Positive	Negative	Average	Positive	Negative	Average
visible cracking[1]	149.3 (33.56)	141.9 (31.89)	145.6 (32.73)	2.21 (0.087)	2.23 (0.088)	2.22 (0.087)
proportional limit	153.1 (34.42)	141.4 (31.80)	147.3 (33.11)	1.81 (0.071)	2.27 (0.089)	2.04 (0.080)
stiffness change	143.4 (32.23)	145.9 (32.80)	144.6 (32.52)	2.26 (0.089)	2.26 (0.089)	2.26 (0.089)

[1]Point 596 in positive loading direction, and point 608 in negative loading direction.

Table A.9 Initial Stiffnesses Inferred from Experimental Data for Wall Specimen 14

Points	Cycles	Peak Shear Force V, kN (kips)		Peak Displacement Δ_o, mm (in.)		Cycle Effective Slope K_o	Initial Stiffness K†
		Positive	Negative	Positive	Negative	kN/mm (kips/in.)	
1-108	E1-E3	65.3 (14.69)	49.55 (11.14)	0.403 (0.01589)	0.328 (0.01293)	156.9 (896.1)	135.0 (770.7)

†$K = 0.86K_o$

Table A.10 Energy Dissipation Indices for Wall Specimen 14

Drift Ratio, Δ/H (%)	0.25	0.5	0.75	1.0	1.25	1.5	1.54[1]
Energy Dissipation Index	10	27	66	100	127	134	138

[1]Drift ratio at maximum lateral displacement ($\Delta=\Delta_{max}$).

Table A.11 Summary of Vertical Reinforcement Strains[1] for Wall Specimen 14

Strain Gage	First Yield[2]		Peak Response			Limit of Reliability	
	Point	Drift[3] (%)	Strain (in/in)	Point	Drift[3] (%)	Point	Drift[3] (%)
VTWO	3025	1.330	0.01480	3211	0.197/1.527	3212	0.165/1.527
VTWI	*NA*	*NA*	0.00144	3023	1.265	3028	1.429
VBWO	1843	0.882/0.906	-0.00417	2394	1.101	*NA*	*NA*
VBWI	*NA*	*NA*	-0.00203	2424	0.136/1.101	3025	1.330
VTEO	1073	0.496	0.00471	1235	0.530/0.530	*NA*	*NA*
VTEI	1873	0.142/0.906	-0.00452	3360	1.446/1.544	*NA*	*NA*
VBEO	*NA*	*NA*	0.00127	2935	1.507	*NA*	*NA*
VBEI	1841	0.875	0.00462	2707	1.109/1.109	*NA*	*NA*

[1]*NA* denotes that strain never achieved the indicated condition.
[2]Strain (tension or compression) first exceeds nominal yield (0.00237).
[3]If two values are shown, the first value is current drift, second value is previous peak drift.

Table A.12 Summary of Horizontal Reinforcement Strains[1] for Wall Specimen 14

Strain Gage	Tension Threshold[2]		First Yield[3]		Peak Strain (in./in.)	Limit of Reliability	
	Point	Drift[4] (%)	Point	Drift[4] (%)		Point	Drift[4] (%)
6NW	655	0.156/0.156	2128	0.848/0.906	-0.00526	*NA*	*NA*
6SW	596	0.155	1074	0.528	0.00319	2203	0.659/0.911
1NE	721	0.188/0.315	1427	0.655	0.00511	*NA*	*NA*
1SE	721	0.188/0.315	1840	0.844	0.00398	*NA*	*NA*
2NE	721	0.188/0.315	1107	0.494	0.00311	*NA*	*NA*
2SE	721	0.188/0.315	1106	0.463	0.00316	*NA*	*NA*
3NE	1075	0.506/0.528	2321	1.076	0.00287	*NA*	*NA*
3SE	1229	0.354/0.528	2322	1.108	0.00290	*NA*	*NA*
4NE	838	0.229/0.254	*NA*	*NA*	0.00264	*NA*	*NA*
4SE	804	0.229/0.254	1945	0.606	0.00335	*NA*	*NA*
3NW	1428	0.686	2313	0.828/0.916	0.00351	*NA*	*NA*
5NE	706	0.253	2378	0.607	0.00637	2986	0.150/1.101
5SE	706	0.253	2194	0.916	0.00496	3035	1.409/1.527
6NE	707	0.230/0.253	2696	0.769/1.101	0.00284	2984	0.087/1.101
6SE	706	0.253	2064	0.910/0.910	0.00440	2990	0.277/1.101
1NW	706	0.253	1784	0.817	0.00341	*NA*	*NA*
1SW	803	0.253/0.253	1784	0.817	0.00302	*NA*	*NA*
2NW	1339	0.531/0.531	*NA*	*NA*	0.00236	*NA*	*NA*
3SW	1426	0.624	2061	0.820/0.910	0.00494	*NA*	*NA*
3NC	706	0.253	1428	0.686	0.00414	*NA*	*NA*
3SC	706	0.253	1781	0.725	0.00385	*NA*	*NA*
4NW	1108	0.527	2193	0.886/0.909	0.00644	*NA*	*NA*
4SW	1108	0.527	2130	0.909/0.909	0.00476	*NA*	*NA*
2SW	1425	0.594	*NA*	*NA*	0.00258	*NA*	*NA*
4NC	720	0.159/0.315	1107	0.494	0.00436	*NA*	*NA*
4SC	720	0.159/0.315	1107	0.494	0.00331	1834	0.662/0.720
5NW	821	0.248/0.248	2183	0.606/0.910	0.01609	3352	1.382/1.507
5SW	723	0.244	1838	0.783	0.02091	3235	0.573/1.507

[1]*NA* denotes that strain never achieved the indicated condition.
[2]Grid tension strain first exceeds 0.0002.
[3]Strain (tension or compression) first exceeds nominal yield (0.00280).
[4]If two values are shown, the first value is current drift, second value is previous peak drift.

Table A.13 Composite Drift Indices for Horizontal Reinforcement Strains in Wall Specimen 14

Condition	Number of Gages	Composite Drift Index (%)	
		Gross[1]	Net[2]
total functional	28	-----	-----
tension threshold	28	0.349	0.349
first yield	25	0.699	0.783

[1]Based on total number of functional gages.
[2]Based on number of gages meeting the limiting condition indicated.

Table A.14 Summary of Masonry Surface (LST) Strains[1] in Wall Specimen 14

Gage Name	Tension Threshold[2]		Compression Threshold[3]		Limit of Reliability		Peak Strain (in./in.)	
	Point	Drift[4] (%)	Point	Drift[4] (%)	Point	Drift[4] (%)	Tension	Comp.
Alpha	*NA*	*NA*	*NA*	*NA*	3358	1.488/1.544	0.00005	0.00140
Beta	*NA*	*NA*	*NA*	*NA*	3358	1.488/1.544	0.00003	0.00049
Cathy	*NA*	*NA*	3028	1.429	3358	1.488/1.544	0.00001	0.00573
Dog	308	0.102	*NA*	*NA*	3358	1.488/1.544	0.03296	0.00039
Ed	248	0.092	*NA*	*NA*	3358	1.488/1.544	0.00013	0.00164
Fox	211	0.079/0.079	*NA*	*NA*	3358	1.488/1.544	0.00011	0.00139
George	380	0.114	*NA*	*NA*	3358	1.488/1.544	0.00129	0.00068
Ivan	*NA*	*NA*	*NA*	*NA*	3254	0.225/1.507	0.00008	0.00073
Jane	2780	1.008/1.120	*NA*	*NA*	3358	1.488/1.544	0.00012	0.00053
King	707	0.230/0.253	*NA*	*NA*	3358	1.488/1.544	0.03864	0.00025
Love	705	0.220	3163	0.510/1.527	3358	1.488/1.544	0.01530	0.00341
Mark	*NA*	*NA*	*NA*	*NA*	3309	0.003/1.527	0.00002	0.00042
Neal	723	0.245	*NA*	*NA*	3358	1.488/1.544	0.02248	0.00021
Opal	785	0.080/0.245	*NA*	*NA*	3358	1.488/1.544	0.02142	0.00039
Paul	82	0.034/0.047	*NA*	*NA*	3254	0.225/1.507	0.01506	0.00007

[1]*NA* denotes that surface strain never achieved the indicated condition.
[2]Surface tension strain magnitude first exceeds 0.0001.
[3]Surface compression strain magnitude first exceeds 0.002.
[4]If two values are shown, the first value is current drift, second value is previous peak drift.

Table A.15 Composite Drift Indices for Masonry Surface (LST) Strains in Wall Specimen 14

Orientation	Number of Gages		Composite Drift Index (%)	
	total functional	tension threshold	Gross[1]	Net[2]
diagonal	4	4	0.337	0.337
transverse	4	3	0.0633	0.0843

[1]Based on total number of functional gages.
[2]Based on number of gages meeting the tension threshold condition.

Table A.16 Summary of Gross (LVDT) Strains[1] in Wall Specimen 14

LVDT Channel	Gage Length (in.)	Threshold[2]		Peak Strain (in./in.)	Limit[2]	
		Point	Drift[3] (%)		Point	Drift[3] (%)
ETBWD	68.17	380	0.114	0.00764	2777	1.095/1.120
WTBED	68.17	536	0.144	0.00399	2777	1.095/1.120
WVTFTG	4.75	4	0.021	0.00884	3358	1.488/1.544
WVTBOT	15.88	483	0.018/0.128	0.00254	3358	1.488/1.544
WVTMID	16.0	721	0.188	0.00147	3101	0.731/1.527
WVTTOP	16.13	324	0.022/0.105	0.00331	2777	1.095/1.120
EVTFTG	4.13	4	0.021	0.01088	3358	1.488/1.544
EVTBOT	16.06	344	0.105/0.105	0.00182	3358	1.488/1.544
EVTMID	16.19	309	0.087/0.102	0.00155	3358	1.488/1.544
EVTTOP	16.0	723	0.245	0.00085	2856	0.886/1.109

[1]*NA* denotes that gross strain never achieved the indicated condition.
[2]Gross strain first exceeds 0.0001.
[3]If two values are shown, the first value is current drift, second value is previous peak drift.

Table A.17 Wall Displacement Profiles (LVDT) for Wall Specimen 14

Point	Cycle Group	Peak Positive Lateral Drift Ratio Along Wall Height[1] (%)					
		BASHOR	BOTHOR	MIDHOR	TOPHOR	SPACER	EWDISP
596	$1.0D_c$	-0.0177	0.0332	0.0719	0.105	0.129	0.155
876	$2.0D_c$	-0.0238	0.0456	0.0986	0.185	0.300	0.342
1074	$3.0D_c$	-0.0284	0.0644	0.140	0.266	0.484	0.528
1381	$4.0D_c$	-0.0332	0.0583	0.176	0.340	0.660	0.719
1787	$5.0D_c$	-0.0325	0.0314	0.232	-----[2]	0.829	0.909
2322	$6.0D_c$	-0.0393	-0.0221	0.248	-----[2]	1.004	1.108
2935	$8.0D_c$	-0.0399	-0.0553	0.268	-----[2]	1.375	1.507

[1]During the D1 cycles.
[2]LVDT removed due to spalling masonry.

Table A.18 Average Ultimate (Gross Area) Shear Stresses for Wall Specimen 14[1]

Method	Reinforcement (Gross) Ratio (%)		Average Ultimate Shear Stresses, MPa (psi)					Ratio, v_n/v_u
			Calculated				Test, v_u	
	ρ_v	ρ_h	v_m	v_s	v_a	v_n		
M-F/nominal[2]	0.410	0.110	0.2110 (30.60)	0.2641 (38.30)	0.1365 (19.80)	0.6116 (88.70)	0.8545 (123.9)	0.716
M-F/actual[3]	0.410	0.110	0.2865 (41.56)	0.3745 (54.32)	0.1660 (24.08)	0.8270 (120.0)	0.8543 (123.9)	0.968
M-F/comp.[4]	0.410	0.110	0.3095 (44.89)	0.3745 (54.32)	0.1779 (25.80)	0.8618 (125.0)	0.8543 (123.9)	1.009
modified M-F/actual[3]	0.410	0.110	0.2359 (34.22)	0.3084 (44.73)	0.1535 (22.27)	0.6978 (101.2)	0.8543 (123.9)	0.817
modified M-F/comp.[4]	0.410	0.110	0.2548 (36.96)	0.3084 (44.73)	0.1633 (23.68)	0.7265 (105.4)	0.854 (123.9)	0.850

[1] L = 1422 mm (56 in.); H/L = 1.0

[2] t_g = 193.5 mm (7.62 in.); t_f = 31.8 mm (1.25 in.); f'_m = 13.79 MPa (2000 psi); f_{yv} = 413.7 MPa (60 ksi); f_{yh} = 413.7 MPa (60 ksi)

[3] t_g = 194.8 mm (7.67 in.); t_f = 33.8 mm (1.33 in.); f'_m = 14.48 MPa (2100 psi); f_{yv} = 445.3 MPa (64.58 ksi); f_{yh} = 586.7 MPa (85.09 ksi)

[4] t_g = 194.8 mm (7.67 in.); t_f = 33.8 mm (1.33 in.); f'_m = 16.89 MPa (2450 psi); f_{yv} = 445.3 MPa (64.58 ksi); f_{yh} = 586.7 MPa (85.09 ksi)

Table A.19 Calculated and Measured Shear Strengths at Ultimate for Shear Wall 14

Method	Shear Strength at Ultimate, kN (kips)						V_n/V_u
	V_m	V_s	V_a	$V_{lim,1}$	$V_{lim,2}$	V_n	
M-F	85.76 (19.28)	103.77 (23.33)	49.29 (11.08)	-----	-----	238.82 (53.69)	1.009
modified M-F	70.62 (15.88)	85.45 (19.21)	45.24 (10.17)	-----	-----	201.3 (45.26)	0.850
NEHRP	100.28 (22.54)	96.5 (21.69)	89.1 (20.03)	-----	-----	222.5 (50.03)	0.940
UBC	63.6 (14.29)	178.2 (40.07)	-----	171.5 (38.57)	218.6 (49.16)	171.5 (38.57)	0.725
Shing	107.4 (24.15)	137.8 (30.98)	11.8 (2.65)	-----	-----	257.05 (57.79)	1.086
measured, V_u	236.7 (53.22)						

t_g = 194.8 mm (7.67 in.); t_f = 33.8 mm (1.33 in.); f'_m = 16.89 MPa (2450 psi)

f_{yv} = 445.3 MPa (64.58 ksi); f_{yh} = 586.7 MPa (85.09 ksi)

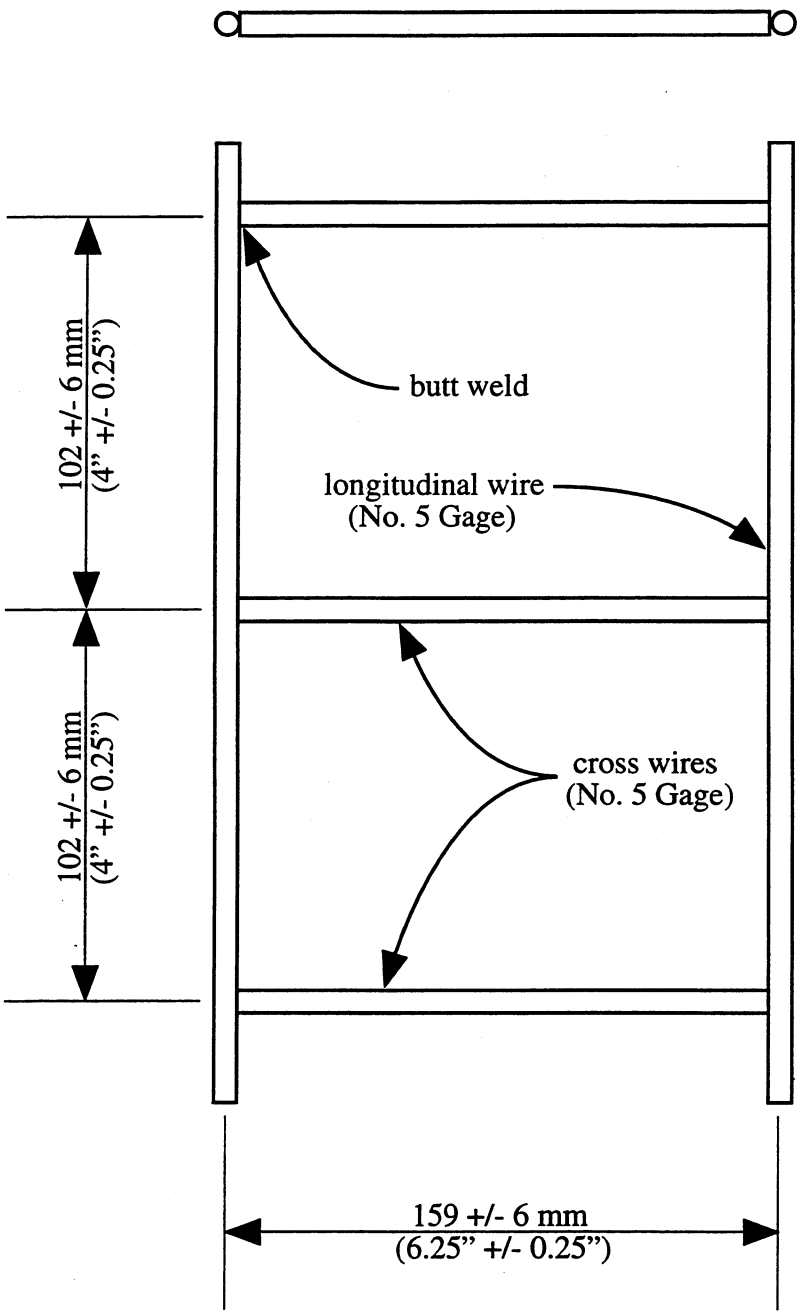

Dimensions are in mm (in.)

Fig. A.1 Welded Wire Grid Configuration for Wall Specimen 14

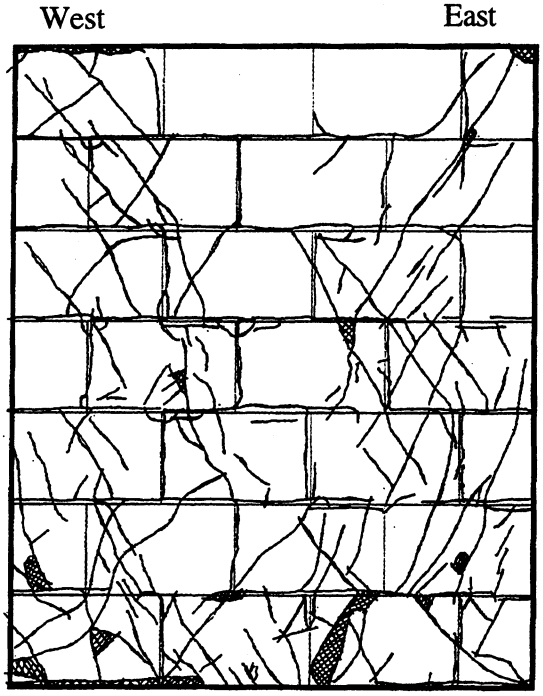

Fig. A.2 Final Crack Pattern for South Face of Wall Specimen 14

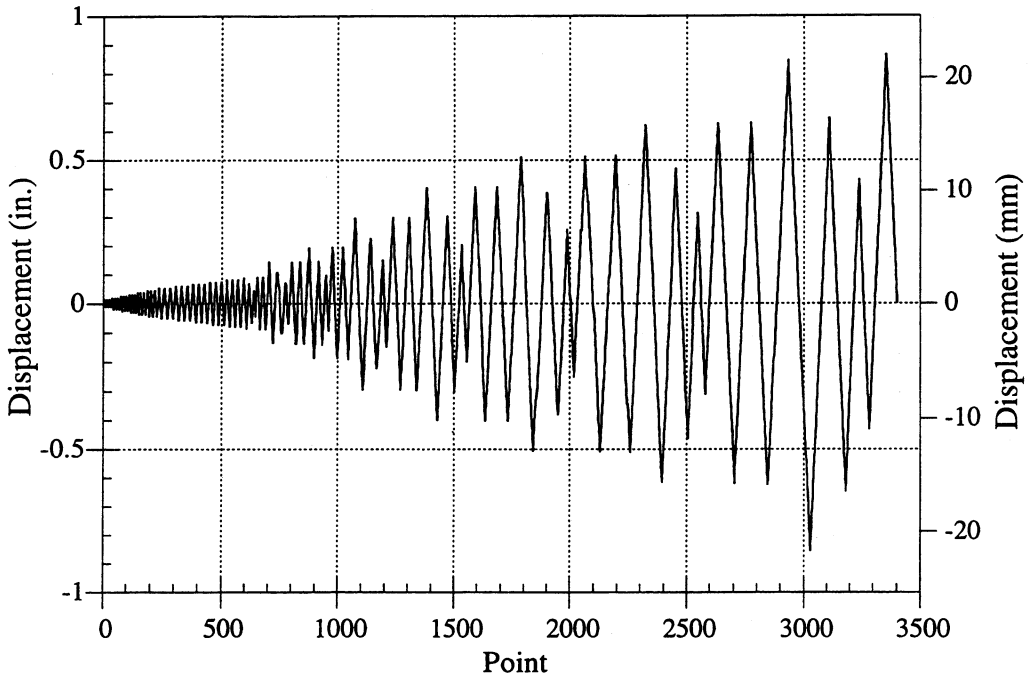

Fig. A.3 In-Plane Lateral Displacement History for Wall Specimen 14

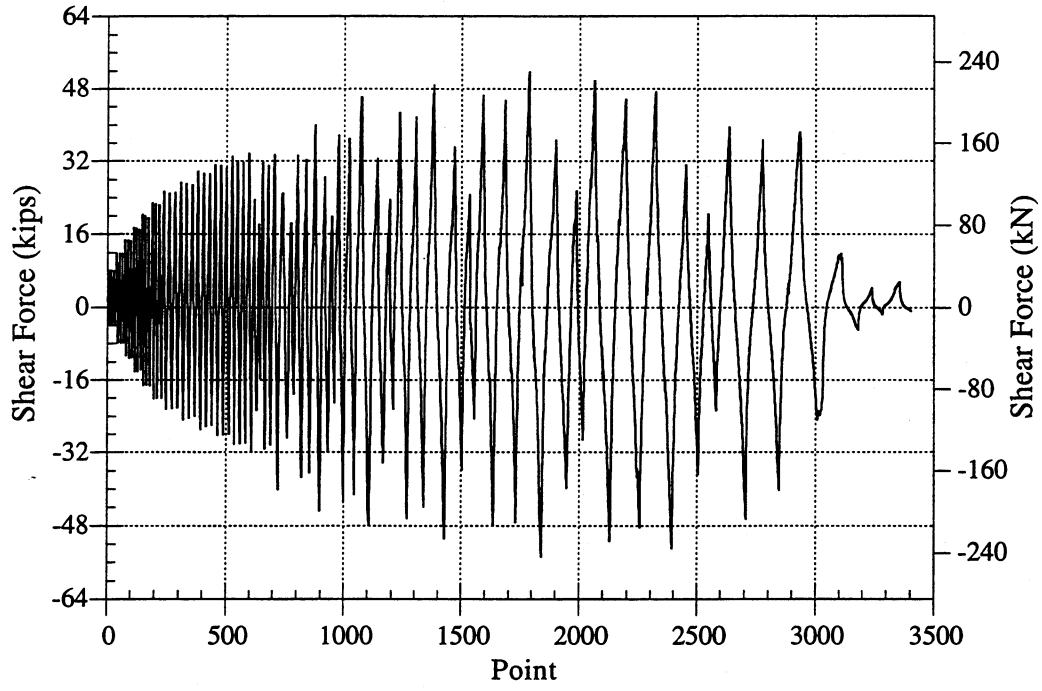

Fig. A.4 Shear Force History for Wall Specimen 14

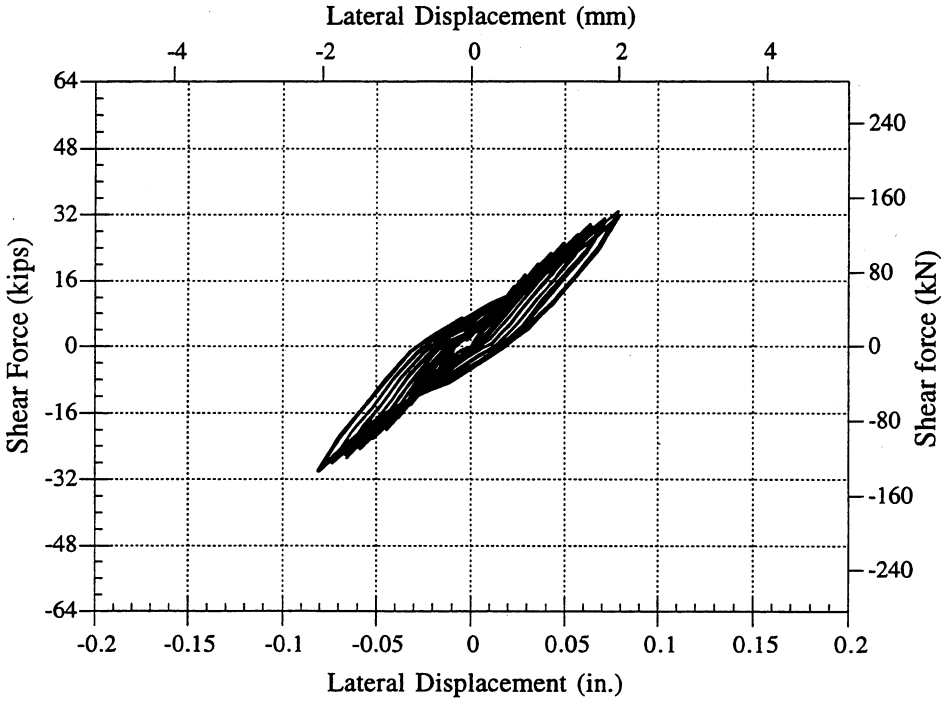

a) Elastic Cycles (Points 1-589)

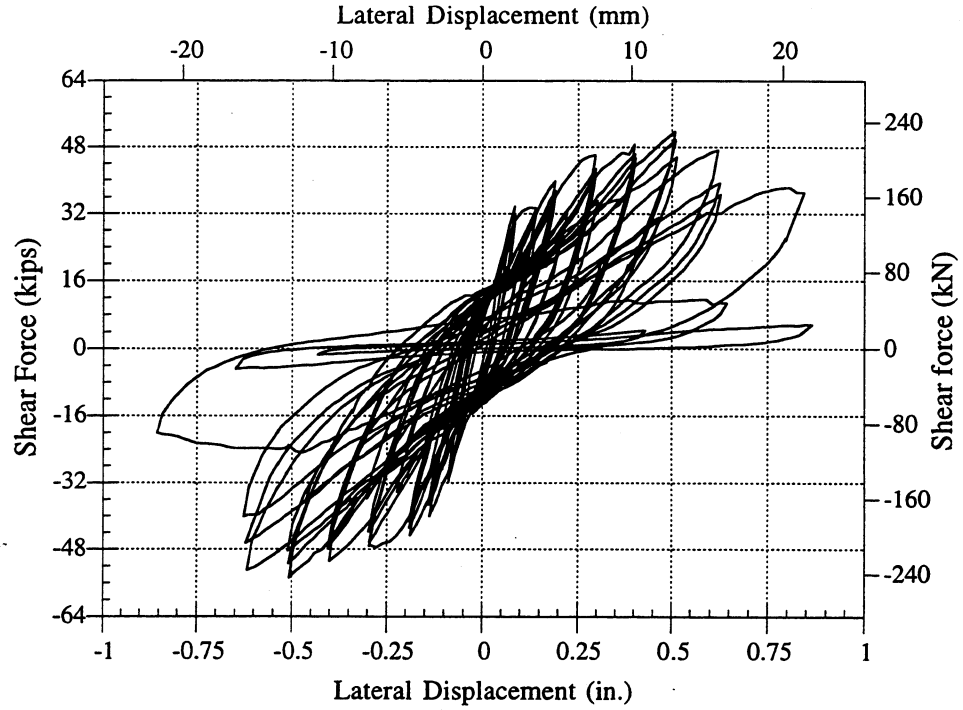

b) Inelastic Cycles (Points 589-3404)

Fig. A.5 Force-Displacement Relations for Wall Specimen 14

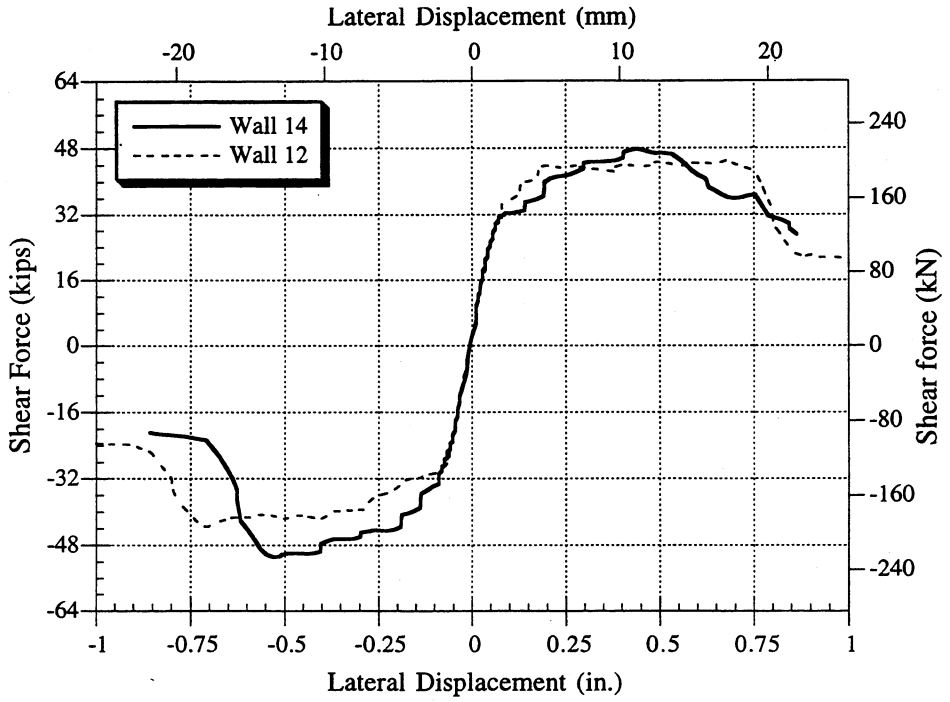

Fig. A.6 Force-Displacement Envelopes for Wall Specimen 14

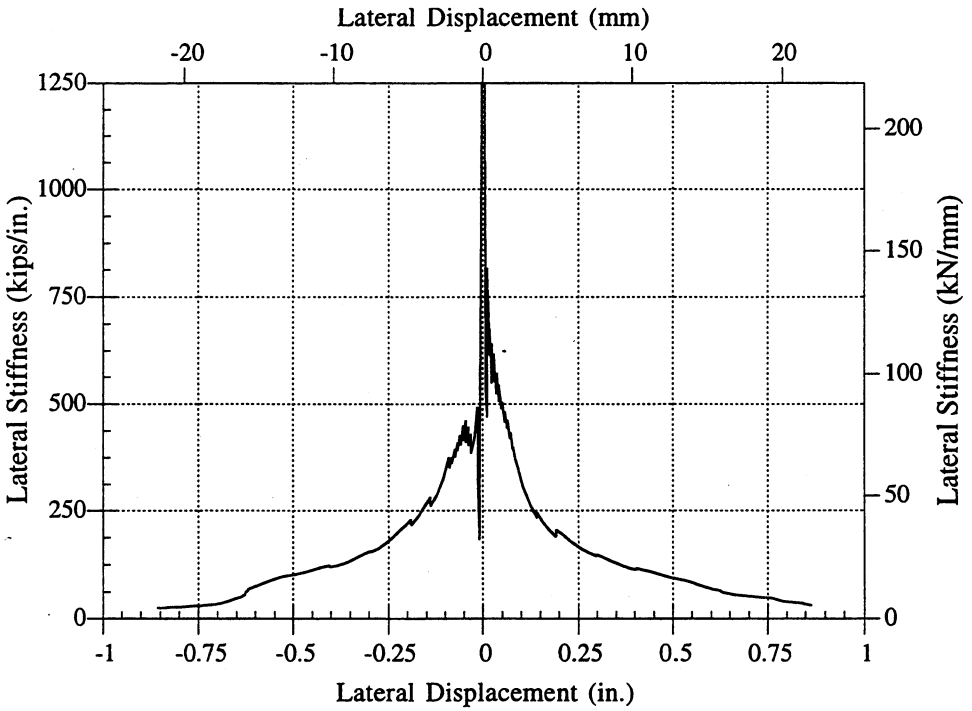

Fig. A.7 Lateral Stiffness Envelope for Wall Specimen 14

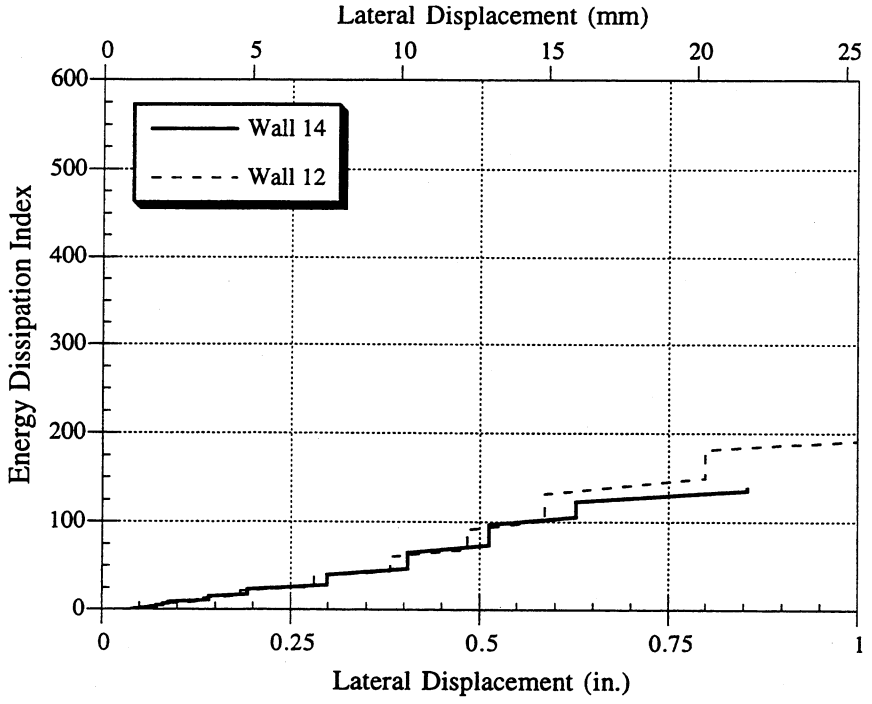

Fig. A.8 Energy Dissipation for Wall Specimen 14

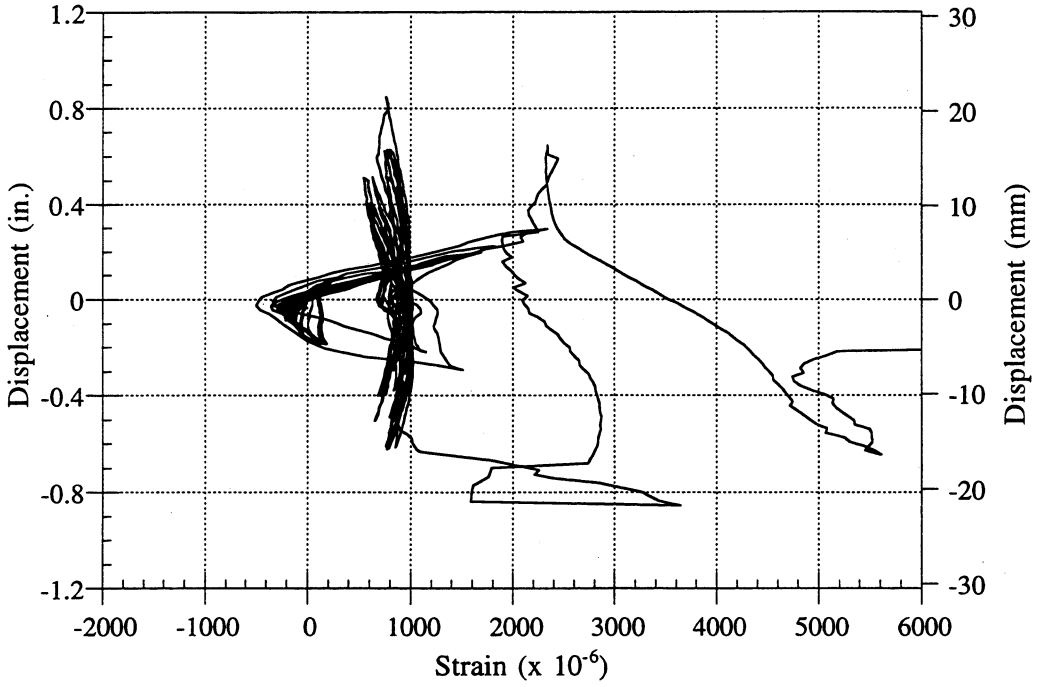

a) Gage VTWO

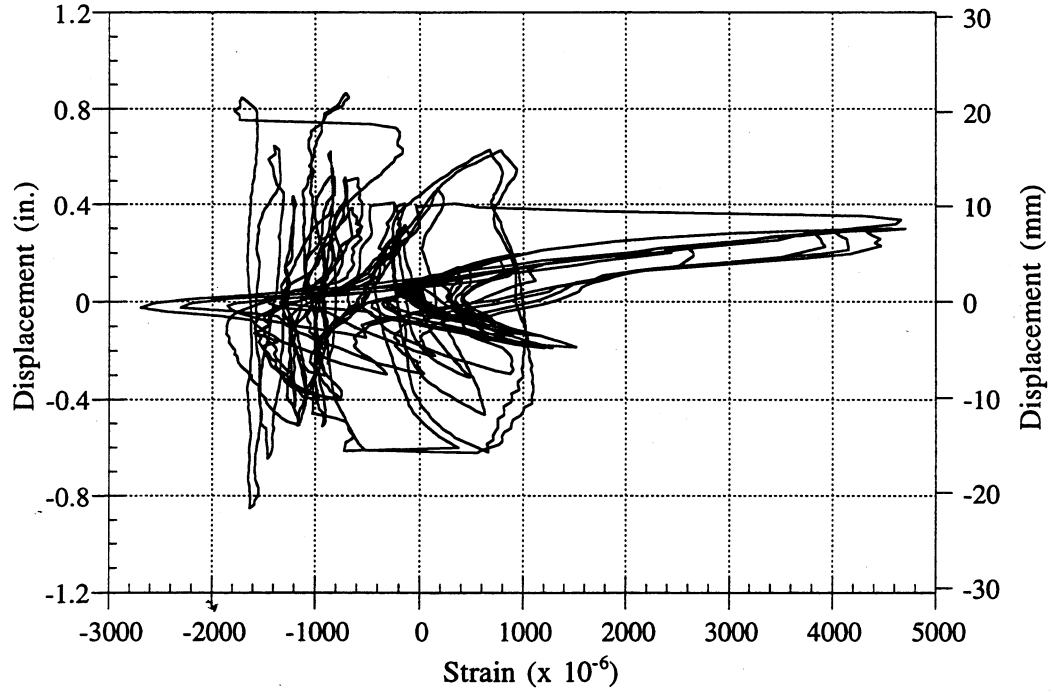

b) Gage VTEO

Fig. A.9 Strains in Vertical Bars vs. Drift in Wall Specimen 14

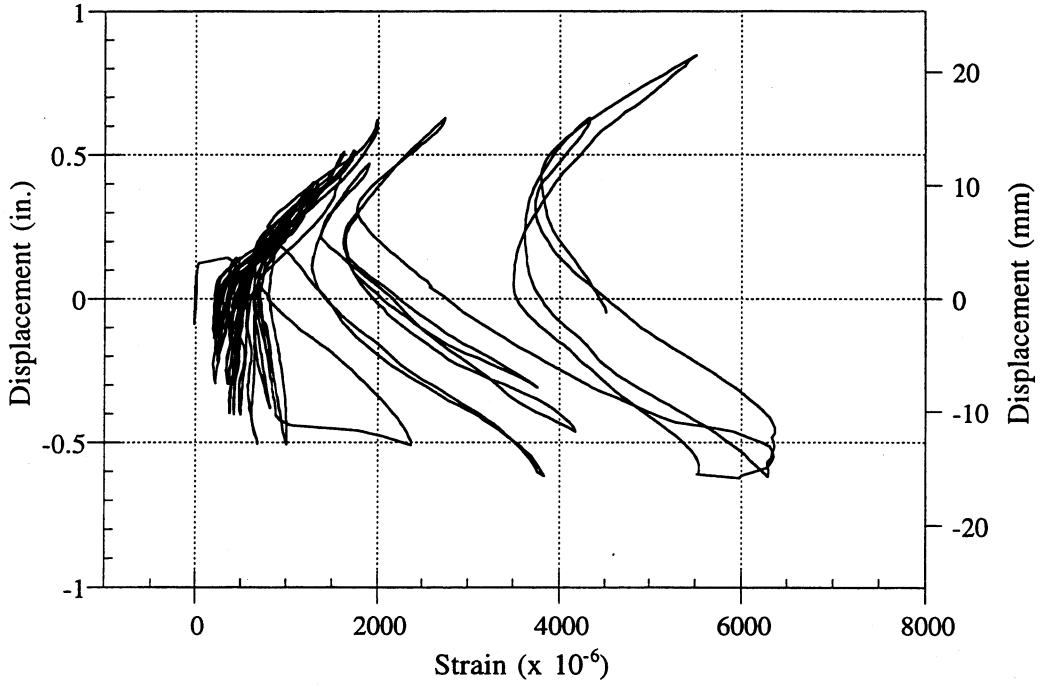

a) Gage 5NE

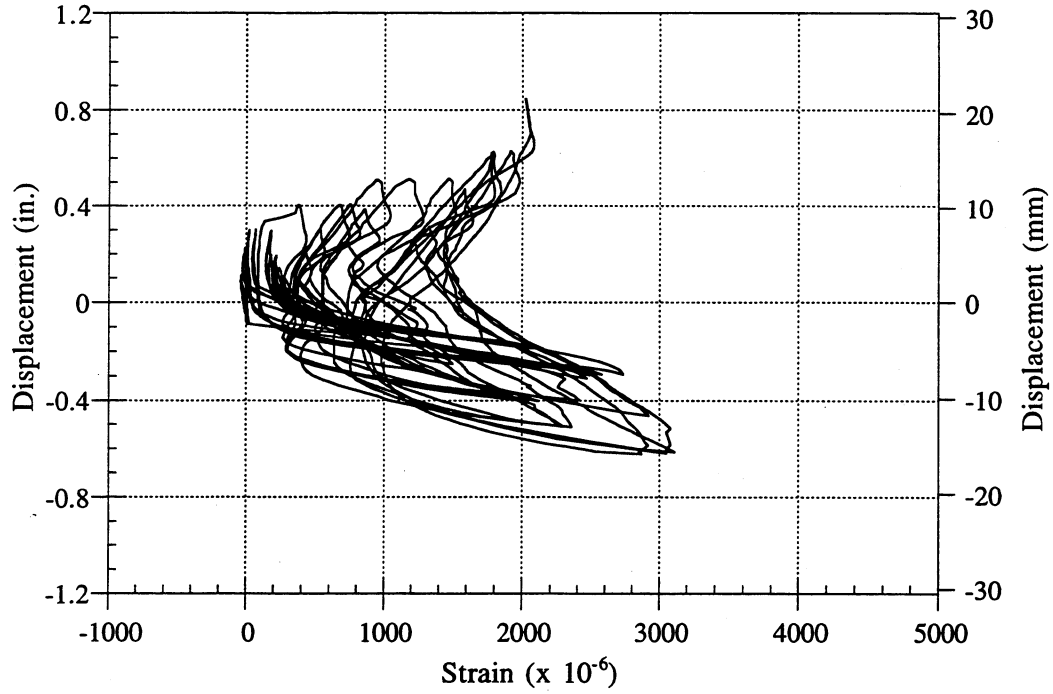

b) Gage 2NE

Fig. A.10 Strains in Horizontal Grids vs. Drift in Wall Specimen 14

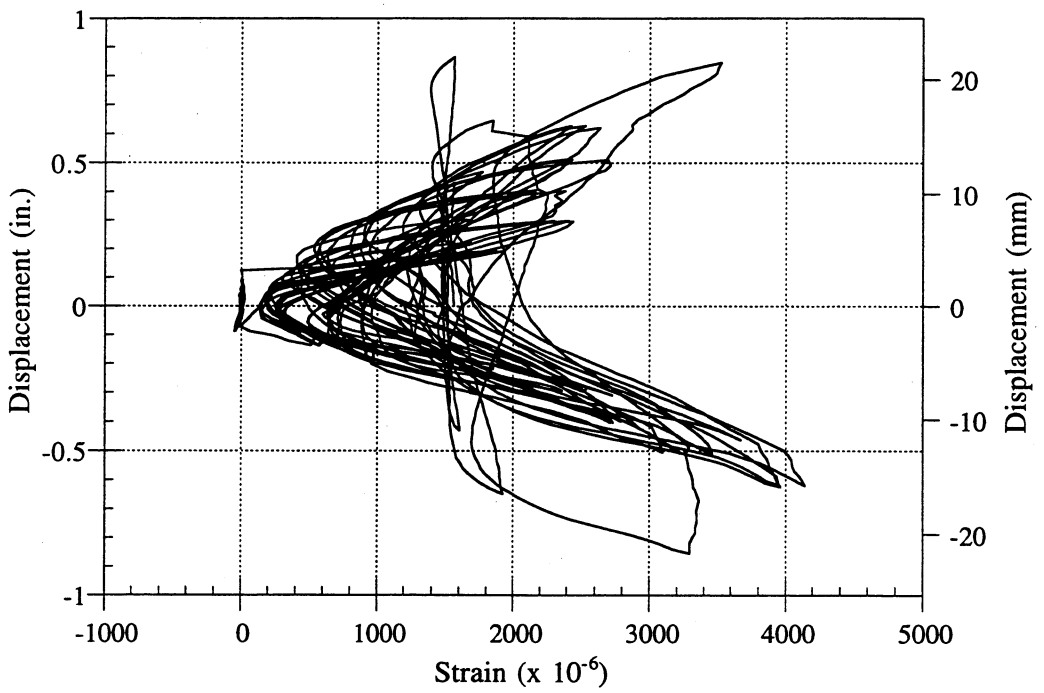

c) Gage 3NC

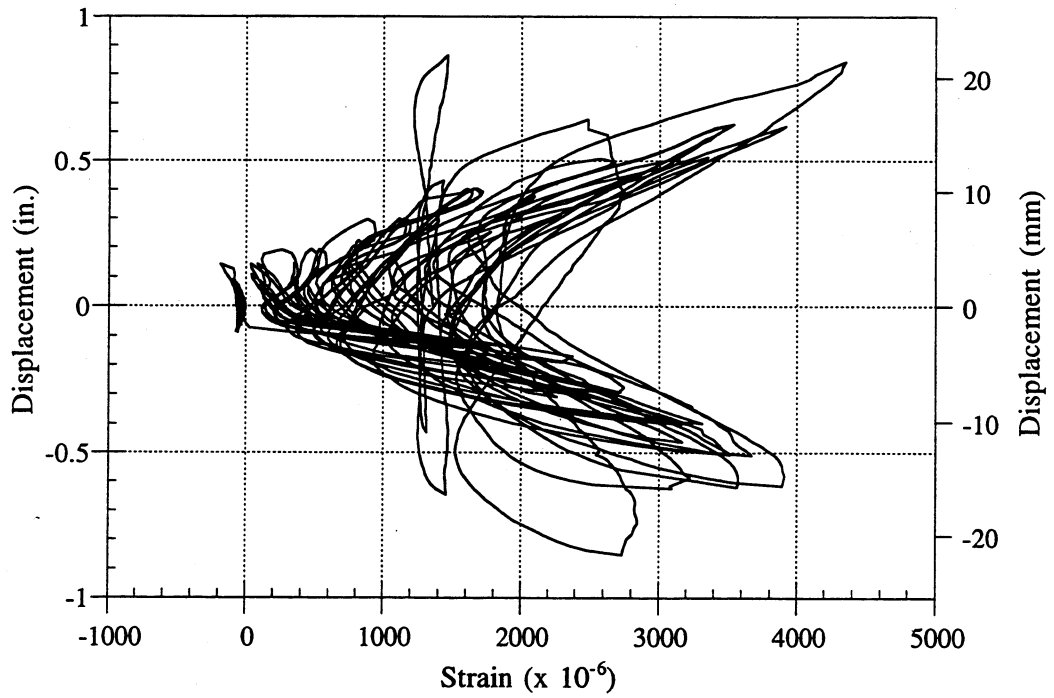

d) Gage 4NC

Fig. A.10 (Cont'd)

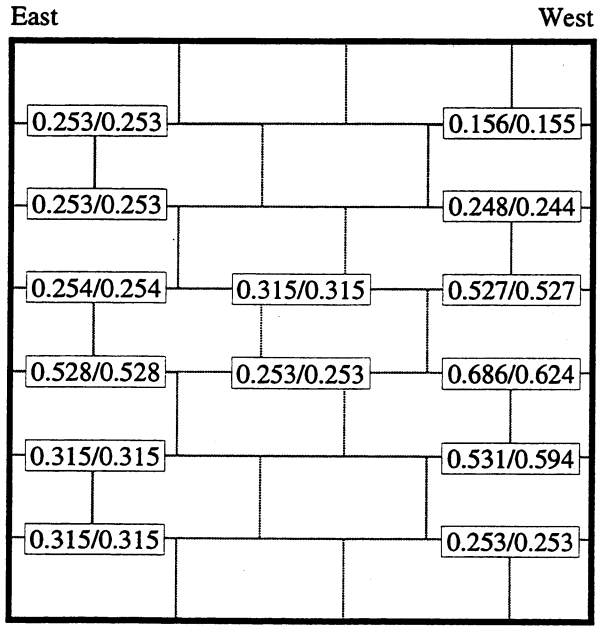

a) At Tension Threshold

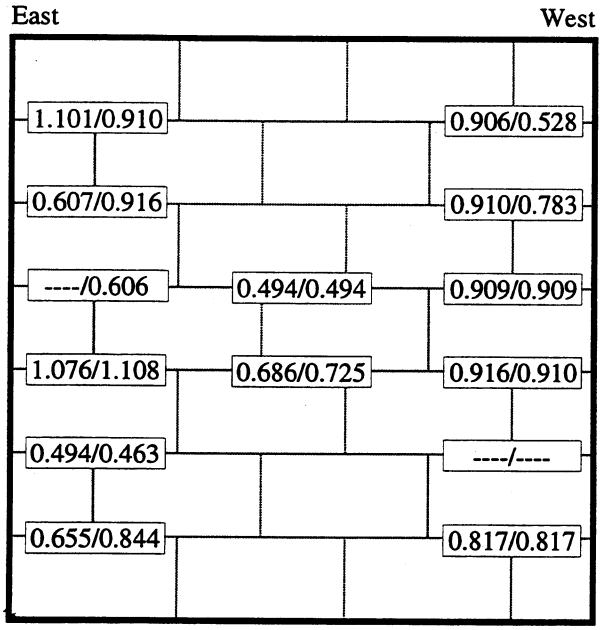

b) At First Yield

Fig. A.11 Drift Ratios (%) at Target Horizontal Reinforcement Strains for Wall Specimen 14

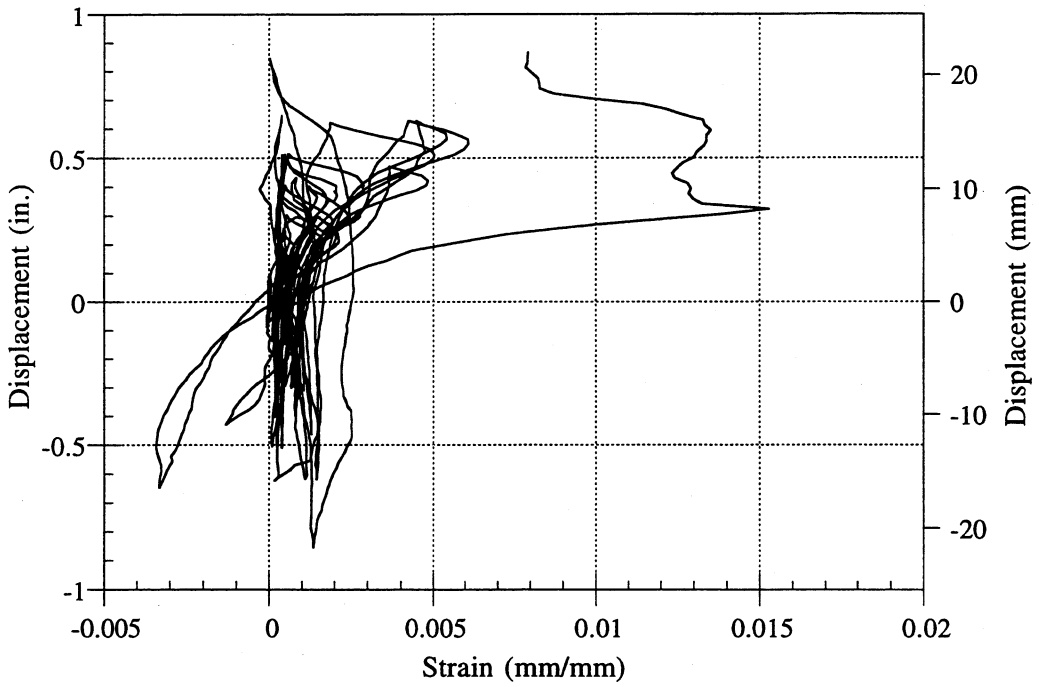

a) Transducer LOVE

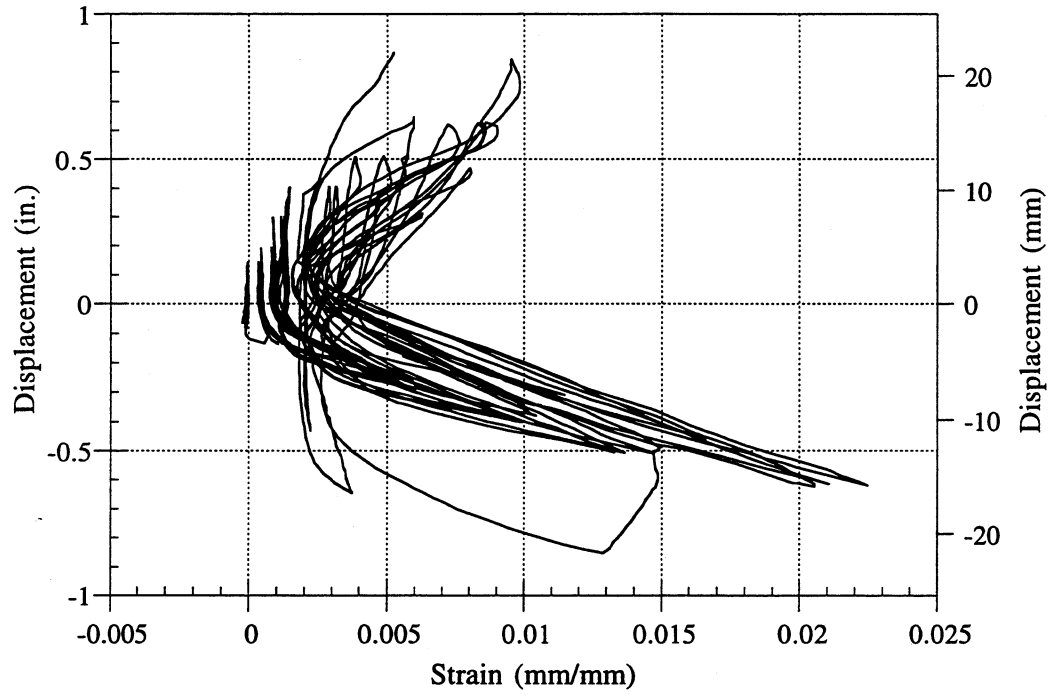

b) Transducer NEAL

Fig. A.12 Masonry Surface Strains vs. Drift in Wall Specimen 14

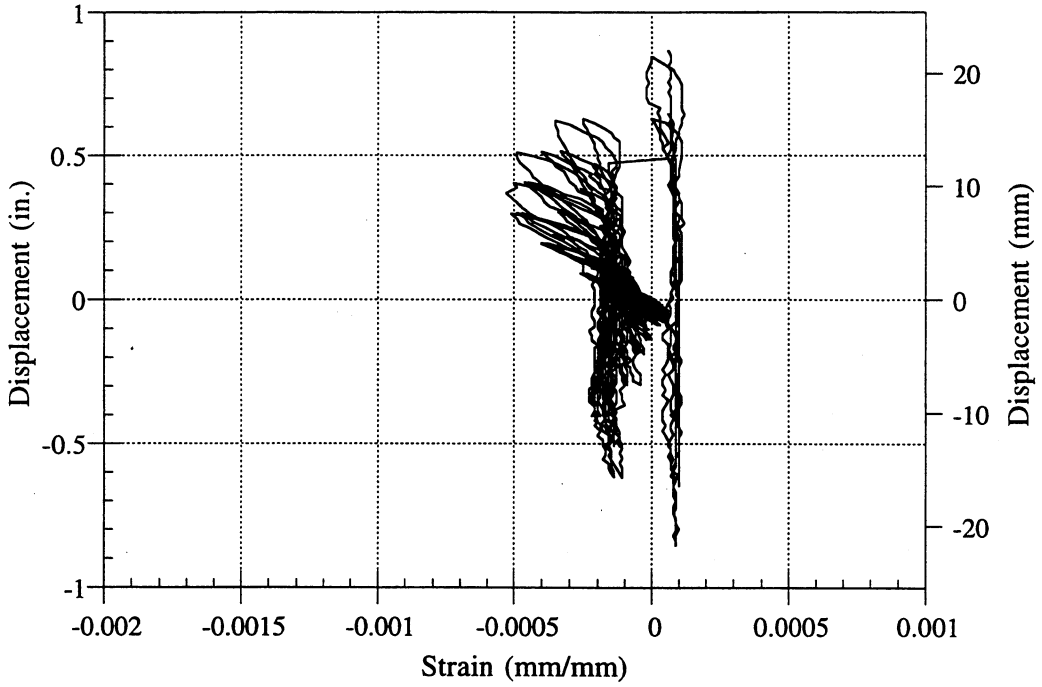

c) Transducer JANE

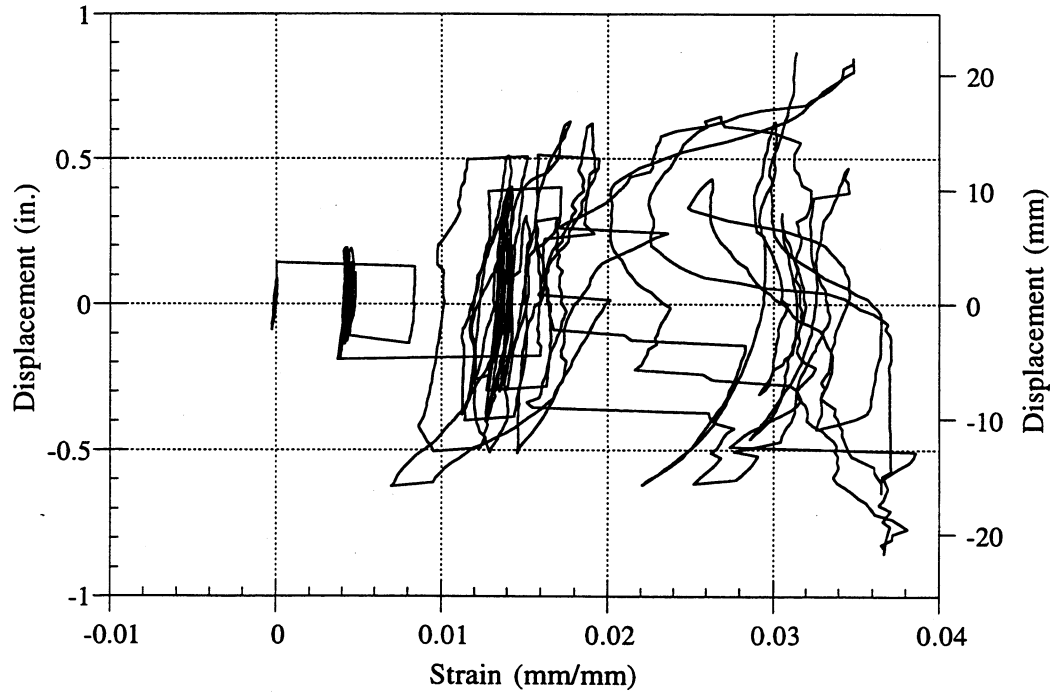

d) Transducer KING

Fig. A.12 (Cont'd)

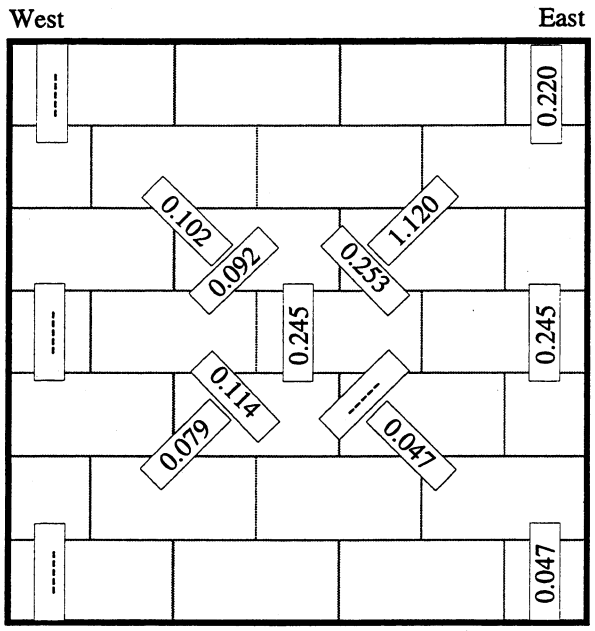

a) Drift Ratios (%) at Tension Threshold

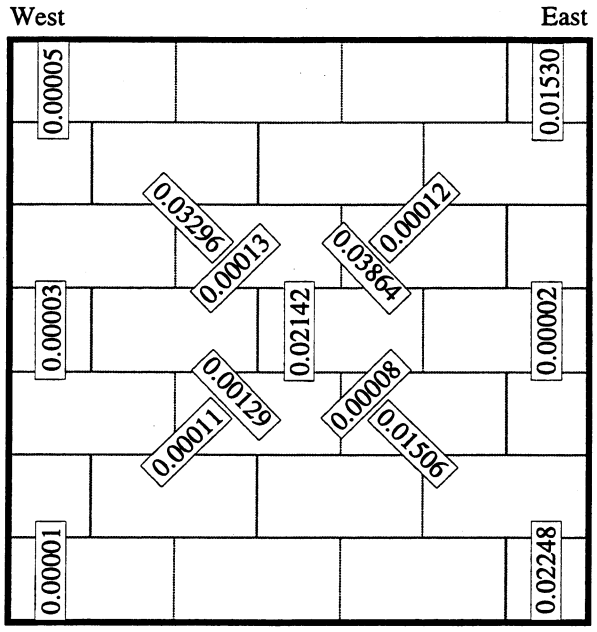

b) Peak Tension Strain Response

Fig. A.13 Masonry Surface Tension Strain Response (LST) for Wall Specimen 14

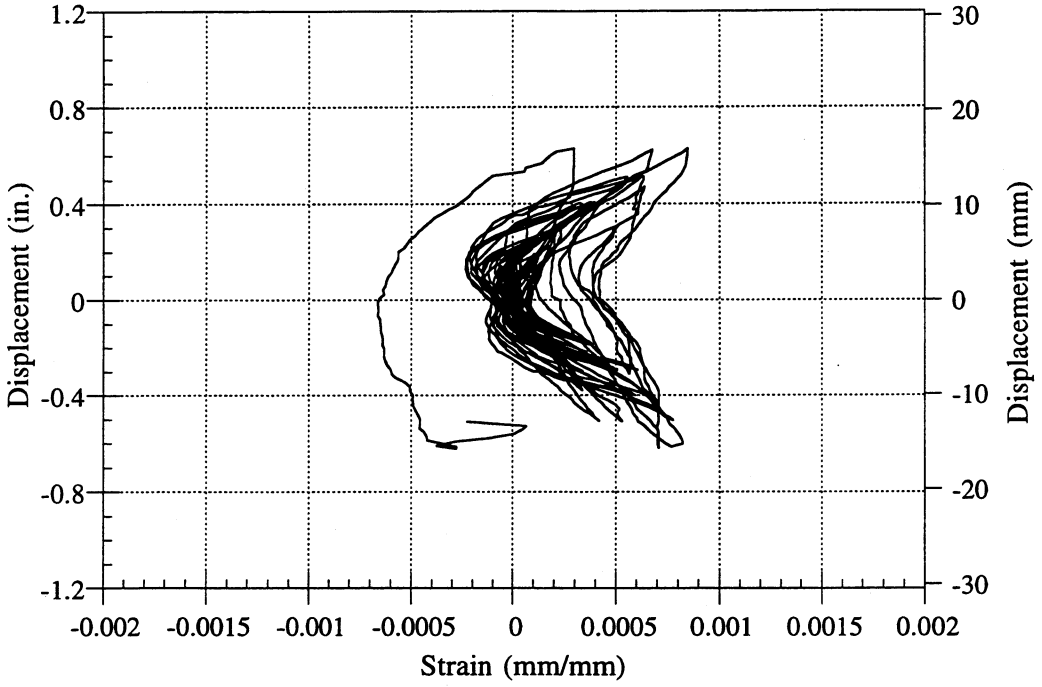

a) Transducer EVTTOP

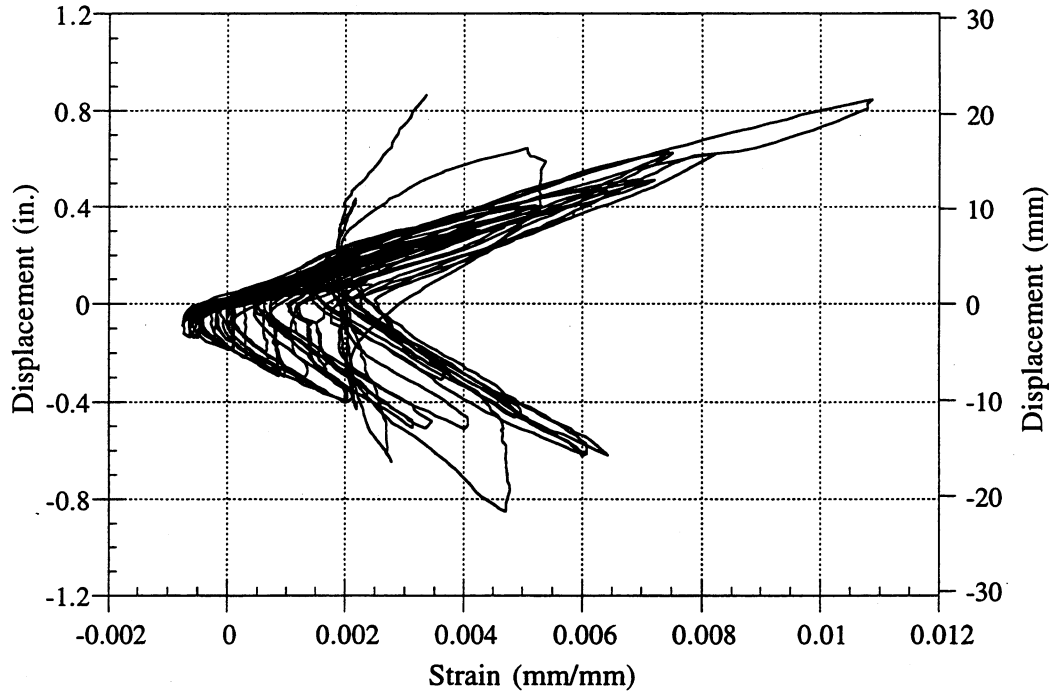

b) Transducer EVTFTG

Fig. A.14 Gross (LVDT) Strains vs. Drift in Wall Specimen 14

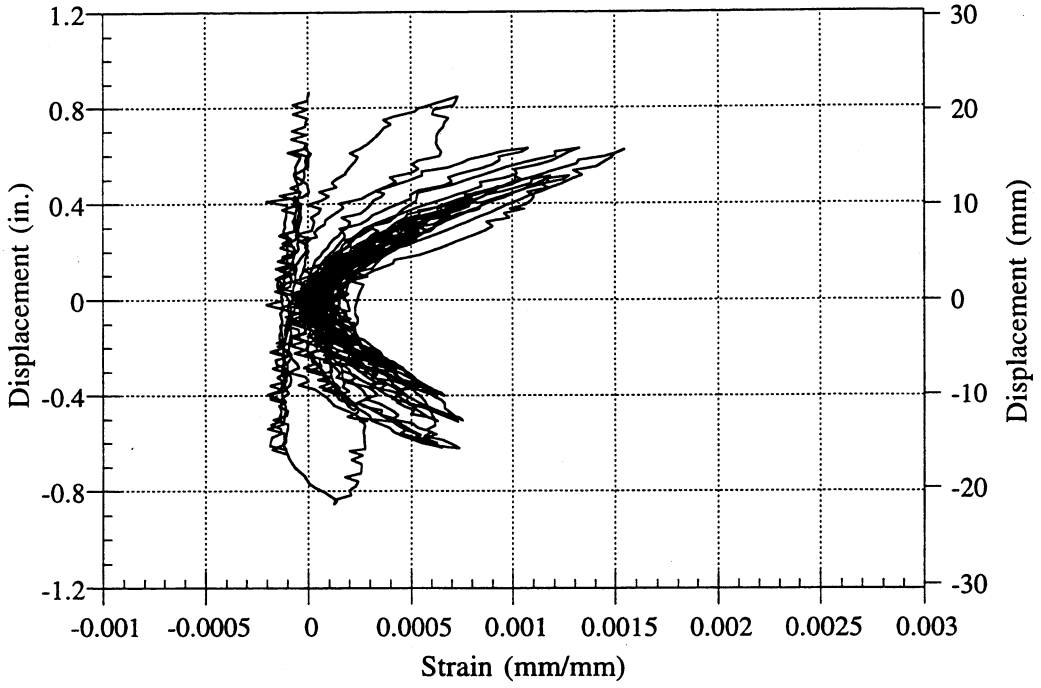

c) Transducer EVTMID

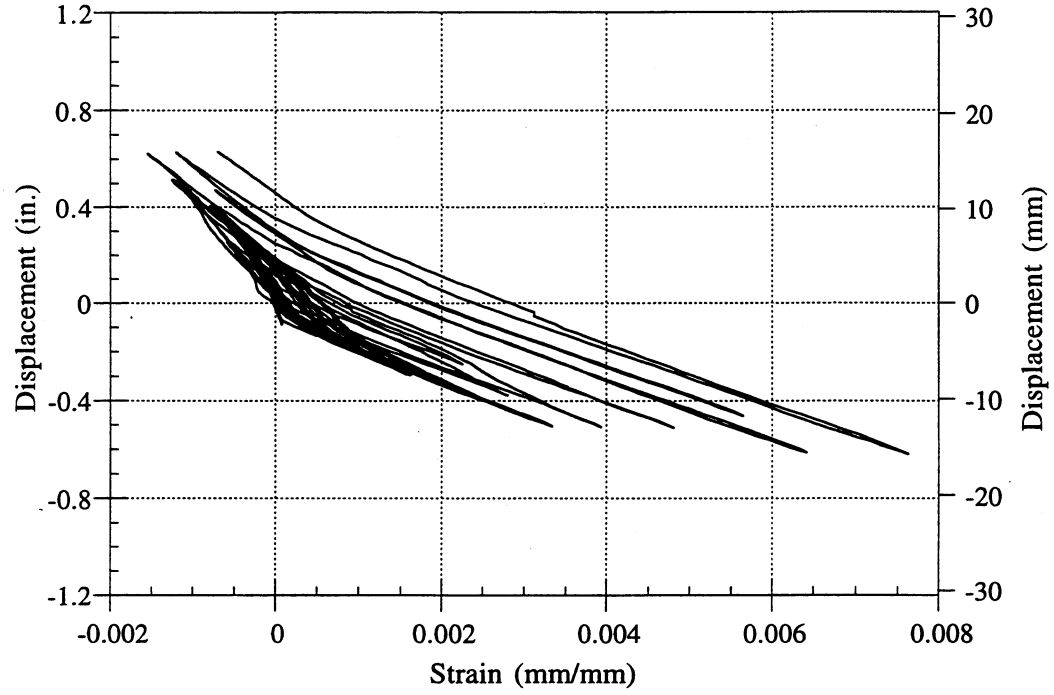

d) Transducer ETWBD

Fig. A.14 (Cont'd)

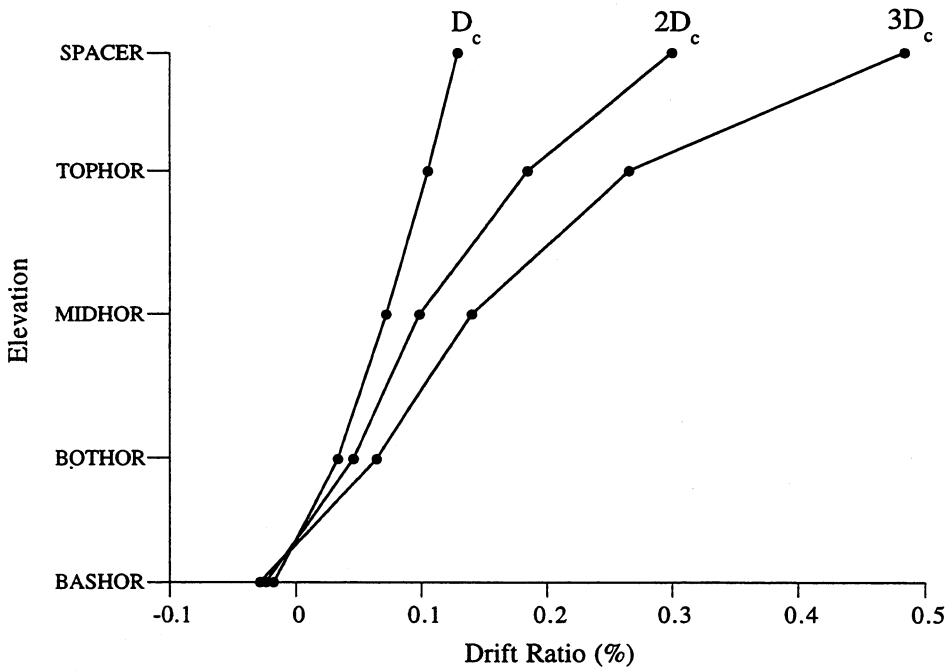

Fig. A.15 Displaced Profiles for Wall Specimen 14

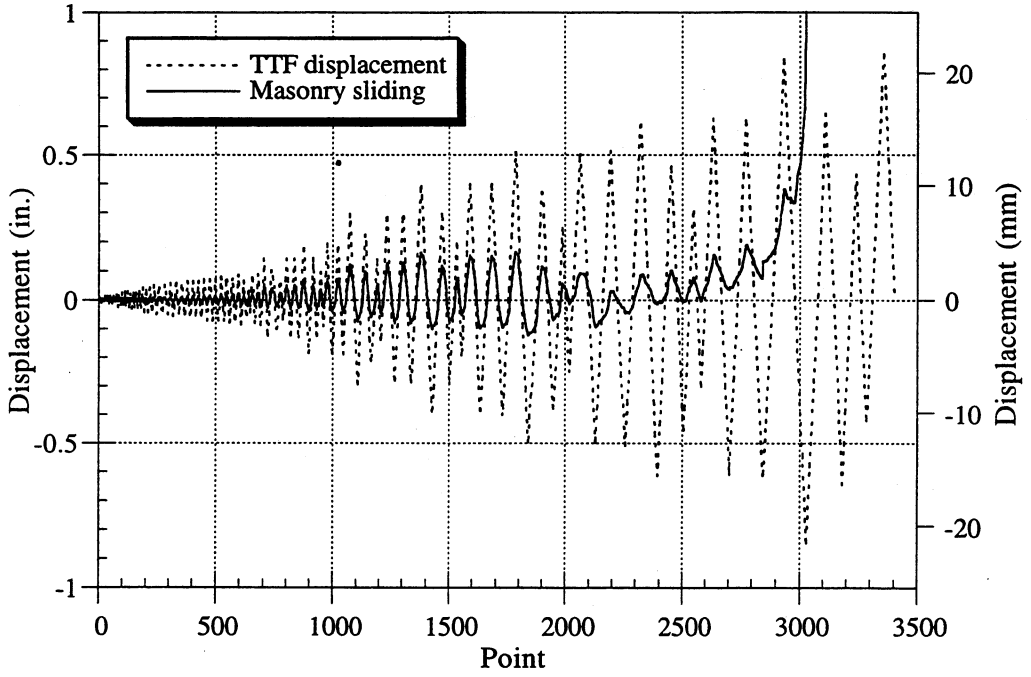

a) Along Top of Masonry

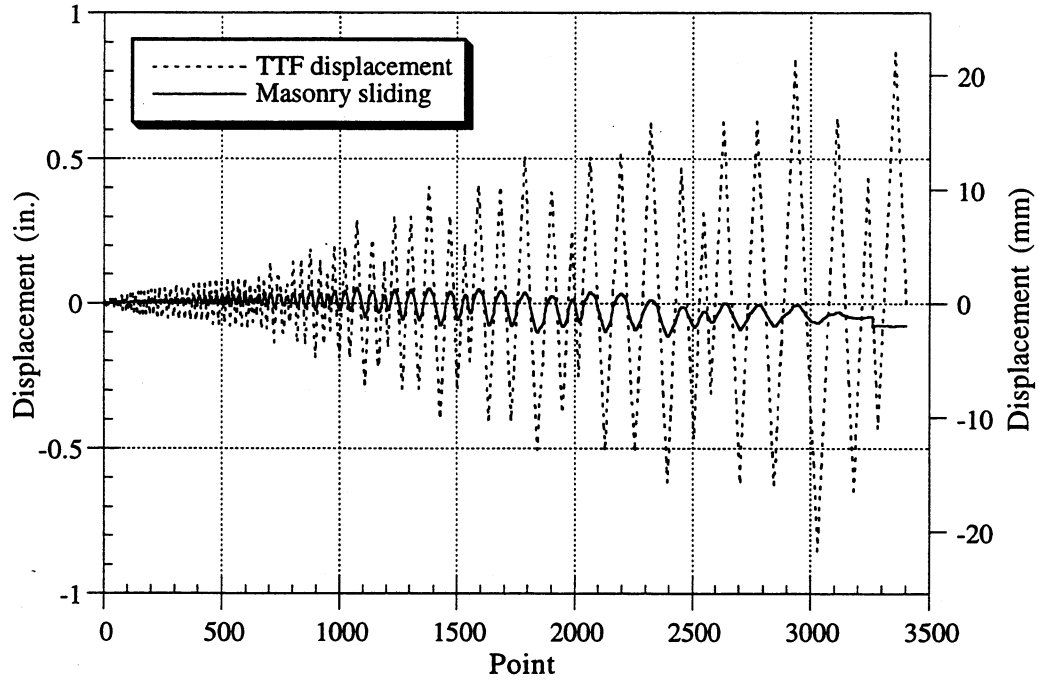

b) Along Bottom of Masonry

Fig. A.16 Masonry Sliding Response in Wall Specimen 14

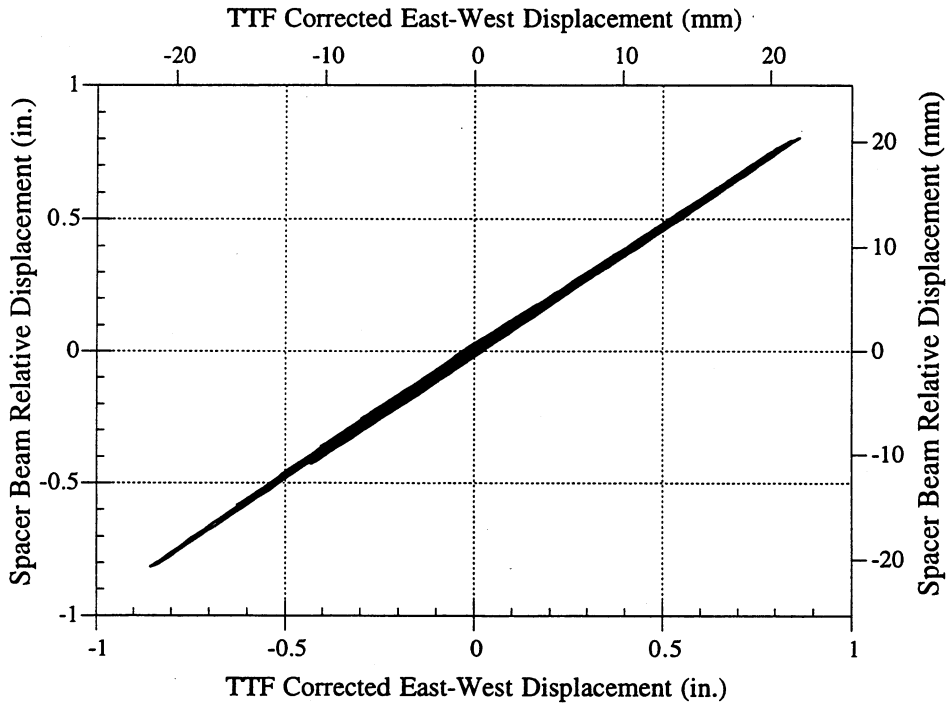

Fig. A.17 Correlation Between TTF and External Displacements for Wall Specimen 14